OPTIMUM DESIGN AND 3D CAD/CAE SIMULATION OF SPIROID AND WORM GEARS

Yongle Song

A thesis submitted in partial fulfilment of the requirements of

The Nottingham Trent University

for the degree of

Doctor of Philosophy

October 2001

ProQuest Number: 10290223

All rights reserved

INFORMATION TO ALL USERS
The quality of this reproduction is dependent upon the quality of the copy submitted.

In the unlikely event that the author did not send a complete manuscript
and there are missing pages, these will be noted. Also, if material had to be removed,
a note will indicate the deletion.



ProQuest 10290223

Published by ProQuest LLC (2017). Copyright of the Dissertation is held by the Author.

All rights reserved.
This work is protected against unauthorized copying under Title 17, United States Code
Microform Edition © ProQuest LLC.

ProQuest LLC.
789 East Eisenhower Parkway
P.O. Box 1346
Ann Arbor, MI 48106 – 1346

FOR REFERENCE ONLY

The Nottingham Trent University
Libraries & Learning Resources
SHORT LOAN COLLECTION

Date	Time	Date	Time
-XX DEC 2003	REF		
-9 DEC 2003	REF		
16 DEC 2003	REF 8.55pm		
-6 FEB 2004	Ref		
-6 XXX 2004	Ref		

Please return this item to the issuing library.
Fines are payable for late return.

THIS ITEM MAY NOT BE RENEWED

Short Loan 03

40 0720644 6

10334468

To Hong, Ruoyu and my parents

ABSTRACT

This thesis describes research conducted by the author on the optimum design and 3D CAD/CAE virtual simulation of spiroid and worm gear drives. Three major contributions have been made: (1) an innovative approach to obtain favourable localised tooth contact, (2) a novel 3D parametric modelling methodology – *virtual gear manufacturing* (VGM), and (3) a feasible procedure for loaded multi-tooth contact analysis using an advanced finite element method. These techniques developed are illustrated using two types of spiroid gears including a conventional spiroid gear drive (whose pinion is a conical worm) and a helicon gear drive (whose pinion is a cylindrical worm), and three types of cylindrical worm gears including ZA, ZN and ZI.

Favourable localised tooth contact is achieved by modifying the worm tooth surface. With this approach, only the worm cutter's geometrical angles and mounting position need to be adjusted. This approach is simpler and more economical than existing gear tooth modification methods because it can be implemented in standard gear hobbing machines without any modification to the hob geometry. Numerical simulations of the localised tooth contact have been conducted. The results confirm that the proposed gear modifying method can provide substantially improved localised bearing contact and is largely insensitive to misalignments. In addition, the modified spiroid and worm gears have significant advantages over conventional designs such as better lubrication conditions, higher load capacity, longer working life and lower manufacturing costs.

The VGM methodology developed includes virtual manufacturing of worm and gears within a computer software environment, creation of 3D parametric and adaptable gear models, and utilisation of the VGM models to simulate gear mesh, to analyse the contact pattern, and to detect tooth interference. Unlike conventional 3D modelling methods, the VGM method does not require complicated mathematical modelling and therefore the difficulties associated with the solution of nonlinear meshing equations can be avoided. In contrast to the existing modern computerised gear theory that can only numerically simulate the meshing of gearing in point or line contact, the VGM method has the capability to visually simulate the general regional contact problems. Consequently, the VGM method can help to significantly reduce the manufacturing cost in the design stage.

The 3D gear models, created in Pro/Engineer using the VGM method, are imported into ANSYS via the IGES interface for the loaded multi-tooth contact analysis. Evaluation of solid and contact elements for nonlinear gear contact analysis has been conducted. Advanced techniques have been developed for 3D gear model geometry cleanup, 3D gear geometry data transferring via the IGES interface and 3D finite element model meshing. 14 full multi-teeth contact finite element models of spiroid and worm gears have been created. The loaded tooth contact stresses and deformations of spiroid and worm gear drives under different operating positions have been analysed. The results of the tooth stresses and tooth load shares successfully simulate the real gear operation. The FE models enable the loaded tooth contact pattern, stress distribution, contact force distribution and load share to be fully examined for the first time. This is impossible for conventional theoretical methods and experimental methods. Using the procedures and techniques developed in this research, researchers and engineers will be able to conduct and gain substantial benefits from the loaded gear tooth contact analysis.

ACKNOWLEDGEMENTS

The author was financially supported by a bursary awarded by the Nottingham Trent University. The author is grateful for this support.

I would like to express my greatest gratitude and appreciation to my Directors of studies, Professor D Su, Professor C R Gentle and Dr. A Ianakiev, for all the excellent guidance and help, and for their patience over the past three years. Their knowledge and experience have been invaluable in the development of this thesis.

The author wishes to thank Mrs Doreen Corlett, Research Administrative Assistant, for her kindly help during my PhD study.

I would also like to express my appreciation for all the help and advice given by the members of academic and technical staff and fellow researchers. Although it is not possible to enumerate all concerned, I would like to especially thank Karim, Geza, Karen, my friends and colleague, for their help.

Finally, I must express my continued gratitude to my family, especially, my wife, Hong, without whose love, support, patience and forbearance over the past three years the work would never have been completed. I must also thank to my lovely daughter Ruoyu, who brought me a very enjoyable life during the candidature. To them I dedicate this thesis.

PUBLICATIONS ARISING FROM THIS WORK

1. Su, D., **Song, Y.** and Gentle, C. R., "Numerical Analysis of Spiroid Gears With Localised Tooth Contact Manufactured in a New Economical Method", Special Issue of International Journal of Gearing & Transmission, November 2000, No.3, UK, pp.13-21.

2. **Song, Y.** and Su, D., "Gear Solid Modelling and Tooth Contact Analysis: State of the Art", Proceedings of The International Conference on Mechanical Transmissions, Chongqing, China, 5-9 April, 2001, pp.148-153.

3. **Song, Y.**, Su, D, Ianakiev, A. and Gentle, R., "Loaded Multi-tooth Contact Analysis of Spiroid Gears by General Surface-to-Surface Contact Analysis Using the Finite Element Method", Proceedings of The International Conference on Mechanical Transmissions, Chongqing, China, 5-9 April, 2001, pp. 131-136.

4. **Song, Y.**, Su, D, and Gentle, R., "Optimum Design and Numerical Simulation of Localised Tooth Contact of Helicon Gears", Proceedings of The International Conference on Mechanical Transmissions, Chongqing, China, 5-9 April, 2001, pp. 142-147.

5. **Song, Y.** and Su, D., "Three Dimensional Virtual Manufacturing of Worm Gears", Proceedings of International Conference on Gearing, Transmissions and Mechanical Systems, Nottingham, UK, 3-6 July 2000, pp.119-128.

6. **Song, Y.,** Su, D. and Gentle, R., "A Novel Approach of 3D Spiroid Gear Modelling", Proceedings of 3rd International Conference on Mechanics & Materials in Design, Orlando, USA, May 29-31, 2000, pp.59-61.

7. Su, D and **Song, Y.**, "Numerical Modelling of Spiroid Gears With Localised Tooth Contact", Proceedings of International Conference on Gearing,

Transmissions and Mechanical Systems, Nottingham, UK, 3-6 July 2000, pp.75-89.

8. **Song, Y.,** Su, D. and Gentle, R., "Optimum Design of Spiroid Gearing With the Aid of 3D Virtual Manufacturing Method", Poster Proceedings of the 4th International Conference on Adaptive Computing in Design and Manufacture, Plymouth, UK, 26-28 April 2000, pp.51-54.

9. Su, D and **Song, Y.,** "A Novel Approach of Obtaining Localised Tooth Contact for Spiroid Gear Drives", Proceedings of 8th International Power Transmission and Gearing Conference, ASME Design Engineering Technical Conferences, Baltimore, USA, 10-13 September 2000.

10. Su, D., Yang, F. and **Song, Y.**, "A CAD Approach for Reducing Worm Gearing's Sensitivity To Manufacturing and Assembly Errors", Proceedings of International Conference on Computer Aided Production Engineering, Durham, U.K., 19-21 April, 1999, pp.101-108.

NOTATION

$\alpha^{(i)}$	blade profile angles for generating line I (i=I) and II (i=II)
ΔE	the shortest centre distance error
ΔL	the axial displacement error
$\Delta\gamma$	the misalignment of the shaft angle
$\Delta\theta_{wheel}$	the increment of wheel rotating angle
ϕ_1	generalised parameter of motion
ϕ'_2	the rotation angles of the gear
ϕ'_w	the rotation angles of the pinion
γ	pinion shaft angle
φ_1	generalised parameter of motion
λ_b	the lead angle of the worm base cylinder
λ_h	lead angles of the hob
λ_w	lead angles of the worm
Σ_i	generating (i=1) and generated (i=2) surfaces
θ_h	the hob tooth surface parameter
θ_w	the modified pinion surface parameter
ω_{wheel}	the angular velocity of wheel
ω_{hob}	the angular velocity of hob
$\omega^{(i)}$	angular velocity vector of worm (i=1) and gear (i=2) rotation
$\boldsymbol{\omega}_w^{(w)}$	the angular velocity of worm represented in coordinate system S_w
$\boldsymbol{\omega}_w^{(2)}$	the angular velocity of gear represented in coordinate system S_w
ξ	the setting adjustment of cutter's blade mount angle
ρ	the load share of gear tooth
E	offset of the worm
$\mathbf{E}_w$	the distance vector from the origin O_p of S_p to the origin O_2 of S_2
$\mathbf{F}_i$	the contact force on the i tooth
L	axial position of the worm

$\mathbf{L}_{ij}$	coordinate transformation matrix (3×3) from coordinate system i to coordinate system j.
m_{21}	gear ratio
$\mathbf{M}_{ij}$	homogeneous coordinate transformation matrix (4×4) from coordinate system i to coordinate system j.
$\mathbf{n}$	unit normal to the surface
$\mathbf{N}$	normal to the surface
N_1	number of threads of the worm pinion
N_2	number of teeth of the gear
p	the screw parameter of the worm.
$\mathbf{p}_{ax}$	screw parameter vectors in axial direction
$\mathbf{p}_t$	screw parameter vectors in perpendicular direction to the axial direction
$\mathbf{r}$	the position vector of worm pinion tooth surface
$\mathbf{r}_1$	the position vector of the worm surface
$\mathbf{r}_{1h}$	the position vector of hob surface in coordinate system S_1
$\mathbf{r}_{1w}$	the position vector of worm surface represented in coordinate system S_w
$\mathbf{r}_2$	the position vector of spiroid gear surface
r_b	the radius of base cylinder of the worm
$\mathbf{r}_f^{(2)}$	the position vector of gear surface in coordinate system S_f
$\mathbf{r}_f^{(w)}$	the position vector of pinion surface represented in coordinate system S_f
r_{ph}	radii of pitch cylinders of the hob
r_{pw}	radii of pitch cylinders of the worm
S_1	coordinate system rigidly connected to the hob
S_2	coordinate system rigidly connected to the gear
S_b	coordinate system rigidly connected to the hob and pinion's cutter
S_f	coordinate system rigidly connected with the frame
S_w	coordinate systems rigidly connected to the worm.
S_h	coordinate systems rigidly connected to the hob
S_p	stationary system connected to the frame
S_r	coordinate systems rigidly connected to the imaginary rack
S_g	coordinate system rigidly connected to the hob and the gear
t	the number of starts of worm.
T	the number of teeth of wheel.

$\mathbf{T}_i$	is the torque contributed by tooth i (I=A, B, C, D, E)
$\mathbf{T}_{app}$	is the total applied torque vector
$u^{(I)}$	the distance parameter of a point on the straight blade of side I
$u^{(II)}$	the distance parameter of a point on the straight blade of side II
u_w	the modified pinion surface parameters
u_h	the hob surface parameter
$\mathbf{v}_1^{(12)}$	the relative velocity of gear to pinion

Other symbols are defined in the text.

ABBREVIATIONS

CAD	Computer Aided Design
CAE	Computer Aided Engineering
CS	Coordinate System
DOF	Degree of Freedom
FE	Finite Element
FEA	Finite Element Analysis
FEM	Finite Element Method
ICCG	Incomplete Choleskey Conjugate Gradient
JCG	Jacobi Conjugate Gradient
LTCA	Loaded Tooth Contact Analysis
IGES	Initial Graphics Exchange Specification
PC	Personal Computer
PCG	Preconditioned Conjugate Gradient
RGM	Real Gear Manufacturing
TCA	Tooth Contact Analysis
VGM	Virtual Gear Manufacturing
ZA worm	Stand for Archimedean worm
ZI worm	Stand for Involute worm

LIST OF FIGURES

Figure 1.1 Worm gear drive 1
Figure 1.2 Spiroid and helicon gear drives 2
Figure 1.3 Comparison of worm, spiroid, hypoid and bevel gearing. 3
Figure 2.1 Axial profiles of grinding wheels for generation of a hob and a worm (from Seol et al 1996a) 17
Figure 2.2 Line of tangency (helix) between the hob and the worm (from Seol et al 1996a) 17
Figure 2.3 Hob mounting position 18
Figure 2.4 Schematic of crowning of worm thread surface 18
Figure 2.5 Tangency of pitch cylinders of worm and hob: $\Delta\lambda$ is the crossing angle of axes, Δr is the shortest centre distance (from Seol et al 1996) 22
Figure 2.6 Representation of two generating racks (from Seol et al 1996) 23
Figure 2.7 Interaction of parabolic and linear functions (from Litvin 1999) 24
Figure 2.8 Meshed spiral bevel gear (from Fong and Tsay 1991) 29
Figure 2.9 Dual-lead worm gear (from Tsay et al 1995) 29
Figure 2.10 Conventional 3D worm gear modelling procedures (from Su et al 1999b) 31
Figure 2.11 Tooth numbering convention (from Gosselin et al 1995) 36
Figure 2.12 Finite element model for the gear (from Litvin et al 1996) 37
Figure 2.13 Illustration of loaded gear tooth contact forces (from Zhang and Fang 1997) 38
Figure 2.14 Seven-teeth model used in finite element analysis (from Handschuh and Bibel 1999) 40
Figure 2.15 Hourglass contact element model (from Qin and Qin 2000) 40
Figure 3.1 Pinion and hob tooth profile 44
Figure 3.2 Tangent to hob and modified pinion tooth surface 44
Figure 3.3 Coordinate systems in tapered spiroid pinion 46
Figure 3.4 Pinion cutter's movement in relation to the coordinate systems 46
Figure 3.5 Cutter's two cutting edges I and II in coordinate system S_b 47
Figure 3.6 Right hand hob thread surface (mm) 48
Figure 3.7 Coordinate systems for modified pinion 51

Figure 3.8 Axial section profile of hob thread and modified pinion thread (Side I)ξ=2°, $\Delta\alpha$=0.252° (unit: mm)....56
Figure 3.9 Difference in hob and pinion's axial section profile (Side I) $\Delta Z=Z_{\text{hob thread}} - Z_{\text{modified pinion thread}}$ ξ=2°, $\Delta\alpha$=0.252° (unit: mm)....56
Figure 3.10 Axial section of hob thread and modified pinion thread (Side II) ξ=-2.5°, $\Delta\alpha$=0.255 (unit: mm)....56
Figure 3.11 Difference in hob and pinion's axial section profile: $\Delta Z=Z_{\text{hob thread}} - Z_{\text{modified pinion thread}}$ (Side II) ξ=2.5°, $\Delta\alpha$=0.255° (unit: mm)....57
Figure 3.12 Coordinate system applied for spiroid gear generation....60
Figure 3.13 Gear tooth surface....67
Figure 3.14 Gear tooth surface (Zoomed)....67
Figure 3.15 Coordinate system for simulation of meshing....72
Figure 3.16 Coordinate systems S_m and S_n....75
Figure 3.17 Localised contact path in the gear tooth surface....88
Figure 4.1 Pinion and hob tooth profile....91
Figure 4.2 Coordinate systems for a helicon pinion....92
Figure 4.3 Pinion cutter's movement in relation to the coordinate systems....93
Figure 4.4 The cutter's two cutting edges I and II in coordinate system S_b....94
Figure 4.5 Right hand helicon hob thread surface....94
Figure 4.6 Coordinate systems for modified pinion....95
Figure 4.7 Axial section profile of hob thread and modified pinion thread (Side I) ξ=2°, $\Delta\alpha$=0.196°, (unit: mm)....98
Figure 4.8 Difference in hob and pinion's axial section profile: $\Delta Z=Z_{\text{hob thread}} - Z_{\text{modified pinion thread}}$ side I (unit: mm)....99
Figure 4.9 Axial section of hob thread and modified pinion thread (Side II) ξ=-2°, $\Delta\alpha$=0.141°, (unit: mm)....99
Figure 4.10 Difference in hob and pinion's axial section profile: $\Delta Z=Z_{\text{hob thread}} - Z_{\text{modified,}}$ (Side II), (unit: mm)....99
Figure 4.11 Generation of helicon gear....102
Figure 4.12 Coordinate system for simulation of meshing....104
Figure 4.13 Localised tooth contact path of helicon gear drive in meshing (mm)....105
Figure 5.1 Coordinate systems for a ZA worm....108
Figure 5.2 The cutter's two cutting edges I and II in coordinate system S_b....108

Figure 5.3 ZA Hob tooth thread surfaces (unit: inch) 109
Figure 5.4 Coordinate systems for the modified worm 111
Figure 5.5 Axial section of hob thread and modified worm thread (Side II) ξ=-2°, $\Delta\alpha$=0.0501°, α=16.24°, (unit: mm) 111
Figure 5.6 Difference in hob and worm's axial section profile: $\Delta Z=Z_{\text{hob thread}} - Z_{\text{modified}}$, (Side II), (unit: mm) 112
Figure 5.7 Coordinate system applied for worm gear generation 113
Figure 5.8 ZA gear surface contact lines 120
Figure 5.9 Contact line on ZA VGM model 121
Figure 5.10 Contact lines on ZA worm surface (unit: inch) 122
Figure 5.11 Coordinate system for the simulation of meshing 122
Figure 5.12 Localised tooth contact path of ZA worm gear drive in meshing (mm) 123
Figure 6.1 Diagram of RGM and VGM methods 127
Figure 6.2 Diagram of spiroid gear configuration 129
Figure 6.3 Procedure for the virtual manufacturing and meshing simulation of spiroid gearing 131
Figure 6.4 Axial section of cutter 132
Figure 6.5 Diagram of helical sweep cut 133
Figure 6.6 Spiroid pinion cutting procedure 133
Figure 6.7 Spiroid gear hob sweep profile and section 134
Figure 6.8 Diagram of virtual spiroid gear hobbing process 134
Figure 6.9 Diagram of spiroid gear assembly 135
Figure 6.10 Spiroid gear tooth contact path 136
Figure 6.11 Diagram of interference (The highlighted area) 136
Figure 6.12 Section view of meshing 137
Figure 6.13 Helicon gear drive 137
Figure 6.14 Over cutting the gear top land (Red surfaces) 139
Figure 7.1 RGM and VGM hobbing process diagrams 143
Figure 7.2 Cross section of ZA worm 144
Figure 7.3 ZA worm thread axial proportions used in example 145
Figure 7.4 ZI worm cross section (3 starts) 146
Figure 7.5 Procedure of 3D simulation of worm gear hobbing and tooth contact analysis 147

Figure 7.6 Section of cylinder base construction 148
Figure 7.7 Helical sweep profile and sweep section 148
Figure 7.8 Worm blank and model 149
Figure 7.9. Axial-section of worm tooth profile 151
Figure 7.10. Axial-section of worm tooth profile 152
Figure 7.11 Illustration of virtual worm cut procedure: (a) worm blank (b) One thread cut (c) 3 threads cut (d) shaft added 153
Figure 7.12 Sweep profile of a ZA gear hob 154
Figure 7.13 Patterning dimensions for ZA wheel bobbing 155
Figure 7.14 ZA worm gear 156
Figure 7.15 Wheel cutter tooth profile in axial section 157
Figure 7.16 Zoomed wheel cutting tooth 158
Figure 7.17 Illustration of the worm gear virtual manufacturing process: (a) Gear blank, (b) Chamfered, (c) First cut, (d) Full cut, (e) Finished gear 158
Figure 7.18 Worm and gear assembly 159
Figure 7.19 Worm gear mesh and global interference check 160
Figure 7.20 Holroyd involute worm gear (6-start worm) 161
Figure 7.21 Holroyd involute worm gear (single start worm) 161
Figure 7.22 Worm gear contact pattern (ratio 1/50) 162
Figure 7.23 Experimental results of tooth contact (gear ratio: 1/50) 163
Figure 7.24 Tooth section profile along the gear face width 164
Figure 8.1 Spiroid pinion meshed by Pro/Mesh 171
Figure 8.2 Worm gear tooth meshed in HyperMesh 172
Figure 8.3 Contact shell element mesh in HyperMesh 173
Figure 8.4 Revolve cross section of spiroid gear blank 175
Figure 8.5 Spiroid gear manufacturing 176
Figure 8.6 Gear smoothed side I surface (yellow colour) and root surface (red colour) 177
Figure 8.7 Extension of side I surface and root surface 178
Figure 8.8 Spiroid gear surface contact lines (Side II) 180
Figure 8.9 Gear tooth surface constituted by the contact lines 180
Figure 8.10 Zoomed radical changes of curvature in gear surface smooth (Side II) 181
Figure 8.11 A few cut spiroid gear blank 182
Figure 8.12 Datum plane for gear tooth section cutting 183

Figure 8.13 Patterned datum planes 183
Figure 8.14 Gear tooth profile datum curve sketch 184
Figure 8.15 Datum curve sketch in root fillet area 185
Figure 8.16 Gear tooth cross section cut 186
Figure 8.17 Gear tooth section profile and datum curves 187
Figure 8.18 Smoothed tooth surfaces 187
Figure 8.19 Gear partial teeth 188
Figure 8.20 Gear blank and the smooth tooth surfaces 189
Figure 8.21 The transformed tooth surfaces 189
Figure 8.22 Cut the tooth using surfaces 190
Figure 8.23 Cut one tooth and copy the surface 191
Figure 8.24 Pattern the surfaces 191
Figure 8.25 Pinion blank and one portion tooth 193
Figure 8.26 Pinion tooth sweep cross section 193
Figure 8.27 (a) Pinion tooth patterned; (b) Inner patterned surface 195
Figure 8.28 (a) Tooth surfaces copied; (b) The copied tooth surfaces transformed.. 195
Figure 8.29 Geometry cleanup finished spiroid gear assembly model 196
Figure 8.30 CONTA174 3D surface-to-surface contact element (8 nodes) 203
Figure 8.31 TARGE170 target surface element 203
Figure 8.32. SOLID92 3D 10-node tetrahedral structural solid element 204
Figure 8.33. SOLID95 3D 20-node structural solid element 205
Figure 8.34 Multi-tooth contact model meshed with tetrahedral elements 205
Figure 8.35 Gear tooth contact stress pattern (geometry imported via ANSYS default option) 209
Figure 8.36 Nodal coordinate systems 210
Figure 8.37 Pinion separated surfaces and volumes 211
Figure 8.38 Diagram of spiroid pinion meshing 213
Figure 8.39 The procedure of the creation of gear tooth areas for 3D mapped meshing 214
Figure 8.40 Diagram of gear tooth mesh 215
Figure 8.41 Whole spiroid gear mesh 216
Figure 8.42 Full hexahedral element mesh spiroid gear FE model 217
Figure 8.43 A full simplified spiroid gear model 218
Figure 8.44 A simplified spiroid gear finite element model 218

Figure 8.45 Contact and target elements in the models....220
Figure 8.46 Simplified full model with hexahedral elements....224
Figure 8.47 Full spiroid gear model's constraint and loading scheme....224
Figure 8.48 Simplified full spiroid gear model's constraint and loading scheme....225
Figure 8.49 Zoomed loading and constraint for the spiroid gear inner surface....226
Figure 8.50 Local mesh refinements in potential contact region in spiroid gear teeth....227
Figure 8.51 Spiroid submodel hexahedral element mesh....228
Figure 8.52 Submodel stress pattern (pinion part)....230
Figure 8.53 Submodel stress pattern (gear part)....230
Figure 8.54 Seven spiroid gear models with different contact positions....232
Figure 8.55 Spiroid gear tooth indexes....233
Figure 8.56 Gear tooth Von Mises stress pattern at contact position 1, load step 1, substep 4....234
Figure 8.57 Pinion tooth Von Mises stress pattern at contact position 1, load step 1, substep 4....235
Figure 8.58 Pinion tooth Von Mises stress cross section pattern at contact position 1, load step 1, substep 4....235
Figure 8.59 Gearset assembly Von Mises stress section distribution at contact position 1, load substep 4....236
Figure 8.60 Gear tooth Von Mises stress pattern at contact position 2, load step 1, substep 4....237
Figure 8.61 Pinion tooth Von Mises stress pattern in contact position 2, load step 1, substep 4....238
Figure 8.62 Gearset assembly Von Mises stress section distribution at contact position 2, load substep 4....238
Figure 8.63 Pinion tooth Von Mises stress pattern at contact position 3, load step 1, substep 4....239
Figure 8.64 Gear tooth Von Mises stress pattern in contact position 3, load step 1, substep 4....239
Figure 8.65 Gear tooth Von Mises stress pattern at contact position 4, load step 1, substep 4....240
Figure 8.66 Pinion tooth Von Mises stress pattern at contact position 4, load step 1, substep 4....241

Figure 8.67 Gear tooth Von Mises stress pattern at contact position 5, load step 1, substep 4 241
Figure 8.68 Pinion tooth Von Mises stress pattern at contact position 5, load step 1, substep 4 242
Figure 8.69 Gear tooth Von Mises stress pattern at contact position 6, load step 1, substep 4 243
Figure 8.70 Pinion tooth Von Mises stress pattern at contact position 6, load step 1, substep 4 243
Figure 8.71 Gear tooth Von Mises stress pattern at contact position 7, load step 1, substep 4 244
Figure 8.72 Pinion tooth Von Mises stress pattern at contact position 7, load step 1, substep 4 245
Figure 8.73 Zoomed gear tooth Von Mises stress pattern at contact position 7, load substep 4 245
Figure 8.74 Gear tooth Von Mises stress cross section pattern at contact position 1, load step 1, substep 4, section 1 246
Figure 8.75 Gear tooth Von Mises stress cross section pattern at contact position 1, load step 1, substep 4, section2 246
Figure 8.76 Gear tooth Von Mises stress cross section pattern at contact position 1, load step 1, substep 4, section 3 247
Figure 8.77 Gear tooth Von Mises stress cross section pattern at contact position 1, load step 1, substep 4, section 4 247
Figure 8.78 Gear tooth Von Mises stress cross section pattern at contact position 1, load step 1, substep 4, section 5 248
Figure 8.79 Gear tooth Von Mises stress cross section pattern at contact position 1, load step 1, substep 4, section 6 248
Figure 8.80 Gear tooth Von Mises stress cross section pattern at contact position 1, load step 1, substep 4, section 7 249
Figure 8.81 Gear tooth Von Mises stress cross section pattern at contact position 1, load step 1, substep 4, section 1, section 8 249
Figure 8.82 Gear tooth contact forces at contact position 1,load substep 4 250
Figure 8.83 Gear tooth load share in whole gear applied torque at position 1 251
Figure 8.84 Gear tooth contact forces at contact position 1 252
Figure 8.85 Gear tooth contact forces at contact position 2, load step 1, substep 4..252

Figure 8.86 Gear tooth contact forces at contact position 2 253
Figure 8.87 Gear tooth load share in whole gear applied torque at position 2 254
Figure 8.88 Gear tooth contact forces at contact position 3, load step 1, substep 4 ..254
Figure 8.89 Gear tooth load share in whole gear applied torque, at position 3 255
Figure 8.90 Gear tooth contact forces at contact position 3 255
Figure 8.91 Gear tooth contact forces at position 4, load step 1, substep 4 256
Figure 8.92 Gear tooth contact forces at contact position 4 257
Figure 8.93 Gear tooth load share in whole gear applied torque at position 4 257
Figure 8.94 Gear tooth contact forces at contact position 5, load step 1, substep 4 ..258
Figure 8.95 Gear tooth load share in whole gear applied torque at position 5 258
Figure 8.96 Gear tooth contact forces at contact position 5 259
Figure 8.97 Gear tooth contact forces at contact position 6, load step 1, substep 4 ..259
Figure 8.98 Gear tooth load share in whole gear applied torque at position 6 260
Figure 8.99 Gear tooth contact forces at contact position 6 260
Figure 8.100 Gear tooth contact forces at contact position 7, load step 1, substep 4261
Figure 8.101 Gear tooth contact forces at contact position 7 262
Figure 8.102 Gear tooth load share in whole gear applied torque at position 7 262
Figure 8.103 Gear tooth contact forces and Von Mises stress distribution at contact position 7, load substep 4. 263
Figure 9.1 Generation of involute worm surface 272
Figure 9.2 Worm cross section involute curve 272
Figure 9.3 Axial tooth profile of worm I (mm) 274
Figure 9.4 Axial tooth profile of hob I (mm) 274
Figure 9.5 Worm gear calliper depth and thickness diagram 275
Figure 9.6 Worm I axial tooth profile pitch=21.3017 mm 276
Figure 9.7 Wheel cutter I axial tooth profile pitch=20.8181 mm 277
Figure 9.8 Wheel cutter's axial section tooth profile 277
Figure 9.9 Worm axial section tooth profile 278
Figure 9.10 Wheel cutter's sweep profile 279
Figure 9.11 Generation of worm I 279
Figure 9.12 3D model of worm I 280
Figure 9.13 Single thread of wheel cutter I 281
Figure 9.14 Generation of wheel cutter I 281
Figure 9.15 3D model of worm gear 282

Figure 9.16 Contact pattern 1 283
Figure 9.17 Contact pattern 2 283
Figure 9.18 Contact pattern 3 284
Figure 9.19 Contact pattern 4 284
Figure 9.20 Contact pattern 5 284
Figure 9.21 Cylinder protrusion on six threads of worm I for FEA 285
Figure 9.22 Sweep section of inner helical surfaces 286
Figure 9.23 Generation of inner helical sweep surfaces 286
Figure 9.24 Rebuilt worm geometry for FEA 287
Figure 9.25 Revolving section for enlarged gear blank 288
Figure 9.26 Enlarged gear blank 288
Figure 9.27 Gear blank with a few cuts 289
Figure 9.28 Zoomed gear tooth cuts 289
Figure 9.29 Section for revolving surface 290
Figure 9.30 Surfaces patterned 291
Figure 9.31 Datum curves created on the cut tooth edges 292
Figure 9.32 Datum curves for gear tooth 293
Figure 9.33 (a) Datum curves (b) Surfaces created by datum curves 293
Figure 9.34 Revolving section for gear blank 295
Figure 9.35 (a) Gear blank and quilts (b) The quilt transformed 296
Figure 9.36 (a) Patterned quilts (b) Gear cut by quilts 296
Figure 9.37 (a) Project the curve; (b) Transform the projected curve 297
Figure 9.38 (a) Create quilts for tooth cutting; (b) Cut using quilts 297
Figure 9.39 (a) Copy tooth surfaces; (b) Transform the tooth surfaces 298
Figure 9.40 Gear tooth surfaces for exporting 299
Figure 9.41 Single gear tooth 300
Figure 9.42 Gear tooth divided volume for mapped meshing 301
Figure 9.43 Gear assembly for FEA 301
Figure 9.44 Worm thread mesh 303
Figure 9.45 Extrude the inner cylinder mesh 303
Figure 9.46 Inner cylinder meshed 304
Figure 9.47 Whole worm mesh 304
Figure 9.48 Gear tooth surface dividing 305
Figure 9.49 Four gear teeth volumes 306

Figure 9.50 Single tooth volume dividing 306
Figure 9.51 Illustration of gear tooth mapped meshing process 307
Figure 9.52 Fourth gear teeth and worm mesh 308
Figure 9.53 Holroyd worm gearset I assembly mesh 308
Figure 9.54 Detect separated area and mesh 309
Figure 9.55 Adding target elements 311
Figure 9.56 Adding contact elements 312
Figure 9.57 Set material ID for contact pair 312
Figure 9.58 Real constants for contact element 312
Figure 9.59 Contact pairs in Holroyd worm gear set I 313
Figure 9.60 Worm gear constraints and loading scheme 314
Figure 9.61 Six worm gear FE models with different contact positions 316
Figure 9.62 Gear I contact stresses (load step 1, substep 6), position 1 317
Figure 9.63 Gear I contact forces (load step 1, substep 6), position 1 318
Figure 9.64 Worm I contact forces and stress pattern (load step 1, substep 6), position 1 318
Figure 9.65 Gear I contact stresses (load step 1, substep 6), position 2 319
Figure 9.66 Worm I contact stresses and reaction forces (load step 1, substep 6), position 2 320
Figure 9.67 Worm I Von Mise stresses (load step 1, substep 6), position 2 320
Figure 9.68 Gear I contact forces (load step 1, substep 7), position 3 321
Figure 9.69 Gear I contact stresses (load step 1, substep 7), position 3 321
Figure 9.70 Worm I contact stresses (load step 1, substep 7), position 3 322
Figure 9.71 Gear I contact stresses (load step 1, substep 6), position 4 323
Figure 9.72 Gear I contact stresses and forces (load step 1, substep 6), position 4 ..323
Figure 9.73 Worm I contact stresses (load step 1, substep 6), position 4 324
Figure 9.74 Gear I contact stresses and forces (load step 1, substep 6), position 5 ..324
Figure 9.75 Worm I contact stresses, position 5 325
Figure 9.76 Gear I contact stresses (load step 1, substep 6), position 6 326
Figure 9.77 Worm I contact stresses (load step 1, substep 6), position 6 326
Figure 9.78 Gear I contact stresses (load step 1, substep 6), position 1 327
Figure 9.79 Gear I contact stresses (load step 1, substep 6), position 2 327
Figure 9.80 Gear I contact stresses (load step 1, substep 6), position 3 328
Figure 9.81 Gear I contact stresses (load step 1, substep 6), position 4 328

Figure 9.82 Gear I contact stresses (load step 1, substep 6), position 5 329
Figure 9.83 Gear I contact stresses (load step 1, substep 6), position 6 329
Figure 9.84 Worm gear tooth load share at position 1 330
Figure 9.85 Worm gear tooth contact forces at contact position 1 330
Figure 9.86 Worm gear tooth load share at position 2 331
Figure 9.87 Worm gear tooth contact forces at contact position 2 332
Figure 9.88 Worm gear tooth load share at position 3 332
Figure 9.89 Worm gear tooth contact forces at contact position 3 333
Figure 9.90 Worm gear tooth load share at position 4 333
Figure 9.91 Worm gear tooth contact forces at contact position 4 334
Figure 9.92 Worm gear tooth load share at position 5 334
Figure 9.93 Worm gear tooth contact forces at contact position 5 335
Figure 9.94 Worm gear tooth load share at position 6 335
Figure 9.95 Worm gear tooth contact forces at contact position 6 336
Figure 9.96 Gear tooth coarse mesh 337
Figure 9.97 Denser mesh of one tooth submodel 337
Figure 9.98 Gear tooth stresses 338
Figure 9.99 Submodel stress pattern (contact side, uniform contour) 338
Figure 9.100 Submodel stress pattern (contact side, non-uniform contour) 339
Figure 9.101 Gear stress pattern (non-contact side) 339
Figure 9.102 Submodel stress pattern (non-contact side, non-uniform contour) 340
Figure 10.1 Comparison between conventional gear modelling method and VGM .347

CONTENTS

ABSTRACT.....i

ACKNOWLEDGEMENTS.....ii

PUBLICATIONS ARISING FROM THIS RESEARCH.....iii

NOTATION.....v

ABBREVIATIONS.....viii

LIST OF FIGURES.....ix

CONTENTS.....xx

CHAPTER 1 Introduction **1**

1.1 WORM, SPIROID AND HELICON GEARS.....1

1.2 BACKGROUND AND RESEARCH APPROACH 3

1.2.1 Localised Tooth Bearing Contact.....3

1.2.2 3D Gear Modelling and Virtual Simulation.....4

1.2.3 Loaded Tooth Contact Analysis.....5

1.3 AIMS AND OBJECTIVES 5

1.4 MAJOR ACHIEVEMENTS.....6

1.4.1 A Novel Approach for Obtaining Localised Tooth Contact Pattern.....6

1.4.2 Virtual Gear Manufacturing Method.....7

1.4.3 Nonlinear Tooth Contact Analysis and Techniques.....9

1.5 STRUCTURE OF THE THESIS.....10

CHAPTER 2 Literature Review **15**

2.1 RESEARCH ON LOCALISED TOOTH CONTACT OF WORM AND SPIROID GEAR DRIVES.....15

2.1.1 Obtaining Localised Tooth Contact by Modifying Worm Tooth Surface 16

2.1.2 Obtain Localised Tooth Contact By Modifying Wheel Tooth Surface ..19

2.1.3 Localised Tooth Contact Analysis 25

2.1.4 Research on Spiroid Gearing.....26

2.2 3D MODELLING OF GEAR DRIVES 28

2.3 FINITE ELEMENT ANALYSIS IN GEAR RESEARCH 33
2.3.1 Single Tooth Finite Element Analysis 34
2.3.2 Multi-Tooth Contact Analysis.....39
2.4 CONCLUSIONS 41

CHAPTER 3 Optimum Design and Numerical Simulation of Spiroid Gears 43

3.1 INTRODUCTION 43
3.2 OVERVIEW OF THE METHOD 43
3.3 THE SPIROID GEAR HOB AND PINION SURFACE EQUATIONS.....45
3.3.1 Equations of Spiroid Gear's Hob Tooth Surface 45
3.3.2 The Normal to the Hob Tooth Surface.....48
3.3.3 Equations of Modified Pinion Tooth Thread Surface 50
3.3.4 The Unit Normal to the Modified Pinion Tooth Surface 57
3.4 SPIROID GEAR SURFACE EQUATIONS 59
3.5 DETECTION OF UNDERCUTTING.....68
3.6 NUMERICAL SIMULATION.....71
3.6.1 Spiroid Gearing Parameters 71
3.6.2 Worm Pinion and Gear Tooth Surface Equations.....72
3.6.3 Normal to the Pinion and Gear Tooth Surfaces in Coordinate System S_f 74
3.6.4 Meshing Equations at Localised Bearing Points.....82
3.6.5 Meshing Simulation 86
3.7 CONCLUSIONS 89

CHAPTER 4 Numerical Simulation of Localised Tooth Contact of Helicon Gears 90

4.1 INTRODUCTION 90
4.2 METHOD OF MODIFICATION.....91
4.3 THE HELICON GEAR HOB AND PINION SURFACE EQUATIONS.....91
4.3.1 Equations of Helicon Gear Hob Tooth Surface 91
4.3.2 Equations of Modified Pinion Tooth Thread Surface 94
4.4 GEAR SURFACE EQUATIONS.....100
4.5 NUMERICAL SIMULATION.....102

4.6 CONCLUSIONS 104

CHAPTER 5 Localised Bearing Contact of ZA Worm Gear Drives 107

5.1 INTRODUCTION 107
5.2 THE HOB AND WORM SURFACE EQUATIONS 107
5.2.1 Equations of Hob Tooth Surface 107
5.2.2 Equations of Modified Worm Tooth Thread Surface 109
5.3 GEAR SURFACE EQUATIONS 112
5.4 NUMERICAL SIMULATION 121
5.5 CONCLUDING REMARKS 124

CHAPTER 6 3D Modelling of Spiroid Gears Using the VGM Method 125

6.1 INTRODUCTION 125
6.2 THEORY OF VIRTUAL MANUFACTURING 127
6.3 VIRTUAL MANUFACTURING OF A SPIROID GEAR 128
6.3.1 Design of Spiroid Gear 128
6.3.2 Virtual Manufacturing of A Tapered Worm 132
6.3.3 Virtual Manufacturing of Spiroid Gear 133
6.4 GEAR ASSEMBLY AND MODEL ANALYSIS 134
6.4.1 Spiroid Gear Set Assembly 134
6.4.2 Model Analysis 135
6.5 SOME ASPECTS OF THE VIRTUAL MANUFACTURING METHOD 137
6.5.1 Parametric and Accurate Model for Finite Element Analysis 137
6.5.2 Simulation of Localised Tooth Contact 138
6.5.3 Visual Tool for Gear Design Optimisation 139
6.6 CONCLUSIONS 140

CHAPTER 7 3D Virtual Manufacturing of Worm Gears 141

7.1 INTRODUCTION 141
7.2 PRINCIPLE OF VIRTUAL MANUFACTURING FOR WORM GEAR 142
7.3 VIRTUAL MANUFACTURING OF WORM GEAR DRIVES 143
7.3.1 Design of ZA and ZI Worm Gears 143
7.3.2 Worm Cut 146

7.3.3 Wheel Hobbing 152
7.3.4 Worm Gear Drive Assembly 159
7.4 HOLROYD 3D VGM WORM GEAR MODELS 160
7.5 CONCLUSIONS 163

CHAPTER 8 Loaded Multi-Tooth Contact Analysis of Spiroid Gears 165

8.1 INTRODUCTION 165
8.1.1 General 165
8.1.2 Previous Work in Gear Tooth Stress Analysis 167
8.1.3 Experimental Testing of Gears 168
8.1.4 Multi-Tooth Finite Element Contact Analysis 168
8.2 EVALUATION OF FINITE ELEMENT PREPROCESSORS 170
8.3 GEOMETRY DATA TRANSFERRING INTERFACE 174
8.4 GENERATION OF 3D MODEL AND GEOMETRY CLEANUP 174
8.4.1 Generation of 3D Geometrical Model 174
8.4.2 Gear Geometry Cleanup 176
8.4.3 Pinion Geometry Rebuilt 192
8.4.4 Gear Assembly Model Exporting Set Up 196
8.5 ASSUMPTIONS OF GEAR TOOTH CONTACT ANALYSIS 197
8.6 GENERAL SURFACE-TO-SURFACE CONTACT ALGORITHM 198
8.6.1 Contact Algorithm 200
8.6.2 The Selection of Contact Element and Target Element 203
8.7 THE SELECTION OF SOLID ELEMENTS 204
8.7.1 Solid Elements 204
8.7.2 Higher Order Tetrahedral Elements vs. Hexahedral Elements 206
8.8 GENERATION OF THE 3D FINITE ELEMENT MODELS 207
8.8.1 Importing 3D Models via the IGES Interface 207
8.8.2 Coordinate Systems 210
8.8.3 Generation of Pinion Mesh 211
8.8.4 Generation of Gear Mesh 213
8.8.5 Generation of Contact and Target Elements 219
8.9 APPLICATION OF THE LOAD AND BOUNDARY CONSTRAINTS 223
8.10 SOLVER SELECTION 226

8.11 ADVANCED TECHNIQUES 227
8.11.1 Gear Contact Region Mesh Refining Technique 227
8.11.2 Submodel Technique 228
8.12 RESULTS AND DISCUSSION 231
8.12.1 Stress Distribution 233
8.12.2 Load Distribution 250
8.13 CONCLUSIONS 264

CHAPTER 9 Loaded Tooth Contact Analysis of Worm Gears 266

9.1 INTRODUCTION 266
9.2 GENERATION OF 3D WORM GEAR MODELS 267
9.2.1 Worm Gear Design 267
9.2.2 Worm and Hob Axial Tooth Profiles 271
9.2.3 Generation of 3D Worm and Hob Models 277
9.2.4 Generation of Gear Model 282
9.3 UNLOADED TOOTH CONTACT PATTERNS 282
9.4 GEOMETRY CLEANUP 285
9.4.1 Geometry Cleanup of Worm I 285
9.4.2 Wheel Geometry Cleanup 287
9.5 GENERATION OF 3D FINITE ELEMENT MODELS 302
9.5.1 Importing Model via the IGES Interface 302
9.5.2 Worm Model Mesh 303
9.5.3 Gear Model Mesh 305
9.6 GENERATION OF CONTACT ELEMENTS 310
9.7 LOAD AND BOUNDARY CONSTRAINTS 313
9.8 RESULTS AND ANALYSIS 315
9.8.1 Stress Pattern 317
9.8.2 Load Distribution 330
9.8.3 Submodel 336
9.9 DISCUSSION AND CONCLUSIONS 340

CHAPTER 10 Conclusions 343

10.1 OBTAINING LOCALISED TOOTH CONTACT FOR SPIROID AND HELICON GEARS 344
10.1.1 Existing Methods of Obtaining Localised Tooth Contact 344
10.1.2 A Novel Approach for Obtaining Favourable Localised Tooth Contact of Spiroid and Helicon Gears 344
10.2 3D PARAMETRIC MODELLING AND VIRTUAL SIMULATION OF SPIROID AND WORM GEARS 345
10.3 LOADED MULTI-TOOTH CONTACT ANALYSIS OF SPIROID AND WORM GEARS USING THE FINITE ELEMENT METHOD 349
10.3.1 Conventional Loaded Tooth Contact Analysis Methods 349
10.3.2 Nonlinear Tooth Contact Analysis and Techniques 350
10.3.3 Loaded Multi-Tooth Contact Analysis of Spiroid Gear 350
10.3.4 Multi-Tooth Contact Analysis of Worm Gears 352
10.4 A BRIEF SUMMARY 353
10.4.1 Three Major Achievements 353
10.4.2 Completed Work 354
10.4.3 Numerical Models Developed 355
10.4.4 VGM Models Developed 355
10.4.5 FE Models Developed for LTCA 356
10.4.6 Experimental Work 356
10.5 SUGGESTION FOR FUTURE WORK 356
10.5.1 3D Parametric Modelling of Gear Drives 356
10.5.2 Loaded Multi-Tooth Contact Finite Element Analysis 356
10.5.3 Dynamic Response of Gear Drives Using Finite Element Method 357

REFERENCES 358
APPENDIX A NUMERICAL RESULTS OF LOCALISED TOOTH CONTACT OF SPIROID GEAR 374
APPENDIX B NUMERICAL RESULTS OF LOCALISED TOOTH CONTACT OF HELICON GEAR 379
APPENDIX C NUMERICAL RESULTS OF LOCALISED TOOTH CONTACT OF ZA WORM GEAR 383
APPENDIX D HOLROYD WORM GEAR DATA SET II AND 3D MODELS 386
APPENDIX E WORM GEAR EXPERIMENT 393

APPENDIX F EXTENDED SUMMARIES OF SOME METHODS MENTIONED IN CHAPTER 2.....421

CHAPTER 1 Introduction

The concept of worm and spiroid gearing has been briefly introduced. The aims and objectives of this research and the layout of this thesis have been presented.

1.1 WORM, SPIROID AND HELICON GEARS

Three types of gear drives, namely worm, spiroid and helicon gears, are investigated in this research. They are widely used in industry to transmit power and motion between non-intersecting and non-parallel shafts.

In most cases, worm gears provide right-angle power flows with a high gear ratio (see Figure 1.1). Worm gear drives have many important properties such as: high loading capacity, large reduction ratio, low noise and vibration, compact size and self-locking capacity.

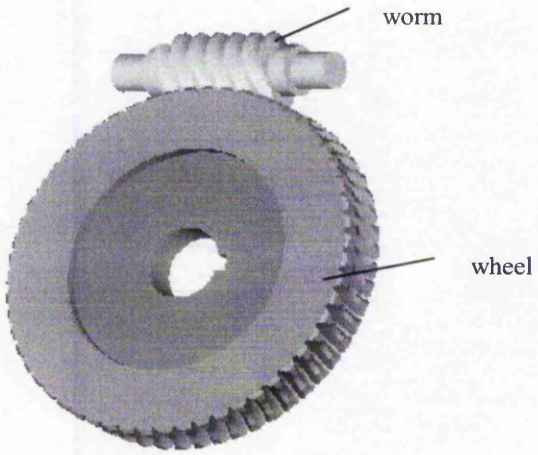
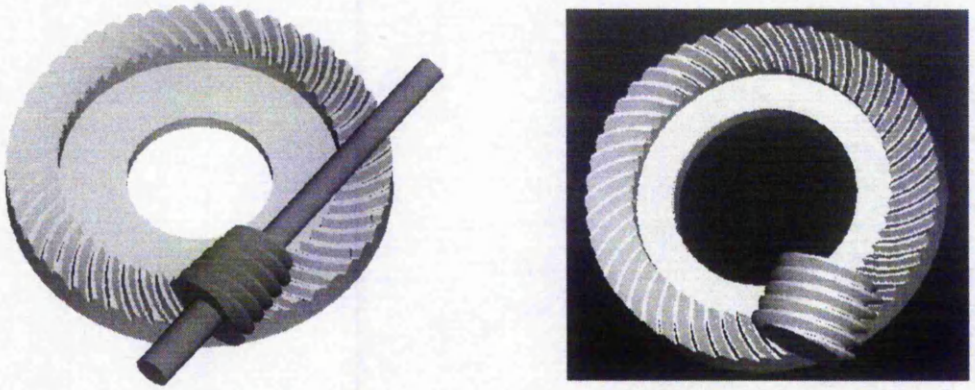


Figure 1.1 Worm gear drive

The spiroid is a kind of skew-axis gearing which has a tapered worm pinion with an angle of elevation of 5° or 10° on one side (see Figure 1.2 (a)). A helicon gear is similar to the spiroid gear but its pinion is a cylindrical worm (see Figure 1.2 (b)).

The gear of a spiroid or a helicon set has its thread on its gear face, resembling a high-pitch-angle bevel gear. Like most other skew axis concepts, spiroid and helicon are primarily screw action gears while by comparison, spur, helical and bevel gear are primarily rolling action gears.



(a) Spiroid gear drive (b) Helicon gear drive

Figure 1.2 Spiroid and helicon gear drives

Both spiroid and helicon gear sets have more teeth in contact than an equivalent size worm gear set. The primary difference between spiroid and helicon is their minimum ratio capabilities and the range of acceptable offsets. The minimum ratio of a spiroid is about 10:1 but for a helicon, the minimum ratio could be only 4:1 due to its lack of taper. In the range of ratios where either a spiroid or a helicon might be used, the spiroid has higher load-carrying capacity for a given size. The helicon pinion is somewhat simpler to make since its threads are not cut on a tapered blank.

Spiroid or helicon gears fit in between bevel and worm gears in terms of ratio (see Figure 1.3), and generally they provide better performance than worm gears. Spiroid mesh characteristics give more favourable tooth contact conditions, ideal lubrication film formation and contact line movement, thus permitting the use of optimum hardenable steels for both gear and pinion. They also have many other advantages such as: uniform durability, high shock strength, quiet operation, material selection versatility and compact package.

The combination of a high ratio in compact arrangements, low cost when mass-produced, and good load-carrying capacity makes the spiroid-type gear attractive in many situations.

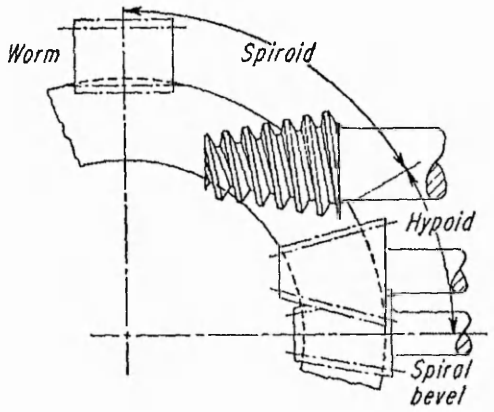


Figure 1.3 Comparison of worm, spiroid, hypoid and bevel gearing.

(from Duke and Walton 1999)

1.2 BACKGROUND AND RESEARCH APPROACH

1.2.1 Localised Tooth Bearing Contact

Gear tooth surfaces are generated as the envelope to the family of worm surfaces. The gear generating process duplicates the meshing of worm and gear. The gear must be generated by a hob, which is identical to the worm of the drive. Three key design parameters must be identical to the worm gear drive, namely, the ratio of their angular velocities, the crossing angle and the shortest distance between the axes of the hob and the gear.

The surfaces of the helicon, spiroid and worm gears generated by the above method are in line contact at every instant. They are sensitive to misalignments which will inevitably arise in the manufacturing and assembly process. In reality, due to errors of alignment and manufacturing, the surface contact may be shifted to the edge of the gear surfaces or even became an edge contact, which will reduce the working life of the gear drives.

In order to reduce the sensitivity to manufacturing and assembly errors, much attention has been focused on optimum design of the gear tooth profile. The main idea of this gear optimum design is to obtain favourable localised tooth contact by modifying the gear tooth profile. A number of approaches exist for modifying the gear tooth profile using computerised simulation of tooth contact, and a great deal of contributions in this area have been made (Su, et al, 1999b; Donno and Litvin, 1999a; Litvin, et al, 1992, 1998, 1999; Seol, et al, 1996; Chang, 1997, Chang & Tsay, 1998). However, the modifying methods they proposed in worm and spiroid gears are difficult to implement on standard gear hobbing machines.

1.2.2 3D Gear Modelling and Virtual Simulation

Worm and spiroid gear drives have such complex tooth geometry that 3D gear models are essential to view the tooth contact patterns and to detect the possible interferences in modified gear drives. 3D gear models are also necessary in *loaded tooth contact analysis* (LTCA) using the *finite element method* (FEM). However, to build three-dimensional models of spiroid and worm gears using currently available methods is not an easy task. Livtin et al. (1996) and Tsay et al (1995) built a 3D model of worm gear by calculating many sections of a worm gear tooth. In their approaches, complicated numerical models were involved and a set of unknowns from the surface and meshing equations had to be solved. It is easy to find the solution for a part of the surface but it is usually very difficult to obtain the full surface solution from these meshing equations. Su et al (1998) proposed a 3D modelling method in which numerical methods are used to get the contact lines' coordinates. The contact lines are used to stitch a quilt in 3D software. These quilts are trimmed according to the worm design parameters and then the trimmed quilts are transformed into a solid tooth. All these methods mentioned above are very complicated, time-consuming, non-parametric, inflexible for changes and do not directly reflect the nature of gear manufacturing.

1.2.3 Loaded Tooth Contact Analysis

One of the major concerns in modern gear research is the determination of the tooth contact stresses and load sharing using the finite element method. There are very few research papers published in this area, but of the papers published, the research mainly focused on a single gear tooth, not on all teeth involved in the contact (Litvin, et al, 1996; Gosselin, et al, 1995; Tsay, et al, 1995). The single tooth analyses obviously do not reflect the real multi-tooth contact situation involved. The research work in this area is still in its infancy due to the extremely complicated worm and spiroid gear tooth geometry and contact conditions. No satisfactory LTCA work for the spiroid and worm gear drives has been so far carried out.

1.3 AIMS AND OBJECTIVES

The aims of this research are mainly concerned with the optimum design and 3D CAD/CAE simulation of spiroid and worm gear drives. The approaches used to achieve the above aims consist of three main parts. The first part is the development and numerical simulation of a new type of spiroid, helicon and worm gear design with favourable localised tooth contact. The second part is the development of a novel CAD methodology for rapid parametric solid modelling of spiroid and worm gears. This will be achieved by virtual simulation of the gear manufacturing process. The models will allow the interference and contact paths of spiroid and worm gears to be visually investigated and controlled. The third part of this research is the development of a general and feasible FEA procedure for loaded multi-tooth tooth contact problem of spiroid and worm gears. This will include geometry cleanup, model importation, model meshing, loading scheme, stress pattern and load sharing analysis.

The objectives of this research are summarized as follows:

- Develop a new method to achieve localised bearing contact for spiroid and worm gears. The new method should be able to be implemented easily to the standard gear hobbing machines and it will therefore be more cost-effective.

- Develop mathematical models of modified worm and spiroid gear surfaces and meshing; develop software to calculate the surfaces and meshing of modified worm and spiroid gears; determine localised contact paths and transmission errors.
- Develop a novel CAD modelling method, *virtual gear manufacturing* (VGM), for worm and spiroid gear drives which will directly reflect the nature of gear manufacturing.
- Apply VGM to model worm and spiroid gear drives through simulation of the gear manufacturing process and simulate the meshing of worm and spiroid gear tooth surfaces in a virtual environment.
- Develop a general and feasible finite element modelling method for multi-tooth contact analysis of worm and spiroid gears using the advanced surface-to-surface contact algorithm.
- To create a reliable *finite element analysis* (FEA) procedure in order to predict the contact stresses and deformations of a loaded spiroid gear drive using ANSYS.
- Investigate the tooth contact stress patterns, deformations and load sharing of spiroid gear drives.

1.4 MAJOR ACHIEVEMENTS

Three original contributions have been achieved for the optimum design and 3D CAD/CAE simulation of spiroid and worm gears in this PhD research. They are:

1.4.1 A Novel Approach for Obtaining Localised Tooth Contact Pattern

A novel approach has been developed to obtain a favourable localised tooth contact for spiroid and worm gears. The localised contact is achieved by modifying the pinion (or worm) tooth surface. With this approach, only the pinion (or worm) cutter's geometrical angles and mounting position need to be adjusted. The meshing theory of the modified gear surface has been established and the mathematical models of gear tooth surfaces have been deduced. Programs have been written to obtain the modification parameters and to solve the nonlinear meshing equations of helicon,

spiroid and Archimedean worm gears. The numerical meshing simulations of localised tooth contact of helicon, spiroid and Archimedean worm gear have been conducted. The results of the numerical simulations confirm that the proposed gear modifying method provides a substantially improved localised bearing contact and any edge contacts are avoided.

This new approach is capable of being implemented in standard gear hobbing machines. It is more economical than the existing methods for the modification of gear teeth. The modified spiroid and worm gearing have significant advantages over conventional ones such as less sensitivity to misalignments, more favourable lubrication conditions, higher load capacity, longer working life and lower manufacturing costs.

1.4.2 Virtual Gear Manufacturing Method

A novel parametric solid modelling methodology, *virtual gear manufacturing* (VGM), has been first proposed and then developed by the author for 3D modelling of worm and spiroid gear drives. The new approach for generating 3D gear models is a virtual manufacturing process of worm and wheel. The principle of VGM is to simulate the practical gear hobbing process to cut a gear in the advanced 3D CAD package Pro/Engineer. The methodology and techniques have been developed for 3D spiroid and worm gear modelling. The VGM models can be used to simulate gear meshing, to analyse the contact pattern and to detect any possible tooth interference in a new gear design.

The VGM method is regarded by the author as a novel approach for the following reasons:

(1) The VGM process visualises and animates both the conventional and modern meshing theory of gearing. Unlike the modern computerised gear theory which can only simulate the meshing of gearing in point or line contact, the VGM process can visually simulate the more general regional contact problems.

(2) The VGM method produces 3D gear models much faster than the conventional gear modelling methods. The increased speed is not just double or triple the original but in a geometrical order for complex gears such as worm and spiroid gears. Solving the meshing equation in conventional gear modelling methods is time consuming and is extremely difficult for worm and spiroid gears. Unlike conventional 3D gear modelling methods, the VGM method does not utilise the coordinates of points on the gear tooth surface to build the solid gear model. Therefore, the extreme difficulty in obtaining the full solutions of gear surface points from the non-linear meshing equations can be avoided. The VGM method directly models the gears from the gear proportions. Therefore, the VGM method can model the gearset much faster than conventional gear modelling methods.

(3) The VGM gear model is more accurate than models built by conventional gear modelling methods. The solutions of the conventional models that are based on modern gear meshing theory are the coordinates of the points on the contact lines. In the root fillet area where no contact resides, there is no information available from the equation of meshing. Therefore in conventional gear modelling methods it is difficult to find the solution of root areas and so correspondingly it is also difficult to construct the whole accurate tooth surfaces. The VGM model simulates the gear manufacturing process and naturally produces the root fillet areas.

(4) The VGM method can successfully create the gear 3D models that the conventional gear modelling method may fail in doing. For example, the VGM method easily produces the worm gear set II (see Figure D.7 Gear set II assembly). The gear set II design data was provided by the Holroyd Gear Company. According to the design engineer in the company, the gear commercial software used in the Holroyd Gear Company cannot find the coordinates of the whole gear surface. The software can only find partial surface points. Without the coordinates of points on the gear surfaces, the conventional gear modelling method cannot even start the modelling process!

(5) The VGM models are parametric and very flexible to incorporate changes if needed. Gear finite element analysis and design optimisations require that the gear models are flexible for modifications. The VGM method has a significant advantage over conventional methods in flexibility due to its parametric characteristics.

(6) The VGM method is a novel approach. It is completely different from conventional 3D gear modelling method not only in concept but also in procedure. By using the VGM method, the difficult gear meshing theory will better be understood by new learners.

(7) The VGM method can significantly reduce the manufacturing cost in the early production stage because it can visually detect and fix the problems in new gear design before expensive prototypes are built.

Based on the new modelling method, 1 ZA worm gear, 3 ZI worm gears, 1 helicon and 1 spiroid gear drive have been virtually hobbed in Pro/Engineer. The worm and spiroid gear models have been assembled and run in a virtual 3D environment. With the new VGM models, simulations of the meshing of spiroid and worm gears have been conducted and animated. The worm and spiroid tooth contact paths have been determined in a virtual 3D environment.

1.4.3 Nonlinear Tooth Contact Analysis and Techniques

Gear tooth contact analysis is a highly nonlinear problem and extremely difficult to solve. The work in this area is still in its infancy.

A feasible and general finite element method has been developed to analyse the multi-tooth contact pattern for spiroid and worm gears. In this research, with the virtual manufacturing method, 14 full multi-tooth contact finite element models of spiroid and worm gears have been developed. The 3D geometrical models of spiroid and worm gear drives were exported to ANSYS from Pro/Engineer. The evaluation of solid and contact elements for nonlinear gear contact finite element analysis has been conducted. The techniques for 3D gear model geometry cleanup, importing the 3D

gear model via the IGES interface and 3D finite element meshing have been developed for spiroid and worm gears. The tooth contact stresses and deformations of spiroid and worm gear drives under load have been fully analysed. The FE models enable the loaded tooth contact pattern, stress distribution, contact force distribution and load share to be fully understood for the first time. This is impossible for the conventional theoretical methods and experimental methods.

By using the procedures and techniques developed in this research, researchers and engineers will be able to conduct and gain benefits from the loaded gear tooth contact analysis.

1.5 STRUCTURE OF THE THESIS

The structure of the thesis begins with the introduction, followed by the literature review, then the main research work and finally the conclusion. The introduction and literature review are presented in Chapters 1 and 2 respectively. The research work consists of three main parts. **Part I** includes Chapters 3, 4 and 5. In Part I, a novel approach to obtaining preferable localised tooth contact of gear drives has been developed. This method has applied to spiroid gears in Chapter 3, to helicon gears in Chapter 4 and to Archimedean worm gears in Chapter 5. **Part II** includes Chapters 6 and 7. An original rapid parametric 3D modelling method has been developed for worm and spiroid gears in this part. Chapter 6 illustrates the principle of the virtual gear manufacturing method. Spiroid and helicon gears have been virtually manufactured on computer using the VGM method. Chapter 7 deals with the 3D parametric modelling and virtual simulation of ZA and ZI worm gears. **Part III** includes Chapter 8 and Chapter 9. Chapter 8 presents a feasible and reliable finite element procedure to analyse the complex loaded gear tooth contact problems together with all the related techniques for nonlinear multi-tooth contact analysis such as model importation, geometry cleanup, 3D model meshing, contact elements creation, rotating constraints and results analysis. Chapter 9 mainly deals with the loaded tooth contact problem for worm gear drives. Some special techniques for worm gear geometry cleanup and 3D model meshing have been developed in Chapter 9. Chapter 10 concludes the work completed in this research and suggests further work for future research.

The subject matter in the following chapters is briefly summarised as follows.

Chapter 2 Literature Review

An extensive literature search has been carried out on the state of research on worm and spiroid gears. Research work on the localised tooth contact of worm and spiroid gear, gear three-dimensional modelling methods and loaded tooth contact analysis have been reviewed.

Chapter 3 Optimum Design and Numerical Simulation of Spiroid Gears

A new approach to obtaining localised bearing contact of spiroid gear drives has been developed. The localised contact is achieved by modifying the pinion tooth surface. With this approach, only the pinion cutter's geometrical angles and mounting position need to be adjusted, and hence, it is simpler and more economical than other methods. In this chapter, the following are presented: overview of this approach, surfaces and meshing equations for modified spiroid gear tooth geometry, and results of computer simulation. The results of the numerical simulation confirm that the proposed modification of the tooth geometry permits localised bearing contact.

Chapter 4 Numerical Simulation of Localised Tooth Contact of Helicon Gears

The innovative approach developed in the preceding chapter is applied on the helicon gears to obtain the preferred localised bearing contact. The surface equations of the helicon gear, hob and pinion are derived. The parameters for the modification of the pinion have been determined. Programs have been written to obtain the coordinates of the helicon gear and the modified pinion's surfaces. Computerised simulation of localised tooth contact has been conducted based on the established numerical model of helicon gear drives. The results of numerical simulation show that the proposed modification of the tooth geometry permits a localised bearing contact.

Chapter 5 Localised Bearing Contact of ZA Worm Gear Drives

This chapter presents the method to obtaining the favourable localised tooth contact pattern for the Archimedean worm gears. The modifying parameters of the worm tooth surface have been determined. The gear tooth surface equations have been derived. A program has been written to calculate the ZA gear tooth surface coordinates and simulate the meshing of localised tooth contact. The meshing simulation of the modified Archimedean worm gear has been conducted. The results of the numerical simulation prove that the proposed method has achieved a good localised tooth contact pattern.

Chapter 6 3D Modelling of Spiroid Gears Using the VGM Method

The virtual gear manufacturing (VGM) method has been first proposed and developed for gear 3D modelling and simulation. The VGM method is totally different from existing 3D modelling methods in gear research and design software because the principle of the VGM is to simulate the gear hobbing process to generate the complex gear tooth geometry using advanced computer aided design software. The method of virtual hobbing of spiroid gears has been developed and illustrated. Some topics related to the virtual gear manufacturing method and modern gear theory have been also addressed in this chapter. A detailed example of virtual manufacturing of spiroid gears has been presented. The advantages of VGM have been discussed and demonstrated.

Chapter 7 3D Virtual Manufacturing of Worm Gears

The method of 3D parametric modelling of worm gears has been studied in this chapter. The virtual gear manufacturing method has been extended for the hobbing of worm gears. The method for the 3D modelling of Archimedean worm gear and involute worm gear has been studied in detail. Two types of worm gear sets have been virtually manufactured in Pro/Engineer. The worm and gear are assembled into a worm gear set according to the design. The tooth surface interference, meshing and contact pattern of the worm gear have been simulated in the three dimensional virtual environment.

Chapter 8 Loaded Multi-Tooth Contact Analysis of Spiroid Gears

This chapter presents the detailed procedures for the loaded tooth contact analysis of spiroid gears using the finite element method. Gear tooth contact problems are highly nonlinear and extremely difficult to solve. There have been no comparable solutions presented in the open literature to date.

This chapter aims to establish a feasible and reliable procedure using the finite element method to analyse complex loaded gear tooth contact problems. Eight full multi-tooth finite element models have been developed to determine the contact stresses in spiroid gears. The spiroid gear models are generated by the VGM method. The geometrical models are then imported into the commercial CAE software ANSYS 5.6 to mesh and solve.

The techniques of importing IGES models, geometry cleanup, meshing model, generating contact elements and simulating boundary constraints have been addressed in detail. In this chapter, the newest and most advanced surface-to-surface contact algorithm is first used to simulate the spiroid gear tooth contact. The presented procedures are feasible and much more efficient than those using gap elements to simulate the gear contact problems. The procedures and techniques developed in this chapter can also be applied to other gear types such as worm gear, hypoid and spiral bevel gear etc.

Chapter 9 Loaded Tooth Contact Analysis of Worm Gears

After the successful analysis of loaded spiroid gear tooth contact problems, the procedures and techniques developed in previous chapter are applied to analyse the real gear tooth contact stresses of worm gears that are provided by the Holroyd Gear Company. A full finite element model using hexahedral elements has been developed to determine the contact force and stresses in a modified Holroyd involute worm gear set. The 3D geometrical worm gear models are generated using the virtual gear manufacturing method. The model's geometry cleanup techniques, which are different from those for the spiroid gear due to their completely different tooth geometry, are newly developed in this chapter. The models are exported from Pro/Engineer and imported into ANSYS via the IGES interface. The whole worm gear assemblies are

meshed in ANSYS 5.6. Some new techniques have been developed for gear and worm meshing with hexahedral elements. The solution techniques for generating an accurate general surface-to-surface contact element model have been presented. The contact forces and stress pattern have been evaluated.

Chapter 10 Conclusions

A summary of the conclusions drawn throughout the thesis is presented in this chapter. The major topics covered in this thesis are discussed and concluded, which include the mathematical modelling of differential geometry of modified worm gear design, tooth contact analysis, 3D modelling using the virtual gear manufacturing method and loaded tooth contact analysis using general surface-to-surface contact element techniques. Further work for the optimum design and 3D CAD/CAE simulation of spiroid and worm gears has been suggested.

Appendix A presents the numerical results of localised tooth contact of a spiroid gear

Appendix B presents the numerical results of localised tooth contact of a helicon gear

Appendix C presents the numerical results of localised tooth contact of a worm gear

Appendix D presents the design data of the Holroyd worm gear set II and the 3D models created using the virtual gear manufacturing method.

Appendix E presents the experimental work on the contact and efficiency of the Holroyd worm gears.

Appendix F lists some related formulae about using oversized hob and tooth contact analysis reviewed in Chapter 2.

CHAPTER 2 Literature Review

An extensive literature search has been carried out on research on worm and spiroid gears. The research work on localised tooth contact of worm and spiroid gears, gear three-dimensional modelling methods and loaded gear tooth contact analyses has been reviewed.

2.1 RESEARCH ON LOCALISED TOOTH CONTACT OF WORM AND SPIROID GEAR DRIVES

With the existing design of worm and spiroid gears, the contact tooth pair is in line contact at every instant. It is very sensitive to misalignment that occurs inevitably during the manufacturing and assembly processes. The errors of misalignment such as the change of the shaft angle, the shortest centre distance or the axial displacement of the gear set will cause a shift in the bearing contact pattern from line contact to edge contact. It also results in large transmission errors and induces significant vibration of drives with multi-thread worms.

The current method of obtaining a favourable location and sufficient area of the bearing contact is based on the initial running-in of the assembled worm or spiroid gear drives. A small load is applied in the initial stages and then the load is gradually increased until a polished area appears on the gear teeth. However, the process can take a long time, up to 100-150 hours.

Thus, a method of shortening the initial running-in times and obtaining a more favourable tooth contact pattern has become a subject of extensive research in modern gear industry. One of the major approaches is the controllable modification of the conjugate surfaces, or so-called preferred localised tooth contact methods. Instead of pursuing perfect theoretical "line contact", these methods concentrate on achieving a practical contact pattern of "localised contact" or " preferred point contact". The obvious advantage of the preferred localised tooth contact method is that less time is

required for the worm gear to run-in under load, and the contact can be located at a preferable position. The other advantages are as follows: better lubrication conditions, less sensitivity to errors, improved contact stability and better meshing quality.

A localised tooth contact pattern may be achieved by modifying the tooth geometry of an existing design. There are existing ways to achieve the localised tooth contact pattern, which can basically be categorised into two kinds: one is to achieve localised tooth contact by modifying the worm surface; the other is by modifying the mating gear tooth surface.

2.1.1 Obtaining Localised Tooth Contact by Modifying Worm Tooth Surface

Seol and Litvin proposed three approaches for localised tooth contact in 1996. The first approach (Seol and Litvin, 1996a) is about the method of mismatching the worm with the hob, which is briefly described below. The other two methods will be outlined in Section 2.1.2.

In Seol et al's first approach, the hob and the worm have the same pitch diameter and coincident axes but different cross-section profile. This approach provided a longitudinal bearing contact on the worm-gear tooth surface. The localisation of bearing contact of a K worm gear drive was presented. The mismatch of the K worm gear drive was achieved by mismatch of tool surfaces used for generation of the hob and worm surfaces. A cone surface and a surface of revolution were used for generation of the worm and the hob respectively, as shown in Figure 2.1. The worm's tooth profile is a special curved-spline. The hob and the worm thread surfaces were in tangency along the helix L_{wh} as shown in Figure 2.2. In order to obtain the special curved cross-section of worm surface, a special grinding wheel had to be used in the above method. It is expensive to use the special grinding wheels for mass production. That's why this method fails to be widely used in the gear industry. However, the gearset geometry modified by the above method is better than the other methods that will be reviewed later in this chapter. If a cheap and feasible method can be found to produce the special geometry of worm, this approach will be very valuable for the gear industry.

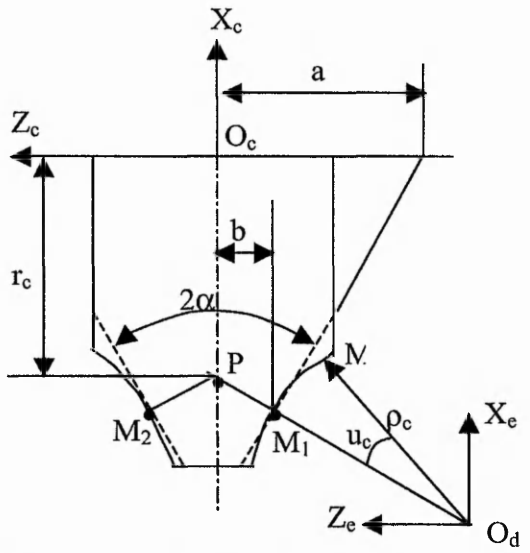


Figure 2.1 Axial profiles of grinding wheels for generation of a hob and a worm (from Seol et al 1996a)

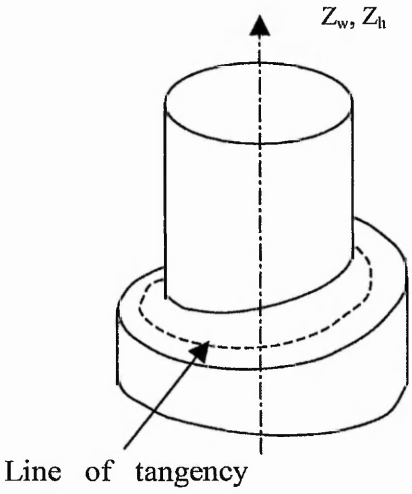


Figure 2.2 Line of tangency (helix) between the hob and the worm (from Seol et al 1996a)

Su et al (1999a, 1999b), and Yang et al (1998) proposed a downsized worm method for localised tooth contact of involute worm gear drives. In their approach, a smaller diameter worm is used. The worm and the hob have the same type of involute surfaces but the worm has a smaller diameter. When cutting the gear, the hob is installed with a small angle to the gear blank to achieve the localisation of bearing contact (see Figure 2.3). The modification of the wheel tooth surface is based on altering the mounting angle θ_h of the hob. The parameters of the hob remain

unchanged while the mounting angle is altered to achieve the designed tooth surfaces. In order to avoid interference, the worm's diameter is made smaller than the hob's. The lead angle of the worm is also changed which is determined by tooth contact analysis. The principle of this approach is similar to the second method presented by Seol and Litvin (1996a) where an oversized hob was used.

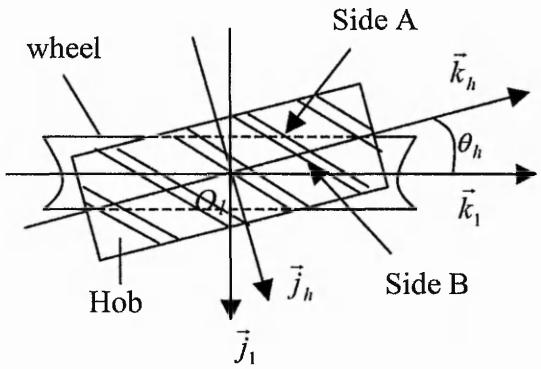
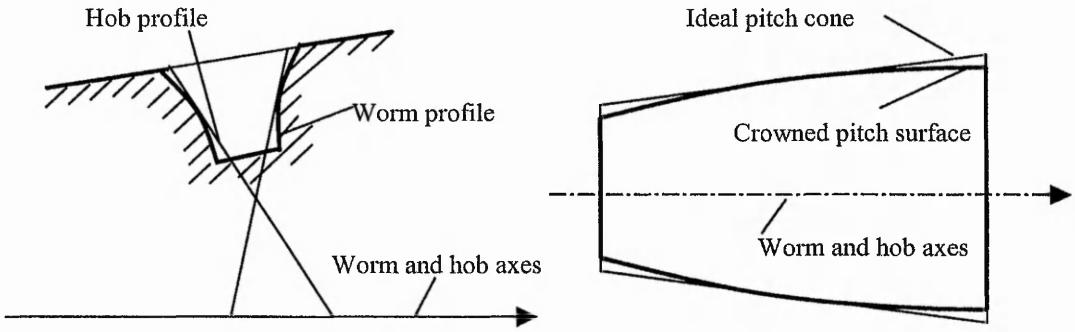


Figure 2.3 Hob mounting position



(a) Profile Crowning (b) Longitudinal Crowning

Figure 2.4 Schematic of crowning of worm thread surface

Litvin and Donno (1997) proposed a crowning of the worm tooth profile for spiroid gear drives. The modified tooth geometry achieved localised bearing contact and reduced the level of transmission errors. The worm thread surface is modified with respect to the hob thread surface that generates the gear tooth surface. The modification is accomplished as a combination of profile and longitudinal crowning

of the worm thread surface (see Figure 2.4). However, how the modified worm thread surface could be achieved was not addressed in their approach.

In 1999, Litvin and Donno proposed a method to achieve the modified worm thread surface. In their approach, the worm is ground by a cone with a special curved axial profile that is identical to the worm profile illustrated in Figure 2.4. Such a special cone is very difficult to produce since the axial profile is curved. The convex shape also makes the cone wear away quickly and therefore increases the manufacturing cost. In other words, the special cone is too *expensive* to be used in mass manufacture.

2.1.2 Obtain Localised Tooth Contact By Modifying Wheel Tooth Surface

In 1961, Ufert proposed a trial and error method to obtain the localised tooth-bearing pattern by modifying the wheel tooth (Yang, 2000). In his method, the gear teeth were over hobbed in two sides. Extra tooth surfaces from both sides of the gear tooth were cut off so that the contact was localised on the middle of the tooth. This method mainly depends on expertise; is very rough and it is difficult to control the cutting position and, therefore, difficult to control the quality and the stability of the localised contact.

Considerable attention has been drawn to the oversized hob method to modify the wheel tooth profile in order to obtain localized tooth contact. The work related to this method found in the literature is reviewed in the rest of this section.

Janninck (1988) developed a mathematical model to predict the initial contact pattern, as well as the surface separation topology over the entire worm gear tooth surface. The equations and procedures were presented for analysis of initial tooth contact. The problem that arose from using a hob duplicated in the set was addressed and the use of oversized hobs was discussed. Janninck pointed out that errors of manufacturing may in certain cases be introduced deliberately to improve bearing contact. The crowning could be applied to the worm gear tooth surface. The longitudinal direction crowning could be achieved by adjusting the amount of hob oversize. The radial direction crowning could be obtained by inducing a tip and root flank easement.

Simon (1988) investigated the manufacturing of high precision hobs for worm surface generation. To improve the worm gear drive unfavourable instantaneous contact line locations, Simon (1993) analysed the grinding wheel optimal setting angles to ensure the precision of the resharpened hob for worm gear manufacturing. Simon (1994) also presented a worm gear drive with double arc profiles to obtain favourable position of the instantaneous contact line, high load carrying capacity of the oil film, and reduced elastohydrodynamic lubrication power losses.

Colbourne (1989) proposed a method for designing oversized hob cutters to cut worm gears to achieve the localised tooth contact. He also investigated the influence of the oversize of the hob on its service life. The backlash was assumed a constant value in his study. Colbourne (1993, 1994) also examined the curvature and undercutting of worm gear surfaces. He observed that the friction coefficient of the entry region was larger than that of the exit region in the worm gear meshing. Colbourne suggested that an oversized hob cutter would be employed to cut the worm gear set that was in point contact. Though the use of an oversized hob this has achieved better localised contact, but his method cannot avoid tooth interference arising from this practice.

Seol and Litvin (1996a) presented a second method to modify the existing geometry of worm gear drives by the application of an oversized hob. In this approach, the localisation of the bearing contacts are achieved by adopting an oversized hob whose pitch diameter was increased with respect to the worm of the gear drive. The principle of the approach is illustrated in Figure 2.5. The hob and the worm are in imaginary internal tangency and their axes are crossed. The pitch cylinder of the hob is larger than that of the worm, $\Delta\lambda$ and Δr are the crossing angle and the shortest centre distance between the axes respectively. Point P of tangency of the hob and the worm pitch cylinders belongs to the shortest distance between the hob and the worm-gear. The normals to surfaces Σ_h, Σ_w and Σ_g pass through point P and the surfaces mentioned above are in simultaneous tangency at the beginning of meshing.

The hob is provided with the same type of thread surfaces as the worm. This means that in applications using a K-worm, a K-hob should be provided as well. Therefore, the hob must be ground by a cone with the same profile angle. However, the shortest

distance between the axes of the grinding cone and the hob to be ground should be increased with Δr. It is obvious that surfaces Σ_h and Σ_g of the hob and the wheel being generated are at every instant in line contact, but surfaces Σ_w and Σ_g are at every instant in point contact. The chosen oversize Δr affects the magnitude of the major axis of the instantaneous contact ellipse and the level of transmission errors. According to Seol and Litvin (1996a), to generate the worm gear by an oversized hob, the following conditions must be satisfied:

$$E_{hg}=E_{wg}+\Delta r, \qquad \gamma_{hg}=90°-\Delta\gamma \tag{2.1.1}$$

Where $\Delta r=r_{ph}-r_{pw}$; r_{ph} and r_{pw} are the radii of the pitch cylinders of the hob and the worm, respectively; $\Delta\gamma=\lambda_w-\lambda_h$; λ_w and λ_h are the lead angles of the worm and the hob, respectively. This approach provides a bearing contact directed across the worm-gear tooth surface.

This method is easy to implement in practice. The use of an oversized hob can obtain localisation of tooth bearing contact, but results in interference between worm and wheel tooth surfaces. The thread surfaces of the oversized hob and the worm interfere by each other in the neighbourhood of the point of tangency. Therefore, positive transmission errors may occur in the process of meshing the modified worm gear drives. However, only negative transmission errors are acceptable in the process of meshing of worm gear drives to provide favourable conditions of force transmission. There were no effective methods to avoid this problem in the above approach.

Seol and Litvin (1996a) also presented their third approach for localisation of bearing contact of the worm gear tooth. In this approach, the oversized hob is designed as a conjugated one to the worm. This means that the hob and the worm thread surface have a common enveloping surface that is the surfaces of an imaginary rack simultaneously in mesh with the worm and the hob. The hob and the worm are again in internal tangency (Figure 2.5), and their axes are crossed. However, the types of helicoid surfaces of the hob and the worm differ from each other. An extended summary of the method is given in Appendix F, Section F.1.

This approach is better than the second approach because (1) the oversize hob does not cause transmission errors at all in the case of an aligned gear drive; and (2) the designed worm-gear drive is less sensitive to errors of alignment. However, this approach still will cause interference between gear tooth surfaces.

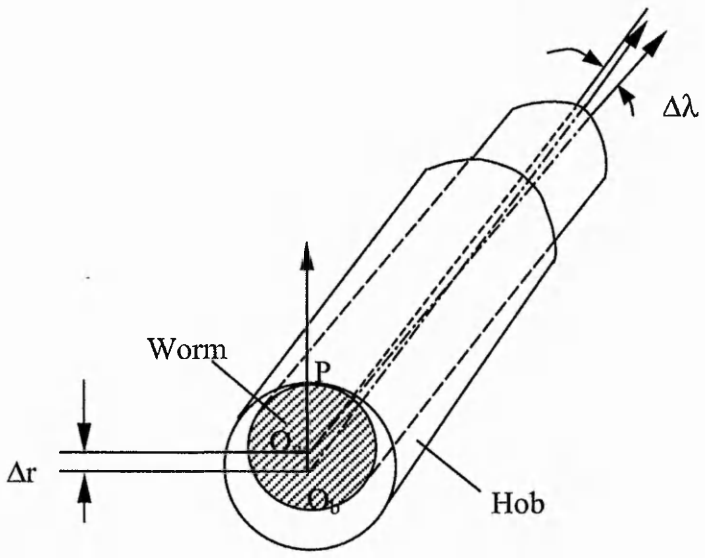


Figure 2.5 Tangency of pitch cylinders of worm and hob: Δλ is the crossing angle of axes, Δr is the shortest centre distance (from Seol et al 1996)

In 1996, Seol and Litvin presented another paper for the localisation of Involute, Klingelnberg and Flender type worm gears. Their approach aimed to reduce the sensitivity of worm gear drives to misalignment and the level of maximal transmission errors. In addition to the application of an oversized hob, a pre-designed parabolic function of transmission errors is applied in the modification of worm gear drives. According to the authors, such a function is able to absorb misalignment that may cause significant vibration. It was proposed to obtain the parabolic function of transmission errors by variation of the shortest distance between the hob and the worm gear during the process of generation.

The proposed approach is based on the generation of the worm gear by a hob of an increased diameter in comparison with the worm. The hob and the worm are in internal tangency as shown in Figure 2.5. Special conjugation of the hob and the worm thread surfaces must be required. Though the hob and the worm gear are in line

contact during the process of generation, the generated worm gear tooth surface and the worm are in point contact in the process of their meshing. Further information of the method is given in Appendix F, Section F.2.

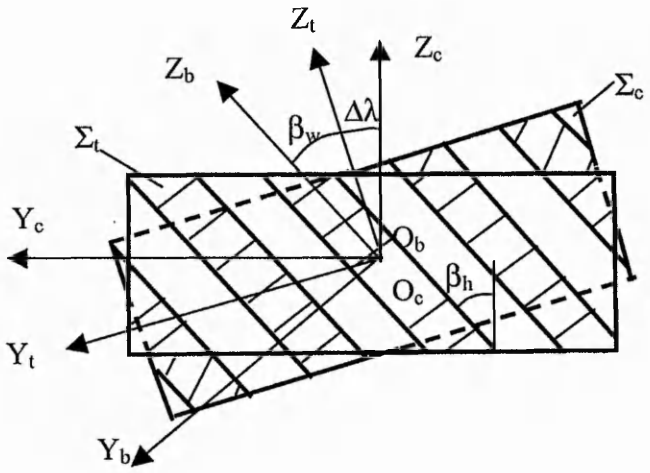


Figure 2.6 Representation of two generating racks (from Seol et al 1996)

According to Seol and Litvin (1996a), the localised tooth contact meshing can be simulated by the following equations:

$$\mathbf{r}_f^{(1)}(u_1,\theta_1,\phi_1)-\mathbf{r}_f^{(2)}(u_2,\theta_2,\phi_2)=0 \qquad (2.1.2)$$

$$\mathbf{n}_f^{(1)}(u_1,\theta_1,\phi_1)-\mathbf{n}_f^{(2)}(u_2,\theta_2,\phi_2)=0 \qquad (2.1.3)$$

However, according to the present gear-meshing program, the solutions of the above equation are not unique. In fact, the above equations cannot naturally prove that the design of hob has indeed achieved a localised tooth contact. It has not been proved yet in theory that the above equations can avoid interference in multi-teeth engagement. Equations (2.1.2) and (2.1.3) have six unknowns but only five independent equations. One unknown, say $\phi 1$, usually used as an input value, then one set of solutions can be obtained, say (u1, u2, $\theta 1$, $\theta 2$, $\phi 1$, $\phi 2$). Then consider that $\phi 1$, $\phi 2$ are the known variables; another set of solutions can be obtained by equations (2.1.2) and one of equations (2.1.3). This set value may not satisfy the remaining

equation (2.1.3). If the remaining equation (2.1.3) is satisfied, then there will be no tooth interference. If it is not, then the tooth interference exists.

The above method, using an imaginary rack, is a valid approach, but it shows clearly that the process of obtaining the hob tooth surface is very complex. This method also cannot avoid the interference in multi-teeth engagement.

Donno and Litvin (1999b) proposed an approach using an oversized hob for design and generation of low noise, stable bearing contact worm gear drives. The approach is quite similar to Seol and Litvin's (1996a). The varied plunging of the worm generating tool is also applied to get longitudinal crowning of the worm. The approach had been applied to a Klingelnberg type of worm gear drive.

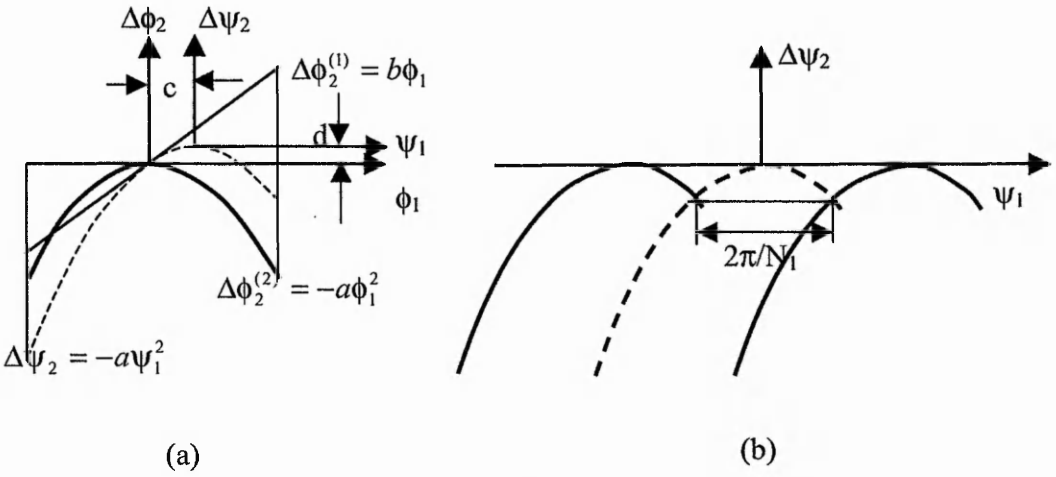


Figure 2.7 Interaction of parabolic and linear functions (from Litvin 1999)

In research into the localisation of gear tooth bearing contact, Litvin and co-workers (1989b, 1992, 1994, 1995, 1996, 1999) proposed that in addition to the localisation of the contact, a pre-designed parabolic function could absorb almost all linear transmission functions of transmission errors caused by misalignment. Figure 2.7(a) shows the interaction of a linear function $\Delta\phi_2^{(1)}(\phi_1) = b\phi_1$ with a parabolic function $\Delta\phi_2^{(2)}(\phi_1) = -a\phi_1^2$. The resulting function is again a parabolic function $\Delta\psi_2(\psi_1) = -a\psi_1^2$ with the same parabola coefficient "a". The origin of $\Delta\psi_2(\psi_1)$ is

shifted with respect to origin of $\Delta\phi_2^{(2)}(\phi_1)$ by d and c as shown in Figure 2.7 (a). Point A* and B* of function $\Delta\psi_2(\psi_1)$ correspond to points A and B of $\Delta\phi_2^{(2)}(\phi_1)$. Figure 2.7 (b) shows that the function of transmission errors $\Delta\psi_2(\psi_1)$ is a periodic continuous parabolic function.

Litvin and Donno (1998) and Donno and Litvin (1999b) proposed an additional modification to the oversized hob method initially developed by Seol and Litvin (1996a, 1996b). In addition to profile crowning, Litvin further modified the gear drives with longitudinal crowning of the worm to provide a parabolic function of negative transmission errors that is able to absorb the linear functions of transmission errors and reduce vibration. Litvin and Donno have applied this method for modification of K worm gear drives (Donno and Litvin, 1999b) and spiroid gear drives (Litvin and Donno1998, Donno and Litvin 1999a). In comparison with the modification method Seol and Litvin proposed in 1996a, this approach has some advantages such as the transmission errors becoming parabolic rather than linear. However, the fundamental problem of interference that arose from the use of the oversize hob still has not been solved.

2.1.3 Localised Tooth Contact Analysis

Tooth Contact Analysis (TCA) is considered as one of the major achievements in modern gear research (Litvin 1995). Since Baxter (1961) first proposed the theoretical principles of TCA for the analysis of hypoid gears, valuable contributions have been made in the development of TCA technology by the engineers of Gleaon Works (1981), Litvin and Gutman (1981a, 1981b, 1981c) and others.

Litvin and Zhang (1989) applied a pre-designed parabolic function of transmission errors with a controlled magnitude for tooth profile modifications of helical gears. They found that such a function of transmission errors could absorb the linear transmission errors caused by assembly misalignment and reduce the level of noise and vibration.

Litvin and Kin (1992) used the TCA method to simulate the meshing contact of a misaligned ZI worm gear drive. Their approach made it possible to determine the transfer point of the transmission errors and the shift of bearing contact caused by misalignment.

Litvin, Egelja and Donno (1998) presented a paper to derive the formulae to determine the envelope surfaces for a family of parametric tooth surfaces, which were represented in parametric form. Litvin, Egelja and Donno (1998) also derived the conditions of the singularities on envelope surfaces. The sufficient conditions of existence of envelope E_1 and E_2 on generating and generated tooth surfaces Σ_1 and Σ_2 were first presented. The necessary condition of coincidence of E_2 with the edge of regression on Σ_2 was also provided.

Fish and Munro (1999) investigated the worm gear production and operating processes and identified the manufacturing error sources relative to a theoretical ideal contact. The measurements of component form, transmission error and marking pattern from several manufactured gear sets were used to quantify individual contributions to the cumulative contact error. Fish and Munro (1999) developed a computer program that calculated the gear tooth form, transmission error and contact marking pattern of a gear set including any effects of manufacturing and operating error sources. According to Fish and Munro, the characteristics of a worm gear set can be accurately predicted once all elements of the design and manufacture are modelled.

2.1.4 Research on Spiroid Gearing

The spiroid gear drive was invented in 1954 by Oliver Saari and then such drives were produced by the Illinois Tool Work Company (Litvin, 1998). The spiroid has two types: helicon – with a cylinder worm; and spiroid – with a taper worm. The tooth profile is not symmetrical. It has a low pressure angle side and a high pressure angle side. The low side is preferred for driving.

There are few publications and little information for spiroid gearing design and manufacturing. Spiroid gearing has many advantages such as high torque capacity,

uniform durability rating, high shock strength, quiet operation, compact package, low cost when mass-produced. Many military applications of spiroid gearing make it of strategic importance (Kirov 1999), but there is little information on spiroid gearing available in the open literature. In Dudley's *Handbook of Practical Gear Design* (1984), some design systems for spiroid and helicon gears have been simply addressed but no explanation is available.

Kirov (1999) presented the main elements of a methodology for the design of spiroid hobs. It was based on conventional methodologies for the design of worm and conical hobs. Kirov investigated the critical elements of effective spiroid hob design and recommended standard modules for spiroid hob. He also discussed the problems of hob-design parameters, geometry, profiling, strength calculations and machine tool adaptation.

Abadjiev and Petrova (1997) developed a mathematical model to describe the surface of meshing of a spiroid gear set. The conditions for the existence of undercutting in the region of meshing was discussed.

Huang et al (1993) presented a new method for the analysis of the lubrication performance of spiroid gears, which combined elastohydrodynamic lubrication analysis with loaded tooth contact analysis. Because oversimplified assumptions are used, the solutions of this method are approximate. Only to a limited extent, did it reflect the lubrication performance of spiroid gears. However, it established the relationship between lubrication performance and the design, manufacture, and operating conditions of spiroid gears. It can be considered that Huang et al's approach laid the foundation for further studies.

In spiroid gear production, the wear of the abrasive grinding wheel causes changes in its diameter. This leads to diameter ratio and axial distance alteration during enveloping the tool and the work piece (pinion). Therefore it significantly affects the geometrical accuracy of the machined profile for the case of a given tool profile. Dudas et al (1996) presented a new technology, the use of a tool that changed its shape during the machining process, to solve this problem. However, this method

requires the application of numerical controlled machines and cannot be implemented in conventional machines.

Duke and Walton (1999) addressed some aspects of Spiradrive gearing efficiency (Spiradrive® is a registered trade-mark of The Davall Gears Company Ltd. It is a spiroid gearing.). They observed that the efficiency of lubricated metal gear combinations followed the same general rules as that of worm gearing. The worm spiral angle dominated the efficiency of a gearset and the higher the spiral angle the higher the efficiency.

2.2 3D MODELLING OF GEAR DRIVES

More and more researchers are interested in the methods of gear solid modelling. The *Question and Answer* pages of the *Gear Industry Home Page* (Gear Industry, accessed on 22 April 1999) has received numerous questions asking how to model gears in solid modelling applications such as AutoCAD, SolidWork and Pro/Engineer.

The geometry of gears such as worm, spiroid and hypoid gears are extremely complex. The contact lines, contact paths and tooth profiles of gear drives published in the literature before 1990 were mostly 2D drawings. With the rapid development of computer hardware and CAD software, many researchers are engaged with 3D CAD models of gear drives.

Fong and Tsay (1991) presented a wire frame 3D model of a circular-cut spiral bevel gear (Figure 2.8). The following procedures are used to construct the model:

(1) Solve the mathematical model;
(2) Obtain the top land by solving a set of meshing and face cone equations;
(3) Obtain the wire frame of the outer cone by solving a set of equations;
(4) Again by solving a set of equations, draw the tooth surface.

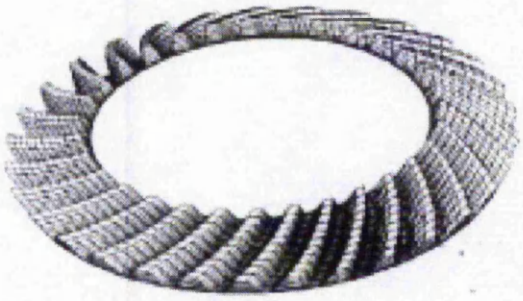


Figure 2.8 Meshed spiral bevel gear (from Fong and Tsay 1991)

This method is time-consuming and not flexible to change. Another shortcoming of this method is that it is unable to generate the information of the root fillet. The spiral bevel gear shown in Figure 2.8 has no root fillet.

Tsay et al (1995) presented a 3D dual-lead worm gear model built in AutoCAD. Bair and Tsay (1998a, 1998b) modelled a ZK-type dual-lead worm gear drive. The 3D ZK worm gear drive was modelled by applying the developed gear set mathematical model. The points of worm and gear surfaces were obtained after solving a set of complicated meshing equations derived from the mathematical model. Then the graphical techniques were used to construct the 3D model. The three-dimensional computer graph of dual-lead worm gear surface is shown in Figure 2.9. This method is time-consuming and is not flexible to incorporate changes.

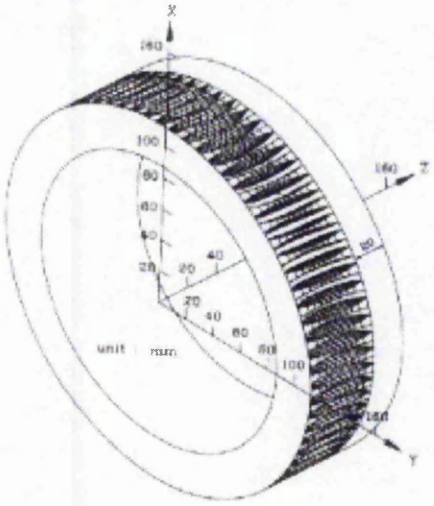


Figure 2.9 Dual-lead worm gear (from Tsay et al 1995)

Litvin et al (1996) presented a hypoid gear drive model mesh for finite element analysis. In this model, the surfaces of the gear and the pinion were created using 20 two-dimensional cross-section profiles. The two-dimensional profiles were obtained using the plane that was perpendicular to the axis of rotation of the pinion to cut the pinion surface. Similarly the two-dimensional profiles were obtained by the intersection of the gear surfaces and the plane passing through the axis of the head cutter. The gear model thus was constructed in a 3D CAD software package.

Su et al (1999b) presented a more advanced 3D modelling method for involute worm gear drives in Pro/Engineer. Figure 2.10 shows the procedures used to model worm gears. Comparing with previous 3D modelling methods, Su et al's method has a major advantage in that it requires less mathematical calculations because it directly trims the tooth surfaces and other gear boundary surfaces in Pro/Engineer. The 3D model can be used for the analysis of contact path and interference. However, the fundamental principle of Su et al's modelling method is the same as those mentioned above. It still involves the complicated solutions of non-linear meshing equations. Furthermore, the model is non-parametric. Qin and Qin (2000) also used a similar procedure to produce a 3D hourglass worm gear model.

The available gear design packages nowadays are all based on complicated mathematical models and the accuracy of their solid graphic ability is limited. In contrast, CAD packages have great graphic ability, but they have limited calculation ability and only finite step calculations can be performed. The gear surfaces are constructed by connecting the points together. All 3D gear modelling methods available in current gear design software or literature are based on the following procedures:

- Establish the mathematical model of gear drives according to the manufacturing process and gear meshing theory.
- Calculate the coordinates of points on the contact lines.
- Export the points' coordinates into a neutral file format, e.g., IGES, STEP.
- Import these points' data into a 3D CAD package.

- Construct the datum points into contact curves.
- Construct the curves into surfaces.
- Trim the surfaces according to design parameters (tooth width, tip and root diameters, etc.).
- Pattern the tooth surfaces to get the teeth.
- Transfer the surface features into a solid gear model.

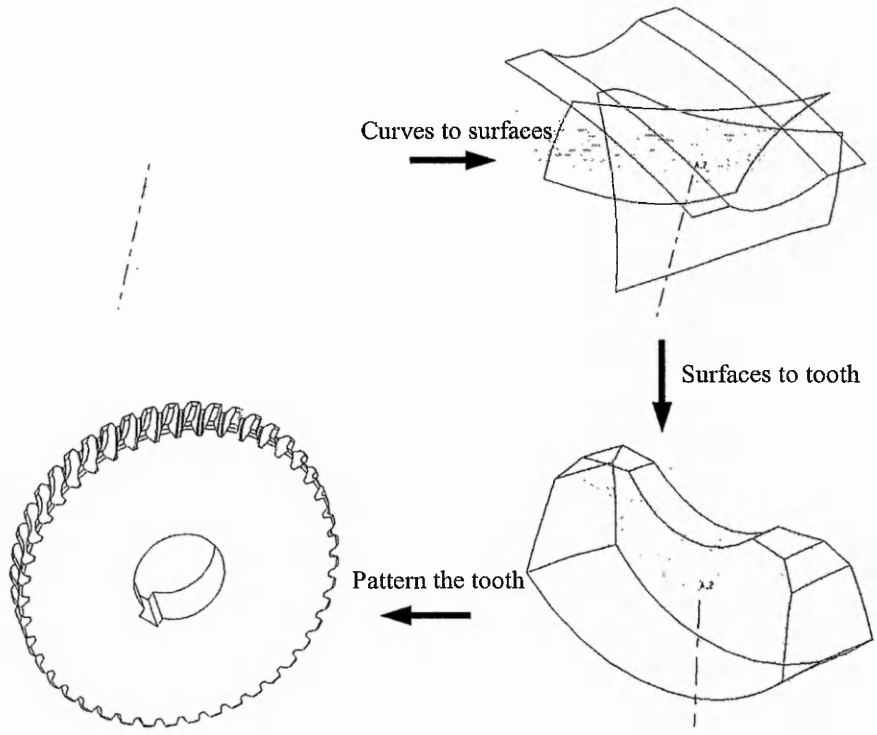


Figure 2.10 Conventional 3D worm gear modelling procedures (from Su et al 1999b)

However, this procedure involves solving the complicated non-linear equations. It is very difficult to find solutions for all the points on the surfaces. Another shortcoming of this method is that it is unable to generate the root fillet. This is because there is no root fillet information available from the equations of meshing. As is well accepted, the root fillet is critical in gear stress and deformation analysis. Furthermore, it is an implicit process with little flexibility for quick modelling and modifications.

Those 3D modelling methods mentioned above are time-consuming and not flexible for changes which are very important in quick modelling and optimisation.

Since the worm and spiroid gear have very complicated tooth geometry, it is very difficult to create 3D models of worm and spiroid gear using conventional modelling methods. One objective of this research is to develop a novel 3D modelling method that can directly and rapidly model the gears in CAD software without involving any complicated calculations. The model should be parametric and directly reflect the gear manufacturing process.

Prior to the introduction of parametric modelling, most programs created engineering models via 2D drawings, 3D wire frames or 3D surface models. In each case, full product descriptions, down to the proper dimensioning scheme and tolerances, were impossible. This was changed with the introduction of parametric modelling.

Parametric modelling allows the design engineer to use the characteristic parameters of a product to *drive* the design of that product. In the case of gear design, key dimensions that would describe the gear being designed such as diametral pitch, pressure angle, root radius and web thickness could be used as the parameters to define the gear. Furthermore, the parameters do not have to be geometric. They can also capture key process information such as case hardening specifications, quality grades, metallurgical properties and even load classifications for the gear being designed.

Programs like Pro/Engineer use these parameters in conjunction with the program's features to generate the shape of the gear and to add in all the essential information to create a product model. In creating a tooth profile, for example, the parametric dimensional information dictates the shape of the tooth and non-geometric parametric information specifies things like the required case hardening depth or the non-destructive test requirements.

While all of these features and abilities are very useful to the designer, they do not deal with the question of the complexity of the calculations needed to define a gear tooth nor the tendency toward approximation inherent in CAD/CAM programs.

Clearly, something more is needed. A new method, completely different from existing methods, needs to be developed to solve the above problem. The method should directly model the worm and spiroid gears in Pro/Engineer without involving any complicated mathematical calculations.

2.3 FINITE ELEMENT ANALYSIS IN GEAR RESEARCH

Due to the complexity of the gear tooth geometry, it is very difficult to use an analytical method to accurately estimate gear stress, deformation and load sharing. The existing calculation methods are mainly based on over-simplified assumptions and formulae developed from the experimental work. A major difficulty associated with experimental investigations is the construction and preparation of models and the accuracy with which the stresses can be determined. Analytical techniques, on the other hand, invariably make some over-simplified assumptions and are limited to symmetric tooth profiles.

The *Finite element method* (FEM) is a well established powerful and reliable tool for engineering analysis. Finite element modelling of the gear pair is highly desirable in order to avoid costly prototyping, particularly where no standard calculations are available. In modern gear research, especially in the late 1990s, researchers are increasingly interested in applying FEM to gear stresses, deformation and load sharing analysis.

However, there are few research papers published in this area. The limited research work available mainly focused on one single gear tooth, not on all teeth involved in the contact region. This obviously does not reflect the real situation. The research work in this area is still in its infancy due to the extremely complicated worm and spiroid gear tooth geometry and contact conditions. No satisfactory work of loaded tooth contact analysis for the worm and spiroid gear drives has so far been carried out.

2.3.1 Single Tooth Finite Element Analysis

Wilcox and Coleman (1973) applied a 2D finite element model to analyse the gear root fillet stresses. The finite element model has been used to analyse tensile fillet stress in generated tooth shapes incorporating either symmetric or asymmetric profiles. Special attention has been given to the asymmetric profiles where no reliable formulae are available. The results of FEA are used to develop a new simplified stress formula that gives tensile fillet stress as a function of geometric tooth shape and general loading conditions.

Moriwaki et al (1993) presented the global local finite element method to a gear stress analysis (GLFEM). The GLFEM is a numerical analysis technique which combines finite element solutions and classical analytical ones on the basis of the energy principle. In this method, the classical analytical solutions are given an almost exact stress field to the elements in which the stress varies very rapidly and where the stress concentration is found. A fine subdivision, therefore, is not required. In the application of the conventional finite element method to gear tooth analysis, a fine subdivision is required especially at the positions near the tooth bottom and the load applied point. There is only two-dimensional analysis available for common use. Therefore, Moriwaki's method is advanced in this aspect. However, the GLFEM is still unable to deal with the complicated multi-teeth contact stress and deformation analysis.

Dabnichki and Crocombe (1999) applied the finite element method to model the local contact conditions in spur gear teeth. In order to obtain a more precise solution of the dynamic gear contact problem, the author applied repeated impact loading in the model.

However, 2D models in which a linear variation of loading across the face width is assumed are incapable of accurately modelling the effects of nonlinear tooth modifications such as crowning and nonlinear lead correction. 3D finite element models are thus needed for gear stress analysis.

Simon (1993) applied the finite element method to analyse the stresses of the worm and the double enveloping gear. He calculated stress distributions in the worm thread and the gear tooth, investigated the influence of the design parameters and the load position on deflections and stresses. On the basis of the calculated results, by using regression analysis and interpolation functions, equations are derived for the calculation of deflections and stresses in the worm thread and in the gear tooth of double enveloping worm gears.

Gosselin et al (1995) presented a loaded tooth contact analysis method to predict the motion error of spiral bevel gear sets. In order to simplify the complexity of the problem, a few general assumptions were made: (1) there is neither friction in the contact zone nor the presence of lubricant that can affect the distribution of the contact pressure, and create an oil film of varying thickness between meshing teeth; (2) displacements due to tooth deflection, shearing or contact deformation are sufficiently small that the tooth surface normal at the contact point is not affected; (3) the gear tooth surface coordinates, contact points along the path of contact, bearing pattern, tooth surface curvatures and principal directions and contact stresses are calculated from unloaded tooth contact analysis; (4) contact is assumed Hertzian and there are no boundary corrections made for edge contact. These can be changed to reflect different operating conditions and the path of contact and contact parameters are then recalculated accordingly; (5) tooth coupling effects are neglected, e.g. the movement of one tooth due to a load applied on an adjacent tooth, although such effects may alter load sharing.

The following two load sharing compatibility conditions were also applied:

- The pinion and the gear blank rotation caused by the displacement of any tooth under load must be the same for all simultaneously meshing tooth pairs (see Figure 2.11). This includes tooth bending deflection and shearing displacement, contact deformation and profile separation due to profile mismatch.
- The sum of the torque contribution of each meshing tooth pair must be equal to the total applied torque.

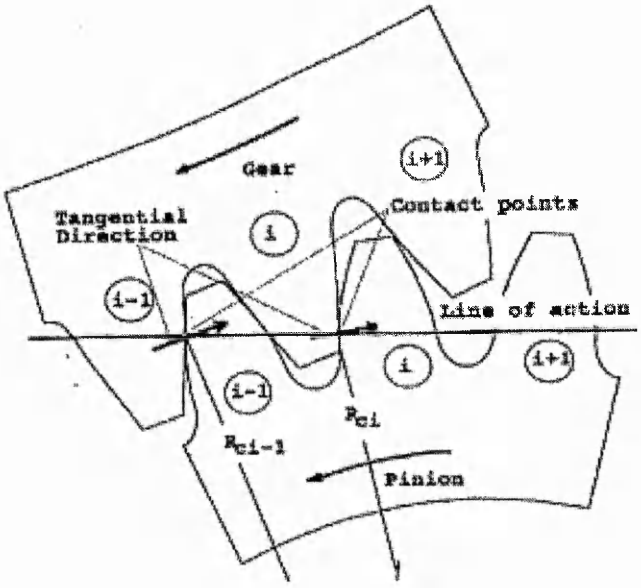


Figure 2.11 Tooth numbering convention (from Gosselin et al 1995)

Gosselin et al (1995) derived a formula for the calculation of load sharing amongst meshing teeth of spiral bevel gears. In their approach, the finite element method was used to determine the tooth displacements under bending and shearing. The classic Hertz theory is applied to obtain the gear tooth contact deformations. The obvious shortcoming of their approach is that it is based on oversimplified assumptions. The tooth coupling effects are neglected even though they are a major factor in the calculations of the loading sharing between mating teeth.

Litvin et al (1996) assumed that the gear contact force at a given position was spread over the area of the contact ellipse. The distribution of the contact force over the contact surface was a semi-ellipsoid. The contact force and its distribution over the contact ellipse, the tooth deflection, the load sharing and the real contact ratio were thus determined by assumption of displacement compatible condition. In Litvin et al's approach, the contact forces were determined first. Then the contact ellipse and the distribution of contact force were determined. Finite element method is applied to the single gear tooth with a solid rim to obtain the tooth deflection and stresses (see Figure 2.12).

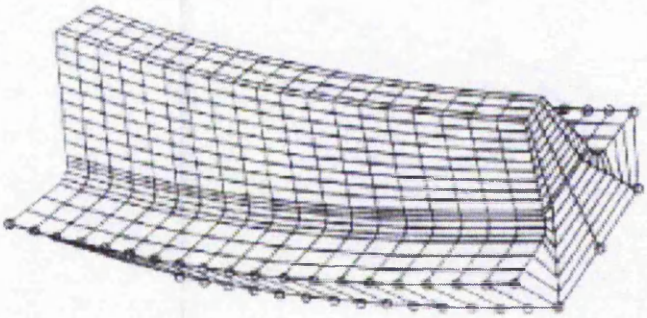


Figure 2.12 Finite element model for the gear (from Litvin et al 1996)

Litvin et al's LTCA method is similar to Gosselin et al's. The blank rotation compatibility condition applied in their approach is an oversimplified assumption. It assumes that if the total position error for a current pair of teeth P_j (j=1, ... s) is $\Delta\theta_j$, then the total position errors in the pairs of teeth being in contact under load must be the same, i.e.,

$$\Delta\theta_1 = \Delta\theta_2 = \ldots = \Delta\theta_s \qquad (2.3.1)$$

This assumption is suitable for rigid body motion; however, the gear teeth are elastic. In the above method, the relation between contact force and deformation is also assumed to be linear. This is not true because the relationship of contact force and deformation is nonlinear.

Zhang and Fang (1997, 1999) presented a model for the analysis of transmission errors of helical gears under load. Zhang and Fang also applied the TCA method first to obtain the position of contact points, tooth surface curvatures, transmission errors without tooth surface deformation and contact ellipses under light load. The TCA is actually used as the pre-processor for loaded tooth contact analysis (LTCA). The LTCA model is based on the long-axis of the contact ellipse that is determined in TCA, i.e., along the relative principal direction at which the relative normal curvature between the two contacting surfaces is the minimum. Using finite element modelling, the deformation of the gear tooth in the direction of surface normal, the gap between the tooth surfaces along the relative principal direction and the transmission error are

related to the distributed load in a system of linear equations that are subjected to a set of non-linear constraints. This system is then solved by a programming technique to determine the transmission errors during a meshing cycle.

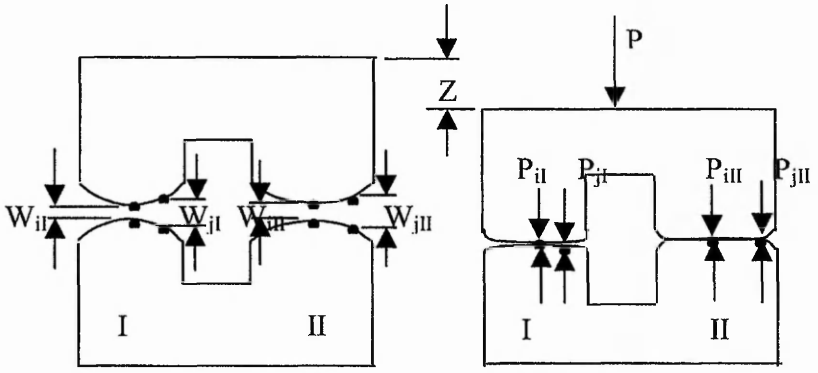


Figure 2.13 Illustration of loaded gear tooth contact forces (from Zhang and Fang 1997)

The model for the tooth contact analysis under load is illustrated in Figure 2.13. As shown in Figure 2.13, two pairs of teeth, denoted by I and II, are in contact at a particular instant during the meshing cycle. For simplicity, the contact load between the two contacting tooth surfaces is assumed to be distributed along the relative principal direction. The tooth curve in Figure 2.13 is the intersection between the tooth surface and the normal plane along the principal direction. In Zhang and Fang's approach, the flexibility matrix is also determined by the finite element method.

Zhang and Fang's approach provided a way for the analysis of loaded tooth contact problems. However, the approach is still limited in TCA that assumes the gear is a rigid body. The model used only one tooth, which obviously does not agree with the real situation. In their approach, the finite element method is only used as a tool to determine the flexibility matrix. The approach is still based on over simplified assumptions.

Su, Yang and Gentle (2000) calculated the meshing stiffness and tooth stress of worm gears using the finite element method. The approach used in Su et al's research is similar to Gosselin et al's and Litvin et al's. The same oversimplified rotation deformation compatibility condition is used. The contact pressures in the contact

region are obtained from assumption (assumed to be Hertzian distribution), not from calculations. A single finite element tooth model is used to calculate the stiffness matrix of teeth. The contact path and contact points are calculated from the unloaded tooth contact analysis.

In all the approaches mentioned above, the position of contact points, tooth surface curvatures and contact ellipses under *load* are all obtained from the *unloaded* tooth contact analysis. The contact forces of multi-teeth contact are all deduced from an over-simplified deformation compatible assumption. The gear tooth models used are single tooth models. The finite element method is only used either as a tool to determine the flexibility matrix or just to calculate the stresses by applying a theoretical contact force on the model. In order to investigate the real tooth contact stresses, a more sophisticate multi-tooth contact model is inevitably necessary.

2.3.2 Multi-Tooth Contact Analysis

Handschuh and Bibel (1999) applied a seven-tooth non-linear finite element model (three pinion teeth and four gear teeth) to simulate 3D multi-tooth contact (see Figure 2.14). The geometrical model was built using the conventional 3d modelling method. First the meshing equation and gear surface equations were established according to the gear kinematics. These equations were solved to get the datum points on the contact lines. Then these datum points were imported to build the spiral bevel gears.

In their analysis, gap elements were used to simulate contact in the initial finite element modelling. However, the alignment of gap elements normal to the complex surfaces was numerically tedious and time-consuming.

Qin and Qin (2000) presented an eight-tooth finite element model of an hourglass worm gear to investigate the load sharing and stresses as shown in Figure 2.15.

The multi-tooth models have obvious advantages over the 2D models and the single tooth 3D models in simulating more closely real gear contact situations. However, the multi-tooth FEA models used by Handschuh and Bibel (1999) and Qin and Qin (2000) are still partial models. The boundary constraints used still have differences

from the real situations. In a real situation, the partial model's boundary surfaces still have rotational and translational deformation but this is very difficult to implement in partial models. The boundary conditions of the models, especially for the non-linear contact stress analysis, have critical effects on the contact force, positions, directions and may greatly affect the accuracy of results. It can even make the results invalid. A full three-dimensional model including the entire pinion and gear would improve the model simulation ability.

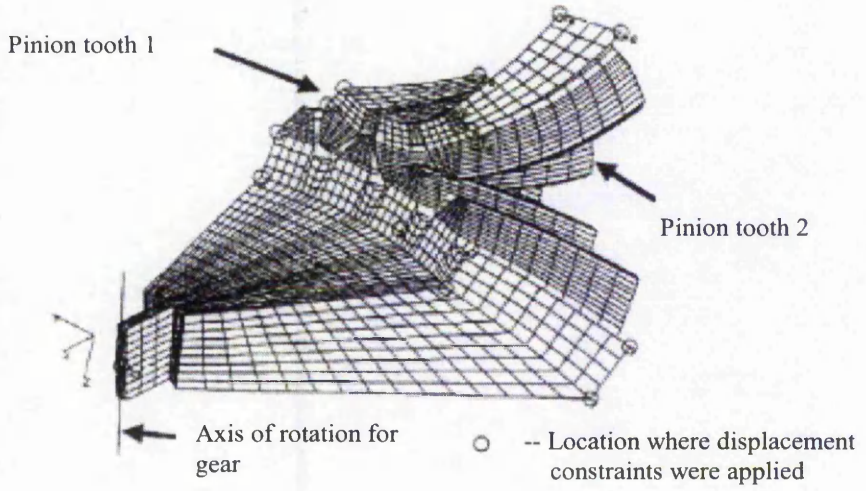


Figure 2.14 Seven-teeth model used in finite element analysis (from Handschuh and Bibel 1999)

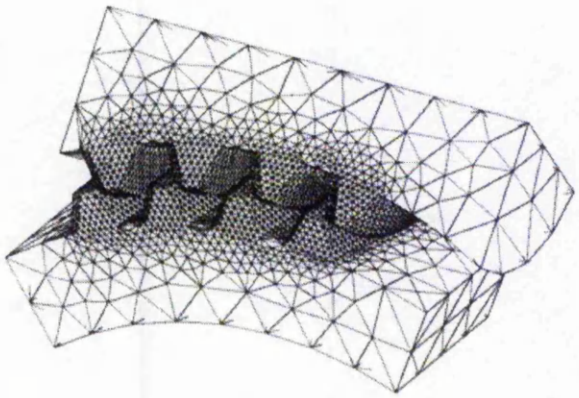


Figure 2.15 Hourglass contact element model (from Qin and Qin 2000)

The existing research utilised gap elements to simulate the contact situation and estimate the contact deformations and forces involved. By using gap elements, the contact paths have to be determined from the classic tooth contact analysis. It seems

contradictory that loaded tooth contact analysis uses unloaded tooth contact paths. The gap element nodes have to be prescribed on the contact path according to the results of the unloaded tooth contact analysis. However, alignment of gap elements normal to the complex surface was numerically tedious. This makes the gear FEA work very difficult.

The latest development in gear multi-tooth contact analysis is the application of the full gear model and the latest general surface-to-surface contact element technique. The general tooth surface-to-surface contact element method can calculate the contact automatically and can determine the contact force, directions and even can evaluate the effects of friction. This technique makes the gear FEA work much easier.

2.4 CONCLUSIONS

Currently there are no efficient methods to modify the worm and spiroid gear drives to obtain the localised tooth contact. The existing method to obtain a favourable bearing contact of a gear tooth is based on the initial running-in of the gearset under load. This is time-consuming and costly. Many modification methods proposed by researchers (Colbourne, 1989, Seol and Litvin, 1996a, Litvin and Kim, 1997, Livtin and Donno 1998, Donno and Litvin, 1999) are based on using an oversized hob to cut the gear. These methods can achieve localisation of bearing contact of worm gear drives but the use of an oversized hob will cause interference between the meshing teeth of the worm and wheel. Designing the hob and worm with the same pitch diameter and coincident axes but different cross-section profile is a good method. This method does not cause interference in the meshing teeth. However, this approach requires a specially designed hob with curved cross-section profiles that are difficult to produce and can be very expensive. In short, all the approaches mentioned above have made great contributions to achieving the localised gear tooth bearing contact, however, they are difficult to implement using standard gear hobbing machines.

No literature concerning the direct modelling of the worm or spiroid gear in advanced CAD packages has been identified. With the rapid development of computer and solid modelling techniques, more and more researchers are interested in rapid parametric solid modelling of gear drives. However, the currently available methods

for solid modelling of gear drives are all based on mathematical models, which require solutions to complicated non-linear equations.

Most work reported did not present an effective method to analyse the tooth behaviour under load. The conventional TCA assumes the gear surface as a rigid body. The deformation of the two contacting teeth is simplified by an elastic approach that is uniformly imposed over the whole tooth surface. The contact between a pair of teeth is assumed to be spread over an elliptic area centred at the point of contact. This is obviously not a true reflection of the real situation. In reality, especially when the gears are under heavy load, the deformation and load distribution on the gear tooth surfaces can affect the meshing characteristics and consequently the gear transmission errors may significantly differ from those that are computed by the TCA analysis.

No satisfactory work on tooth contact analysis under load for the worm and spiroid gear drives has so far been carried out. Due to the complexity of the gear drives, there are few mutli-tooth contact analysis models reported. Most researchers only developed single tooth finite element models. This is better than the conventional method based on beam theory but the single tooth model still does not reflect the real situation. The research work in this area is still in its infancy due to the extremely complicated worm and spiroid gear tooth geometry and contact conditions.

Therefore, there is a need to develop novel techniques to cater for the problems identified from the literature review.

CHAPTER 3 Optimum Design and Numerical Simulation of Spiroid Gears

A novel approach to obtaining localised bearing contact of spiroid gear drives has been developed. The localised contact is achieved by modifying the pinion tooth surface. With this approach, only the pinion cutter's geometrical angles and mounting position need to be adjusted, and hence it is simpler and more economical than other methods. In this chapter the following topics are presented: an overview of the approach, equations for modified spiroid gear tooth geometry, and computer simulation results. The results confirm that the proposed modification of the tooth geometry permits localisation of the bearing contact.

3.1 INTRODUCTION

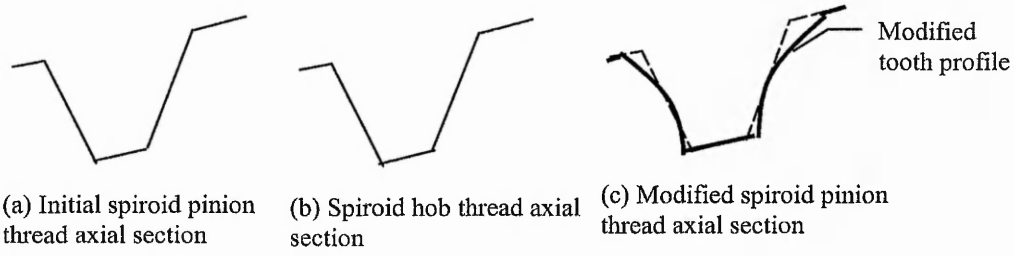
Spiroid gears are cut with a tapered hob which is identical to the spiroid pinion. The hobbing process duplicates the operation of the spiroid gearing (Abadjiev and Petrova, 1997, Kirov, 1999). Such a spiroid gear drive has an instantaneous line contact between the pinion and the face gear. However, it is sensitive to misalignment which causes a large shift of the bearing contact to the edge.

In this chapter, a new method is presented to achieve localised bearing contact for spiroid gears. With this method, the localised contact is achieved by slightly adjusting two mounting angles of the pinion cutter when the pinion is cut. This method can be implemented on conventional equipment at no extra cost and is much simpler and more economical than existing methods.

3.2 OVERVIEW OF THE METHOD

The conventional spiroid pinion considered here is an Archimedean tapered worm. The spiroid gear is produced using a spiroid hob whose thread profile is identical to the spiroid pinion. Such a spiroid gear drive has an instantaneous line contact between the pinion and the gear tooth surfaces and therefore is sensitive to errors such as

misalignment. A solution widely accepted in both research and industrial practice is to localise the tooth contact to reduce the sensitivity.



(a) Initial spiroid pinion thread axial section

(b) Spiroid hob thread axial section

(c) Modified spiroid pinion thread axial section

Figure 3.1 Pinion and hob tooth profile

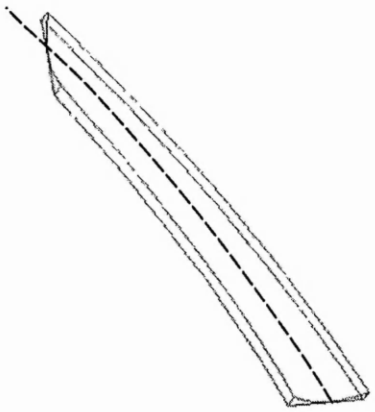


Figure 3.2 Tangent to hob and modified pinion tooth surface

In this research, a novel method has been developed to achieve the localised tooth contact for spiroid gears. The basic idea is to modify the pinion's tooth surface, while its mating gear is produced using a standard hob. The mismatch between the pinion and the gear results in a localised contact on the tooth surfaces. The localised position can be predesigned. Figure 3.1(a) shows the pinion's initial tooth profile (i.e. no modification), which is identical to the hob used to cut the gear shown in Figure 3.1 (b); Figure 3.1 (c) shows the modified pinion's tooth profile. If the modified pinion and hob are put into the same coordinate system, they will be tangent to a spiral helix curve as shown in Figure 3.2.

The mismatch is achieved by modifying the pinion tooth surface. The method to achieve the modification can be briefly described as follows: the geometrical angles of the pinion cutter's cutting edges are changed from the original $\alpha^{(I)}$ and $\alpha^{(II)}$ (see Figure 3.4(a)) to ($\alpha^{(I)}+\Delta\ \alpha^{(I)}$) and ($\alpha^{(II)}+\Delta\ \alpha^{(II)}$) respectively, and the cutter's position is changed as well (see Figure 3.7). Such a modified pinion will get the desired localised tooth bearing contact that has been verified in the tooth contact analysis described in Section 3.6.

Since the above modifications only change the mounting angles of the pinion cutter's blade, the modified pinion can be manufactured using the same machine and equipment. Therefore, it can significantly reduce the cost.

3.3 THE SPIROID GEAR HOB AND PINION SURFACE EQUATIONS

3.3.1 Equations of Spiroid Gear's Hob Tooth Surface

The coordinate systems used for the spiroid gear's hob and pinion surfaces are shown in Figure 3.3. The coordinate system $S_1(O_1, X_1,Y_1,Z_1)$ is rigidly connected to the hob. The coordinate system $S_b(O_b, X_b,Y_b,Z_b)$ is rigidly connected to the hob and pinion's cutter, with its origin O_b situated at the intersection point of the straight lines of cutting edges I and II.

The hob surfaces are generated by the two cutting edges I and II which are at the axial plane of the hob. The cutter moves along a space spiral helix. The cutter's movement can be described as the combination of three simultaneous motions: (1) rotating around the pinion centre axis; (2) translational moving along the pinion centre axis; (3) moving inwards into the pinion's centre. Figure 3.4 shows the cutter's two different positions during its movement: the origin O_{b0} is at the initial position of the cutter's movement. After the cutter is rotated about axis Z_1 with angle θ, the coordinate system S_b's original position is reached at $O_{b\theta}$.

The vector of the pinion cutter's cutting edges, i.e. the generatrices of the pinion tooth surface, in coordinate system S_b is given by

$$\mathbf{r}_b^{(i)}(u_h) = \begin{Bmatrix} u_h \cos\alpha^{(i)} \\ 0 \\ \mp u_h \sin\alpha^{(i)} \end{Bmatrix} \tag{3.3.1}$$

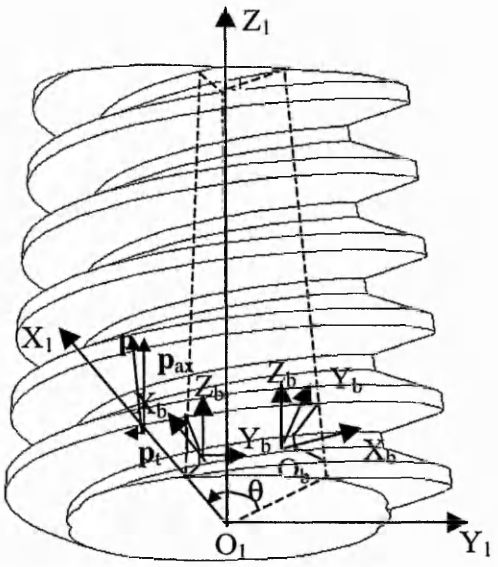


Figure 3.3 Coordinate systems in tapered spiroid pinion

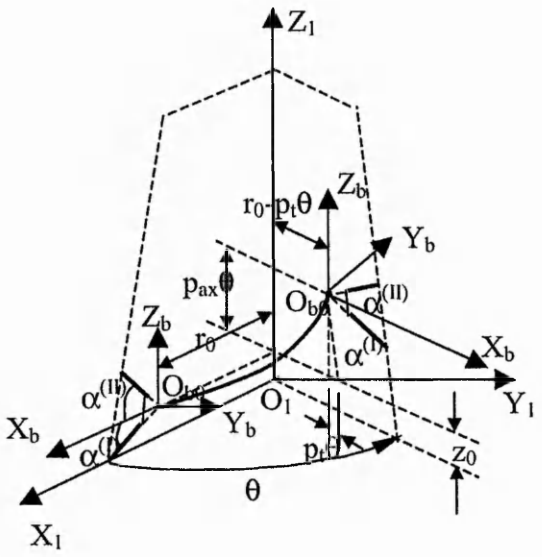


Figure 3.4 Pinion cutter's movement in relation to the coordinate systems

where, as shown in Figure 3.5, u_h is the surface parameter. $\alpha^{(i)}$ is the angles of generatrix, i=I, II indicating the two cutting edges respectively, and the sign "–" is for i=I and the sign "+" is for i=II.

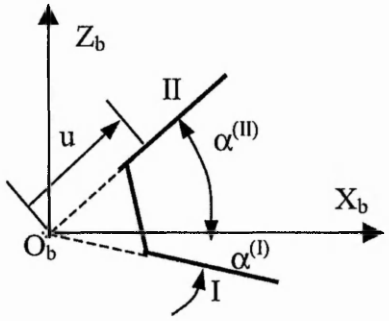


Figure 3.5 Cutter's two cutting edges I and II in coordinate system S_b

The hob tooth surface is thus obtained as

$$\mathbf{r}_{1h}^{(i)}(u_h, \theta_h) = \mathbf{M}_{1b} \cdot \mathbf{r}_b^{(i)}(u_h) \tag{3.3.2}$$

where θ_h is the hob tooth surface parameter; $\mathbf{M}_{1b}$ is the transformation matrix from coordinate system S_b to S_1,

$$\mathbf{M}_{1b} = \begin{bmatrix} \cos\theta_h & -\sin\theta_h & 0 & (r_0 + p_t \cdot \theta_h) \cdot \cos\theta_h \\ \sin\theta_h & \cos\theta_h & 0 & (r_0 + p_t \cdot \theta_h) \cdot \sin\theta_h \\ 0 & 0 & 1 & z_0 + p_{ax} \cdot \theta_h \\ 0 & 0 & 0 & 1 \end{bmatrix} \tag{3.3.3}$$

where p_t is the screw parameter in the direction perpendicular to the hob axis, and p_{ax} is the screw parameter in the axial direction.

Substituting Equation (3.3.3) into Equation (3.3.2), the spiroid hob surface equation is then rewritten as

$$\mathbf{r}_{1h}^{(i)}(u_h,\theta_h)=\begin{Bmatrix}(u_h\cos\alpha^{(i)}+r_0+p_t\cdot\theta_h)\cdot\cos\theta_h\\(u_h\cos\alpha^{(i)}+r_0+p_t\cdot\theta_h)\cdot\sin\theta_h\\\mp u_h\sin\alpha^{(i)}+p_{ax}\cdot\theta_h+z_0\\1\end{Bmatrix} \tag{3.3.4}$$

As a numerical example from Equation (3.3.4), Figure 3.6 shows the surface of the spiroid gear hob used in the example of numerical tooth contact analysis described in Section 3.6.

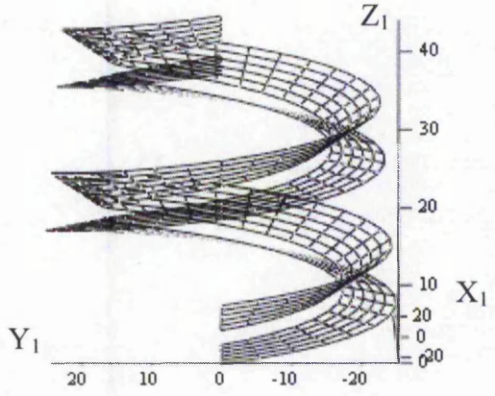


Figure 3.6 Right hand hob thread surface (mm)

3.3.2 The Normal to the Hob Tooth Surface

The hob surface normal can be given by the following equations:

$$\mathbf{N}_{1h}=\frac{\partial\mathbf{r}_{1h}}{\partial u_h}\times\frac{\partial\mathbf{r}_{1h}}{\partial\theta_h} \tag{3.3.5}$$

Substituting Equation (3.3.4) into the first part of the right side of Equation (3.3.5), we get

$$\frac{\partial\mathbf{r}_{1h}}{\partial u_h}=\begin{Bmatrix}\cos\alpha^{(i)}\cdot\cos\theta_h\\\cos\alpha^{(i)}\cdot\sin\theta_h\\\mp\sin\alpha^{(i)}\end{Bmatrix} \tag{3.3.6}$$

Similarly, the second part of the right side of Equation (3.3.5) will be obtained as follows

$$\frac{\partial \mathbf{r}_{1h}}{\partial \theta_h} = \begin{Bmatrix} -(u_h \cdot \cos\alpha^{(i)} + r_0 + p_t \cdot \theta_h) \cdot \sin\theta_h + p_t \cdot \cos\theta_h \\ (u_h \cdot \cos\alpha^{(i)} + r_0 + p_t \cdot \theta_h) \cdot \cos\theta_h + p_t \cdot \sin\theta_h \\ p_{ax} \end{Bmatrix} \tag{3.3.7}$$

With Equation (3.3.4), Equation (3.3.7) can be simplified as

$$\frac{\partial \mathbf{r}_{1h}}{\partial \theta_h} = \begin{Bmatrix} -y_{1h} + p_t \cdot \cos\theta_h \\ x_{1h} + p_t \cdot \sin\theta_h \\ p_{ax} \end{Bmatrix} \tag{3.3.8}$$

By substituting Equations (3.3.6), (3.3.8) into Equation (3.3.5) and following the rules of a vector product gives

$$\mathbf{N}_{1h} = \begin{vmatrix} \mathbf{i}_1 & \mathbf{j}_1 & \mathbf{k}_1 \\ \cos\alpha^{(i)} \cdot \cos\theta_h & \cos\alpha^{(i)} \cdot \sin\theta_h & \mp\sin\alpha^{(i)} \\ -y_{1h} + p_t \cdot \cos\theta_h & x_{1h} + p_t \cdot \sin\theta_h & p_{ax} \end{vmatrix}$$

The above equation can be written in the following form

$$\mathbf{N}_{1h} = \mathbf{N}_{1hx} \cdot \mathbf{i}_1 + \mathbf{N}_{1hy} \cdot \mathbf{j}_1 + \mathbf{N}_{1hz} \cdot \mathbf{k}_1 \tag{3.3.9}$$

where

$$N_{1hx} = p_{ax} \cdot \cos\alpha^{(i)} \cdot \sin\theta_h \pm \sin\alpha^{(i)} \cdot (x_{1h} + p_t \cdot \sin\theta_h) \tag{3.3.10}$$

$$N_{1hy} = -p_{ax} \cdot \cos\alpha^{(i)} \cdot \cos\theta_h \mp \sin\alpha^{(i)} \cdot (-y_{1h} + p_t \cdot \cos\theta_h) \tag{3.3.11}$$

$$N_{1hz} = (u_h \cdot \cos\alpha^{(i)} + r_{01} + p_t \cdot \theta_h) \cdot \cos\alpha^{(i)} \tag{3.3.12}$$

The unit normal to the hob tooth surface is thus obtained as

$$\mathbf{n}_{1h}(u_h,\theta_h)=\frac{1}{\sqrt{(N_{1hx})^2+(N_{1hy})^2+(N_{1hz})^2}}\mathbf{N}_{1h}(u_h,\theta_h) \tag{3.3.13}$$

3.3.3 Equations of Modified Pinion Tooth Thread Surface

With the method developed in this project, the generatrix of the modified spiroid pinion tooth surface is still a straight line, but the angle is changed with increments $\Delta\alpha^{(I)}$ for side I, $\Delta\alpha^{(II)}$ for side II, as shown in Figure 3.7. In addition, the cutter's position is different from the original setting, which is illustrated in Figure 3.7 using the coordinate system rigidly connected to the cutter. The new setting is represented using coordinate system S_m (O; X_m,Y_m,Z_m), and its position is determined as follows:

1. Plane $Z_mO_mY_m$, where the generating line lies, rotates from the initial plane $Z_bO_bY_b$ about axis Z_b with angle ξ;
2. S_m moves to a new position with its origin O_m away from O_b with Δx, Δy, Δz, while the axis Z_m is kept parallel to Z_b .

Angle ξ may be different for the two cutting edges I and II. It is determined by the calculation results.

The position vector of the generating line expressed in coordinate system S_m is

$$\mathbf{r}_m^{(i)}(u_w)=\begin{Bmatrix} u_w\cos(\alpha^{(i)}+\Delta\alpha^{(i)}) \\ 0 \\ \mp u_w\sin(\alpha^{(i)}+\Delta\alpha^{(i)}) \end{Bmatrix} \tag{3.3.14}$$

where i=I, II, indicating the generating lines I and II respectively.

The modified pinion thread surface can be obtained from the modified cutter surfaces through a series of transformations.

$$\mathbf{r}_{1w}^{(i)}(u_w, \theta_w) = \mathbf{M}_{1b} \cdot \mathbf{M}_{bm} \cdot \mathbf{r}_m^{(i)}(u_w) \tag{3.3.15}$$

where $\mathbf{M}_{bm}$ is the transformation matrix from S_m to S_b,

$$M_{bm} = \begin{bmatrix} \cos\xi & \sin\xi & 0 & \Delta x \\ -\sin\xi & \cos\xi & 0 & \Delta y \\ 0 & 0 & 1 & \Delta z \\ 0 & 0 & 0 & 1 \end{bmatrix} \tag{3.3.16}$$

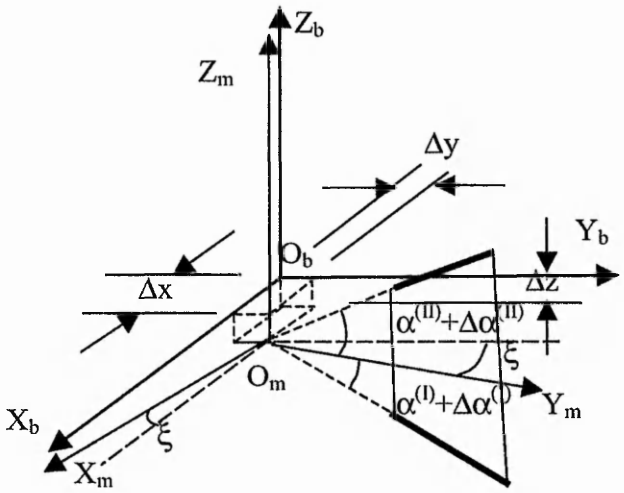


Figure 3.7 Coordinate systems for modified pinion

With Equations (3.3.7) and (3.3.3), the modified spiroid pinion surface equation is then obtained as follows

$$\mathbf{r}_{1w}^{(i)}(u_w, \theta_w) = \begin{Bmatrix} (u_w \cos(\alpha^{(i)} + \Delta\alpha^{(i)}) \cdot \cos\xi + \Delta x + r_0 + p_t \cdot \theta_w) \cdot \cos\theta_w \\ -(\Delta y - u_w \cos(\alpha^{(i)} + \Delta\alpha^{(i)}) \cdot \sin\xi) \cdot \sin\theta_w \\ (u_w \cos(\alpha^{(i)} + \Delta\alpha^{(i)}) \cdot \cos\xi + \Delta x + r_0 + p_t \cdot \theta_w) \cdot \sin\theta_w \\ +(\Delta y - u_w \cos(\alpha^{(i)} + \Delta\alpha^{(i)}) \cdot \sin\xi) \cdot \cos\theta_w \\ \mp u_w \sin(\alpha^{(i)} + \Delta\alpha^{(i)}) + p_{ax} \cdot \theta_w + z_0 + \Delta z \\ 1 \end{Bmatrix} \tag{3.3.17}$$



At the pre-designed contact point M(x_M,y_M,z_M), the gear hob surface parameter is $u_h = u_h^{(M)}$ and the pinion surface parameter is $u_w = u_w^{(M)}$. The other surface parameters of hob and pinion are the rotating angles of generatrices. They have the equal angles at point M, i.e.

$$\theta_h^{(M)} = \theta_w^{(M)} \tag{3.3.18}$$

At the pre-designed contact point M, the modified pinion and the hob thread surfaces should have the same coordinates. That is

$$\mathbf{r}_{1w}(u_w^{(M)}, \theta_w^{(M)}) = \mathbf{r}_{1h}(u_h^{(M)}, \theta_h^{(M)}) \tag{3.3.19}$$

At point M, the modified pinion and the hob thread surfaces should be in tangent to each other in order to achieve smooth transmission. Given a plane y = kx (considered in three dimensional coordinate system, in which k=tan(φ) and φ is an arbitrary angle) to intersect to the pinion and hob thread surface, there will be two curves obtained: one curve (C_w) is from the intersection with the worm pinion tooth thread; the other (C_h) is from the intersection with the hob. Both curves should be tangent to each other at point M, and hence have the same tangency at point M, i.e.

$$\left.\frac{dz^{(w)}}{dr_{xy}^{(w)}}\right|u = u_w^{(M)} = \left.\frac{dz^{(h)}}{dr_{xy}^{(h)}}\right|u = u_h^{(M)} \tag{3.3.20}$$

where, the superscript w and h indicate pinion and hob respectively, superscript M indicates the contact point M, and

$$dr_{xy} = \frac{x \cdot dx + y \cdot dy}{\sqrt{x^2 + y^2}} \tag{3.3.21}$$

Both curves are in the same plane y=kx. For side I, the curvature of curve C_h should be smaller than that of curve C_w so that the modified pinion tooth will not interfere

with its mating gear but make contact with it at point M. For side II, in contrast, the curvature of curve C_h should be larger than that of curve C_w. That is

$$\left.\frac{d^2 z^{(h)}}{dr_{xy}^2}\right|_{r_{xy} \neq r_M} < \left.\frac{d^2 z^{(w)}}{dr_{xy}^2}\right|_{r_{xy} \neq r_M} \quad \text{(Side I)} \tag{3.3.22}$$

$$\left.\frac{d^2 z^{(h)}}{dr_{xy}^2}\right|_{r_{xy} \neq r_M} > \left.\frac{d^2 z^{(w)}}{dr_{xy}^2}\right|_{r_{xy} \neq r_M} \quad \text{(Side II)} \tag{3.3.23}$$

From Equation (3.3.19), at contact point M, the three equations were obtained as follows

$$\begin{aligned}&(u_w^{(M)} \cos(\alpha^{(i)} + \Delta\alpha^{(i)}) \cdot \cos\xi + \Delta x + r_0 + p_t \cdot \theta_w^{(M)}) \cdot \cos\theta_w^{(M)} \\ &- (\Delta y - u_w \cos(\alpha^{(i)} + \Delta\alpha^{(i)}) \cdot \sin\xi) \cdot \sin\theta_w^{(M)} \\ &= (u_h^{(M)} \cos\alpha^{(i)} + r_0 + p_t \cdot \theta_h^{(M)}) \cdot \cos\theta_h^{(M)}\end{aligned} \tag{3.3.24}$$

$$\begin{aligned}&(u_w^{(M)} \cos(\alpha^{(i)} + \Delta\alpha^{(i)}) \cdot \cos\xi + \Delta x + r_0 + p_t \cdot \theta_w^{(M)}) \cdot \sin\theta_w^{(M)} \\ &+ (\Delta y - u_w^{(M)} \cos(\alpha^{(i)} + \Delta\alpha^{(i)}) \cdot \sin\xi) \cdot \cos\theta_w^{(M)} \\ &= (u_h^{(M)} \cos\alpha^{(i)} + r_0 + p_t \cdot \theta_h^{(M)}) \cdot \sin\theta_h^{(M)}\end{aligned} \tag{3.3.25}$$

$$\begin{aligned}&\mp u_w^{(M)} \sin(\alpha^{(i)} + \Delta\alpha^{(i)}) + p_{ax} \cdot \theta_w^{(M)} + z_0 + \Delta z \\ &= \mp u_h^{(M)} \sin\alpha^{(i)} + p_{ax} \cdot \theta_h^{(M)} + z_0\end{aligned} \tag{3.3.26}$$

For the sake of simplification, let $\theta_h^{(M)} = \theta_w^{(M)} = \theta$. Collecting terms and rewriting the above three equations, we have

$$\begin{aligned}&(u_w^{(M)} \cos(\alpha^{(i)} + \Delta\alpha^{(i)}) \cdot \cos\xi + \Delta x - u_h^{(M)} \cos\alpha) \cdot \cos\theta \\ &= (\Delta y - u_w^{(M)} \cos(\alpha^{(i)} + \Delta\alpha^{(i)}) \cdot \sin\xi) \cdot \sin\theta\end{aligned} \tag{3.3.27}$$

$$\begin{aligned}&(u_w^{(M)} \cos(\alpha^{(i)} + \Delta\alpha^{(i)}) \cdot \cos\xi + \Delta x - u_h^{(M)} \cos\alpha) \cdot \sin\theta \\ &= -(\Delta y - u_w^{(M)} \cos(\alpha^{(i)} + \Delta\alpha^{(i)}) \cdot \sin\xi) \cdot \cos\theta\end{aligned} \tag{3.3.28}$$

$$\Delta z = \mp u_h^{(M)} \sin\alpha - (\mp) u_w^{(M)} \sin(\alpha + \Delta\alpha) \tag{3.3.29}$$

To simply the above equations, introduce the symbol

$$\beta = (u_w^{(M)} \cos(\alpha^{(i)} + \Delta\alpha^{(i)}) \cdot \cos\xi + \Delta x - u_h^{(M)} \cos\alpha) \tag{3.3.30}$$

$$\kappa = (\Delta y - u_w^{(M)} \cos(\alpha^{(i)} + \Delta\alpha^{(i)}) \cdot \sin\xi) \tag{3.3.31}$$

Thus, Equations (3.3.27), (3.3.28) can be simplified as follows

$$\beta \cos\theta = \kappa \sin\theta \tag{3.3.32}$$

$$\beta \sin\theta = -\kappa \cos\theta \tag{3.3.33}$$

Multiplying the left term and the right term of Equation (3.3.32) with the left and the right term of Equation (3.3.33) respectively and rearranging the equations, we have

$$(\beta^2 + \kappa^2) \cdot \sin\theta \cdot \cos\theta = 0 \tag{3.3.34}$$

Considering that $\sin\theta \cdot \cos\theta = \frac{1}{2}\sin 2\theta$, and for any given arbitrary value of θ Equation (3.3.34) should be satisfied. The only solution of Equation (3.3.34) is that the other term of above equation must equal to zero. Thus the following equation will be obtained

$$\beta^2 + \kappa^2 = 0 \tag{3.3.35}$$

To find the real solution of Equation (3.3.35) will naturally yield the following two equations

$$\beta = 0 \tag{3.3.36}$$

$$\kappa = 0 \tag{3.3.37}$$

Substituting Equations (3.3.36), (3.3.37) into Equations (3.3.30), (3.3.31) gives

$$u_w^{(M)} \cos(\alpha^{(i)} + \Delta\alpha^{(i)}) \cdot \cos\xi + \Delta x - u_h^{(M)} \cos\alpha^{(i)} = 0 \tag{3.3.38}$$

$$\Delta y - u_w^{(M)} \cos(\alpha^{(i)} + \Delta\alpha^{(i)}) \cdot \sin\xi = 0 \tag{3.3.39}$$

The translational displacements of the origin O_b to O_m are thus derived by rewriting Equations (3.3.38), (3.3.39) and (3.3.29) as follows

$$\Delta x = -u_w^{(M)} \cos(\alpha^{(i)} + \Delta\alpha^{(i)}) \cdot \cos\xi + u_h^{(M)} \cos\alpha^{(i)} \tag{3.3.40}$$

$$\Delta y = u_w^{(M)} \cos(\alpha^{(i)} + \Delta\alpha^{(i)}) \cdot \sin\xi \tag{3.3.41}$$

$$\Delta z = \mp u_h^{(M)} \sin\alpha^{(i)} - (\mp) u_w^{(M)} \sin(\alpha^{(i)} + \Delta\alpha^{(i)}) \tag{3.3.42}$$

Assuming ξ, $\Delta\alpha$ and the point M's coordinates are given, the modification parameters Δx, Δy, Δz can be obtained. The angles ξ and $\Delta\alpha$ are calculated using the tangent condition expressed by Equations (3.3.20) - (3.3.23).

Figure 3.8 to Figure 3.11 show one example of the tooth profiles of the modified pinion and the hob used to cut the mating spiroid gear. Their major design parameters are listed in Table 3.1.

Figure 3.8 and Figure 3.9 show the tooth profile results related to the generating line of side I with modifying parameters ξ=2° and $\Delta\alpha$=0.0044°. Figure 3.8 shows the tooth profiles of the hob and the modified pinion in the axial section. The differences between them are clearly indicated in Figure 3.9. Similarly, the tooth profile results for side II with ξ= -2.5° and $\Delta\alpha$=0.255° are shown in Figure 3.10 and Figure 3.11. Note that the ξ values are different. For the given example, the contact point is pre-designed at the middle of the tooth surface as shown in Figure 3.9 and Figure 3.11.

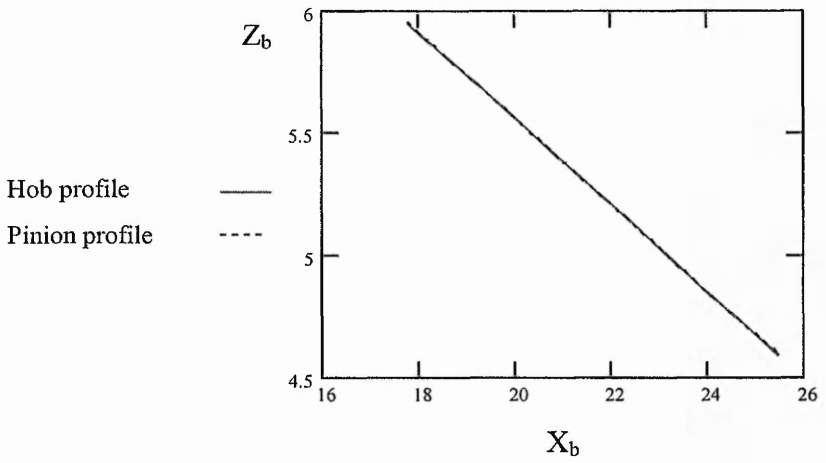


Figure 3.8 Axial section profile of hob thread and modified pinion thread (Side I)ξ=2°, $\Delta\alpha$=0.252° (unit: mm)

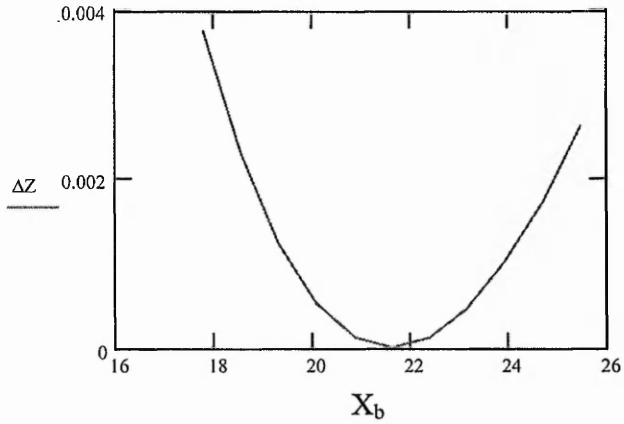


Figure 3.9 Difference in hob and pinion's axial section profile (Side I) $\Delta Z=Z_{\text{hob thread}} - Z_{\text{modified pinion thread}}$ ξ=2°, $\Delta\alpha$=0.252° (unit: mm)

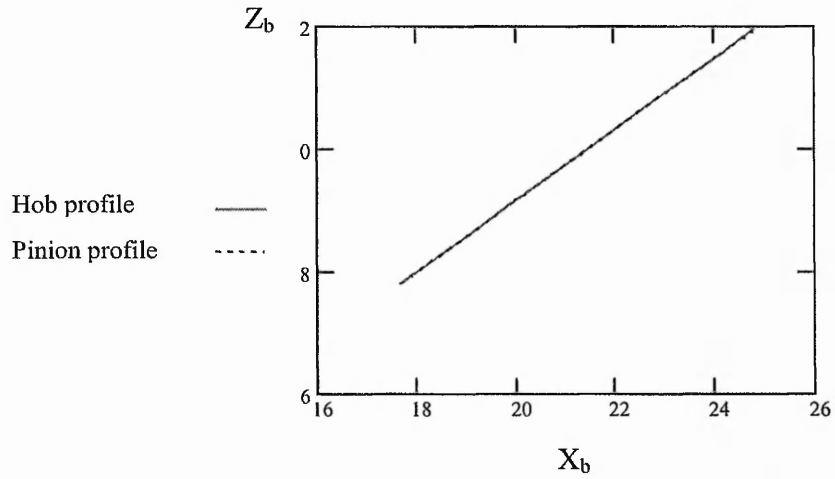


Figure 3.10 Axial section of hob thread and modified pinion thread (Side II) ξ=-2.5°, $\Delta\alpha$=0.255 (unit: mm)

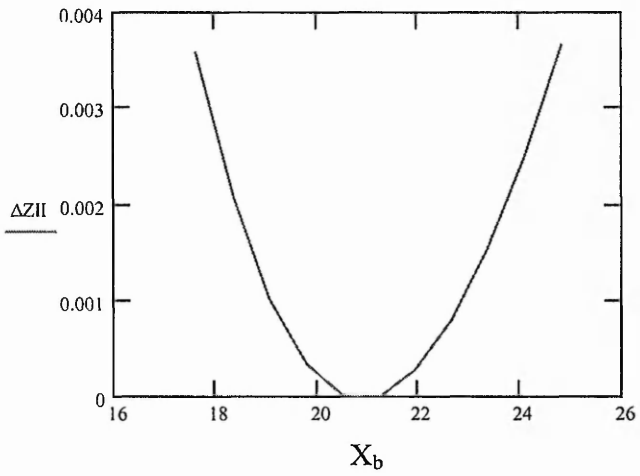


Figure 3.11 Difference in hob and pinion's axial section profile: $\Delta Z=Z_{\text{hob thread}} - Z_{\text{modified pinion thread}}$ (Side II) $\xi=2.5°$, $\Delta\alpha=0.255°$ (unit: mm)

3.3.4 The Unit Normal to the Modified Pinion Tooth Surface

The unit normal to themodified pinion surface can be calculated from its surface equations by the following equation

$$\mathbf{n}_{1w}(u_w,\theta_w)=\frac{\dfrac{\partial \mathbf{r}_{1w}}{\partial u_w}\times\dfrac{\partial \mathbf{r}_{1w}}{\partial \theta_w}}{\left|\dfrac{\partial \mathbf{r}_{1w}}{\partial u_w}\times\dfrac{\partial \mathbf{r}_{1w}}{\partial \theta_w}\right|} \tag{3.3.43}$$

The surface equation of modified pinion $\mathbf{r}_{1w}$ is represented in Equation (3.3.17). The first term of above equation thus can be derived as follows

$$\frac{\partial \mathbf{r}_{1w}}{\partial u_w}=\begin{Bmatrix}\cos(\alpha^{(i)}+\Delta\alpha^{(i)})\cdot\cos(\theta_w-\xi)\\ \cos(\alpha^{(i)}+\Delta\alpha^{(i)})\cdot\sin(\theta_w-\xi)\\ \mp\sin(\alpha^{(i)}+\Delta\alpha^{(i)})\end{Bmatrix} \tag{3.3.44}$$

The unit surface normal is a complex expression and is most conveniently calculated using a computer program. In order to write the computing codes easily and clearly, Equation (3.3.44) is rewritten in the following form

$$\frac{\partial \mathbf{r}_{1w}}{\partial u_w} = \begin{Bmatrix} r_{ux}^{(w)} \\ r_{uy}^{(w)} \\ r_{uz}^{(w)} \end{Bmatrix} \tag{3.3.45}$$

The other term of Equation (3.3.43) is derived in a similar manner and expressed as follows

$$\frac{\partial \mathbf{r}_{1w}}{\partial \theta_w} = \begin{Bmatrix} -y_{1w} + p_t \cdot \cos\theta_w \\ x_{1w} + p_t \cdot \sin\theta_w \\ p_{ax} \end{Bmatrix} \tag{3.3.46}$$

Equation (3.3.46) is further rewritten as follows

$$\frac{\partial \mathbf{r}_{1w}}{\partial \theta_w} = \begin{Bmatrix} r_{\theta x}^{(w)} \\ r_{\theta y}^{(w)} \\ r_{\theta z}^{(w)} \end{Bmatrix} \tag{3.3.47}$$

Therefore the normal to the pinion tooth surface can be derived as

$$\mathbf{N}_{1w}(u_w, \theta_w) = \frac{\partial \mathbf{r}_{1w}}{\partial u_w} \times \frac{\partial \mathbf{r}_{1w}}{\partial \theta_w} = \begin{vmatrix} \mathbf{i}_w & \mathbf{j}_w & \mathbf{k}_w \\ r_{ux}^{(w)} & r_{uy}^{(w)} & r_{uz}^{(w)} \\ r_{\theta x}^{(w)} & r_{\theta y}^{(w)} & r_{\theta z}^{(w)} \end{vmatrix} \tag{3.3.48}$$

For the sake of simplicity, writing the pinion normal in the following form

$$\mathbf{N}_{1w}(u_w, \theta_w) = N_{1wx} \cdot \mathbf{i}_w + N_{1wy} \cdot \mathbf{j}_w + N_{1wz} \cdot \mathbf{k}_w \tag{3.3.49}$$

where

$$N_{1wx} = \begin{vmatrix} r_{uy}^{(w)} & r_{uz}^{(w)} \\ r_{\theta y}^{(w)} & r_{\theta z}^{(w)} \end{vmatrix} = r_{uy}^{(w)} \cdot r_{\theta z}^{(w)} - r_{uz}^{(w)} \cdot r_{\theta y}^{(w)} \tag{3.3.50}$$

$$N_{1wy} = -\begin{vmatrix} r_{ux}^{(w)} & r_{uz}^{(w)} \\ r_{\theta x}^{(w)} & r_{\theta z}^{(w)} \end{vmatrix} = r_{uz}^{(w)} \cdot r_{\theta x}^{(w)} - r_{ux}^{(w)} \cdot r_{\theta z}^{(w)} \tag{3.3.51}$$

$$N_{1wz} = \begin{vmatrix} r_{ux}^{(w)} & r_{uy}^{(w)} \\ r_{\theta x}^{(w)} & r_{\theta y}^{(w)} \end{vmatrix} = r_{ux}^{(w)} \cdot r_{\theta y}^{(w)} - r_{uy}^{(w)} \cdot r_{\theta x}^{(w)} \tag{3.3.52}$$

Finally the unit normal to the modified pinion tooth surface is obtained as follows

$$\mathbf{n}_{1w}(u_w, \theta_w) = \frac{1}{\sqrt{(N_{1wx})^2 + (N_{1wy})^2 + (N_{1wz})^2}} \mathbf{N}_{1w}(u_w, \theta_w) \tag{3.3.53}$$

3.4 SPIROID GEAR SURFACE EQUATIONS

The spiroid gear tooth is an envelope of the spiroid hob tooth surface. The gear surface is constituted by the instantaneous contact lines between the hob and the gear when they are in mesh. To derive the spiroid gear tooth surface, the following coordinate systems are used:

1. $S_f(O_f;X_f,Y_f,Z_f)$: stationary system connected to the frame with its origin situated on the gear axis
2. $S_p(O_p;X_p,Y_p,Z_p)$: stationary system connected to the frame with its origin situated on the pinion axis
3. $S_w(O_w;X_w,Y_w,Z_w)$: rigidly connected to the pinion
4. $S_1(O_1;X_1,Y_1,Z_1)$: rigidly connected to the hob
5. $S_2(O_2;X_2,Y_2,Z_2)$: rigidly connected to the gear

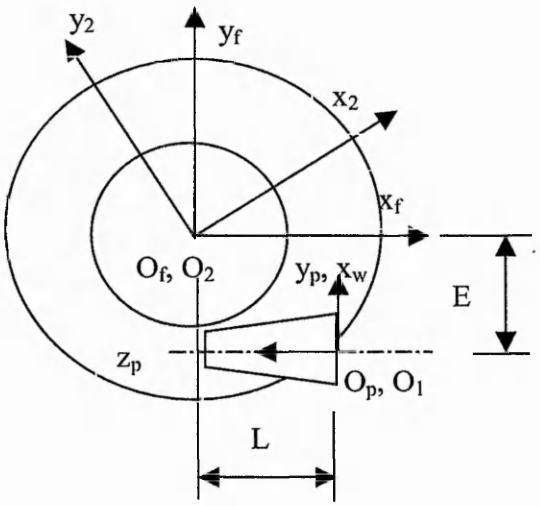
The spiroid gear surface can be represented as follows

$$\mathbf{r}_2(u_h, \theta_h, \phi_1) = \mathbf{M}_{21} \cdot \mathbf{r}_{1h}(u_h, \theta_h) \tag{3.4.1}$$

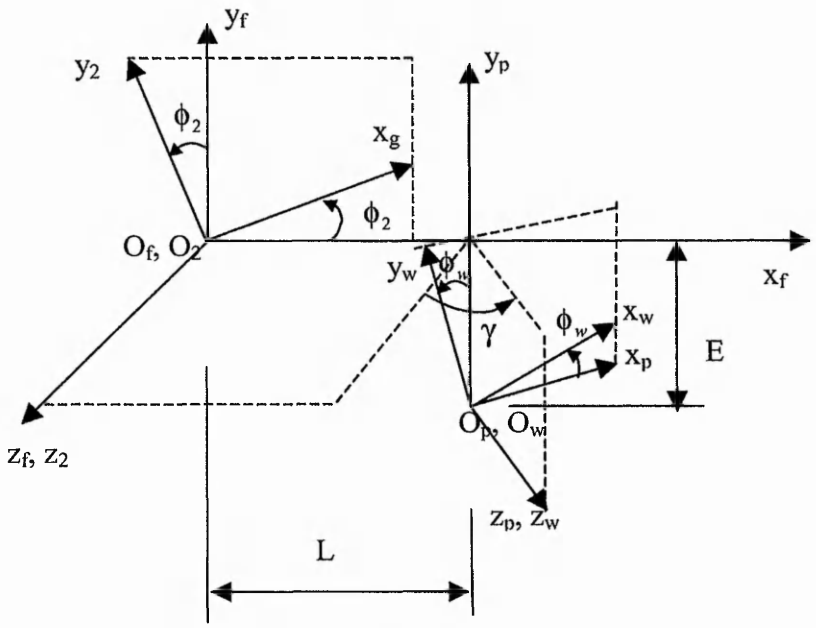
The variables of the spiroid gear surface should satisfy the meshing equation of spiroid gear drives

$$\mathbf{N}_{1h} \cdot \mathbf{v}_1^{(12)} = 0 \qquad (3.4.2)$$

In which $\mathbf{M}_{21}$ is the homogeneous transformation matrix from the coordinate system S_1 to S_2; $\mathbf{N}_1$ is the normal to the pinion surface; and $\mathbf{v}_1^{(12)}$ is the relative velocity between the gear and the pinion.



(a) Setting of gear generation



(b) Coordinate systems

Figure 3.12 Coordinate system applied for spiroid gear generation

The homogeneous transformation matrix from the coordinate system S_1 to S_2 can be derived as follows

$$\mathbf{M}_{21} = \mathbf{M}_{2f} \cdot \mathbf{M}_{fp} \cdot \mathbf{M}_{p1} \tag{3.4.3}$$

where, $\mathbf{M}_{p1}$ is the homogeneous transformation matrix from the coordinate system S_1 to S_p and expressed as follows

$$\mathbf{M}_{p1} = \begin{bmatrix} \cos\phi_1 & -\sin\phi_1 & 0 & 0 \\ \sin\phi_1 & \cos\phi_1 & 0 & 0 \\ 0 & 0 & 1 & 0 \\ 0 & 0 & 0 & 1 \end{bmatrix} \tag{3.4.4}$$

$\mathbf{M}_{2f}$ is the homogeneous transformation matrix from the coordinate system S_f to S_2 and expressed as follows

$$\mathbf{M}_{2f} = \begin{bmatrix} \cos\phi_2 & \sin\phi_2 & 0 & 0 \\ -\sin\phi_2 & \cos\phi_2 & 0 & 0 \\ 0 & 0 & 1 & 0 \\ 0 & 0 & 0 & 1 \end{bmatrix} \tag{3.4.5}$$

The homogeneous transformation matrix $\mathbf{M}_{fp}$ from S_p to S_f is represented as follows

$$\mathbf{M}_{fp} = \begin{bmatrix} \cos\gamma & 0 & \sin\gamma & L \\ 0 & 1 & 0 & -E \\ -\sin\gamma & 0 & \cos\gamma & 0 \\ 0 & 0 & 0 & 1 \end{bmatrix} \tag{3.4.6}$$

By following the product rule of matrix algebra, the homogeneous coordinate transformation from S_1 to S_2 is derived.

$$\mathbf{M}_{21}=\mathbf{M}_{2f}\cdot\mathbf{M}_{fp}\cdot\mathbf{M}_{p1}$$

$$=\begin{bmatrix} \cos\phi_1\cdot\cos\phi_2\cdot\cos\gamma & -\sin\phi_1\cdot\cos\phi_2\cdot\cos\gamma & \cos\phi_2\cdot\sin\gamma & L\cos\phi_2-E\sin\phi_2 \\ +\sin\phi_1\cdot\sin\phi_2 & +\cos\phi_1\cdot\sin\phi_2 & & \\ -\cos\phi_1\cdot\sin\phi_2\cdot\cos\gamma & \sin\phi_1\cdot\sin\phi_2\cdot\cos\gamma & -\sin\phi_2\cdot\sin\gamma & -L\sin\phi_2-E\cos\phi_2 \\ +\sin\phi_1\cdot\cos\phi_2 & +\cos\phi_1\cdot\cos\phi_2 & & \\ -\cos\phi_1\cdot\sin\gamma & \sin\phi_1\cdot\sin\gamma & \cos\gamma & 0 \\ 0 & 0 & 0 & 1 \end{bmatrix} \quad (3.4.7)$$

The elements of 3×3 submatrix of $\mathbf{M}_{21}$ represent the direction cosines of the unit vectors ($\mathbf{i}_1$, $\mathbf{j}_1$, $\mathbf{k}_1$) in the coordinate system S_2.

$$\mathbf{L}_{21}=\begin{bmatrix} \cos\phi_1\cos\phi_2\cos\gamma & -\sin\phi_1\cos\phi_2\cos\gamma & \cos\phi_2\sin\gamma \\ +\sin\phi_1\sin\phi_2 & +\cos\phi_1\sin\phi_2 & \\ -\cos\phi_1\sin\phi_2\cos\gamma & \sin\phi_1\sin\phi_2\cos\gamma & -\sin\phi_2\sin\gamma \\ +\sin\phi_1\cos\phi_2 & +\cos\phi_1\cos\phi_2 & \\ -\cos\phi_1\sin\gamma & \sin\phi_1\sin\gamma & \cos\gamma \end{bmatrix} \quad (3.4.8)$$

For most cases, the axes of pinion and spiroid gear are perpendicular to each other, i.e. γ=-90°, hence $\mathbf{M}_{21}$ can be simplified as follows

$$\mathbf{M}_{21}=\begin{bmatrix} \sin\phi_1\cdot\sin\phi_2 & \cos\phi_1\cdot\sin\phi_2 & -\cos\phi_2 & L\cos\phi_2-E\sin\phi_2 \\ \sin\phi_1\cdot\cos\phi_2 & \cos\phi_1\cdot\cos\phi_2 & \sin\phi_2 & -L\sin\phi_2-E\cos\phi_2 \\ -\cos\phi_2 & \sin\phi_2 & 0 & 0 \\ 0 & 0 & 0 & 1 \end{bmatrix} \quad (3.4.9)$$

The relative velocity of worm pinion and gear represented in coordinate system S_1 can be obtained from the following relationship

$$\mathbf{v}_1^{(12)}=(\boldsymbol{\omega}_1^{(1)}-\boldsymbol{\omega}_1^{(2)})\times\mathbf{r}_1-\mathbf{E}_1\times\boldsymbol{\omega}_1^{(2)} \quad (3.4.10)$$

where

$\boldsymbol{\omega}_1^{(1)}$ is the rotational velocity of the worm represented in coordinate system S_1

$\boldsymbol{\omega}_1^{(2)}$ is the rotational velocity of the gear represented in coordinate system S_1

$\mathbf{r}_1$ is the position vector of worm surface represented in coordinate system S_1

$\mathbf{E}_1$ is the distance vector from O_p to O_2. O_p is the origin of coordinate system S_p and O_2 is the origin of coordinate system S_2.

The rotation speed of worm represented in coordinate system S_1 is written as

$$\boldsymbol{\omega}_1^{(1)} = \omega_1 \cdot \mathbf{k}_1 \tag{3.4.11}$$

The angular rotating speed of gear represented in coordinate system S_2 is written as

$$\boldsymbol{\omega}_2^{(2)} = \omega_2 \cdot \mathbf{k}_2 \tag{3.4.12}$$

The distance vector from O_p to O_2 represented in coordinate system S_f

$$\mathbf{E}_f = \overline{O_p O_2} = -L \cdot \mathbf{i}_f + E \cdot \mathbf{j}_f \tag{3.4.13}$$

The distance vector from O_p to O_2 represented in coordinate system S_1 can be obtained from the vector from O_p to O_2 represented in coordinate system S_f by multiplying a series of transformation matrices.

$$\mathbf{E}_1 = \overline{O_p O_2} = \mathbf{L}_{1f} \cdot \mathbf{E}_f = \mathbf{L}_{1p} \cdot \mathbf{L}_{pf} \cdot \mathbf{E}_f \tag{3.4.14}$$

where, $\mathbf{L}_{1p}$ is 3×3 transformation matrix from coordinate system S_p to S_1 and $\mathbf{L}_{pf}$ is 3×3 transformation matrix from coordinate system S_f to S_p

The above two transformation equations can be acquired directly from Figure 3.12.

$$\mathbf{L}_{1p} = \begin{bmatrix} \cos\phi_1 & \sin\phi_1 & 0 \\ -\sin\phi_1 & \cos\phi_1 & 0 \\ 0 & 0 & 1 \end{bmatrix} \tag{3.4.15}$$

$$\mathbf{L}_{pf} = \begin{bmatrix} \cos\gamma & 0 & -\sin\gamma \\ 0 & 1 & 0 \\ \sin\gamma & 0 & \cos\gamma \end{bmatrix} \tag{3.4.16}$$

Substituting Equations (3.4.15), (3.4.16) and (3.4.13) into Equation (3.4.14), the centre distance in coordinate system S_1 are expressed as follows

$$\mathbf{E}_1 = \begin{Bmatrix} -L\cos\phi_1 \cdot \cos\gamma + E \cdot \sin\phi_1 \\ L\sin\phi_1 \cdot \cos\gamma + E \cdot \cos\phi_1 \\ -L \cdot \sin\gamma \end{Bmatrix} \tag{3.4.17}$$

The angular speed of the gear in coordinate system S_1

$$\boldsymbol{\omega}_1^{(2)} = \mathbf{L}_{12} \cdot \boldsymbol{\omega}_2^{(2)} = \omega_2 \cdot (-\cos\phi_1 \cdot \sin\gamma \cdot \mathbf{i}_1 - \sin\phi_1 \cdot \sin\gamma \cdot \mathbf{j}_1 + \cos\gamma \cdot \mathbf{k}_1) \tag{3.4.18}$$

where $\mathbf{L}_{12}$ is the 3×3 transformation matrix from coordinate system S_2 to S_1. It can be derived as

$$\mathbf{L}_{12} = \mathbf{L}_{1p} \cdot \mathbf{L}_{pf} \cdot \mathbf{L}_{f2} \tag{3.4.19}$$

where transformation matrices $\mathbf{L}_{1p}$, $\mathbf{L}_{pf}$ and $\mathbf{L}_{f2}$ can be obtained from Figure 3.12 as follows

$$\mathbf{L}_{1p} = \begin{bmatrix} \cos\phi_1 & \sin\phi_1 & 0 \\ -\sin\phi_1 & \cos\phi_1 & 0 \\ 0 & 0 & 1 \end{bmatrix} \tag{3.4.20}$$

$$\mathbf{L}_{f2} = \begin{bmatrix} \cos\phi_2 & -\sin\phi_2 & 0 \\ \sin\phi_2 & \cos\phi_2 & 0 \\ 0 & 0 & 1 \end{bmatrix} \tag{3.4.21}$$

$$\mathbf{L}_{pf} = \begin{bmatrix} \cos\gamma & 0 & -\sin\gamma \\ 0 & 1 & 0 \\ \sin\gamma & 0 & \cos\gamma \end{bmatrix} \tag{3.4.22}$$

Substituting the above three equations into Equation (3.4.19), we have

$$\mathbf{L}_{12} = \begin{bmatrix} \cos\phi_1\cos\phi_2\cos\gamma & -\cos\phi_1\sin\phi_2\cos\gamma & -\cos\phi_1\sin\gamma \\ +\sin\phi_1\sin\phi_2 & +\sin\phi_1\cos\phi_2 & \\ -\sin\phi_1\cos\phi_2\cos\gamma & \sin\phi_1\sin\phi_2\cos\gamma & \sin\phi_1\sin\gamma \\ +\cos\phi_1\sin\phi_2 & +\cos\phi_1\cos\phi_2 & \\ \cos\phi_2\sin\gamma & -\sin\phi_2\sin\gamma & \cos\gamma \end{bmatrix} \tag{3.4.23}$$

Substituting Equation (3.4.12) and (3.4.23) into (3.4.18), the angular speed of the gear in coordinate system S_1 is derived as follows

$$\boldsymbol{\omega}_1^{(2)} = \omega_2 \cdot (-\cos\phi_1 \cdot \sin\gamma \cdot \mathbf{i}_1 - \sin\phi_1 \cdot \sin\gamma \cdot \mathbf{j}_1 + \cos\gamma \cdot \mathbf{k}_1) \tag{3.4.24}$$

Substituting Equations (3.4.11), (3.4.17) and (3.4.24) into Equation (3.4.10) gives

$$\mathbf{v}_1^{(12)} = (\boldsymbol{\omega}_1^{(1)} - \boldsymbol{\omega}_1^{(2)}) \times \mathbf{r}_1 - \mathbf{E}_1 \times \boldsymbol{\omega}_1^{(2)}$$

$$= \begin{vmatrix} \mathbf{i}_1 & \mathbf{j}_1 & \mathbf{k}_1 \\ \omega_2 \cos\phi_1 \sin\gamma & -\omega_2 \sin\phi_1 \sin\gamma & \omega_1 - \omega_2 \cos\gamma \\ x_1 & y_1 & z_1 \end{vmatrix}$$

$$- \begin{vmatrix} \mathbf{i}_1 & \mathbf{j}_1 & \mathbf{k}_1 \\ -L\cos\phi_1 \cos\gamma + E\sin\phi_1 & L\sin\phi_1 \cos\gamma + E\cos\phi_1 & -L\sin\gamma \\ -\omega_2 \cos\phi_1 \sin\gamma & \omega_2 \sin\phi_1 \sin\gamma & \omega_2 \cos\gamma \end{vmatrix}$$

The above equation can be written in the following form

$$\mathbf{v}_1^{(12)} = v_{1x}^{(12)} \cdot \mathbf{i}_1 + v_{1y}^{(12)} \cdot \mathbf{j}_1 + v_{1z}^{(12)} \cdot \mathbf{k}_1 \tag{3.4.25}$$

where

$$\begin{aligned} v_{1x}^{(12)} &= -z_1\omega_2 \sin\phi_1 \sin\gamma - y_1(\omega_1 - \omega_2 \cos\gamma) \\ &\quad - \omega_2 \cos\gamma \cdot (L\sin\phi_1 \cos\gamma + E\cos\phi_1) - L\omega_2 \sin\phi_1 \sin^2\gamma \end{aligned} \tag{3.4.26}$$

$$\begin{aligned} v_{1y}^{(12)} &= -z_1\omega_2 \cos\phi_1 \sin\gamma + x_1(\omega_1 - \omega_2 \cos\gamma) \\ &\quad + \omega_2 \cos\gamma \cdot (-L\cos\phi_1 \cos\gamma + E\sin\phi_1) - L\omega_2 \cos\phi_1 \sin^2\gamma \end{aligned} \tag{3.4.27}$$

$$\begin{aligned} v_{1z}^{(12)} &= y_1\omega_2 \cos\phi_1 \sin\gamma + x_1\omega_2 \sin\phi_1 \sin\gamma \\ &\quad - \omega_2 \cos\phi_1 \sin\gamma \cdot (L\sin\phi_1 \cos\gamma + E\cos\phi_1) \\ &\quad - \omega_2 \sin\phi_1 \sin\gamma(-L\cos\phi_1 \cos\gamma + E\sin\phi_1) \end{aligned} \tag{3.4.28}$$

With Equations (3.3.9), (3.4.25), the meshing equation (3.4.2) can be written as

$$f(u_h, \theta_h, \phi_1) = N_{1x} \cdot v_{1x}^{(12)} + N_{1y} \cdot v_{1y}^{(12)} + N_{1z} \cdot v_{1z}^{(12)} \tag{3.4.29}$$

The gear surfaces are thus expressed by the following equations

$$\begin{cases} f(u_h, \theta_h, \phi_1) = 0 \\ \mathbf{r}_2(u_h, \theta_h, \phi_1) \end{cases} \tag{3.4.30}$$

The tooth surface constituted by contact lines can be obtained by solving Equation (3.4.30). Figure 3.13 shows two sides of one gear tooth surface. One side is meshing with the hob tooth side I and the other side is meshing with hob tooth side II. Figure 3.14 is the zoomed picture of Figure 3.13. The contact lines and contact path are clearly shown in Figure 3.14.

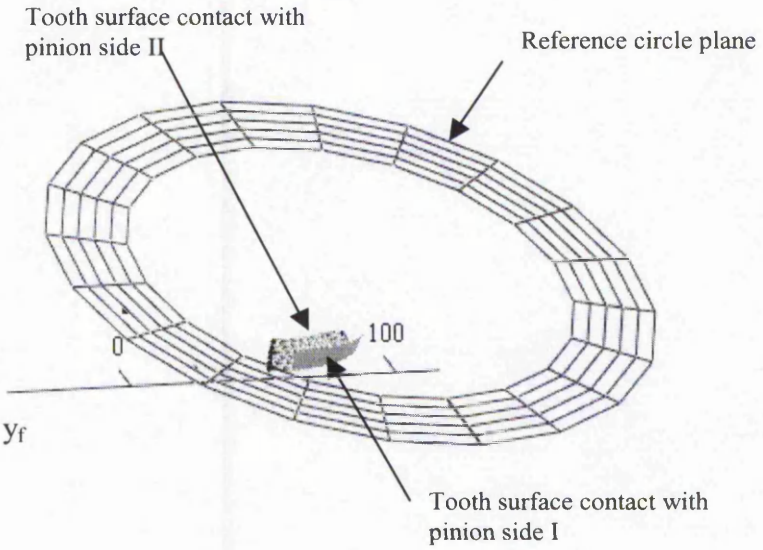


Figure 3.13 Gear tooth surface

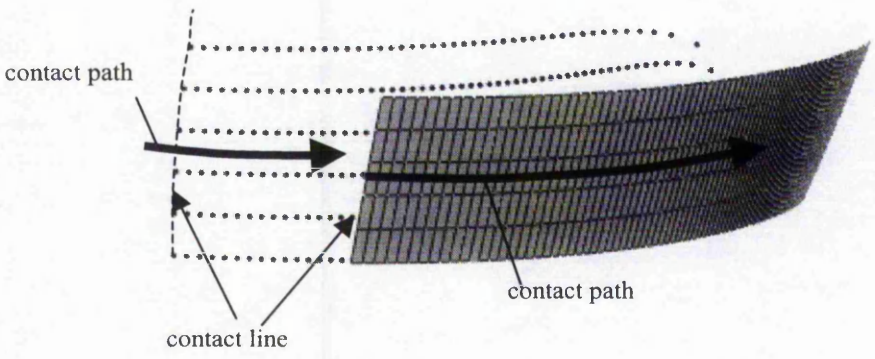


Figure 3.14 Gear tooth surface (Zoomed)



3.5 DETECTION OF UNDERCUTTING

Gear undercut will reduce the gear's loading capacity and working life. Avoiding undercutting in gear design is an important problem. If the generated spiroid gear surfaces exhibit singularities then the spiroid gear design has an undercutting problem, i.e. the gear tooth will be undercut in the process of generation. The theory of determining singularities of surfaces is a very complex topic in differential geometry. The equations of determination of the singularities of surfaces have been developed by Zalgaller (1975) and Litvin (1984, 1989, 1994). In this chapter, the theory of singularities of surface developed by Litvin (1994) has been used to detect if there is an undercutting problem.

The necessary condition for the existence of singularities on surface Σ_2 is represented by the following equations

$$\mathbf{r}_2(u_h,\theta_h,\varphi_1), \qquad f(u_h,\theta_h,\varphi_1)=0 \qquad F(u_h,\theta_h,\varphi_1)=0 \tag{3.5.1}$$

where

$\mathbf{r}_2$	the position vector of the spiroid gear surface
u_h, θ_h	surface parameters of the hob
φ_1	generalised parameter of motion
f=0	meshing equation

Equation F=0 may be derived considering that

$$\Delta_1=0, \qquad \Delta_2=0, \qquad \Delta_3=0 \tag{3.5.2}$$

where

$$\Delta_1 = \begin{vmatrix} \frac{\partial x_1}{\partial u_1} & \frac{\partial x_1}{\partial \theta_1} & -v_{x1}^{(12)} \\ \frac{\partial y_1}{\partial u_1} & \frac{\partial y_1}{\partial \theta_1} & -v_{y1}^{(12)} \\ f_u & f_\theta & -f_\phi \frac{d\phi}{dt} \end{vmatrix} \tag{3.5.3}$$

$$\Delta_2 = \begin{vmatrix} \frac{\partial x_1}{\partial u_1} & \frac{\partial x_1}{\partial \theta_1} & -v_{x1}^{(12)} \\ \frac{\partial z_1}{\partial u_1} & \frac{\partial z_1}{\partial \theta_1} & -v_{z1}^{(12)} \\ f_u & f_\theta & -f_\phi \frac{d\phi}{dt} \end{vmatrix} \tag{3.5.4}$$

$$\Delta_3 = \begin{vmatrix} \frac{\partial y_1}{\partial u_1} & \frac{\partial y_1}{\partial \theta_1} & -v_{y1}^{(12)} \\ \frac{\partial z_1}{\partial u_1} & \frac{\partial z_1}{\partial \theta_1} & -v_{z1}^{(12)} \\ f_u & f_\theta & -f_\phi \frac{d\phi}{dt} \end{vmatrix} \tag{3.5.5}$$

Instead of Equation (3.5.2), the following equation can be used.

$$g(u_1,\theta_1,\phi_1) = \begin{vmatrix} f_u & f_\theta & f_\phi \\ \left(\frac{\partial \mathbf{r}_1}{\partial u_1}\right)^2 & \left(\frac{\partial \mathbf{r}_1}{\partial u_1}\right)\cdot\left(\frac{\partial \mathbf{r}_1}{\partial \theta_1}\right) & \left(\frac{\partial \mathbf{r}_1}{\partial u_1}\right)\cdot \mathbf{v}_1^{(12)} \\ \left(\frac{\partial \mathbf{r}_1}{\partial \theta_1}\right)\cdot\left(\frac{\partial \mathbf{r}_1}{\partial u_1}\right) & \left(\frac{\partial \mathbf{r}_1}{\partial \theta_1}\right)^2 & \left(\frac{\partial \mathbf{r}_1}{\partial \theta_1}\right)\cdot \mathbf{v}_1^{(12)} \end{vmatrix} \tag{3.5.6}$$

To avoid the appearance of singularities, the generating surface Σ_1 by line L_1 may be determined as

$$\mathbf{r}_1(u_h,\theta_h), \qquad f(u_h,\theta_h,\varphi_l) = 0 \qquad F(u_h,\theta_h,\varphi_l) = 0 \tag{3.5.7}$$

Line L_1 on surface Σ_1 is formed by regular points of Σ_1 but generates singular points on Σ_2.

Singular points on Σ_2 may form a line that is the envelope E_2 to contact line on Σ_2. This line is also the edge of regression on Σ_2. The sufficient conditions that the envelope to contact lines on generated surface Σ_2 exists are described as follows:

If at point $M(u_0, \theta_0, \phi_0)$ the following conditions are observed,

$$\mathbf{r}_2(u,\theta,\phi) \qquad f(u,\theta,\phi) = 0 \qquad g(u,\theta,\phi) = 0 \tag{3.5.8}$$

$$\begin{vmatrix} f_u & f_\theta \\ g_u & g_\theta \end{vmatrix} \neq 0 \tag{3.5.9}$$

$$h = \begin{vmatrix} g_u & g_\theta & g_\phi \\ \left(\frac{\partial \mathbf{r}_1}{\partial u_1}\right)^2 & \left(\frac{\partial \mathbf{r}_1}{\partial u_1}\right)\cdot\left(\frac{\partial \mathbf{r}_1}{\partial \theta_1}\right) & \left(\frac{\partial \mathbf{r}_1}{\partial u_1}\right)\cdot \mathbf{v}_1^{(12)} \\ \left(\frac{\partial \mathbf{r}_1}{\partial \theta_1}\right)\cdot\left(\frac{\partial \mathbf{r}_1}{\partial u_1}\right) & \left(\frac{\partial \mathbf{r}_1}{\partial \theta_1}\right)^2 & \left(\frac{\partial \mathbf{r}_1}{\partial \theta_1}\right)\cdot \mathbf{v}_1^{(12)} \end{vmatrix} \neq 0 \tag{3.5.10}$$

Then, in the neighbourhood of point M the envelope to the family of contact lines E_2 is a regular curve.

The above theory is applied in the present analysis to determine if in the present example design there exists an undercutting problem. Programs have been written using MathCAD. The calculated results show that no undercutting problem exists in the present spiroid gear design. The program can also be used to detect undercutting problems in other gear types.

3.6 NUMERICAL SIMULATION

3.6.1 Spiroid Gearing Parameters

In order to evaluate the shift of bearing contact in the modified spiroid gear drive caused by misalignment, a numerical example of a spiroid gear drive is presented here. The tapered pinion has two starts and the gear has 51 teeth and its gear ratio is 25.5. The centre distance of the spiroid gear assembly is 70 mm. The other parameters of the spiroid gear design are calculated according to the gear ratio and the centre distance. The main parameters of the spiroid gear drive are listed in Table 3.1.

Table 3.1Main parameters of spiroid gearset (right hand) (mm)

Ratio	25.5
Number of threads on pinion	2
Number of teeth on gear	51
Mounting distance of pinion	109
Mounting distance of gear	43.27
Outside diameter of gear	209.55
Inner diameter of gear tooth tip	153.67
Centre distance	70
Gear form	Tapered

To conduct the numerical simulation of meshing, a spiroid gear tooth contact analysis program has been developed. The coordinate system for the simulation is shown in Figure 3.15, which takes into account the errors including axial displacement error, centre distance error and misalignment. The meshing algorithm is based on the condition that the pinion surface and gear surface are continuously tangent to each other at the contact points and therefore they have the same unit normal vector.

3.6.2 Worm Pinion and Gear Tooth Surface Equations

The position vector of the gear surface in coordinate system S_f can be obtained from the product of the transformation matrix $\mathbf{M}'_{f2}$ and the position vector of gear surface in coordinate system S_2

$$\mathbf{r}_f^{(2)}(u_h, \theta_h, \phi_1, \phi_2') = \mathbf{M}'_{f2} \cdot \mathbf{r}_2 = \mathbf{M}'_{f2} \cdot \mathbf{M}_{21}(\phi_1) \cdot \mathbf{r}_{1h}(u_h, \theta_h) \tag{3.6.1}$$

where

$\mathbf{r}_f^{(2)}$ is the position vector of gear surface in coordinate system S_f;

u_h, θ_h are the hob surface parameters.

ϕ_1 is the rotation angle of the hob.

ϕ'_2 is the rotation angle of the gear.

$\mathbf{r}_{1h}$ is the position vector of hob surface in coordinate system S_1, Equation (3.3.4).

$\mathbf{M}_{21}$ is the transformation matrix, Equation (3.4.7).

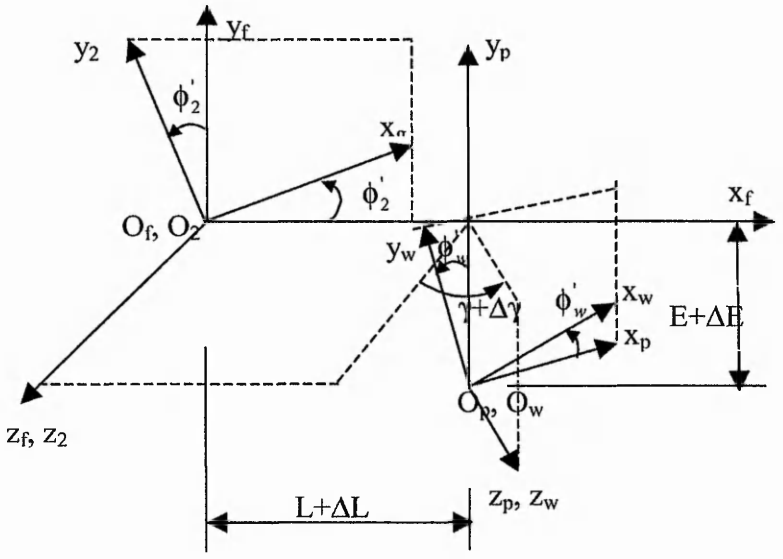


Figure 3.15 Coordinate system for simulation of meshing

The transformation matrix $\mathbf{M}'_{f2}$ can be written as follows

$$\mathbf{M}'_{f2} = \begin{bmatrix} \cos\phi'_2 & -\sin\phi'_2 & 0 & 0 \\ \sin\phi'_2 & \cos\phi'_2 & 0 & 0 \\ 0 & 0 & 1 & 0 \\ 0 & 0 & 0 & 1 \end{bmatrix} \tag{3.6.2}$$

Similarly, the position vector of the tapered worm pinion surface represented in coordinate system S_f can be obtained from the product of the transformation matrix $\mathbf{M}'_{fw}$ and the position vector of worm surface represented in coordinate system S_w

$$\mathbf{r}_f^{(w)}(u_w, \theta_w, \phi'_w, \Delta L, \Delta E, \Delta\gamma) = \mathbf{M}'_{fw} \cdot \mathbf{r}_w = \mathbf{M}'_{fp} \cdot \mathbf{M}'_{pw} \cdot \mathbf{r}_{1w}(u_w, \theta_w) \tag{3.6.3}$$

where

$\mathbf{r}_{1w}(u_w, \theta_w)$ is the position vector of the modified pinion surface, Equation (3.3.17).

$\mathbf{r}_f^{(w)}$ is the position vector of the pinion surface represented in coordinate system S_f

u_w, θ_w are the modified pinion surface parameters

ϕ'_w is the rotation angle of the pinion

ΔL is the axial displacement error

ΔE is the shortest centre distance error

$\Delta\gamma$ is the misalignment of the shaft angle

The transformation matrix from coordinate system S_p to S_f is represented as follows

$$\mathbf{M}'_{fp} = \begin{bmatrix} \cos(\gamma+\Delta\gamma) & 0 & \sin(\gamma+\Delta\gamma) & L+\Delta L \\ 0 & 1 & 0 & -(E+\Delta E) \\ -\sin(\gamma+\Delta\gamma) & 0 & \cos(\gamma+\Delta\gamma) & 0 \\ 0 & 0 & 0 & 1 \end{bmatrix} \tag{3.6.4}$$

The transformation matrix from coordinate system S_w to S_p is represented as follows

$$\mathbf{M}'_{pw} = \begin{bmatrix} \cos\phi'_w & -\sin\phi'_w & 0 & 0 \\ \sin\phi'_w & \cos\phi'_w & 0 & 0 \\ 0 & 0 & 1 & 0 \\ 0 & 0 & 0 & 1 \end{bmatrix} \tag{3.6.5}$$

3.6.3 Normal to the Pinion and Gear Tooth Surfaces in Coordinate System S_f

The unit normal to the pinion surface represented in coordinate system S_f can be deduced from the unit normal to the pinion surface in coordinate system S_1 as follows

$$\mathbf{n}_f^{(w)}(u_w, \theta_w, \phi'_w, \Delta\gamma) = \mathbf{L}'_{fw} \cdot \mathbf{n}_{1w}(u_w, \theta_w) \tag{3.6.6}$$

in which, $\mathbf{n}_{1w}(u_w, \theta_w)$ is the unit normal to the modified pinion surface represented in Equation (3.3.53); $\mathbf{L}'_{fw}$ is a transformation matrix from coordinate system S_m to S_f.

The unit normal to the gear surface represented in coordinate system S_f also can be derived as follows

$$\mathbf{n}_f^{(2)}(u_h, \theta_h, \phi_1, \phi'_2) = \mathbf{L}'_{f1} \cdot \mathbf{n}_{1h}(u_h, \theta_h) \tag{3.6.7}$$

where $\mathbf{n}_{1h}(u_h, \theta_h)$ is the unit normal to the hob's surface represented in Equation (3.3.53); $\mathbf{L}'_{f1}$ is a transformation matrix from coordinate system S_1 to S_f.

The transformation matrices $\mathbf{L}'_{fw}$ and $\mathbf{L}'_{f1}$ can be derived by two different methods. The two different methods are presented in the following sections.

3.6.3.1 Determination of Transformation Matrices 1

When $\mathbf{M}'_{fw}$ has been determined, $\mathbf{L}'_{fw}$ can be easily calculated from $\mathbf{M}'_{fw}$. It can be shown that matrix $\mathbf{L}'_{fw}$ is equal to the first 3x3 submatrix of $\mathbf{M}'_{fw}$.

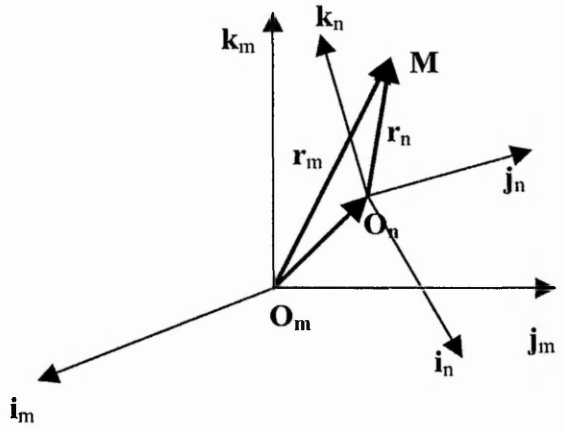


Figure 3.16 Coordinate systems S_m and S_n

The above relation can be described as follows:

Assume that surface Σ represented in coordinate system S_m as position vector $\mathbf{r}_m(u,\theta)$ and represented in coordinate system S_n as position vector $\mathbf{r}_n(u,\theta)$, then they have the following position and normal relationships:

$$\mathbf{r}_n(u,\theta) = \mathbf{M}_{nm} \cdot \mathbf{r}_m(u,\theta) \tag{3.6.8}$$

$$\mathbf{N}_n(u,\theta) = \mathbf{L}_{nm} \cdot \mathbf{N}_m(u,\theta) \tag{3.6.9}$$

where $\mathbf{M}_{nm}$ is the position vector transformation matrix from coordinate system S_m to coordinate system S_n. $\mathbf{L}_{nm}$ is the normal vector transformation matrix from coordinate system S_m to coordinate system S_n.

If the transformation matrix $\mathbf{M}_{nm}$ is obtained and written as follows

$$\mathbf{M}_{nm}=\begin{bmatrix} a_{11} & a_{12} & a_{13} & a_{14} \\ a_{21} & a_{22} & a_{23} & a_{24} \\ a_{31} & a_{32} & a_{33} & a_{34} \\ 0 & 0 & 0 & 1 \end{bmatrix}$$

$$=\begin{bmatrix} (\mathbf{i}_n\cdot\mathbf{i}_m) & (\mathbf{i}_n\cdot\mathbf{j}_m) & (\mathbf{i}_n\cdot\mathbf{k}_m) & (\overline{O_nO_m}\cdot\mathbf{i}_m) \\ (\mathbf{j}_n\cdot\mathbf{i}_m) & (\mathbf{j}_n\cdot\mathbf{j}_m) & (\mathbf{j}_n\cdot\mathbf{k}_m) & (\overline{O_nO_m}\cdot\mathbf{j}_m) \\ (\mathbf{k}_n\cdot\mathbf{i}_m) & (\mathbf{k}_n\cdot\mathbf{j}_m) & (\mathbf{k}_n\cdot\mathbf{k}_m) & (\overline{O_nO_m}\cdot\mathbf{k}_m) \\ 0 & 0 & 0 & 1 \end{bmatrix} \qquad (3.6.10)$$

$$=\begin{bmatrix} \cos(x_n,x_m) & \cos(x_n,y_m) & \cos(x_n,z_m) & x_n^{(O_m)} \\ \cos(y_n,x_m) & \cos(y_n,y_m) & \cos(y_n,z_m) & y_n^{(O_m)} \\ \cos(z_n,x_m) & \cos(z_n,y_m) & \cos(z_n,z_m) & z_n^{(O_m)} \\ 0 & 0 & 0 & 1 \end{bmatrix}$$

Then the normal vector transformation matrix $\mathbf{L}_{nm}$ can be obtained as the 3×3 submatrix of $\mathbf{M}_{nm}$, represented by the direction cosines of the unit vector $(\mathbf{i}_m,\mathbf{j}_m,\mathbf{k}_m)$ in the coordinate system S_n,

$$\mathbf{L}_{nm}=\begin{bmatrix} a_{11} & a_{12} & a_{13} \\ a_{21} & a_{22} & a_{23} \\ a_{31} & a_{32} & a_{33} \end{bmatrix}=\begin{bmatrix} \cos(x_2,x_1) & \cos(x_2,y_1) & \cos(x_2,z_1) \\ \cos(y_2,x_1) & \cos(y_2,y_1) & \cos(y_2,z_1) \\ \cos(z_2,x_1) & \cos(z_2,y_1) & \cos(z_2,z_1) \end{bmatrix} \qquad (3.6.11)$$

This has been proved by the author as follows.

According to Litvin (1995), an element of Matrix $\mathbf{L}_{nm}$ can be represented by a respective determinant of the second order. For instance,

$$a_{11}=\begin{vmatrix} a_{22} & a_{23} \\ a_{32} & a_{33} \end{vmatrix},\qquad a_{23}=(-1)\begin{vmatrix} a_{11} & a_{12} \\ a_{31} & a_{32} \end{vmatrix} \qquad (3.6.12)$$

The normal to the surface Σ in coordinate system S_m can be obtained from the following equation:

$$\mathbf{N}_m(u,\theta)=\frac{\partial\mathbf{r}_m}{\partial u}\times\frac{\partial\mathbf{r}_m}{\partial\theta} \qquad (3.6.13)$$



Similarly, the normal to the surface Σ represented in coordinate system S_n is obtained from

$$\mathbf{N}_n(u,\theta)=\frac{\partial \mathbf{r}_n}{\partial u}\times\frac{\partial \mathbf{r}_n}{\partial \theta} \tag{3.6.14}$$

Equation (3.6.13) can be derived by following the rules of vector product as follows

$$\mathbf{N}_m(u,\theta)=\begin{vmatrix} \mathbf{i}_m & \mathbf{j}_m & \mathbf{k}_m \\ \frac{\partial x_m}{\partial u} & \frac{\partial y_m}{\partial u} & \frac{\partial z_m}{\partial u} \\ \frac{\partial x_m}{\partial \theta} & \frac{\partial y_m}{\partial \theta} & \frac{\partial z_m}{\partial \theta} \end{vmatrix}=N_{mx}\cdot\mathbf{i}_m+N_{my}\cdot\mathbf{j}_m+N_{mz}\cdot\mathbf{k}_m \tag{3.6.15}$$

where

$$N_{mx}=\begin{vmatrix} \frac{\partial y_m}{\partial u} & \frac{\partial z_m}{\partial u} \\ \frac{\partial y_m}{\partial \theta} & \frac{\partial z_m}{\partial \theta} \end{vmatrix} \tag{3.6.16}$$

$$N_{my}=-\begin{vmatrix} \frac{\partial x_m}{\partial u} & \frac{\partial z_m}{\partial u} \\ \frac{\partial x_m}{\partial \theta} & \frac{\partial z_m}{\partial \theta} \end{vmatrix} \tag{3.6.17}$$

$$N_{mz}=\begin{vmatrix} \frac{\partial x_m}{\partial u} & \frac{\partial y_m}{\partial u} \\ \frac{\partial x_m}{\partial \theta} & \frac{\partial y_m}{\partial \theta} \end{vmatrix} \tag{3.6.18}$$

Equation (3.6.14) can be obtained in a similar way.

$$\mathbf{N}_n(u,\theta)=\frac{\partial \mathbf{r}_n}{\partial u}\times\frac{\partial \mathbf{r}_n}{\partial \theta}=\frac{\partial(\mathbf{M}_{nm}\cdot\mathbf{r}_m)}{\partial u}\times\frac{\partial(\mathbf{M}_{nm}\cdot\mathbf{r}_m)}{\partial \theta} \tag{3.6.19}$$

Substituting Equation (3.6.10) into the first term of the above equation's right hand side has

$$\frac{\partial(\mathbf{M}_{nm}\cdot\mathbf{r}_m)}{\partial u}=\begin{Bmatrix} a_{11}\dfrac{\partial x_m}{\partial u}+a_{12}\dfrac{\partial y_m}{\partial u}+a_{13}\dfrac{\partial z_m}{\partial u} \\ a_{21}\dfrac{\partial x_m}{\partial u}+a_{22}\dfrac{\partial y_m}{\partial u}+a_{23}\dfrac{\partial z_m}{\partial u} \\ a_{31}\dfrac{\partial x_m}{\partial u}+a_{32}\dfrac{\partial y_m}{\partial u}+a_{33}\dfrac{\partial z_m}{\partial u} \end{Bmatrix} \tag{3.6.20}$$

Substituting Equation (3.6.10) into the second term of the right hand side of Equation (3.6.19) has

$$\frac{\partial(\mathbf{M}_{nm}\cdot\mathbf{r}_m)}{\partial \theta}=\begin{Bmatrix} a_{11}\dfrac{\partial x_m}{\partial \theta}+a_{12}\dfrac{\partial y_m}{\partial \theta}+a_{13}\dfrac{\partial z_m}{\partial \theta} \\ a_{21}\dfrac{\partial x_m}{\partial \theta}+a_{22}\dfrac{\partial y_m}{\partial \theta}+a_{23}\dfrac{\partial z_m}{\partial \theta} \\ a_{31}\dfrac{\partial x_m}{\partial \theta}+a_{32}\dfrac{\partial y_m}{\partial \theta}+a_{33}\dfrac{\partial z_m}{\partial \theta} \end{Bmatrix} \tag{3.6.21}$$

The vector product of Equation (3.6.20) and (3.6.21) yields

$$\begin{aligned}\mathbf{N}_n(u,\theta)&=\begin{vmatrix} \mathbf{i}_m & \mathbf{j}_m & \mathbf{k}_m \\ a_{11}\dfrac{\partial x_m}{\partial u}+a_{12}\dfrac{\partial y_m}{\partial u}+a_{13}\dfrac{\partial z_m}{\partial u} & a_{21}\dfrac{\partial x_m}{\partial u}+a_{22}\dfrac{\partial y_m}{\partial u}+a_{23}\dfrac{\partial z_m}{\partial u} & a_{31}\dfrac{\partial x_m}{\partial u}+a_{32}\dfrac{\partial y_m}{\partial u}+a_{33}\dfrac{\partial z_m}{\partial u} \\ a_{11}\dfrac{\partial x_m}{\partial \theta}+a_{12}\dfrac{\partial y_m}{\partial \theta}+a_{13}\dfrac{\partial z_m}{\partial \theta} & a_{21}\dfrac{\partial x_m}{\partial \theta}+a_{22}\dfrac{\partial y_m}{\partial \theta}+a_{23}\dfrac{\partial z_m}{\partial \theta} & a_{31}\dfrac{\partial x_m}{\partial \theta}+a_{32}\dfrac{\partial y_m}{\partial \theta}+a_{33}\dfrac{\partial z_m}{\partial \theta} \end{vmatrix} \\ &=N_{nx}\cdot\mathbf{i}_m+N_{ny}\cdot\mathbf{j}_m+N_{nz}\cdot\mathbf{k}_m\end{aligned} \tag{3.6.22}$$

where, the first term of the above equation's right hand side is

$$\begin{aligned}\mathbf{N}_{nx} &= \begin{vmatrix} a_{21}\frac{\partial x_m}{\partial u}+a_{22}\frac{\partial y_m}{\partial u}+a_{23}\frac{\partial z_m}{\partial u} & a_{31}\frac{\partial x_m}{\partial u}+a_{32}\frac{\partial y_m}{\partial u}+a_{33}\frac{\partial z_m}{\partial u} \\ a_{21}\frac{\partial x_m}{\partial \theta}+a_{22}\frac{\partial y_m}{\partial \theta}+a_{23}\frac{\partial z_m}{\partial \theta} & a_{31}\frac{\partial x_m}{\partial \theta}+a_{32}\frac{\partial y_m}{\partial \theta}+a_{33}\frac{\partial z_m}{\partial \theta} \end{vmatrix} \\ &= (a_{21}\frac{\partial x_m}{\partial u}+a_{22}\frac{\partial y_m}{\partial u}+a_{23}\frac{\partial z_m}{\partial u})(a_{31}\frac{\partial x_m}{\partial \theta}+a_{32}\frac{\partial y_m}{\partial \theta}+a_{33}\frac{\partial z_m}{\partial \theta}) \\ &-(a_{21}\frac{\partial x_m}{\partial \theta}+a_{22}\frac{\partial y_m}{\partial \theta}+a_{23}\frac{\partial z_m}{\partial \theta})(a_{31}\frac{\partial x_m}{\partial u}+a_{32}\frac{\partial y_m}{\partial u}+a_{33}\frac{\partial z_m}{\partial u})\end{aligned} \tag{3.6.23}$$

Expanding Equation (3.6.23) gives

$$\begin{aligned}\mathbf{N}_{nx} &= a_{21}\frac{\partial x_m}{\partial u}\cdot a_{31}\frac{\partial x_m}{\partial \theta}+a_{21}\frac{\partial x_m}{\partial u}\cdot a_{32}\frac{\partial y_m}{\partial \theta}+a_{21}\frac{\partial x_m}{\partial u}\cdot a_{33}\frac{\partial z_m}{\partial \theta} \\ &+a_{22}\frac{\partial y_m}{\partial u}\cdot a_{31}\frac{\partial x_m}{\partial \theta}+a_{22}\frac{\partial y_m}{\partial u}\cdot a_{32}\frac{\partial y_m}{\partial \theta}+a_{32}\frac{\partial y_m}{\partial u}\cdot a_{33}\frac{\partial z_m}{\partial \theta} \\ &+a_{22}\frac{\partial y_m}{\partial u}\cdot a_{31}\frac{\partial x_m}{\partial \theta}+a_{22}\frac{\partial y_m}{\partial u}\cdot a_{32}\frac{\partial y_m}{\partial \theta}+a_{32}\frac{\partial y_m}{\partial u}\cdot a_{33}\frac{\partial z_m}{\partial \theta} \\ &-a_{21}\frac{\partial x_m}{\partial \theta}\cdot a_{31}\frac{\partial x_m}{\partial u}-a_{21}\frac{\partial x_m}{\partial \theta}\cdot a_{31}\frac{\partial x_m}{\partial u}-a_{21}\frac{\partial x_m}{\partial \theta}\cdot a_{31}\frac{\partial x_m}{\partial u} \\ &-a_{21}\frac{\partial x_m}{\partial \theta}\cdot a_{31}\frac{\partial x_m}{\partial u}-a_{21}\frac{\partial x_m}{\partial \theta}\cdot a_{31}\frac{\partial x_m}{\partial u}-a_{21}\frac{\partial x_m}{\partial \theta}\cdot a_{31}\frac{\partial x_m}{\partial u}\end{aligned} \tag{3.6.24}$$

Rewriting the above equation has

$$\begin{aligned}\mathbf{N}_{nx} &= a_{21}a_{32}(\frac{\partial x_m}{\partial u}\frac{\partial y_m}{\partial \theta}-\frac{\partial x_m}{\partial \theta}\frac{\partial y_m}{\partial u})+a_{21}a_{33}(\frac{\partial x_m}{\partial u}\frac{\partial z_m}{\partial \theta}-\frac{\partial x_m}{\partial \theta}\frac{\partial z_m}{\partial u}) \\ &+a_{22}a_{31}(\frac{\partial y_m}{\partial u}\frac{\partial x_m}{\partial \theta}-\frac{\partial y_m}{\partial \theta}\frac{\partial x_m}{\partial u})+a_{22}a_{33}(\frac{\partial y_m}{\partial u}\frac{\partial z_m}{\partial \theta}-\frac{\partial y_m}{\partial \theta}\frac{\partial z_m}{\partial u}) \\ &+a_{23}a_{31}(\frac{\partial z_m}{\partial u}\frac{\partial x_m}{\partial \theta}-\frac{\partial z_m}{\partial \theta}\frac{\partial x_m}{\partial u})+a_{23}a_{32}(\frac{\partial z_m}{\partial u}\frac{\partial y_m}{\partial \theta}-\frac{\partial z_m}{\partial \theta}\frac{\partial y_m}{\partial u}) \\ &= (a_{21}a_{32}-a_{22}a_{31})(\frac{\partial x_m}{\partial u}\frac{\partial y_m}{\partial \theta}-\frac{\partial x_m}{\partial \theta}\frac{\partial y_m}{\partial u}) \\ &+(a_{21}a_{33}-a_{23}a_{31})(\frac{\partial x_m}{\partial u}\frac{\partial z_m}{\partial \theta}-\frac{\partial x_m}{\partial \theta}\frac{\partial z_m}{\partial u}) \\ &+(a_{22}a_{33}-a_{23}a_{32})(\frac{\partial y_m}{\partial u}\frac{\partial z_m}{\partial \theta}-\frac{\partial y_m}{\partial \theta}\frac{\partial z_m}{\partial u})\end{aligned} \tag{3.6.25}$$

This equation can be rewritten in the following form

$$\mathbf{N}_{nx} = \begin{vmatrix} a_{21} & a_{22} \\ a_{31} & a_{32} \end{vmatrix} \cdot \begin{vmatrix} \frac{\partial x_m}{\partial u} & \frac{\partial y_m}{\partial u} \\ \frac{\partial x_m}{\partial \theta} & \frac{\partial y_m}{\partial \theta} \end{vmatrix} + \begin{vmatrix} a_{21} & a_{23} \\ a_{31} & a_{33} \end{vmatrix} \cdot \begin{vmatrix} \frac{\partial x_m}{\partial u} & \frac{\partial z_m}{\partial u} \\ \frac{\partial x_m}{\partial \theta} & \frac{\partial z_m}{\partial \theta} \end{vmatrix} + \begin{vmatrix} a_{22} & a_{23} \\ a_{32} & a_{33} \end{vmatrix} \cdot \begin{vmatrix} \frac{\partial y_m}{\partial u} & \frac{\partial z_m}{\partial u} \\ \frac{\partial y_m}{\partial \theta} & \frac{\partial z_m}{\partial \theta} \end{vmatrix} \tag{3.6.26}$$

With Equations (3.6.12), (3.6.16), (3.6.17) and (3.6.18), the above equation can be simplified as follows

$$N_{nx} = a_{11}N_{mx} + a_{12}N_{my} + a_{13}N_{mz} \tag{3.6.27}$$

The second term and third term of Equation (3.6.26) can be derived in the same manner and represented as follows

$$N_{ny} = a_{21}N_{mx} + a_{22}N_{my} + a_{23}N_{mz} \tag{3.6.28}$$

$$N_{nz} = a_{31}N_{mx} + a_{32}N_{my} + a_{33}N_{mz} \tag{3.6.29}$$

Rewriting Equations (3.6.27) to (3.6.29) in matrix form has

$$\begin{Bmatrix} N_{nx} \\ N_{ny} \\ N_{nz} \end{Bmatrix} = \begin{bmatrix} a_{11} & a_{12} & a_{13} \\ a_{21} & a_{22} & a_{23} \\ a_{31} & a_{32} & a_{33} \end{bmatrix} \cdot \begin{Bmatrix} N_{mx} \\ N_{my} \\ N_{mz} \end{Bmatrix} \tag{3.6.30}$$

Substituting Equation (3.6.11) into the above equation yields

$$\mathbf{N}_n(u,\theta) = \mathbf{L}_{nm} \cdot \mathbf{N}_m(u,\theta) \tag{3.6.31}$$

The relationship between the position transformation matrix and the normal transformation matrix is thus proved.

3.6.3.2 Determination of Transformation Matrices 2

The advantage of the second method is that it reduces the length of the programming codes and calculation times. Method 2 still uses the relationships of method 1 but it derives the normal transformation matrices in a clearer way using the transformation rules between different coordinate systems.

The normal transformation matrix from coordinate system S_w to S_f can be obtained by the product of the transformation matrices from S_w to S_p and from S_p to S_f.

$$\mathbf{L}'_{fw} = \mathbf{L}'_{fp} \cdot \mathbf{L}'_{pw} \tag{3.6.32}$$

The normal transformation matrices from coordinate system S_w to S_p and from S_p to S_f can be written directly from Figure 3.15.

$$\mathbf{L}'_{fp} = \begin{bmatrix} \cos(\gamma+\Delta\gamma) & 0 & \sin(\gamma+\Delta\gamma) \\ 0 & 1 & 0 \\ -\sin(\gamma+\Delta\gamma) & 0 & \cos(\gamma+\Delta\gamma) \end{bmatrix} \tag{3.6.33}$$

$$\mathbf{L}'_{pw} = \begin{bmatrix} \cos\phi'_w & -\sin\phi'_w & 0 \\ \sin\phi'_w & \cos\phi'_w & 0 \\ 0 & 0 & 1 \end{bmatrix} \tag{3.6.34}$$

The normal transformation matrix from coordinate system S_1 to S_f can be obtained by the product of the transformation matrices from S_1 to S_2 and from S_2 to S_f.

$$\mathbf{L}'_{f1} = \mathbf{L}'_{f2} \cdot \mathbf{L}_{21} \tag{3.6.35}$$

where $\mathbf{L}_{21}$ is presented in Equation (3.4.8); The normal transformation matrices from coordinate system S_2 to S_f can be obtained directly from Figure 3.15.

$$\mathbf{L}_{f2}^{'}=\begin{bmatrix}\cos\phi_2^{'} & -\sin\phi_2^{'} & 0\\ \sin\phi_2^{'} & \cos\phi_2^{'} & 0\\ 0 & 0 & 1\end{bmatrix} \tag{3.6.36}$$

3.6.4 Meshing Equations at Localised Bearing Points

The relative velocity of the gear to the worm $\mathbf{v}_w^{(w2)}$ in coordinate system S_w can be written as follows

$$\mathbf{v}_w^{(w2)}=(\boldsymbol{\omega}_w^{(w)}-\boldsymbol{\omega}_w^{(2)})\times\mathbf{r}_{1w}-\mathbf{E}_w\times\boldsymbol{\omega}_w^{(2)} \tag{3.6.37}$$

where

$\boldsymbol{\omega}_w^{(w)}$ is the angular velocity of worm in coordinate system S_w

$\boldsymbol{\omega}_w^{(2)}$ is the angular velocity of gear in coordinate system S_w

$\mathbf{r}_{1w}$ is the position vector of worm surface in coordinate system S_w

$\mathbf{E}_w$ is the vector of O_p to O_2, O_p is the origin of the coordinate system S_p and O_2 is the origin of the coordinate system S_2

The rotation speed of the worm in coordinate system S_w is written as

$$\boldsymbol{\omega}_w^{(w)}=\omega_w\cdot\mathbf{k}_w \tag{3.6.38}$$

The rotation speed of gear in coordinate system S_2 is written as

$$\boldsymbol{\omega}_2^{(2)}=\omega_2\cdot\mathbf{k}_2 \tag{3.6.39}$$

The vector from O_p to O_2 in coordinate system S_f is

$$\mathbf{E}_f^{'}=\overline{O_pO_2}=-(L+\Delta L)\cdot\mathbf{i}_f+(E+\Delta E)\cdot\mathbf{j}_f \tag{3.6.40}$$

The vector from O_p to O_2 in coordinate system S_w can be obtained from the vector from O_p to O_2 in coordinate system S_f by multiplying by a series of transformation matrices.

$$\mathbf{E}_w = \overline{O_p O_2} = \mathbf{L}'_{wf} \cdot \mathbf{E}'_f = \mathbf{L}'_{wp} \cdot \mathbf{L}'_{pf} \cdot \mathbf{E}'_f \tag{3.6.41}$$

The normal transformation matrices from coordinate system S_p to S_w and from S_f to S_p can be written directly from Figure 3.15.

$$\mathbf{L}'_{pf} = \begin{bmatrix} \cos(\gamma+\Delta\gamma) & 0 & -\sin(\gamma+\Delta\gamma) \\ 0 & 1 & 0 \\ \sin(\gamma+\Delta\gamma) & 0 & \cos(\gamma+\Delta\gamma) \end{bmatrix} \tag{3.6.42}$$

$$\mathbf{L}'_{wp} = \begin{bmatrix} \cos\phi'_w & \sin\phi'_w & 0 \\ -\sin\phi'_w & \cos\phi'_w & 0 \\ 0 & 0 & 1 \end{bmatrix} \tag{3.6.43}$$

Substituting above two equations and Equation (3.6.40) into Equation (3.6.41) yields

$$\mathbf{E}_w = \begin{Bmatrix} -(L+\Delta L)\cdot\cos\phi'_w \cdot \cos(\gamma+\Delta\gamma) + (E+\Delta E)\cdot\sin\phi'_w \\ (L+\Delta L)\cdot\sin\phi'_w \cdot \cos(\gamma+\Delta\gamma) + (E+\Delta E)\cdot\cos\phi'_w \\ -(L+\Delta L)\cdot\sin(\gamma+\Delta\gamma) \end{Bmatrix} \tag{3.6.44}$$

The rotating speed of the gear in coordinate system S_w can be transformed from the rotating speed $\boldsymbol{\omega}_2^{(2)}$ by multiplying by the appropriate transformation matrix.

$$\boldsymbol{\omega}_w^{(2)} = \mathbf{L}'_{w2} \cdot \boldsymbol{\omega}_2^{(2)} \tag{3.6.45}$$

where $\mathbf{L}'_{w2}$ is the transformation matrix from coordinate system S_2 to S_w. It can be obtained by a series transformation processes illustrated as follows

$$\mathbf{L}'_{w2} = \mathbf{L}'_{wp} \cdot \mathbf{L}'_{pf} \cdot \mathbf{L}'_{f2} \tag{3.6.46}$$

The transformation matrix $\mathbf{L}'_{f2}$ is presented in Equation (3.6.36); the other two transformation matrices are presented in Equations (3.6.42) and (3.6.43).

By substituting Equations (3.6.36), (3.6.42) and (3.6.43) into Equation (3.6.46), the product of the matrices of Equation (3.6.46) is obtained as follows

$$\mathbf{L}'_{w2} = \begin{bmatrix} (\mathbf{L}'_{w2})_{11} & (\mathbf{L}'_{w2})_{12} & (\mathbf{L}'_{w2})_{13} \\ (\mathbf{L}'_{w2})_{21} & (\mathbf{L}'_{w2})_{22} & (\mathbf{L}'_{w2})_{23} \\ (\mathbf{L}'_{w2})_{31} & (\mathbf{L}'_{w2})_{32} & (\mathbf{L}'_{w2})_{33} \end{bmatrix} \tag{3.6.47}$$

where

$$(\mathbf{L}'_{w2})_{11} = \cos\phi'_w \cdot \cos\phi'_2 \cdot \cos(\gamma + \Delta\gamma) + \sin\phi'_w \cdot \sin\phi'_2 \tag{3.6.47a}$$

$$(\mathbf{L}'_{w2})_{12} = -\cos\phi'_w \cdot \sin\phi'_2 \cdot \cos(\gamma + \Delta\gamma) + \sin\phi'_w \cdot \sin\phi'_2 \tag{3.6.47b}$$

$$(\mathbf{L}'_{w2})_{13} = -\cos\phi'_w \cdot \sin(\gamma + \Delta\gamma) \tag{3.6.47c}$$

$$(\mathbf{L}'_{w2})_{21} = -\sin\phi'_w \cdot \cos\phi'_2 \cdot \cos(\gamma + \Delta\gamma) + \cos\phi'_w \cdot \sin\phi'_2 \tag{3.6.47d}$$

$$(\mathbf{L}'_{w2})_{22} = \sin\phi'_w \cdot \sin\phi'_2 \cdot \cos(\gamma + \Delta\gamma) + \cos\phi'_w \cdot \cos\phi'_2 \tag{3.6.47e}$$

$$(\mathbf{L}'_{w2})_{23} = \sin\phi'_w \cdot \sin(\gamma + \Delta\gamma) \tag{3.6.47f}$$

$$(\mathbf{L}'_{w2})_{31} = \cos\phi'_2 \cdot \sin(\gamma + \Delta\gamma) \tag{3.6.47g}$$

$$(\mathbf{L}'_{w2})_{32} = -\sin\phi'_2 \cdot \sin(\gamma + \Delta\gamma) \tag{3.6.47h}$$

$$(\mathbf{L}'_{w2})_{33} = \cos(\gamma + \Delta\gamma) \tag{3.6.47i}$$

Substituting Equation (3.6.47) into Equation (3.6.45) yields

$$\boldsymbol{\omega}_w^{(2)} = \begin{Bmatrix} -\omega_2' \cdot \cos\phi_w' \cdot \sin(\gamma+\Delta\gamma) \\ \omega_2' \cdot \sin\phi_w' \cdot \sin(\gamma+\Delta\gamma) \\ \omega_2' \cdot \cos(\gamma+\Delta\gamma) \end{Bmatrix} \tag{3.6.48}$$

Substituting Equations (3.3.17), (3.6.44), (3.6.38), (3.6.48) into Equation (3.6.37) has

$$\begin{aligned} \mathbf{v}_w^{(w2)} &= (\boldsymbol{\omega}_w^{(w)} - \boldsymbol{\omega}_w^{(2)}) \times \mathbf{r}_w - \mathbf{E}_w \times \boldsymbol{\omega}_w^{(2)} \\ &= \begin{vmatrix} \mathbf{i}_w & \mathbf{j}_w & \mathbf{k}_w \\ \omega_2' \cos\phi_w' \sin(\gamma+\Delta\gamma) & -\omega_2' \sin\phi_w' \sin(\gamma+\Delta\gamma) & \omega_w' - \omega_2' \cos(\gamma+\Delta\gamma) \\ x_w & y_w & z_w \end{vmatrix} \\ &- \begin{vmatrix} \mathbf{i}_w & \mathbf{j}_w & \mathbf{k}_w \\ [-(L+\Delta L)\cos\phi_w' \cos(\gamma+\Delta\gamma) & [(L+\Delta L)\sin\phi_w' \cos(\gamma+\Delta\gamma) & -(L+\Delta L)\sin(\gamma+\Delta\gamma) \\ +(E+\Delta E)\sin\phi_w'] & +(E+\Delta E)\cos\phi_w'] & \\ -\omega_2' \cos\phi_w' \sin(\gamma+\Delta\gamma) & \omega_2' \sin\phi_w' \sin(\gamma+\Delta\gamma) & \omega_2' \cos(\gamma+\Delta\gamma) \end{vmatrix} \end{aligned} \tag{3.6.49}$$

The results of above equation can be written in the following format

$$\mathbf{v}_w^{(w2)} = v_{wx}^{(w2)} \cdot \mathbf{i}_w + v_{wy}^{(w2)} \cdot \mathbf{j}_w + v_{wz}^{(w2)} \cdot \mathbf{k}_w \tag{3.6.50}$$

where

$$\begin{aligned} v_{wx}^{(w2)} &= -z_w\omega_2' \sin\phi_w' \sin(\gamma+\Delta\gamma) - y_w(\omega_w' - \omega_2' \cos(\gamma+\Delta\gamma)) \\ &-(L+\Delta L)\omega_2' \sin\phi_w' \sin^2(\gamma+\Delta\gamma) \\ &-\omega_2' \cos(\gamma+\Delta\gamma) \cdot ((L+\Delta L)\sin\phi_w' \cos(\gamma+\Delta\gamma) + (E+\Delta E)\cos\phi_w') \end{aligned} \tag{3.6.51}$$

$$\begin{aligned} v_{wy}^{(w2)} &= -z_w\omega_2' \cos\phi_w' \sin(\gamma+\Delta\gamma) + x_w(\omega_w' - \omega_2' \cos(\gamma+\Delta\gamma)) \\ &-(L+\Delta L)\omega_2' \cos\phi_w' \sin^2(\gamma+\Delta\gamma) \\ &+\omega_2' \cos(\gamma+\Delta\gamma) \cdot (-(L+\Delta L)\cos\phi_w' \cos(\gamma+\Delta\gamma) + (E+\Delta E)\sin\phi_w') \end{aligned} \tag{3.6.52}$$

$$v_{wz}^{(w2)} = y_w\omega_2^{'}\cos\phi_w^{'}\sin(\gamma+\Delta\gamma) + x_w\omega_2^{'}\sin\phi_w^{'}\sin(\gamma+\Delta\gamma)$$
$$-\omega_2^{'}\sin\phi_w^{'}\sin(\gamma+\Delta\gamma)\cdot(-(L+\Delta L)\cos\phi_w^{'}\cos(\gamma+\Delta\gamma)+(E+\Delta E)\sin\phi_w^{'})$$
$$-\omega_2^{'}\cos\phi_w^{'}\sin(\gamma+\Delta\gamma)\cdot((L+\Delta L)\sin\phi_w^{'}\cos(\gamma+\Delta\gamma)+(E+\Delta E)\cos\phi_w^{'}) \quad (3.6.53)$$

The meshing equation of the modified worm pinion and gear with misalignments is thus written as

$$\mathbf{N}_{1w}\cdot\mathbf{v}_w^{(w2)} = 0 \quad (3.6.54)$$

Substituting Equation (3.6.50) into the above equation has the meshing equation

$$N_{1wx}\cdot v_{wx}^{(w2)} + N_{1wy}\cdot v_{wy}^{(w2)} + N_{1wz}\cdot v_{wz}^{(w2)} = 0 \quad (3.6.55)$$

3.6.5 Meshing Simulation

Consider the gear assembly with misalignments in the centre distance, an axial displacement error and shaft angle amounting error, when the pinion and the gear are in mesh, the coordinates of their contact points must be the same, i.e.

$$\mathbf{r}_f^{(2)} = \mathbf{r}_f^{(w)} \quad (3.6.56)$$

Meanwhile, at the contact points, the unit normals to the pinion and the gear must be in the same direction, i.e.

$$\mathbf{n}_f^{(w)} = \mathbf{n}_f^{(2)} \quad (3.6.57)$$

According to the theory of meshing, at the contact points, they should still satisfy the meshing equations, i.e.

$$\mathbf{N}_{1w}\times\mathbf{v}_w^{(w2)} = 0 \quad (3.6.58)$$

The equations for simulating the localised tooth contact of the spiroid gears are therefore summarised as follows

$$\mathbf{r}_f^{(w)}(u_w,\theta_w,\phi_w^{'},\Delta L,\Delta E,\Delta\gamma)=\mathbf{r}_f^{(2)}(u_h,\theta_h,\phi_1,\phi_2^{'}) \tag{3.6.59}$$

$$\mathbf{n}_f^{(w)}(u_w,\theta_w,\phi_w^{'},\Delta\gamma)=\mathbf{n}_f^{(2)}(u_h,\theta_h,\phi_1,\phi_2^{'}) \tag{3.6.60}$$

$$\mathbf{N}_{1w}\times\mathbf{v}_{1w}^{(w2)}=0 \tag{3.6.61}$$

where

$\mathbf{r}_f^{(w)}$ - position vector of the pinion surface in coordinate system S_f

$\mathbf{r}_f^{(2)}$ - position vector of the gear surface in coordinate system S_f

u_w, θ_w - the modified pinion surface parameters

ϕ'_w - the rotation angles of the pinion

ϕ'_2 - the rotation angles of the gear

ΔL - axial displacement error

ΔE - shortest centre distance error

$\Delta\gamma$ - misalignment of the shaft angle

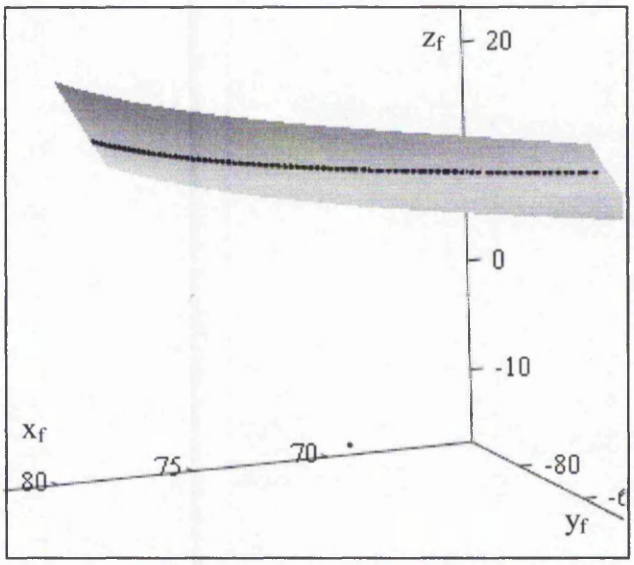
Equations (3.6.59)-(3.6.61) have seven unknowns but there are only six independent scalar equations since $\left|\mathbf{n}_f^{(w)}\right|=\left|\mathbf{n}_f^{(2)}\right|=1$ in Equation (3.6.60). The worm rotation angle ϕ'_w is used as an input so Equations (3.6.59)-(3.6.61) can be solved.

The localised tooth contact paths are shown in Figure 3.17. They are based on the calculated results from the tooth contact analysis. They clearly show that the proposed modification to the geometry permits a localised bearing contact (Figure 3.17).

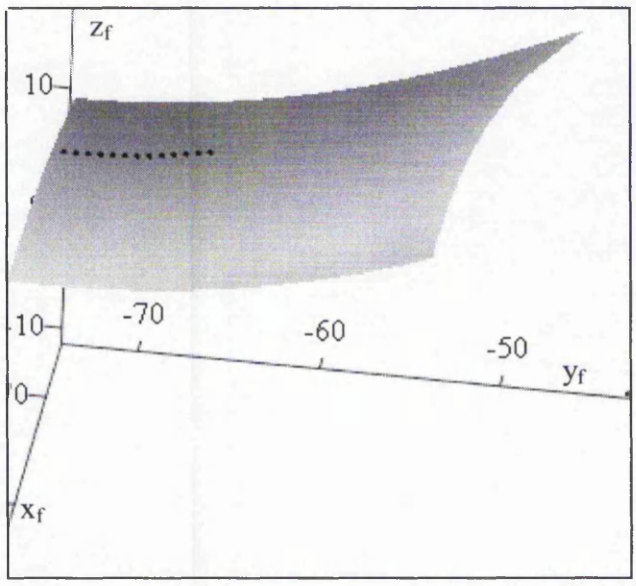
Using the solved surface equations, the paths of contact on the contacting surfaces and the shift of the bearing contact caused by misalignment can be determined. The function $\phi_2^{'}(\phi_w^{'})$ is the transmission function of the misaligned gear drive and the

deviations $\Delta\phi_2'$ of this function from the theoretical one represent the transmission errors caused by misalignment. Thus, we have

$$\Delta\phi_2' = \phi_2'(\phi_w') - \frac{N_1}{N_2}\phi_w' \tag{3.6.47}$$



(a) $\Delta\gamma$=2′, ΔE=ΔL=0, ξ=2°, $\Delta\alpha$=0.252° (Side I)



(b) $\Delta\gamma$=2′, ΔE=ΔL=0, ξ=-2.5°, $\Delta\alpha$=0.25°(Side II)

Figure 3.17 Localised contact path in the gear tooth surface



3.7 CONCLUSIONS

A new method has been developed to obtain localised tooth contact for spiroid gear drives by modifying the pinion tooth surface. With this method, the localised contact is achieved by slightly adjusting two mounting angles of the pinion cutter when the pinion is cut. This method can be implemented on conventional equipment without extra cost. This is much simpler and more economical than existing methods. In this chapter, the following work has been presented:

- The detailed description of the modification principles including the change of cutting edge's mounting angle and re-setting of the cutter location has been presented.
- Equations regarding the geometry of the hob, the modified pinion and the spiroid gear have been derived.
- Program codes for calculating the gear surfaces, pinion surfaces, tooth contact paths and transmission errors have been written.
- The results of numerical simulation of the tooth contact have confirmed that the proposed modification to the geometry permits a localised bearing contact.

CHAPTER 4 Numerical Simulation of Localised Tooth Contact of Helicon Gears

The approach developed in the preceding chapter is applied to obtain the favourable localised bearing contact of helicon gear drives. The surface equations of the helicon gear, hob and pinion are derived. The parameters for the modification of the pinion have been determined. Programs have been written to obtain the coordinates of the helicon gear and the modified pinion's surfaces. Computerised simulation of localised tooth contact has been conducted. The results of numerical simulation show that the proposed modification of the tooth geometry permits a favourable localised bearing contact.

4.1 INTRODUCTION

The helicon gear drive belongs to the spiroid family and is used for the transmission of power between non-intersecting and non-parallel axes shafts. While a spiroid gear drive has a tapered worm pinion, a helicon gear drive has a cylindrical worm pinion (see Figure 1.2).

The generating process of helicon gears is similar to spiroid gears and worm gears. Helicon gears are cut by a cylindrical hob. The hob is identical to its worm pinion except that it has blades and flutes for cutting. The hobbing process is the same as the operation of the helicon gears. Such a helicon gear drive has line contact between the pinion and the face gear and is sensitive to misalignment that inevitably arises from the manufacturing and assembly processes. This will cause an undesirable shift of the bearing contact to the edge of the teeth and would reduce its working life.

In this research, the method of modification developed in the preceding chapter is applied to helicon gears to achieve the preferred localised tooth contact. The numerical models of the helicon gear, hob and the modified pinion have been established. The parameters for the modified pinion cut setting have been determined and illustrated. Programs have been written to simulate the localised tooth contact based on the established numerical models.

4.2 METHOD OF MODIFICATION

The conventional helicon pinion considered in this research is an Archimedean cylindrical worm. The helicon gear is produced using a helicon hob whose thread profile is identical to the helicon pinion. Such a helicon gear drive has instantaneous line contact between the pinion and gear tooth surfaces and therefore is sensitive to misalignment. Localising the tooth contact can reduce this sensitivity.

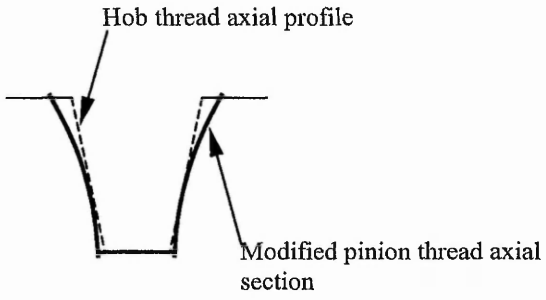


Figure 4.1 Pinion and hob tooth profile

The basic idea to achieve localised tooth contact for helicon gearing is to mismatch the gear and pinion's geometry. The mismatch between gear and pinion can be achieved by a mismatch of the gear's standard hob and pinion. The mismatch of hob and pinion can be achieved by modifying the pinion's tooth surface. Figure 2 shows the hob's tooth profile and the modified pinion's tooth profile. From the pre-designed conditions, this mismatch between the pinion and the gear will result in a preferred localised contact on the tooth surfaces.

4.3 THE HELICON GEAR HOB AND PINION SURFACE EQUATIONS

4.3.1 Equations of Helicon Gear Hob Tooth Surface

Two coordinate systems are used for the helicon hob and its cutter (see Figure 4.2). The coordinate system $S_1(O_1, X_1,Y_1,Z_1)$ is rigidly connected to the hob. The coordinate system $S_b(O_b, X_b,Y_b,Z_b)$ is rigidly connected to the hob's cutter, with its origin O_b situated at the intersection point of the straight lines of cutting edges I and II

(see Figure 4.4). The hob surfaces are generated by the two cutting edges I and II which are in the axial plane of the hob. The track of the cutter's movement is a space helix curve. Figure 4.3 shows the cutter's two positions during its movement: the origin O_{b0} is at the initial position of the cutter's movement. After the cutter is rotated about axis Z_1 with angle θ, the coordinate system S_b's original position is reached at $O_{b\theta}$.

The vector of the generatrices of the hob tooth surface represented in coordinate system S_b is given by

$$\mathbf{r}_b^{(i)}(u) = \begin{Bmatrix} u\cos\alpha^{(i)} \\ 0 \\ \mp u\sin\alpha^{(i)} \end{Bmatrix} \tag{4.3.1}$$

where, as shown in Figure 4.4, u is the surface parameter; $\alpha^{(i)}$ is the angle of generatrix, i=I, II indicates the two cutting edges respectively, and the negative sign "–" is for the side I (i=I) and the positive sign "+" is for side II (i=II).

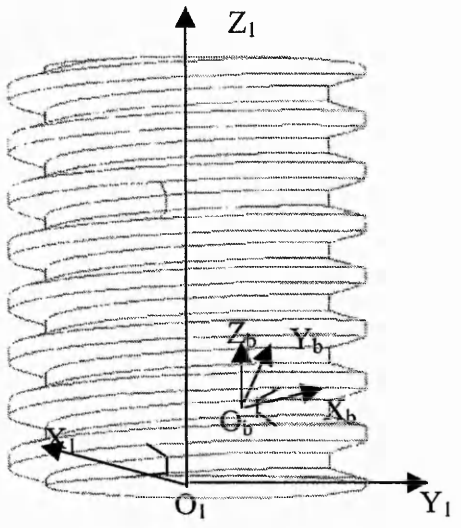


Figure 4.2 Coordinate systems for a helicon pinion

The hob tooth surface is thus obtained as

$$\mathbf{r}_1^{(i)}(u,\theta) = \mathbf{M}_{1b} \cdot \mathbf{r}_b^{(i)}(u) \tag{4.3.2}$$

where $\mathbf{M}_{1b}$ is the transformation matrix from coordinate system S_b to S_1,

$$\mathbf{M}_{1b} = \begin{bmatrix} \cos\theta & -\sin\theta & 0 & r_0 \cdot \cos\theta \\ \sin\theta & \cos\theta & 0 & r_0 \cdot \sin\theta \\ 0 & 0 & 1 & z_0 + p \cdot \theta \\ 0 & 0 & 0 & 1 \end{bmatrix} \tag{4.3.3}$$

where p is the screw parameter.

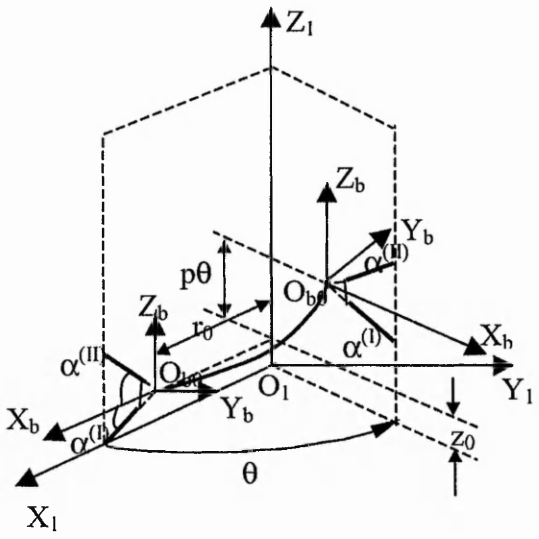


Figure 4.3 Pinion cutter's movement in relation to the coordinate systems

Substituting Equation (4.3.3) into Equation (4.3.2), the helicon hob surface equation is then obtained as follows

$$\mathbf{r}_b^{(i)}(u,\theta) = \begin{Bmatrix} (u\cos\alpha^{(i)} + r_0)\cdot\cos\theta \\ (u\cos\alpha^{(i)} + r_0)\cdot\sin\theta \\ \mp u\sin\alpha + p\cdot\theta + z_0 \\ 1 \end{Bmatrix} \tag{4.3.4}$$

As a numerical example of the use of Equation (4.3.4), Figure 4.5 shows the surface of the helicon gear hob used later in the example of numerical tooth contact analysis.

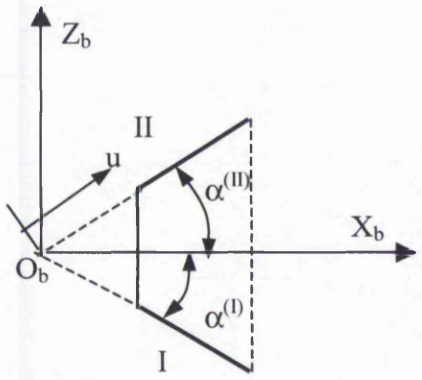


Figure 4.4 The cutter's two cutting edges I and II in coordinate system S_b

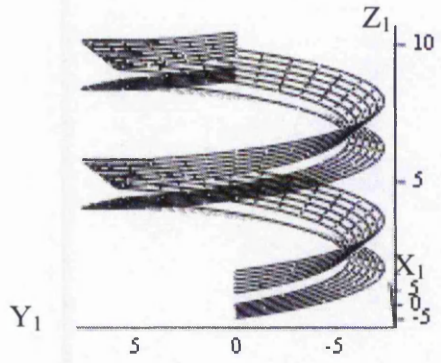


Figure 4.5 Right hand helicon hob thread surface

4.3.2 Equations of Modified Pinion Tooth Thread Surface

The coordinate systems for the modified pinion's cutter are shown in Figure 4.6. The generatrices of the modified helicon pinion tooth surface are still a straight line, but the angles are changed with increments $\Delta\alpha^{(I)}$ for side I, $\Delta\alpha^{(II)}$ for side II, as shown in Figure 4.6. In addition, the cutter's position is different from the original setting, which is illustrated in Figure 4.6. The coordinate system S_m (O_m; X_m,Y_m,Z_m) is rigidly connected to the cutter. The new setting is represented in coordinate system S_m and its position is determined as follows

- Plane $Z_mO_mY_m$, where the generating line lies, is rotated from the initial plane $Z_bO_bY_b$ about Z_b with angle ξ;

- S_m moves to a new position with its origin O_m away from O_b with Δx, Δy, Δz, while keeping axis Z_m parallel to Z_b .

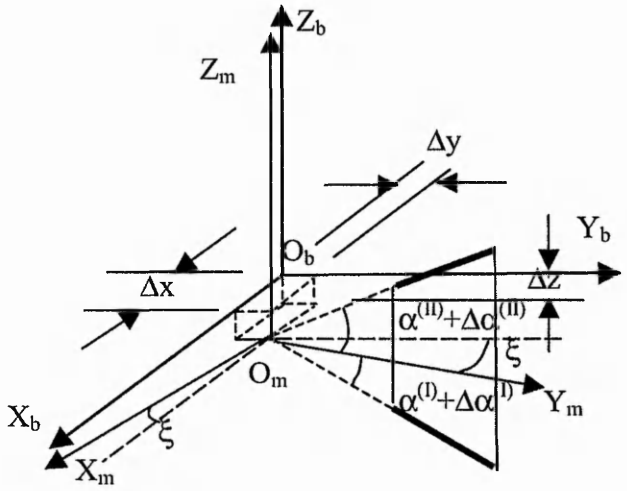


Figure 4.6 Coordinate systems for modified pinion

The generating line vector in coordinate system S_m is expressed as

$$\mathbf{r}_m^{(i)}(u) = \begin{Bmatrix} u\cos(\alpha^{(i)} + \Delta\alpha^{(i)}) \\ 0 \\ \mp u\sin(\alpha^{(i)} + \Delta\alpha^{(i)}) \end{Bmatrix} \tag{4.3.5}$$

where i=I, II, indicating the generating lines I and II respectively.

The modified pinion thread surface can be obtained by

$$\mathbf{r}_{1w}^{(i)}(u,\theta) = \mathbf{M}_{1b} \cdot \mathbf{M}_{bm} \cdot \mathbf{r}_m^{(i)}(u) \tag{4.3.6}$$

where $\mathbf{M}_{bm}$ is the transformation matrix from S_m to S_b,

$$M_{bm} = \begin{bmatrix} \cos\xi & \sin\xi & 0 & \Delta x \\ -\sin\xi & \cos\xi & 0 & \Delta y \\ 0 & 0 & 1 & \Delta z \\ 0 & 0 & 0 & 1 \end{bmatrix} \tag{4.3.7}$$

With Equation (4.3.7), and (4.3.3), the modified helicon pinion surface equation is then rewritten as

$$\mathbf{r}_{1w}^{(i)}(u,\theta) = \begin{Bmatrix} (u\cos(\alpha^{(i)} + \Delta\alpha^{(i)})\cdot\cos\xi + \Delta x + r_0)\cdot\cos\theta \\ -(\Delta y - u\cos(\alpha^{(i)} + \Delta\alpha^{(i)})\cdot\sin\xi)\cdot\sin\theta \\ (u\cos(\alpha^{(i)} + \Delta\alpha^{(i)})\cdot\cos\xi + \Delta x + r_0)\cdot\sin\theta \\ +(\Delta y - u\cos(\alpha^{(i)} + \Delta\alpha^{(i)})\cdot\sin\xi)\cdot\cos\theta \\ \mp u\sin(\alpha^{(i)} + \Delta\alpha^{(i)}) + p\cdot\theta + z_0 + \Delta z \\ 1 \end{Bmatrix} \tag{4.3.8}$$

In order to achieve the favourable localised tooth contact, the following two conditions must be satisfied:

(1) At the pre-designed contact point M, the coordinates of the hob and the pinion's thread must be the same, which ensures that the hob and the pinion are in contact. This will lead to

$$\mathbf{r}_{1w}(u,\theta)\Big|_{u=u_M^{(p)}} = \mathbf{r}_{1h}(u,\theta)\Big|_{u=u_M^{(h)}} \tag{4.3.9}$$

where

$\mathbf{r}_{1w}$ is the position vector of the modified worm pinion thread surface

$\mathbf{r}_{1h}$ is the position vector of the hob thread surface

u and θ are the surface parameters

(2) At the given contact point $M(x_M, y_M, z_M)$, the modified pinion and the hob thread surfaces must be tangentral to each other.

Since the pinion and the hob of a helicon gear drive are cylindrical worms, their tooth profiles are identical in any two arbitrary axial sections. Therefore the above three dimensional tangent condition can be simplified into two-dimensional conditions, as described below.

The pinion and hob thread surface intersect with the plane of $X_1O_1Z_1$ of coordinate system S_1 will yield two curves: one curve (C_p) is from the intersection with the pinion tooth thread; the other (C_h) is from the intersection with the hob. Both curves should be tangent to each other at point M, and hence have the same tangency at point M, i.e.

$$\left.\frac{dz^{(p)}}{dx}\right|_{u=u_M^{(p)}} = \left.\frac{dz^{(h)}}{dx}\right|_{u=u_M^{(h)}} = \tan\alpha^{(i)} \tag{4.3.10}$$

where, the superscripts p and h indicate pinion and hob respectively, subscript M indicates the contact point M.

For side I, the curvature of curve C_h should be smaller than that of curve C_p so that the modified pinion tooth will not interfere with its mating gear but make contact with it at point M. For side II, in contrast, the curvature of curve C_h should be greater than that of curve C_p. Therefore

$$\left.\frac{d^2z^{(h)}}{dx^2}\right|_{x\neq x_M} < \left.\frac{d^2z^{(p)}}{dx^2}\right|_{x\neq x_M} \quad \text{(Side I)} \tag{4.3.11}$$

$$\left.\frac{d^2z^{(h)}}{dx^2}\right|_{x\neq x_M} > \left.\frac{d^2z^{(p)}}{dx^2}\right|_{x\neq x_M} \quad \text{(Side II)} \tag{4.3.12}$$

Substituting Equations (4.3.4), (4.3.8) into Equation (4.3.9), through a series of mathematical operations, the following equations can finally be derived

$$\Delta x = -u_M^{(p)}\cos(\alpha^{(i)}+\Delta\alpha^{(i)})\cdot\cos\xi + u_M^{(h)}\cos\alpha \tag{4.3.13}$$

$$\Delta y = u_M^{(p)} \cos(\alpha^{(i)} + \Delta\alpha^{(i)}) \cdot \sin\xi \tag{4.3.14}$$

$$\Delta z = \mp u_M^{(h)} \sin\alpha^{(i)} - (\mp) u_M^{(p)} \sin(\alpha^{(i)} + \Delta\alpha^{(i)}) \tag{4.3.15}$$

Given ξ, $\Delta\alpha$ and the point M's coordinates, the modification parameters Δx, Δy, Δz can be obtained. The angles ξ and $\Delta\alpha$ are calculated using the tangent condition given by Equations (4.3.10).

Figure 4.7 and Figure 4.9 show one example of the tooth profiles of the modified pinion and the hob used to cut the mating helicon gear. Their major design parameters are listed in Table 4.1. Figure 4.7 and Figure 4.8 show the tooth profile results related to the generating line of side I with ξ=2° and $\Delta\alpha$=0.196°. Figure 4.7 shows the tooth profiles of the hob and the modified pinion in the axial section. X_b and Z_b in Figure 4.7 are the hob tooth profile coordinate in coordinates sytem S_b (see Figure 4.4). The differences between them are clearly indicated in Figure 4.8. Similarly, the tooth profile results for side II with ξ= -2° and $\Delta\alpha$=0.141° are shown in Figure 4.9 and Figure 4.10. Note that the ξ values are different. For the given example, the contact point is pre-designed near the middle of the tooth surface as shown in Figure 4.8 and Figure 4.10.

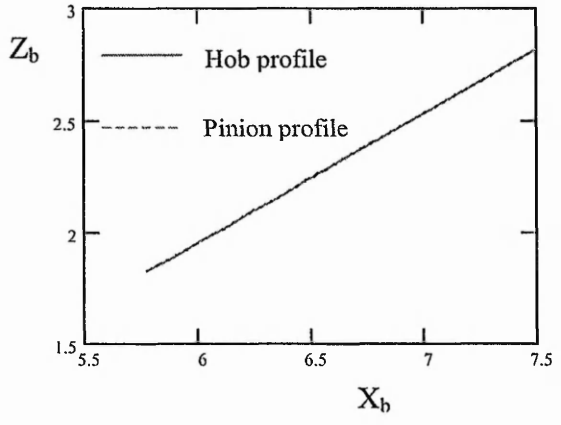


Figure 4.7 Axial section profile of hob thread and modified pinion thread (Side I) ξ=2°, $\Delta\alpha$=0.196°, (unit: mm)

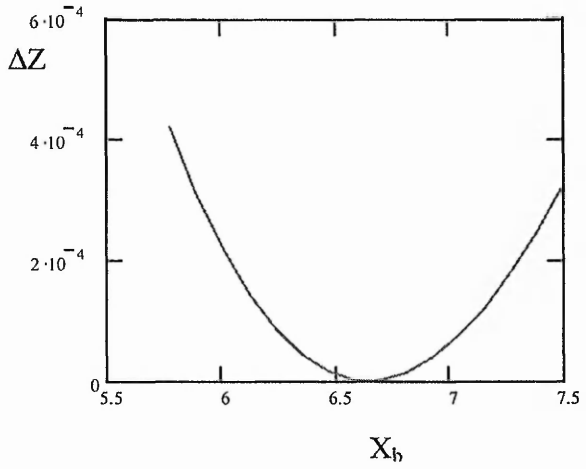


Figure 4.8 Difference in hob and pinion's axial section profile: $\Delta Z=Z_{\text{hob thread}} - Z_{\text{modified pinion thread side I}}$ (unit: mm)

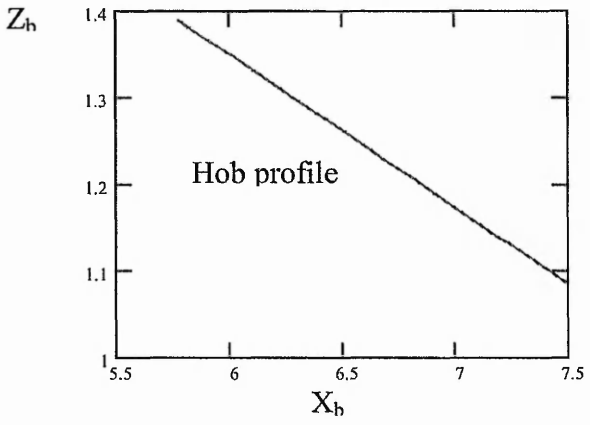


Figure 4.9 Axial section of hob thread and modified pinion thread (Side II) ξ=-2°, $\Delta\alpha$=0.141°, (unit: mm)

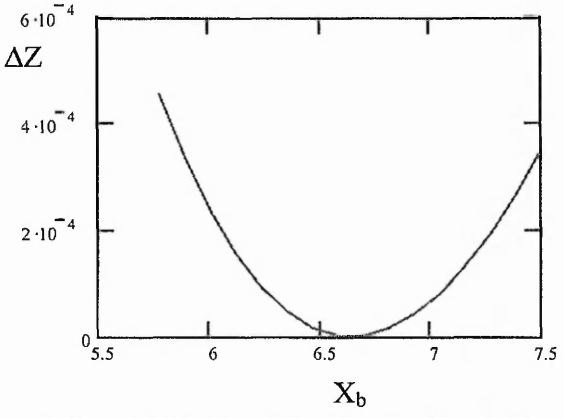


Figure 4.10 Difference in hob and pinion's axial section profile: $\Delta Z=Z_{\text{hob thread}} - Z_{\text{modified, (Side II),}}$ (unit: mm)

4.4 GEAR SURFACE EQUATIONS

The helicon gear tooth surface is generated by a hob and is an envelope of the hob tooth surface. The gear surface is constituted by the instantaneous contact lines between the hob and the gear when they are in mesh. To derive the helicon gear tooth surface, the following coordinate systems are used:

1. $S_f(O_f;X_f,Y_f,Z_f)$: stationary system connected to the frame with its origin situated on the gear axis
2. $S_p(O_p;X_p,Y_p,Z_p)$: stationary system connected to the frame with its origin situated on the pinion axis
3. $S_w(O_w;X_w,Y_w,Z_w)$: rigidly connected to the pinion
4. $S_1(O_1;X_1,Y_1,Z_1)$: rigidly connected to the hob
5. $S_2(O_2;X_2,Y_2,Z_2)$: rigidly connected to the gear

The surface equations of the helicon gear can be obtained from the following two equations.

$$\mathbf{N}_1 \cdot \mathbf{v}_1^{(12)} = 0 \tag{4.4.1}$$

$$\mathbf{r}_2(u,\theta,\phi_1) = \mathbf{M}_{21} \cdot \mathbf{r}_1(u,\theta,\phi_1) \tag{4.4.2}$$

where $\mathbf{N}_1$ is the normal to the hob surface, $\mathbf{v}_1^{(12)}$ is the relative velocity of the hob and the gear represented in coordinate system S_1, and $\mathbf{M}_{21}$ is the homogenous transformation matrix from S_1 to S_2.

$$\mathbf{N}_1 = \frac{\partial \mathbf{r}_1}{\partial u} \times \frac{\partial \mathbf{r}_1}{\partial \theta} = N_{1x} \cdot \mathbf{i}_1 + N_{1y} \cdot \mathbf{j}_1 + N_{1z} \cdot \mathbf{k}_1 \tag{4.4.3}$$

where

$$N_{1x} = p \cdot \cos\alpha \cdot \sin\theta \pm \sin\alpha \cdot x_1 \tag{4.4.4}$$

$$N_{1y} = -p \cdot \cos\alpha \cdot \cos\theta \pm \sin\alpha \cdot y_1 \tag{4.4.5}$$

$$N_{1z} = (u \cdot \cos\alpha + r_{01}) \cdot \cos\alpha \tag{4.4.6}$$

The relative velocity $\mathbf{v}_1^{(12)}$ of the hob and gear in coordinate system S_1 can be obtained from the following equation

$$\begin{aligned} \mathbf{v}_1^{(12)} &= (\boldsymbol{\omega}_1^{(1)} - \boldsymbol{\omega}_1^{(2)}) \times \mathbf{r}_1 - \mathbf{E}_1 \times \boldsymbol{\omega}_1^{(2)} \\ &= v_{1x}^{(12)} \cdot \mathbf{i}_1 + v_{1y}^{(12)} \cdot \mathbf{j}_1 + v_{1z}^{(12)} \cdot \mathbf{k}_1 \end{aligned} \tag{4.4.7}$$

where

$$\begin{aligned} v_{1x}^{(12)} = & -z_1\omega_2 \sin\phi_1 \sin\gamma - y_1(\omega_1 - \omega_2 \cos\gamma) \\ & - \omega_2 \cos\gamma \cdot (L \sin\phi_1 \cos\gamma + E \cos\phi_1) \\ & - L\omega_2 \sin\phi_1 \sin^2\gamma \end{aligned} \tag{4.4.8}$$

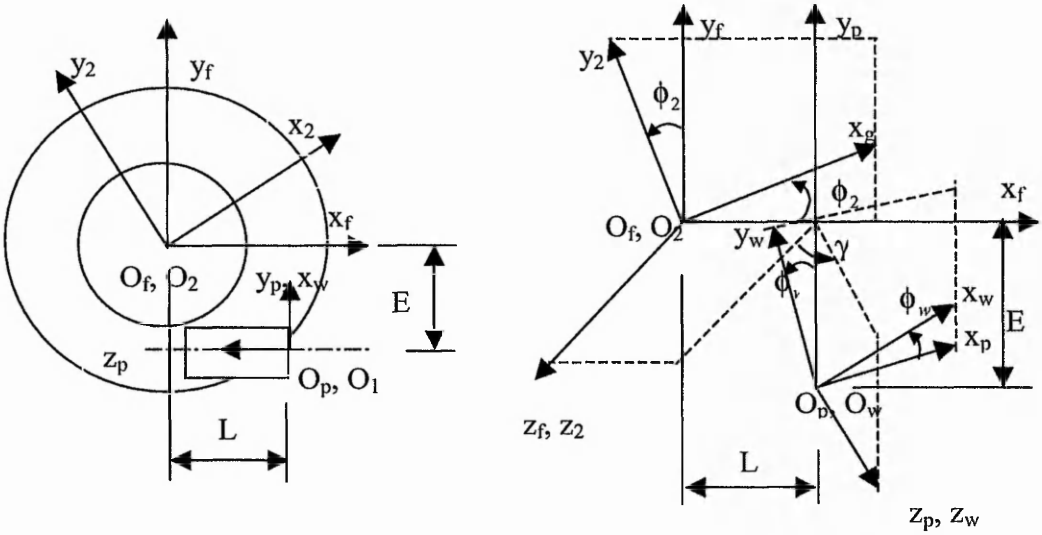
$$\begin{aligned} v_{1y}^{(12)} = & -z_1\omega_2 \cos\phi_1 \sin\gamma + x_1(\omega_1 - \omega_2 \cos\gamma) \\ & + \omega_2 \cos\gamma \cdot (-L \cos\phi_1 \cos\gamma + E \sin\phi_1) \\ & - L\omega_2 \cos\phi_1 \sin^2\gamma \end{aligned} \tag{4.4.9}$$

$$\begin{aligned} v_{1z}^{(12)} = & \, y_1\omega_2 \cos\phi_1 \sin\gamma + x_1\omega_2 \sin\phi_1 \sin\gamma \\ & - \omega_2 \cos\phi_1 \sin\gamma \cdot (L \sin\phi_1 \cos\gamma + E \cos\phi_1) \\ & - \omega_2 \sin\phi_1 \sin\gamma (-L \cos\phi_1 \cos\gamma + E \sin\phi_1) \end{aligned} \tag{4.4.10}$$

The transformation matrix $\mathbf{M}_{21}$ is obtained by

$$\mathbf{M}_{21}=\mathbf{M}_{2f}\cdot\mathbf{M}_{fp}\cdot\mathbf{M}_{p1}$$

$$=\begin{bmatrix} \cos\phi_1\cdot\cos\phi_2\cdot\cos\gamma & -\sin\phi_1\cdot\cos\phi_2\cdot\cos\gamma & & \\ +\sin\phi_1\cdot\sin\phi_2 & +\cos\phi_1\cdot\sin\phi_2 & \cos\phi_2\cdot\sin\gamma & L\cos\phi_2-E\sin\phi_2 \\ -\cos\phi_1\cdot\sin\phi_2\cdot\cos\gamma & \sin\phi_1\cdot\sin\phi_2\cdot\cos\gamma & & \\ +\sin\phi_1\cdot\cos\phi_2 & +\cos\phi_1\cdot\cos\phi_2 & -\sin\phi_2\cdot\sin\gamma & -L\sin\phi_2-E\cos\phi_2 \\ -\cos\phi_1\cdot\sin\gamma & \sin\phi_1\cdot\sin\gamma & \cos\gamma & 0 \\ 0 & 0 & 0 & 1 \end{bmatrix} \quad (4.4.11)$$



(a) Gearset (b) Coordinate systems

Figure 4.11 Generation of helicon gear

4.5 NUMERICAL SIMULATION

In order to evaluate the shift of the bearing contact for the modified helicon gear drive that is caused by misalignment, a numerical example of a helicon gear drive is presented here. The main parameters of the helicon gear drive are listed in Table 4.1.

To conduct the numerical simulation of meshing, a helicon gear tooth contact analysis program written in MathCAD has been developed. The coordinate system for the

simulation is shown in Figure 4.12, which takes into account the errors including axial displacement error, centre distance error and misalignment. The meshing algorithm is based on the condition that the pinion surface is tangent continuously with gear surface at the contact points and therefore they have the same unit normal vector.

Table 4.1 Main parameters of helicon gearset (right hand)

Ratio	25.5
Number of pinion threads	2
Number of gear teeth	51
Mounting distance of pinion	19.4725 mm
Mounting distance of gear	11.5 mm
Outside diameter of gear	48 mm
Inner diameter of gear tooth tip	35.232 mm
Centre distance	16 mm

Thus the following equations are derived

$$\mathbf{r}_f^{(w)}(u_w,\theta_w,\phi_w^{'},\Delta L,\Delta E,\Delta\gamma)=\mathbf{r}_f^{(2)}(u\ ,\theta\ ,\phi_1,\phi_2^{'}) \tag{4.5.1}$$

$$\mathbf{n}_f^{(w)}(u_w,\theta_w,\phi_w^{'},\Delta\gamma)=\mathbf{n}_f^{(2)}(u,\theta\ ,\phi_1,\phi_2^{'}) \tag{4.5.2}$$

$$\mathbf{N}_1\cdot\mathbf{v}_1^{(12)}=0 \tag{4.5.3}$$

where

$\mathbf{r}_f^{(w)}$ - position vector of the pinion in coordinate system S_f

$\mathbf{r}_f^{(2)}$ - position vector of the gear in coordinate system S_f

u_w, θ_w - the modified pinion surface parameters

ϕ'_w - the rotation angle of the pinion

ϕ'_2 - the rotation angle of the gear

ΔL - axial displacement error

ΔE - shortest centre distance error

$\Delta\gamma$ - misalignment of the shaft angle

Equations (4.5.1)-(4.5.3) have seven unknowns but there are only six independent scalar equations since $\left|\mathbf{n}_f^{(w)}\right| = \left|\mathbf{n}_f^{(2)}\right| = 1$ in Equation (4.5.2). The worm rotation angle ϕ'_w is used as input so Equation (4.5.1)-(4.5.3) can be solved.

The localised tooth contact path is shown in Figure 4.13 and is based on the calculation results of tooth contact analysis. It clearly shows that the proposed modification of the geometry permits a localised bearing contact (see Figure 4.13).

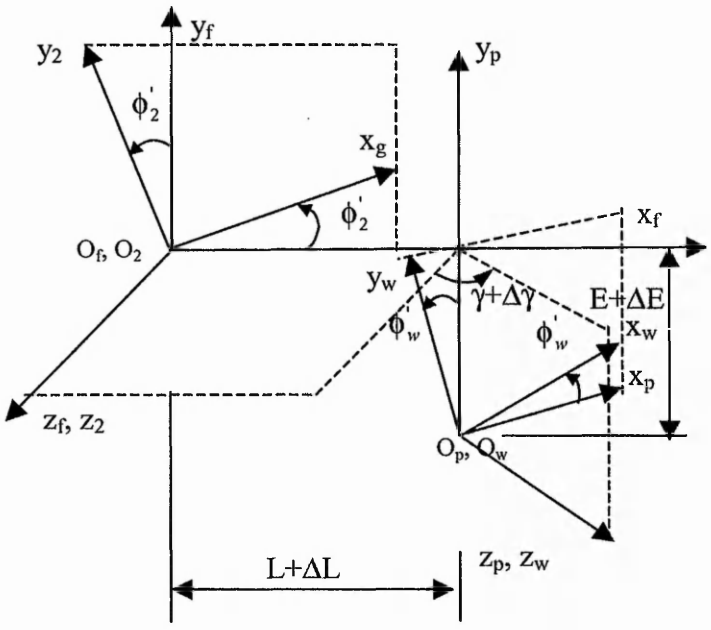
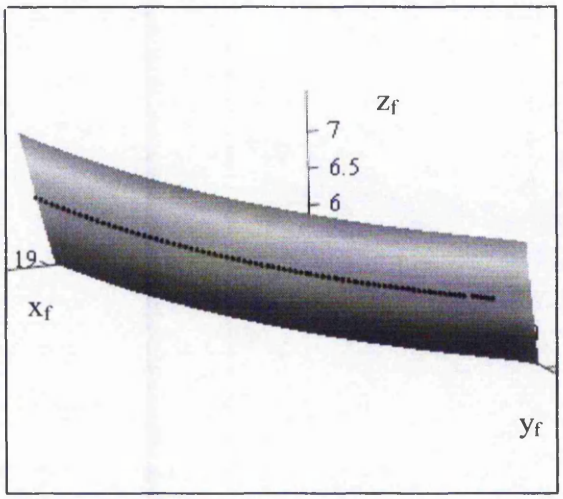


Figure 4.12 Coordinate system for simulation of meshing

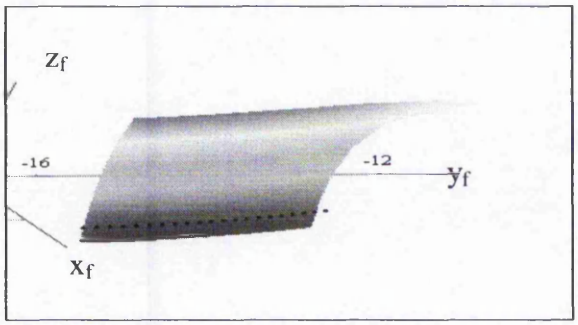
4.6 CONCLUSIONS

The novel method is applied to helicon gear drives to obtain the favourable bearing contact pattern. The modification is achieved by adjusting the mounting angles and positions of pinion's cutter. With the new method, the helicon gear is still generated by a standard hob. Therefore, it is very easy to implement in manufacturing process

without increasing extra cost. The proposed method can achieve the optimum performance of helicon gear with pre-designed tooth contact patterns.



(a) (side I),$\Delta\gamma=2'$, $\Delta E=\Delta L=0$, $\xi=2°$, $\Delta\alpha=0.196°$



(b) (side II),$\Delta\gamma=2'$, $\Delta E=\Delta L=0$, $\xi=-2°$, $\Delta\alpha=0.141°$

Figure 4.13 Localised tooth contact path of helicon gear drive in meshing (mm)

In this chapter, the following have been achieved:

- The parameters of the cutter's mounting angle and positions have been derived and demonstrated in an example design of a helicon gear.
- The equations of the hob, the modified pinion and the helicon gear surfaces have been presented.

- Programs have been written in MathCAD to obtain the coordinates of hob, pinion and gear tooth surfaces. Numerical modelling and simulation of tooth meshing with the pre-designed contact pattern have been conducted.
- Results of the numerical simulation of the tooth contact show that the proposed modification to the geometry permits a favourable localised bearing contact.

CHAPTER 5 Localised Bearing Contact of ZA Worm Gear Drives

The novel method for obtaining localised tooth contact has been extended to Archimedean worm gears. The equations of the modified worm and gear tooth surfaces have been derived. The meshing simulation of a modified Archimedean worm gear has been conducted. The results of the numerical simulation prove that the proposed method has achieved a good localised tooth contact pattern.

5.1 INTRODUCTION

The Archimedean worm gear is also called a ZA worm gear and is widely used in industry. It has a cylindrical worm and a gear (see Figure 1.1). The surface generating method for an Archimedean worm is the same as that of a helicon pinion, and so the same modification method is applied to the ZA worm gear to obtain the favoured tooth contact pattern. The modified worm is the same as that for a helicon gear. The ZA gear surface, however, is quite different from a helicon gear.

5.2 THE HOB AND WORM SURFACE EQUATIONS

The derivations of hob and modified worm are the same as those for a helicon gear as presented in the preceding chapter. For the purpose of convenience, only the final equations of hob and worm surfaces are given in the following sections. The detailed derivations are similar to those presented in the preceding chapter.

5.2.1 Equations of Hob Tooth Surface

The coordinate systems used for the Archimedean wheel cutter and worm are shown in Figure 5.1. The coordinate system $S_1(O_1, X_1,Y_1,Z_1)$ is rigidly connected to the hob and situated at the centre of the hob or worm. The coordinate system $S_b(O_b, X_b,Y_b,Z_b)$ is rigidly connected to the worm cutter, with its origin O_b situated at the intersection point of the straight lines of cutting edges I and II.

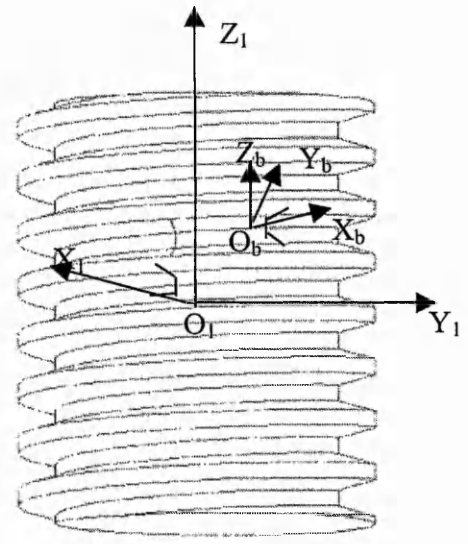


Figure 5.1 Coordinate systems for a ZA worm

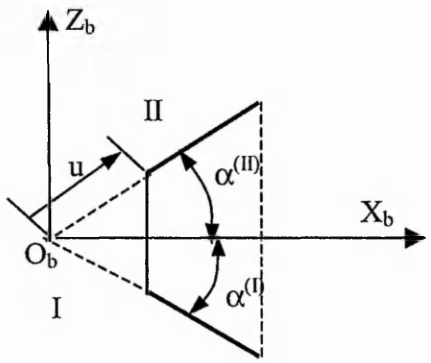


Figure 5.2 The cutter's two cutting edges I and II in coordinate system S_b

The vector of the worm cutter's cutting edges, i.e. the generatrices of the worm tooth surface in coordinate system S_b is given by

$$\mathbf{r}_h^{(i)}(u) = \begin{Bmatrix} u\cos\alpha^{(i)} \\ 0 \\ \mp u\sin\alpha^{(i)} \end{Bmatrix} \tag{5.2.1}$$

where, as shown in Figure 5.2, u is the surface parameter, $\alpha^{(i)}$ are the angles of generatrix, i=I, II indicating the two cutting edges respectively, and the negative sign

"-" is for i=I and the positive sign "+" is for i=II. For an Archimedean worm gear, $\alpha^{(I)}= \alpha^{(II)}= \alpha$.

The hob tooth surface is obtained in the same manner as the helicon pinion and can be written as follows

$$\mathbf{r}_h^{(i)}(u,\theta) = \begin{Bmatrix} (u\cos\alpha^{(i)} + r_0)\cdot\cos\theta \\ (u\cos\alpha^{(i)} + r_0)\cdot\sin\theta \\ \mp u\sin\alpha + p_{ax}\cdot\theta + z_0 \\ 1 \end{Bmatrix} \tag{5.2.2}$$

As a numerical example using Equation (5.2.2), Figure 5.3 shows the surface of the ZA gear hob, which is used in the example of numerical tooth contact analysis described in the following sections.

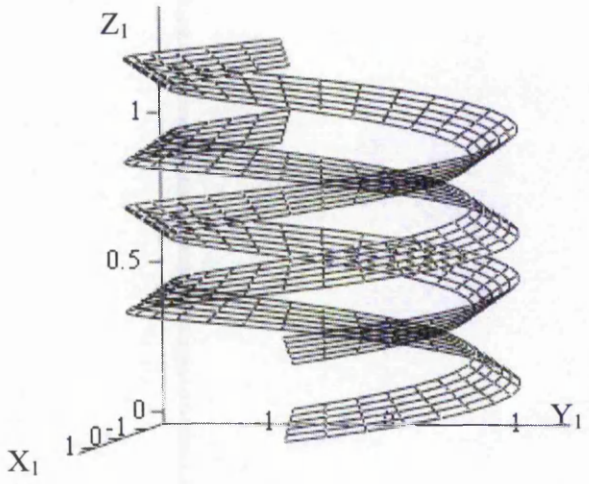


Figure 5.3 ZA Hob tooth thread surfaces (unit: inch)

5.2.2 Equations of Modified Worm Tooth Thread Surface

The generatrix of the modified worm tooth surface is still a straight line, but the angle is changed with increments $\Delta\alpha^{(I)}$ for side I, $\Delta\alpha^{(II)}$ for side II, as shown in Figure 5.4. In addition, the cutter's position is different from the original setting, which is illustrated in Figure 5.4 using the coordinate system rigidly connected to the cutter.

The new setting is represented using system S_m (O; X_m,Y_m,Z_m) and its position is determined by the following steps:

1. Plane $Z_mO_mY_m$, where the generating line lies in, rotates from the initial plane $Z_bO_bY_b$ around Z_b with angle ξ;
2. S_m moves to a new position with its origin O_m away from O_b with Δx, Δy, Δz, while keeping axis Z_m parallel to Z_b .

Angle ξ may be different for the two cutting edges I and II and is determined by the calculated results.

The derivation of the modified worm surface equation is the same as that for the modified pinion of a helicon gear drive as presented in the preceding chapter. The equation of the modified worm tooth surface is then written as follows

$$\mathbf{r}_{1w}^{(i)}(u,\theta)=\begin{Bmatrix}(u\cos(\alpha^{(i)}+\Delta\alpha^{(i)})\cdot\cos\xi+\Delta x+r_0)\cdot\cos\theta\\-(\Delta y-u\cos(\alpha^{(i)}+\Delta\alpha^{(i)})\cdot\sin\xi)\cdot\sin\theta\\(u\cos(\alpha^{(i)}+\Delta\alpha^{(i)})\cdot\cos\xi+\Delta x+r_0)\cdot\sin\theta\\+(\Delta y-u\cos(\alpha^{(i)}+\Delta\alpha^{(i)})\cdot\sin\xi)\cdot\cos\theta\\\mp u\sin(\alpha^{(i)}+\Delta\alpha^{(i)})+p_{ax}\cdot\theta+z_0+\Delta z\\1\end{Bmatrix} \tag{5.2.3}$$

The modification parameters Δx, Δy, Δz can be obtained from the following equations

$$\Delta x=-u_M^{(p)}\cos(\alpha^{(i)}+\Delta\alpha^{(i)})\cdot\cos\xi+u_M^{(h)}\cos\alpha \tag{5.2.4}$$

$$\Delta y=u_M^{(p)}\cos(\alpha^{(i)}+\Delta\alpha^{(i)})\cdot\sin\xi \tag{5.2.5}$$

$$\Delta z=\mp u_M^{(h)}\sin\alpha^{(i)}-(\mp)u_M^{(p)}\sin(\alpha^{(i)}+\Delta\alpha^{(i)}) \tag{5.2.6}$$

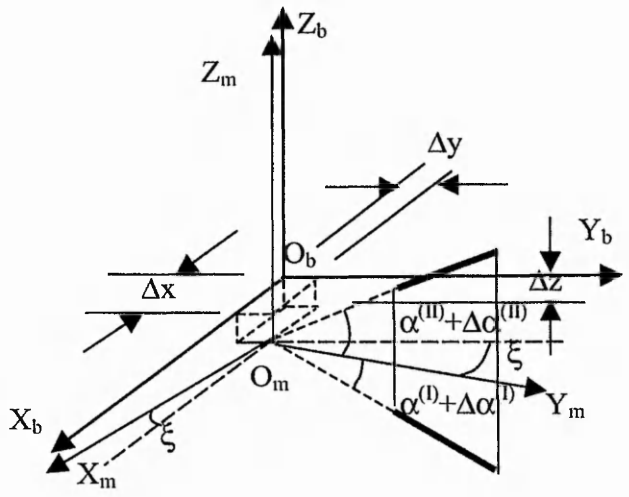


Figure 5.4 Coordinate systems for the modified worm

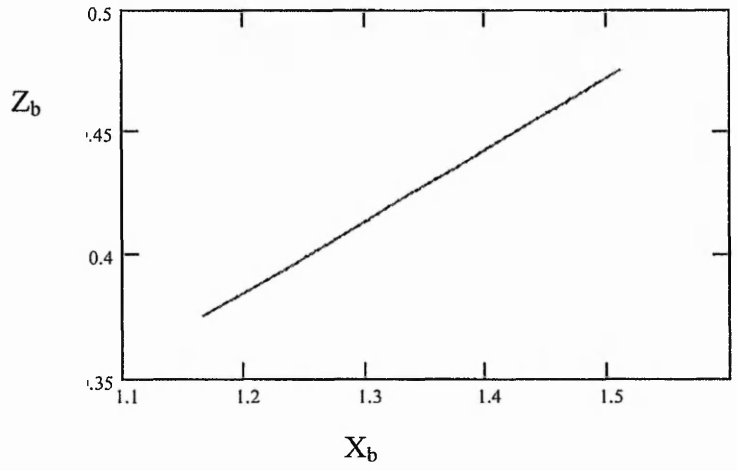


Figure 5.5 Axial section of hob thread and modified worm thread (Side II) ξ=-2°, $\Delta\alpha$=0.0501°, α=16.24°, (unit: mm)

Given ξ, $\Delta\alpha$ and the point M's coordinates, the modification parameters Δx, Δy, Δz can be obtained. Figure 5.5 shows one example of the tooth profiles of the modified worm and hob used to cut the mating gear. Their major design parameters are listed in Table 5.1. Figure 5.5 and Figure 5.6 show the tooth profile results related to the generating line of side I with ξ=2° and $\Delta\alpha$=0.0501°. Figure 5.5 shows the tooth profiles of the hob and the modified worm in axial section. The differences between

them are clearly indicated in Figure 5.6. Since side II has the same pressure angle as side I, so only the side I modification needs to be calculated.

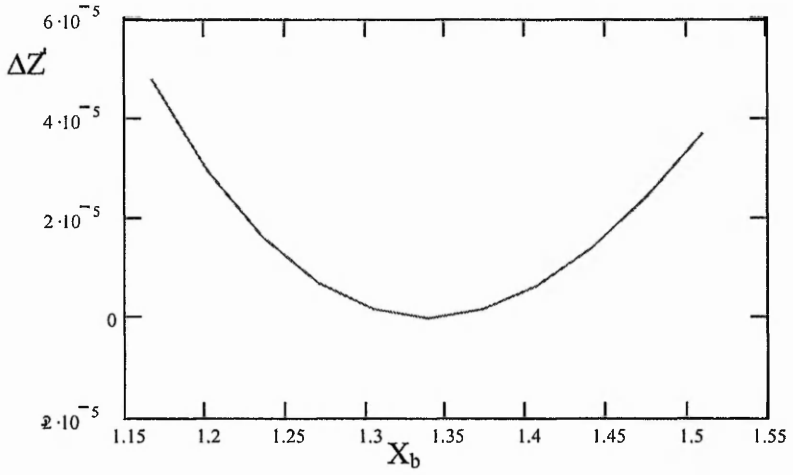


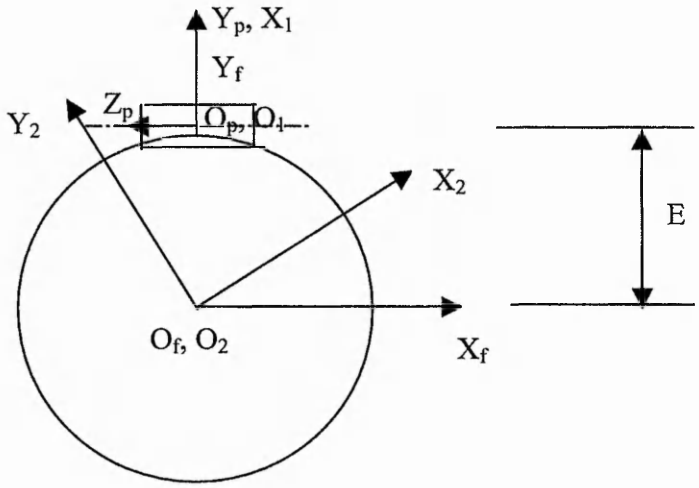
Figure 5.6 Difference in hob and worm's axial section profile: $\Delta Z=Z_{hob\ thread} - Z_{modified}$, (Side II), (unit: mm)

Table 5.1 Main Design Parameters of ZA Worm, Wheel Cutter and Gear (inch)

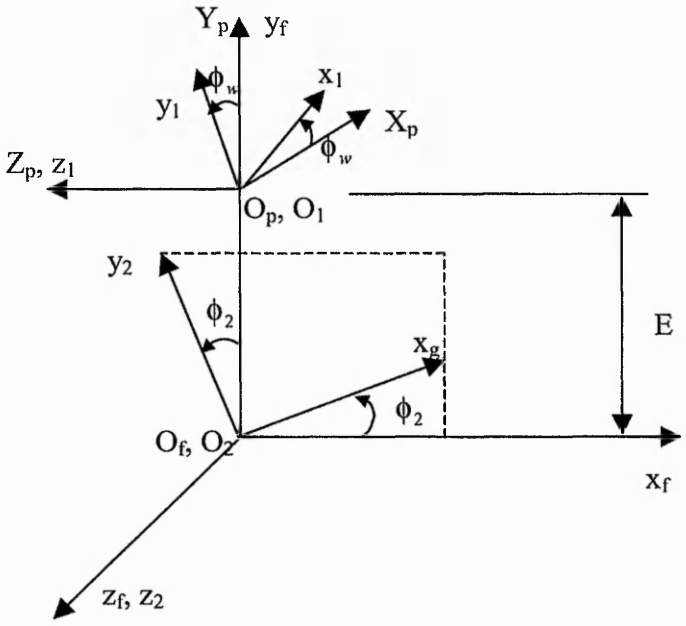
	Worm	Wheel Cutter	Wheel
Root Diameter	2.6318	2.6318	-------
Pitch Diameter	2.7608	2.7608	-------
Outside Diameter	3.3184	3.3184	9.8086
Lead	0.5	0.5	-------
Number of Threads (Teeth)	1	1	60
Gear Centre Distance	6.125	6.125	6.125
Wheel Throat Radius	-------	-------	4.7841
Wheel Tooth Face Width	-------	-------	2.00

5.3 GEAR SURFACE EQUATIONS

Figure 5.7 shows the coordinate systems used for the derivation of the ZA gear surface equations. The following coordinate systems are used:



(a) Setting of Gear Generation



(b) Coordinate systems

Figure 5.7 Coordinate system applied for worm gear generation

1. $S_f(O_f;X_f,Y_f,Z_f)$: stationary system connected to the frame with its origin situated on the gear axis
2. $S_p(O_p;X_p,Y_p,Z_p)$: stationary system connected to the frame with its origin situated on the worm axis



3. $S_w(O_w;X_w,Y_w,Z_w)$: rigidly connected to the worm
4. $S_1(O_1;X_1,Y_1,Z_1)$: rigidly connected to the hob
5. $S_2(O_2;X_2,Y_2,Z_2)$: rigidly connected to the gear

The ZA gear surface can be represented as follows

$$\mathbf{r}_2(u_h,\theta_h,\phi_1)=\mathbf{M}_{21}\cdot\mathbf{r}_{1h}(u_h,\theta_h) \tag{5.3.1}$$

The variables of the spiroid gear surface should satisfy the meshing equation of ZA gear drives

$$\mathbf{N}_{1h}\cdot\mathbf{v}_1^{(12)}=0 \tag{5.3.2}$$

where $\mathbf{M}_{21}$ is the homogeneous transformation matrix from the coordinate system S_1 to S_2. $\mathbf{N}_1$ is the normal to the worm surface. $\mathbf{v}_1^{(12)}$ is the relative velocity between the gear and the worm.

The homogeneous transformation matrix from the coordinate system S_1 to S_2 can derived as follows

$$\mathbf{M}_{21}=\mathbf{M}_{2f}\cdot\mathbf{M}_{fp}\cdot\mathbf{M}_{p1} \tag{5.3.3}$$

where $\mathbf{M}_{p1}$ is the homogeneous transformation matrix from the coordinate system S_1 to S_p and is expressed as

$$\mathbf{M}_{p1}=\begin{bmatrix}\cos\phi_1 & -\sin\phi_1 & 0 & 0\\ \sin\phi_1 & \cos\phi_1 & 0 & 0\\ 0 & 0 & 1 & 0\\ 0 & 0 & 0 & 1\end{bmatrix} \tag{5.3.4}$$

$\mathbf{M}_{2f}$ is the homogeneous transformation matrix from the coordinate system S_f to S_2 and is expressed as

$$\mathbf{M}_{2f} = \begin{bmatrix} \cos\phi_2 & \sin\phi_2 & 0 & 0 \\ -\sin\phi_2 & \cos\phi_2 & 0 & 0 \\ 0 & 0 & 1 & 0 \\ 0 & 0 & 0 & 1 \end{bmatrix} \tag{5.3.5}$$

The homogeneous transformation matrix $\mathbf{M}_{fp}$ from S_p to S_f is

$$\mathbf{M}_{fp} = \begin{bmatrix} 0 & 0 & -1 & 0 \\ 0 & 1 & 0 & E \\ 1 & 0 & 0 & 0 \\ 0 & 0 & 0 & 1 \end{bmatrix} \tag{5.3.6}$$

Therefore,

$$\begin{aligned} \mathbf{M}_{21} &= \mathbf{M}_{2f} \cdot \mathbf{M}_{fp} \cdot \mathbf{M}_{p1} \\ &= \begin{bmatrix} \sin\phi_1 \cdot \sin\phi_2 & \cos\phi_1 \cdot \sin\phi_2 & -\cos\phi_2 & E\sin\phi_2 \\ \sin\phi_1 \cdot \cos\phi_2 & \cos\phi_1 \cdot \cos\phi_2 & \sin\phi_2 & E\cos\phi_2 \\ \cos\phi_1 & -\sin\phi_1 & 0 & 0 \\ 0 & 0 & 0 & 1 \end{bmatrix} \end{aligned} \tag{5.3.7}$$

The elements of 3×3 submatrix of $\mathbf{M}_{21}$ represent the direction cosines of the unit vectors ($\mathbf{i}_1$, $\mathbf{j}_1$, $\mathbf{k}_1$) in the coordinate system S_2.

$$\mathbf{L}_{21} = \begin{bmatrix} \sin\phi_1 \sin\phi_2 & \cos\phi_1 \sin\phi_2 & -\cos\phi_2 \\ \sin\phi_1 \cos\phi_2 & \cos\phi_1 \cos\phi_2 & \sin\phi_2 \\ \cos\phi_1 & -\sin\phi_1 & 0 \end{bmatrix} \tag{5.3.8}$$

The relative velocity of the worm and gear represented in coordinate system S_1 can be obtained from following relationship

$$\mathbf{v}_1^{(12)} = (\boldsymbol{\omega}_1^{(1)} - \boldsymbol{\omega}_1^{(2)}) \times \mathbf{r}_1 - \mathbf{E}_1 \times \boldsymbol{\omega}_1^{(2)} \tag{5.3.9}$$

where

$\boldsymbol{\omega}_1^{(1)}$ is the angular velocity of the worm in coordinate system S_1

$\boldsymbol{\omega}_1^{(2)}$ is the angular velocity of the gear in coordinate system S_1

$\mathbf{r}_1$ is the position vector of the worm surface in coordinate system S_1

$\mathbf{E}_1$ is the distance vector from O_p to O_2. O_p is the origin of coordinate system S_p and O_2 is the origin of coordinate system S_2.

The rotation speed of the worm represented in coordinate system S_1 is written as

$$\boldsymbol{\omega}_1^{(1)} = \omega_1 \cdot \mathbf{k}_1 \tag{5.3.10}$$

The angular speed of the gear represented in coordinate system S_2 is written as

$$\boldsymbol{\omega}_2^{(2)} = \omega_2 \cdot \mathbf{k}_2 \tag{5.3.11}$$

The distance vector from O_p to O_2 in coordinate system S_f is

$$\mathbf{E}_f = \overline{O_p O_2} = -E \cdot \mathbf{j}_f \tag{5.3.12}$$

The distance vector from O_p to O_2 in coordinate system S_1 can be obtained from the vector from O_p to O_2 represented in coordinate system S_f by multiplying a series of transformation matrices.

$$\mathbf{E}_1 = \overline{O_p O_2} = \mathbf{L}_{1f} \cdot \mathbf{E}_f = \mathbf{L}_{1p} \cdot \mathbf{L}_{pf} \cdot \mathbf{E}_f \tag{5.3.13}$$

where $\mathbf{L}_{1p}$ is a 3×3 transformation matrix from coordinate system S_p to S_1 and $\mathbf{L}_{pf}$ is a 3×3 transformation matrix from coordinate system S_f to S_p.

The above two transformation equations can be obtained directly from Figure 5.7.

$$\mathbf{L}_{1p} = \begin{bmatrix} \cos\phi_1 & \sin\phi_1 & 0 \\ -\sin\phi_1 & \cos\phi_1 & 0 \\ 0 & 0 & 1 \end{bmatrix} \tag{5.3.14}$$

$$\mathbf{L}_{pf} = \begin{bmatrix} 0 & 0 & 1 \\ 0 & 1 & 0 \\ -1 & 0 & 0 \end{bmatrix} \tag{5.3.15}$$

Substituting Equations (5.3.12), (5.3.14) and (5.3.15) into (5.3.13), the centre distance of the gear axis and the worm axis in coordinate system S_1 are derived and written as follows

$$\mathbf{E}_1 = \begin{Bmatrix} -E \cdot \sin\phi_1 \\ -E \cdot \cos\phi_1 \\ 0 \end{Bmatrix} \tag{5.3.16}$$

The rotational angular speed of the gear in coordinate system S_1 is

$$\boldsymbol{\omega}_1^{(2)} = \mathbf{L}_{12} \cdot \boldsymbol{\omega}_2^{(2)} \tag{5.3.17}$$

in which $\mathbf{L}_{12}$ is the 3×3 transformation matrix from coordinate system S_2 to S_1.

$$\mathbf{L}_{12} = \mathbf{L}_{1p} \cdot \mathbf{L}_{pf} \cdot \mathbf{L}_{f2} \tag{5.3.18}$$

where transformation matrices $\mathbf{L}_{1p}$, $\mathbf{L}_{pf}$ and $\mathbf{L}_{f2}$ can be obtained from Figure 5.7 as follows

$$\mathbf{L}_{1p} = \begin{bmatrix} \cos\phi_1 & \sin\phi_1 & 0 \\ -\sin\phi_1 & \cos\phi_1 & 0 \\ 0 & 0 & 1 \end{bmatrix} \tag{5.3.19}$$

$$\mathbf{L}_{f2} = \begin{bmatrix} \cos\phi_2 & -\sin\phi_2 & 0 \\ \sin\phi_2 & \cos\phi_2 & 0 \\ 0 & 0 & 1 \end{bmatrix} \tag{5.3.20}$$

Substituting the above two equations and Equation (5.3.15) into Equation (5.3.18) has

$$\mathbf{L}_{12}=\begin{bmatrix}\sin\phi_1\sin\phi_2 & \sin\phi_1\cos\phi_2 & \cos\phi_1\\ \cos\phi_1\sin\phi_2 & \cos\phi_1\cos\phi_2 & -\sin\phi_1\\ \cos\phi_2\sin\gamma & \sin\phi_2 & 0\end{bmatrix} \tag{5.3.21}$$

Substituting Equation (5.3.21) and (5.3.11) into (5.3.17), the angular speed of the gear represented in coordinate system S_1 is derived as

$$\boldsymbol{\omega}_1^{(2)}=\omega_2\cdot(\cos\phi_1\cdot\mathbf{i}_1-\sin\phi_1\cdot\mathbf{j}_1) \tag{5.3.22}$$

Substituting Equations (5.3.11), (5.3.13) and (5.3.22) into Equation (5.3.9) gives

$$\begin{aligned}\mathbf{v}_1^{(12)}&=(\boldsymbol{\omega}_1^{(1)}-\boldsymbol{\omega}_1^{(2)})\times\mathbf{r}_1-\mathbf{E}_1\times\boldsymbol{\omega}_1^{(2)}\\&=\begin{vmatrix}\mathbf{i}_1 & \mathbf{j}_1 & \mathbf{k}_1\\ -\omega_2\cos\phi_1 & \omega_2\sin\phi_1 & \omega_1\\ x_1 & y_1 & z_1\end{vmatrix}-\begin{vmatrix}\mathbf{i}_1 & \mathbf{j}_1 & \mathbf{k}_1\\ -E\sin\phi_1 & -E\cos\phi_1 & 0\\ \omega_2\cos\phi_1 & -\omega_2\sin\phi_1 & 0\end{vmatrix}\end{aligned}$$

The above equation can be written as

$$\mathbf{v}_1^{(12)}=v_{1x}^{(12)}\cdot\mathbf{i}_1+v_{1y}^{(12)}\cdot\mathbf{j}_1+v_{1z}^{(12)}\cdot\mathbf{k}_1 \tag{5.3.23}$$

where

$$v_{1x}^{(12)}=z_1\omega_2\sin\phi_1-y_1\omega_1=\omega_1(z_1\cdot m_{21}\cdot\sin\phi_1-y_1) \tag{5.3.24}$$

$$v_{1y}^{(12)}=\omega_1(z_1\cos\phi_1 m_{21}+x_1) \tag{5.3.25}$$

$$v_{1z}^{(12)}=\omega_1(-y_1 m_{21}\cos\phi_1-x_1 m_{21}\sin\phi_1-m_{21}E) \tag{5.3.26}$$

The generated hob surface normal is given by the following equations:

$$\mathbf{N}_1=\frac{\partial\mathbf{r}_1}{\partial u}\times\frac{\partial\mathbf{r}_1}{\partial\theta} \tag{5.3.27}$$

Substituting Equation (5.2.2) into the first term of the right side of Equation (5.3.27) has

$$\frac{\partial \mathbf{r}_1}{\partial u} = \begin{Bmatrix} \cos\alpha \cdot \cos\theta \\ \cos\alpha \cdot \sin\theta \\ \mp \sin\alpha \end{Bmatrix} \tag{5.3.28}$$

Similarly,

$$\frac{\partial \mathbf{r}_1}{\partial \theta} = \begin{Bmatrix} -(u \cdot \cos\alpha + r_0) \cdot \sin\theta \\ (u \cdot \cos\alpha + r_0) \cdot \cos\theta \\ p_{ax} \end{Bmatrix} \tag{5.3.29}$$

Using Equation (5.2) to simplify Equation (5.35) gives

$$\frac{\partial \mathbf{r}_1}{\partial \theta} = \begin{Bmatrix} -y_1 \\ x_1 \\ p_{ax} \end{Bmatrix} \tag{5.3.30}$$

Substituting Equations (5.3.29), (5.3.30) into Equation (5.3.28) yields

$$\begin{aligned} \mathbf{N}_1 &= \begin{vmatrix} \mathbf{i}_i & \mathbf{j}_1 & \mathbf{k}_1 \\ \cos\alpha \cdot \cos\theta & \cos\alpha \cdot \sin\theta & \mp \sin\alpha \\ -y_1 & x_1 & p_{ax} \end{vmatrix} \\ &= \mathbf{N}_{1x} \cdot \mathbf{i}_1 + \mathbf{N}_{1y} \cdot \mathbf{j}_1 + \mathbf{N}_{1z} \cdot \mathbf{k}_1 \end{aligned} \tag{5.3.31}$$

where

$$N_{1x} = p_{ax} \cdot \cos\alpha \cdot \sin\theta \pm \sin\alpha \cdot x_1 \tag{5.3.32}$$

$$N_{1y} = -p_{ax} \cdot \cos\alpha \cdot \cos\theta \pm \sin\alpha \cdot y_1 \tag{5.3.33}$$

$$N_{1z} = (u \cdot \cos\alpha + r_0) \cdot \cos\alpha \tag{5.3.34}$$

From Equations (5.3.31) and (5.3.23), the meshing equation (5.3.2) can be written as

$$f(u_h, \theta_h, \phi_1) = N_{1x} \cdot v_{1x}^{(12)} + N_{1y} \cdot v_{1y}^{(12)} + N_{1z} \cdot v_{1z}^{(12)} \tag{5.3.35}$$

The gear surface can thus be expressed by the following equations

$$\begin{cases} f(u_h, \theta_h, \phi_1) = 0 \\ \mathbf{r}_2(u_h, \theta_h, \phi_1) \end{cases} \tag{5.3.36}$$

The tooth surface constituted by contact lines can be obtained by solving Equation (5.3.36). Figure 5.8 shows datum points on one side of the gear tooth surface (generated by side I of hob generating lines) calculated from a program written in MathCAD. Since both sides of hob thread have the same pressure angles, only one side of the gear surface is needed.

The example of a ZA gear has a high reduction ratio (1/60). The gear with such a high reduction ratio makes it difficult to find all the solutions for contact lines on the gear surfaces because the contact points near the middle of the gear tooth are very sensitive to the initial input guess values. The bandwidth for the initial guess values are very narrow. The solutions have multiple roots and it is very easy to jump to other undesired solutions. The desired root is very difficult to obtain. The present program can only automatically get the two ends of the contact lines on the gear tooth surface as shown in Figure 5.8.

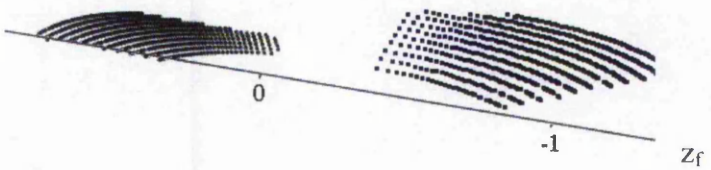


Figure 5.8 ZA gear surface contact lines



Figure 5.9 Contact line on ZA VGM model

Current commercial gear software also fails to find all the contact points on surfaces for high reduction ratio gears. For example, the Holroyd worm gear II (which will be studied in a later chapter) has a reduction ratio of 1/50 which is lower than 1/60 in the present example. According to Fish (2000), the software they use cannot obtain all the contact points on the surface of the Holroyd worm gear II. If surface points cannot be obtained from the solutions, conventional 3D modelling methods are unable to model 3D worm gears with high reduction ratios. However, using the virtual gear manufacturing method developed in this research (see Chapters 6 and 7), such problems are easily overcome. Figure 5.9 shows the VGM model and its contact lines on the gear surfaces which are very similar to those obtained from the numerical solutions. The contact lines on the worm surface are shown in Figure 5.10.

5.4 NUMERICAL SIMULATION

In order to evaluate the shift in the bearing contact which is caused by misalignment for the modified worm gear drive, a numerical example of a worm gear drive is presented here. The main parameters of the worm gear drives are listed in Table 5.1. The worm is a single start worm and the gear has 60 teeth.

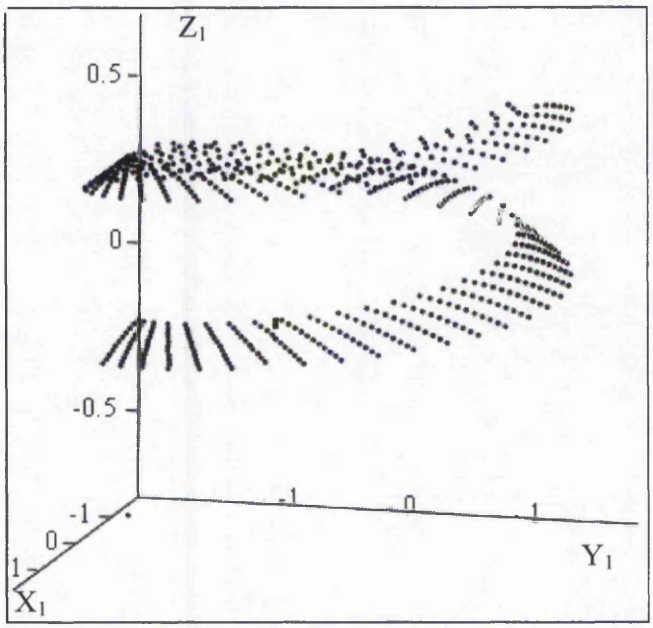


Figure 5.10 Contact lines on ZA worm surface (unit: inch)

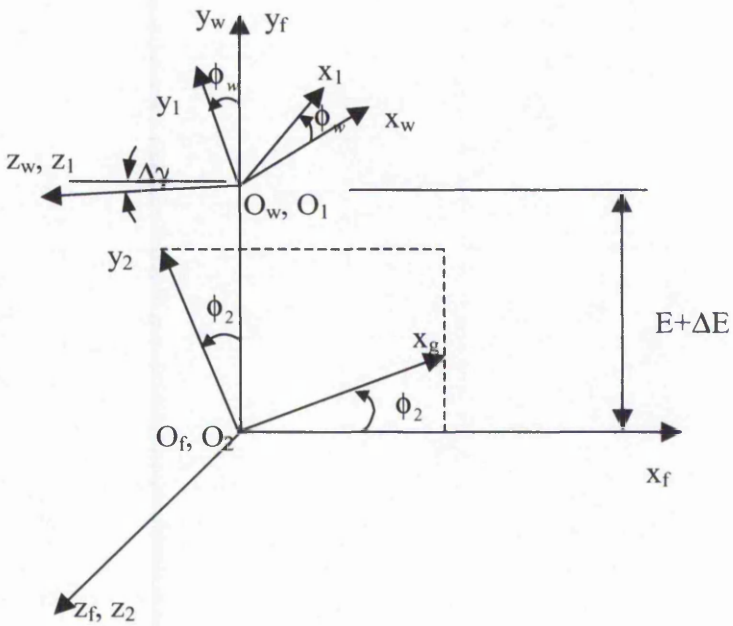


Figure 5.11 Coordinate system for the simulation of meshing

To conduct the numerical simulation of meshing, a ZA worm gear tooth contact analysis program has been developed in MathCAD. The coordinate system for the

simulation is shown in Figure 5.11, which takes into account the errors including axial displacement error, centre distance error and misalignment. The meshing algorithm is based on the condition that the worm surface and gear surface are continuously tangent to each other at the contact points and therefore they have the same unit normal vector. Thus the following equations are derived,

$$\mathbf{r}_f^{(w)}(u_w,\theta_w,\phi_w^{'},\Delta L,\Delta E,\Delta\gamma)=\mathbf{r}_f^{(2)}(u_1,\theta_1,\phi_1,\phi_2^{'}) \tag{5.4.1}$$

$$\mathbf{n}_f^{(w)}(u_w,\theta_w,\phi_w^{'},\Delta\gamma)=\mathbf{n}_f^{(2)}(u_1,\theta_1,\phi_1,\phi_2^{'}) \tag{5.4.2}$$

$$\mathbf{N}_1\times\mathbf{v}_1^{(12)}=0 \tag{5.4.3}$$

where

$\mathbf{r}_f^{(w)}$ - position vector of the worm in coordinate system S_f

$\mathbf{r}_f^{(2)}$ - position vector of the gear in coordinate system S_f

u_w, θ_w - the modified worm surface parameters

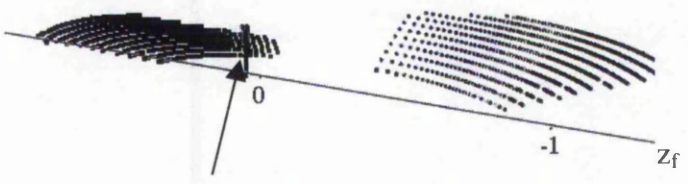
ϕ'_w - the rotation angle of the worm

ϕ'_2 - the rotation angle of the gear

ΔL - axial displacement error

ΔE - shortest centre distance error

$\Delta\gamma$ - misalignment of the shaft angle



Localised tooth contact path

Figure 5.12 Localised tooth contact path of ZA worm gear drive in meshing (mm)



Equations(5.4.1)-(5.4.3) have seven unknowns but there are only six independent scalar equations since $\left|\mathbf{n}_f^{(w)}\right| = \left|\mathbf{n}_f^{(2)}\right| = 1$ in Equation (5.4.1). The worm rotation angle ϕ'_w is used as input so Equation (5.4.1)-(5.4.3) can be solved.

The localised tooth contact path is shown in Figure 5.12, which is based on the calculated results from the tooth contact analysis. It clearly shows that the proposed modification of the geometry enables the bearing contact to be localised.

5.5 CONCLUDING REMARKS

The novel modification method has been applied to obtain favourable localised tooth contact for ZA gear drives. This modification method is much simpler than existing methods and can be implemented on standard hobbing machines. The following work has been completed in this chapter:

- Equations have been derived for the geometry of the hob, the modified worm and ZA gear.
- Programs have been written to obtain the hob, worm and gear surfaces and to simulate localised gear meshing.
- Results of a numerical simulation of tooth contact have confirmed that the proposed modification to the geometry permits a favourable localised bearing contact.

CHAPTER 6 3D Modelling of Spiroid Gears Using the VGM Method

The virtual gear manufacturing method has been proposed for rapid 3D modelling of spiroid gears. The new method is based on obtaining the gear tooth surfaces directly in advanced CAD packages by simulating the gear manufacturing process. The model generation procedure is a virtual manufacturing process for spiroid gearing. Compared with conventional gear 3D modelling methods, the virtual gear manufacturing method is a completely different approach. It is a visual and direct method and does not involve any solutions of nonlinear equations. The newly designed gear drives can be virtually assembled and run on a computer to check the clearance or interference between the tooth surfaces. The effects of misalignments on the gear tooth contact can also be visually investigated. The gear models are parametric and therefore are very suitable for the optimum design of gearing. An example of the virtual manufacturing of a spiroid gear drive is presented. The pinion and gear are assembled into a spiroid gear set according to the design. Then the spiroid gear set is virtually run on the computer. The conflict, meshing and contact paths of the spiroid gear tooth surfaces have been simulated in a 3D virtual environment. A helicon gear drive is also created using the virtual gear manufacturing method.

6.1 INTRODUCTION

The geometry of gears such as worm, spiroid and hypoid gears are extremely complex. With the rapid development of computer hardware and CAD software, many researchers are engaged with 3D CAD models of gear drives. The existing 3D gear modelling methods are extremely difficult and time-consuming because they involve the solution of complicated non-linear equations. The conventional modelling methods are implicit processes with little flexibility for fast modelling and modifications and also do not directly reflect the nature of gear manufacturing.

The novel virtual gear manufacturing method developed for 3D spiroid gear modelling in this research has overcome the shortcomings of conventional solid modelling methods. The new method does not need to establish a complicated gear mathematical model and can directly model gears in Pro/Engineer.

The theory and techniques for the virtual manufacturing of spiroid gears have been presented in the following sections. The principle of this new approach is to directly simulate the practical spiroid gear hobbing mechanism in order to generate the complex geometry of the spiroid gear tooth using an advanced 3D CAD package. The model generating procedure is a virtual manufacturing process for spiroid gears. Unlike conventional methods, in which the gear tooth surfaces are constituted by datum points gained from the meshing equations, the spiroid gears are virtually hobbed on the computer using the new method. The new approach to gear modelling directly reflects the nature of the gear manufacturing process and hence is more accurate than conventional methods. It is very difficult for conventional methods to obtain the root fillet datum points which are not included in the meshing equations and are critical in tooth stress analysis.

The theory of the virtual spiroid gear manufacturing method can also be applied to other gear types such as worm gears. The model produced by this new method can be used to simulate the meshing between the pinion and the gear, to analyse the contact pattern and to detect any tooth interference that may occur during tooth engagement.

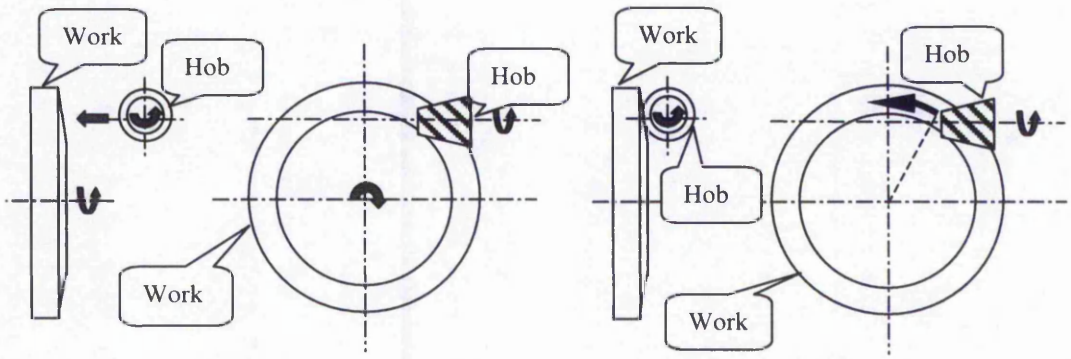
As an example, a 3D spiroid gear drive model, based on the new method, has been virtually manufactured on a computer using Pro/Engineer. After the spiroid pinion and gear hobbing were finished, the pinion and gear were assembled into a spiroid gear set according to the design specifications. Then the spiroid gear set has been virtually run on a computer. The conflict, meshing and contact path of the spiroid gear tooth surfaces have been simulated in a 3D virtual environment.

The proposed virtual manufacturing modelling method is a new and visual method in gear research. It is easy to check undercutting, interference and the contact tooth path when gears are in mesh. It is a very powerful tool in gear design and research since the designers can investigate the contact zone and adjust the design parameters to obtain better contact patterns. The method has great flexibility for gear optimum design and finite element analysis since it is parametric. It is particularly useful for gear design because it can visualise and settle any performance problems before prototypes are built. Therefore, it can help to reduce the manufacturing cost in the early production stage.

6.2 THEORY OF VIRTUAL MANUFACTURING

Spiroid gears can be cut using a standard machine by a spiroid hob that is identical to the spiroid pinion. The hobbing process simulates the operation of the spiroid gear drives.

In Real Gear Manufacturing (RGM), the generation of a gear tooth is a continuous indexing process in which both the cutting tool and the work piece rotate in a constant relationship while the hob is being fed into the work. As the hob is fed across the work once, all the teeth in the work are completely formed (see Figure 6.1 (a)). The Virtual Gear Manufacturing (VGM) method is similar to the real gear hobbing process but, in VGM, the gear blank is static and the hob rotates about two axes simultaneously. One rotation is about the hob's own axis, the other is about the gear blank axis. However, the relative movements of the gear blank and the hob in VGM are the same. When the hobbing process is finished, the same gear will be produced in VGM and RGM.



(a) RGM of Spiroid Gear (b) VGM of Spiroid Gear

Figure 6.1 Diagram of RGM and VGM methods

In RGM, the hob is basically a worm that has been fluted and has form-relieved teeth. The flutes provide the cutting edges. Each tooth is relieved radially to provide a clearance behind the cutting edge, allowing the faces of the teeth to be sharpened

while retaining the original tooth profile. In VGM, however, only the tooth profile is needed and tooth-relief is not required.

Both in VGM and RGM, the generating process of cutting gears is the same. The teeth of the hob are cut into the gear blank in succession, and each in a slightly different position. Each hob tooth cuts its own profile and the accumulation of these cuts produces a curved form on the gear teeth. The gear teeth are formed a little at a time in a series of cuts.

The main difference between RGM and VGM is that in RGM, the hob has to be fed slowly into depth due to the blade strength limitation but in VGM, without those limitations, the hob reaches the depth straight away.

6.3 VIRTUAL MANUFACTURING OF A SPIROID GEAR

6.3.1 Design of Spiroid Gear

A 3D model of spiroid gearing was presented as an example to illustrate the virtual gear manufacturing method. The present example of a spiroid gear drive is right hand type. The centre distance between the pinion axis and the gear axis is 70mm. The tapered pinion has two threads and the face gear has 51 teeth and the gear ratio is 25.5. The configurations of spiroid gear are shown in Figure 6.2. Its primary design parameters are listed in Table 6.1.

Table 6.1 The spiroid gearing tooth primary parameters

Centre distance	70 mm
Gear ratio	25.50
Number of face gear teeth	51
Number of pinion teeth	2

Currently, there is no standard available for spiroid gear design in the open literature. The method introduced in Dudley's Gear Handbook was used to calculate the other design parameters. The basic approach to the establishment of the spiroid gear tooth

form is to establish the pinion-tooth form first and then develop a gear-tooth form that is conjugate to it.

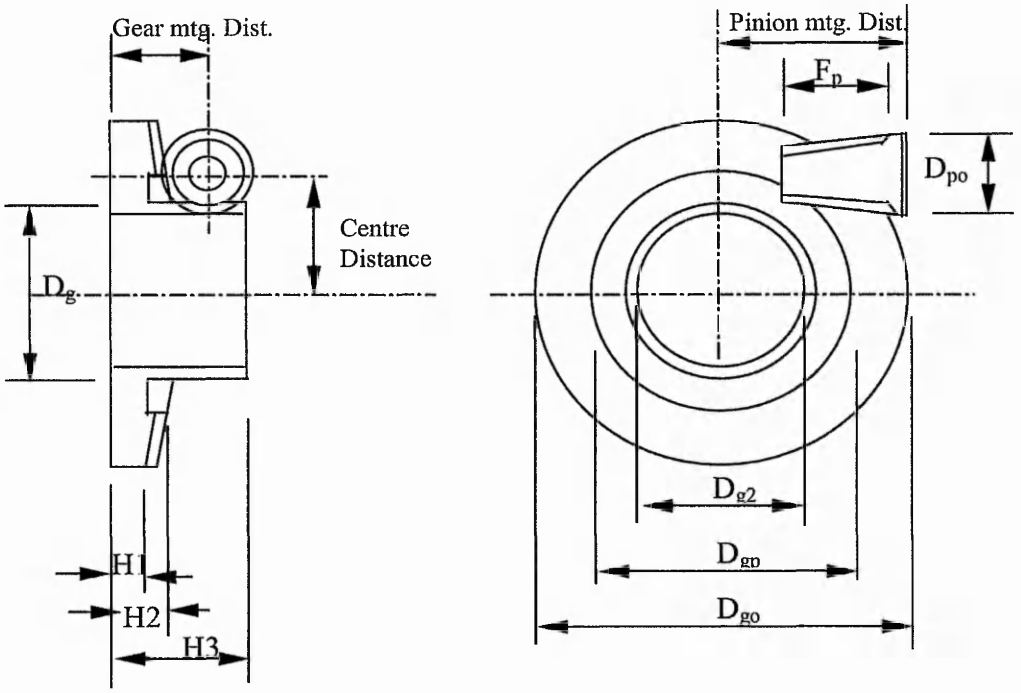


Figure 6.2 Diagram of spiroid gear configuration

The tooth form of the spiroid gear is comprised of teeth with different pressure angles on each side of the teeth: a "low" pressure angle side and a "high" pressure angle side. The choice of pressure angle will control the extent of the fields of conjugate action of the teeth. The values of pinion taper angles have been standardized by the Illinois Tool Work in order to achieve the best general-purpose gearing. For the sake of convenience, these standard values are copied from Dudley's Gear Hand Book (1962) and listed in Table 6.2.

Table 6.2 Standard tooth and gear-blank relationships, spiroid and helicon gears

1. "Sigma" angle σ_P=40° (standard)	
2.Pinion taper angle τ vs. gear face angle γ	
Pinion taper angle τ (degree)	Gear face angle γ (degree)
5	8

7	11	
10	14	
3. Gear ratio	m_G=10:1 higher	
4. Number of teeth in gear	Varies with centre distance	
5.Tentative pressure angle selection		
	Pressure angle selection	
Ratio	Low side	High side
$M_G \leq 16:1$	15°	35°
$M_G > 16:1$	10°	30°

The design procedure for spiroid gear differs somewhat from other types of gears. The centre distance is the basic starting point for the calculation of spiroid tooth proportions. Then the lead and the pinion "zero" plane radius are calculated. The tooth proportions and the blank proportions are calculated based on the pinion zero plane radius. The spiroid tooth proportions calculated for the present example are listed in Table 6.3.

Table 6.3 Spiroid gear tooth proportions (calculated)

Parameter	**Value of Calculation**
"Sigma" angle	40°
Taper angle	5°
Pressure angle (high side)	30°
Pressure angle (low side)	10°
Pinion pitch radius	3.75 mm
Gear pitch radius	88.178 mm
Pinion conical lead	18.371 mm
Pinion working depth	7.563416 mm
Gear point diameter	154.126 mm
Pinion axis to high point plane	14.0288 mm
Pinion outside diameter (large end)	51.7126 mm
Gear outside diameter	210 mm
Pinion face width	51.156 mm

Parameter	Value of Calculation
"Sigma" angle	40°
Gear axis to pinion point	83.461 mm
Clearance	0.6937836 mm
Land widths	1.837096 mm

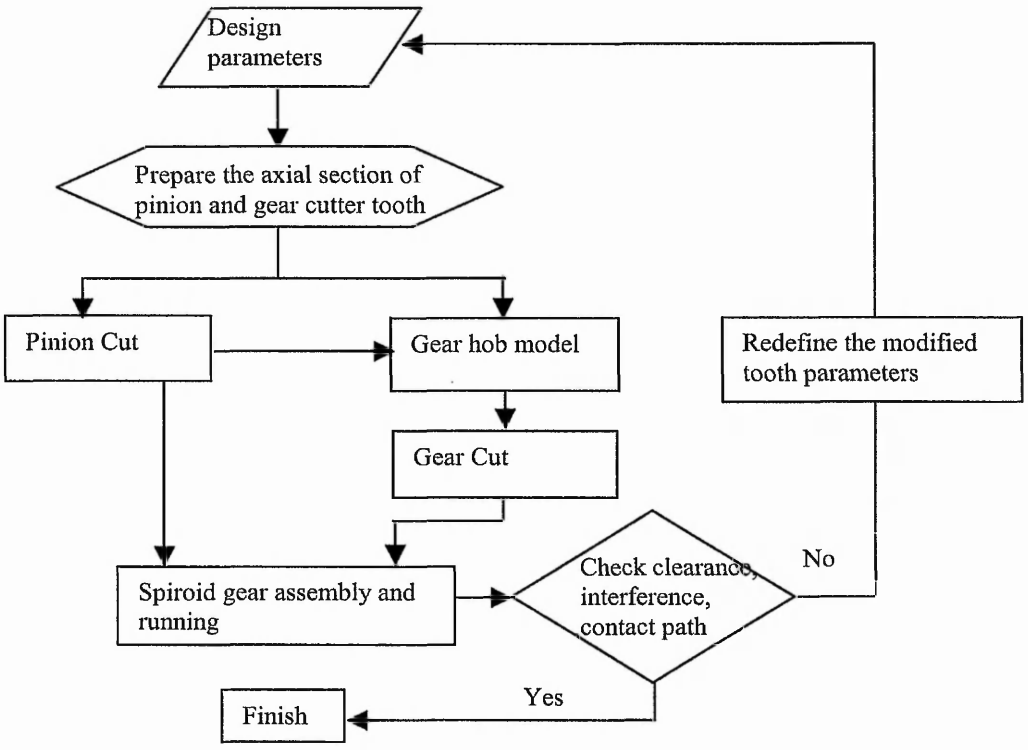


Figure 6.3 Procedure for the virtual manufacturing and meshing simulation of spiroid gearing

The spiroid tooth proportions will be used to build the 3D models of spiroid gears. The virtual manufacturing procedure of a spiroid gear is shown in Figure 6.3. The design parameters are prepared first and then the pinion and hob's axial sections are calculated. For a spiroid pinion and hob, the axial section tooth profiles are straight lines with different pressure angles. Once the axial sections are ready, the pinion and hob's geometry can be constructed. The gear's tooth surface is an envelope of the hob surface and is a generated surface. After the spiroid gear solid model is generated, the gear and the pinion are assembled together. Then the assembly model can be used to check the global interference between gear and pinion with different misalignments. The assembly model is also used to simulate the gear operation and to examine the

contact path and pattern. If the design has problems, the gear is redesigned. The above procedure is repeated until a good design is achieved.

6.3.2 Virtual Manufacturing of A Tapered Worm

To cut the tapered worm is a relatively simple task. A pinion cone blank is first created according to pinion proportions (Figure 6.6(a)). The *Revolving Protrusion* function in Pro/Engineer is used to produce the cone.

The tapered worm is cut by the advanced *helical sweep* function. The sweep profile is aligned to the pinion blank's outside surface (see Figure 6.5 (a)). The centre line of the helical sweep feature is collinear with the pinion's axis. The sweep profile is rotating about the centre line when the cutting is underway. The start point of the sweep profile is below the bottom of blank cone. The sweep section is used to cut the pinion's thread. It is identical to the cutter's axial section in practical worm cutting (see Figure 6.4). The thread is cut when the sweep section moves from the start point along the sweep profile in a spiral helical screw motion as shown in Figure 6.5 (a). Figure 6.6(b) shows the pinion that has finished one *helical sweep cut.*

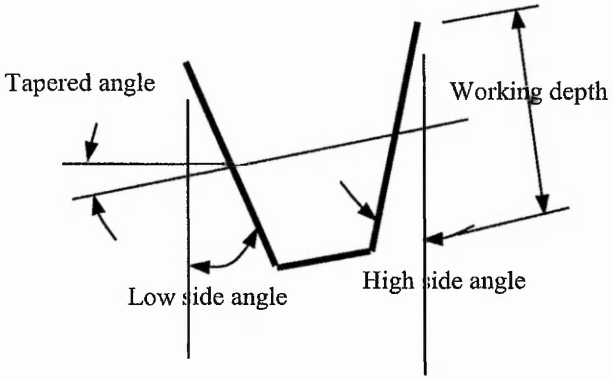
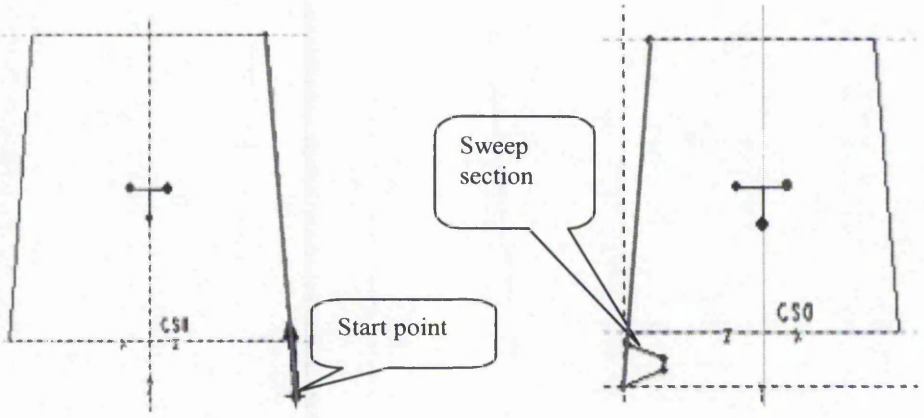


Figure 6.4 Axial section of cutter

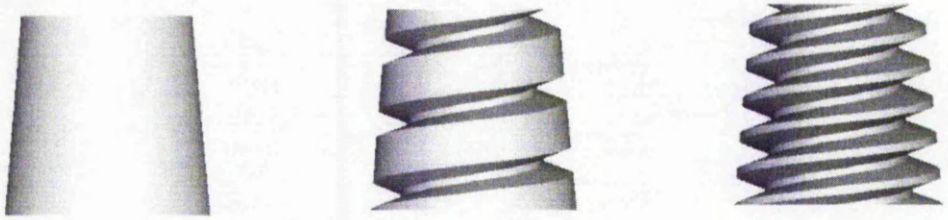
In the present example, the pinion is a two-start worm. The second thread of tapered pinion is cut using the advanced *pattern* function. In order to pattern the one thread cut, a datum plane 'on the fly' should be created as the sketching datum plane for the sweep profile. This 'on the fly' datum plane will provide the angular leading dimension for patterning. With the rotational angle leader, the cut can be patterned

straight away with a 180° increment. The final tapered pinion is created as shown in Figure 6.6(c).



(a) Sweep profile (b) Sweep section

Figure 6.5 Diagram of helical sweep cut



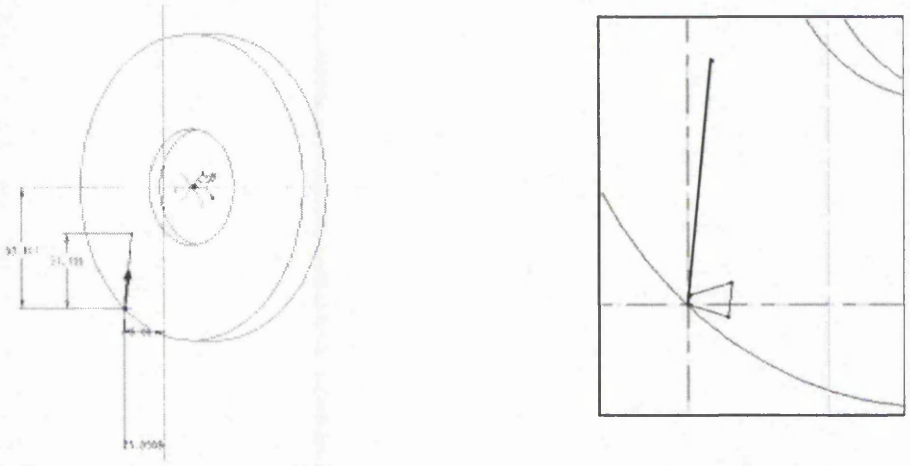
(a) Pinion blank (b) One thread cut (c) Full Cut

Figure 6.6 Spiroid pinion cutting procedure

6.3.3 Virtual Manufacturing of Spiroid Gear

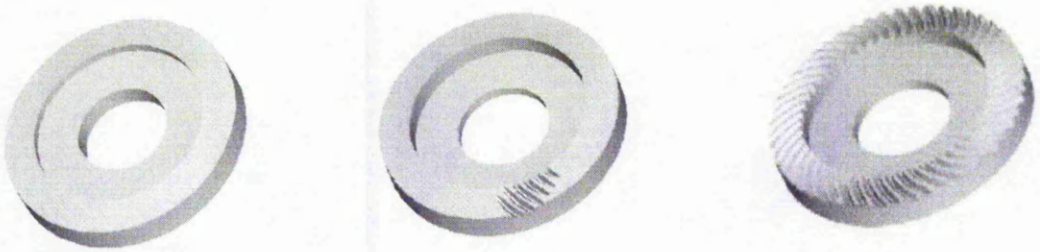
The process of spiroid gear cutting is much more complicated than the process of pinion cutting. The first step is to create a gear blank with the design specifications (Figure 6.8 (a)). The hobbing sweep profile is sketched on the datum plane 'on the fly' which offers the rotational dimension leader (Figure 6.7 (a)). The sweep section, which is identical to the tapered hob tooth axial section, will sweep in a screw motion along the sweep profile (Figure 6.7 (b)). The pitch of the hob is input as the pitch of the screw motion. One helical sweep cut will be obtained as shown in Figure 6.8(b).

The whole face gear can be virtually produced by patterning the helical sweep cut rotating about two axes simultaneously (see Figure 6.8 (c)).



(a) Sweep profile (b) Sweep section

Figure 6.7 Spiroid gear hob sweep profile and section



(a) Spiroid gear blank (b) One cut (c) Full cut

Figure 6.8 Diagram of virtual spiroid gear hobbing process

6.4 GEAR ASSEMBLY AND MODEL ANALYSIS

6.4.1 Spiroid Gear Set Assembly

After the spiroid pinion and gear hobbing is finished, the pinion and gear are assembled into a spiroid gear set according to the design specifications. The Pro/Assembly module was used to assemble the spiroid gear set. With the *Mate Offset* option, the pinion and the gear were assembled together. Then with the *Modify* function, the pinion was rotated into position. Figure 6.9 illustrates the process of

pinion and gear assembly. The interference of pinion and gear was checked until they fit according to design and without interference. The spiroid gear set can run virtually on a computer by changing the mounting angle of gear and pinion, in which the value of pinion and gear rotation is determined according to the gear ratio.

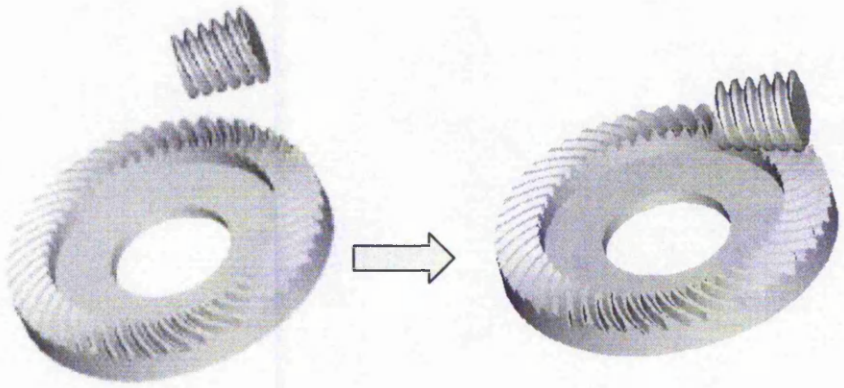


Figure 6.9 Diagram of spiroid gear assembly

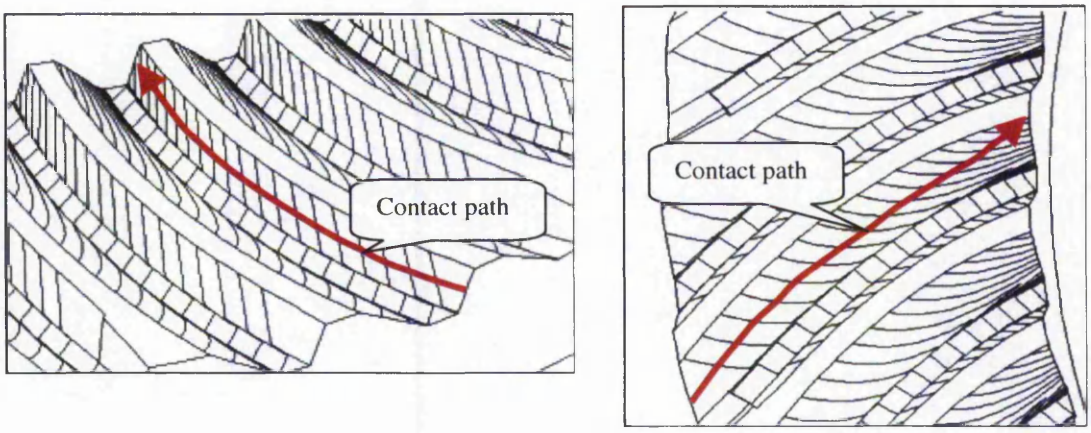
6.4.2 Model Analysis

Since the hobbing process duplicated the operation of gear meshing, it is possible to view the tooth contact path and determine the contact line (Shown in Figure 6.10.). In conventional modelling methods, the tooth contact lines and contact paths have to be solved from the nonlinear meshing equations.

Figure 6.10 (a) shows the spiroid gear tooth side I contact lines and contact path. They are the same as the contact lines and contact path calculated from the numerical modelling in Chapter 3. Figure 6.10 (b) shows the tooth side II contact lines and contact path. The contact lines near the gear inner surface have high curvature, for which it is very difficult to find the solutions in conventional gear modelling methods.

The interference between the mating teeth is easy to check by using the model analysis function. The highlighted regions in Figure 6.11 shows the interferences due to the misalignments of gear drive.

It is very convenient to get any desired tooth profile and sections. The sections can be obtained by *X-section* function or simply by cutting the gear to view the section. Figure 6.12 is an example of a section to view the pinion and gear tooth contact. Tooth profile curves, surface normal, clearance or interference part volume are convenient to observe by the modal analysis. The width of spiroid gear top land can be measured by the *measure function.* The above data are very difficult to acquire using conventional numerical methods.



(a) Contact path in driving side (b) Contact path in coasting side

Figure 6.10 Spiroid gear tooth contact path

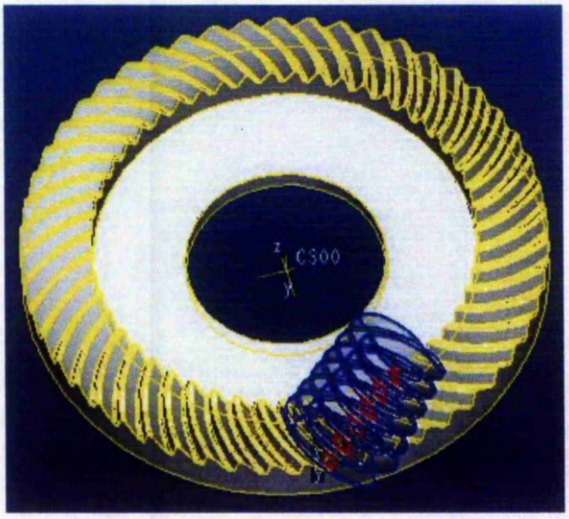


Figure 6.11 Diagram of interference (The highlighted area)

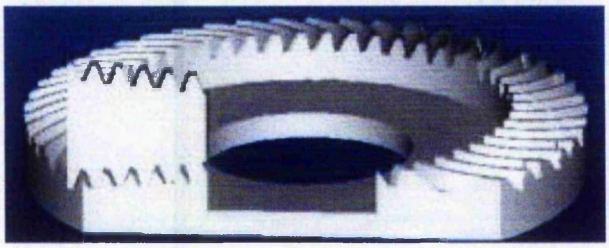


Figure 6.12 Section view of meshing

The helicon gear is similar to the spiroid gear except that its pinion is a cylindrical worm. The virtual manufacturing method has also been applied to the production of a helicon gear. The design parameters are the same as the example in Chapter 4 (see Table 4.1 Main parameters of helicon gearset (right hand)). The 3D modelling procedure for the helicon gear is the same as that for the spiroid gear. Figure 6.13 shows 3D model created for a helicon gear drive.

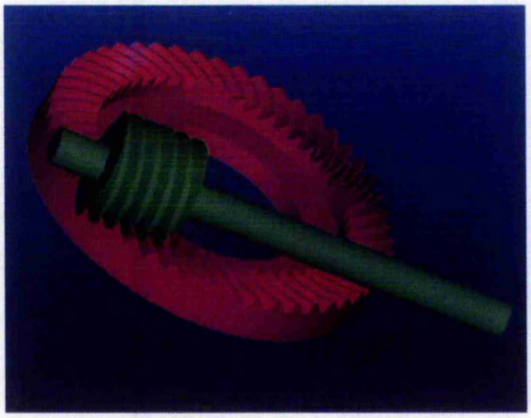


Figure 6.13 Helicon gear drive

6.5 SOME ASPECTS OF THE VIRTUAL MANUFACTURING METHOD

6.5.1 Parametric and Accurate Model for Finite Element Analysis

If conventional solid modelling methods are used to construct the gear models, the meshing equations have to be used to obtain the conjugated gear surface datum points. Then according to the design specifications, the quilts that have been

constituted by the datum curves of contact lines are trimmed. However, the equations of gear meshing do not contain any information about those parts of the tooth surface that are not a part of the conjugated surface, e.g. the tooth fillet. Conventional 3D modelling methods for gear have many limitations. The virtual manufacturing method naturally produces the tooth fillet just as in practical gear hobbing. The tooth fillet is very critical in finite element analysis of tooth stress, deformation, stiffness and load sharing. In gear optimum design and finite element analysis, parametric and accurate models are required. The virtual manufacturing method not only provides such models but also offers the easiest and quickest way so far to make such models.

6.5.2 Simulation of Localised Tooth Contact

One of the major trends in the optimum design of skew axis gears is to obtain the localised tooth bearing contact by mismatch between the gear and pinion surfaces. Such a localised bearing contact can reduce the sensitivity of gear drives to misalignments such as manufacturing and assembly errors.

Numerous computerised analyses have been undertaken to determine gear geometry optimum design. One of the most important achievements has been the computer analysis of tooth contact. However, for modified gear drives, even tooth contact analysis method finds it difficult to detect the contact path and several simplified assumptions have to be adopted.

In order to simulate the meshing of modified gear drives, modern tooth contact analysis assumes that the modified gears have point contact and the contact point between the pinion and gear teeth has the same coordinate and surface normal (Note that in practice, no gears are in real point contact. They are in regional contact under load).

The above assumption will yield five independent equations but there are six unknowns. In tooth contact analysis, one unknown parameter is used as an input and thus the nonlinear equations can be solved. However, the obvious problem in this assumption is that according to the theory of gear meshing, at the tooth contact point the surface normal and relatively velocity should satisfy the equation of meshing, i.e.

$n_1 \cdot v_1^{(12)} = 0$. But in meshing simulation, this fundamental equation in the theory of gear meshing is entirely ignored. Why? Because if the meshing equation is considered, there will be no solution at all. There are still no efficient ways yet to simulate the meshing of modified gear drives with existing methods. However, by using the virtual gear manufacturing method, the modified gear tooth contact region and contact path can be simulated efficiently.

6.5.3 Visual Tool for Gear Design Optimisation

In the example of the spiroid gear, the hob and the face gear blank dimensions were calculated using the method described in Dudley's Gear Handbook and have been found to conflict with each other during the virtual manufacturing process. The highlighted over cut (red colour surfaces) is clearly shown in Figure 6.14. The interference problem was fixed quickly because the cause of interference was easy to diagnose via the visual aid of the virtual manufacturing model. As can be seen, the main problem in this case is that the distance between the hob axis and the gear blank is slightly smaller than the correct design. After the distance was adjusted, the interference resulting from the initial design was soon eliminated. This example illustrates a potential economic benefit since it can fix the problem before a practical gear prototype is built.

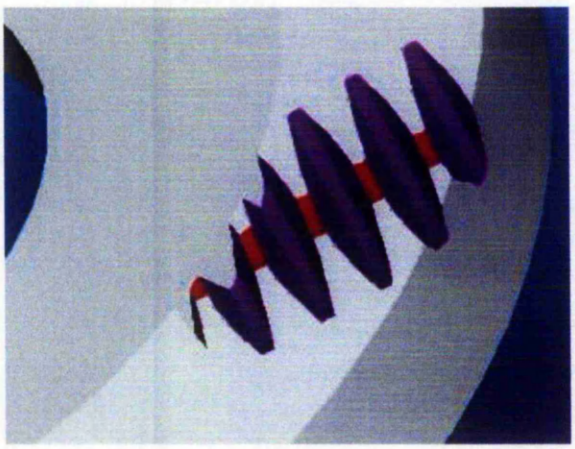


Figure 6.14 Over cutting the gear top land (Red surfaces)

The advantage of this VGM method is that any design conflicts in the model will be visually apparent at the design stage. The model is easy to manipulate. It is also very flexible with regard to change, and so is very useful for gear optimisation. The designers can fix the design problem visually in a virtual environment.

6.6 CONCLUSIONS

A novel approach, the 3D virtual spiroid gear manufacturing method, has been proposed instead of the conventional 3D modelling method. The theory and techniques of the virtual manufacturing of spiroid gears have also been presented.

A 3D spiroid gear drive model has been virtually manufactured on a computer using Pro/Engineer. The design parameters, calculated using the method introduced in Dudley's Gear Handbook, have been found to conflict with each other during the virtual manufacturing process. The conflict has been spotted and fixed visually in the 3D environment during the virtual hobbing process. The pinion and gear are assembled into a spiroid gear set according to the design. The spiroid gear set is virtually run on the computer. The conflict, meshing and contact path of the spiroid gear tooth surfaces have been simulated in a 3D virtual environment.

A 3D model of helicon gear drive has also been created using the virtual gear manufacturing method.

This proposed virtual manufacturing method is a new and visual method in modern gear research. The VGM models have great flexibility for gear optimum design and preparing a finite element model. The VGM method can visualise and settle performance problems before the prototypes are built. It can help to reduce the manufacturing cost early in the production stage. Therefore the VGM method is a very useful tool for both industrial gear design and academic research.

CHAPTER 7 3D Virtual Manufacturing of Worm Gears

A new virtual gear manufacturing method has been developed for rapid 3D modelling of worm gears. The principle of the new approach is to simulate the worm gear hobbing process to generate the complex tooth surface in Pro/Engineer. 3D ZA and ZI worm gear models have been virtually manufactured using Pro/Engineer. The tooth surface interference, tooth meshing and contact path of the worm gear drive have been simulated in the three dimensional virtual environment.

7.1 INTRODUCTION

A worm gear drive has complex tooth geometry. Due to its advantages such as compact size, high transmission ratio, smooth transmission and low level noise, worm gear drives are used in a wide variety of applications in modern industry. Researchers have paid much attention to improving the performance of worm gears and to establish numerical models of worm gears (Donno and Litvin, 1998; Chang, Tsay, 1998; Seol and Litvin, 1996a; Litvin, 1994, 1995). In recent years attempts have been made to apply the finite element method to analyse the stresses, deformation and load sharing of gear drives (Litvin et al, 1996, Handschuh and Bibel, 1999). However, it is not an easy task to build a three-dimensional model of a worm gear for finite element analysis. The conventional gear 3D modelling methods are very complicated, time-consuming, non-parametric and difficult to change.

In this chapter, a three dimensional *virtual gear manufacturing* (VGM) method has been proposed to produce the worm gears. Unlike conventional 3D modelling methods, the VGM method does not involve any complicated mathematical modelling and hence the complicated solution of non-linear meshing equations can be avoided. The model generation procedure is a virtual manufacturing process for worm gears. The VGM model can be used to simulate the meshing between the worm and gear, to analyse the contact pattern and to detect any tooth interference that may occur during tooth engagement.

7.2 PRINCIPLE OF VIRTUAL MANUFACTURING FOR WORM GEAR

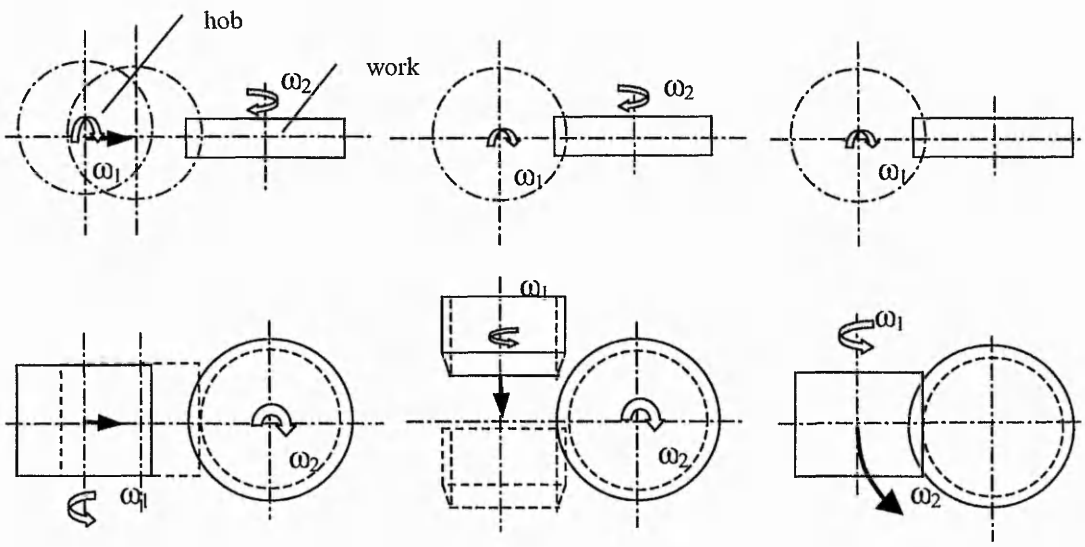
The worm thread is a helical sweep feature. It can be cut by using a *helical sweep cut* or created by *helical sweep protrusion*. The tooth surface of a gear is generated by a hob which is identical to the worm. The generation of a gear tooth is a continuous indexing process in which both the hob and the work piece rotate in a constant relationship while the hob is being fed into the gear blank. As the hob is fed across the gear blank once, all the teeth in the gear blank are completely formed. Generally speaking, there are two types of manufacturing method for worm gears producing. The first is the radial feed method in which the hob is fed into the gear blank in a radial direction as shown in Figure 7.1(a). The other one is the tangential feed method in which the hob is fed into the work piece in the tangential direction (see Figure 7.1 (b)).

The worm gear VGM method is similar to the practical gear hobbing process except that in VGM the gear blank is static and the hob rotates about two axes simultaneously (see Figure 7.1 (c)). One rotation is about hob's own axis and the other is about the gear blank axis. However, the relative movement of the gear blank and the hob in VGM and real gear manufacturing (RGM) is the same, so when the hob process is finished, the same gears will be produced in VGM and RGM.

The VGM method for 3D worm gear modelling has many advantages including:

- It directly reflects the manufacturing process - the worm gear is produced on computer using the virtual cutting process which is a simulation of the cutting process applied in practical manufacturing. The VGM method does not require a complex mathematical model of the worm and wheel tooth surfaces.
- It is parametric and very flexible for changing – suitable for FEM modelling and optimum design;
- It is economic - it allows researchers and engineers to virtually manufacture their new gear designs on a computer, and fixes any performance problems before expensive prototypes are built.

- It is a valuable visualisation tool for gear researchers and engineers - the worm gear set can be assembled and virtually run on computer to check for interference or to see the localised tooth contact pattern.



(a) Radial feed in RGM (b) Tangential feed in RGM (c) Hob motion in VGM

Figure 7.1 RGM and VGM hobbing process diagrams

7.3 VIRTUAL MANUFACTURING OF WORM GEAR DRIVES

In order to illustrate the virtual gear manufacturing method clearly, a single thread ZA worm and a multi-start ZI worm are used as examples. The virtual manufacturing method can be used to generate all of the other types of worm gears. The procedure for 3D VGM of worm gear hobbing and tooth contact analysis is shown in Figure 7.5.

7.3.1 Design of ZA and ZI Worm Gears

7.3.1.1 ZA Worm Gear Proportions

A ZA worm tooth profile is a ruled surface that is generated by a straight line while it performs a screw motion with respect to the worm axis. The generating line intersects the worm axis and the axial section of the worm surface in a straight line. The cross

section of the ZA worm is an Archimedean spiral (see Figure 7.2). The ZA worm gear used as an example here has a single start worm. The worm has one thread and the worm gear has 60 teeth. The main dimensions of the present worm gear are listed in Table 7.1. The centre distance between the worm axis and gear axis is 6.125 inches. The thread leads of worm and hob are identical (0.5 inches). The axial pitch of the worm is 0.5 inches and its lead angle is 3.3725°. The worm tooth axial section is shown in Figure 7.3. The two edges of this tooth section represent the two cutting edges of the hob. In the virtual manufacturing process, it will represent as the two cutting edges too.

Table 7.1 Main Design Parameters of ZA Worm, Wheel Cutter and Gear (inch)

	Worm	Wheel Cutter	Wheel
Root Diameter	2.6318	2.6318	
Pitch Diameter	2.7008	2.7008	
Outside Diameter	3.3184	3.3184	9.8086
Lead	0.5	0.5	
Number of Threads (Teeth)	1	1	60
Gear Centre Distance	6.125	6.125	6.125
Wheel Throat Radius			4.7841
Wheel Tooth Face Width			2.00

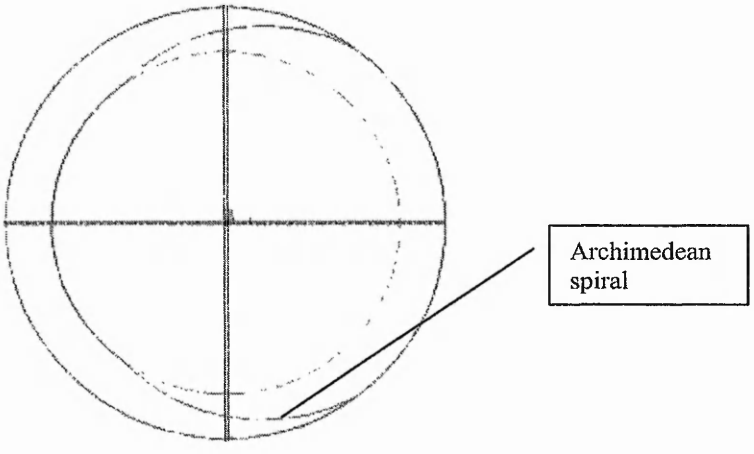


Figure 7.2 Cross section of ZA worm

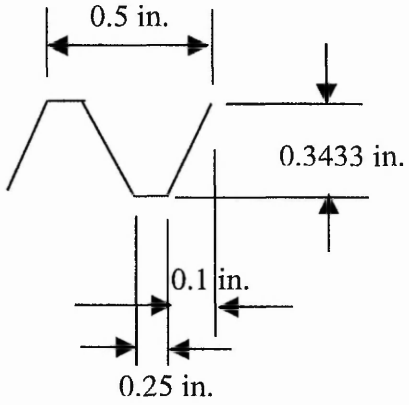


Figure 7.3 ZA worm thread axial proportions used in example

7.3.1.2 ZI Worm Gear Proportions

A ZI worm surface is a screw involute surface. Such a surface is generated by a straight line that performs a screw motion about the worm axis being a tangent to the helix on the base cylinder of the worm. The cross section of the worm surface is an involute curve (see Figure 7.4). In order to illustrate the generation of a multi-start worm, a 3-start ZI worm gear is used as an example. Its main design parameters are shown in Table 7.2.

Table 7.2 Main Design Parameters of ZI Worm, Wheel Cutter and Gear: T/t/q/m=56/3/10.590/8.500, normal pressure angle: 22.5° (unit: mm)

	Worm	Wheel Cutter	Wheel
Base Diameter	49.477	49.985	
Root Diameter	71.029	75.336	
Pitch Diameter	90.018	91.034	
Outside Diameter	106.995	111.303	499.999
Lead	80.112	79.898	
Number of Threads (Teeth)	3	3	56
Gear Centre Extension	283.000	0.508	283.00
Wheel Throat Radius			37.160
Wheel tooth Face Width			78.03

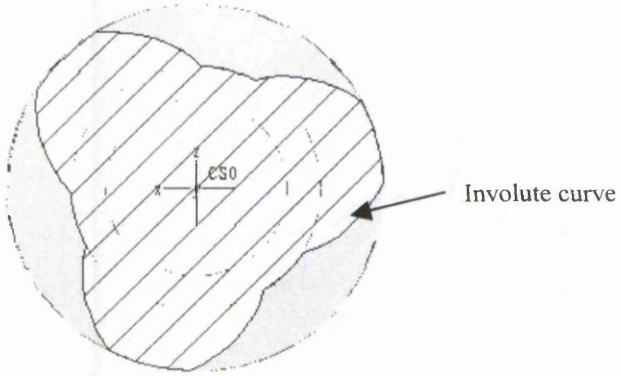


Figure 7.4 ZI worm cross section (3 starts)

The first step is to prepare worm, hob and gear design parameters. According to the design parameters, the through axial section profile of the worm and hob is calculated and constructed in a CAD package. The worm is cut by a *helical sweep cut* in Pro/Engineer. The gear is cut using the *patterning helical sweep cut* function, which simulates the simultaneous rotation of the two axes in the real manufacturing process. The principle of gear cutting is shown in Figure 7.1(c).

After the worm and gear have been cut, they are assembled together according to the design parameters. The worm gear set can be virtually run on a computer and their contact path and any interference between worm and gear can be visually and quantitatively checked. The worm gear tooth profile, curvature and normal can be determined through the model analysis function.

7.3.2 Worm Cut

7.3.2.1 ZA Worm Cut

To generate the worm model, the first step is to create the worm cylinder base. The cylinder base can be protruded either by *extrusion* or *revolution*. If the extrusion method is used, the cylinder cross circle is needed and a depth value is entered for protrusion. If the revolution method is used, the cylinder axial section is needed and a

value of 360° is entered for revolution (see Figure 7.6). The cylinder base so produced is shown in Figure 7.8(a).

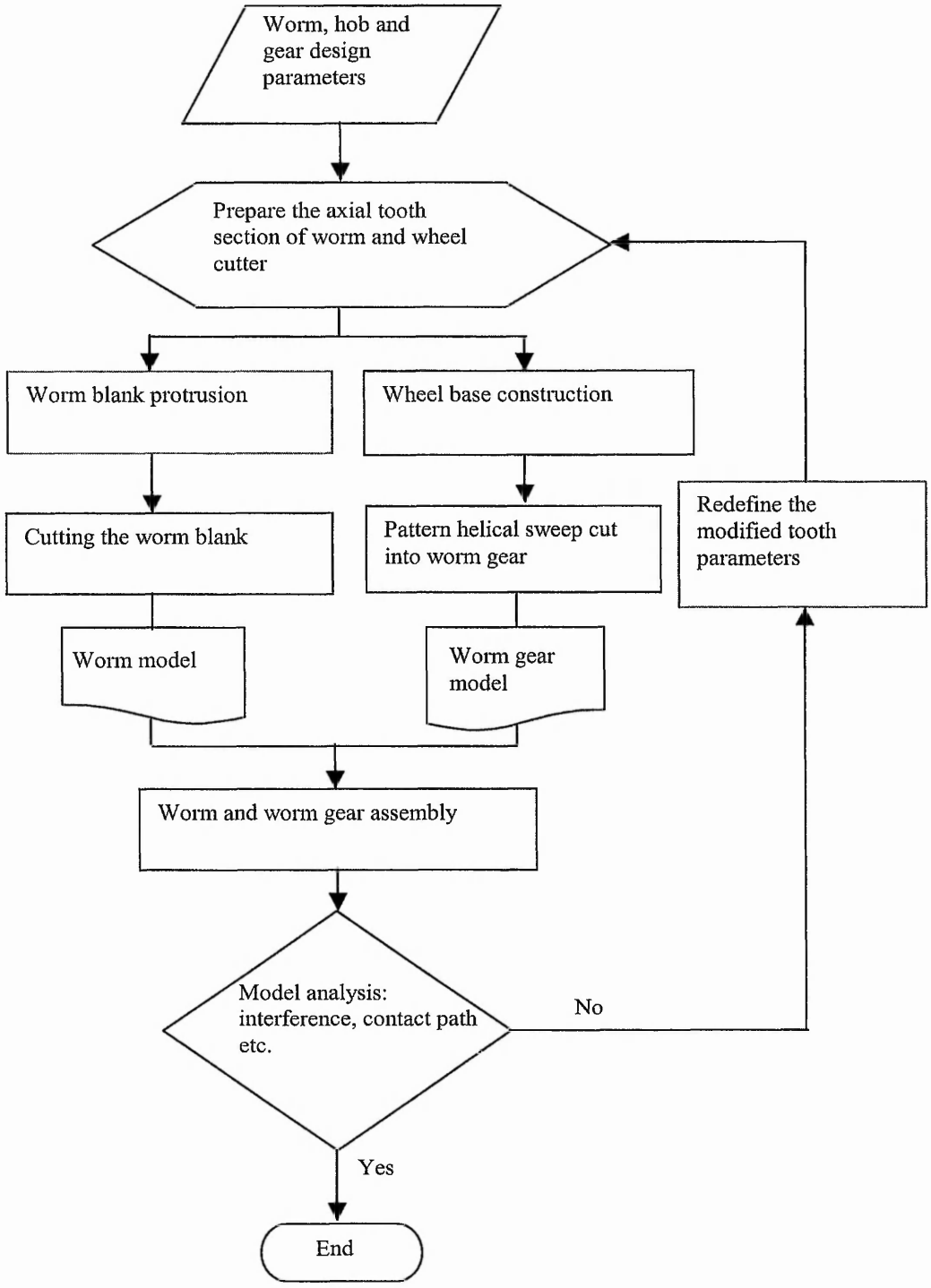


Figure 7.5 Procedure of 3D simulation of worm gear hobbing and tooth contact analysis

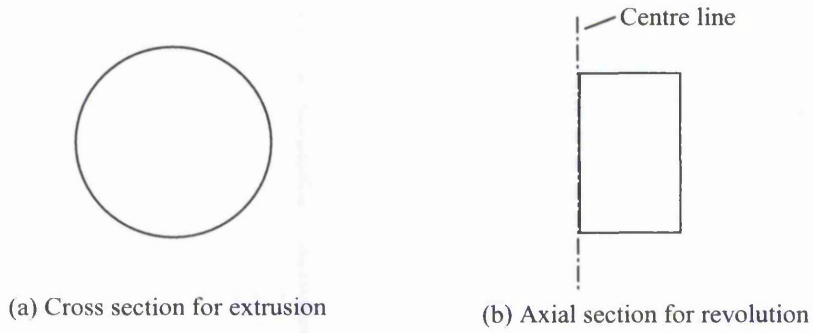


Figure 7.6 Section of cylinder base construction

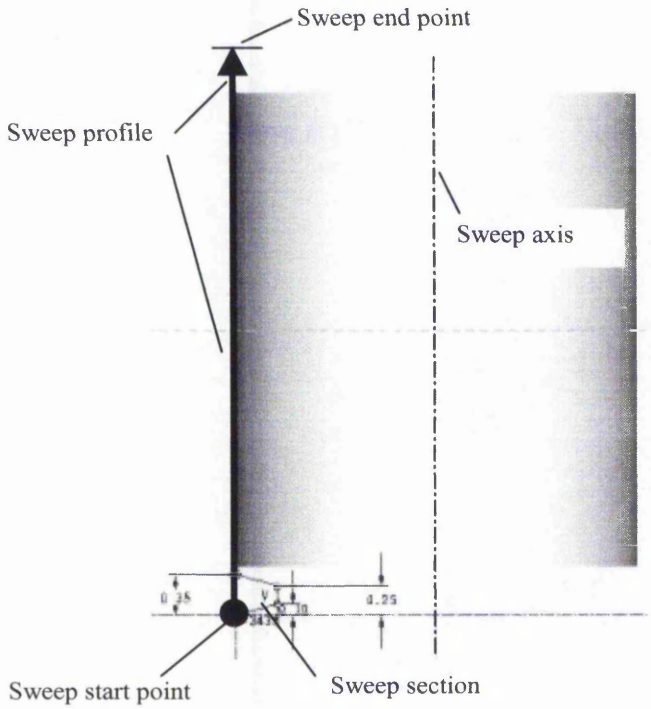
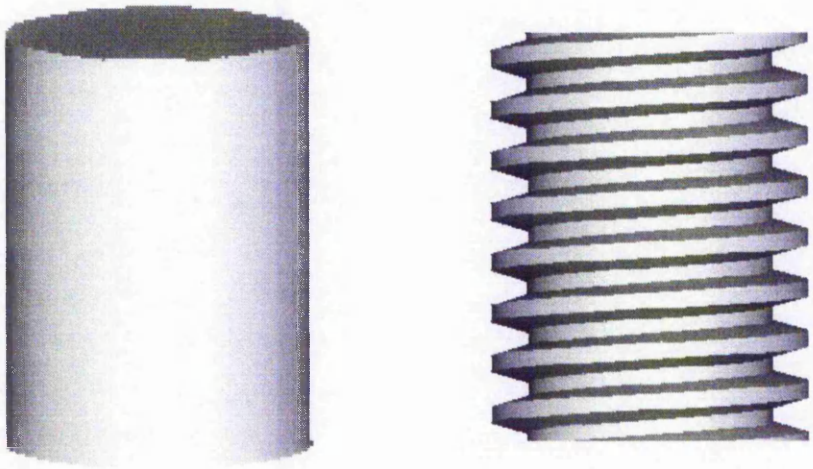


Figure 7.7 Helical sweep profile and sweep section

The worm cutting is produced by the function *helical sweep cut* in Pro/Engineer. The *helical sweep cut* will sweep the *sweep section* along the *sweep profile* and rotate about the sweep axis that is coaxial with the worm blank (see Figure 7.7). The swept path is a helix curve. The swept section is identical to the section of the blade in practice that is installed in the axial section of the worm. All the material of the worm cylinder base in the swept path of the swept section is cut out.

In Figure 7.7, the sweep profile is aligned with the edge of the cylinder base. The start point for the sweep profile is some distance from the bottom of cylinder. The reason for this is that it will be convenient for later assembly. The sweep end point should have enough distance from the top of the cylinder to ensure that the full thread can be cut. The final worm, cut by the *helical sweep cut*, is shown in Figure 7.8(b).



(a) Worm blank (b) Worm model

Figure 7.8 Worm blank and model

For ZN type worm cutting, the procedure is similar to that for ZA worm cutting. However, in ZN cutting, the section is swept normal to the helix, so when the *helical sweep cut* is applied, the *normal to trajectory* option should be selected.

7.3.2.2 ZI Worm Cut

A worm cylinder base with its outside diameter identical to the worm outside diameter is produced in Pro/Engineer first. The advanced constructing feature option, *helical sweep cut,* is used to simulate the worm tooth cutting process. In order to achieve this, the tooth cutter profile is needed. For a ZA worm, the cutter's cutting edge, i.e. the generating line of the worm tooth surface is a straight line placed in the through axis plane, so the sweep section is easy to obtain. In the case of a ZI worm, the through axis section of the worm tooth is needed for the *helical sweep cut.* The

sweep section of a ZI worm is a curved section. This section can be obtained from the tooth surface equation. The ZI worm tooth surface can be written as

$$\mathbf{r}_1 = \begin{pmatrix} x_1 \\ y_1 \\ z_1 \end{pmatrix} = \begin{pmatrix} r_b \cdot \cos\theta + u \cdot \cos\lambda_b \cdot \sin\theta \\ r_b \cdot \sin\theta - u \cdot \cos\lambda_b \cdot \cos\theta \\ -u \cdot \sin\lambda_b + p\theta \end{pmatrix} \tag{7.1}$$

where, $\mathbf{r}_1$ is the position vector of the worm surface, r_b is the radius of the base cylinder of the worm, λ_b is the lead angle of the worm, and p is the screw parameter of the worm.

Let $x_1=0$, we have

$$r_b \cdot \cos\theta + u \cdot \cos\lambda_b \cdot \sin\theta = 0 \tag{7.2}$$

Rearranging the equation gives

$$u = -r_b \cot\theta \sec\lambda_b \tag{7.3}$$

Substituting u for y_1, we have

$$y_1 = r_b \csc\theta \tag{7.4}$$

The surface parameter θ is thus obtained

$$\theta = \arcsin\frac{r_b}{y_1} \qquad (0 < \theta < \frac{\pi}{2}) \tag{7.5}$$

or

$$\theta = \pi - \arcsin\frac{r_b}{y_1} \qquad (\pi > \theta \geq \frac{\pi}{2}) \tag{7.6}$$

Using Equations (7.3), (7.5) and (7.6), the through axis section curve of a ZI worm tooth is obtained as follows

$$z_1 = \tan\lambda_b \sqrt{y_1^2 - r_b^2} + p \arcsin\frac{r_b}{y_1} \qquad (0 < \theta < \frac{\pi}{2}) \qquad (7.7)$$

$$z_1 = -\tan\lambda_b \sqrt{y_1^2 - r_b^2} + p(\pi - \arcsin\frac{r_b}{y_1}) \qquad (\pi > \theta \geq \frac{\pi}{2}) \qquad (7.8)$$

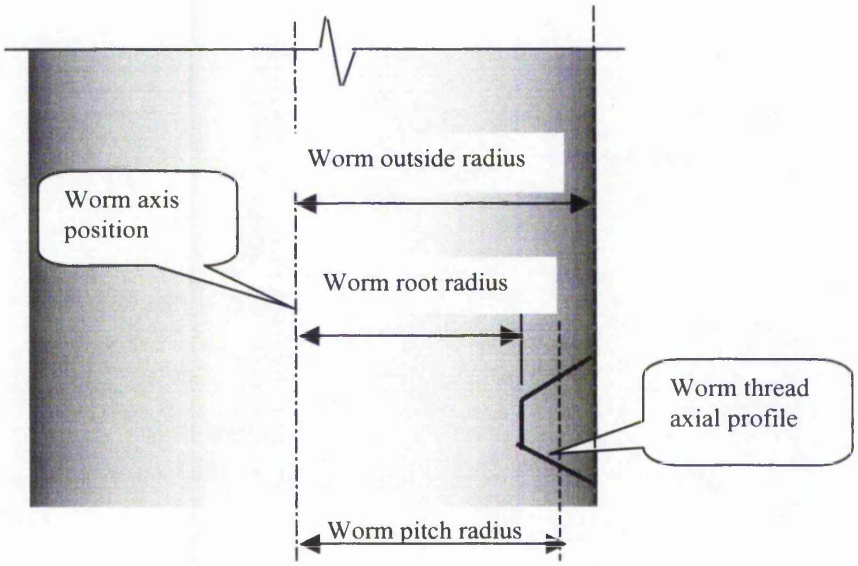


Figure 7.9. Axial-section of worm tooth profile

From the above equations, the through axial section curve datum points are calculated and saved in a text file. Then the cross-section is produced in Pro/Engineer Sketcher Mode as follows:

- Sketch a simple 3 point spline and dimension the spline to a local coordinate system
- Modify the simple spline into the desired curve by reading the coordinates of the points from the saved data text file.

According to the design parameters, the axial tooth section can thus be determined. The final through axis section is shown in Figure 7.10. After the through axial cross section of the worm tooth profile is produced, the helical sweep profile is determined according to wheel design parameters. The following procedure for preparing the

sweep profile and sweep section for a ZI worm gear are the same as for a ZA worm gear. After the worm helical pitch is inputted, the first helical sweep cut is applied to the worm blank cylinder and a single thread is obtained as shown in Figure 7.11(b).

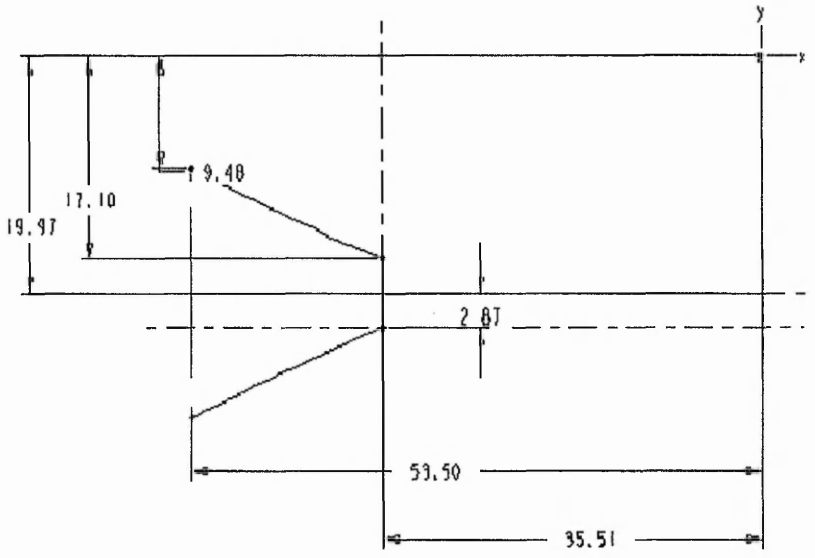


Figure 7.10. Axial-section of worm tooth profile

In this example, the worm has 3 starts. To produce the 3-start worm, the sketching plane should be created as a datum plane 'on the fly' with an angular leading dimension. With the angular leading dimension, the other two threads are created by patterning the single *helical sweep cut* as shown in Figure 7.11 (c). Finally, the shaft is added to complete the worm (see Figure 7.11 (d)).

7.3.3 Wheel Hobbing

7.3.3.1 ZA Wheel Hobbing

The wheel is much more difficult to produce than the worm. The wheel teeth are conjugate with the worm teeth and the wheel tooth surfaces are generated by a hob. In practical wheel tooth cutting, the hob is identical to the worm.

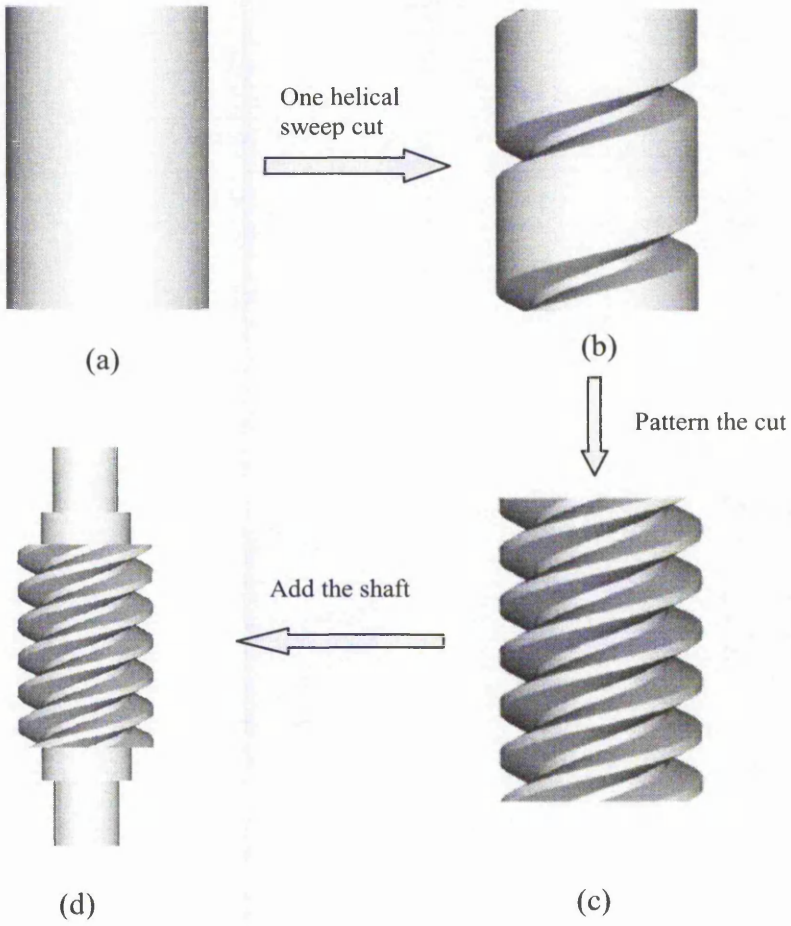


Figure 7.11 Illustration of virtual worm cut procedure: (a) worm blank (b) One thread cut (c) 3 threads cut (d) shaft added

The hobbing process duplicates the operation of worm gear drives. So the wheel tooth surface can be conjugate with the worm surface. The wheel surfaces are the envelopes of the hob surfaces. The virtual hobbing process is the same as the real operation of a worm gear drive, so that the wheel such produced can mesh with the worm.

The most difficult part in simulating wheel hobbing is how to rotate the worm and wheel axes simultaneously with a given speed ratio. It is impossible for most CAD packages, such as AutoCAD, to rotate parts around two perpendicular axes simultaneously. Pro/Engineer has the capacity of performing *helical sweep cut* about a single axis, so it is not difficult to cut the worm. However, it is quite difficult to cut the wheel since the wheel surfaces are the envelopes of the worm tooth surfaces. During the process of hobbing, the hob has to rotate about two perpendicular axes simultaneously.

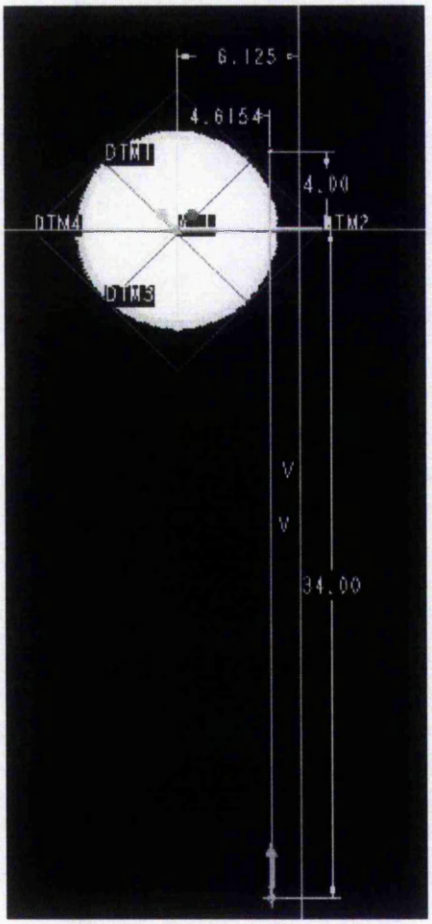


Figure 7.12 Sweep profile of a ZA gear hob

This difficulty was overcome by the author by introducing a translational relation between the axial rotation and the helical sweep cut starting distance. It is a parametric method and easy to use.

The cut thread of a hob is simulated by a *helical sweep cut* feature in Pro/Engineer. The *helical sweep profile* is sketched on datum plane DTM2 as shown in Figure 7.12. The reference plane is sketched during the feature construction (DTM4 in Figure 7.12) so that it can provide an angular leader. So the *helical sweep cut* can be patterned to simulate the rotation of the hob about the gear axis.

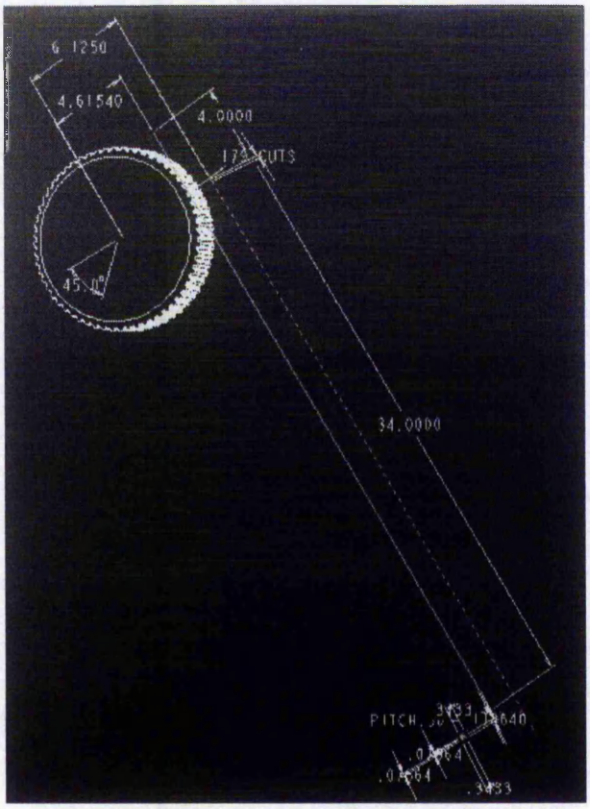


Figure 7.13 Patterning dimensions for ZA wheel bobbing

The rotation of the hob about its own axis is simulated by changing the position of the starting point of the *helical sweep profile* for the *helical sweep cut*. When the starting distance advances the distance of one pitch, the hob rotates about its own axis exactly one circle, i.e., 360°. So the hob's rotation can be simulated by patterning the dimension of the starting point of its *helical sweep profile* with a constant increment. The constant increment has the following relationship with the hob's rotation angle.

$$\Delta S = \frac{\Delta\theta_{hob}}{360} \cdot p \tag{7.9}$$

in which ΔS is the increment of starting point position, $\Delta\theta_{hob}$ is the increment of hob rotation angle and p is the pitch of the hob.

The rotation of the hob and the wheel blank has the following relationship

$$\omega_{wheel} = \omega_{hob} \cdot \frac{t}{T} \tag{7.10}$$

$$\Delta\theta_{wheel} = \Delta\theta_{hob} \cdot \frac{t}{T} \tag{7.11}$$

where,

ω_{wheel} is the angular velocity of wheel

ω_{hob} is the angular velocity of hob

$\Delta\theta_{wheel}$ is the increment of wheel rotation angle

t is the number of starts of the worm.

T is the number of teeth of the wheel.

Using Equation (7.9) and (7.11), the relationship between the two patterning dimensions can be obtained as follows

$$\Delta\theta_{wheel} = \frac{360}{p} \cdot \frac{t}{T} \cdot \Delta S \tag{7.12}$$

Since the translational position of the starting point is used to simulate the hob's rotation, the hob's start point begins a long distance from the DTM4 (see Figure 7.12). This distance should long enough for patterning.

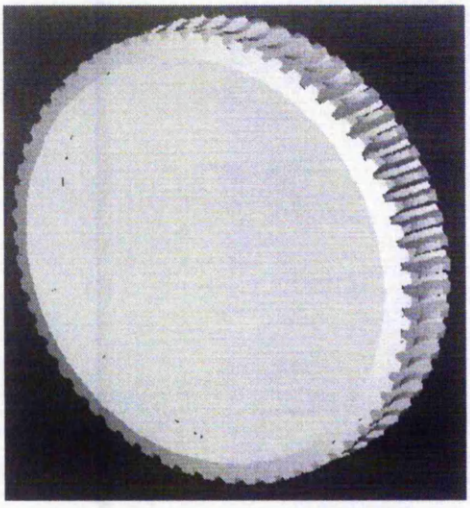


Figure 7.14 ZA worm gear

Figure 7.13 shows all the dimensions in the wheel hobbing. The angular dimension 45.0° is the wheel rotating leader and the dimension 34.0000 is the translational leader for the hob starting point. When the above two dimension leaders are patterned simultaneously, the real gear hobbing process is simulated. After the patterning is finished, the gear is created. Figure 7.14 shows the created 3D ZA gear model.

7.3.3.2 ZI Wheel Hobbing

The procedure for hobbing a gear for a ZI hob is the same as that for a ZA hob. The virtual wheel cutter's axial tooth profile is shown in Figure 7.15. There are three tooth axial profiles because the hob has 3-start.

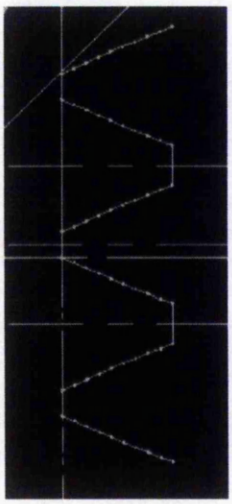


Figure 7.15 Wheel cutter tooth profile in axial section

The mounting relation of the wheel cutter's axis and the wheel blank is similar to that for a ZA gear. The axes of the wheel cutter and the wheel are perpendicular to each other. The wheel blank and its cutter rotate about their own axes with a constant ratio as shown by Equations (7.10) and (7.11).

Figure 7.16 shows a zoomed unfinished gear tooth hob profile and the cutting trails can be clearly seen. In this example, the wheel rotating angle per cutting step is $\Delta\theta_{wheel}$ =2.143° and the cut tooth profile looks good (see Figure 7.16).

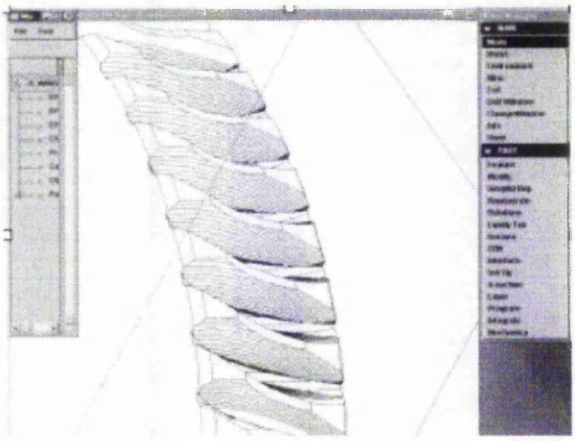


Figure 7.16 Zoomed wheel cutting tooth

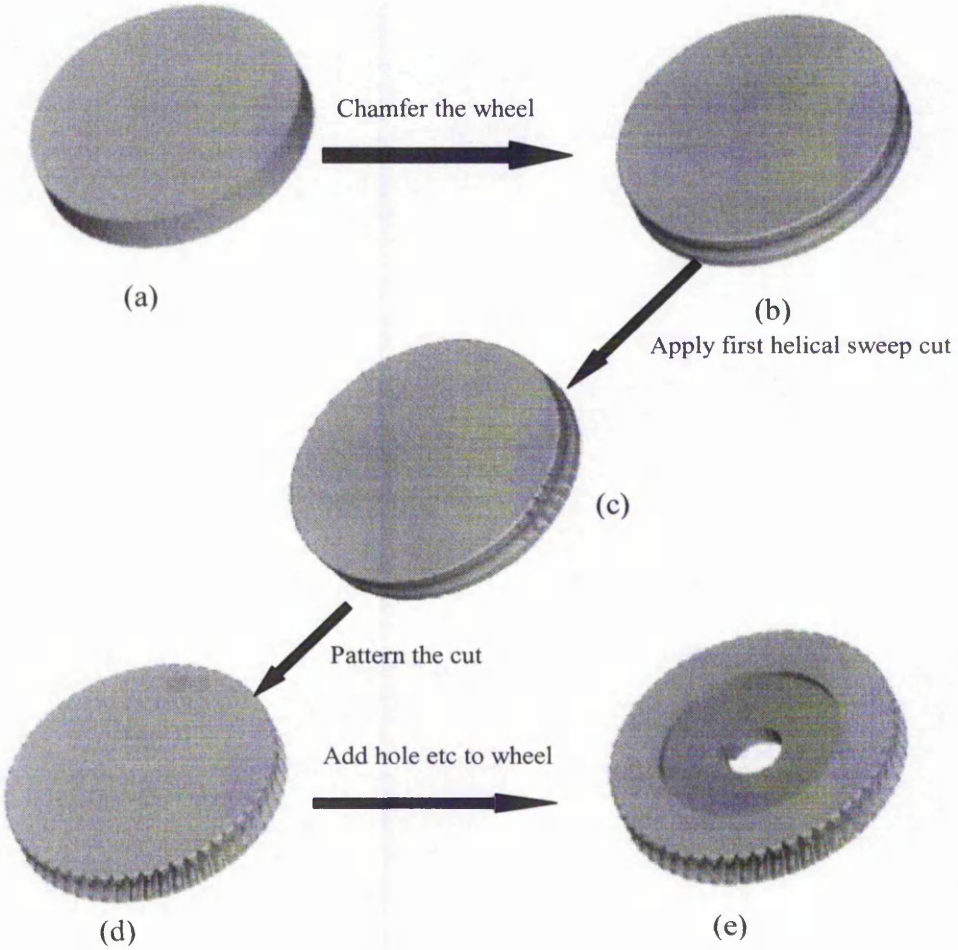


Figure 7.17 Illustration of the worm gear virtual manufacturing process: (a) Gear blank, (b) Chamfered, (c) First cut, (d) Full cut, (e) Finished gear

The worm gear virtual manufacturing process is illustrated in Figure 7.17. Firstly the gear blank is prepared and chamfered and the gear throat is cut. After that, the wheel cutter is mounted on the wheel, then the wheel blank and the cutter are rotated simultaneously which is achieved by *patterning* the *helical sweep cut* feature. When the cutting process is finished, the hole is cut and the gear is ready for assembly and model analysis. The virtual cut gear method is identical to the tangential feed method in real gear manufacturing.

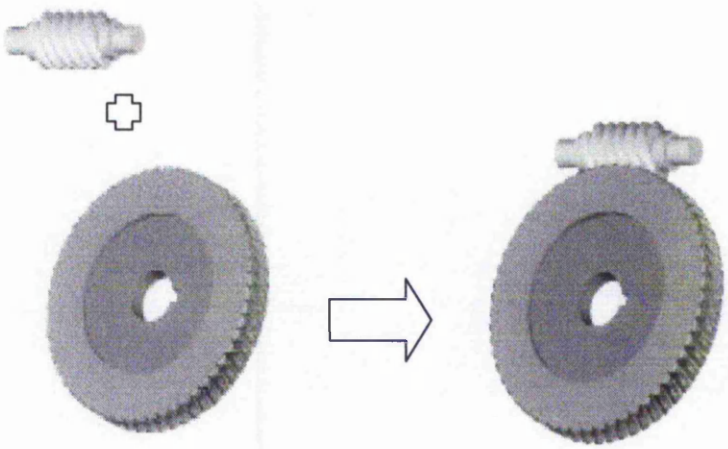
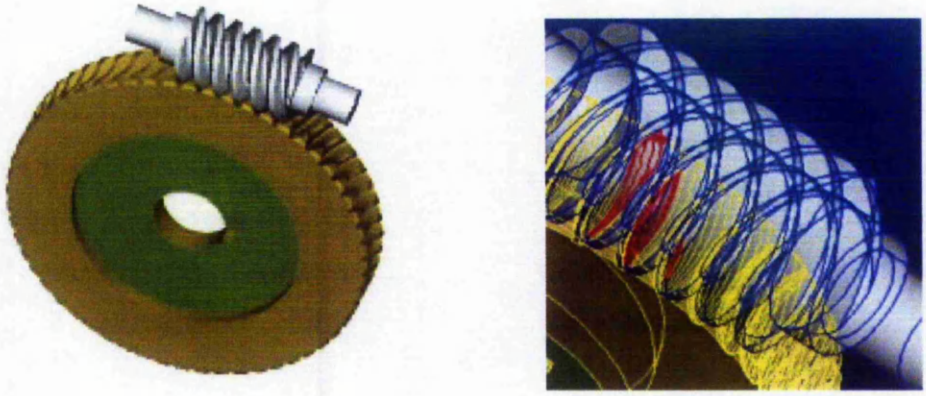


Figure 7.18 Worm and gear assembly

7.3.4 Worm Gear Drive Assembly

The produced worm and wheel models are assembled in the Pro/Assembly module according to their space mounting relationship, shown in Figure 7.18. The options used for the worm gear assembly are *Mate*, *Mate Offset*. It is also possible to use the coordinate system to assemble the worm gear set. After the assembly, use *Modify/Modify Assembly/Move/* option to create the rotational leader. With the rotational leader, the gear drive can be virtually run on a computer and its meshing conditions, including any localised tooth contact path and tooth interference can be checked. The 3D worm gear model can be further exported to a FE package to conduct finite element analysis and optimisation design.

Using the assembly model, the three-dimensional simulation of localised tooth contact can be conducted. The tooth contact pattern and the moving direction of the localised contact area can be predicted; moreover, any interference between the modified tooth surfaces can be detected and hence can be avoided at the design stage.



(a) Worm gear in mesh (b) Zoomed contact area

Figure 7.19 Worm gear mesh and global interference check

Figure 7.19 (a) shows the worm gear in mesh. Its design specifications are given in Table 7.2. Figure 7.19 (b) shows the zoomed tooth contact pattern between the worm and the gear during their engagement. The contact pattern is highlighted (red region) in the picture.

7.4 HOLROYD 3D VGM WORM GEAR MODELS

The VGM method have been applied to create two involute worm gears designed by Holroyd (a gear manufacturing company in UK). The first gear set has a lower reduction ratio (6/31) and its worm has six starts. The 3D VGM model which has been created is shown in Figure 7.20. The second gear set has a higher reduction ratio (1/50) and the finished 3D VGM model is shown in Figure 7.21. The first worm gear set will be used to build a finite element model (see Chapter 9).

An experiment on a worm gear provided by Holyroyd has been conducted (see Appendix E). The experimental results of tooth contact show that all the contact

zones at different instances spread over almost the whole tooth width (see Figure 7.23). This is quite different from the localised tooth contact pattern reported in the literature (Yang et al 1998), which happens at the partial width of the tooth surface. In order to understand this phenomenon, the virtual simulation of the tooth contact of the Holroyd worm gear (ratio: 1/50) was conducted. The 3D worm and gear models were produced using the virtual gear manufacturing method based on the Holroyd design and manufacturing specifications. After the models were created, they were assembled.

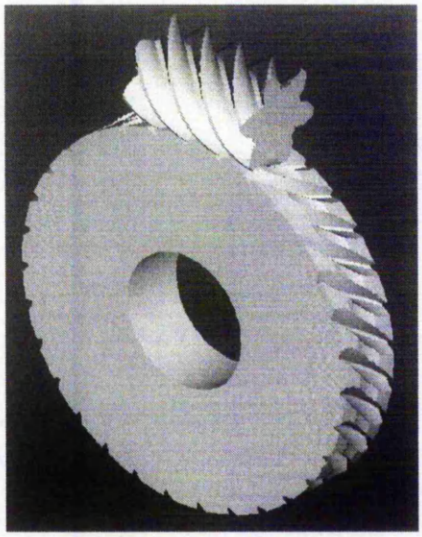


Figure 7.20 Holroyd involute worm gear (6-start worm)

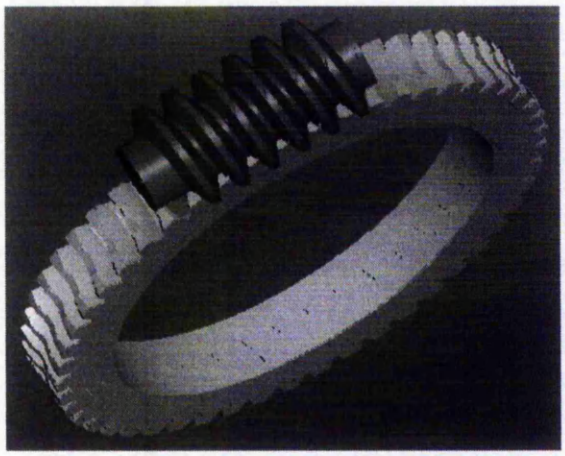


Figure 7.21 Holroyd involute worm gear (single start worm)

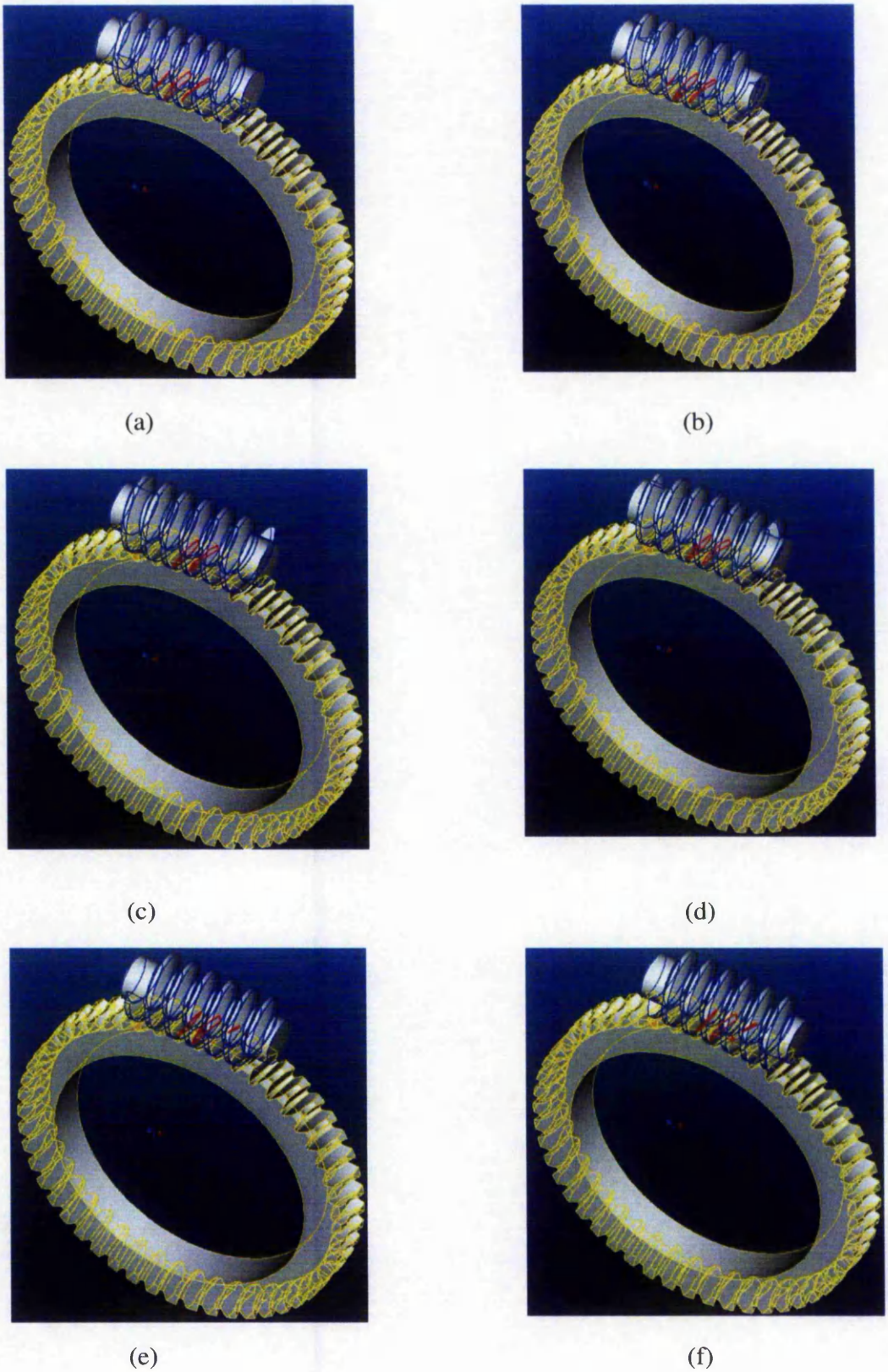


Figure 7.22 Worm gear contact pattern (ratio 1/50)

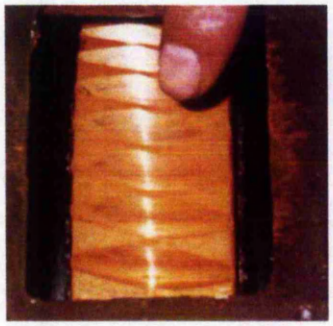


Figure 7.23 Experimental results of tooth contact (gear ratio: 1/50)

The contact patterns of the Holroyd worm gear with a gear ratio 1/50 at different contact positions are shown in Figure 7.22. In the simulation, the gear is static while the worm rotates in two directions simultaneously: one is about its own axis and the other is about the gear axis. The ratio of the two axis rotational speeds is identical to the gear ratio. The simulation of the gear operation is conducted at six different positions. The six positions cover the whole period of a gear tooth in contact so that the full gear operation can be simulated. From the pictures, the contact patterns (highlighted by the red enclosed line) can be clearly seen in the gear tooth. Such a contact pattern will result in the contact areas exactly the same as that shown in Figure 7.23. This shows the advantage of the VGM method. The experimental run-in is neither able to find the real contact patterns nor the changes of the contact regions in operation. With the virtual simulation of the gear meshing, how the contact patterns change with the different operating stages can be clearly animated (see Figure 7.22). Another advantage of the VGM model is that it is easy to obtain the gear tooth section profiles. Figure 7.24 shows how it is possible to obtain any desired tooth section and profile curve data in Pro/Engineer. This is a very useful tool for gear designers.

7.5 CONCLUSIONS

The method of the virtual gear manufacturing has been developed for the rapid 3D modelling of worm gears. This new method simulates the gear hobbing process to

model the complex geometry of the worm gear tooth on a computer. The methodology has been developed to simulate a hob's two-axis simultaneous rotation.

One ZA and one ZI worm gears have been used as examples to illustrate how 3D VGM worm gear models are created. The 3D models are created in Pro/Engineer and the whole modelling process is fast and does not involve any complicated mathematical calculations. Two Holroyd worm gear models have also been created and the contact patterns have been examined. The operation of a Holroyd worm gear has been animated in a 3D environment.

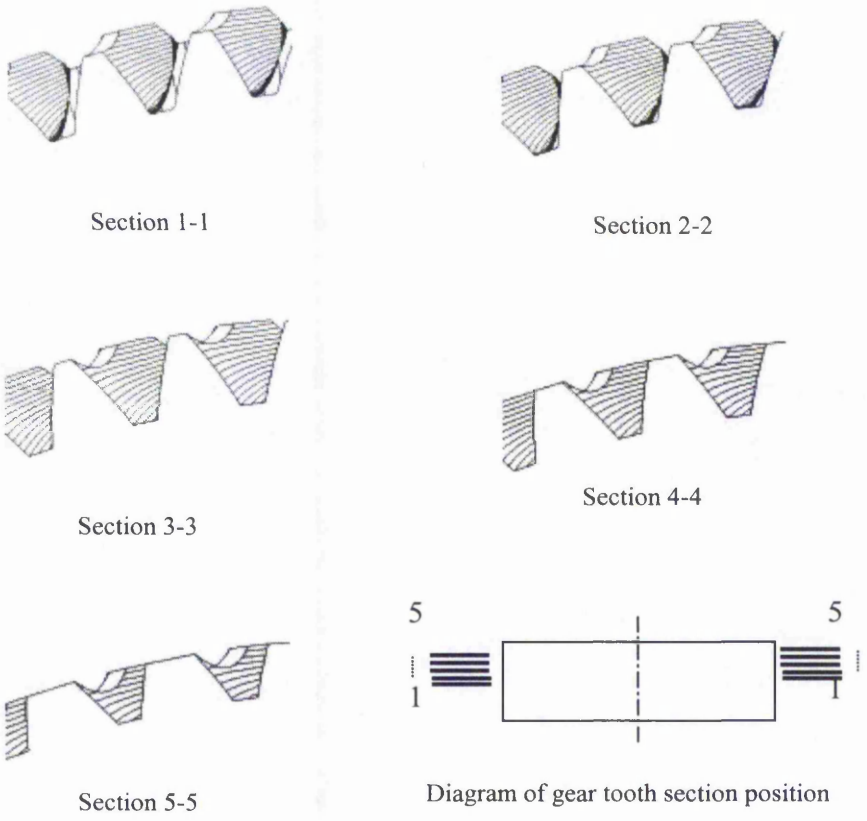


Figure 7.24 Tooth section profile along the gear face width

CHAPTER 8 Loaded Multi-Tooth Contact Analysis of Spiroid Gears

A multi-tooth finite element model has been developed to determine the contact forces and stresses in spiroid gears. The virtual manufacturing modelling method has been used for generating the 3D spiroid gear tooth model. The multi-tooth contact model is then imported into a commercial finite element software package to build the finite element model. The contact boundaries are simulated by general surface-to-surface contact elements that are more suitable than gap elements in the simulation of real tooth contact. The solution technique for generating an accurate general surface-to-surface contact element model has been addressed. The procedure for performing three-dimensional stress analysis of spiroid gears in meshing has been developed. The contact forces and stress pattern have been evaluated.

8.1 INTRODUCTION

8.1.1 General

Spiroid gear teeth have such a complex geometrical shape that no feasible stress analysis solutions have so far been developed for any given set of gear teeth. Conventional methods fail to predict the gear tooth stress and load distributions accurately.

With the rapid development of computer software and hardware, it is now possible to accurately predict the gear tooth contact stresses and deformations using the finite element method. However, loaded gear tooth contact analysis is a highly nonlinear problem and hence is extremely difficult to solve. It is one of the most complex problems to accurately predict how a multi-tooth contact will perform. The regions of contact are generally unknown until the model is run. Depending on the loads, materials, boundary conditions and other factors, the tooth surfaces can get into and go out of contact with each other in an unpredictable and abrupt manner. Loaded tooth contact analysis takes a lot of time to set up and requires comprehensive

understanding of the principles of the nonlinear algorithms and the object to be solved.

In this research, feasible procedures and techniques for loaded gear tooth contact analysis using the finite element method have been developed. By using these procedures and techniques, researchers and engineers will be able to conduct and gain benefits from the loaded gear tooth contact analysis. More accurate tooth stresses, contact forces and load sharing between the mating teeth can be acquired and visually displayed.

This chapter has 13 sections. In the introduction, previous work in gear tooth stress analysis is briefly reviewed. The difficulties and limitations of experimental testing of gears and multi-tooth finite element analysis will be discussed. Section 8.2 evaluates four available preprocessors can be used for complicated gear models. The data transfer interface is discussed in Section 8.3. In Section 8.4, the 3D spiroid gear geometry model is generated and the necessary geometry cleanup and rebuild work will be presented. The assumptions of gear tooth contact analysis are introduced in Section 8.5. Section 8.6 discusses the contact algorithm that has been used in the present analysis and some considerations in selecting the proper contact element for the spiroid gear contact models. Section 8.7 introduces the selection of solid elements for the contact models. The model importation, coordinate systems and mesh generation of models are introduced and the problems in the process have also been discussed in Section 8.8. In Section 8.9, the application of a load and the technique of applying the boundary conditions to ensure the gear set rotating about their own axes but are fixed along the axial directions have been developed. In Section 8.10, the considerations regarding the selection of the most appropriate solver and the choice of analysis options for the analysis of the spiroid gear contact problem have been covered. Section 8.11 introduces two advanced techniques: gear contact region mesh refining and submodelling. The results of the contact analysis have been discussed in Section 8.12. The detailed stress distribution, contact region shifting, contact force and load sharing have been analysed and illustrated. The results show that the 3D contact models successfully simulate the meshing of spiroid gears. Section 8.13 briefly summarises the work completed in this chapter and some of the experience in 3D multi-tooth contact analysis.

8.1.2 Previous Work in Gear Tooth Stress Analysis

Spiroid gears are used to transmit power and motion between intersecting shafts. Accurate prediction of the tooth stresses is important for gear design. However, in practice, it is still difficult to predict the stresses in spiroid gears using currently available analyses due to the complicated tooth geometry and multi-tooth contact characteristics.

Attempts have been made by previous investigators to relate tensile fillet stresses observed in statically loaded gear teeth to the geometric appearance of the tooth. As early as 1893, Wilfred Lewis applied elementary beam theory to symmetrical tooth profiles by inscribing a parabola to represent a beam of uniform strength. As a result of the uniform strength assumption the Lewis formula was unable to deal effectively with the abrupt changes in tooth section that occur in the tooth fillet region. Furthermore, for teeth with high-pressure angles a radial component of load exists that tends to modify the stresses produced by the applied bending moment.

In 1938, Merritt added a term to the Lewis formula that accounted for the radial component of the load which was assumed to act along the vertical centreline of the symmetric tooth. At this point neither the Lewis nor the Merritt formula was able to take into account abrupt changes in tooth section.

Lewis and Merritt's work is obviously not accurate since the gear tooth was simply modelled as a beam. Traditional methods cannot solve the complex geometry contact problem.

The methods of load distribution analysis currently used in practical gear design are usually based on one of the modern gear rating standards such as AGMA 218, BS436, ISO 6336/DP. In these analyses, the contact and bending stresses are first calculated for idealised "perfect" gears. The values so calculated are then modified by introducing various load distribution factors that account for the effect of alignment errors and inaccurate manufacturing. To estimate the load distribution factors all the existing gear rating standards assume the gear teeth to behave as a series of thin slices



that deflect independently. This approach clearly fails to model the contact teeth properly since the buttressing effect of adjacent tooth sections tends to flatten the load distribution.

8.1.3 Experimental Testing of Gears

It is possible, though, to do experiments on a gearset test rig to determine the load sharing and contact stress patterns. However, experimental work on gear testing has three shortcomings: (1) it is expensive because the test needs a special test rig and the existing gear prototyping is also costly; (2) it is very difficult to obtain the real gear tooth contact force, region and stress distribution with currently available test methods. Due to the special running-in characteristics of a gearset, it is very hard to observe the exact contact regions in a multi-tooth contact problem. It is also difficult to place the strain gauges in the gear root fillet areas. In most cases, the tested gears have to be specially designed in the root areas to allow enough room for the strain gauges. However, in so doing, the stresses in the real gear set are only approximately obtained; (3) the results of gear experimental tests are only suitable to those particular gears with the same design features. Many factors (e.g. lead angle, pitch, tilt angle, mounting misalignment, material properties and different loading conditions) all affect the test results.

8.1.4 Multi-Tooth Finite Element Contact Analysis

Handschuh et al (1999) presented a seven-tooth non-linear finite element model, comprising of three pinion teeth and four gear teeth, to simulate the 3D multi-tooth contact of spiral bevel gears. Qin et al (2000) presented an eight-tooth finite element model of an hourglass worm gear to investigate the load sharing and tooth contact stresses. Although the above multi-tooth contact models are more realistic in simulating the simultaneous contact of gear under load than those in previous research, they still have two major shortcomings:

1. It is difficult to generate the model. This is due to the fact that gap elements were used to predict the penetrations between the simultaneous contact teeth. Since the loaded contact paths are never known until the finite element model

has been run, the unloaded contact paths calculated by tooth contact analysis have to be used instead of the loaded tooth contact path in finite element analysis. Furthermore, the process of alignment of the gap elements in the anticipated contact paths is numerically tedious and practically inexecutable.

2. The application of boundary constraints is problematic since only partial models are used. The boundary conditions in the analyses, whatever constraint schemes are applied, cannot ideally simulate the real stresses and deformations in the model's boundary surfaces. The boundary conditions affect the force equilibrium and therefore have a great impact on the results. As it is well known, the boundary condition is a critical factor in non-linear contact analysis and may make the results totally useless if it is not properly applied.

In order to overcome the above shortcomings in multi-tooth contact analysis, the general surface-to-surface contact element technique, the latest development in nonlinear contact analysis, is used in gear multi-tooth contact analysis in this research. It is more convenient and more suitable to simulate the real tooth contact using surface-to-surface contact elements than using gap elements. The primary difference between the gap element and surface-to-surface element technique is the ability to account for large deformation and large relative part sliding, without requiring knowledge of the exact location of the contact areas beforehand. The general surface-to-surface contact element techniques can calculate the tooth contact automatically and determine the contact forces and the effects of friction on the contact stresses. Surface-to-surface elements also eliminate the need for compatible meshes across contacting parts. This technique makes the gear finite element model more efficient. The surface-to-surface technique accounts for real-world interaction between parts of an assembly. These contact elements use a target surface and a contact surface to form a contact pair. Once formed, the real-world interaction among parts of an assembly can be simulated.

The gear tooth contact analysis is a difficult task for the occasional user. Nowadays CAD and FEA software is very sophisticated and difficult to learn. The complex geometries of gear sets and the difficulty of nonlinear contact analysis make gear

tooth contact analysis even harder. The VGM method developed in the preceding chapters has overcome some of the difficulties of 3D geometrical modelling of gears. The VGM method requires little knowledge about the theory of gear meshing. By using the VGM method, a 3D gear model can be produced quickly and accurately. Now in this chapter, a feasible procedure for developing a full spiroid gear finite element contact model will be presented. Though those procedures are applied to spiroid gears in this chapter, most of them are applicable to other types of gears.

8.2 EVALUATION OF FINITE ELEMENT PREPROCESSORS

Gear models have very complex surfaces. The selection of suitable preprocessor is the first important step in the gear multi-tooth contact analysis. In this research, four finite element pre-processors (FEMB, Pro/Mesh, ANSYS preprocessor, HyperMesh) have been learnt and evaluated for the 3D meshing of gears.

FEMB is a pre-processor supplied with LS-DYNA3D. FEMB has the best user interface among the four evaluated preprocessors. It is easy to learn. FEMB has the option of importing a model's geometry via the IGES (IGES stands for the Initial Graphics Exchange Specification) format. However, when the gear IGES files were imported, the program always responded that the iges.dll is not available and failed to import any geometry. It is very difficult to model the gear directly on FEMB. So FEMB was not selected as the pre-processor to be used in the first instance.

Pro/Mesh was the second pre-processor to be evaluated since it is one module of Pro/Engineer and the VGM models were created in Pro/Engineer. The models built in Pro/Mesh have high geometrical accuracy. When it is properly set up in the config.pro file, Pro/Mesh can directly output models to the ANSYS solver. After the modelling is solved, the resultant data can be inputted back to Pro/Mesh for post-processing. This has obvious advantages in post-processing due to the powerful functions of Pro/Engineer. However, Pro/Mesh lacks the advanced surface-to-surface contact elements that need to be used for gear tooth contact analysis. One alternative method is to export the element and nodal data and then add the general tooth contact elements in the ANSYS pre-processor. However, in doing so, the element data file is written in a file with the extension .ans and the database file is read from an input

option in ANSYS. This makes the model very inflexible for modifying and adjusting and also makes the selection of elements very difficult. Another limit of Pro/Mesh is that it has only tetrahedral elements available for 3D meshing. Pro/Mesh uses tetrahedrons as mesh elements. Known as 'tet', these are tiny geometrical pyramids with three-sided bases. If the model is meshed with too few elements, the elements tend to elongate which makes solving them take too long. Within reason the more elements that are used, the *flatter* the tets are, and the faster the ANSYS solution.

Comparing Pro/Mesh with the ANSYS preprocessor, Pro/Mesh almost always meshes the model and generally does it more quickly. However, the element quality has to be very carefully checked.

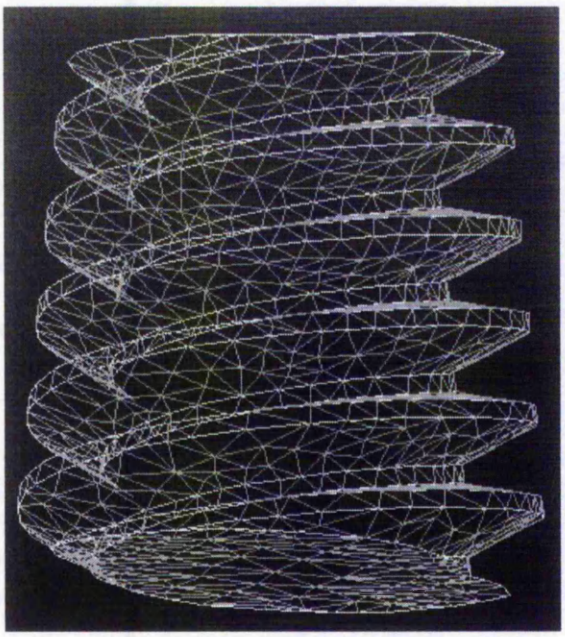


Figure 8.1 Spiroid pinion meshed by Pro/Mesh

The ANSYS mesh is of much higher quality and more accurate especially when the mesh is not trivial. According to the case study of "Cummins Boost Power & Durability of New Signature 600 Diesel Engine" (BENCHmark, January 1999), a Pro/Engineer mesh totalling 90,000 elements would not solve, but a refined mesh totalling 130,000 elements in ANSYS ran in about an hour.

A full gear model with tetrahedral element mesh has far more nodes than the limit of the ANSYS software available (University high option, maximum node number is 32,000). Figure 8.1 shows one of the spiroid pinions meshed with tetrahedral elements during the evaluation stage.

HyperMesh is a very popular and powerful pre- and post-processor for most FE commercial software such as ANSYS, ABAQUS and LS-DYNA etc. Its meshing ability for curved surfaces using shell elements is very impressive. HyperMesh also has a powerful geometry cleanup ability. It is very convenient to do surface partitions and surface edge gap merging in HyperMesh. In the beginning, a lot of time was spent on HyperMesh and some test models were meshed. Figure 8.2 shows a quarter worm tooth meshed with hexahedral elements in HyperMesh. Figure 8.3 shows the contact elements built in HyperMesh in a partial spiroid gear model. However, HyperMesh was found not suitable for gear contact element model for two reasons: (1) HyperMesh does not have the general surface-to-surface contact elements CONTAC174, TARGET170; (2) HyperMesh model has lower geometrical accuracy, a price to pay for its powerful geometry cleanup ability. For non-contact finite element analysis, the lower geometrical accuracy may not cause any serious effects. But for gear nonlinear contact analysis, it will change the contact positions and contact regions and consequently make the results invalid. After the gear model is imported, some edge gaps in HyperMesh are greater than 0.2 mm which is unacceptable for gear tooth contact analysis.

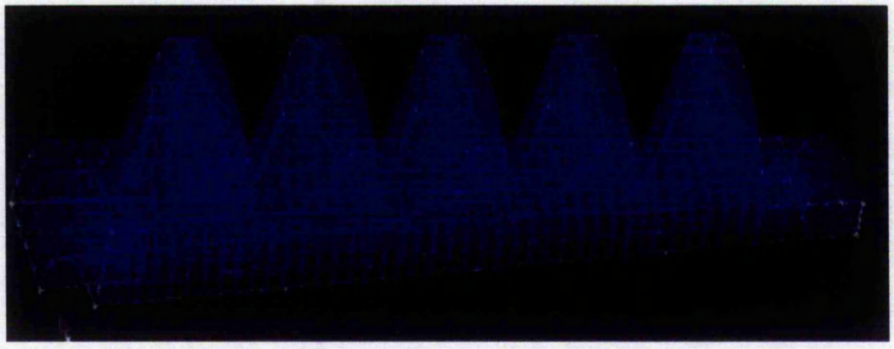


Figure 8.2 Worm gear tooth meshed in HyperMesh

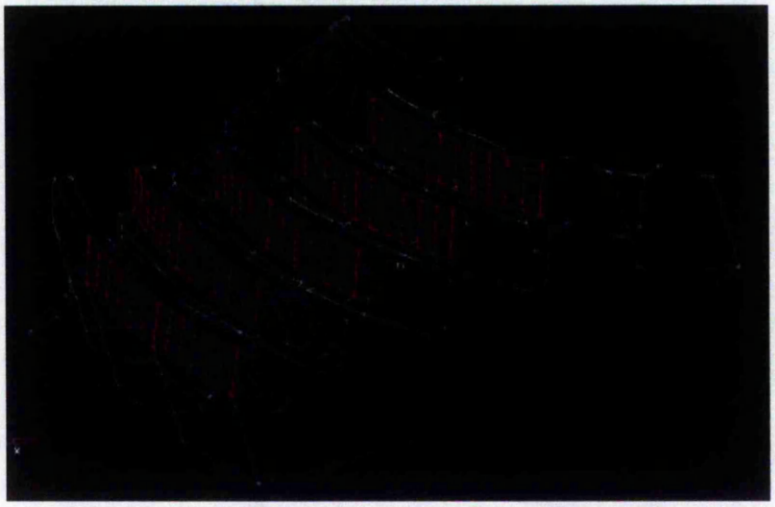


Figure 8.3 Contact shell element mesh in HyperMesh

ANSYS has its own pre-processor. ANSYS preprocessor's surface partition and merging function are not so powerful as HyperMesh's. However, ANSYS's IGES interface is one of the most robust in industry. The geometry imported into ANSYS via an IGES file has higher accuracy than that imported into HyperMesh according to the trial examples conducted in this research.

The following conclusions can be drawn from the evaluation and experience of using the four preprocessors.

- Regarding the ability for solid meshing, the ANSYS preprocessor is generally more efficient than HyperMesh. Its IGES engine is also more robust than HyperMesh's.
- Regarding the 3D model shade display function, ANSYS is better than HyperMesh.
- Regarding the ability to control the mesh density, ANSYS is the best of the four.
- HyperMesh's shell mesh function is better than the ANSYS preprocessor. The density of shell mesh can be controlled by the mouse picking and the change will be displayed simultaneously. The ANSYS preprocessor is still robust for shell meshing.

- Using tetrahedral elements to mesh, Pro/Mesh is the fastest among the four preprocessors but the ANSYS preprocessor has the best element quality. It is very easy to refine the tetrahedral mesh. HyperMesh has to mesh the surface first and then mesh the surface enclosed volume.
- Regarding the ease of use, FEMB is the best of the four
- For a hexahedral element mesh, no preprocessors have refining ability.

8.3 GEOMETRY DATA TRANSFERRING INTERFACE

The geometry data transferring interfaces were reviewed before the geometrical models were exported and imported. According to Adams and Askenazi (1999), the STEP and PARAsolid files are better than IGES and transferring geometrical data using IGES files will usually cause problems. ANSYS has a Pro/E interface, but due to budget restrictions, the Pro/Engineer data transfer interface was not available for this research. The IGES interface was the only available choice.

The ANSYS IGES interface has the options to control the imported accuracy while HyperMesh has not. This makes the ANSYS preprocessor more suitable than HyperMesh. The gear models are imported via the IGES interface and the data transferring process requires good knowledge of IGES. However, importing the gear geometry via the IGES did not run smoothly in the beginning. To import a gear set geometry with as high accuracy as possible, there was a lot of work needed to be done, e.g., understanding how the IGES define the surfaces. A lot of configurations have to be properly set before the geometry can be successfully imported. These difficulties were finally overcome after a substantial amount of time reading manuals, discussions with FEA experts and lots of trial runs.

8.4 GENERATION OF 3D MODEL AND GEOMETRY CLEANUP

8.4.1 Generation of 3D Geometrical Model

In this research, a three dimensional spiroid gear set model has been virtually manufactured in the advanced CAD software package Pro/Engineer as described in

Chapter 6. The 3D model is exported as an IGES file first and then the IGES file is imported to the finite element analysis package ANSYS 5.6 to build the finite element model for loaded tooth contact analysis.

First, an enlarged gear blank was protruded by using the *revolve* function. The section used for revolving is shown in Figure 8.4. In order to obtain a high accuracy smooth tooth surface for subsequent geometry cleanup, the gear blank was created a little larger than the original gear design proportions to ensure that the smoothed surface would be big enough to trim. This is because at both ends of the cutting tooth, the contact lines are not aligned with the end surfaces (see Figure 8.6). So, a slightly larger gear blank is necessary since the contact lines will be used to constitute the smoothed surface. In this case, the inner surface radius was 3 mm smaller and outside radius was 3 mm greater.

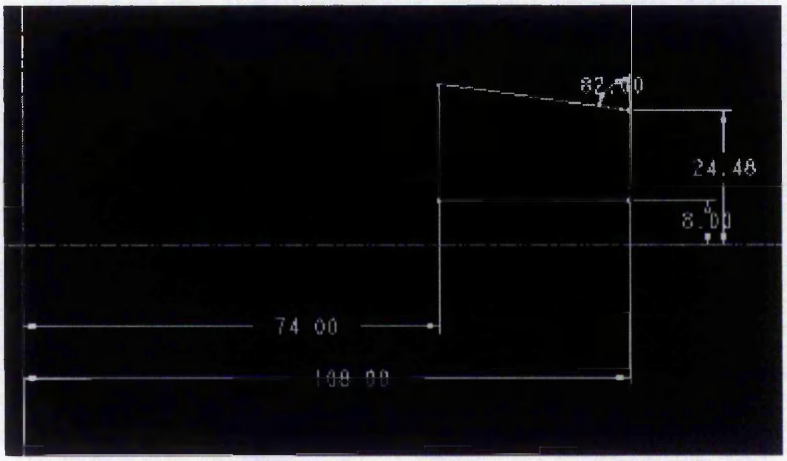


Figure 8.4 Revolve cross section of spiroid gear blank

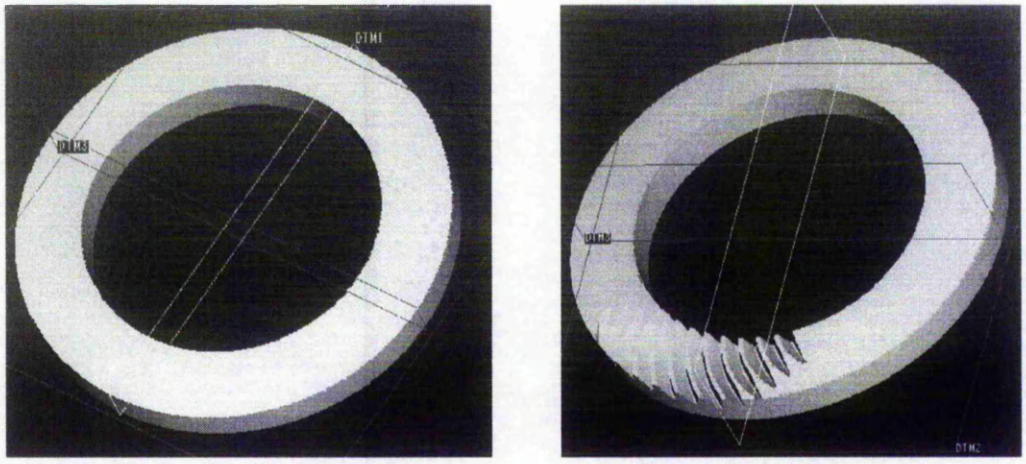
During the geometry cleanup, the gear blank will be reconstructed using the original design proportions. The revolved gear blank is shown in Figure 8.5 (a). To get the smoothed tooth surface, only one gear tooth is needed. So the gear blank is only needs to be cut partially as shown in Figure 8.5 (b).

8.4.2 Gear Geometry Cleanup

Why do the 3D models need geometry cleanup? There are several reasons for this.

First, the VGM model has many small areas in the tooth surfaces due to the nature of hobbing. In FEA, those small areas are unwanted and will cause mesh problems. Those small features should be removed or smoothed. Other small features such as small fillets and chamfers, which are not necessary, have to be removed too.

Second, the CAD file may have been created in a way that the model is visually correct in Pro/Engineer but causes problems for a finite element analysis tool (such as gaps and overlaps between areas).



(a) Blank (b) Partially cut

Figure 8.5 Spiroid gear manufacturing

Third, the CAD program may define entities in a manner that it is not entirely conformant with a particular format. For example, in the present model, the pinion created by the *helical sweep cut* function looked perfect in Pro/Engineer but after the pinion was imported to ANSYS, the cut geometry failed to display and caused an error. The ANSYS preprocessor cannot interpret the *helical sweep cut* geometry. To solve this problem, the pinion model had thus to be redefined using the features that ANSYS can interpret (see Section 8.4.3).

Fourth, duplicate lines and keypoints are possible when transferring a model as an IGES file. This often happens with CAD models due to the tolerances and practices that they were created with. These solid models need to be cleaned up with ANSYS commands that merge duplicated entities together.

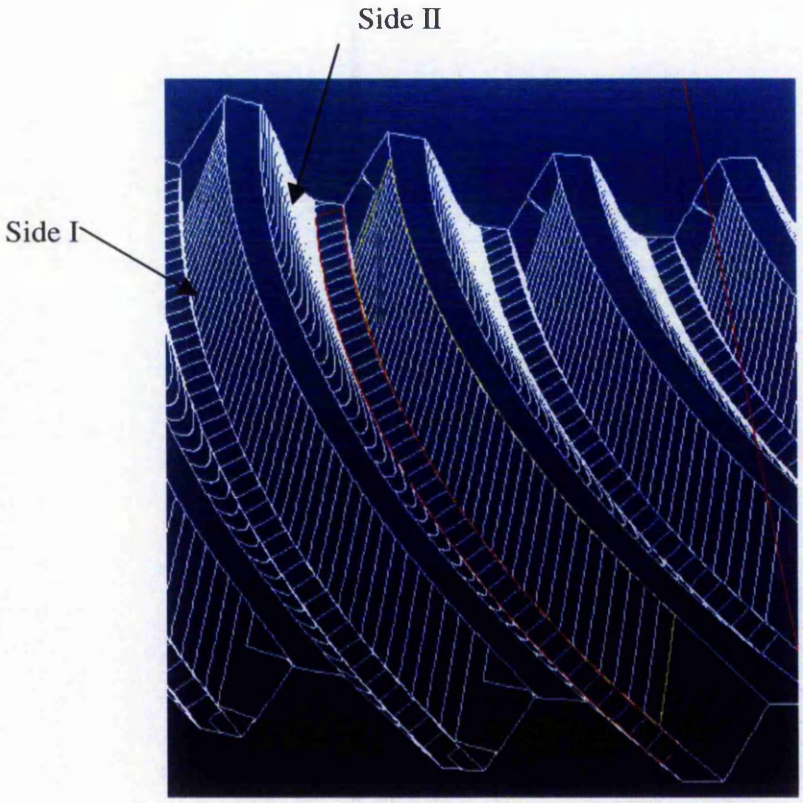


Figure 8.6 Gear smoothed side I surface (yellow colour) and root surface (red colour)

As for most finite element geometrical models, the VGM models need geometry cleanup to make the surfaces smooth. The geometry cleanup is undertaken much easier in Pro/Engineer than in the ANSYS preprocessor. In order to make the meshing of the spiroid gear easier in ANSYS, the spiroid gear needed to be partitioned as desired. This work was also much easier to perform in Pro/Engineer than in the ANSYS pre-processor. The pinion geometry was constructed in Pro/Engineer using a *helical sweep cut*. This feature produces a long helical strip twist surface. When the long helical surface was exported as an IGES file and then imported to ANSYS, the ANSYS preprocessor failed to display such a surface and resulted in a large tolerance

error. So the pinion tooth surface needed to be reconstructed to make the tooth surface shorter. This work was done using the *protrusion* and *pattern* functions.

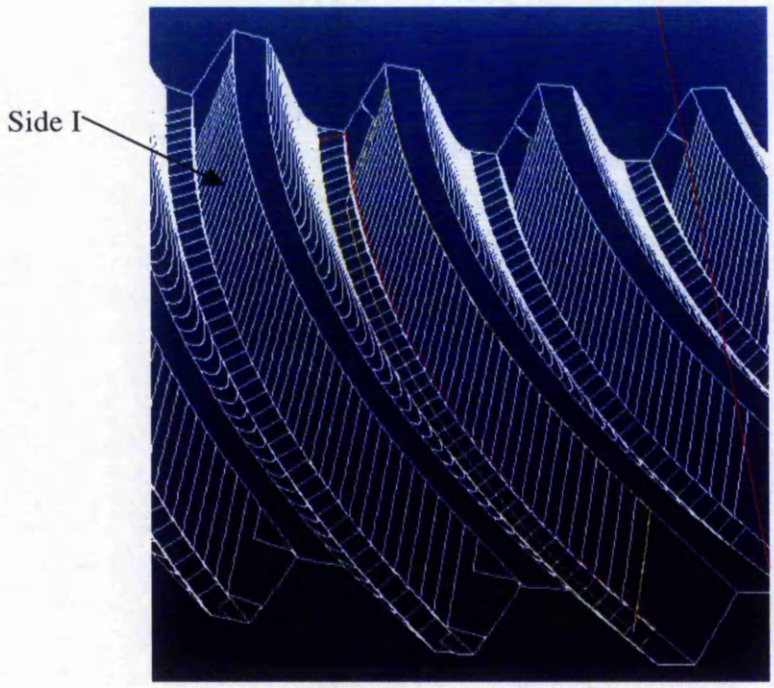


Figure 8.7 Extension of side I surface and root surface

The purpose of the gear geometry cleanup is to eliminate the small areas created in the virtual hobbing process and to smooth the tooth surfaces.

The side I of the gear tooth have more regular contact paths (see Figure 8.6). This side is conveniently smoothed out in Pro/Engineer using the advanced Pro/Surface module. The side I surface smoothed by the contact lines is shown in Figure 8.6. The advanced surface function *Boundaries* was used to construct the side I surface.

The construction procedure is described as follows (using Pro/Engineer 2000i):

Step 1: In the **Feature** main menu, select **Create**;
Step 2: In the **FEAT Class** menu; select the **Surface** option and then click **Done**;
Step 3: In the pop up **SRF OPTS** menu, select **Advanced** and then click **Done**;
Step 4: In the pop up **ADV FEAT OPT** menu, select **Boundaries**, then click **Done**;

Step 5: In the pop up **BNDRS OPT** menu, select **Blended Surf**, then click **Done**;

Step 6: In the pop up **CRV OPTS** menu, click **First Dir**;

Step 7: In **Select Item** submenu, choose **Chain** option. Note: the default option is the **Curve** option. The **Curve** option means that the datum curves will be used to blend the surface. Since the edges of small cut areas are used as constituting curves, the **Chain** option should be chosen. Otherwise the contact lines in the gear tooth shown in Figure 8.6 cannot be picked;

Step 8: In the **Chain** submenu, choose option **One by One**;

Step 9: Then pick the first contact line and click **Done** on the **Select** submenu; Remember that the **Done** should be clicked after one contact line is picked. Otherwise it will be found that all the contact lines will be chosen but nothing will be constructed and an error message will appear. After **Done** is clicked, the first curve in the first direction is added;

Step 10: Repeat Steps 8 to 9 until all the contact lines in tooth side I are selected in a continuous order.

Step 11: Click **Done Curve** in **CRV OPTS** menu;

Step 12: Click **Preview** button on the **SURFACE: Blended** sub-window to preview the surface. If it is all right, then click **OK** button in the same row as the **Preview** button. If not, the procedure must be repeated to correct the errors.

The root surface was constructed in the same manner as the side I surface. The red surface shown in Figure 8.6 is the smoothed root area surface. For the convenience of merging the surfaces, the side I smoothed surface and the root surface are extended a small amount as shown in Figure 8.7. The above method is the fastest method to smooth the surface. However, it is not suitable to smooth the tooth surface side II.

Tooth surface side II is much more complicated and irregular (see Figure 8.8). The contact lines in the outside diameter are similar to Side I. But the contact lines vary a lot when the contact moves inward to the gear centre and the curvature of the contact lines changes dramatically.

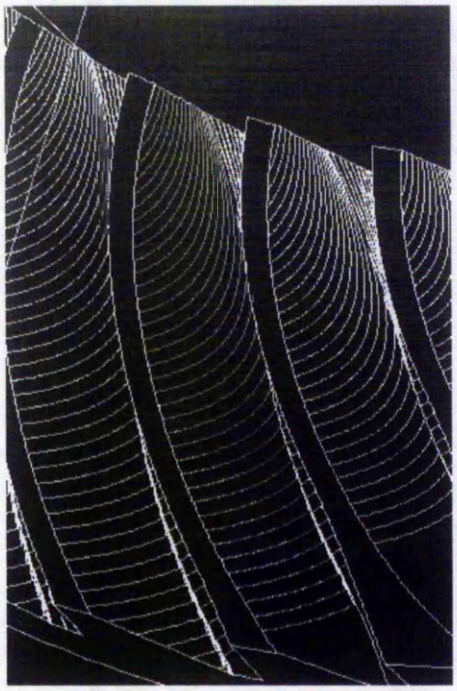


Figure 8.8 Spiroid gear surface contact lines (Side II)

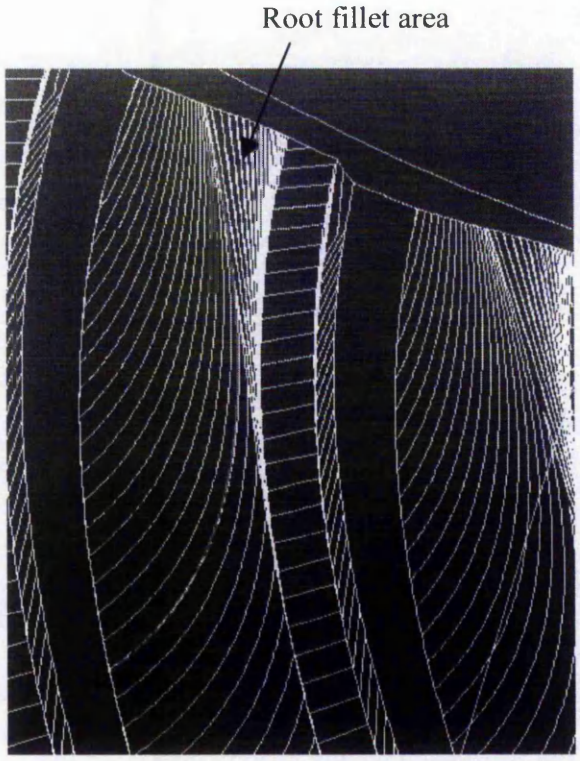


Figure 8.9 Gear tooth surface constituted by the contact lines



Figure 8.10 Zoomed radical changes of curvature in gear surface smooth (Side II)

Using the same methods as for the side I surface to create the smoothed surface, after all the curves were selected (blue lines in Figure 8.8) and the **Done Curve** was clicked, a red curved line appeared near the contact line (see Figure 8.9). This line indicates where the surface curvatures change drastically. Zooming on the red curve showed that it is not a line but the edge of the smooth surface (see Figure 8.10).

Such a radical change in curvature is due to the limits of the surface blend algorithm. The currently available surface algorithm requires the constituting curves' curvature and length must change in a gradually continuous manner. Near the inner surface, the length of contact lines changes abruptly because the contact lines are cut suddenly by the gear blank inner surface.

This is also where the difficulty is for conventional gear modelling methods. If a numerical method is used to calculate the tooth contact lines and points in this area, it is very difficult to obtain a solution since it is so sensitive to the initial guess values that manual intervention is required to obtain the points one by one. This is tedious and requires expertise in meshing theory. Even if the surface points are obtained after

much effort, the problem of how to use these coordinates of points to construct the smooth surfaces still has to be faced. These points have to be constituted into curves and then these curves are used to construct the surfaces. Here the same problem will be met as mentioned above. Another difficulty for conventional numerical method is that it is impossible to obtain the root fillet areas, but the VGM method naturally creates the root fillet areas (see Figure 8.9).

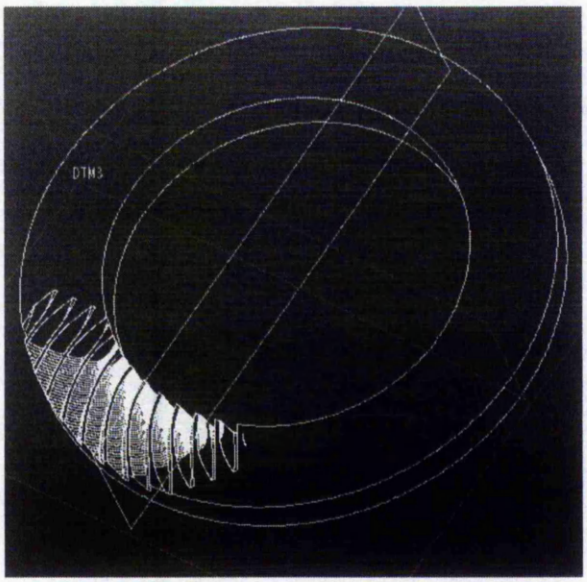


Figure 8.11 A few cut spiroid gear blank

A new method has been developed for smoothing the side II surface. In this new method, a set of datum planes is created first, which is to be used as the sketching plane for cutting the gear's tooth cross-section. Then the tooth cross-section profiles are copied as datum curves. These datum curves have nearly the same length and gradually changed curvatures and therefore they are ideal for the construction of surfaces. Using these datum curves, the complicated gear tooth surface (side II) can be smoothed.

The procedures for the surface smoothing are described as follows. Firstly, one datum plane (DTM4) crossing one tooth surface was created as shown in Figure 8.12. Then the datum plane DTM4 was patterned into a set of datum planes as shown in Figure 8.13.

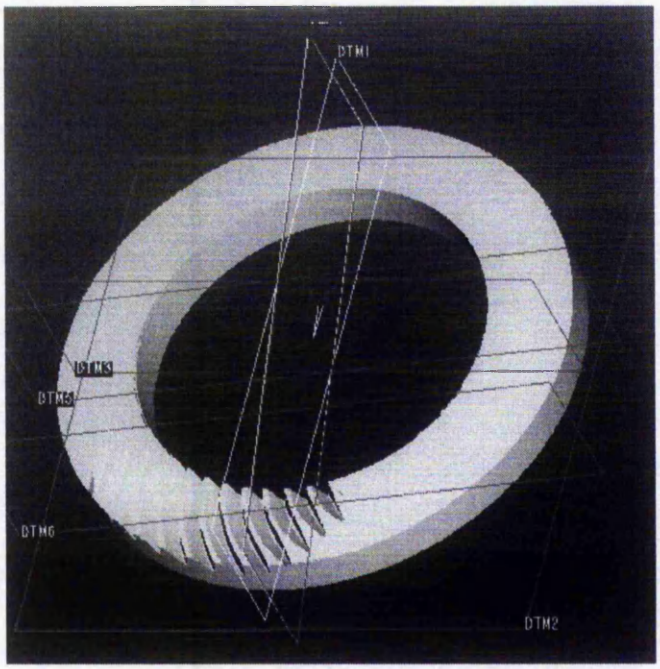


Figure 8.12 Datum plane for gear tooth section cutting

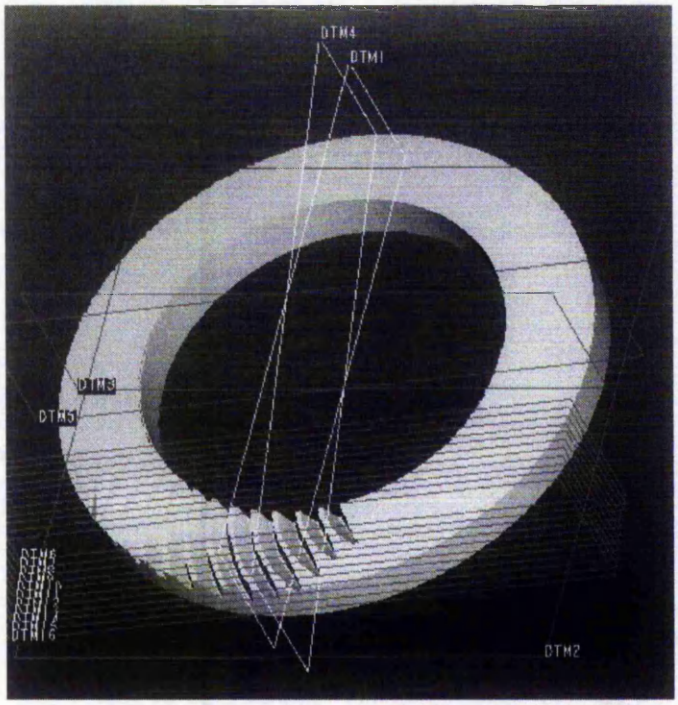


Figure 8.13 Patterned datum planes

After the datum planes have been created, the gear was cut in the first datum plane position by the *extrude* function. In this cut, the datum plane DTM2 (see Figure 8.13) was used as the sketching plane. A line aligning with the datum plane DTM16 was then drawn, which is near the gear outside surfaces. The line's dimension can be arbitrary as long as it is long enough to cut the gear.

Once the first gear tooth section is cut, create the tooth profile datum curve with the *sketch* function and use the datum plane DTM16 as the sketching plane. In Sketcher, zoom in the tooth section to make the tooth profile larger for easier mouse picking (see Figure 8.14).

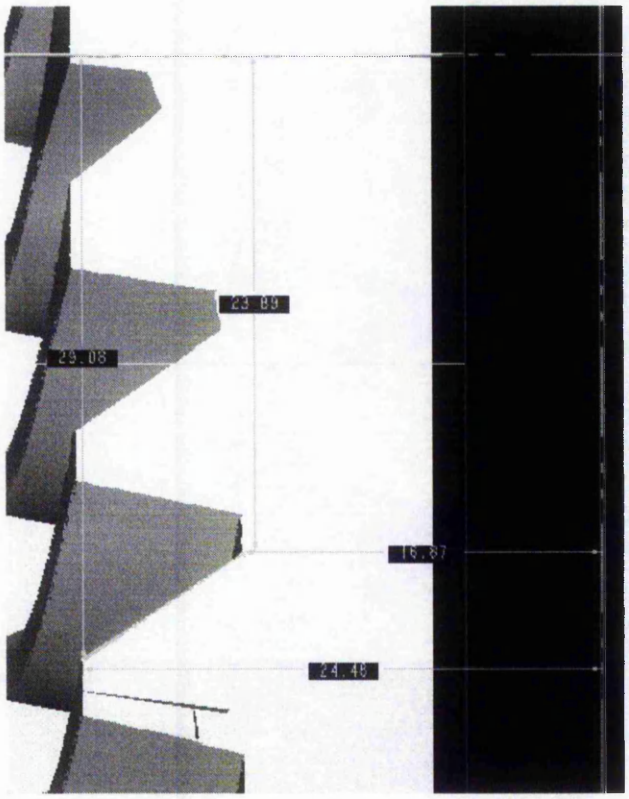


Figure 8.14 Gear tooth profile datum curve sketch

Here, only the gear tooth side II's profile datum curves are needed because surface side I and root area have been constructed. The surface side I and root area can be constructed in the same manner as the side II surface. For a more general case, three

datum curves needed to create separately for the tooth. This is because it will be much easier for ANSYS to mesh with hexahedral elements. If only one datum curve is constructed for the whole tooth section, the smoothed tooth surface will be only one surface. Such a surface is difficult to be divided or partitioned in ANSYS.

In the root fillet area due to the nature of virtual hobbing, there are a lot of very small areas. When the tooth section datum curve is sketched, in the root fillet area there is a set of short zig-zag lines as shown in Figure 8.15. The rule for the tooth profile datum curve sketching is to use vertex points such as the vertex B in Figure 8.15 and not to use vertex points such as A. The reason is that if the hobbing number is increased, then vertex A will be hobbed away to form the root fillets.

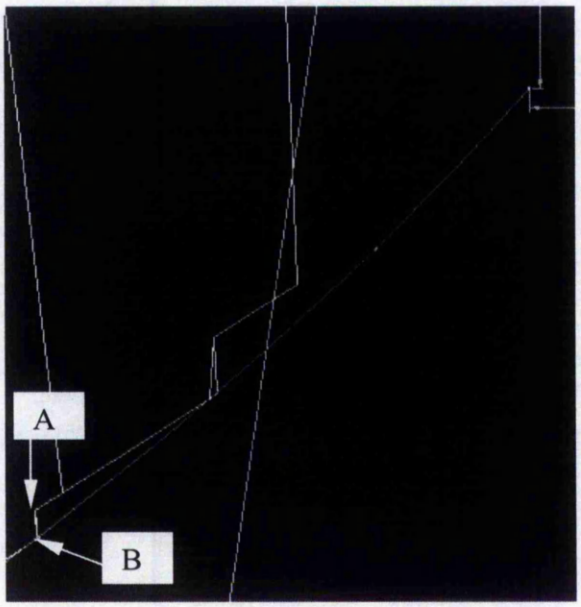


Figure 8.15 Datum curve sketch in root fillet area

After all the three datum curves have been sketched, cut the tooth in the position of the second datum plane and repeat the same procedure to create the second set of datum curves of the tooth profile and so on until all datum curves has been done. Figure 8.16 shows a cut in one of these tooth cross section. Figure 8.17 shows the situation when all these gear section cuts have been completed and the gear tooth datum curves have been constructed. Then these datum curves are used to construct the tooth surface. The procedure for the creation of the surface using datum curves is

nearly the same as the procedure used in the construction of surface side I. In order to use these tooth surfaces to cut out the tooth, the three quilts needed merge into one whole surface. It is easy to be misunderstood here. In the preceding procedure, it was suggested that the whole surface construction scheme should be avoided and now the three separated surfaces have to be merged into one. There is nothing wrong here because the merged whole surface is different from a whole constructed tooth surface. When the gear tooth cut by the merged surface is exported via the IGES, the gear tooth still has three surfaces in the IGES file. However, if the gear tooth cut by the whole surface is exported, there is only one mathematical tooth surface.

In ANSYS, for the purpose of meshing the model with hexahedral elements, it is necessary to divide one tooth surface into three separated surfaces. However, due to the complex surface and the limited CAD function, it is difficult to do this in ANSYS.

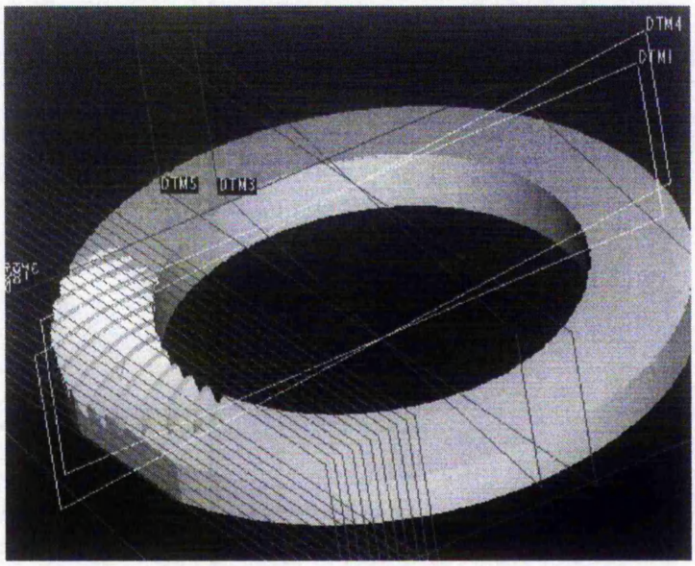


Figure 8.16 Gear tooth cross section cut

The final merged tooth surface is shown in Figure 8.18. It will be used to cut the whole gear. The remaining gear blank solid shown in Figure 8.18 is no use any more and so can be cut off. They cannot be cut off in one cut since Pro/Engineer does not allow all the solids to be cut off. So one half of the gear blank is cut off first and then

the half of the gear blank with original design proportions is constructed. After this, the remaining of gear blank can be cut off (see Figure 8.19).

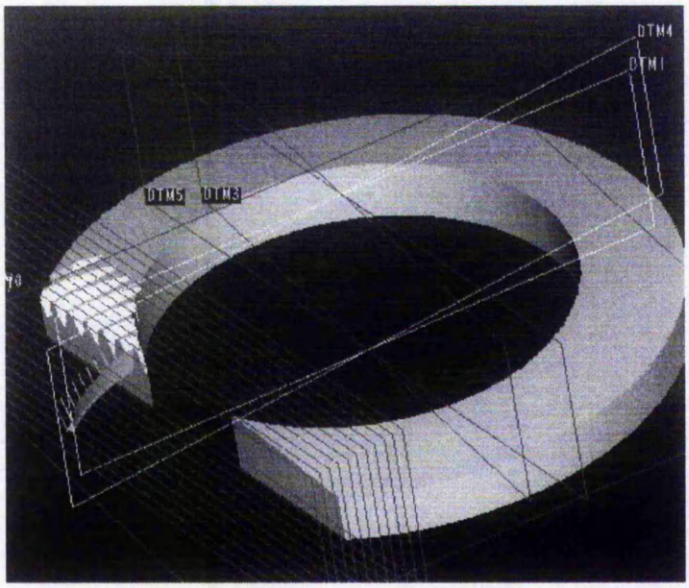


Figure 8.17 Gear tooth section profile and datum curves

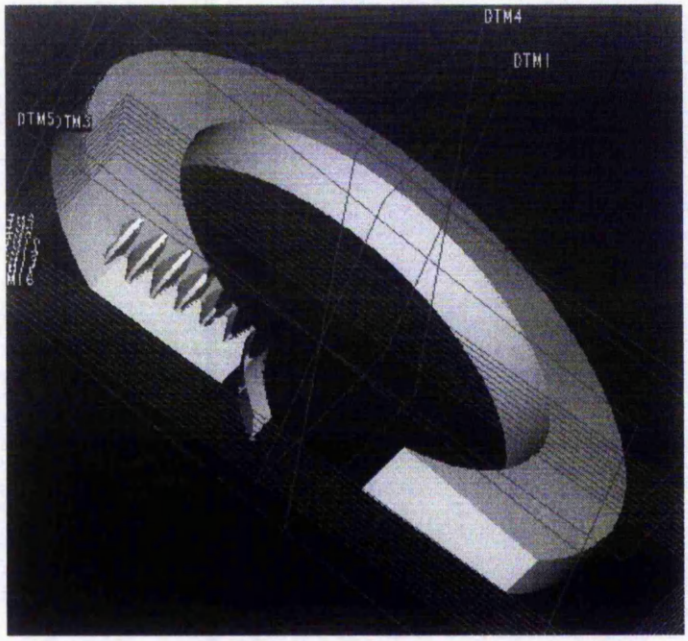


Figure 8.18 Smoothed tooth surfaces

At the beginning, the gear blank was constructed larger than the original design. The reasons for this have been illustrated in the construction of the smoothed surfaces. Now, after the larger gear blank is cut off, the original gear blank is constructed. Figure 8.19 shows that half the gear blank solid with the original design proportion has been constructed. Figure 8.20 shows the merged smoothed tooth surface and the whole gear blank with the original proportions.

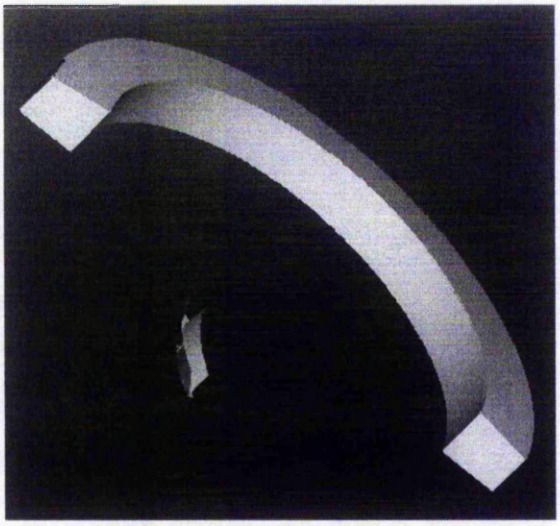


Figure 8.19 Gear partial teeth

The merged surface will be used to cut out the gear teeth. In order to cut out the whole tooth, the merged surface was transformed with a rotational angle (360°/51=7.0588°). Figure 8.21 shows the transformed surface and the original surface. The gear blank was then cut using the merged surface. Figure 8.22 shows the cut tooth in the gear blank.

Now one tooth with three surfaces (two flank surfaces and one top land surface) has been created. For *mapping* the mesh in ANSYS, the gear tooth needed to be further divided below the root surfaces. The curved surface such as area A in Figure 8.23(a) is very difficult to create in ANSYS, and hence has to be created in Pro/Engineer.



Figure 8.20 Gear blank and the smooth tooth surfaces



Figure 8.21 The transformed tooth surfaces

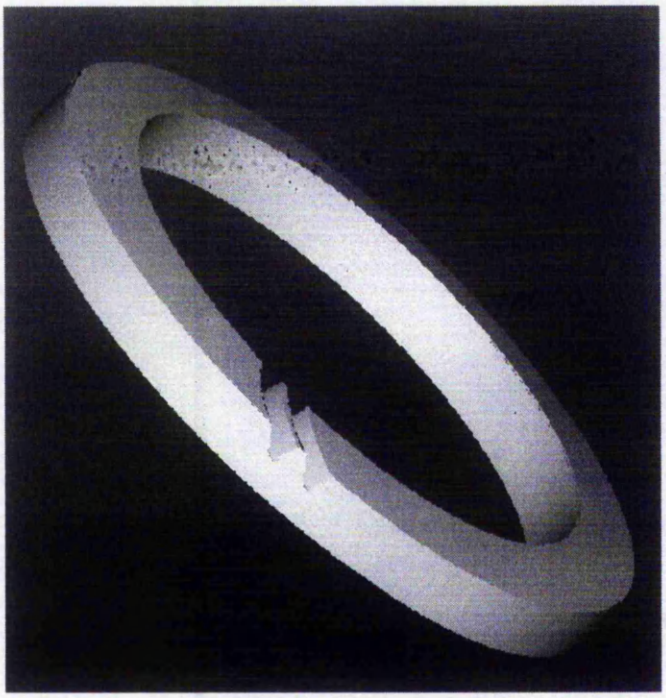
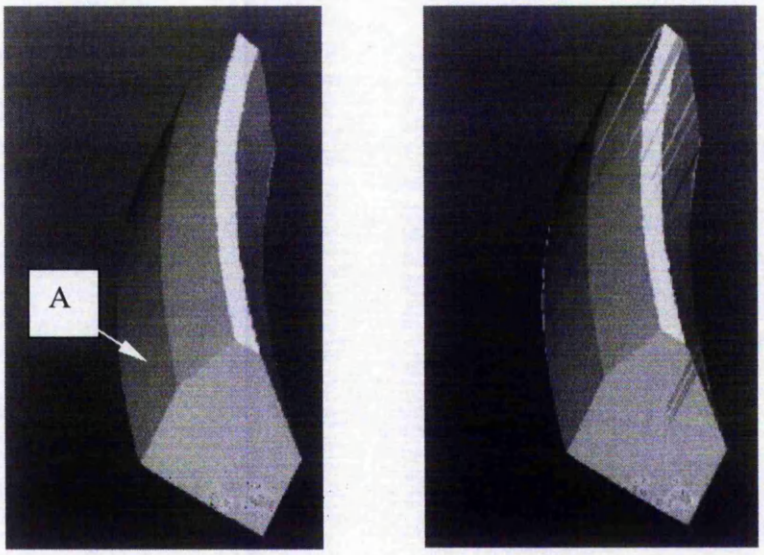


Figure 8.22 Cut the tooth using surfaces

The curved surface can be created by the solid *cut* function. In the sketching plane, select the *use edge* function to create an exact cut along the edge of the tooth flank. Figure 8.23(a) shows the cut tooth with its base.

The gear has 51 teeth so 51 tooth surfaces will be created using the *pattern* function. To achieve this, the original surfaces have to be copied from the solid tooth faces. During the copying process, the *solid* option should be used instead of the *one by one* option. For a surface copied using the *one by one* option, there is no difference shown in Pro/Engineer to a surface copied using the *solid* option. However, after they are imported into ANSYS, there will be a big difference in that the surfaces created by the *one by one* option have a merging problem in ANSYS. The surfaces created by the *solid* option are merged automatically in ANSYS with the IGES file accuracy.

The *pattern* function requires a dimensional leader in the feature. However, there is no such a dimensional leader available in the merged surface. In order to pattern the merged surface, a dimensional leader has to be created. In Pro/Surface module, the advanced surface *tranform* technique can be used to create the rotating angle leader.



(a) One solid tooth (b) The tooth surface copied

Figure 8.23 Cut one tooth and copy the surface

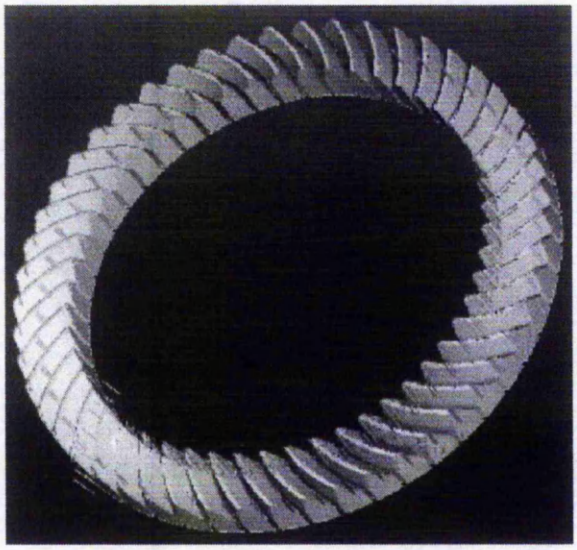


Figure 8.24 Pattern the surfaces

Once the transformed tooth surfaces have been created, the *pattern* function in the **FEAT** menu was used to pattern the whole spiroid gear. Figure 8.24 shows the 51 spiroid gear tooth surfaces. Among them, only one tooth is a solid feature and all the other teeth are just surface features. It does not matter since the IGES interface only

transfers the surfaces, lines or points. The parts below the root areas are not constructed in Figure 8.24 because they will be constructed in ANSYS. With the curved surfaces created in the gear teeth, the root areas and volumes can be easily created using ANSYS geometry tools. If the root areas are created in Pro/Engineer, there will be merging problems after they are imported into ANSYS.

8.4.3 Pinion Geometry Rebuilt

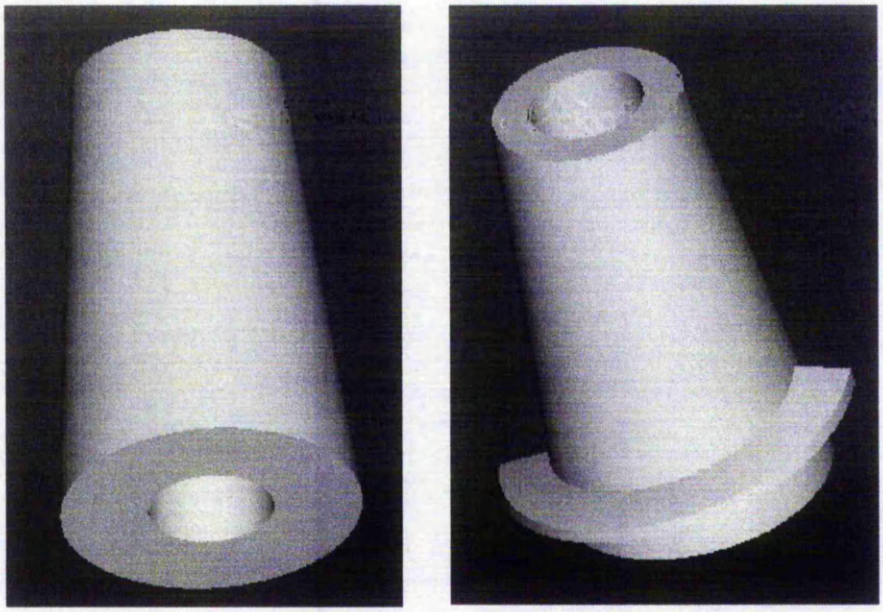
The pinion has two starts and the lead is 18.371 mm. In the beginning, the pinion's geometry was created from a solid cylinder blank by two *helical sweep cuts*. When such a pinion is imported into ANSYS via the IGES, the geometry can be imported successfully if the *default* option is used. Later model trial runs showed that such a model did not meet the required accuracy and the pinion surfaces were not smooth. This issue will be addressed in Section 8.8.1 Importing 3D Models via the IGES Interface.

To solve the above problem, the pinion's surfaces were imported using *Alter no defeature* option. In this option, by using IGES file's accuracy, the geometry can be imported with the desired accuracy. However, the geometry created by a *helical sweep cut* cannot be displayed in ANSYS. The ANSYS IGES engine cannot interpret the *helical sweep cut* geometry properly and the cut geometry cannot be constructed in ANSYS. The pinion geometry has to be rebuilt so that the ANSYS IGES importing engine can interpret it. Instead of constructing the geometry using the *cut* function, the pinion geometry is constructed using the *helical sweep protrusion*.

The pinion created by *helical sweep cut* or *helical sweep protrusion* is identical in Pro/Engineer. But there are differences when they are exported. The protrusion feature can be interpreted successfully when it is imported into ANSYS using *alter no defeature option* while the cut feature failed.

There is no problem to import protrusion features into ANSYS via the IGES. However, the pinion tooth surface in Pro/Engineer is a narrow and long helical spiral surface. It is too narrow and twisting for IGES to transform. It will result in a big tolerance error when it is imported to ANSYS via the IGES. In order to import the

geometry with high accuracy, the pinion was reconstructed again to make the thread less twisted by shortening the thread length. In the mean time, for the sake of reducing the number of nodes, the pinion's solid centre was hollowed by a cylindrical hole where the stress information was not required.



(a) Pinion blank (b) One portion tooth (half lead long)

Figure 8.25 Pinion blank and one portion tooth

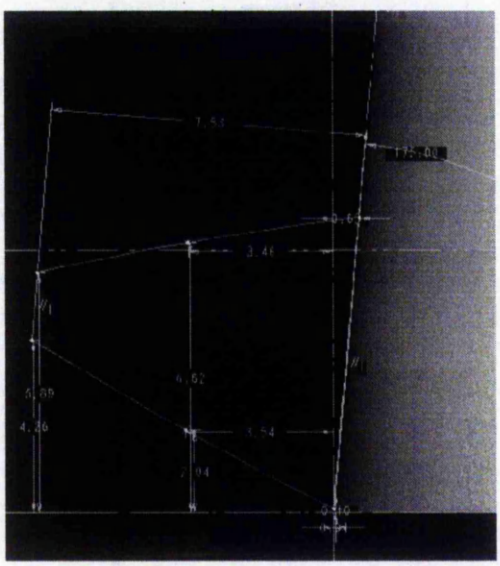


Figure 8.26 Pinion tooth sweep cross section

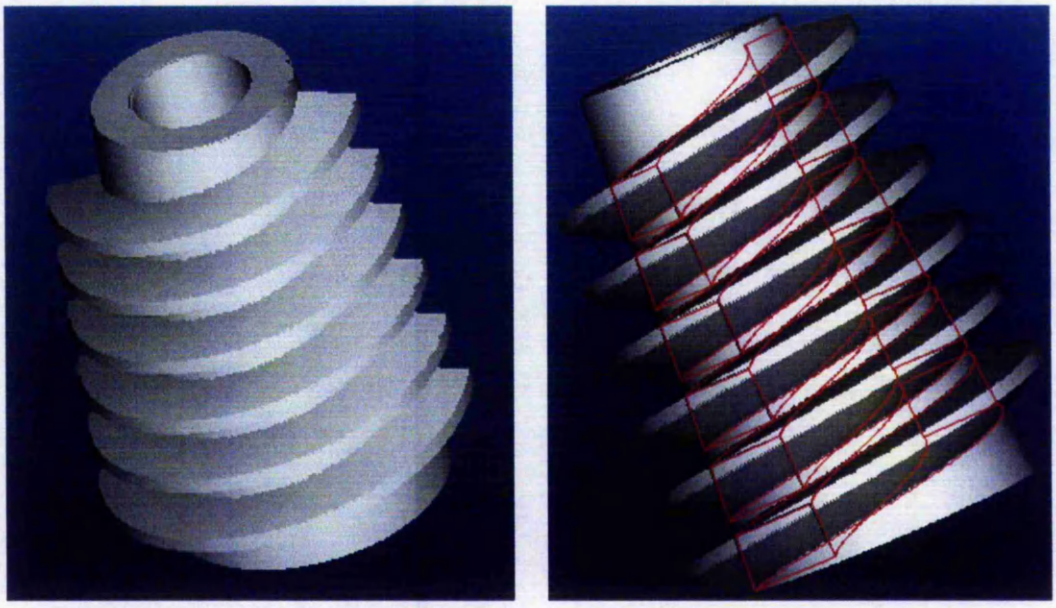
The solution to the long twist surface problem is to make only half a pitch tooth when the feature is constructed with the *helical sweep protrusion* function. Then the *pattern* function is used to pattern a full-length tooth surface.

Figure 8.25 to Figure 8.28 illustrates the whole process of pinion geometry rebuilding. The pinion inner cone tube was created first using the protrusion method with the *revolve* function as shown in Figure 8.25(a). Then the helical sweep thread was created. The thread is not all along the pinion face width but only half the lead length, as shown in Figure 8.25 (b).

The *helical sweep* section is just a reverse to that of helical sweep cut (see Figure 8.26). During the process of sketching, the program will prompt the user to align the section with part of the feature. It is necessary to carefully align the section with the part of the feature here, because the half tooth feature will be used for patterning. An improperly aligned feature will result in an unimaginable feature after it is patterned. The dimension scheme of the section is also worth attention.

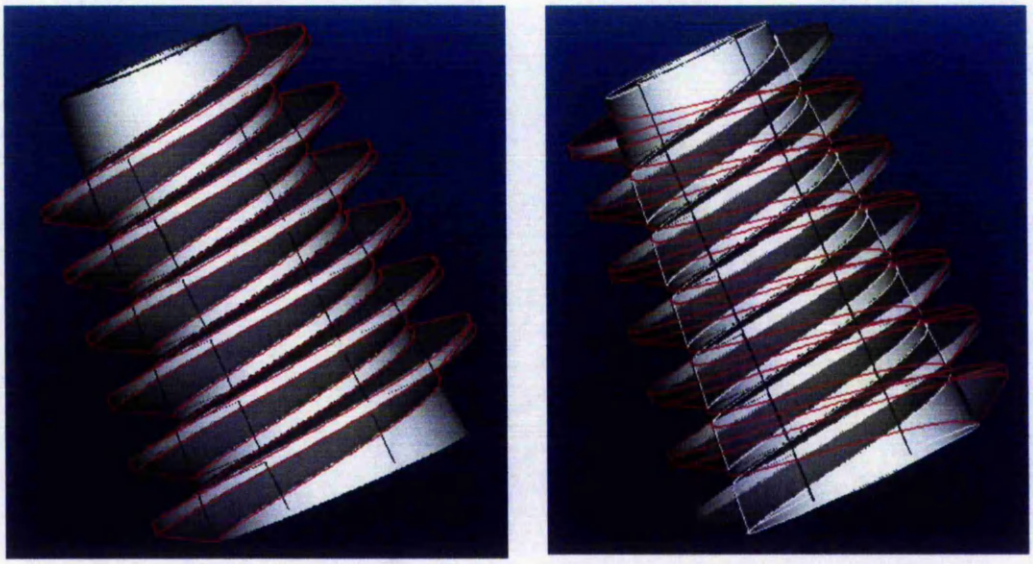
The half pitch tooth thread was then patterned into six half pitch teeth as shown in Figure 8.27 (a). For the mapping mesh in ANSYS, the geometry should be divided into brick-shape blocks. The base of tooth should also have the helical sweep block feature. It is very difficult to construct the *helical sweep* geometry in ANSYS so these surfaces are created in Pro/Engineer using the helical sweep functions. The procedure used here is the same as that for half pitch surfaces. The red surfaces in Figure 8.27 show the created inner helical sweep surface and its patterned surfaces. The other half pitch surfaces are created by transforming the existing tooth surfaces. To do this, the six half pitch solid tooth faces are copied into a surface feature (the highlighted red surfaces) and then the copied surface feature is transformed with a rotational angle of 180° as shown in Figure 8.28 (the red surface is the transformed surface). The inner helical sweep surfaces are transformed in the same manner.

Now the pinion rebuilt geometry has been completed and is ready to be exported for finite element analysis.



(a) (b)

Figure 8.27 (a) Pinion tooth patterned; (b) Inner patterned surface



(a) (b)

Figure 8.28 (a) Tooth surfaces copied; (b) The copied tooth surfaces transformed

8.4.4 Gear Assembly Model Exporting Set Up

After the pinion and gear's geometry cleanup is finished, the gear assembly model (see Figure 8.29) is ready for exporting as an IGES file. In order to transfer the geometry accurately, some important configurations should be set up properly in the config.pro file in Pro/Engineer before the exporting command is executed. From the numerous trials and failure experiences with exporting the gear geometry, the following configurations should be added to the config.pro file of Pro/Engineer.

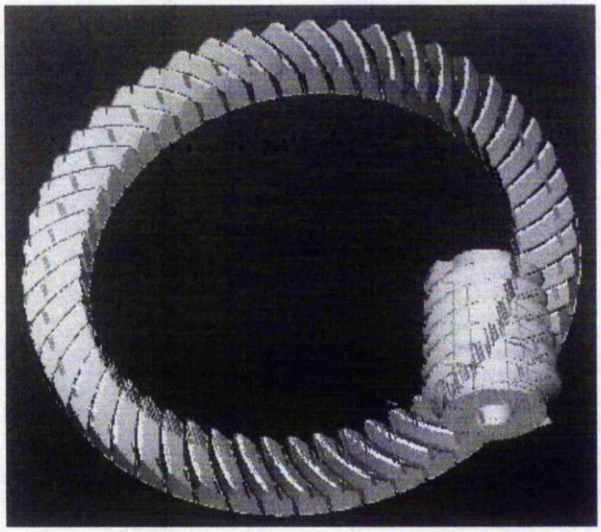


Figure 8.29 Geometry cleanup finished spiroid gear assembly model

intf_out_blanked_entities	no
intef3d_out_surface_deviation	current part accuracy
iges_out_trim_curve_deviation	current accuracy
iges_out_trim_xyz	yes
iges_out_mil_d_28000	no
iges_out_trm_srfs_as_143	no
iges_out_all_srfs_as	128
intf_out_blanked_entities	no
iges_out_spl_crvs_as_126	yes
iges_out_spl_srfs_as_128	yes

In addition to the appropriate set-up configuration file, the model's accuracy must be checked before exporting. The same absolute accuracy (default value is relative accuracy) should be applied to both pinion and gear in the gear assembly.

There are two reasons for not using relative accuracy: (1) Relative accuracy cannot meet the required geometric accuracy for the gear tooth contact analysis. It will also cause problems in later model exporting and importing via the IGES interface. The tolerance errors of relative accuracy in Pro/Engineer are calculated by the product of the relative accuracy and the length of the square that can enclose the part. Tooth dimensions are generally much smaller than the whole gear size. So using relative accuracies will result in big tolerance errors for the tooth surface and fail to satisfy the requirement of accuracy. (2) Relative accuracy will confuse the exporting program. If the relative accuracy is used, both the gear and pinion have their own accuracy. The gear's feature accuracy is not identical to the pinion's even though the same values of relative accuracy are set. This is because the sizes of the gear and pinion are not identical. The exporting program has to decide which accuracy to use from the two different accuracy values.

So if the model is created using the relative accuracy, the model has to be regenerated using the absolute accuracy. Since the contact regions and forces are calculated based on the models, the gear tooth contact analysis requires an extremely high geometrical accuracy, especially in the contact regions. The value of the model absolute accuracy should be set as 0.0001 or smaller.

When the above procedure and set up have been carried out, the IGES exporting command of Pro/Engineer can be executed.

8.5 ASSUMPTIONS OF GEAR TOOTH CONTACT ANALYSIS

In applying the FE method to model the gear tooth contact, two assumptions are made to simplify the simulation process. The assumptions adopted in the present work are given below:

- Sliding friction between the mating gear teeth is neglected, since its effect on deflection is small.
- The gear material is assumed to be homogeneous, isotropic and elastic according to Hooke's law. Thus, the material properties required for the analysis are the Young's modulus of elasticity and Poisson's ratio.

8.6 GENERAL SURFACE-TO-SURFACE CONTACT ALGORITHM

In ANSYS, there are three contact elements available for contact analysis: the node-to-node contact element, the node-to-surface contact element and the general surface-to-surface contact element.

Node-to-node contact elements are typically used to model point-to-point contact applications. To use node-to-node contact elements, the location of contact has to be known beforehand. These types of contact problems usually involve small relative sliding between contacting surfaces. Node-to-node contact elements can also be used to solve a surface-to-surface problem if the nodes of the two surfaces line up, the relative sliding deformation is negligible, and deflections (rotations) of the two surfaces remain small.

Node-to-surface contact element is an advanced technique. The primary difference between the node-to-node and node-to-surface techniques is the ability to account for large deformations and large relative part sliding, without requiring knowledge of the exact location of the contact area beforehand. The node-to-surface technique is suitable for point-to-surface contact problems.

The surface-to-surface contact elements, which were introduced in ANSYS version 5.5 in 2000, are more general contact elements that can be used to simulate surface-to-surface contact problem. The surface-to-surface elements have several advantages over the node-to-surface elements:

- Provide better contact results.



- No restrictions on the shape of the target surface. Surface discontinuities can be physical or due to mesh discretization.
- Require fewer contact elements than the node-to-surface elements, resulting in less disk space and CPU usage and efficient visualisation.

Previous gear finite element work simulated the multi-tooth contact using the gap element technique. The gap analysis technique imposes strict requirements on mesh generation for the entire assembly. To use gap elements, the location of the contact must be calculated beforehand. For loaded gear tooth contact analysis, the loaded tooth contact paths can only be known after the model has been run and cannot be calculated beforehand. The other limits of gap elements are that they usually allow for only relatively small sliding between the gear tooth contact surfaces. So the difficulty in using gap elements is that even if the area of the gear teeth which may come into contact can be accurately guessed, the problems can be solved are limited to those that relative gear teeth sliding is negligible and deflections or rotations of gear remain small. According to the white paper of ANSYS, "Assembly analysis using gap elements can be frustrating. Convergence is typically cumbersome at best, and often insufficient".

To analyse the loaded gear multi-tooth contact problem, the advanced general surface-to-surface contact technique was chosen by the author. This technique can simulate the sliding with closure and separation without requiring knowledge of the exact location of the contact area beforehand. The general surface-to-surface contact elements also eliminate the need for compatible meshes across contacting parts. For gear analysis, the "flexible-to-flexible" type contact elements are used to simulate the tooth contact interfaces. These contact elements use a target surface and a contact surface to form a contact pair. In applying this technique, each target surface node is checked for penetration through the contact surface. If the target surface node does not penetrate, nothing is done. If it does, an interface force is applied between the target surface node and its contact point. The magnitude of this force is proportional to the amount of penetration.

8.6.1 Contact Algorithm

Surface-to-surface contact analysis is a very difficult task. Fully understanding the contact algorithm is important for properly choosing the solver, setting up the right options and judging the solutions. The ANSYS manuals describe some of the contact algorithm but are far from complete. The following is the author's understanding of the contact algorithm that has been learnt during the research process and from discussion with experienced ANSYS stress analysts.

For surface-to-surface contact elements, the augmented Lagrangian method or the penalty method is used for the solution.

The augmented Lagrangian method is an iterative series of penalty updates to find the exact Lagrange multipliers. Compared to the penalty method, the augmented Lagrangian method usually leads to better conditioning and is less sensitive to the magnitude of the contact stiffness coefficient.

Contact elements use a penalty stiffness to help enforce compatibility at the contact interface. Some finite amount of penetration is required mathematically to maintain equilibrium. However, physical contacting bodies do not interpenetrate. In contact analysis, minimum penetration gives best accuracy. Therefore, the penalty stiffness should be very great. However, too large a stiffness will cause convergence difficulties. The model can oscillate with contacting surfaces bouncing off each other. The penalty stiffness is the most important parameter affecting both *accuracy* and *convergence* behaviour. So how to achieve a best solution rests on how to balance the convergence efficiency against the required level of accuracy.

Penetration is controlled by the FTOLN real constant -- a positive number is a scaling factor whereas a negative number is an absolute value for allowable penetration. The finer the gear model mesh is, the lower the penetration. If the resulting penetration is a negligible percentage of the displacements, then the answers (contact pressure, surface stresses, etc.) will probably be very close to the exact results.

When the gear and pinion come into contact with each other, a contact algorithm needs to determine the location of the two bodies relative to each other. In the ANSYS user's manual, there is no explanation about the detecting algorithm. However, the detailed information about how to detect the contacts between two bodies can be found in the LS-DYNA3D user's manual.

Once the contact surface positions are known, in regions where the contact surfaces have penetrated each other, internal forces are applied between these nodes (the magnitudes of which are governed by the specification of contact stiffness) to "push" the surfaces back to reduce the penetration. This process of checking and pushing is iterated several times over until global equilibrium is attained.

The penalty method (pure penalty or augmented Lagrangian method which, essentially, is penalty-method-based) can be explained in a simplified form as follows:

For the nodes in contact, we have

$$\mathbf{F}_c = \mathbf{k}_c \cdot \mathbf{x}_c \tag{8.1}$$

where $\mathbf{F}_c$ is the contact force vector, $\mathbf{k}_c$ is the matrix of contact stiffness, and $\mathbf{x}_c$ is the vector of "penetration" (DOF values). It is assembled into the global equilibrium equations as follows

$$(\mathbf{k}_g + \mathbf{k}_c) \cdot \mathbf{x} = \mathbf{F} \tag{8.2}$$

in which $\mathbf{F}$ is the nodal force vector, $\mathbf{k}_g$ is the global matrix of stiffness, and $\mathbf{x}$ is the vector of nodal displacements.

The impenetrability condition is imposed via a penalty method -- the contact stiffness. The penalty method, in very simplistic terms, just plans a large number into the stiffness matrix which mathematically attempts to zero-out the displacement differences between the surfaces. The bigger the number (based directly on FKN) that

is used on the matrix, the less penetration will occur. The downside of this method is that ideally zero penetration is wanted, so an exceedingly large FKN value would be required. However this causes the global stiffness matrix to become numerically unstable or *ill-conditioned.* Too high a contact stiffness will make convergence difficult. In the present gear contact analysis, when all the options are properly set, the penetrations are around 1.0E-6 and the convergence is good.

There is also a pure Lagrangian method. As another simplified explanation, this time the contact force is represented as a variable by itself in a displacement-based solution. The equations to be solved are (static case):

$$\mathbf{k}\,\mathbf{x} = \mathbf{F} + \mathbf{F}_c \tag{8.3}$$

That means that contact force is solved for explicitly, and the impenetrability condition can easily be satisfied. In the previous example, $\mathbf{F}_c$ is solved by $\mathbf{k}_c\,\mathbf{x}_c$. This time, $\mathbf{F}_c$ is solved for direct penetration.

There are various drawbacks to both methods. The penalty method (including the augmented Lagrangian method) results in finite penetration. However, the good thing is that it can take advantage of iterative solvers like the PCG solver that deal with regular **k** matrices as long as they are not too ill-conditioned. On the other hand, while the pure Lagrangian method results in no penetration, that formulation leads to zero diagonals due to Lagrangian multipliers. Most iterative solvers will choke on zero diagonals. The number of DOF in the equations is increased, too (to account for the Lagrange multipliers) with the pure Lagrange method. The pure Langrage method results in zero penetration so it is not suitable for the PCG solver. The penalty-method is more advantageous in this respect. In the present analysis, the augmented Lagrangian method is used because the PCG solver is chosen for gear tooth contact analysis. The reason that the PCG solver was chosen for this research is addressed in section 8.10.

8.6.2 The Selection of Contact Element and Target Element

In ANSYS, there are 9 types of contact elements available. Among them, the contact element CONTA174 and TARGE170 have been chosen for this research for the gear tooth contact analysis.

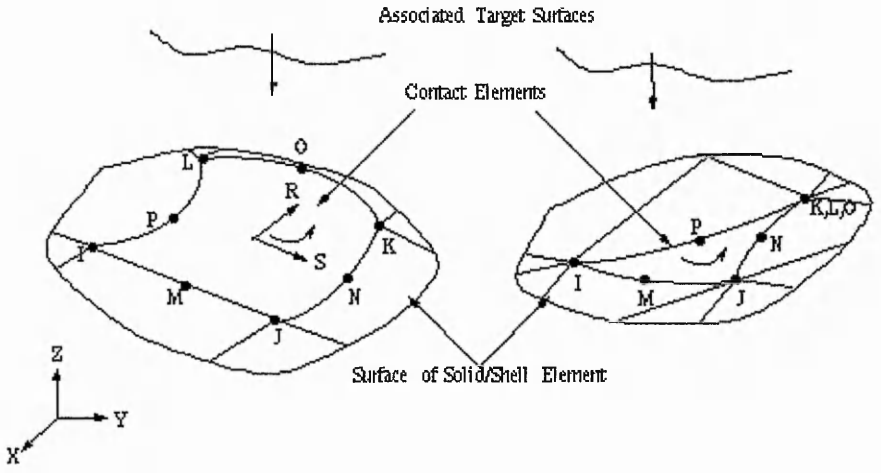


Figure 8.30 CONTA174 3D surface-to-surface contact element (8 nodes)

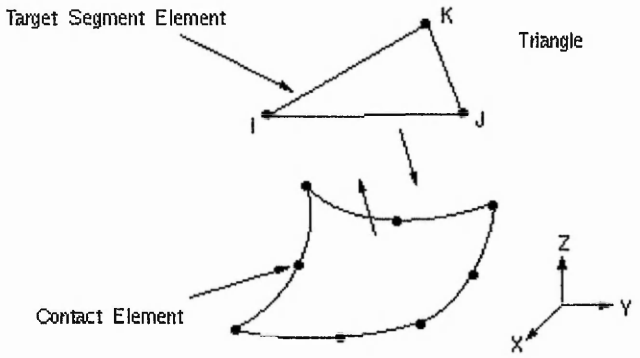


Figure 8.31 TARGE170 target surface element

CONTA174 is a 3D 8-node surface-to-surface contact element (see Figure 8.30). It is used to represent a deformable contact surface that will interact with target surfaces. It is placed on the surfaces of 3D solid elements with mid-nodes. The element has eight nodes and each node has three degrees of freedom: translations in the nodal x, y, and z directions. It has the same geometric characteristics as the solid elements

underneath. Contact occurs when the element surface penetrates one of the target segment elements on a specified target surface.

TARGE170 is a 3D target segment element and is used to represent various 3D "target" surfaces for the associated contact elements. This target surface is paired with its associated contact surface via a shared real constant set. The target elements overlay the solid elements describing the boundary of the deformable target body.

For any target surface definition, the node ordering of the target segment element is critical for proper detection of contact. The nodes must be ordered so that the outward normal to the target surface is defined by the right hand rule. Therefore, for general target segments, the outward normal by the right hand rule is consistent with the external normal.

8.7 THE SELECTION OF SOLID ELEMENTS

8.7.1 Solid Elements

Two element types have been used for the gear model mesh in the present analysis, i.e., SOLID92 and SOLID95.

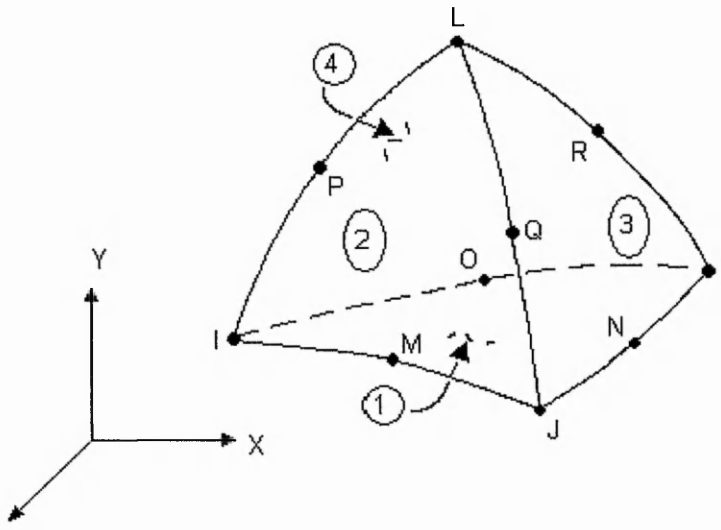


Figure 8.32. SOLID92 3D 10-node tetrahedral structural solid element

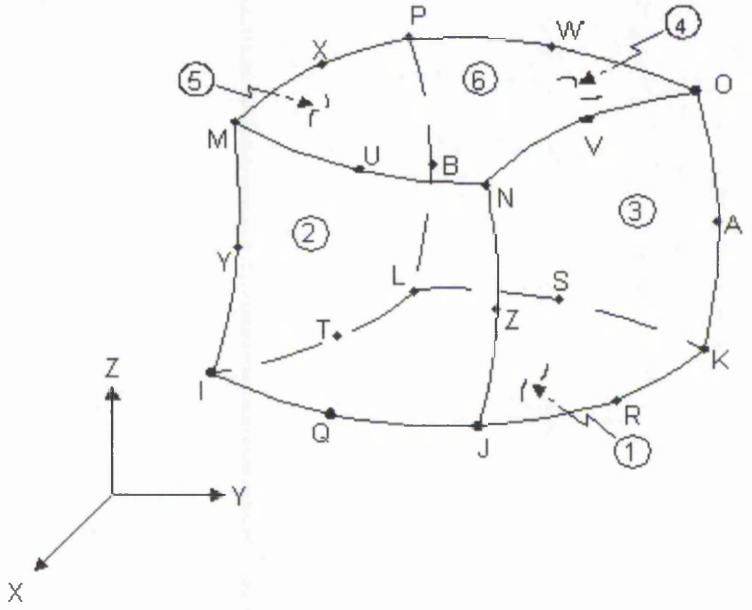


Figure 8.33. SOLID95 3D 20-node structural solid element

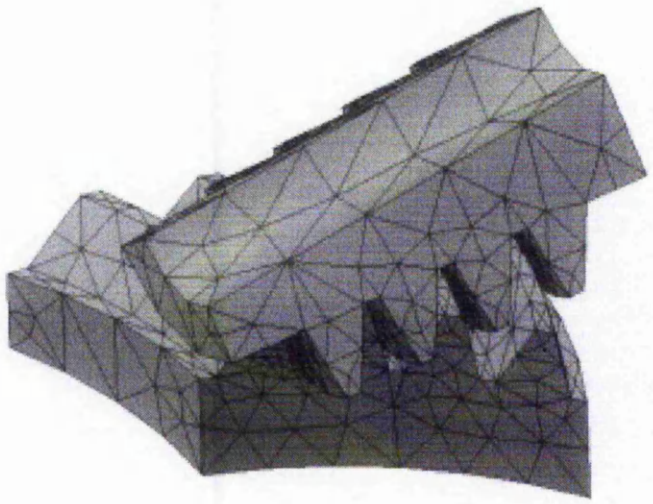


Figure 8.34 Multi-tooth contact model meshed with tetrahedral elements

SOLID92 is a 3D 10-node tetrahedral structural solid element that is usually called "tets" element. It has a quadratic displacement behaviour and is well suited to model irregular meshes. This element has ten nodes and each node has three degrees of freedom: translations in the nodal x, y and z directions as shown in Figure 8.32.



SOLID95 is a higher order version of the 3D 8-node solid element SOLID45. It can tolerate irregular shapes without as much loss of accuracy. SOLID95 elements have compatible displacement shapes and are well suited to model curved boundaries. The element has 20 nodes and each node has three translational DOF in the nodal x, y and z directions (see Figure 8.33).

SOLID92 elements have been used in the present trial model (see Figure 8.34). This element has advantages in the speed of modelling and convenience of model meshing. However, the convergence speed is not as good as SOLID95. Since the model's element size is limited, if "tets" elements are used, the number of nodes within a satisfied mesh density will exceed the nodal limits. However, if the model size is not a problem and also a fast mesh is required, SOLID92 element is not a bad choice. Using mesh refining techniques, the gear assembly model's size also can be decreased (see 8.11.1).

8.7.2 Higher Order Tetrahedral Elements vs. Hexahedral Elements

For loaded tooth contact analysis, in the authors' experience, lower order elements usually have problems with convergence. In contrast, both higher order tetrahedral and hexahedral elements have good accuracy and convergence.

SOLID45 element is a lower order solid element in ANSYS. It is a 3D 8-node brick element with three degrees of freedom at each node. In a simple contact model conducted by the author, the model meshed with SOLID45 elements failed to converge. The same model meshed with higher order element SOLID92 or SOLID95 converged very well so that SOLID45 has been excluded in this research.

High order hexahedral elements can simulate the curved surface so it is suitable for gear tooth surface meshing and will greatly reduce the element number but not compromise the accuracy compared to lower order elements. In order to achieve convergence for the non-linear multi-tooth contact analysis, high order elements are used in this analysis.

The tetrahedral higher order element is the first choice if the computer resources are not a problem. For a large complex finite element model the major portion of the cost is in building the mesh. The biggest advantage in using the tetrahedral element is that it is easy to mesh the complex gear geometry and it usually takes less than one hour. The density of the mesh can also be controlled conveniently. The shortcoming of the tetrahedral mesh is that it usually has many more nodes and elements than a hexahedral element mesh. This shortcoming sometimes can be offset by another advantage of using tetrahedral elements, i.e. it is very convenient to refine the mesh in the interested region such as the contact region. For the areas of little interest, the mesh can be made very coarse. For the possible contact area, the desired fine mesh can be made using the advanced element refine techniques (see Figure 8.50). The present trial model runs showed that it still had good convergence.

A tetrahedral element model is generally not so good in convergence as a hexahedral element model. The problems using tetrahedral elements usually arise in running the models. It takes less time to mesh the model using tetrahedral elements but may take much more time in solving the model.

The higher order hexahedral elements have many advantages over the tetrahedral elements. Though it is difficult to mesh the gear and pinion using hexahedral elements, it will be rewarded when the models are run. The models meshed with hexahedral elements have many fewer nodes and therefore have a significant time reduction compared to models meshed with the tetrahedral elements.

8.8 GENERATION OF THE 3D FINITE ELEMENT MODELS

8.8.1 Importing 3D Models via the IGES Interface

As mentioned in Section 8.4, the 3D spiroid gear models created in Pro/Engineer were imported into ANSYS via the IGES interface. The ANSYS IGES importing capability is among the most robust in the industry. However, for complex geometries like worm gear and spiroid gears, it can seldom import the geometry smoothly without problems. The IGES process basically copies the solid surfaces of the model and translates them into a neutral format that can be accessed by other CAD/CAE

systems. But this process of translation is not always 100% accurate. Aside from the fact that some geometry that might not translate; there is the possibility that the incorrect geometry may be translated into ANSYS.

The gear tooth contact analysis requires precise tooth geometry because the contact forces are governed by the amounts of penetration between the contact surfaces and target surfaces. Therefore, precise tooth geometry is very critical in gear tooth contact analysis.

The importation through IGES files can be tricky. Most of the reasons are linked to the generation process of the part in Pro/Engineer. These problems and the solution techniques have already been addressed in Section 8.4.2. A lot of time has been spent on managing to transfer the precise gear assembly models. During the importing process, many problems were encountered and overcome. The following is some of understanding that has been learnt and noted from the numerous failed and trial importing experience.

ANSYS provides two options for importing IGES files. The first one is the ANSYS recommended option, i.e. the *default* option. This option converts IGES files and defeature the geometry automatically without user intervention. Once the importing is finished, the model's key points are automatically merged. The volumes are created and the model is ready for meshing. The ANSYS manual recommends that the user should always try the *default* option first.

The gear assembly model was first imported using the *default* option in this research. It was very convenient in the beginning. However, the problems became apparent immediately after the model had been imported. The models could not be divided into sub-volumes for hexahedral element meshing. The *default* option utilises a so called enhanced database which is different from the native ANSYS database. After the model is imported, no bottom up feature can be created in ANSYS. Lines and areas cannot be concatenated either, so it is very difficult for the volume to be meshed with hexahedral elements. Thus the tetrahedral elements were used to mesh the model. After the model was run, the results showed that the contact region was not smooth enough. The contact stresses on the contact regions are not smooth but have three 'hot

spots' (see Figure 8.35). This is not the real situation. The reason for this is probably that the curved surfaces imported using the *default* option are internally represented by a grid of flat facets. Nodes that are meshed onto those surfaces (on area interiors) do not follow the original surface as accurately as those at keypoints or those interior to lines, nor as accurately as they would if they had been imported using the *alternate* option. It may result in a numerically non-smoothed area. In gear contact analysis, this could adversely affect the results of analysis.

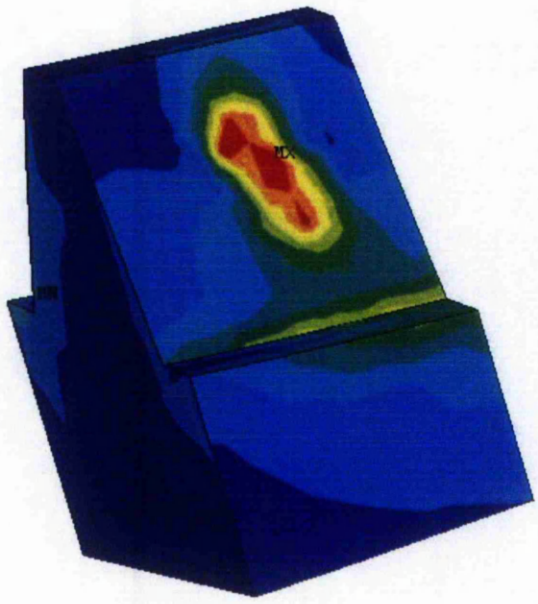


Figure 8.35 Gear tooth contact stress pattern (geometry imported via ANSYS default option)

When the gear geometry was imported, the second option, *alternate* option in ANSYS was used. This option is more difficult to use and that is why ANSYS does not recommend it. The *alternate* option has no capability for automatically creating volumes. For a complex model, this means substantial manual repair. The enhanced set of topological or geometric repair tools is also not available for modelling. However, the *alternate* option also has two critical properties for gear contact analysis. The first one is that the geometry imported using the *alternate* option has higher accuracy than that using the *default* option. This is the major concern in gear tooth contact analysis. Another one is that entities may be operated on as if they are native ANSYS entities after the translation.

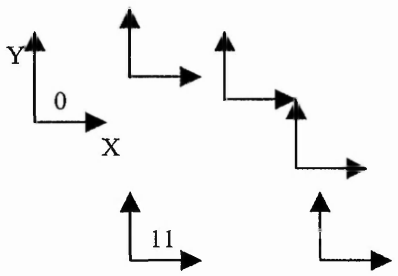
In the importing process of a gear model, the IGES file tolerance should be used. This is very important because the default tolerance is not adequate and must be replaced by the IGES file tolerance. If the default tolerance value is used, it wastes a lot of time to mesh and to run the model, only to finally find the results are inaccurate.

8.8.2 Coordinate Systems

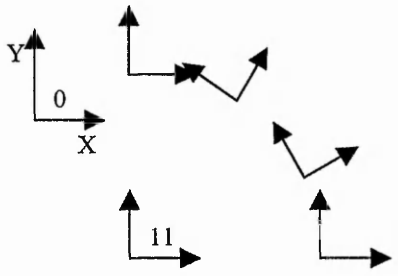
Four types of coordinate system have been used in the gear tooth contact FE analysis. They are global, local, nodal and result coordinate systems.

The global Cartesian coordinate system placed at the centre of gear is used to import the 3D model geometry and locate geometry items (nodes, keypoints, etc.) in space. In addition to the global Cartesian coordinate system, the global cylindrical coordinate system is also used for the convenience since the worm and gear are cylindrical.

Several local cylindrical coordinate systems are used in each gear tooth contact model to locate geometric items and to assist in geometry operations such as copy volumes and meshes.



(a) Default orientation--parallel to global Cartesian system (C.S.0)



(b) Rotated orientation--parallel to local cylindrical system (C.S.11)

Figure 8.36 Nodal coordinate systems

Two nodal cylindrical coordinate systems are used in the analysis to define the degree of freedom directions at each node and the orientation of nodal forces and nodal result data (see Figure 8.36). One nodal cylindrical coordinate system is located at the centre of the gear, which is used to orient the degree of freedom directions of the nodes on the inner ring surface of gear. The other nodal cylindrical coordinate system is located at the centre of the big end surface of the pinion. The desired node sets are rotated into the nodal cylinder coordinate system so that the forces and displacements can be applied in tangential or radial directions to simulate the gear rotation.

The global cylindrical and two nodal coordinate systems were used as result coordinate systems for processing the result data in the ANSYS general postprocessor.

8.8.3 Generation of Pinion Mesh

After the gear assembly model was imported through the *alternate* option, the pinion's surfaces were grouped into a "pinion" component and the gear's surfaces into a "gear" component. It is more convenient to select the geometry by component for the later geometrical processing since the gear assembly model is very complex.

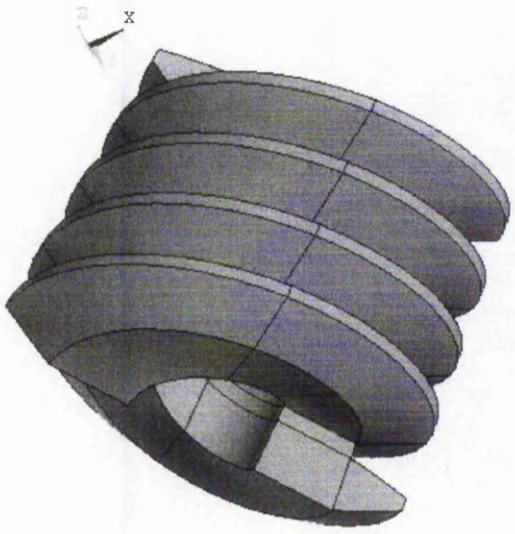


Figure 8.37 Pinion separated surfaces and volumes

Since the pinion will be meshed with hexahedral elements, the pinion's surfaces have to be properly processed to brick-shape blocks. The work plane was used to divide the pinion's threads. For the sake of convenience and clarity, the gear surfaces were unselected and only the pinion geometry was left for processing. The work plane was offset to the pinion's big end plane centre and then was rotated to the desired position. After the *divide* command was issued and all the surfaces of pinion were selected, the command can be executed. The pinion's surface was then divided as shown in Figure 8.37.

There is no area in the place where the work plane cuts. It is necessary for these areas to be created in ANSYS. The work is not difficult since the key points already exist. The necessary straight lines are created using the existing keypoints. The desired areas are thus created one by one by selecting the lines that enclose the area using the *arbitrary* option.

After all the desired areas have been created, the volumes were produced using the *arbitrary* option in ANSYS preprocessor. Each volume contained six areas. The volumes were created one by one by selecting the areas in a continuous order.

After all the volumes were created, the pinion was ready for *map* meshing with hexahedral elements. The number of divisions to each line was assigned. The number of line divisions depends on the model size and the capacity. In this research, the model size is limited to 32, 000 nodes. So the mesh is relatively coarse. Trial runs showed that the higher order SOLID95 elements had a very good performance in simulating the gear tooth with a relatively coarse mesh.

The pinion mesh was created by selecting the volumes in a continuous order. Figure 8.38 illustrates the process of pinion mapped meshing. The volume of the thread was meshed first, then the tooth base was meshed (Figure 8.38 (a) and (b)) and after this, the contiguous thread volumes were meshed (Figure 8.38 (c)). Then the other thread volumes began to be meshed since the pinion had two starts (see Figure 8.38 (d)). The mesh process was repeated until all the pinion volumes have been meshed (Figure 8.38 (h)).

8.8.4 Generation of Gear Mesh

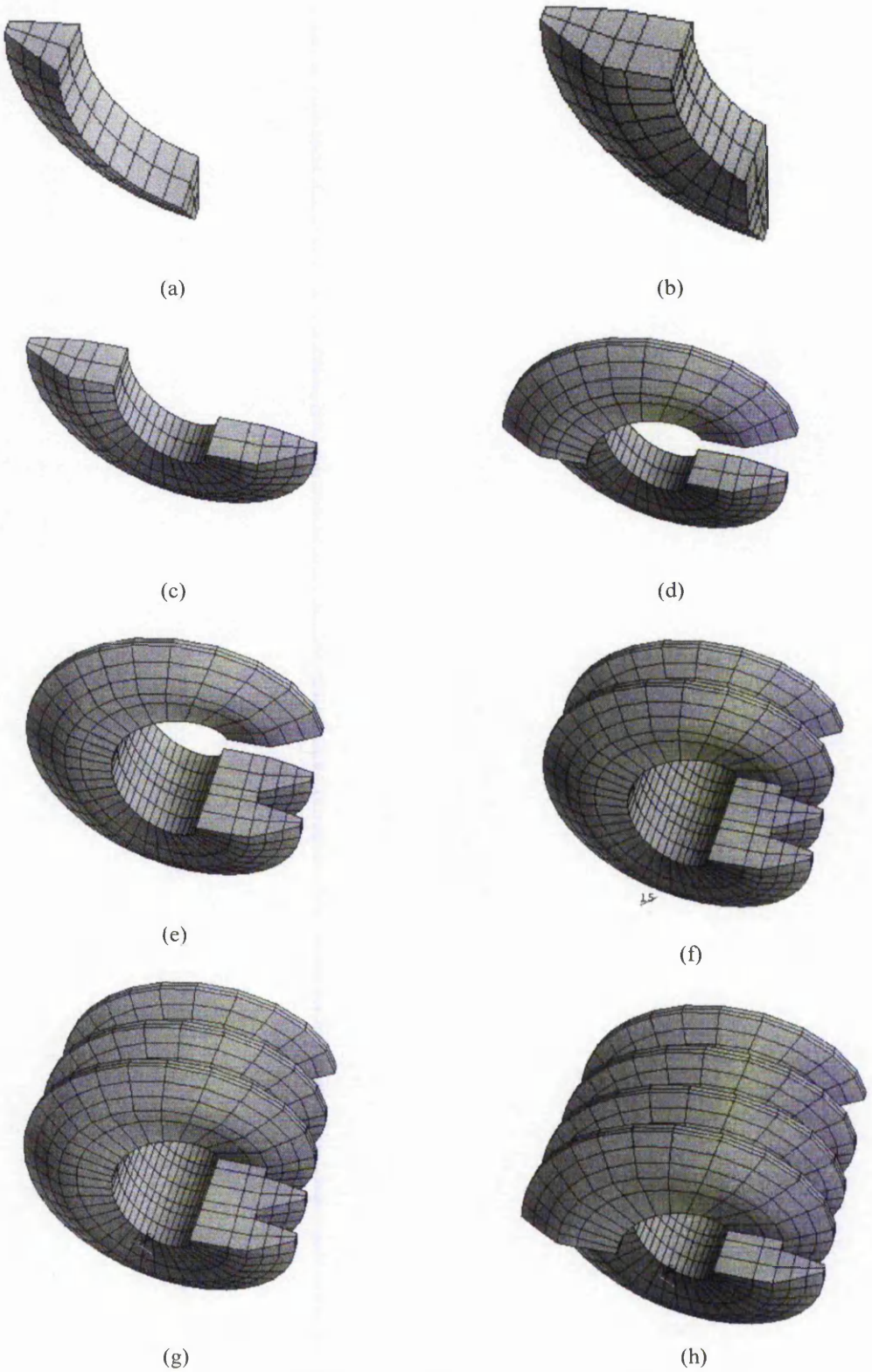
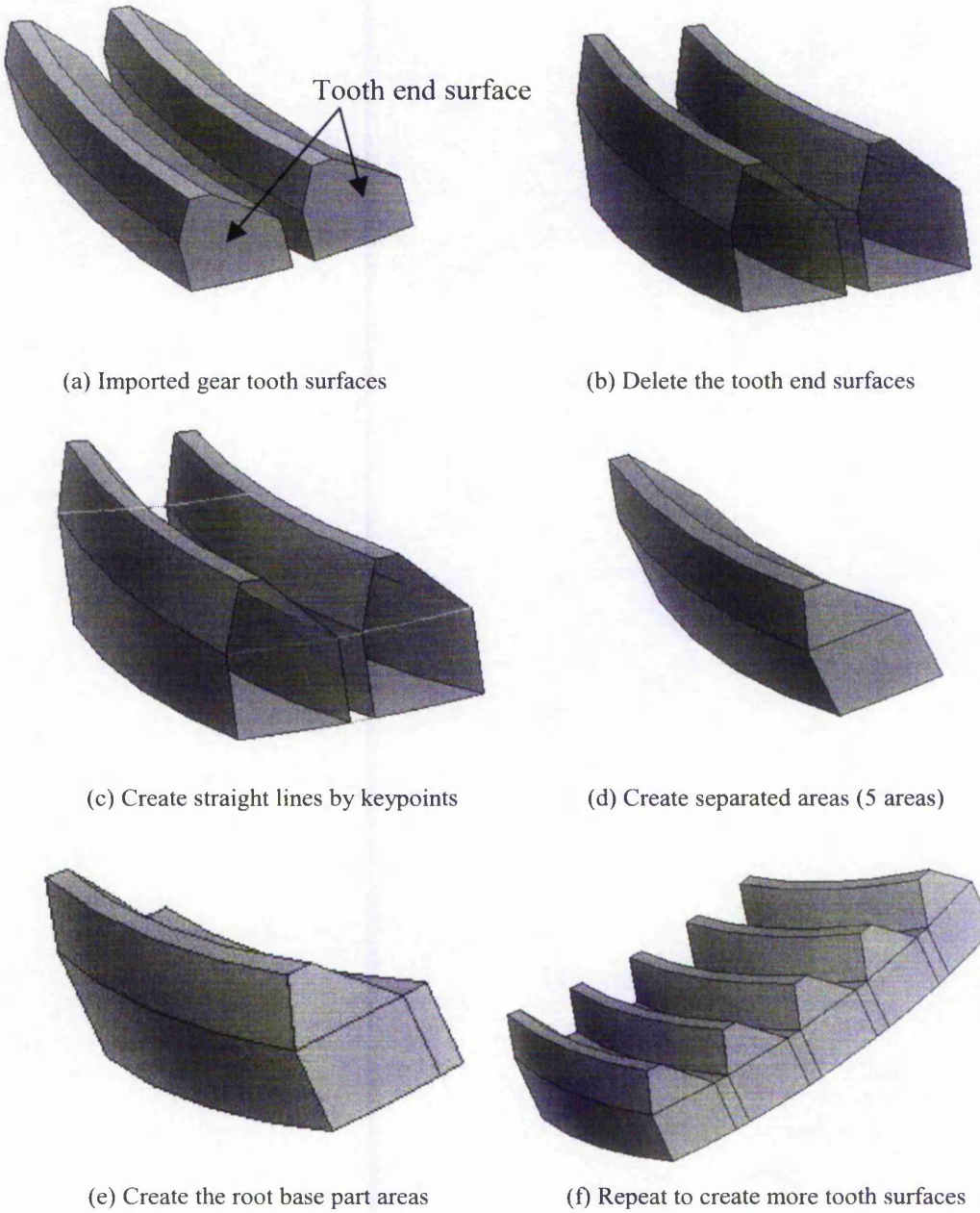


Figure 8.38 Diagram of spiroid pinion meshing

When the gear geometry was imported into ANSYS, the tooth end surfaces of the gear are hexagonal surfaces. Figure 8.39(a) shows the surfaces of two original imported gear teeth. The tooth end surface of gear needs to further divide to four edge surfaces for the purpose of *mapped meshing*. It is difficult to divide this surface using the ANSYS *divide* function because the surface is curved. An easier way is to delete this surface and then to create the two new flat surfaces. Since this surface has little influence on the final calculated results, it was deleted as shown in Figure 8.39(b).



(a) Imported gear tooth surfaces

(b) Delete the tooth end surfaces

(c) Create straight lines by keypoints

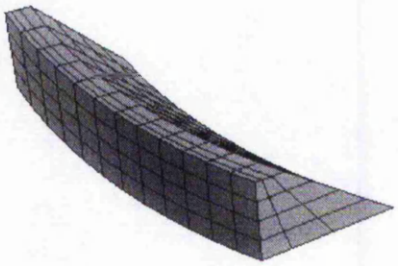
(d) Create separated areas (5 areas)

(e) Create the root base part areas

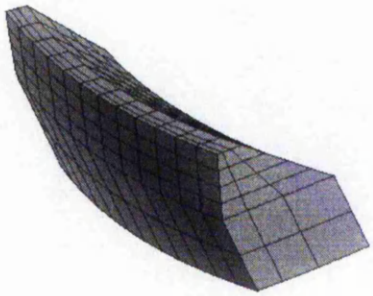
(f) Repeat to create more tooth surfaces

Figure 8.39 The procedure of the creation of gear tooth areas for 3D mapped meshing

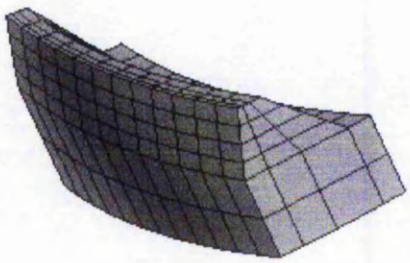
After the end surfaces were deleted, straight lines were created using the existing keypoints as shown in Figure 8.39 (c). For one gear tooth and its base part, five areas need to be created: four areas on both ends and one area that separates tooth from its base.



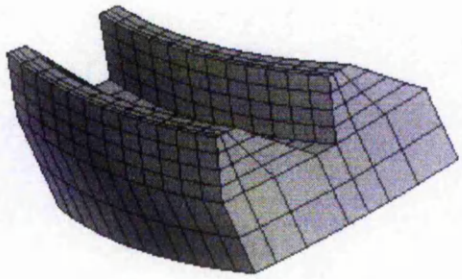
(a) Tooth map meshed



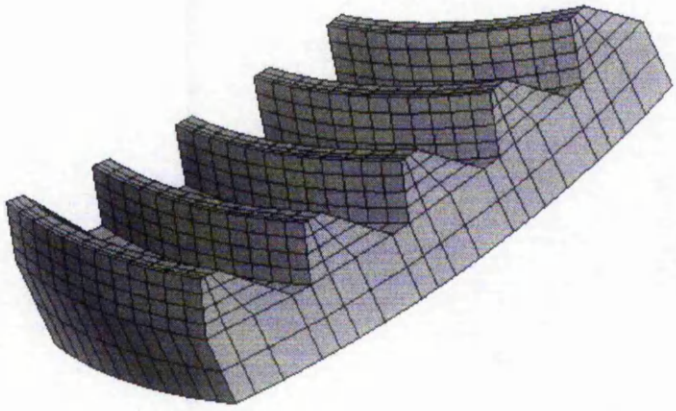
(b) Tooth base meshed



(c) Root base meshed



(d) One more tooth meshed



(e) Five tooth meshed

Figure 8.40 Diagram of gear tooth mesh

After the surfaces were created, the gear tooth volumes could be created from the areas. For one single tooth there are three volumes: the top gear thread, the tooth base part, the root base part. The volumes were created one by one by selecting the six areas that enclosed the volumes.

Four areas have to be created for each root base part as shown in Figure 8.39 (e). Repeating the above process will create all the gear tooth surfaces for mapped meshing. Figure 8.39 (f) shows five gear tooth surfaces have been processed.

Once the gear's volumes were created, the next step was to mesh them with the hexahedral elements. Each line's division was assigned by interactive mouse picking on the screen. The gear model could be rotated if necessary for easier picking by mouse.

After the lines' division was assigned, the meshing process is quite straightforward. Figure 8.40 illustrates the gear tooth mapped meshing process. The gear thread was selected first, then the tooth base part and then the root base part. This process was repeated until all the gear teeth were meshed. In this research, the meshes for five teeth have been created in the above manner. The remaining meshes were created by mesh copying and moving for the sake of convenience. Figure 8.41 shows a full spiroid gear meshed with the hexahedral elements.

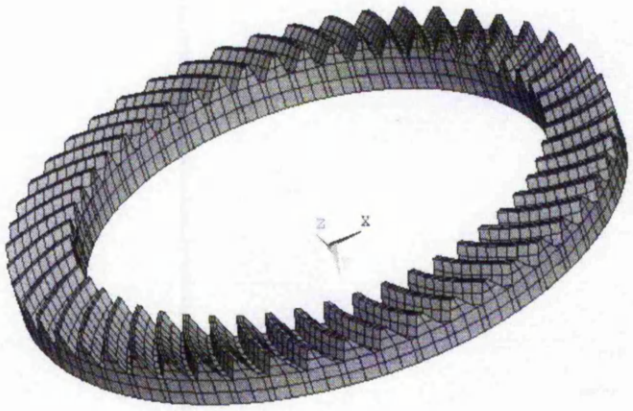


Figure 8.41 Whole spiroid gear mesh

Three types of spiroid gear models have been created in the present analysis. The first type is a partial model. The second type is a full spiroid gear model. The third type is a simplified full spiroid gear model.

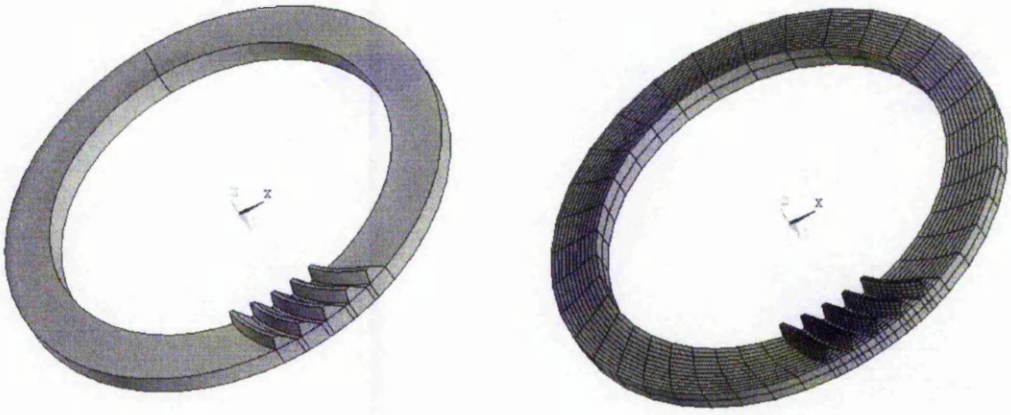
The partial model has four teeth for both pinion and gear. This is the first type of gear model used in this study to analyse the spiroid gear contact stresses. There are two reasons for using the partial models: (1) from the literature review, it was found that partial gear models were used in existing research; (2) it was initially thought that the gear stresses are mainly on the tooth and it is valid to apply displacement constraints sufficiently away from the region of interest (e.g. root of the tooth is OK). However, the trial runs showed that such a partial model is not accurate enough for gear contact analysis. The main reason is concerned with the boundary constraints. The gear tooth contact analysis is very sensitive to the cut boundaries. Simplified constraint schemes cannot simulate the real situation and consequently make the results invalid or with large errors. The second reason is only true if performing a single non-contact tooth stress analysis. This is not the case for the loaded gear contact analysis. Figure 8.34 is a partial model meshed with tetrahedral elements. Figure 8.51 is a partial model meshed with hexahedral elements.



Figure 8.42 Full hexahedral element mesh spiroid gear FE model

The full models have all the gear and pinion teeth. Figure 8.42 shows the full spiroid gear FE model meshed with hexahedral elements. Due to the limits of the number of nodes in the ANSYS university version, the full model has a relatively coarse mesh.

The third type of spiroid gear model is a simplified full gear model. It was created to overcome the model size limit. In order to reduce the model size, those gear teeth not in contact are removed. Such a simplified model has two advantages: (1) fewer nodes and elements, and (2) no boundary constraint problem.



(a) Geometrical model (b) Meshed with SOLID95 element

Figure 8.43 A full simplified spiroid gear model

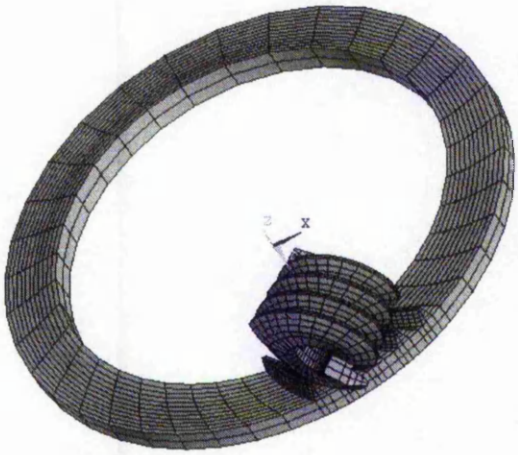


Figure 8.44 A simplified spiroid gear finite element model

For the simplified full model, it is necessary to create the gear tooth base. The creating procedure for this was: (1) create the four curves using the keypoints in the gear tooth base; (2) create the areas using the lines; (3) create the volumes using the areas; (4) mesh the gear tooth base.

The gear tooth base was created in two volumes so the meshing could be controlled in such a manner that there was a denser mesh near the gear tooth and a coarser one at the other end, where the stress is of little interest (see Figure 8.43 (b)). Figure 8.44 shows the simplified full spiroid gear model meshed with SOLID95 elements.

8.8.5 Generation of Contact and Target Elements

Gear tooth contact analysis is a flexible-to-flexible type analysis. The type of contact element selected for the analysis is CONTA174. The type of target element is TARGE170. The reason for choosing these two elements was addressed in Section 8.6.2.

The contact and target elements can be created by commands or by using the contact wizards. In the present analysis, the contact wizard was used to create the contact pairs. Figure 8.45 shows the four contact elements created for the contact analysis.

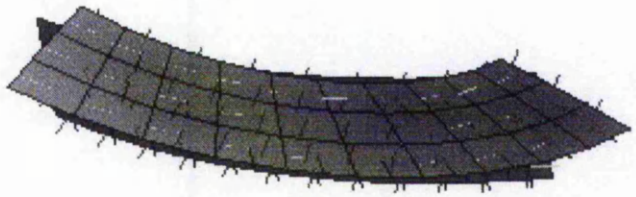
In the tooth contact analysis, the surfaces of the pinion were selected as the target surfaces and the surfaces of gear were selected as the contact surfaces. Since both the gear and pinion surfaces have relatively coarse meshes, due to the limit on the number of nodes in the ANSYS university high option version used in this research, the symmetric contact scheme was applied for the FE models. Each surface is designated to be both a target and a contact surface and two sets of contact pairs between the contacting surfaces have been generated.

The most difficult part in the generation of contact and target element pairs is how to set up the real constants for the contact pairs. ANSYS uses a set of 11 real constants and several element key options to control surface-to-surface contact behaviours. Of the 11 real constants, two (R1 and R2) are used to define the geometry of the target

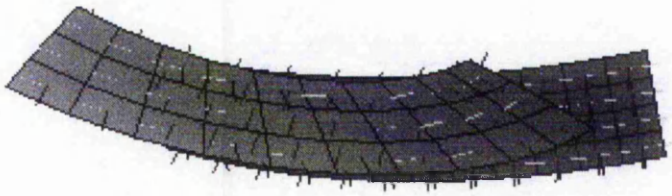
surface elements. The remaining nine are used by the contact surface elements. The 11 real constants are described as follows:



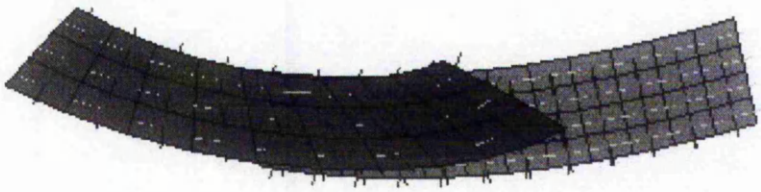
(a) The first pair of contact and target elements



(b) The second pair of contact and target elements



(c) The third pair of contact and target elements



(d) The fourth pair of contact and target elements

Figure 8.45 Contact and target elements in the models

- R1 and R2 define the target element geometry.
- FKN defines a normal contact stiffness factor.

- FTOLN is a factor based on the thickness of the element which is used to calculate allowable penetration.
- ICONT defines an initial closure factor (or adjustment band).
- PINB defines a "pinball" region.
- PMIN and PMAX define an allowable penetration range for initial penetration.
- TAUMAX specifies the maximum contact friction.
- CNOF specifies the positive or negative offset value applied to the contact surface.
- FKOP specifies the stiffness factor applied when contact opens.
- FKT specifies the tangent contact stiffness.
- COHE specifies the cohesion sliding resistance.

If the real constants are not properly set, the model may not converge or may refuse to run. The most important real constants in the present case are FKN, FTOLN and ICONT. They will directly affect the behaviour and results of the model.

The real constant FKN is used to specify either a scaling factor or an absolute value for contact stiffness. The contact stiffness is estimated based on the material properties of the underlying deformable elements. Determining a good stiffness value may require some experimentation on the models. In order to arrive at a good stiffness value, a "trial run" in the spiroid gear model can be conducted as follows:

1. A low value is used to start with. This is because it is better in general, to underestimate this value rather than overestimate it. Penetration problems resulting from a low stiffness are easier to fix than convergence difficulties that arise from a high stiffness. It was found in many cases that convergence failures in contact analysis result from using too large a value for contact stiffness.

2. The penetration and the number of equilibrium iterations used in each substep have to be carefully checked. This check is necessary because if the global convergence difficulty is caused by too much penetration (rather than by

residual forces and displacement increments), FKN may be underestimated. In the next trial run, a larger FKN value is used. If the global convergence requires many equilibrium iterations for achieving the convergence tolerances of residual forces and displacement increments rather than the penetrations, FKN may be overestimated. In the next trial run, a smaller FKN value would be used.

The above procedure was repeated until a good value of stiffness was obtained. Finally, in the spiroid gear tooth contact analysis, the value of 1 was determined for FKN in the present models and good convergence was achieved.

The real constant FTOLN is a factor based on the thickness of the element which specifies an allowable maximum penetration for the augmented Lagrangian method. If FTOLN is set too small, an excessive number of iterations or non-convergence will result. In the spiroid gear analysis, the value of 0.1 was used for FTOLN.

The definition of initial contact is perhaps the most important aspect of building a contact analysis model. The real constant ICONT is used to specify a geometric "tolerance" for ANSYS to use in determining whether two surfaces are initially (at the start of the analysis) in contact. It is used to deal with problems that may otherwise be caused by small errors in coordinate locations due to the finite precision of the computer arithmetic used to calculate numerical information such as coordinate locations.

In the spiroid gear model, the real constant ICONT is used to specify a small initial contact closure between the gear and pinion contact teeth. This is the depth of an "adjustment band" around the target surface. According to ANSYS manual, a positive value for ICONT indicates a scaling factor relative to the depth of the underlying elements. A negative value indicates an absolute contact closure value. Any contact detection points that fall within this adjustment band are internally shifted to be on the target surface. Both positive and negative values have been used in “trial runs”. After a number of trial runs had been conducted, the value of –0.3 was determined for ICONT.

8.9 APPLICATION OF THE LOAD AND BOUNDARY CONSTRAINTS

A loaded gear set usually has only a few pairs of teeth in simultaneous contact. The gear teeth not in contact have low stresses and hence are of little interest. The only interest lies in those teeth in contact, which have high stresses. Based on that, an assumption is widely accepted that the partial models containing these teeth in contact are good enough for gear contact analysis. Previous researchers thus used partial multi-tooth FE models that ignored those teeth not in contact to reduce the number of nodes and elements to save computation time. However, the above assumption is found to be not correct in the present research. As addressed in Section 8.1.4, such a simplification results in incorrect boundary conditions which affect the accuracy of the results.

In the beginning of this research, a few partial models with various boundary assumptions have been built and analysed. This boundary problem was found when the results of the present partial models were examined. The results showed that different boundary constraint schemes resulted in great differences. In order to estimate the effects of boundary conditions in the partial model, a full model with high order solid hexahedral elements (see Figure 8.42) were built. A comparison between the results of the partial model and the full model of a spiroid gear has been made. For the partial model, any changes in the boundary constraints resulted in totally different contact regions. However for the full model, there is no such a boundary constraint problem.

The full model has no such boundary problem but its model size is much larger. To overcome the model size problem, the author has developed two techniques to tackle it. The first technique is to use the advanced submodel technique. The second technique is to simplify the full model to reduce the number of nodes but keep the accuracy. The submodel technique will be addressed in Section 8.11.2.

The simplified full model keeps those tooth pairs in contact and removes the teeth not in contact but keeps the gear base part. The contact tooth pairs meshed with a finer mesh and the bases meshed with a coarse mesh are shown in Figure 8.46. The contact

pattern calculated from the simplified full model has the same pattern as the results of the full model.

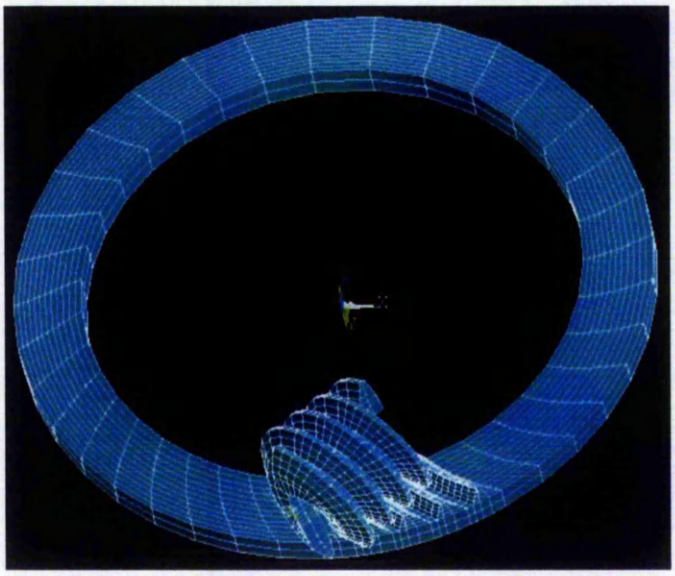


Figure 8.46 Simplified full model with hexahedral elements



Figure 8.47 Full spiroid gear model's constraint and loading scheme

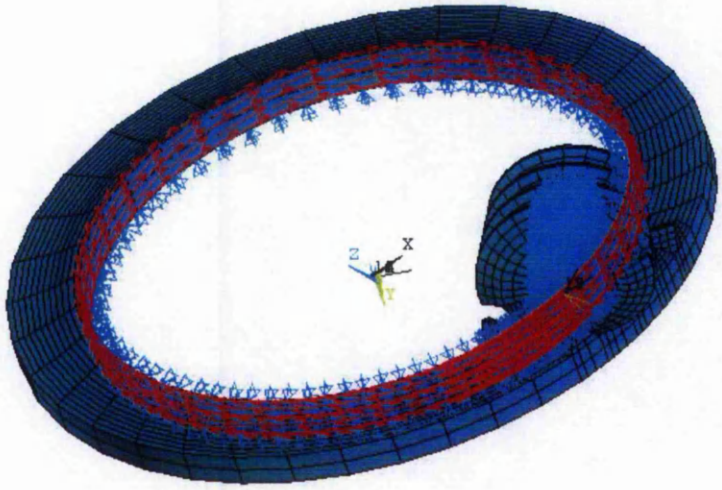


Figure 8.48 Simplified full spiroid gear model's constraint and loading scheme

The simplified full assembly model's boundary condition is applied in the same manner as the full assembly model (see Figure 8.47). To simulate the gear set shaft rotating at a steady speed, the pinion is fixed while the gear is constrained to allow rotation about its own axis. The nodes on the inner cylindrical surfaces of the pinion are fixed in x, y, z translational displacements. To simulate the gear rotation, a local cylindrical coordinate system is created and its origin is situated at the gear's centre. The z-axis of this local cylindrical coordinate system is along the gear axis direction. The nodal coordinate systems of the inner surfaces of the gear are transformed into the local cylindrical coordinate system. The nodal x-axis and z-axis translational displacements are fixed but the y-axis translation displacement is free. Such a constraint scheme will allow the gear to rotate about its own axis.

The applied torque is simulated by the forces applied on the nodes on the inner cylindrical surfaces of the gear. Since the nodes on the gear inner cylindrical surface are transformed into the local cylindrical coordinate system, the applied forces in the y direction are all perpendicular to the gear axis at every instance and therefore a rotating torque is simulated. When the loads are applied, the time step size is set small enough to capture the correct contact zone. The time step size is specified by a number of substeps or the time step size itself. The smooth transfer of contact forces will be disrupted if the time step size is too large.

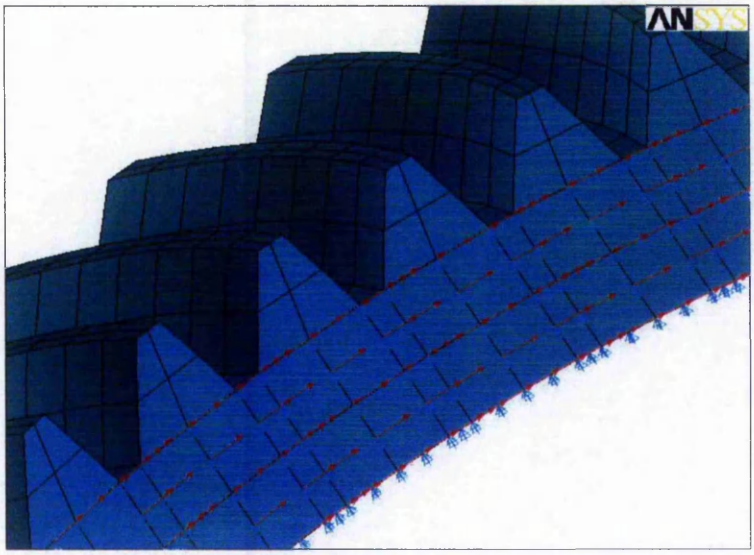


Figure 8.49 Zoomed loading and constraint for the spiroid gear inner surface

8.10 SOLVER SELECTION

There are five solvers available in ANSYS. They are Frontal solver, Sparse Direct solver, Jacobi Conjugate Gradient (JCG) solver, Incomplete Cholesky Conjugate Gradient (ICCG) solver and Preconditioned Conjugate Gradient (PCG) solver. Each solver has its own advantages and disadvantages. Since gear tooth contact analysis takes a long time to solve and the solutions may not converge, it is very important to choose the right solver to acquire the right solution.

The choice of solver depends on three main factors: (1) the type of problem, such as linear or nonlinear, static or dynamic; (2) the model size and (3) the computer hardware. The JCG and ICCG solvers were excluded because they were more suitable for 3D field analysis. The current model's wavefront is more than 3,000. According to the ANSYS manual, when the wavefront is greater than 1,000, the Frontal solver is not economic. Trial runs also confirmed that the Frontal solver took too long to solve the model and therefore was not suitable for the current models. The sparse Direct solver can be used in the present model according to the ANSYS manual. However, several trial runs indicated that if the Sparse Direct solver is used, the solution can be achieved in 12 to 18 hours per run for a 90,000 DOF model using a Pentium II 400MHZ, 128MB SDRAM PC. Sometimes it even takes longer because

it requires a lot of disk writing and reading operations that seriously affect the speed of solution.

The advantage of the PCG solver is that it converges to the solution much faster (4-10 times) than the Sparse Direct solver or JCG solver. The PCG solver applies a very sophisticates preconditioner in its iteration process. Because of its fast convergence, the PCG solver has been tried with the gear contact models. The trial run showed that the PCG solver converged to a solution most quickly.

8.11 ADVANCED TECHNIQUES

Several advanced techniques such as mesh refining, node coupling, submodel and substructure have been tried and used in the spiroid gear contact analysis for different purposes. The two techniques, mesh refining and submodel, are deemed by the author as the most useful and can be used in future loaded gear tooth contact analysis. They are introduced in the following two sections.

8.11.1 Gear Contact Region Mesh Refining Technique

The mesh refining technique has been developed for the gear partial model. ANSYS has the capacity to refine the tetrahedral element meshes in the area of interest, e.g. the tooth contact region in gear contact analysis. For the purpose of reducing the number of nodes, the possible contact region of gear and pinion tooth surface are refined and other parts are meshed with coarser meshes (see Figure 8.50).

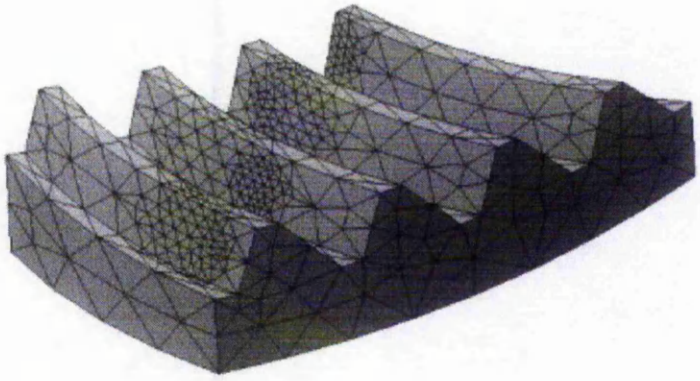


Figure 8.50 Local mesh refinements in potential contact region in spiroid gear teeth

This technique has not been adopted in the present final full FE models due to the nodal number limits of the ANSYS university high option version. If the commercial ANSYS version is used, the number of nodes is not a problem. Then this technique can be applied. It will make the modelling work much easier and also prevent the less significant part of the model from occupying too much computer resources.

8.11.2 Submodel Technique

During the research, the full spiroid gear model has been found necessary for gear contact analysis. For the loaded gear tooth contact analysis, the stresses in the teeth not in contact are of little interest and therefore those teeth not in contact can be meshed with coarser meshes. For those teeth in contact, finer meshes are required. However, the full model size cannot be reduced too much due to the characteristics of mapped meshing. The full model's size is still too large if a reasonably fine mesh is required. Due to the limit on the model size, the meshes of the full model cannot be too fine. So if more accurate tooth stresses in the contact region are to be examined, the submodel technique should be used.

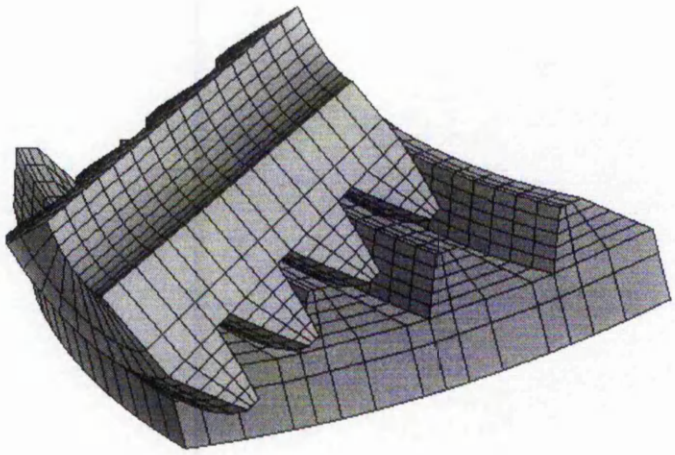


Figure 8.51 Spiroid submodel hexahedral element mesh

To obtain more accurate results in the contact region, reanalysing the entire model with a greater mesh refinement is, of course, always the first thought. However, this

method is time-consuming and costly because the model size is too large. In the present model, it is impossible to use this method.

The alternative method developed was to utilise partial models, created at the beginning of this research, as submodels. Figure 8.51 shows one such partial model meshed with hexahedral elements. Those partial models had problems with boundary constraints. However the real boundary displacements can be taken from the results of the full coarser spiroid gear models by using the submodelling technique. The boundary of the submodel represents a cut through the coarse model. Displacements calculated on the cut boundary of the coarse model are specified as boundary conditions for the submodel. This is a significant difference from the partial model constraint schemes in previous research, in which a few nodes in the boundary surface are fixed.

According to St. Venant's principle, if an actual distribution of forces is replaced by a statically equivalent system, the distribution of stress and strain is altered only near the regions of load application. This implies that stress concentration effects are localised around the concentration region. Therefore, if the boundaries of the gear submodel are far enough away from the stress concentration, reasonably accurate results can be calculated in the submodel.

The obvious benefit of a submodel is to give more accurate results in the contact region. Figure 8.52 shows stresses in the pinion part of a submodel. Figure 8.53 shows the stresses in the gear part of a spiroid submodel.

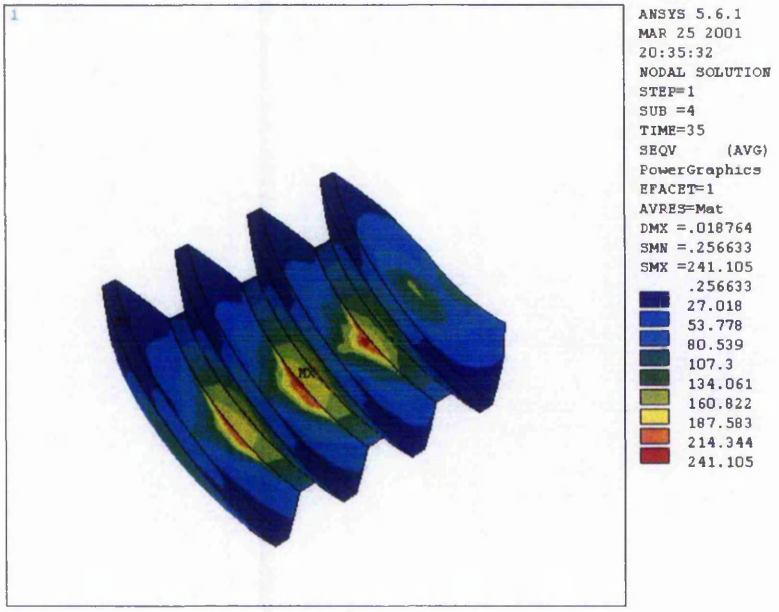


Figure 8.52 Submodel stress pattern (pinion part)

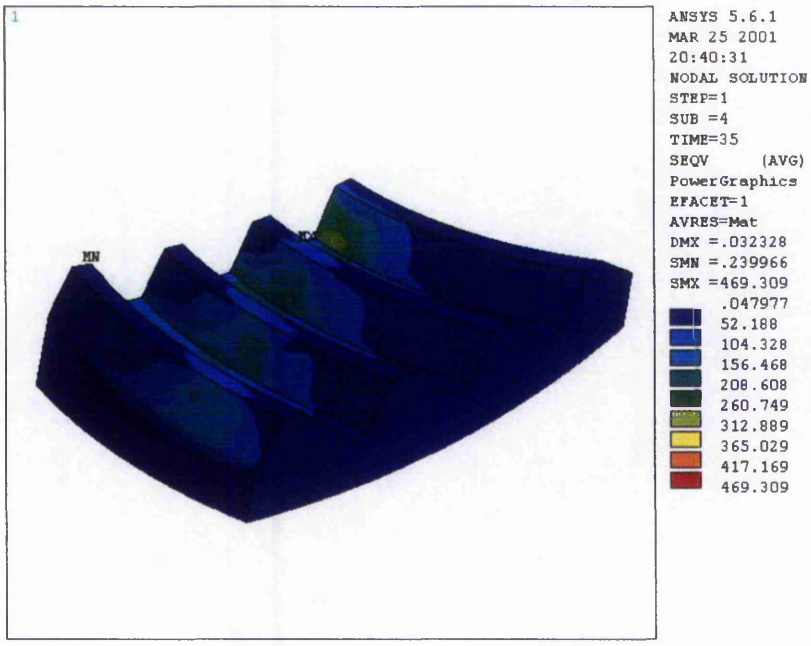


Figure 8.53 Submodel stress pattern (gear part)

8.12 RESULTS AND DISCUSSION

The whole tooth contact process is simulated by seven simplified full models with different contact positions. The seven different positions vary with continuous rotational angle increments 1.008° (360/51/7) for the gear and 25.714° (180/7) for the pinion. Figure 8.54 shows the seven different position models created for the gear contact analysis. The different positional angles of the seven models are listed in Table 8.1.

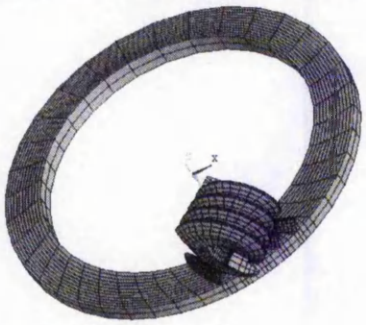
Table 8.1 The different position angles of contact models

	Gear	**Pinion**
Position 1	0°	0°
Position 2	1.008°	25.714°
Position 3	2.017°	51.429°
Position 4	3.025°	77.143°
Position 5	4.034°	102.857°
Position 6	5.042°	128.571°
Position 7	6.050°	154.286°

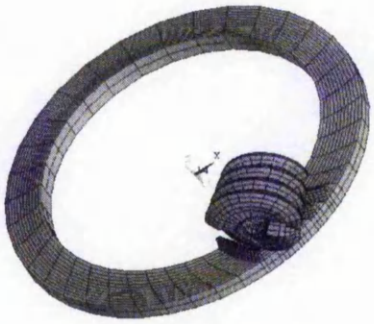
These seven positions cover the engagement period for one tooth pair getting into and out of contact. Therefore, with the seven models, the whole process of one tooth contact can be simulated. Other tooth pairs coming into contact have exactly the same contact patterns as the calculated tooth pair's. So the whole gearset can be simulated with the seven models.

The torque applied to the gear was 332.8Nm. The loads were ramped when they were applied. There is one load step applied in the whole loading process. The one load step was divided into five load substeps. The automatic time stepping option was turned on during the analysis. The time of the first load step was set to 100. When the equilibrium of first load step was achieved, there were finally four load substeps in total. The torque to the gear was applied as y-axis direction forces at the nodes on the

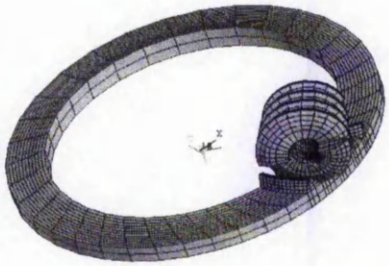
inner cylindrical surfaces in the local cylindrical coordinate system (see Figure 8.48). The materials of the gearset are steels.



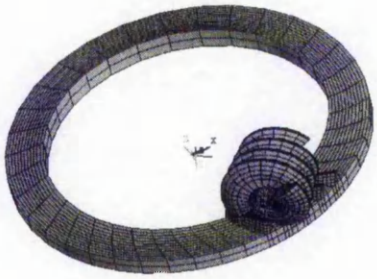
(1) Gear set position 1



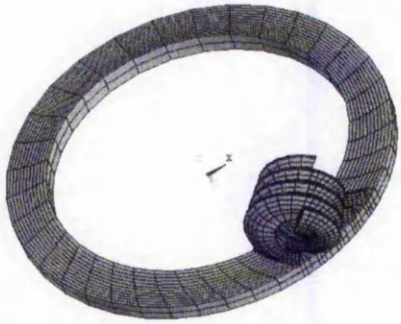
(2) Gear set position 2 model



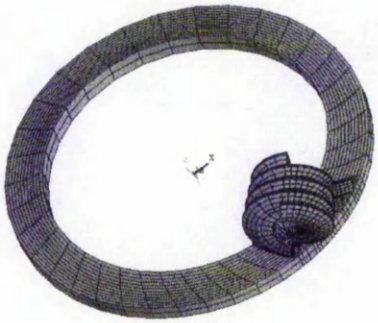
(3) Gear set position 3 model



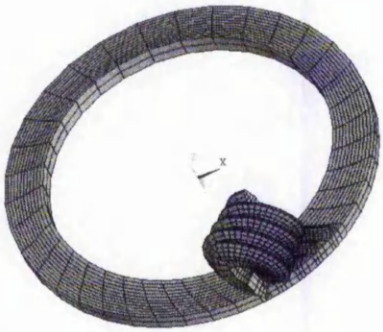
(4) Gear set position 4 model



(5) Gear set position 5 model



(6) Gear set position 6 model



(7) Gear set position 7 model

Figure 8.54 Seven spiroid gear models with different contact positions

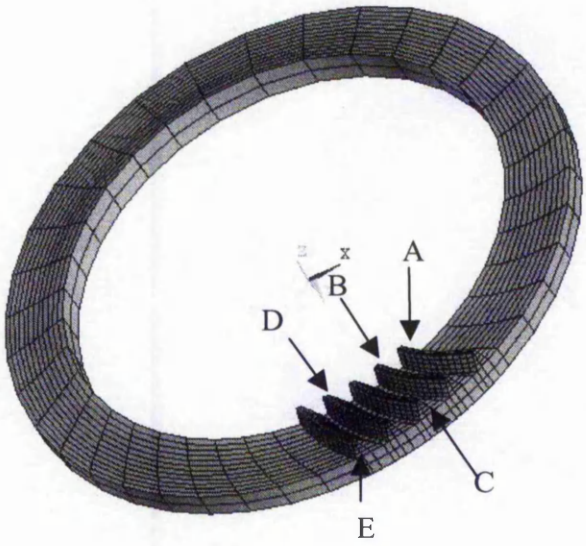


Figure 8.55 Spiroid gear tooth indexes

8.12.1 Stress Distribution

For the sake of convenience, the five teeth of the simplified full spiroid gear models are designated as A, B, C, D and E as shown in Figure 8.55. At the beginning, the gear model is not in contact. For the first load substep, the initial closure constant ICONT is given a negative value of –0.1. When the first substep load is applied, the initial contact is established. After several iterations, the gear model reaches its equilibrium. Then the second substep load is applied. The process is repeated until the last substep load is applied and the final equilibrium is obtained. The solution results are analysed using the postprocessor of ANSYS.

8.12.1.1 Tooth Stresses at Position 1

At position 1, when the first load step is applied, gear tooth A first comes into contact with the pinion. There are four tooth pairs, A, B, C, D in simultaneous contact. The maximum stress in the gear occurs at the entrance contact tooth A and is near the end of tooth A. The contact region in tooth A is near the inner side end, therefore there are less buttressing effects near the contact region. In load substep 1, the maximum Von Mises stress in the gear is 24 MPa. In load substep 4, the maximum Von Mises stress

reaches at 140 MPa. Figure 8.56 shows Von Mises stresses of the gear tooth in load step 1, substep 4. The maximum Von Mises stress in each tooth is in descending order from tooth A to tooth D. Figure 8.56 shows that the maximum Von Mises stress in A and B occurs within the contact region but in C and D, where there is the strongest buttressing effect, it occurs near the root. Although the maximum stress is located near the end of tooth A, the contact force at tooth A is the smallest among the four simultaneous contact teeth (see Figure 8.84).

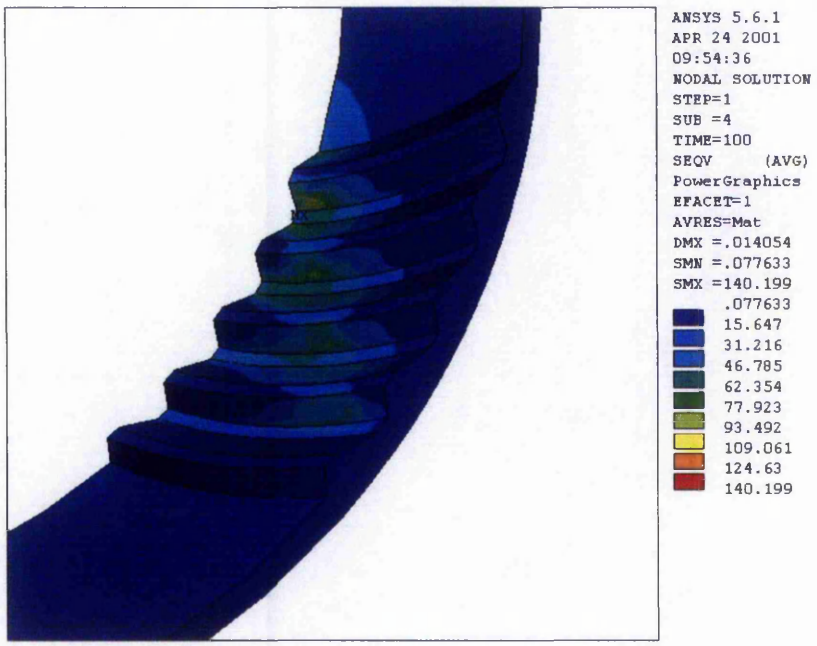


Figure 8.56 Gear tooth Von Mises stress pattern at contact position 1, load step 1, substep 4

Figure 8.57 shows the pinion's Von Mises stress pattern. The maximum Von Mises occurs in the middle tooth (contact with gear tooth C).

In contrast to the gear stress pattern, the maximum Von Mises stress in the pinion tooth which contacts with gear tooth A is the smallest among the pinion teeth as shown in Figure 8.57. This is because the stress in the pinion has a stronger buttressing effect. The pinion's maximum Von Mises stress (88.844 MPa) is smaller than the counterpart gear's (140.199 MPa). The maximum stress in each pinion tooth occurs at the root area below the contact region, not at the centre of the contact region. The shape of maximum stress area is approximately triangular. The stresses

decrease with the distance from the centre of maximum stress. The effective stress area is around one quarter of its circumference. Outside this area, the stress is negligible.

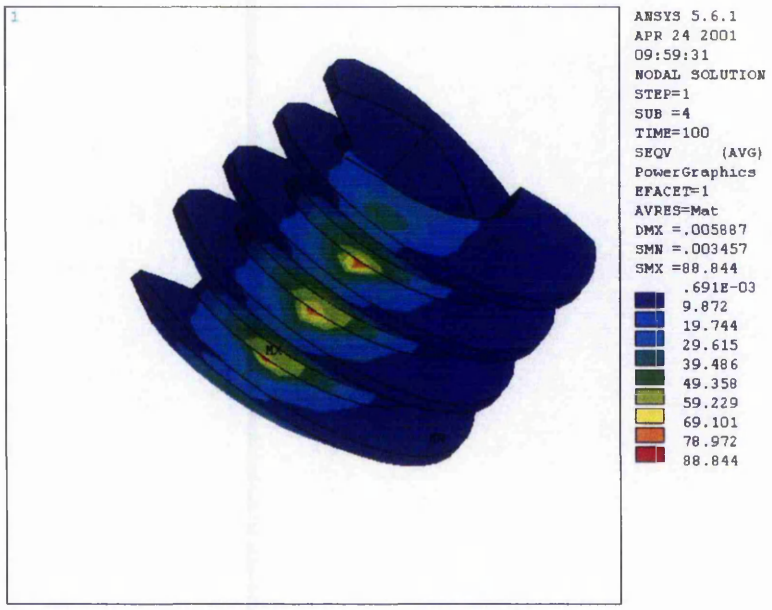


Figure 8.57 Pinion tooth Von Mises stress pattern at contact position 1, load step 1, substep 4

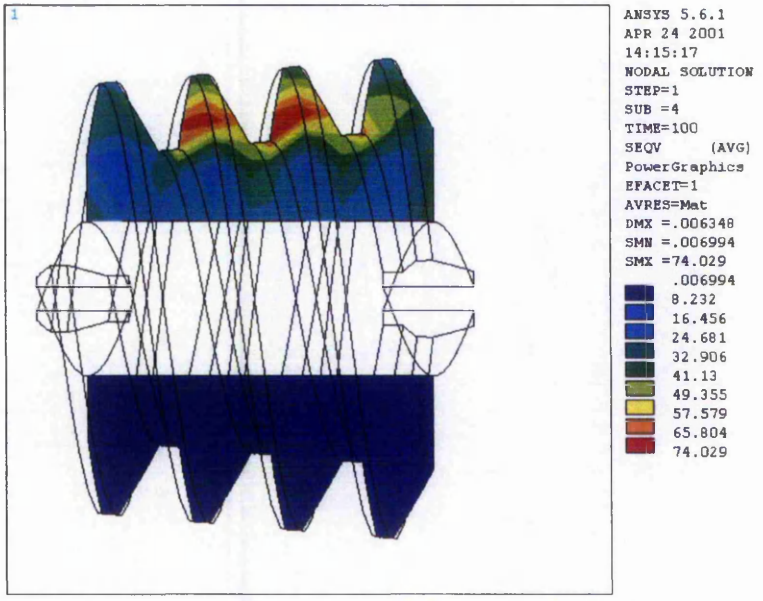


Figure 8.58 Pinion tooth Von Mises stress cross section pattern at contact position 1, load step 1, substep 4

Figure 8.58 shows the pinion's Von Mises stress patterns in the axial cross section through the maximum stress area in the thread that contacts with gear tooth C. From this figure, it can be seen how the stresses distribute across the tooth section which is nearly impossible to see in experimental methods. The maximum stress in each tooth is not located in the same axial plane.

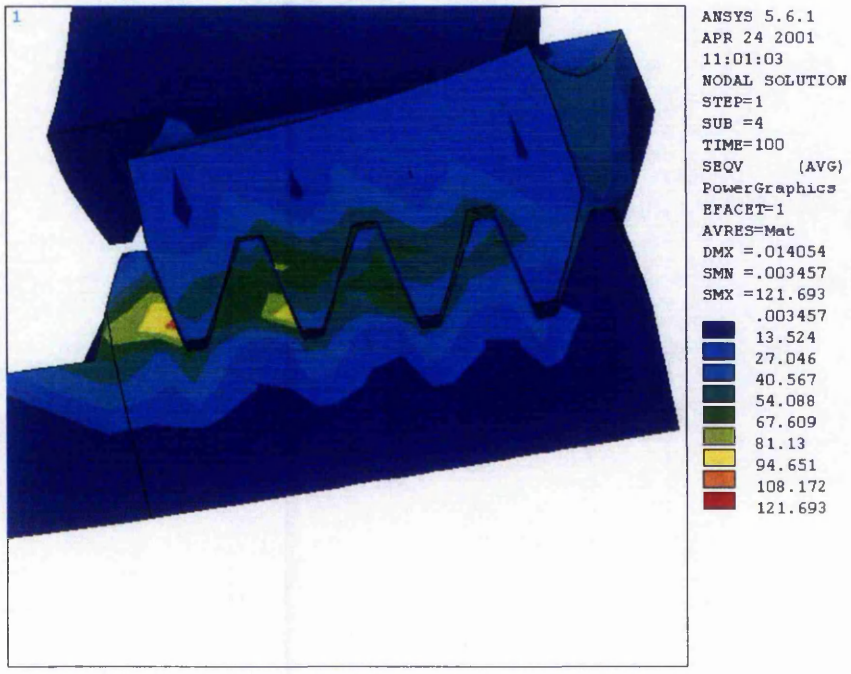


Figure 8.59 Gearset assembly Von Mises stress section distribution at contact position 1, load substep 4

Figure 8.59 illustrates the gear cross section Von Mises stress pattern in the contact region of the gearset assembly for load substep 4. The gear tooth contact stresses decrease from the entrance tooth A to the exiting tooth D. From the stress patterns in gear teeth A and B, it can be clearly seen that the maximum stress is above the root. The stresses decrease with distance from the centre of the maximum stress area.

8.12.1.2 Tooth Stress at Position 2

After the gear rotates an angle of 1.008° and the pinion rotates an angle of 25.714°, the spiroid gear reaches position 2. The contact region in gear tooth A moves to the end of the tooth. The maximum Von Mises stress still occurs at tooth A but the

position is on the edge of tooth. The maximum Von Mises stress increases from position 1 to position 2 and reaches 224.8 MPa for load substep 4 (see Figure 8.60). The other stress patterns are similar to those for position 1, except the contact regions are shifted.

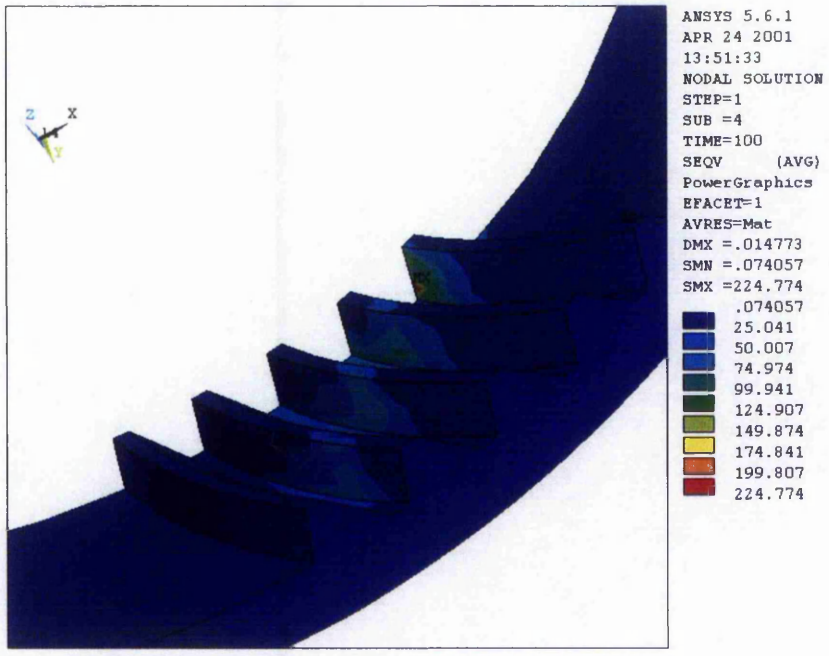


Figure 8.60 Gear tooth Von Mises stress pattern at contact position 2, load step 1, substep 4

The pinion's maximum Von Mises stress also increases. The value of the maximum stress is 116 MPa. Apart from increase in stress value, the pinion's stress pattern at position 2 is very similar to that at position 1. The maximum Von Mises stress still occurs at the tooth that is in contact with gear tooth C and this tooth has the maximum contact forces. It indicates that gear tooth C has the maximum contact forces among the four contact teeth and also has the maximum load share.

Figure 8.62 shows in cross-section the distribution of the Von Mises stress pattern in contact position 2, load substep 4. The pinion is shown at the bottom. This illustrates that the pinion's stress effective depth is not far from the gear tooth root. The deepest effective area occurs below the root. The shape of the edge of the stress effective area is somewhat similar to a sine curve with the highest points in the middle of the root

and the lowest in the middle of the teeth. It also illustrates the relations of the spiroid gear tooth contact.

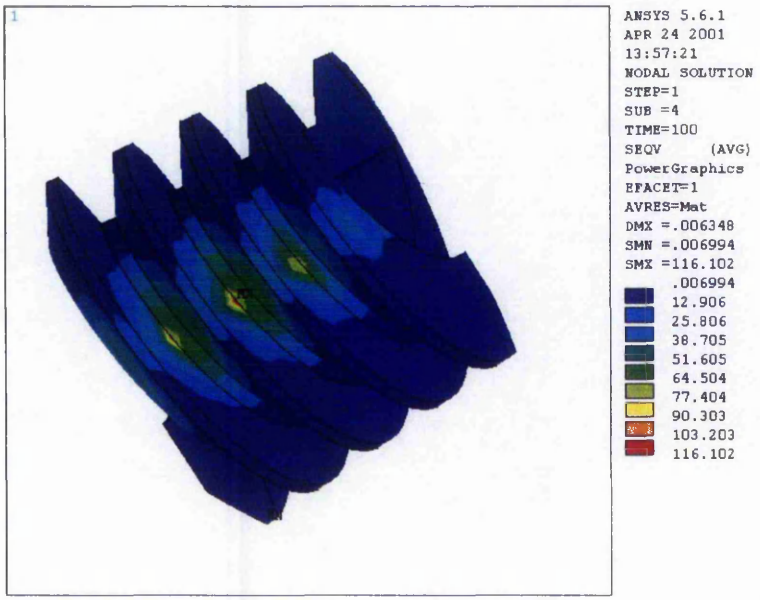


Figure 8.61 Pinion tooth Von Mises stress pattern in contact position 2, load step 1, substep 4

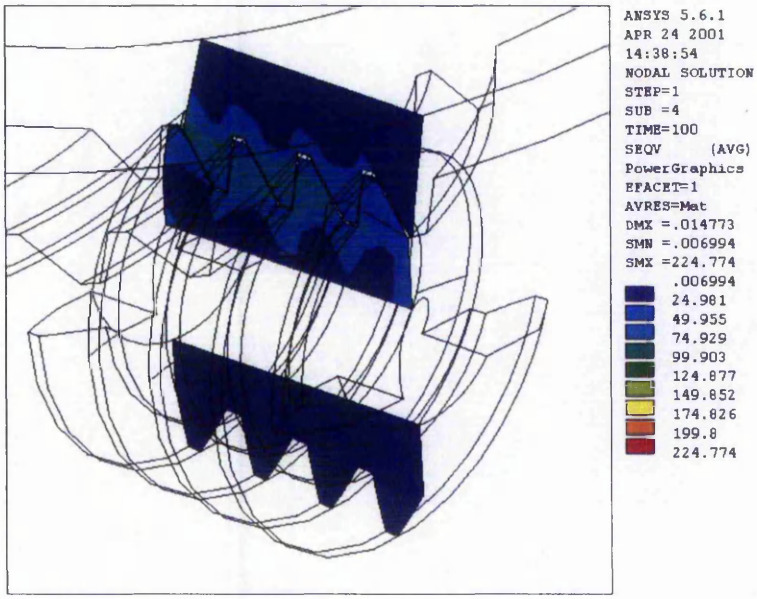


Figure 8.62 Gearset assembly Von Mises stress section distribution at contact position 2, load substep 4

8.12.1.3 Tooth Stress at Position 3

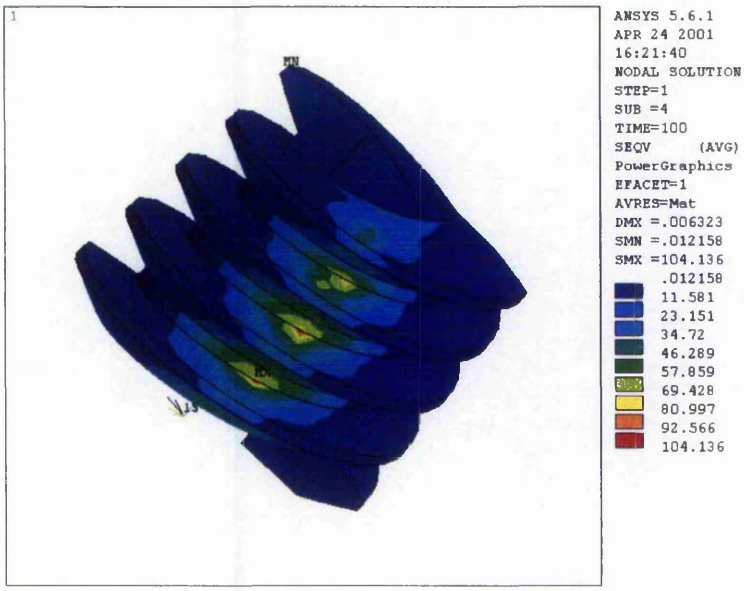


Figure 8.63 Pinion tooth Von Mises stress pattern at contact position 3, load step 1, substep 4

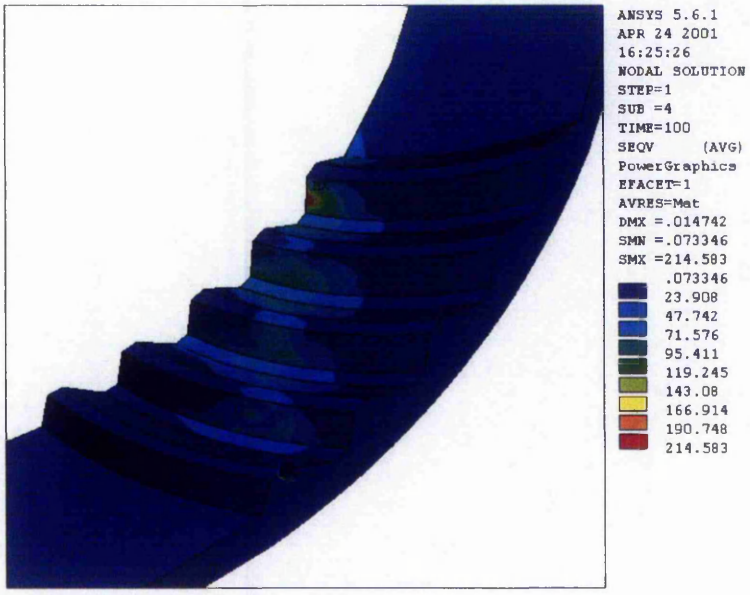


Figure 8.64 Gear tooth Von Mises stress pattern in contact position 3, load step 1, substep 4

When the pinion rotates another 25.714° and the gear 1.008° from position 2, the spiroid gear model reaches position 3. The gear tooth contact stress patterns in substep 4 are shown in Figure 8.60. There are still four gear teeth in simultaneous

contact. The contact on tooth A moves further to the edge. As shown in the Figure 8.64, tooth A is close to going out of contact. The maximum gear Von Mises stress decreases slightly to 214.583 MPa. The pinion's maximum stress is also decreasing from 116 MPa to 104 MPa as shown in Figure 8.63.

8.12.1.4 Tooth Stress at Position 4

At position 4, the gear tooth A exits from contact with the pinion tooth and has no contact force or stress on it (see Figure 8.65). Tooth E has still not come into contact. There are only three pairs of teeth in contact.

The gear's maximum Von Mises stress is 168.256 MPa and is smaller than that at position 2 and 3 (224.774 MPa and 214.583 MPa). This is because the maximum tooth stress for positions 2 and 3 occurred at tooth A which is out of contact. The maximum Von Mises stress now is located at gear tooth B (see Figure 8.65).

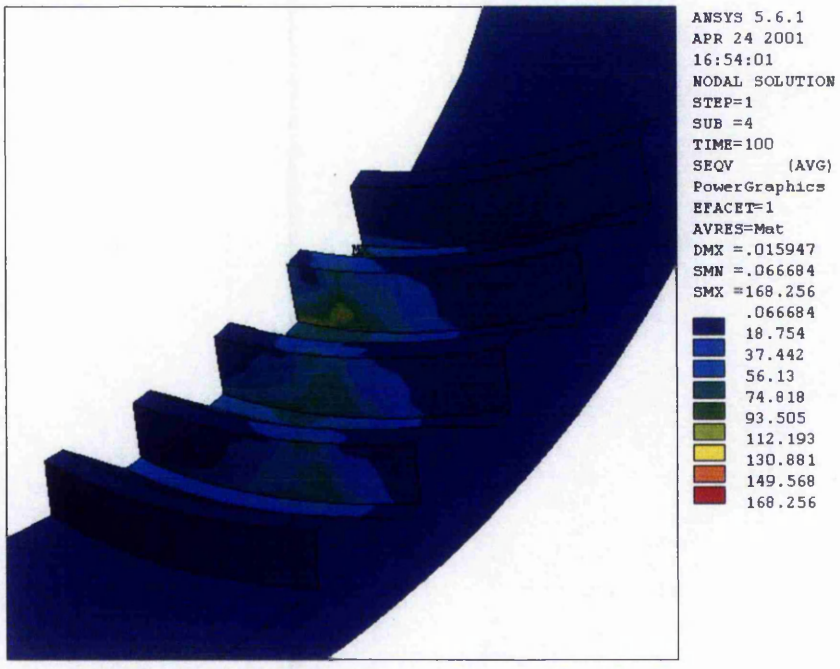


Figure 8.65 Gear tooth Von Mises stress pattern at contact position 4, load step 1, substep 4

Though the gear maximum stress has changed to tooth B from A, the pinion's maximum tooth stress still occurs at the tooth in contact with gear tooth C (see Figure

8.66). This indicates that the gear tooth C still has the maximum contact forces and maximum load share. The maximum pinion Von Mises stress is 122.588 MPa, i.e. increased 18.452 MPa from position 3.

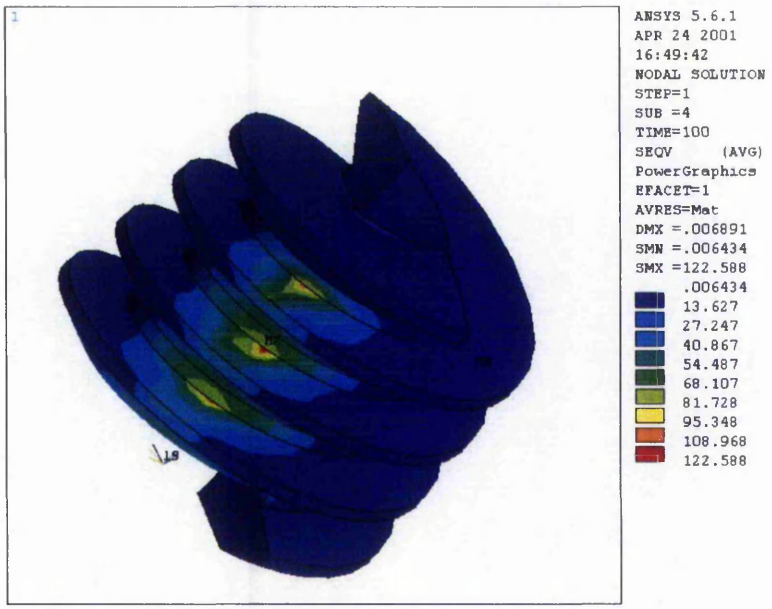


Figure 8.66 Pinion tooth Von Mises stress pattern at contact position 4, load step 1, substep 4

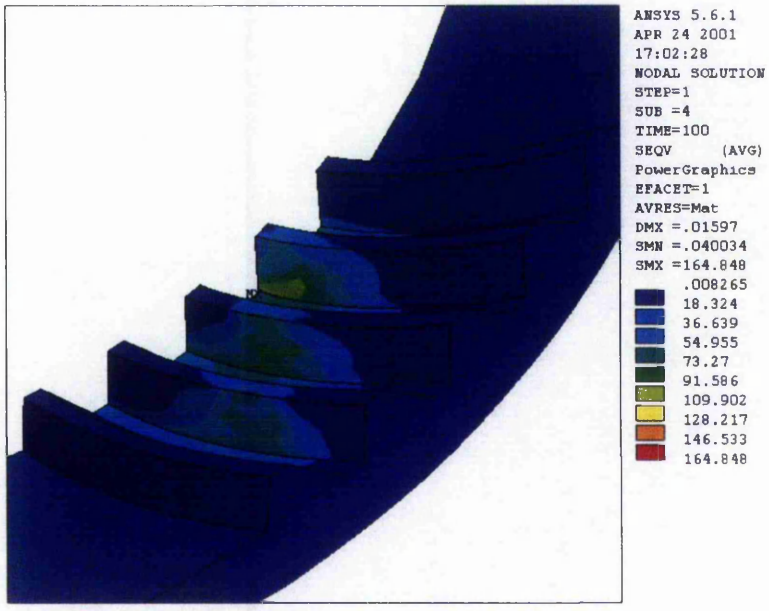


Figure 8.67 Gear tooth Von Mises stress pattern at contact position 5, load step 1, substep 4

8.12.1.5 Tooth Stress at Position 5

At position 5, there are still three tooth pairs in contact. Figure 8.67 and Figure 8.68 show the contact stress patterns for the gear and pinion in load substep 4 at position 5 respectively. Both the gear and pinion stress patterns are quite similar to those at position 4. The magnitudes of the maximum Von Mises stress in both the pinion and gear have change little from that of position 4 - with 1 MPa increment for the pinion and 3.4 MPa decrement for the gear.

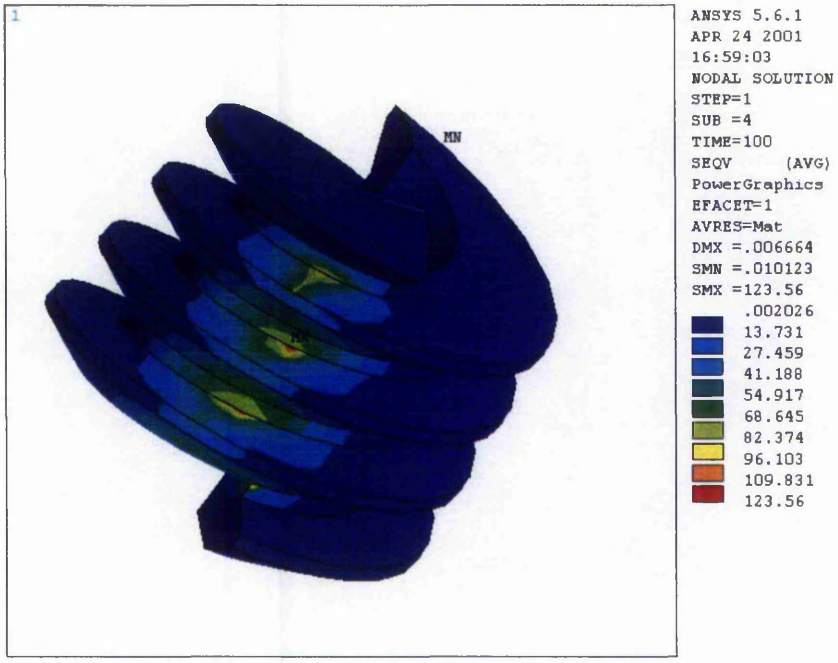


Figure 8.68 Pinion tooth Von Mises stress pattern at contact position 5, load step 1, substep 4

8.12.1.6 Tooth Stress at Position 6

At position 6, the contact status changes from position 5. Gear tooth E comes into contact. There are four tooth pairs in simultaneous contact at this position. The gear maximum stress still occurs at tooth B but its magnitude decreases from 164.848 MPa (at position 5) to 142.455 MPa.

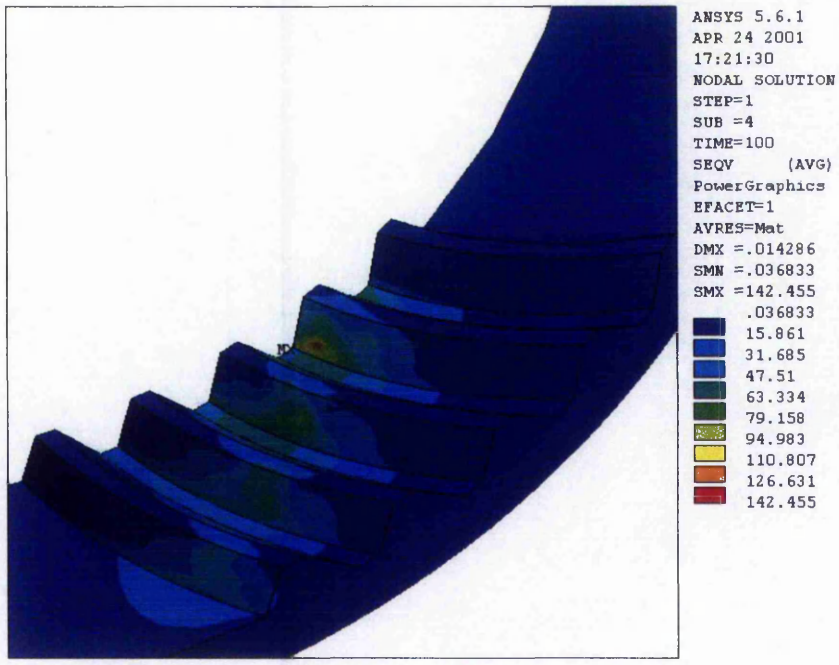


Figure 8.69 Gear tooth Von Mises stress pattern at contact position 6, load step 1, substep 4

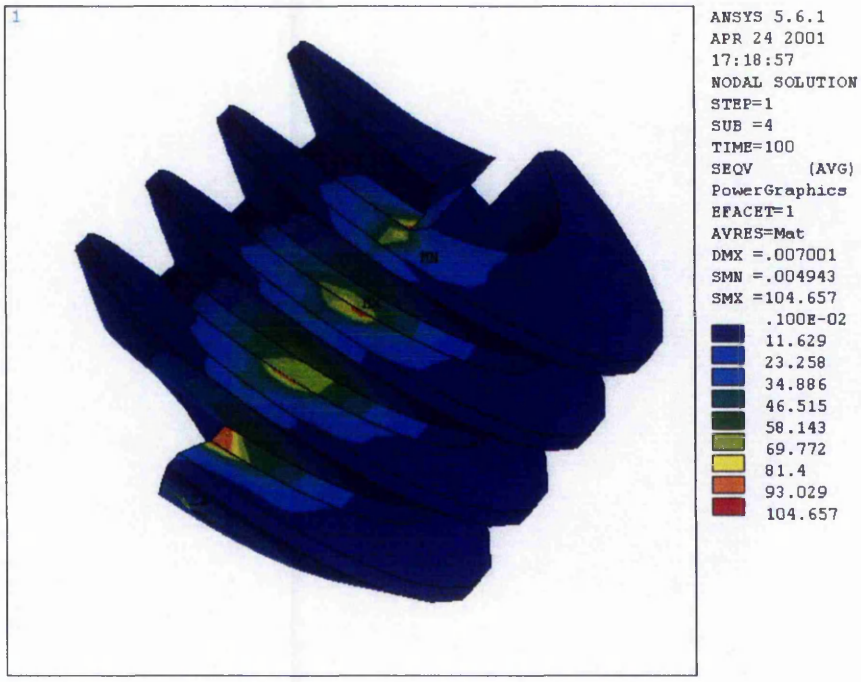


Figure 8.70 Pinion tooth Von Mises stress pattern at contact position 6, load step 1, substep 4

The pinion's maximum Von Mises stress is 104.657 MPa which occurs in the tooth in contact with gear tooth C as shown in Figure 8.70.

8.12.1.7 Tooth Stress at Position 7

At position 7, there are four tooth pairs in contact. Both the pinion and gear contact pattern are similar to those at contact position 1. This is because after position 7, the next contact status will be the same as that at position 1. Figure 8.71 shows the gear stress (Von Mises) pattern at substep 4 in load step 1 at contact position 7. The maximum stress occurs in the entrance contact tooth and the maximum Von Mises stress in the last load substep is 141.186 MPa. Figure 8.73 is the zoomed entrance tooth stress pattern around the contact region. The maximum contact stress is located near the centre of contact regions of the entrance contact tooth.

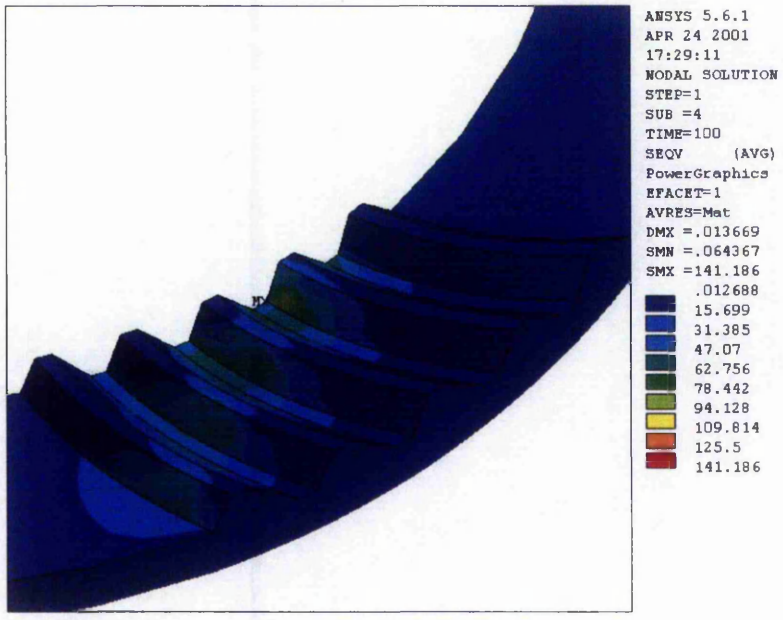


Figure 8.71 Gear tooth Von Mises stress pattern at contact position 7, load step 1, substep 4

The pinion tooth stresses are smaller than those in the gears. At position 7 and load substep 4, the pinion's maximum Von Mises is only 88.158 MPa, whereas the gear maximum Von Mises is 141.186 MPa. Unlike the gear stresses, the maximum stresses in the pinion are all located at the root of the teeth near the contact regions.

Figure 8.74 to Figure 8.81 shows 8 different cross section views of the gear tooth stress at position 1, load substep 4.

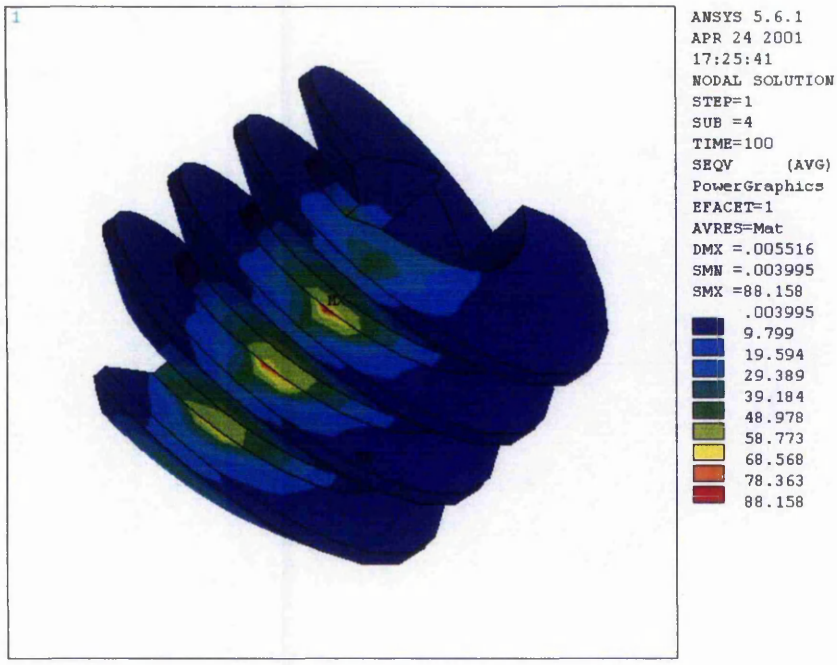


Figure 8.72 Pinion tooth Von Mises stress pattern at contact position 7, load step 1, substep 4

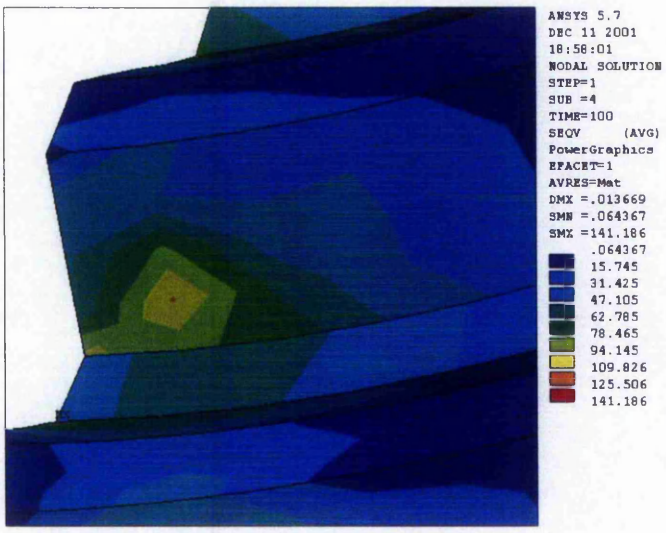


Figure 8.73 Zoomed gear tooth Von Mises stress pattern at contact position 7, load substep 4

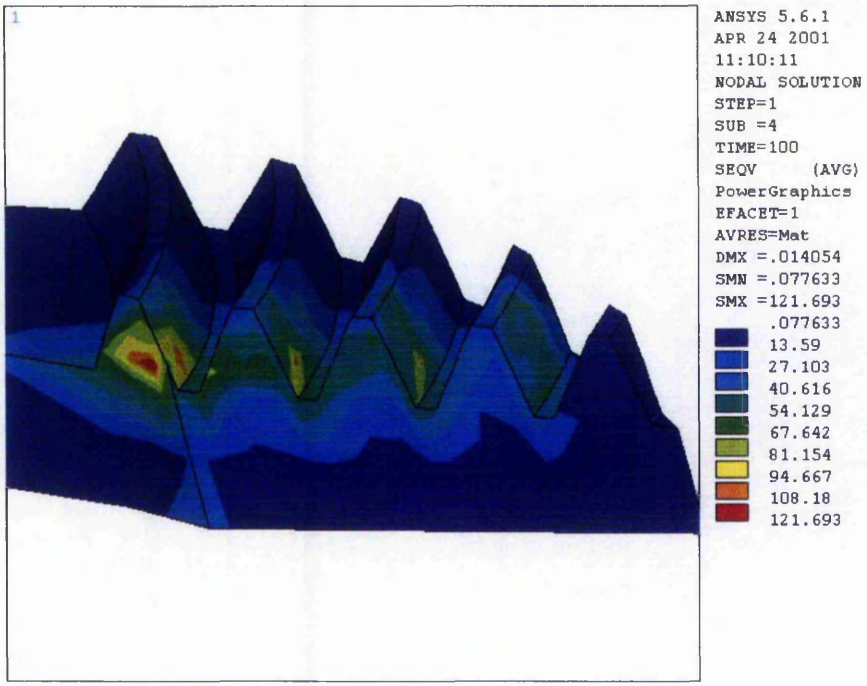


Figure 8.74 Gear tooth Von Mises stress cross section pattern at contact position 1, load step 1, substep 4, section 1

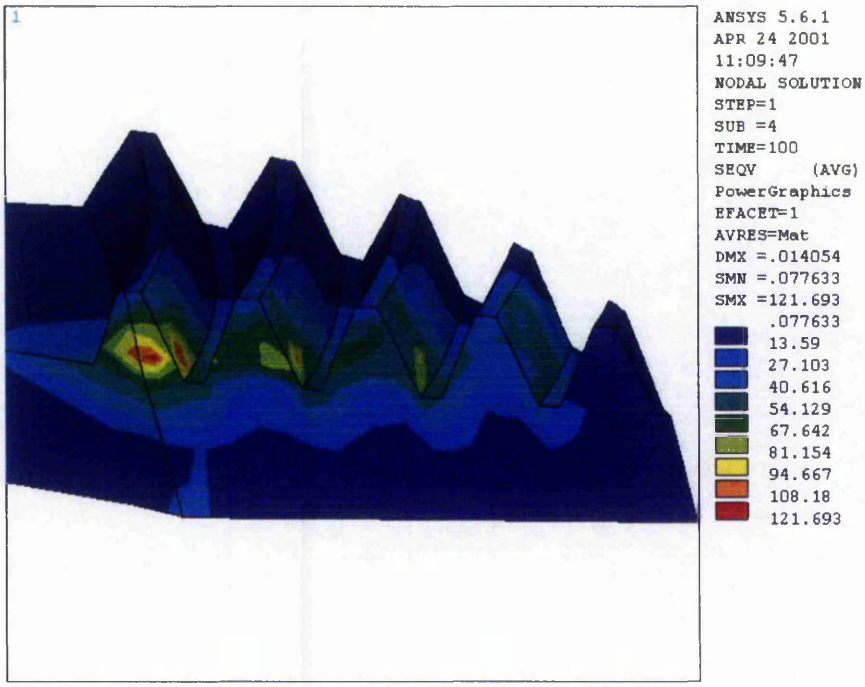


Figure 8.75 Gear tooth Von Mises stress cross section pattern at contact position 1, load step 1, substep 4, section2

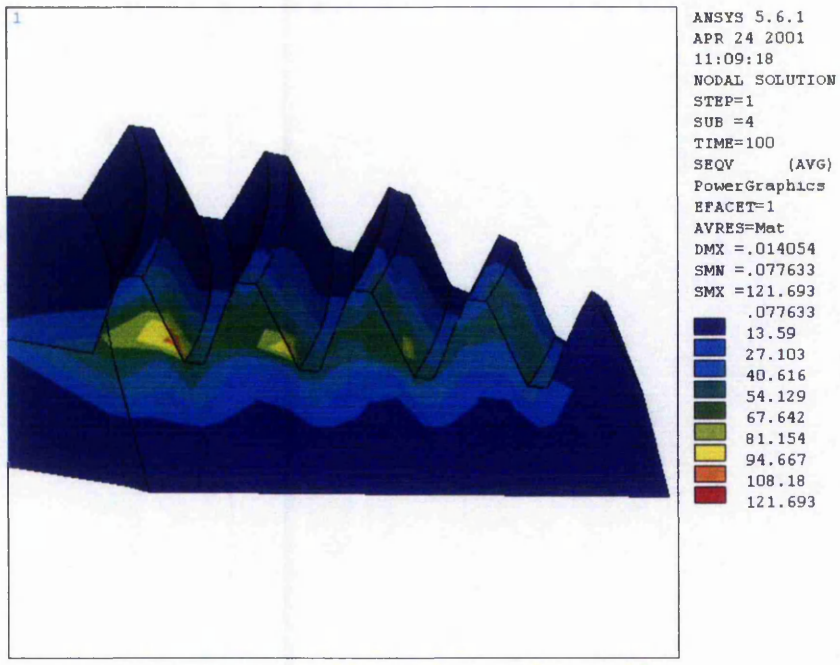


Figure 8.76 Gear tooth Von Mises stress cross section pattern at contact position 1, load step 1, substep 4, section 3

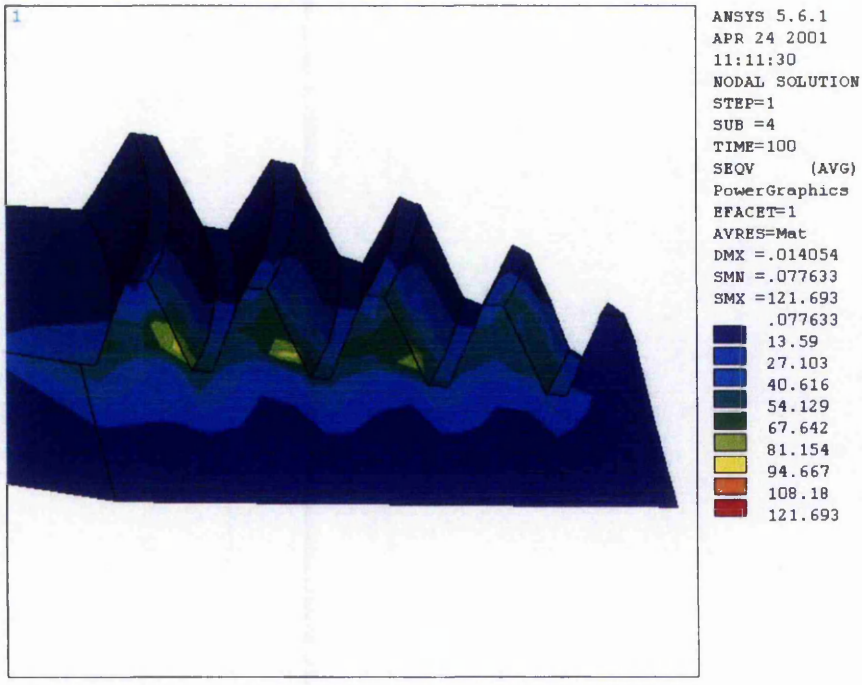


Figure 8.77 Gear tooth Von Mises stress cross section pattern at contact position 1, load step 1, substep 4, section 4

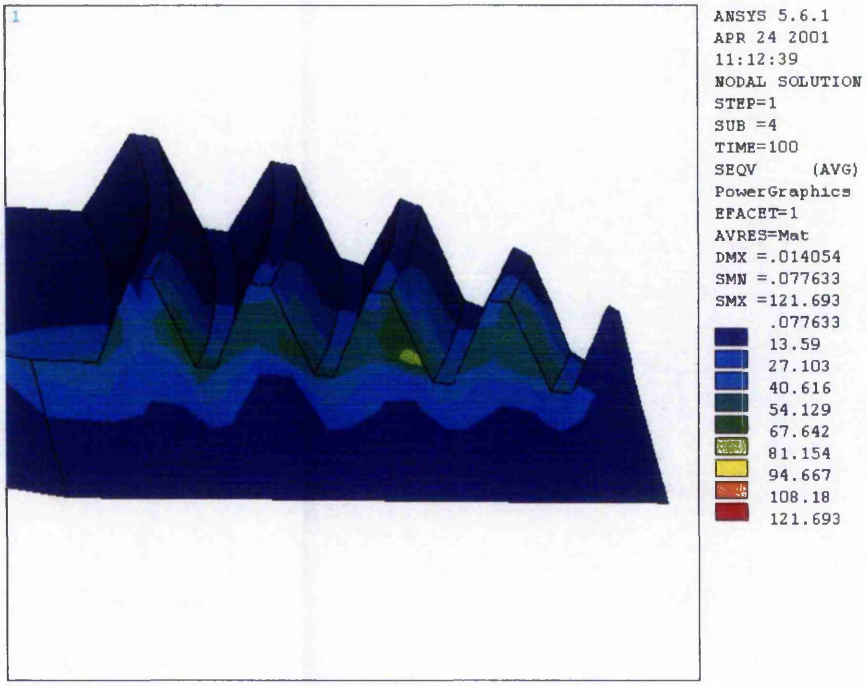


Figure 8.78 Gear tooth Von Mises stress cross section pattern at contact position 1, load step 1, substep 4, section 5

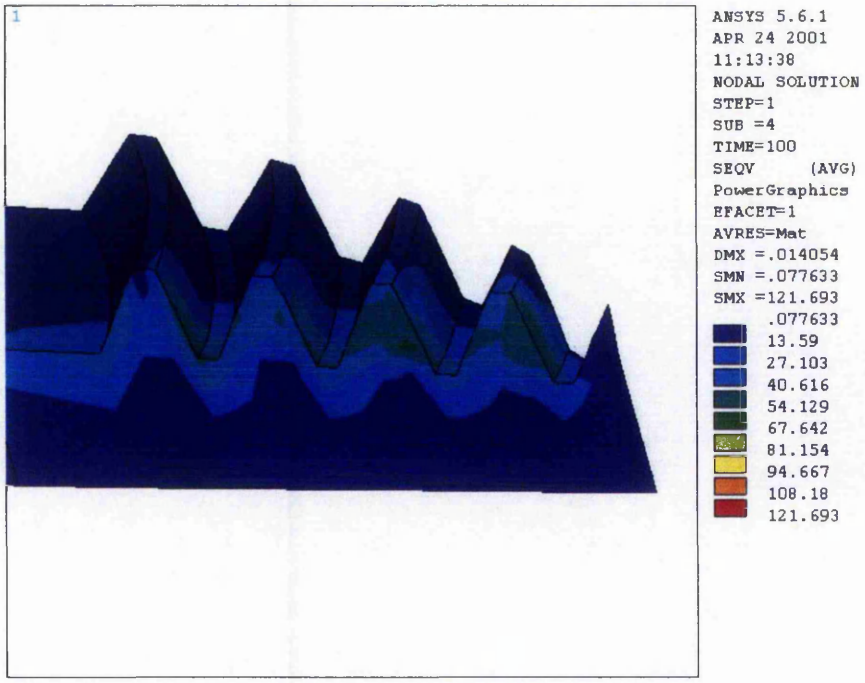


Figure 8.79 Gear tooth Von Mises stress cross section pattern at contact position 1, load step 1, substep 4, section 6

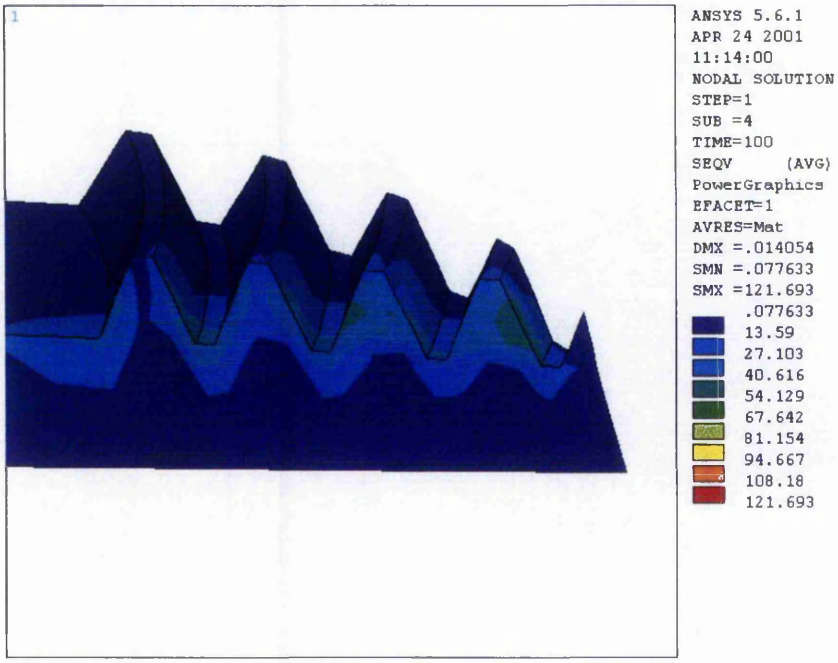


Figure 8.80 Gear tooth Von Mises stress cross section pattern at contact position 1, load step 1, substep 4, section 7

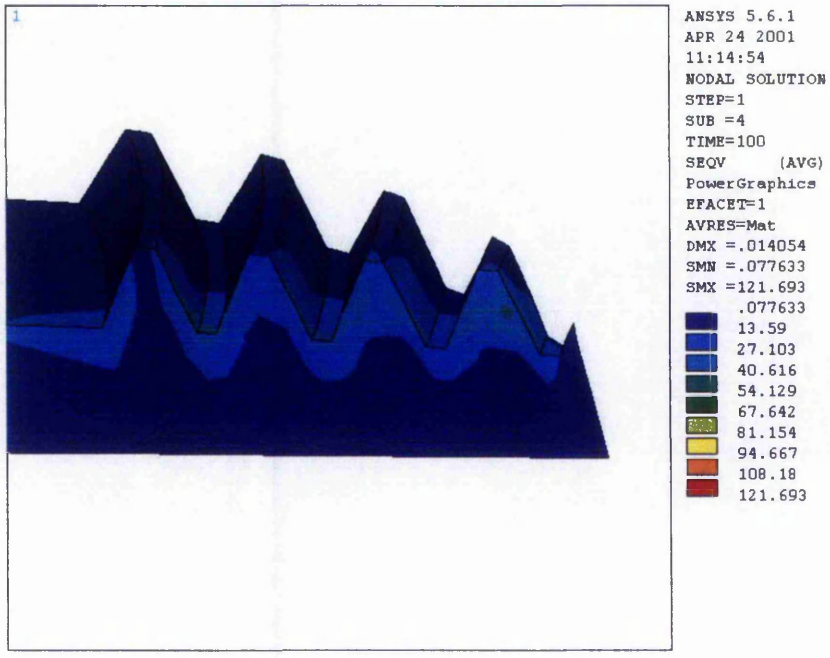


Figure 8.81 Gear tooth Von Mises stress cross section pattern at contact position 1, load step 1, substep 4, section 1, section 8

8.12.2 Load Distribution

8.12.2.1 Load Distribution at Position 1

Figure 8.82 shows the contact forces on the gear tooth at contact position 1. The contact region is an elliptical shape. The maximum contact force is located at the centre of contact region and the contact force decreases from its centre to the edge of contact region.

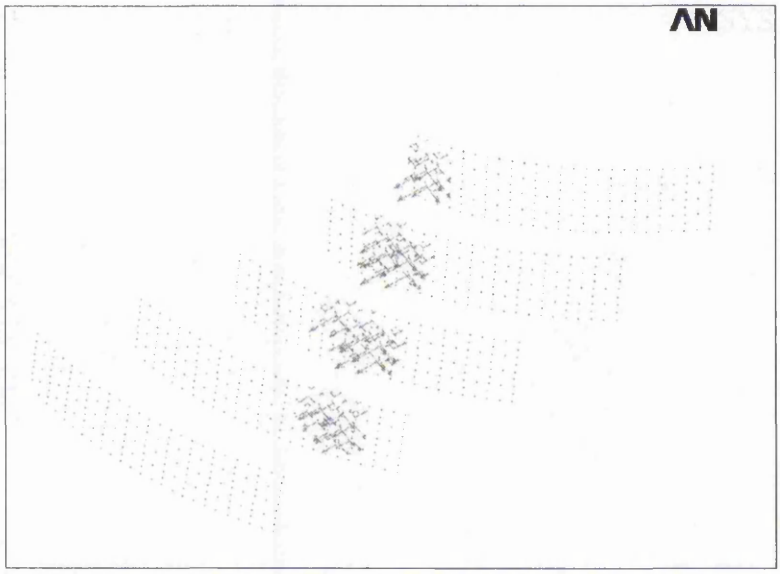


Figure 8.82 Gear tooth contact forces at contact position 1,load substep 4

Table 8.2 Gear tooth contact forces at position 1, load substep 4 (in global Cartesian CS)

	FX (N)	FY (N)	FZ (N)	MX (Nmm)	MY (Nmm)	MZ (Nmm)
TOOTH A	-553.6	-136.3	-445.27	-209.29	51764	-15589.06
TOOTH B	-1063.7	-266.7	-845.67	-2391.5	99082	-28258.29
TOOTH C	-1104.0	-280.7	-887.87	-4716.9	103395	-26855.74
TOOTH D	-831.7	-213.6	-680.75	-5289.8	78501	-18193.65
TOOTH E						
TOTAL	-3553.1	-897.5	-2859.58	-12607.6	332742.3	-88896.74

The contact forces in each tooth at position 1 are summarised in Table 8.2. The forces are expressed in the global Cartesian coordinate system. In this coordinate system, the moment MY is the applied gear torque, which is 332742 Nmm. The moment MX and MZ are resisted by the shaft. Therefore only the applied gear torque MY is discussed here and in the following sections.

The load share is defined here as the ratio of the torque each tooth contributed divided by the applied torque on the gear axis. It is calculated by Equation (8.12.1).

$$\rho_i = \frac{|\mathbf{T}_i|}{|\mathbf{T}_{app}|} \tag{8.12.1}$$

where ρ_i is the load share of the tooth i (i=A, B, C, D, E); $\mathbf{T}_i$ is the torque about the gear axis contributed by the tooth i ; $\mathbf{T}_{app}$ is the whole applied torque about the gear axis.

The gear tooth C has the maximum load share (31%). Tooth B has 30% load share which is slightly lower than tooth C. Though tooth A has the maximum stress, its load share is only 15.5% and is the lowest among the four simultaneous contact teeth. This is because its contact position is near to the edge of tooth and has the smallest buttressing effect among the contact teeth.

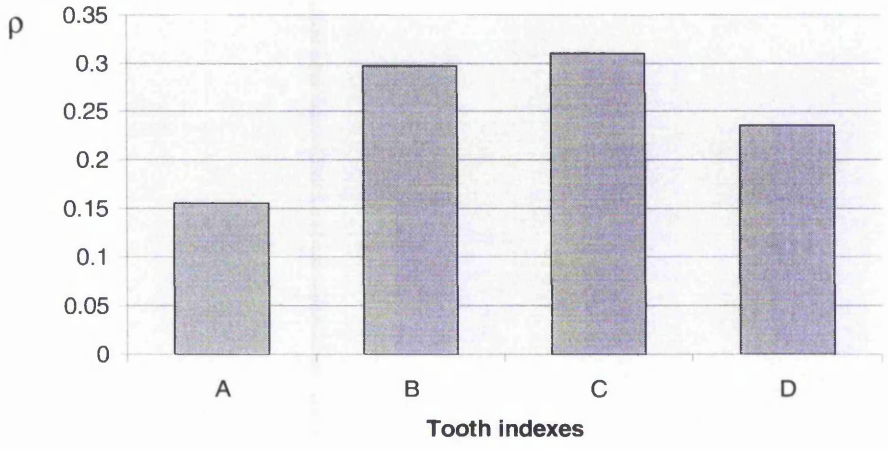


Figure 8.83 Gear tooth load share in whole gear applied torque at position 1

The total contact force in each tooth ($\mathbf{F}_i$) is the vector sum of the nodal forces on the contact region which have different orientations. Here only the magnitude of forces on each tooth is compared. Figure 8.84 shows the magnitude of gear contact forces on each contact tooth. The distribution pattern of contact forces is similar to that of load share. Tooth C has the largest force and tooth A has the smallest contact force.

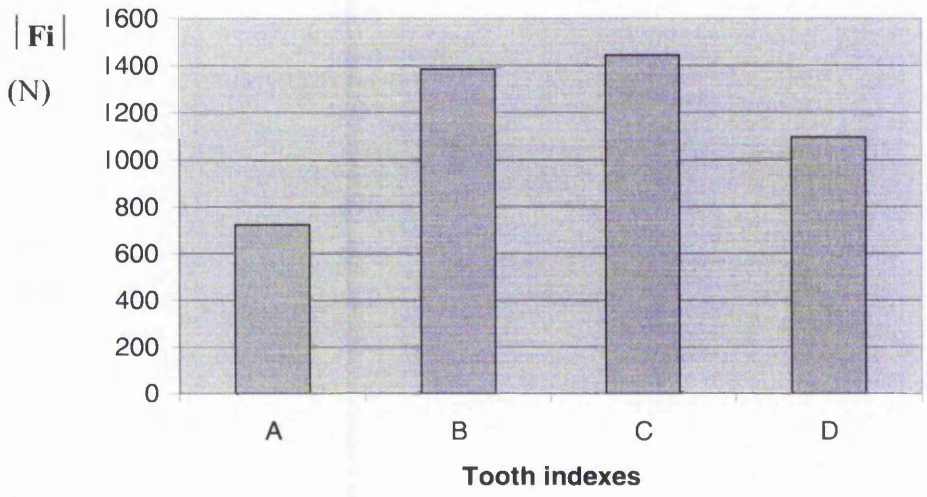


Figure 8.84 Gear tooth contact forces at contact position 1

8.12.2.2 Load Distribution at Position 2

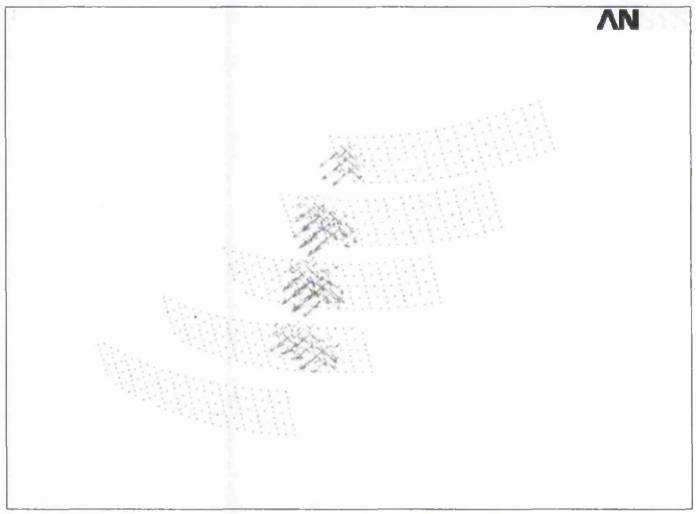


Figure 8.85 Gear tooth contact forces at contact position 2, load step 1, substep 4

Figure 8.85 shows the gear tooth contact force at contact position 2, load substep 4. Table 8.3 lists all the contact forces and their torque attribution in the global Cartesian coordinate system. When the gear rotates, the load share changes as well (see Figure 8.86 and Figure 8.87). Tooth A has the lowest load share and is only 11% of the total gear torque (15.5% at position 1). The two middle teeth have the largest share (63% in total). The load share of tooth D increases to 26% (23% at position 1).

Table 8.3 Gear tooth contact forces at position 2, load substep 4 (in global Cartesian CS)

	FX (N)	FY (N)	FZ (N)	MX (Nmm)	MY (Nmm)	MZ (Nmm)
TOOTH A	-399.0	-97.0	-311.0	-82.0	36908	-11383
TOOTH B	-1106.0	-275.0	-872	-2222.82	102729	-29664
TOOTH C	-1129.0	-286.0	-910.5	-4569.5	105848	-27632
TOOTH D	-926.0	-237.0	-754.0	-5600.0	87255	-18194
TOOTH E						
TOTAL	-3560.5	-896.84	-2850.2	-12474	332742	-20599

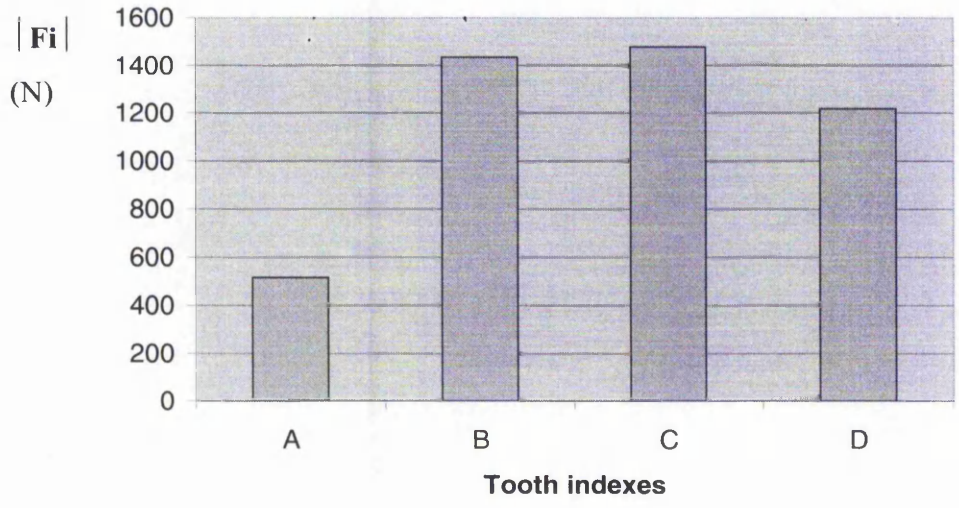


Figure 8.86 Gear tooth contact forces at contact position 2

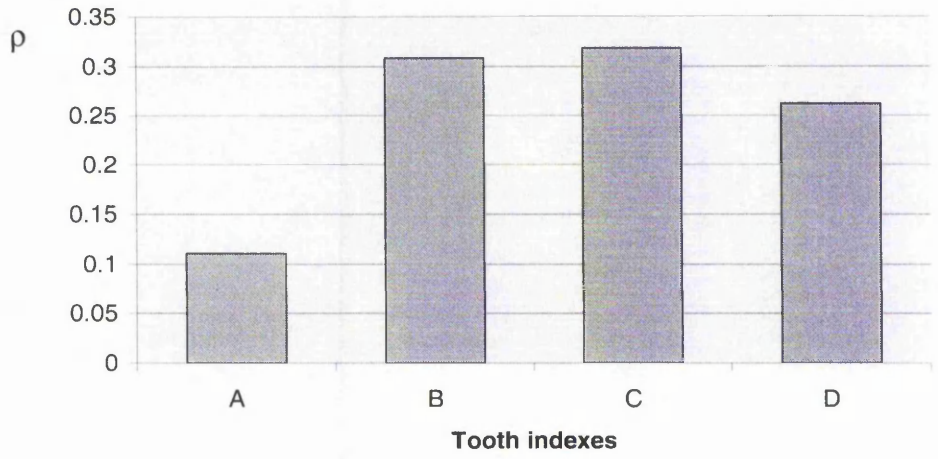


Figure 8.87 Gear tooth load share in whole gear applied torque at position 2

8.12.2.3 Load Distribution at Position 3

At position 3, the situation is quite similar to that at contact position 2. Figure 8.88 shows the gear tooth nodal contact force at contact position 3, load substep 4. Table 8.4 is the contact forces and their torque attribution expressed in global Cartesian coordinates. Comparing with position 2, tooth A and tooth B's load shares still decrease (see Figure 8.89 and Figure 8.90). Tooth C has the maximum load share (32.4%).

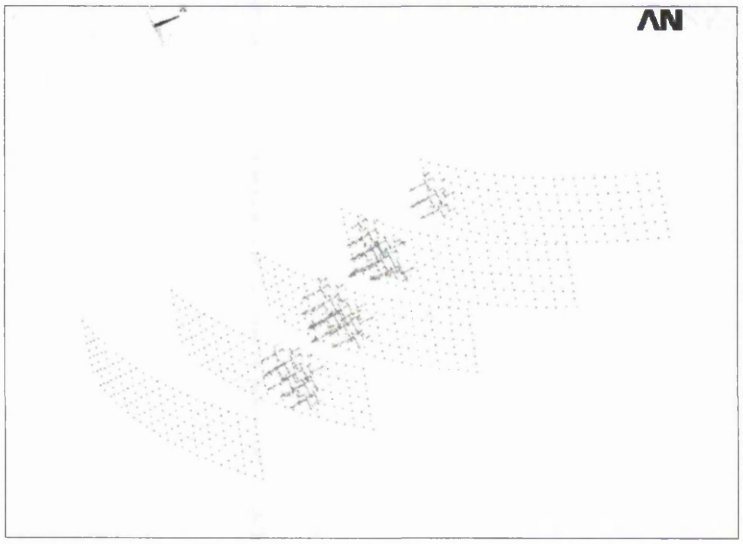


Figure 8.88 Gear tooth contact forces at contact position 3, load step 1, substep 4

Table 8.4 Gear tooth contact forces at position 3, load substep 4 (in global Cartesian CS)

	FX (N)	FY (N)	FZ (N)	MX (Nmm)	MY (Nmm)	MZ (Nmm)
TOOTH A	-375.7	-91.87	-303.3	32.7	35206.6	-10701
TOOTH B	-1075	-267.4	-849.1	-1900.7	99898	-29072
TOOTH C	-1154.9	-292.1	-922.6	-4289.2	107843	-28784
TOOTH D	-954.7	-244.4	-776.2	-5483.2	89793.6	-21560
TOOTH E						
TOTAL	-3560	-895.74	-2851.2	-11640	332742	-90118

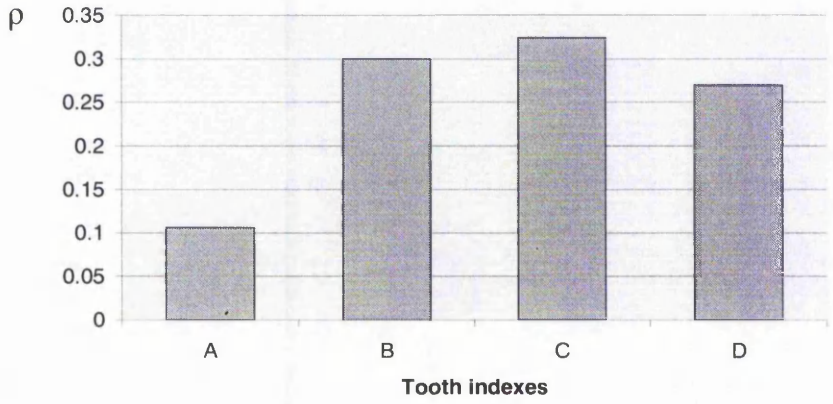


Figure 8.89 Gear tooth load share in whole gear applied torque, at position 3

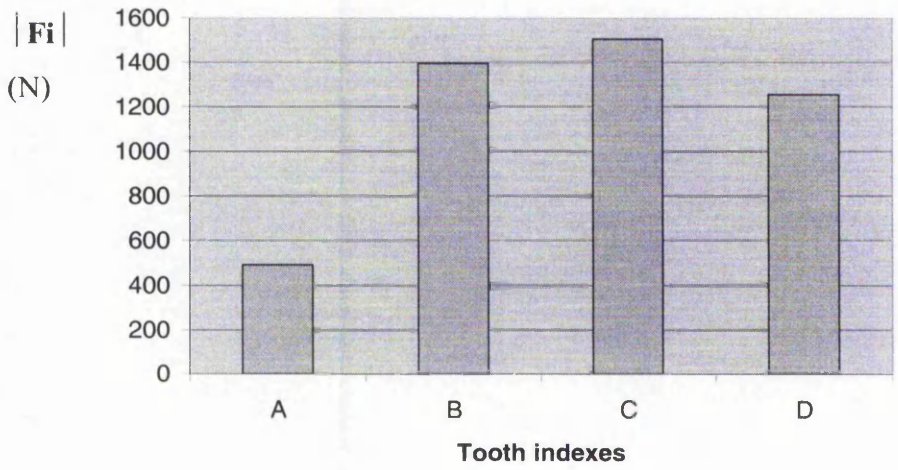


Figure 8.90 Gear tooth contact forces at contact position 3

8.12.2.4 Load Distribution at Position 4

Tooth A exits from contact at position 4 and there are only three tooth pairs in simultaneous contact. The gear tooth nodal contact forces are shown in Figure 8.85. Table 8.5 lists the contact forces and their torque contributions in global Cartesian coordinates. Since tooth A exits from contact, the load shares of the three teeth are all increased. Tooth C still has the maximum load share (37.4%) (see Figure 8.92 and Figure 8.93).

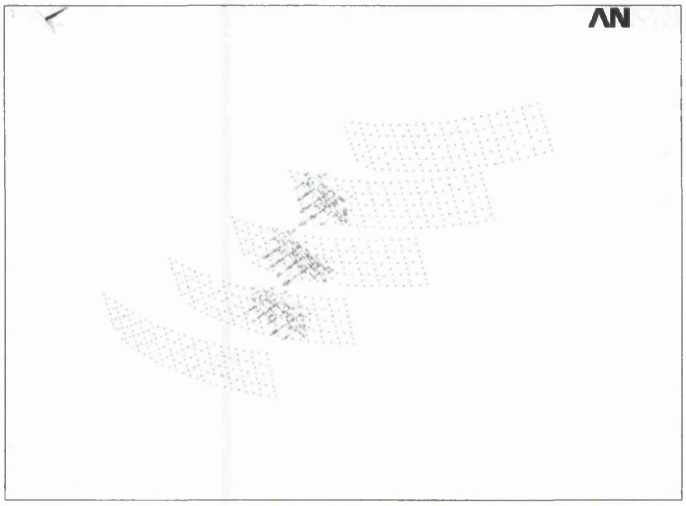


Figure 8.91 Gear tooth contact forces at position 4, load step 1, substep 4

Table 8.5 Gear tooth contact forces at position 4, load substep 4 (in global Cartesian CS)

	FX (N)	FY (N)	FZ (N)	MX (Nmm)	MY (Nmm)	MZ (Nmm)
TOOTH B	-1149.441	-286.9339	-916.2897	-1629.912	107150.2	-31521.73
TOOTH C	-1327.967	-336.2079	-1068.245	-4571.704	124337.5	-33471.32
TOOTH D	-1076.173	-275.7274	-874.6104	-5851.107	101251.5	-24744.80
TOTAL	-3553.581	-898.8692	-2859.145	-12052.72	332739.2	-89737.86

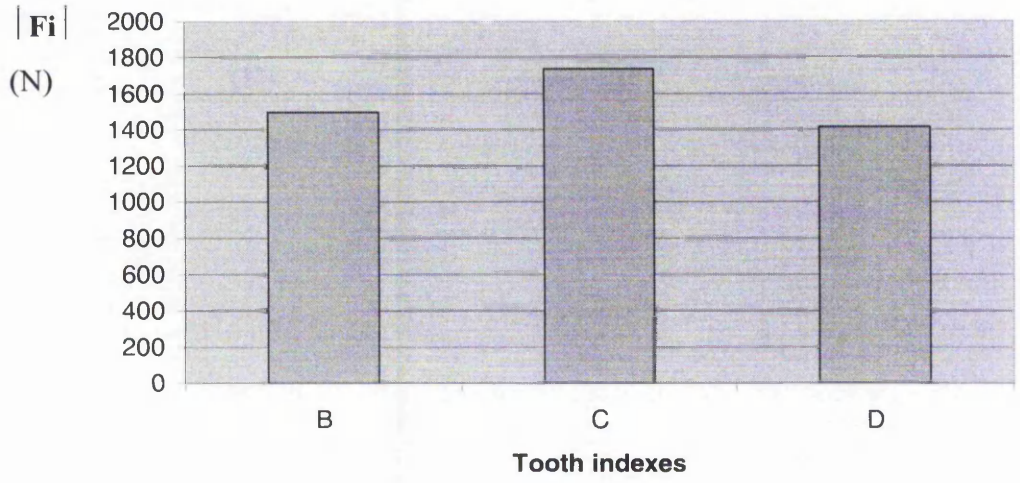


Figure 8.92 Gear tooth contact forces at contact position 4

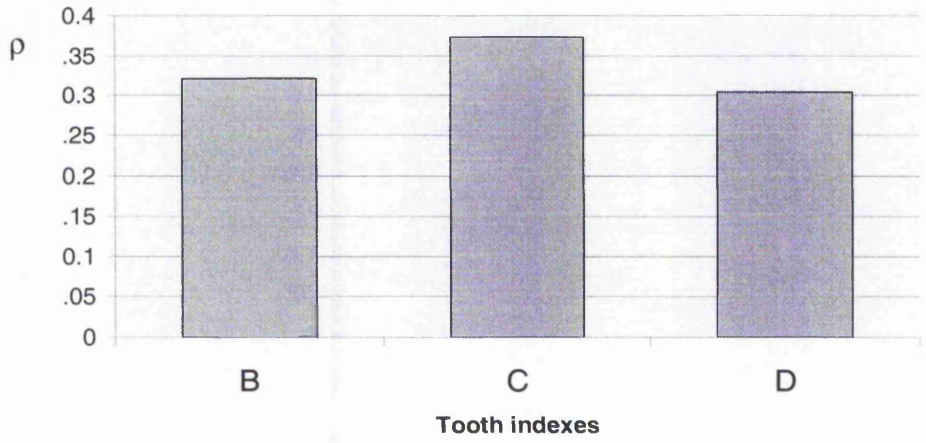


Figure 8.93 Gear tooth load share in whole gear applied torque at position 4

8.12.2.5 Load Distribution at Position 5

At position 5, the load share pattern is similar to that at position 4. There are three tooth pairs in simultaneous contact. Tooth C still has the largest load share. Tooth B's load share decreases while tooth D's load share increases (see Figure 8.95 to Figure 8.94).

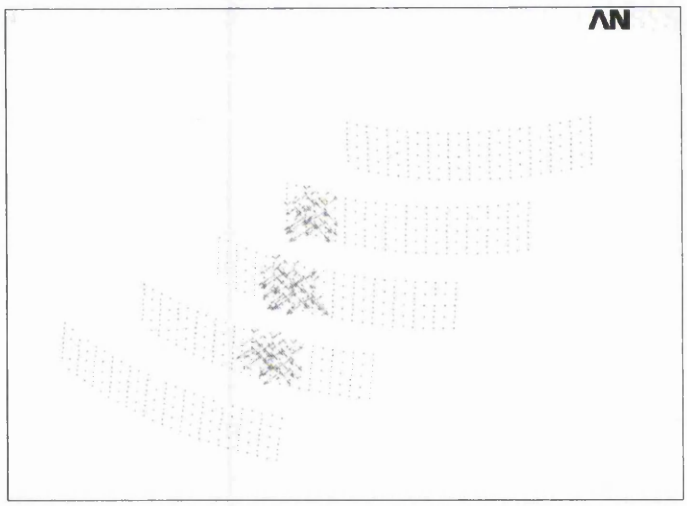


Figure 8.94 Gear tooth contact forces at contact position 5, load step 1, substep 4

Table 8.6 Gear tooth contact forces at position 5, load substep 4 (in global Cartesian CS)

	FX (N)	FY (N)	FZ (N)	MX (Nmm)	MY (Nmm)	MZ (Nmm)
TOOTH A						
TOOTH B	-1037.7	-257.3	-823.46	-1261.65	96551.0	-28579.0
TOOTH C	-1357.7	-342.6	-1085.48	-4287.8	126808	-34697
TOOTH D	-1165.8	-297.8	-941.04	-6010.5	109380	-27196
TOOTH E						
TOTAL	-3561.2	-897.6	-2849.98	-11559.9	332739.6	-90472.9

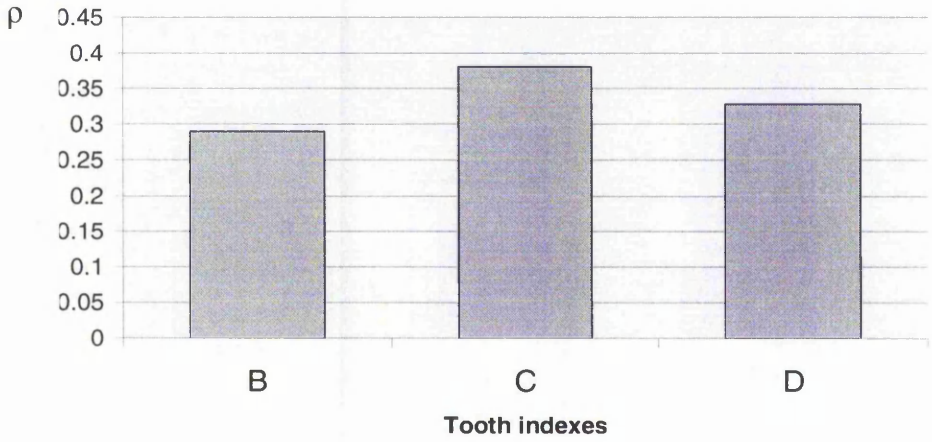


Figure 8.95 Gear tooth load share in whole gear applied torque at position 5

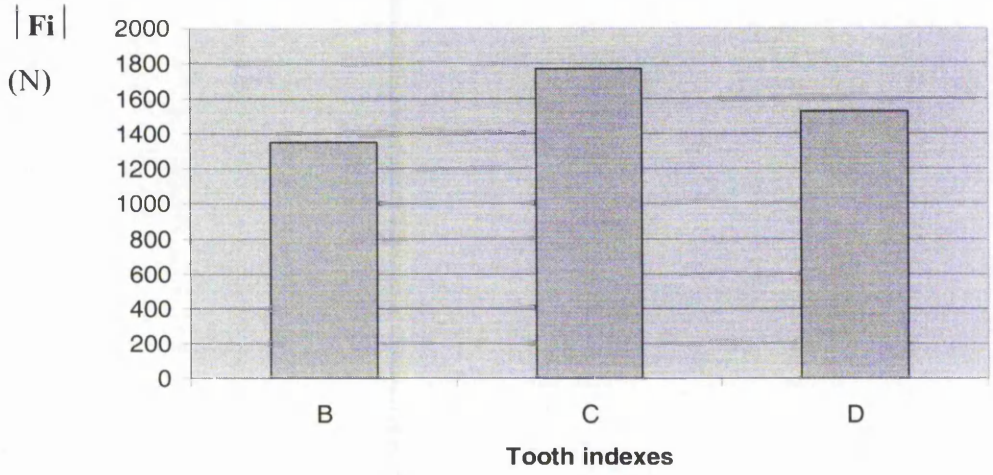


Figure 8.96 Gear tooth contact forces at contact position 5

8.12.2.6 Load Distribution at Position 6

At position 6, the contact status has changed again. Tooth E now is coming into contact. Figure 8.97 shows the gear tooth contact force (FX, FY, FZ) at contact position 6, load substep 4. Table 8.7 summarises the contact forces in each tooth and their torque attribution in global Cartesian coordinate system. Since one more tooth joins into contact, the load share of the other three teeth all drop a little (see Figure 8.98 and Figure 8.99). Tooth C still has the maximum load share (33%). Tooth D has 29.5% load share. The new contacting tooth, E, has 16% load share.

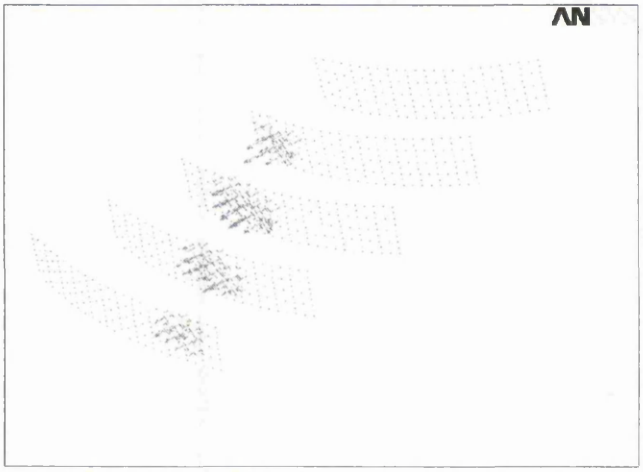


Figure 8.97 Gear tooth contact forces at contact position 6, load step 1, substep 4

Table 8.7 Gear tooth contact forces at position 6, load substep 4 (in global Cartesian CS)

	FX (N)	FY (N)	FZ (N)	MX (Nmm)	MY (Nmm)	MZ (Nmm)
TOOTH A						
TOOTH B	-747.6	-184.4	-589.2	-686.6	69357	-20829
TOOTH C	-1180.2	-296.5	-941.3	-3462.6	110112	-30414
TOOTH D	-1050.0	-267.4	-844.8	-5099.0	98366	-24818
TOOTH E	-586.2	-150.6	-470.7	-3911.3	54906	-12699
TOTAL	-3563.8	-898.9	-2846.0	-13123	332742	-88761

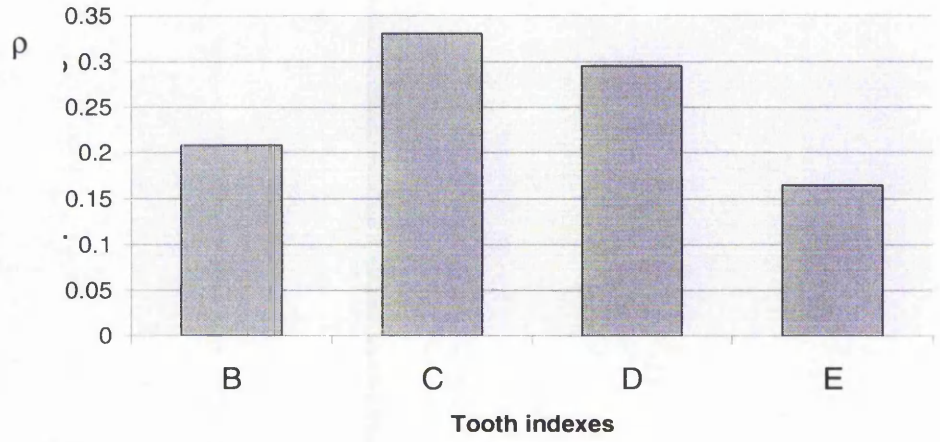


Figure 8.98 Gear tooth load share in whole gear applied torque at position 6

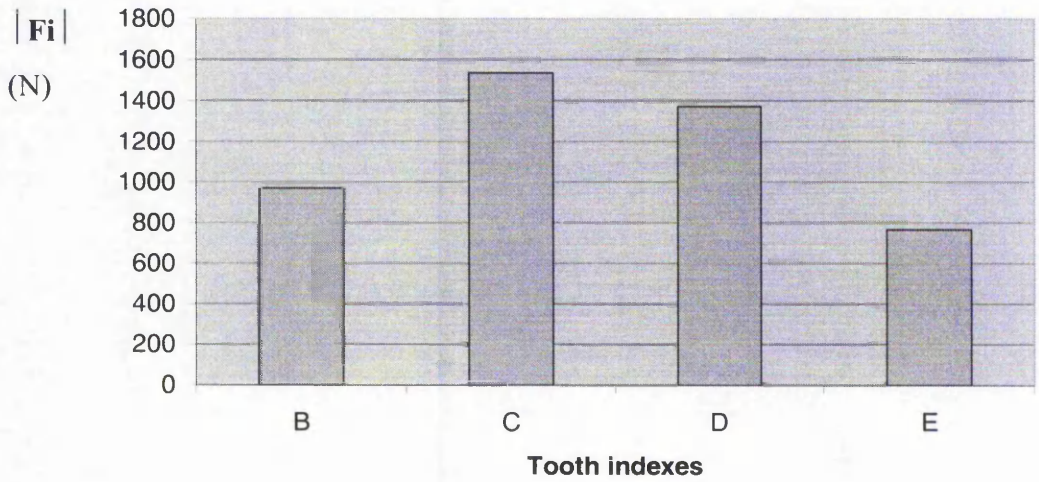


Figure 8.99 Gear tooth contact forces at contact position 6

8.12.2.7 Load Distribution at Position 7

Figure 8.100 shows the gear tooth contact force at contact position 7, load substep 4. Table 8.8 lists all the contact forces and their torque attribution in global Cartesian coordinates. The load share of tooth B decreases from 21% to 18.8% and has its lowest load share. Tooth C has the maximum load share but its load share is decreasing. Meanwhile the load share of tooth D is increasing. In the next contact position, tooth D will have the maximum load share (refer to position 1). The two middle teeth have the largest shares (59% in total).

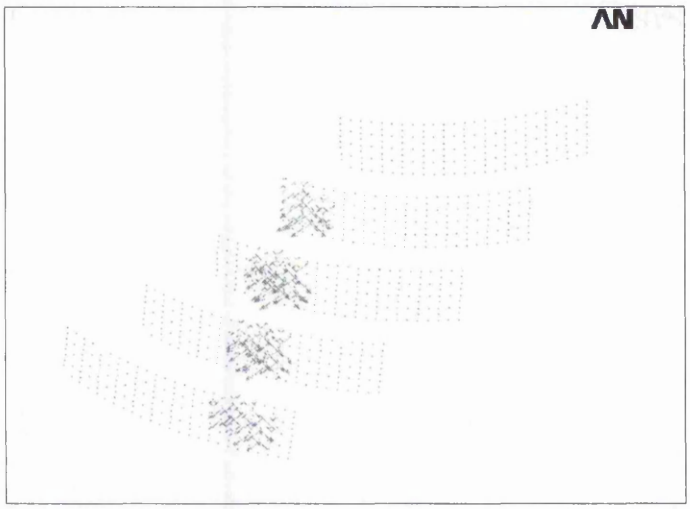


Figure 8.100 Gear tooth contact forces at contact position 7, load step 1, substep 4

Table 8.8 Gear tooth contact forces at position 7, load substep 4 (in global Cartesian CS)

	FX (N)	FY (N)	FZ (N)	MX (Nmm)	MY (Nmm)	MZ (Nmm)
TOOTH A						
TOOTH B	-666.1	-166.1	-542.2	-330.8	62582	-18761
TOOTH C	-1089.3	-274.3	-869.5	-2756	101648	-28652
TOOTH D	-1035.9	-263.7	-835.4	-4752	97135	-24803
TOOTH E	-756.9	-194.4	-618.1	-5009	71378	-16323
TOTAL	-3548.3	-898.4	-2865.0	-12847	332743	-88539

Figure 8.103 illustrate the gear and pinion tooth contact forces and the stress distribution pattern at position 7. The contact force distribution is quite similar to that given by classical Hertzian theory. The maximum contact force is located at the centre of contact region. The shapes of the contact regions are elliptical.

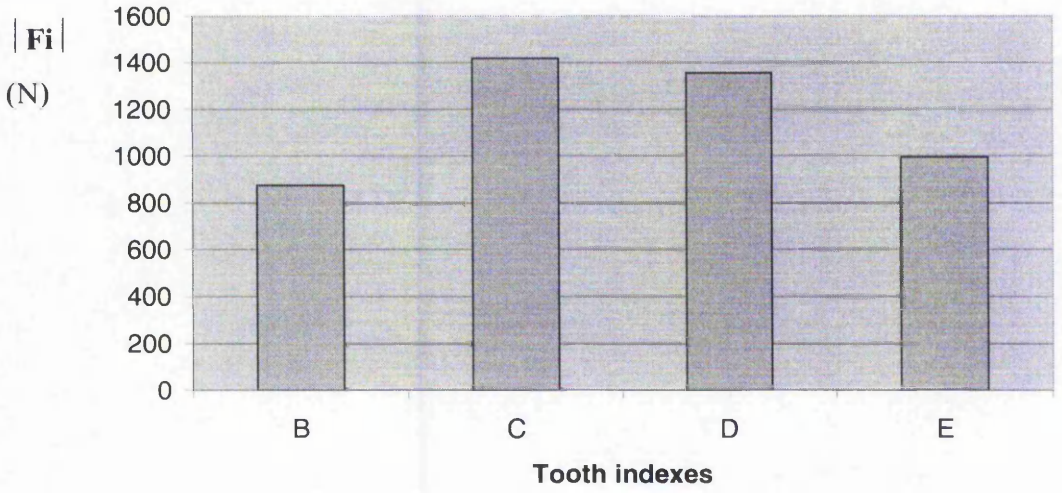


Figure 8.101 Gear tooth contact forces at contact position 7

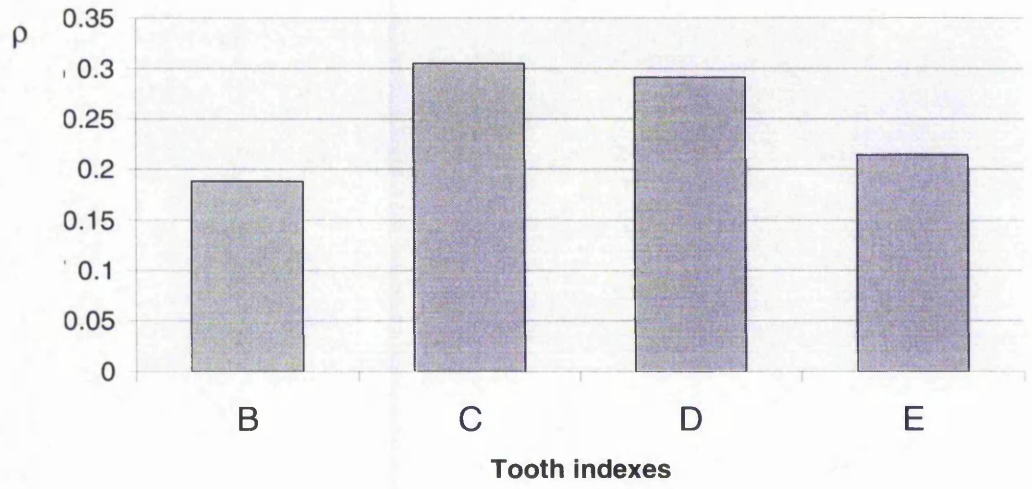


Figure 8.102 Gear tooth load share in whole gear applied torque at position 7

Since the loaded tooth contact analysis work is still in its infancy, there are no reference papers and published experimental data available to validate the finite

element models. In most cases, it is very expensive to do experimental validation. It is also very difficult to obtain loaded tooth contact pattern and stresses by experiment. The validation of the finite element contact model relies mostly on engineering intuition and judgements. Here, three criteria can be used for validation purposes of the loaded spiroid gear tooth contact analysis. Firstly, the contact pattern in each tooth should be correct. In the present model the contact patterns under load are unknown before the model is run. This is different from the traditional method that assumes a contact pattern beforehand. If there is a mistake in preparing the finite element model, the calculated contact pattern will be abnormal and can be identified easily. Secondly, the simulation of gear operation with different positions should be successful. Carefully examination of the positioning of the tooth contact regions during the simulation is required. If the model is right, the movement of the contact pattern will agree well with the actual gear operation. Thirdly, checking on the load share between contacting teeth, the middle tooth always has the largest load share. When the gear rotates, the entrancing gear tooth load share should be gradually increased and the exiting tooth load share should be gradually reduced. Only if the model is right then such results can be achieved.

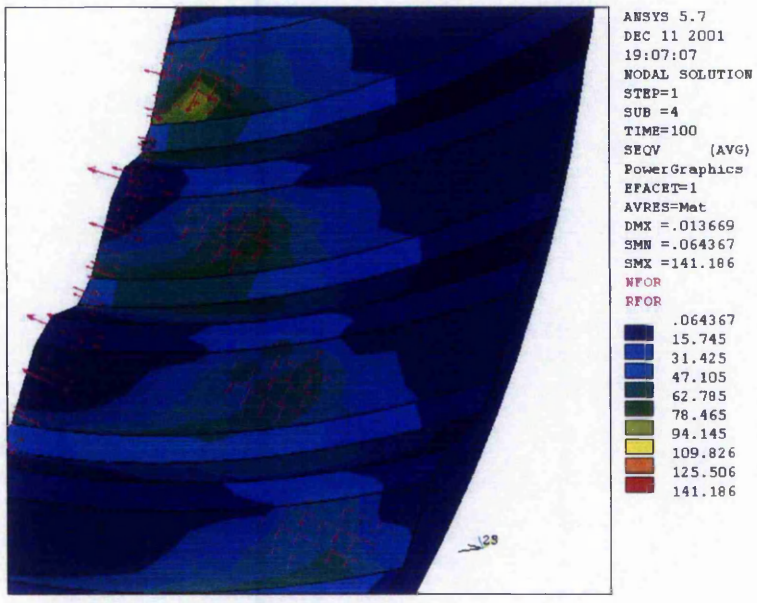


Figure 8.103 Gear tooth contact forces and Von Mises stress distribution at contact position 7, load substep 4.

8.13 CONCLUSIONS

One full spiroid gear model and seven simplified full models have been developed for the loaded multi-tooth contact analysis of spiroid gears. Another ten partial spiroid models and submodels have also been developed during this research.

Feasible procedures for the 3D spiroid gear modelling, geometry cleanup and 3D model generation have been developed and illustrated in this research. The advanced VGM 3D modelling technique allows quick and parametric 3D modelling of spiroid gears. The techniques developed for the spiroid gear geometry cleanup are general and can be used for other types of VGM gear models, e.g., worm gears. The developed FE procedures and techniques make the complicated loaded multi-tooth FE contact analysis simpler and more efficient. These procedures and techniques also make it possible for gear design engineers and researchers using FEM to analyse the loaded tooth contact behaviour of gear drives.

The advanced surface-to-surface contact techniques have been applied in the multi-tooth contact analysis. The contact boundaries are simulated by the general surface-to-surface contact elements that are more convenient and more suitable for simulation of real tooth contact than gap elements. The general tooth surface-to-surface contact techniques calculate the contact and determine the contact forces automatically. This technique makes the gear finite element model more efficient.

The whole range of spiroid gear engagement has been simulated by seven simplified full FE models with different contact positions. The spiroid gear contact stress distribution in the whole gear operation range has been illustrated and discussed in detail. The cross section stress patterns of gear and pinion are also visually presented which is almost impossible for experimental methods. The contact forces and load share of the spiroid gear have been analysed. The relation of the load share, the contact forces and the stresses with the different contact positions have been illustrated. The observed contact region is elliptical and the contact force distribution is similar to that from classical Hertzian contact theory.

The new discoveries in this chapter are summarised below:

1. Full contact models should be used, rather than partial models, for loaded multi-tooth contact analysis. The partial models were found not to be suitable for gear tooth contact analysis in this research. In contrast to the widely used practice that utilise partial models for loaded multi-tooth contact analysis, the partial models were found not to be accurate in the trial runs in the present partial models due to the problem of boundary simulation. This is a significant discovery for the loaded tooth contact analysis.

2. The boundary conditions have a significant influence on the final contact force and tooth stresses.

3. The middle tooth among the simultaneous contact teeth has the largest load share.

4. The load share on a tooth depends on the position of its contact region. The tooth with the contact region in its middle width has the largest load share. The tooth with the contact region near to its edge has the smallest load share.

5. Non-linear multi-tooth contact analysis requires very accurate tooth geometry. Analysts should pay special attention on the accuracy of model after the models are imported and subsequent geometry cleanup.

6. Hexahedral high order elements have very good performance for loaded gear tooth contact analysis.

7. When transferring gear geometry into ANSYS via the IGES interface, the *alternate* option should be used rather than the *default* option for gear contact models.

CHAPTER 9 Loaded Tooth Contact Analysis of Worm Gears

Six full finite element models using hexahedral elements have been developed to determine the contact forces and stresses in modified Holroyd involute worm gears. The 3D geometrical worm gear models are generated using the virtual gear manufacturing method. The model's geometry cleanups are completed in Pro/Engineer. The worm gear assemblies are imported into ANSYS 5.6.1 to build the finite element model. The contact boundaries are simulated by general surface-to-surface contact elements. The solution technique for generating an accurate surface-to-surface contact element model has been addressed. The procedure for performing three-dimensional stress analysis of worm gears in meshing has been developed. The contact forces and stress patterns in the whole gear operating range have been successfully simulated. The changes of load sharing and contact patterns in different positions agree well with the real situations.

9.1 INTRODUCTION

After the finite element contact analyses of spiroid gears had been successfully conducted, the established techniques were applied to the worm gears that were provided by Holroyd, a company specialising in worm gears. The 3D geometrical models were created using the virtual gear manufacturing technique. The unloaded localised tooth contact patterns have been investigated using Pro/Engineer. The 3D gear model's geometry cleanup work was completed in Pro/Engineer. The worm gear geometrical model is then imported into ANSYS to build the 3D finite element model. Due to the completely different geometry between spiroid and worm gears, the geometry cleanup techniques and meshing techniques required for worm gears are quite different from those for spiroid gears; therefore new geometry cleanup techniques and meshing techniques have been specially developed in this chapter.

There are two sets of worm gear data provided by Holroyd. In this chapter, the first worm gear set is used to illustrate how the gear tooth contact analyses are conducted. The second worm gear is not discussed here because the analysis procedure is the same as the first set. The design data and 3D modelling of the second worm gear are presented in Appendix D.

9.2 GENERATION OF 3D WORM GEAR MODELS

The worm gear was virtually hobbed on a computer using the virtual gear manufacturing method. The 3D modelling technique has been described in detail in Chapter 7.

9.2.1 Worm Gear Design

The Holroyd worm gear set studied and described in this chapter is right hand involute type. The worm has 6 threads and the gear has 31 teeth as listed in Table 9.1. The centre distance is fixed to 125 mm. This worm gear design is not a standard one with the quotient of designation being 6.5031, whereas it is usually an integer in standard design. The normal pressure angle is 22.5°. The worm has a very high lead angle (42° 42′).

Table 9.1 Worm gear I reference information

Threads	6
Teeth	31
Centres	125.0000 mm
Hand	Right
Lead Form	Single
Design	Involute Helix
Backlash	0.102 mm
Quotient	6.5031
Module	6.7805
Normal Pressure Angle	22.5
Wheel Oversize	1.27 mm
Wheel Cutter Type	Fly

Since the method of worm gear modification is the commercial confidential to the company, how they modify the worm gear is unknown. However, which parameters

are modified and how much they are modified can be determined by comparison with the standard design of worm gear.

The standard design of a worm gear has been calculated according to the quotient of designation (6.5031) which Holroyd used in this design. The results for standard design of worm gear are listed in Table 9.2. From the calculated data it can be seen how Holroyd modify the parameters of their tooth profile.

For the sake of convenience, the Holroyd worm gear and the standard design worm gear are denoted as worm gear I and worm gear Is respectively. The comparison data of the Holroyd gear design and the standard gear design are listed in Table 9.3 to Table 9.5.

Table 9.2 Design of Involute Helicoid Worm Gear Is (length units: mm)

	Formula	**Value**
Module	m	6.7805
Normal pressure angle	ψ_n	22.5
Diameter quotient	q	6.5031
No. of starts: worm	t	6
No. of teeth : gear	T	31
Ratio	T/t	5.16667
Axial pitch of worm	$m\pi$	21.30157
Worm pitch diameter	mq	44.09427
Gear pitch diameter	mT	210.1955
Centre distance	C=0.5m(T+q)	127.14488
Lead	L=$m\pi t$	127.80941
Lead Angle	$\lambda=\tan^{-1}(t/q)$	42.69577°
Normal Module	$m_n = \frac{m \cdot q}{\sqrt{t^2 + q^2}}$	4.98343
Axial pressure angle	$\psi_a = \tan^{-1}\left(\frac{\tan(\psi_n) \cdot \sqrt{t^2 + q^2}}{q}\right)$	0.51321 (in radian)

Transverse pressure angle	$\psi_t = \tan^{-1}\left(\frac{\tan(\psi_n)\cdot\sqrt{t^2+q^2}}{t}\right)$	0.54835 (in radian)
Base diameter	$d_0 = d\cdot\cos(\psi_t)$	37.62939
Base lead angle	$\lambda_0 = \cos^{-1}\left(\frac{q\cdot\cos(\psi_n)}{\sqrt{t^2+q^2}}\right)$	47.23299
Worm addendum	a=m	6.7805
Worm dedendum	b=m[2.2cos(λ)-1]	4.18304
Wheel addendum	A=m[2cos(λ)-1]	3.18636
Wheel dedendum	B=m[0.2cos(λ)+1]	7.77719
Clearance	c=0.2m cos(λ)	0.99669
Tip diameter of worm	d_a=m(q+2)	57.65527
Outside diameter of wheel	J=D+2A+m	223.34871
Throat diameter of wheel	D_t=D+2A	216.56821
Root diameter of worm	d_r=d-2b	35.72819
Root diameter of wheel	D_r=D-2B	194.64113
Worm minimum face width	$f_p = \sqrt{J^2 - D^2}$	75.51
Wheel maximum face width	$F_e = 2\cdot m\cdot\sqrt{q+1}$	37.15

The calculations show that nearly all the data of the Holroyd worm gear design are the same as the standard design. The Holroyd worm is a standard design as shown in Table 9.3. The wheel's dimensions have small changes in order to be consistent with the fixed centre distance 125 mm (127.1449 mm in the standard design). Holroyd's wheel is 211.0888 mm in outside diameter (223.3487 mm in the standard design), 190.3511 mm in root diameter (194.6411 mm in the standard design) and 208.3766 mm in throat diameter (216.5682 mm in the standard design). The dimensions that have changed are highlighted in the table. From the calculations it can be seen that the wheel cutter is a standard design. However, the Holroyd hob is oversized. Its outside diameter is 60.919 mm which is 2.302 mm oversized. Its root diameter is 40.400 mm which is 3.71 mm larger than that in the standard design.

Table 9.3 Worm I and Is dimensions (length units: mm)

	WORM I	WORM Is
Axial Pitch	21.3017	21.3015
Lead	127.8100	127.8094
Base Diameter	37.6296	37.6294
Pitch Diameter	44.0945	44.0943
Root Diameter	35.728	35.7282
Outside Diameter	57.656	57.65527
Case Depth	1.1438	
Roughing Allowance	0.2540	
Grinding Allowance	0.3048	
Normal Pitch	15.6560	15.656
Lead Angle	42° 42′	42° 41′ 45″
Base Lead Angle	47° 14′	47° 13′ 59″
Tooth Height	10.964	10.9635
Clearance	0.9967	0.9967
Calliper Depth	5.134	
Calliper Thickness	8.511 (Milled)	
Calliper Thickness	8.257 (Ground)	
Calliper Thickness	7.952 (Finished)	

Table 9.4 Wheel I and Is Setting (length units: mm)

	WHEEL I	WHEEL Is
Face width	37.1462	37.1462
Outside Diameter	211.0888	223.3487
Pitch Diameter	210.1964	210.1955
Root Diameter	190.3511	194.6411
Max Shrunk Bore	171.3561	
Max Bolted Bore	175.4007	
Throat Diameter	208.3766	216.56821
Throat Radius	20.8117	20.8117



Table 9.5 Wheel cutter I and Is setting (length units: mm)

	WHEEL CUTTER I	**WHEEL CUTTER Is**
Machine Set Up	Fly	Fly
Axial Pitch	20.8181	20.8181
Lead	124.9086	124.9086
Base Diameter	38.4096	38.4091
Root Diameter	40.400	36.68997
Outside Diameter	60.919	58.6170
Cutting Centres	125.6350	125.3943
Threads	6	6
Normal Pitch	15.6560	15.6560
Lead Angle	41° 14′	41° 14′
Base Lead Angle	45° 59′	45° 59′
Calliper Depth	6.130	
Calliper Thickness	8.054	
Tilt Angle	1° 28′	

9.2.2 Worm and Hob Axial Tooth Profiles

To build the worm and hob, the axial section of the worm and hob tooth profiles are required. In order to obtain the axial section the worm and hob, the surface equations of the worm and hob are needed.

The Holroyd worm gear is an involute type. The surface equation of an involute worm is derived from its generating method which is illustrated in Figure 9.1.

The surface of an involute type worm is generated by a straight-line that performs a screw motion, being tangent to the helix P_0P on the base cylinder. In Figure 9.1, the cutting edge of the tool is tangent to both the base cylinder and the helix curve, the

radius of base cylinder is r_b, and λ_b is the lead angle of the base cylinder of the worm.

The worm cutter is always placed in the tangent plane of the base cylinder. When the cutting tool moves along the screw trajectory, the surface generated by its edge is the tooth profile of the involute worm. The worm tooth profile in cross section is an involute curve (see Figure 9.2).

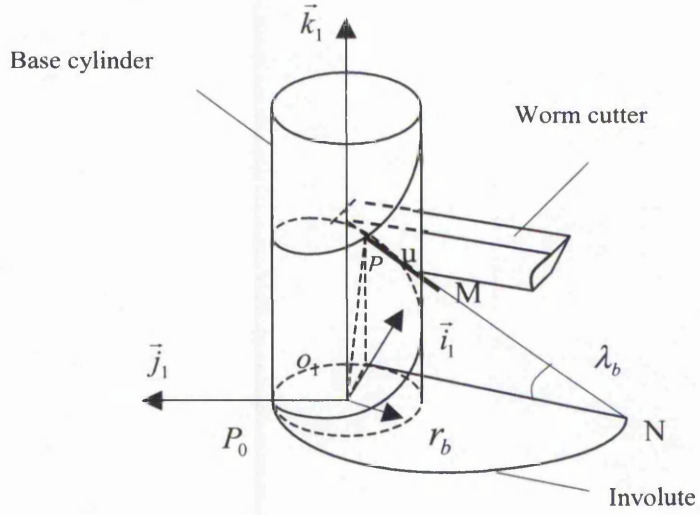


Figure 9.1 Generation of involute worm surface

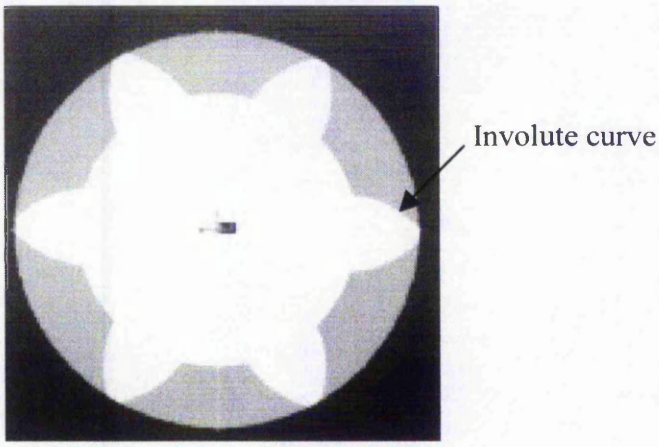


Figure 9.2 Worm cross section involute curve

The involute worm tooth surface can be derived from Figure 9.1 and written as follows

$$\mathbf{r}_1 = \begin{pmatrix} x_1 \\ y_1 \\ z_1 \end{pmatrix} = \begin{pmatrix} r_b \cdot \cos\theta + u \cdot \cos\lambda_b \cdot \sin\theta \\ r_b \cdot \sin\theta - u \cdot \cos\lambda_b \cdot \cos\theta \\ -u \cdot \sin\lambda_b + p\theta \end{pmatrix} \tag{9.1}$$

where,

$\mathbf{r}_1$ is the position vector of the worm surface,

r_b is the radius of base cylinder of the worm,

λ_b is the lead angle of the worm,

p is the screw parameter of the worm.

u and θ are the surface parameters.

The axial section profile of the involute worm can be derived from above equations. Let x_1=0, then

$$r_b \cdot \cos\theta + u \cdot \cos\lambda_b \cdot \sin\theta = 0 \tag{9.2}$$

Rearranging this equation gives

$$u = -r_b \cot\theta \sec\lambda_b \tag{9.3}$$

Substituting u for y_1, then yields

$$y_1 = r_b \csc\theta \tag{9.4}$$

Solving this equation for θ yields

$$\theta = \arcsin\frac{r_b}{y_1} \qquad (0 < \theta < \frac{\pi}{2}) \tag{9.5}$$

$$\theta = \pi - \arcsin\frac{r_b}{y_1} \qquad (\pi > \theta \geq \frac{\pi}{2}) \tag{9.6}$$

Using Equations (9.3), (9.5) and (9.6), the through axis section curve of a ZI worm tooth is obtained as follows

$$z_1 = \tan\lambda_b \sqrt{y_1^2 - r_b^{\,2}} + p \arcsin\frac{r_b}{y_1} \qquad (0 < \theta < \frac{\pi}{2}) \qquad (9.7)$$

$$z_1 = -\tan\lambda_b \sqrt{y_1^2 - r_b^{\,2}} + p(\pi - \arcsin\frac{r_b}{y_1}) \qquad (\pi > \theta \geq \frac{\pi}{2}) \qquad (9.8)$$

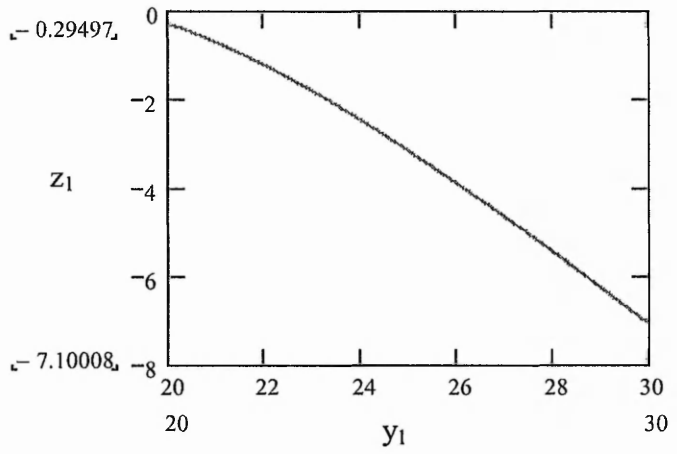


Figure 9.3 Axial tooth profile of worm I (mm)

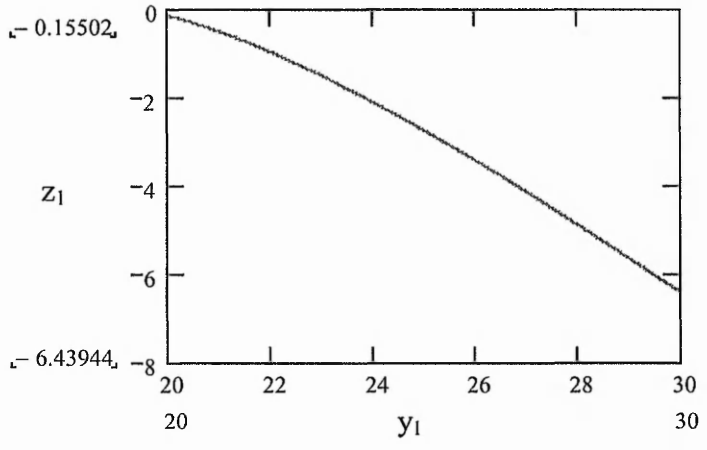
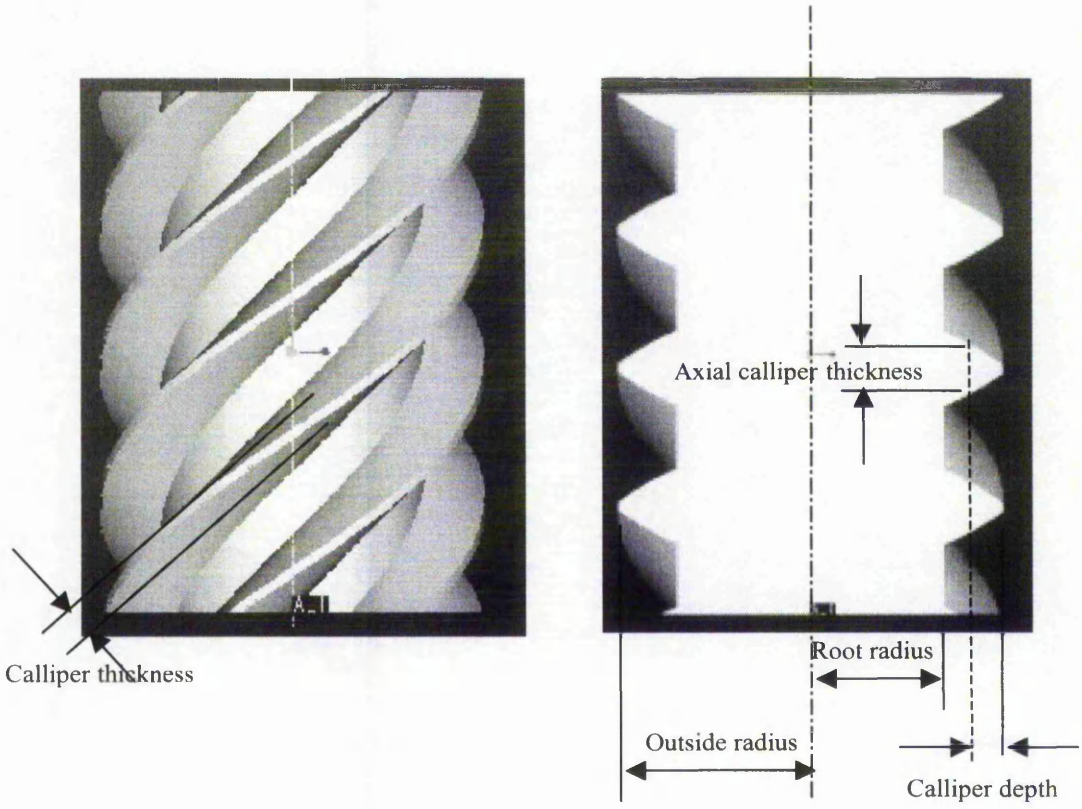


Figure 9.4 Axial tooth profile of hob I (mm)

The axial section of the worm or hob can be calculated numerically. Figure 9.3 shows the Holroyd worm axial tooth profile and Figure 9.4 shows the Holroyd wheel cutter's axial tooth profile. The xm in Figure 9.3 is the radius of the worm and the xw in Figure 9.4 is the radius of the wheel cutter. These axial tooth profiles will be used to construct the solid models of the worm and wheel cutter.

According to the root radius and outside radius of the worm and wheel cutter, the axial tooth profiles can be determined. However, the tooth thickness has to be derived from the calliper tooth thickness listed in Table 9.3 and Table 9.5. The calliper thickness in the tables is measured from the normal section of the worm or wheel cutter (see Figure 9.5 (a)). The relation of calliper depth, calliper thickness and axial calliper thickness is shown in Figure 9.5.



(a) Involute worm gear (b) Axial section of involute worm gear

Figure 9.5 Worm gear calliper depth and thickness diagram

The axial tooth thickness can be obtained from the following equation.

$$T_{ac} = \frac{T_c}{\cos \lambda_c} \tag{9.9}$$

in which, T_{ac} is the axial calliper tooth thickness; T_c is the normal calliper tooth thickness and λ_c is the lead angle of the helix curve. This helix curve is the intersection of the surface of the worm or wheel cutter with a concentric cylindrical surface at the calliper depth.

From the axial calliper tooth thickness, the axial top land width of the worm or wheel cutter can be determined from the following equation.

$$T_{atop} = T_{ac} - 2 \cdot \left| z(r_{ac}) - z(r_{out}) \right| \tag{9.10}$$

in which, T_{atop} is the axial width of the top land, r_{ac} is the radius in the calliper depth, r_{out} is the outside radius of the worm or wheel cutter and z is the function expressed in Equation (9.7) and (9.8).

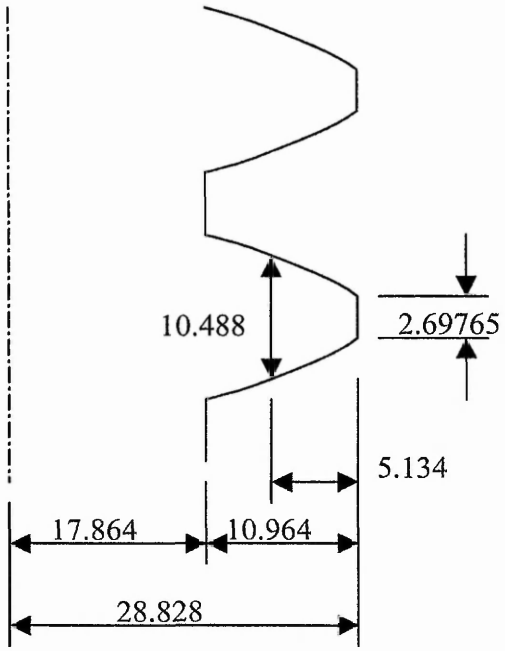


Figure 9.6 Worm I axial tooth profile pitch=21.3017 mm

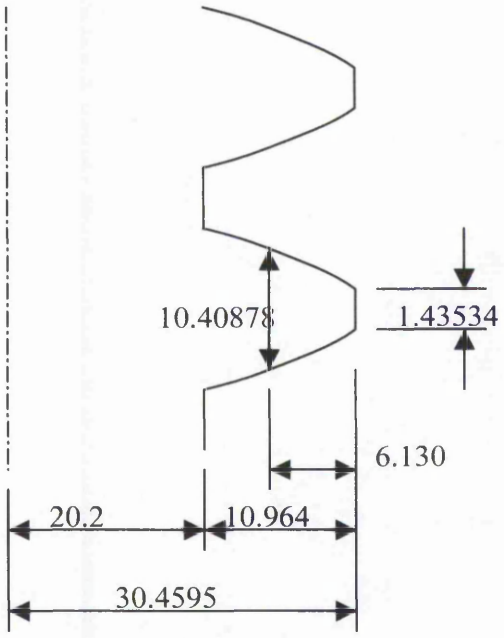


Figure 9.7 Wheel cutter I axial tooth profile pitch=20.8181 mm

The dimensions of the worm axial tooth profile calculated from above equation are shown in Figure 9.6. Figure 9.7 illustrates the dimensions of the wheel cutter's axial tooth profile.

9.2.3 Generation of 3D Worm and Hob Models

With the dimensions of the axial tooth section, the worm and wheel cutter's axial sections are produced in Pro/Engineer Sketcher Mode as follows:

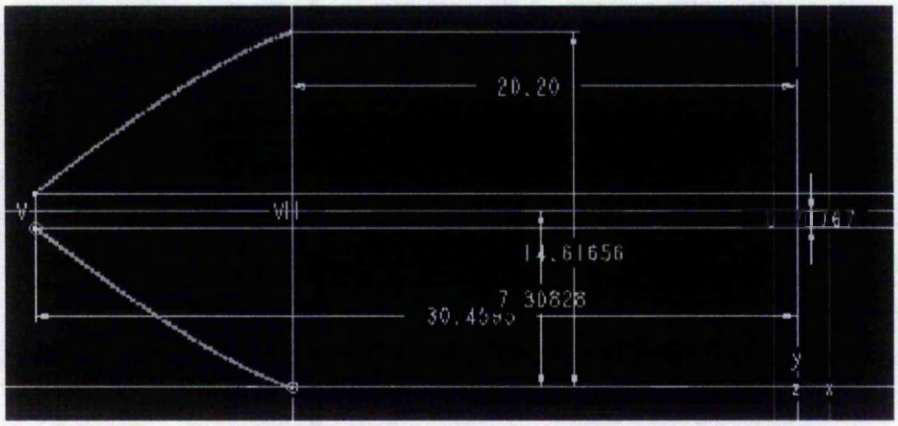


Figure 9.8 Wheel cutter's axial section tooth profile

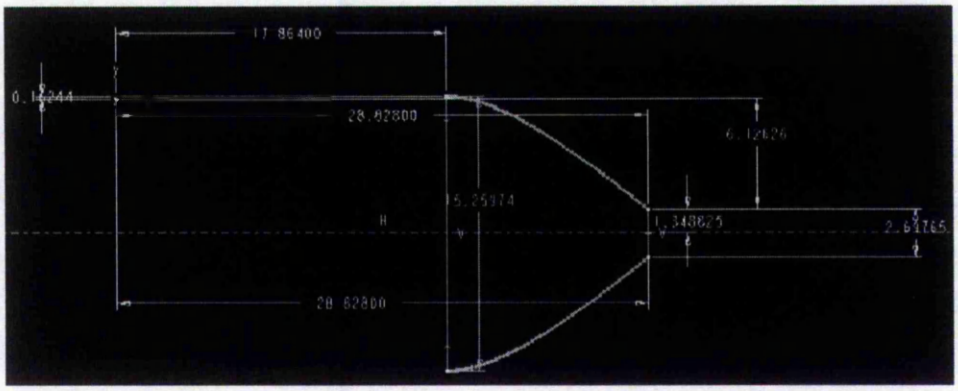


Figure 9.9 Worm axial section tooth profile

In the **Menu Manger**, select **Sketcher**. Then

1. Select the **Spline** option from the submenu **Advanced Geometry**. Sketch a three-point spline.
2. Sketch a local coordinate system.
3. Dimension the three point spline to the local coordinate system using the following procedures: (1) pick the spline twice; (2) pick the local coordinate system. If a message is seen that say that the spline has been dimensioned to the local coordinate system, then the work is done.
4. Modify the local start point and end point of the spline with the dimensions exactly the same as the gear tooth axial profile.
5. Select **Modify** from **Sketcher** menu. Then pick the spline using the mouse. A submenu will appear. Select **Read Points**. In the prompt input window, input the name of the data file, which should be in the working directory.
6. Sketch a centre line, which is at the middle of the tooth thickness.
7. Mirror the spline.
8. Draw the tooth top line and bottom line to form an enclosed section.

The completed axial section of the wheel's cutter is shown in Figure 9.8. This section will be used to hob the wheel blank. Figure 9.9 shows the finished axial section of the worm. This section will be used to generate the worm later.

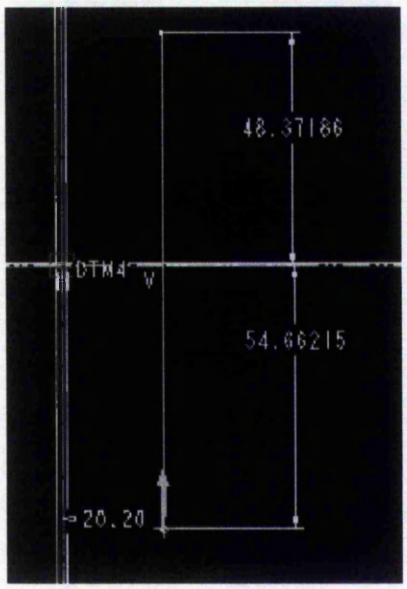
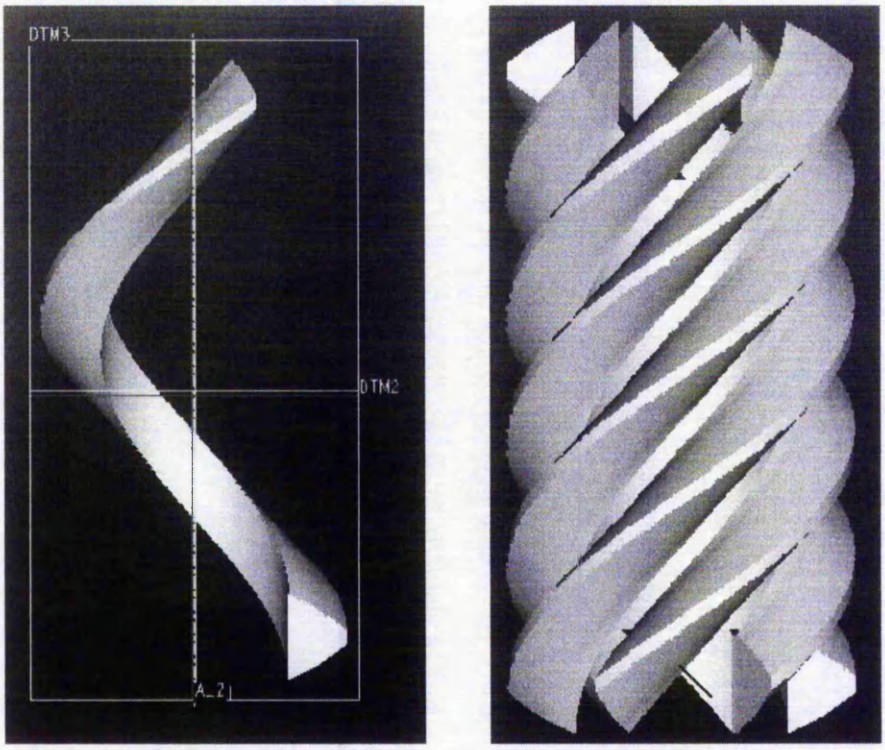


Figure 9.10 Wheel cutter's sweep profile



(a) Single thread (b) Six threads and core column

Figure 9.11 Generation of worm I

The worm and the wheel cutter are generated using the *helical sweep protrusion* function. In the **Feature** menu, Select **Create**; then **Solid/Protrusion/Advance Feat**; then in the pop up menu, select **Helical Sweep /Right Hand/Axial Section**.

After the sketching and reference planes are selected, the sweep profile can be drawn. The completed swept profile of a wheel cutter is shown in Figure 9.10. The sweep profile for the worm is similar to that for the wheel cutter.

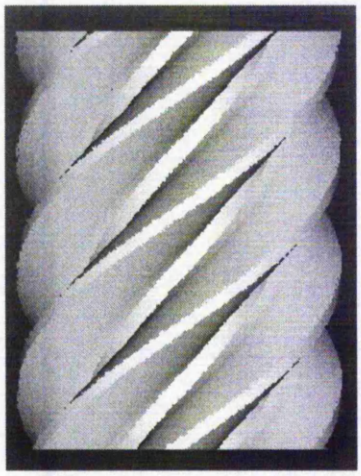


Figure 9.12 3D model of worm I

Since gear tooth contact analysis requires very high accuracy, the default relative accuracy is not suitable. The absolute accuracy is used instead of the relative accuracy and the value is set to 0.0001. With such a high absolute accuracy, it was found that the generating method of the worm and wheel cutter is different from those with lower accuracy. If the relative accuracy is used, the normal practice is to generate the column first, and then to produce the worm or wheel solid model using the *helical sweep cut* or *helical sweep protrusion* function. The generating time of the worm is normally within a few seconds. But with the high absolute accuracy, such a procedure yields the problem that Pro/Engineer will take very long time to calculate (e.g. In one case, the program did not generate one thread in two hours, and the worm has six threads!!!). A lot of time has been spent on overcoming the problem and it was finally found that this is primarily caused by the accuracy. The author considers that this is a problem resulting from Pro/Engineer's internal algorithm. If the accuracy level is relaxed, the geometry can be constructed within seconds.

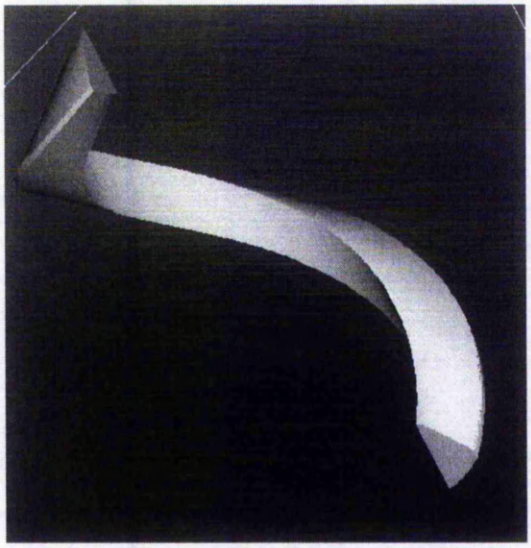
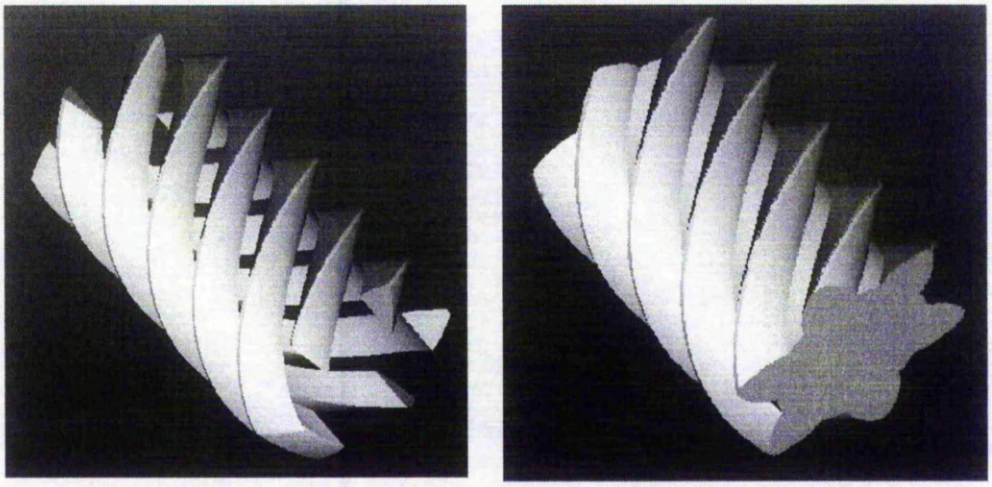


Figure 9.13 Single thread of wheel cutter I



(a) Six threads (b) 3D model

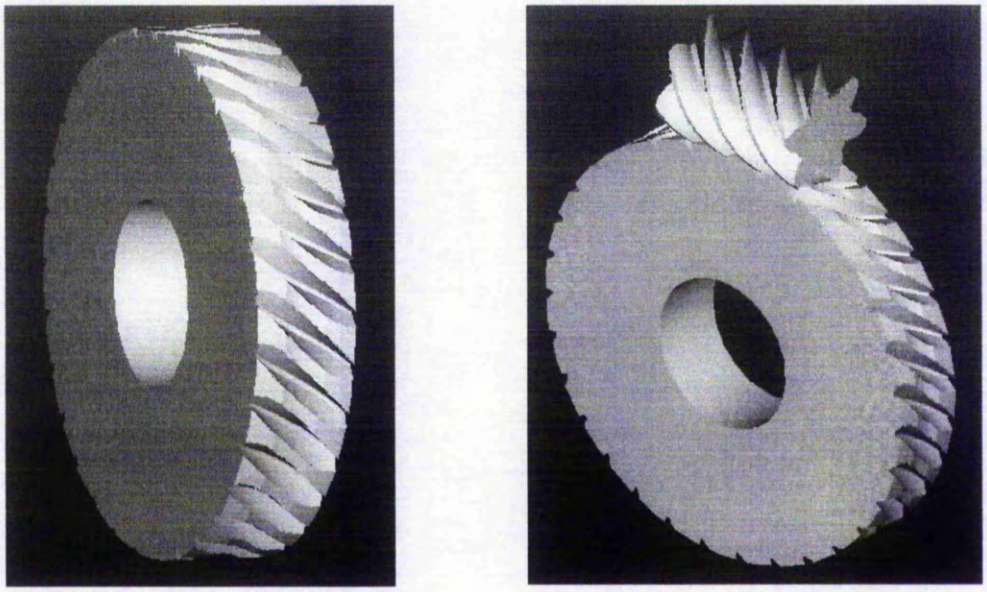
Figure 9.14 Generation of wheel cutter I

So an alternative method to generate the worm and wheel cutter has to be found. The problem can be solved by reversing the procedure used in normal practice. Figure 9.11 and Figure 9.14 shows the procedure for the alternative method used. Instead of creating the column in the first step, the worm or wheel cutter's thread is created first (see Figure 9.11 (a) and Figure 9.13). Then the single thread is patterned into six

threads (see Figure 9.11 (b) and Figure 9.14 (a)). After the six threads have been successfully created, then the core column is protruded. By doing so, the worm or hob geometry can be created quickly. Cutting off the unwanted part, the 3D worm or wheel cutter can be generated. The completed 3D worm and wheel cutter models are shown in Figure 9.12 and Figure 9.14 (b) respectively.

9.2.4 Generation of Gear Model

The generation of the 3D gear model is the same as described in Chapter 6 using the VGM method. The wheel is virtually hobbed by the wheel cutter. The created 3D worm gear model is shown in Figure 9.15 (a). The worm and the gear are assembled together according to its design specifications and are shown in Figure 9.15 (b).



(a) 3D model of gear I (b) Assembly of worm gear I

Figure 9.15 3D model of worm gear

9.3 UNLOADED TOOTH CONTACT PATTERNS

After the wheel's tooth surface is polished using the method described in Section 9.4, the worm gear can be used to analyse the unloaded tooth contact pattern.

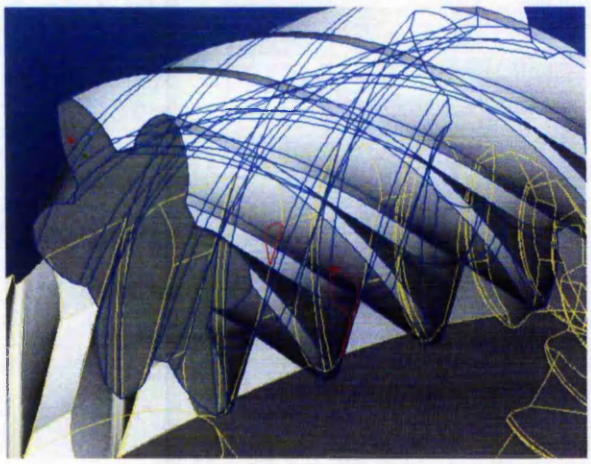


Figure 9.16 Contact pattern 1

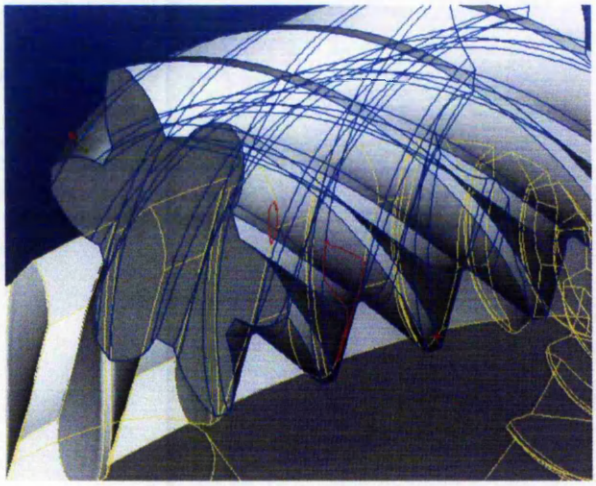


Figure 9.17 Contact pattern 2

The worm gear contact patterns in one tooth operation range (the gear rotates a total angle of 11.6129°, the worm rotates a total angle of 60°) are shown from Figure 9.16 to Figure 9.20. The contact patterns have been presented to a worm gear design engineer at Holroyd's and a worm gear manufacturing engineer at Renold Gears. They confirmed the contact patterns. The shapes of these contact patterns also agree with the results for the loaded gear tooth contact analysis (see Section 9.8.1 Stress Pattern).

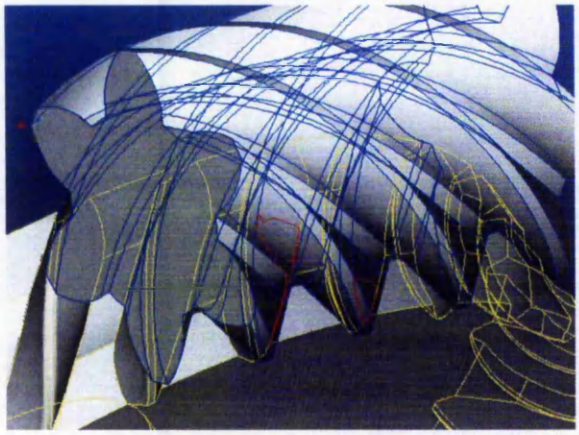


Figure 9.18 Contact pattern 3

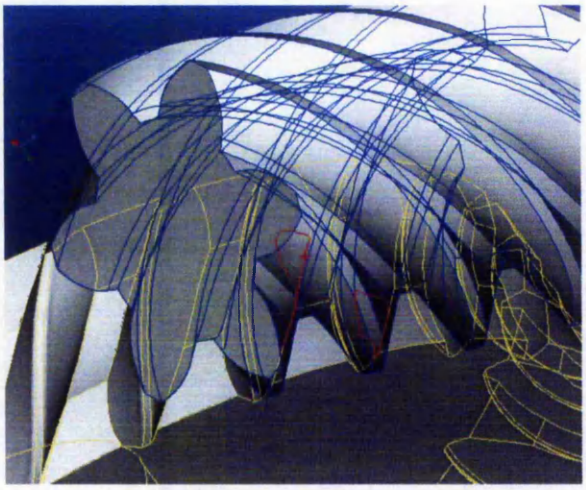


Figure 9.19 Contact pattern 4

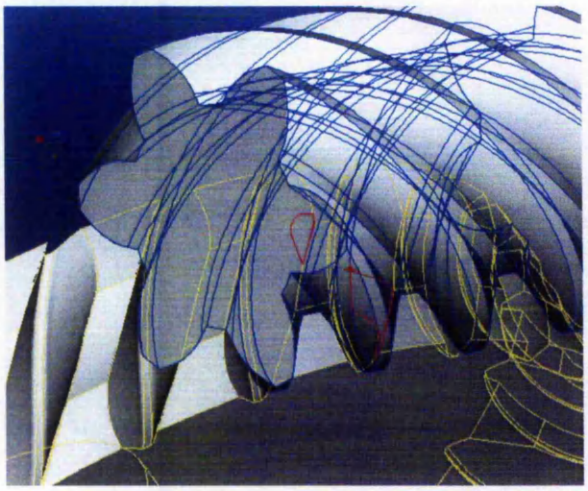


Figure 9.20 Contact pattern 5

9.4 GEOMETRY CLEANUP

9.4.1 Geometry Cleanup of Worm I

The worm and gear was meshed in ANSYS with high order hexahedral elements. As has been discussed in the preceding chapter, the high order hexahedral elements have better performance than other solid elements in nonlinear tooth contact analysis. The high order hexahedral elements can simulate the complicated surface better than tetrahedral elements.

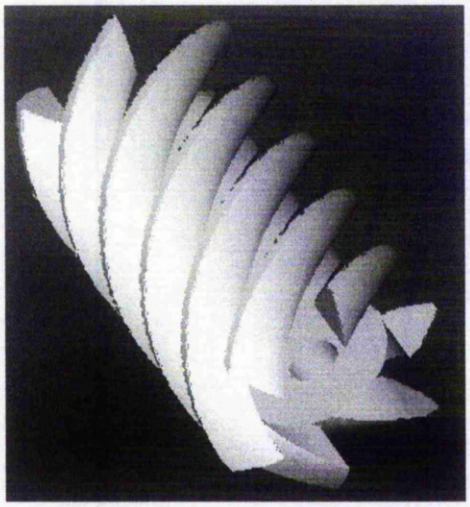


Figure 9.21 Cylinder protrusion on six threads of worm I for FEA

In order to mesh the worm with hexahedral elements, there is still some work to do with the worm geometry. The worm geometry needs to be built as a hexagonal block so that it will be easier for mapped meshing. Pro/Engineer has much more powerful functions in 3D geometrical modelling than ANSYS. It is easier to do these operations in Pro/Engineer rather than in ANSYS.

The stresses in the centre of the worm are of little interest since they have no influence on strength and design. Therefore, the core column of the worm is hollowed out to reduce the model size as shown in Figure 9.21. The six threads are created in the same manner as before.

For the consideration of mapped meshing, a helical sweep surface is created which will make the meshing work in ANSYS much easier. The section for the helical sweep surface is rectangular as shown in Figure 9.22. The outside line of the section is aligned with the outside surface of the cylinder and the inner line of the section is aligned with the surface of the hole.

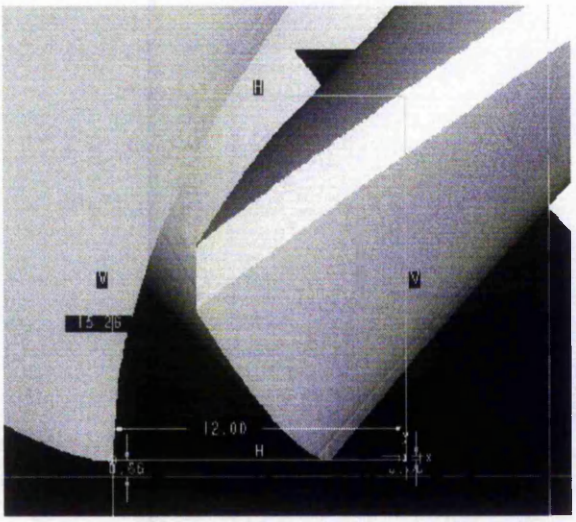
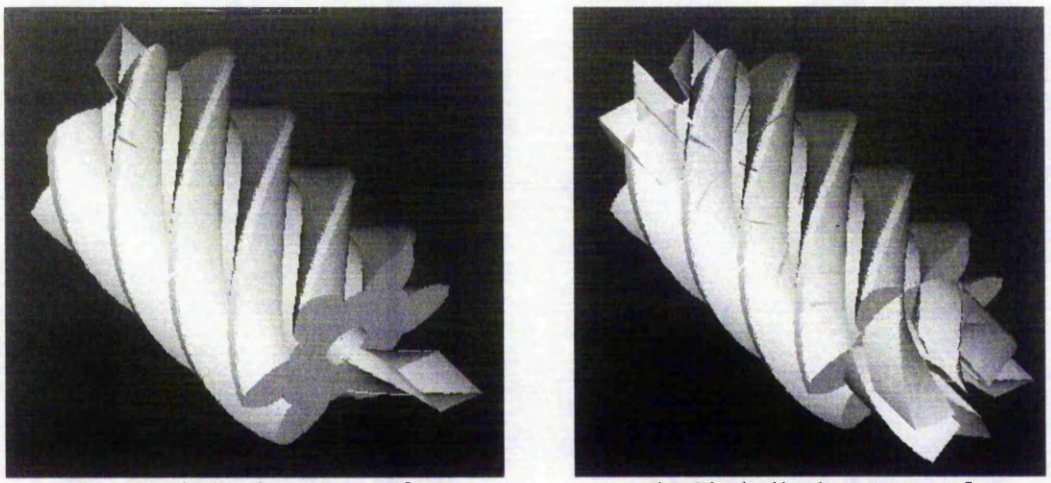


Figure 9.22 Sweep section of inner helical surfaces



(a) One helical sweep surface (b) Six helical sweep surfaces

Figure 9.23 Generation of inner helical sweep surfaces

After the first helical sweep surface is created, it is patterned into six surfaces as shown in Figure 9.23. Finally, the unwanted solids and surfaces can be cut off. Figure 9.24 shows the rebuilt worm geometry that is ready to be exported as an IGES file.

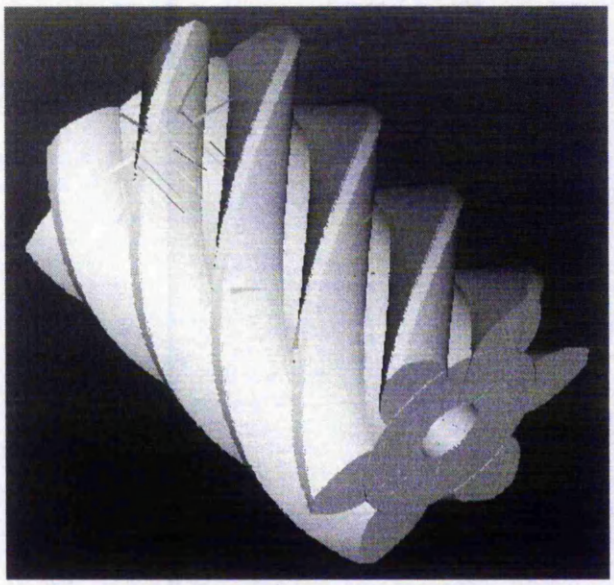


Figure 9.24 Rebuilt worm geometry for FEA

9.4.2 Wheel Geometry Cleanup

The wheel created by the VGM method has many small cut areas. These areas will inevitably cause meshing problems. The techniques developed for spiroid gears cannot be applied to the worm gear tooth smoothing, due to their totally different geometry. It is impossible to use the tooth contact lines to construct the surfaces (see Figure 9.28). The red line in Figure 9.28 is where the surface has been created by the contact lines. The curvatures where the two patches of areas join have an abrupt discontinuity.

The reason for geometry cleanup is that the geometry imported into ANSYS can be easier to mesh. The small areas need to be cleared. In order to smooth the gear tooth surface, a surface was created from the VGM models. This surface was then used to cut out the gear. The procedure for the smoothing of the gear surfaces is illustrated below.

9.4.2.1 Creating Enlarged Gear Blank

An enlarged gear blank is created first so that a larger surface can be obtained. This will be easier for the later tooth cutting technique. The revolving section of the enlarged gear blank is sketched as shown in Figure 9.25. The small radius curve will be revolved to form the gear throat surface. The two straight lines just enclosed by the real gear blank. The above section is revolved into gear blank as shown in Figure 9.26.

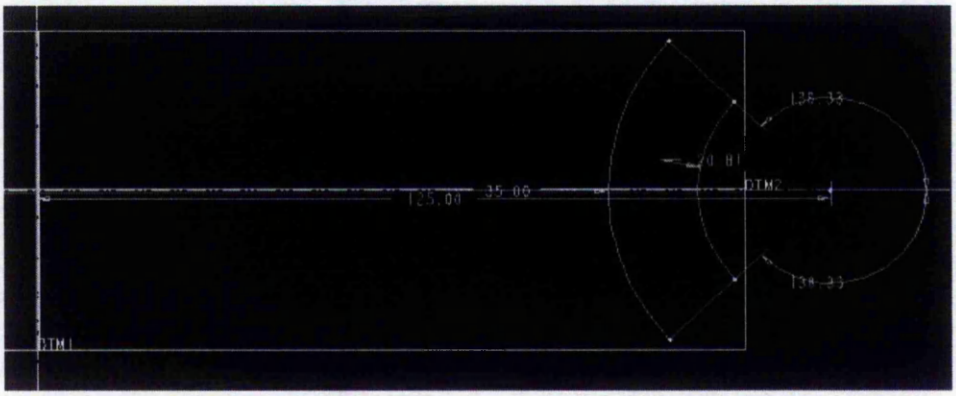


Figure 9.25 Revolving section for enlarged gear blank

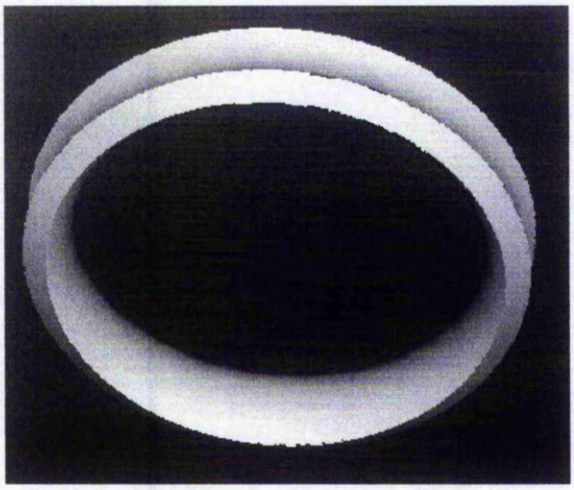


Figure 9.26 Enlarged gear blank

9.4.2.2 Generation of One Complete Gear Tooth

Then the virtual gear manufacturing method is used to hob the enlarged gear blank. Only the surfaces of one complete hobbed tooth are required for tooth smoothing. The partial cut tooth surfaces are shown in Figure 9.27.

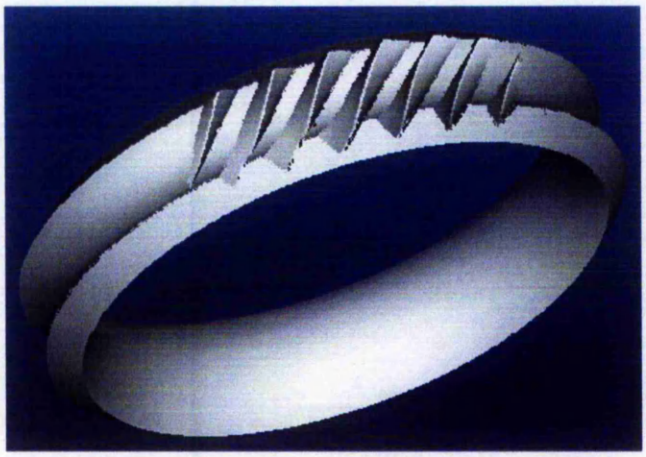


Figure 9.27 Gear blank with a few cuts

Figure 9.28 shows the zoomed tooth of the VGM worm gear model in which only one tooth has the completed generated surfaces. The contact lines are clearly shown in the figures.

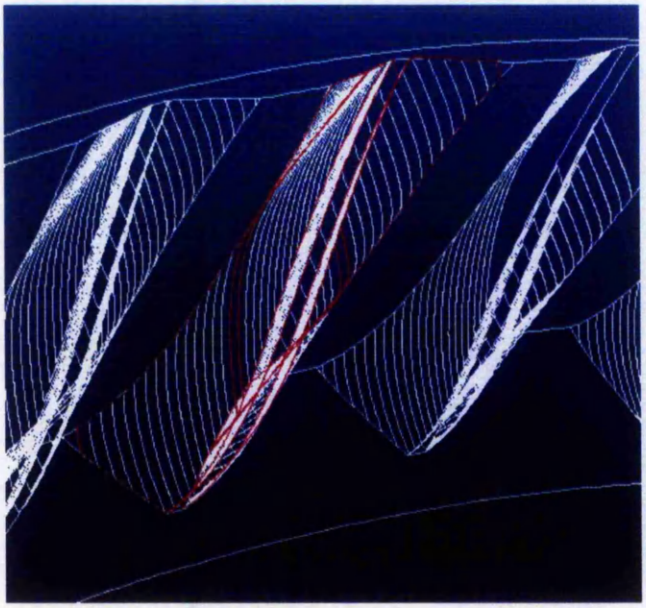


Figure 9.28 Zoomed gear tooth cuts

9.4.2.3 Generation of Cutting Surfaces

To smooth out the tooth surface, the tooth surface curves are needed. The top land of the worm gear consists of three surfaces, which are not tangent to each other. Therefore if the same smoothing technique as that for the spiroid is used, the worm gear tooth surface curves will need to be longer near the middle and shorter near the edges. Such a set of curves is not ideal for constructing the surface because it will result in a large tolerance error of the surface.

A new method was developed in this research to obtain the required curves. In this new method, the revolved surfaces are created and used to cut off the top land of the tooth. The curves are constructed from the edges of the top surface of the remaining tooth. Figure 9.29 shows the section, which is an arc curve and is concentric with the worm, for the revolved surface.

Special attention should be paid to the dimension scheme of the arc curve; otherwise the surface will fail to regenerate or cannot be used for patterning. For example, if the end of the arc is dimensioned to the centre line of the gear, when the surface is patterned, the created surfaces cannot be used for cutting.

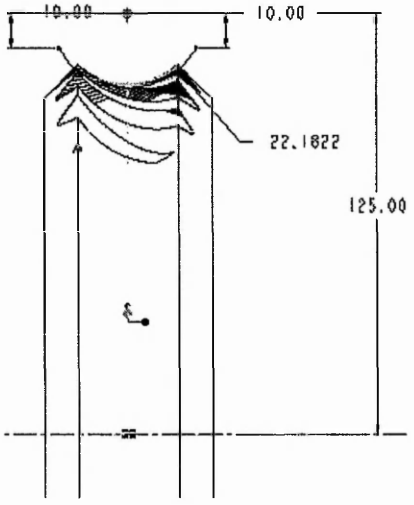


Figure 9.29 Section for revolving surface

After the revolved surface is constructed, the surface is patterned to a set of surfaces as shown in Figure 9.30. These surfaces will be used to cut out the teeth.

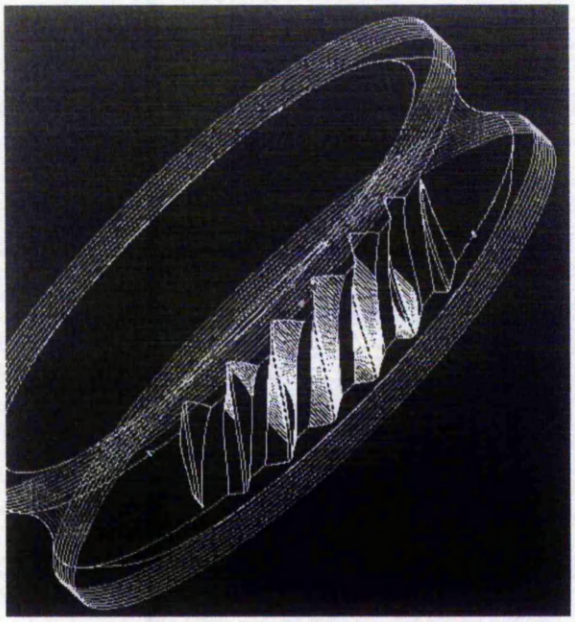


Figure 9.30 Surfaces patterned

9.4.2.4 Creating Datum Curves

Now the datum curves were created. The first set of datum curves was created on the edge of the top land. The *composite curve* function of Pro/Engineer was used to construct the curves. In the *composite curve* function, there are two options: *approximate* and *exact*. The *approximate* option should be selected here since this function will construct the several composite curves into a whole smooth curve. If the *exact* function is selected, then the composite curves are only a set of joint curves, which are not tangent to each other. The procedure for constructing the composite smooth curve is described as follows:

1. In the **Feature** menu, select **Create;**
2. Then choose **Datum** and then **Curves**;

3. Select **Composite** from the pop up menu, which lists many curve generating methods.
4. Choose **Approximate**; do not select the **Exact** option here.
5. In the pop up menu, the **Chain** option should be selected. It is impossible to pick up the small edges of the cut off top land if any other option is selected.
6. Zoom the gear tooth and then select the gear top land edges one by one in a continuous way.
7. After all the small lines are selected, select **Done**.

After the above procedure is completed, a single composite curve was created. Repeat the above procedure to create another smooth datum curve on the edge of tooth top land. The two datum curves created are shown in Figure 9.30 (yellow colour).

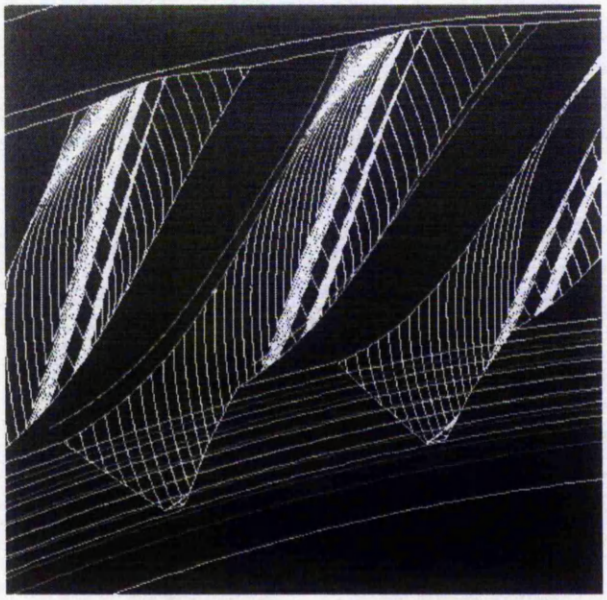
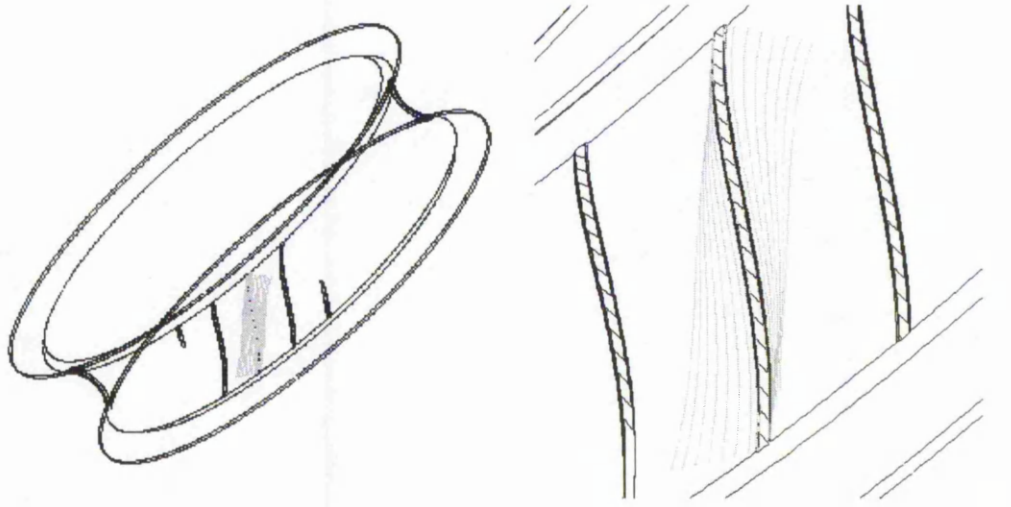


Figure 9.31 Datum curves created on the cut tooth edges

After the top land curves, the second set of datum curves were produced. The gear was cut off a layer using the surface next to the top land. Then the same procedure as step three was used to create the curves. Figure 9.31 shows the two sets of datum curves created. The top curves are created from the edges of top land and the lower curves are created from the edges of the gear tooth, which is cut off a layer by the first quilt next to the gear top land. Repeat the above procedure to create all the datum curves needed.

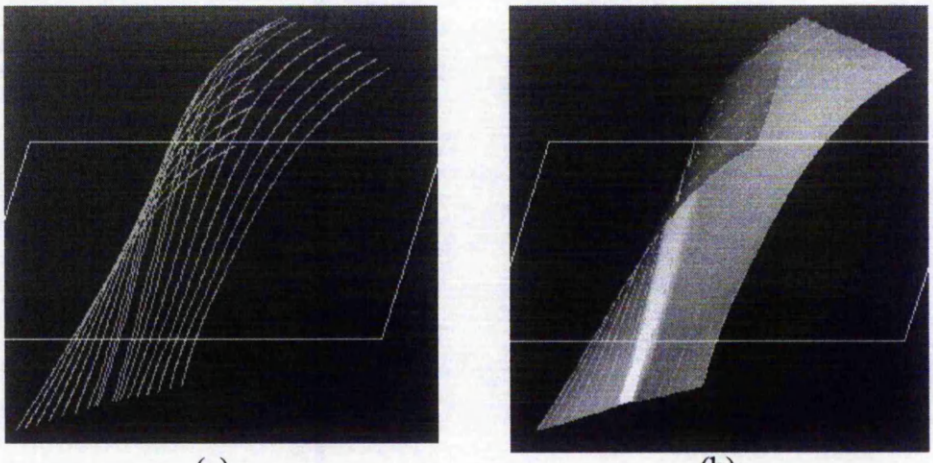
9.4.2.5 Creating Datum Curves in Tooth Fillet Area

The datum curves near the bottom cannot be created using the *approximate* composite curve function. This is because near the fillet area of the bottom, the small edges of the cutting off gear tooth top land are not in tangent to each other any more.



(a) Tooth datum curves (b) Zoomed datum curves

Figure 9.32 Datum curves for gear tooth



(a) (b)

Figure 9.33 (a) Datum curves (b) Surfaces created by datum curves

Another method was developed to construct the datum curves. This method uses the datum points to construct the datum curve. These datum points are created using *On Vertex* option. Select all the vertices of the small edges and create a datum point on every vertex of the small edges of tooth top land. Then the datum curves can be created using the *Through Points* option. The datum points should be picked one by one in a continuous order to construct the datum curves. Figure 9.32 (a) shows all the curves that have been created in the gear and (b) is the zoomed datum curves.

9.4.2.6 Generation of Tooth Surfaces

Once the datum curves have been created, they can be used to construct the surfaces. First, these curves are exported as IGES files. Then these curves are imported back to a new part one by one as shown in Figure 9.33. The curves are then used to construct the surfaces by the following procedure:

1. In the **Feature** main menu, select **Create**;
2. In the **FEAT Class** menu; select the **Surface** option and then click **Done**;
3. In the pop up **SRF OPTS** menu, select **Advanced** and then click **Done**;
4. In the pop up **ADV FEAT OPT** menu, select **Boundaries**, then click **Done**;
5. In the pop up **BNDRS OPT** menu, select **Blended Surf**, then click **Done**;
6. In the pop up **CRV OPTS** menu, click **First Dir**;
7. In **Select Item** submenu, choose **Curve** option.
8. Choose option **One by One**;
9. Then pick the curves one by one in a continuous order.
10. After all the curves on one tooth surface are selected. Click **Done Curve** in **CRV OPTS** menu;
11. Click **Preview** button on the **SURFACE: Blended** sub-window to preview the surface. If it is all right, then click **OK** button. The surface is created.

The surface should consist of three quilts: two tooth quilts and one root quilt. If only one surface is created using all the datum curves, it is very difficult to split it up in ANSYS for mapped meshing. After three quilts are created one by one, they are merged into one surface.

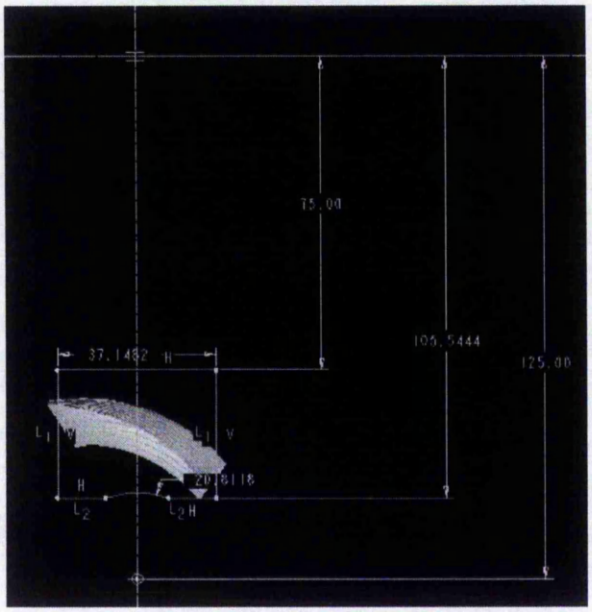


Figure 9.34 Revolving section for gear blank

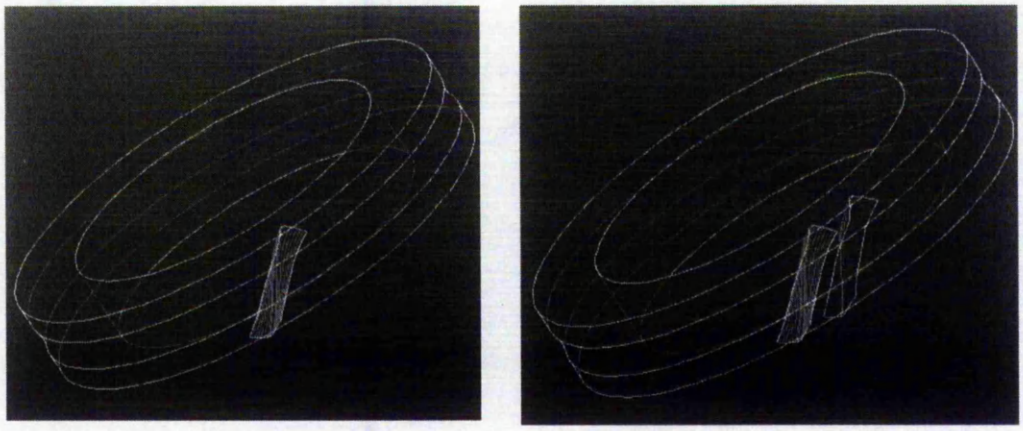
9.4.2.7 Creation of a Gear

A gear blank is created using the *revolving* function for cutting. The revolved section is shown in Figure 9.34. In order to create the exact gear blank, the same default coordinate system and gear axis as the enlarged gear blank are used. After the *revolve* function was activated, the gear blank and the quilts were in one part as shown in Figure 9.35.

The next step is to use these quilts to cut the gear blank. In order to create the 31 teeth, 31 quilts are required. To generate these quilts, the quilts shown in Figure 9.35 (a) are transformed as shown in Figure 9.35 (b).

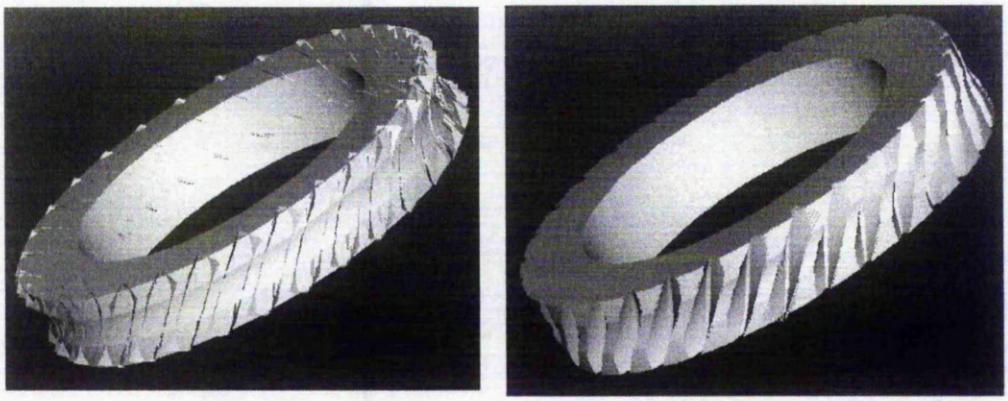
The transformed surface provides an angular leader dimension for patterning. The transformed surface is patterned into 31 surfaces as shown in Figure 9.36 (a). These surfaces are going to be used to cut the gear teeth. Cut the gear using the original transformed surface first; then pattern the cut using the *reference pattern* technique to get the whole gear as shown in Figure 9.36 (b).

The gear is now available for gear assembly and tooth analysis, interference checking and tooth contact path.



(a) (b)

Figure 9.35 (a) Gear blank and quilts (b) The quilt transformed



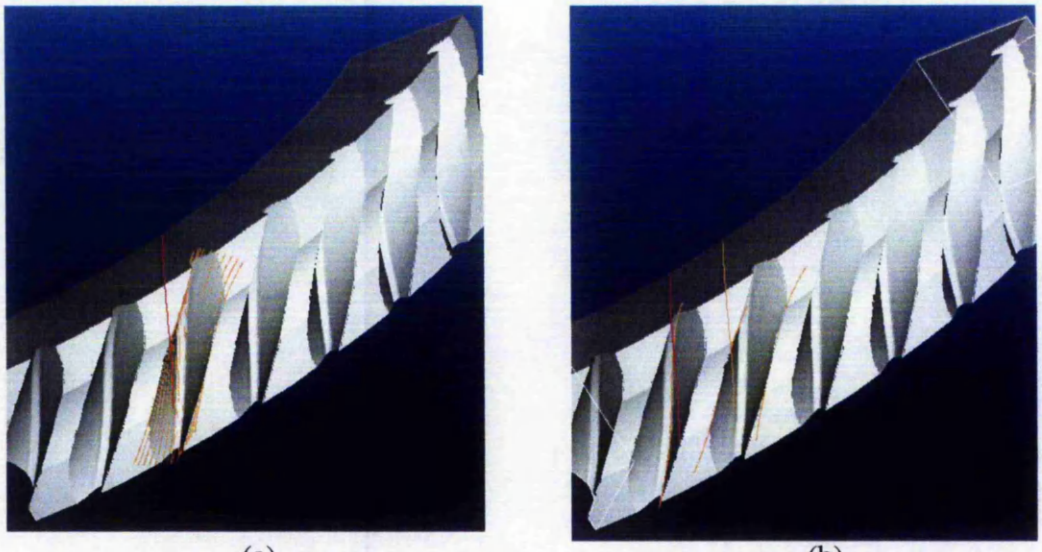
(a) (b)

Figure 9.36 (a) Patterned quilts (b) Gear cut by quilts

9.4.2.8 Single Gear Tooth for FEA

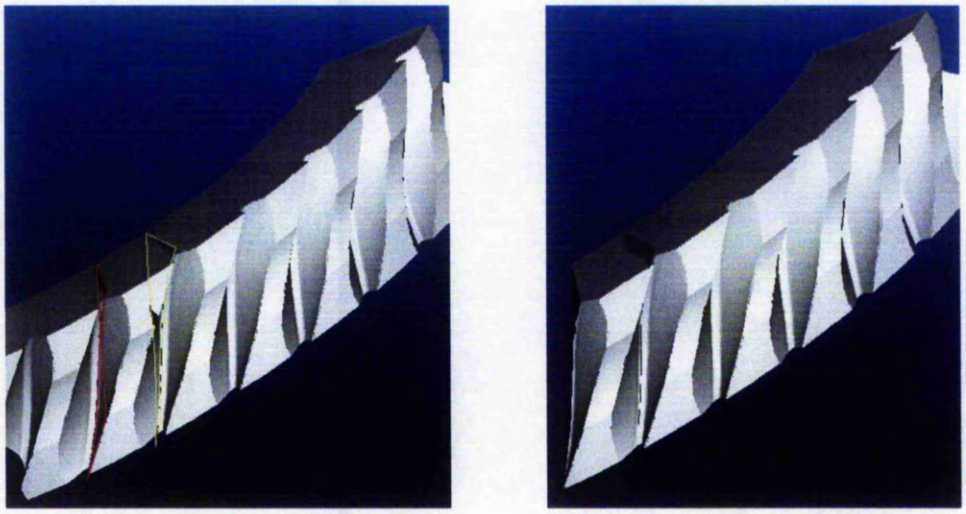
In order to map mesh the gear tooth, the gear geometry needs to be further partitioned. The partition work is done more easily in Pro/Engineer than in ANSYS.

First of all, a single gear tooth was cut. The cutting procedure is described as follows:



(a) (b)

Figure 9.37 (a) Project the curve; (b) Transform the projected curve



(a) (b)

Figure 9.38 (a) Create quilts for tooth cutting; (b) Cut using quilts

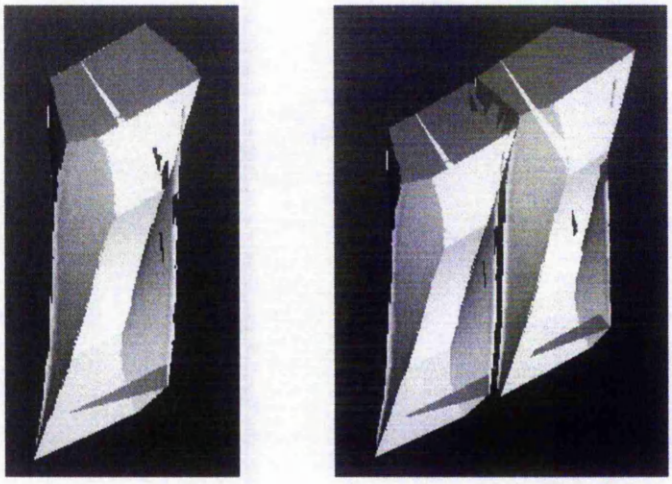
1. Cut a quarter gear from the whole gear as shown in Figure 9.37 (a).
2. Project the root edge curve into the gear inner surfaces. The red line in Figure 9.37 (a) is the projected curve.
3. Transform the project line as shown in Figure 9.37 (b).
4. Create 8 datum points at the end of the project curves and the root surface edge curves.

5. Create two straight-line datum curves using the datum points as shown in Figure 9.38 (a).
6. Create two surfaces using the four datum curves. Figure 9.38 (a) shows these two surfaces (the red and yellow surfaces).
7. Cut the gear using the datum surfaces. Figure 9.38 (b) shows the gear cut by the red quilt shown in Figure 9.38 (a).
8. Cut the tooth using the yellow quilt to get the single tooth.

9.4.2.9 Gear For FEA

The single tooth created will be used to copy the gear tooth surfaces. Why are the gear tooth copied surfaces necessary? This is because the solid single tooth cannot be patterned due to lack of an angular leader dimension. The surface geometry can be transformed and therefore an angular leader dimension can be created for patterning. Figure 9.39 (a) is the single solid tooth plus the copy surface and Figure 9.39 (b) shows the transformed gear tooth surfaces. Comparing Figure 9.38 and Figure 9.39, it can be seen that Pro/Engineer displays the solid geometry with better quality than the surface geometry.

By using the angular leader dimension of the transformed surfaces, the 31 tooth surfaces are patterned as shown in Figure 9.40.



(a) (b)

Figure 9.39 (a) Copy tooth surfaces; (b) Transform the tooth surfaces



Figure 9.40 Gear tooth surfaces for exporting

If the above smoothed model is exported to ANSYS, the gear tooth cannot be map meshed. In ANSYS, the volume should have five or six surfaces for mapped meshing with hexahedral elements.

The gear tooth can be divided into two volumes: the tooth part and its root part. Figure 9.41 shows a single gear tooth. The end surfaces (ACDBFE and GHIJK) can be deleted and recreated as two separate surfaces in ANSYS (use key points to create the straight line e.g. AB; use four lines to construct the areas, ACDB and ABFE). The lower root part is enclosed by six surfaces and is no problem for meshing. The above tooth part volume has 7 surfaces. The gear tooth top land consists of three surfaces (CDLM, LMPN, PNIJ). In ANSYS, two surfaces can be concatenated into one surface for the purpose of meshing. However, ANSYS only allow two surfaces to be concatenated. The third surface cannot be concatenated with the surface that has already been concatenated so the surface and volume need to be further divided.

In order to map mesh, the gear tooth should be divided into blocks as shown in Figure 9.42. This is easy to cut in Pro/Engineer. However, when such a model is imported into ANSYS, it is found that the edges of surface are difficult to merge. HyperMesh usually easily deals with such problems, but the price is a poorer accuracy of the

geometry. The joint surface edges cannot be merged into one if the tolerances is not relaxed. The reason for these problems is that when the surface is written into IGES, the edge curvature constraints are not included. Since gear contact analysis requires very high accuracy, the tolerance for merging cannot be compromised.

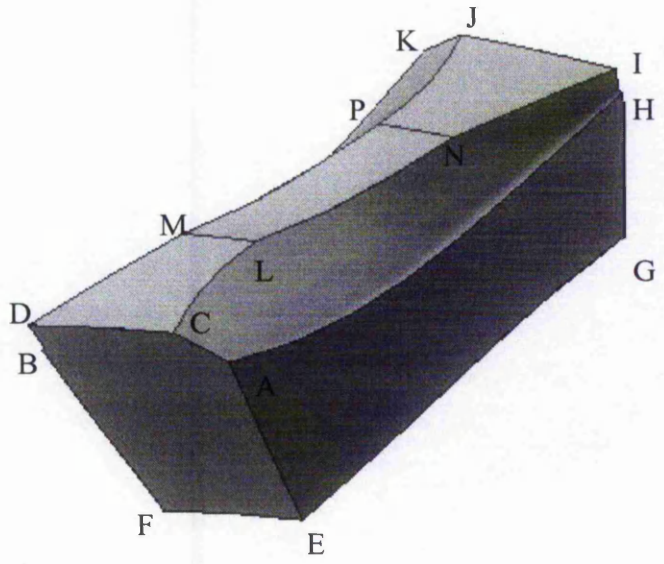


Figure 9.41 Single gear tooth

Another method is to export the whole surface and cut the gear tooth surface in ANSYS using work planes. However, this is also impossible because using the default global tolerance, the work plane cannot align with the top land curves (e.g. curve ML and PN in Figure 9.41). When the cut is finished using the work plane, it will cut out a tiny area and this will cause even more trouble. Obviously, a new method has to be developed.

The new method developed for tackling the division of the gear tooth volume problem in ANSYS is described as follows. Two planes in the joint edges of top land are created by the *revolving* function in Pro/Engineer (see Figure 9.40). The revolved section line is aligned with the top land edge. These two planes are going to be exported together with the 31 gear teeth surfaces. Since these two planes are regular geometry and will be exactly transferred into IGES and also will be exactly imported into ANSYS. So when the geometry is written into an IGES file, the gear tooth top

lines (e.g. curve ML and PN in Figure 9.41) will be forced to locate on the planes and share the same key points. During the importation, they will have the same edge. When these planes and gear teeth are imported into ANSYS, these planes can be used to divide the gear tooth surfaces. Considering the overall transferring tolerance errors of IGES data, the whole gear assembly is imported instead of separated individual items.

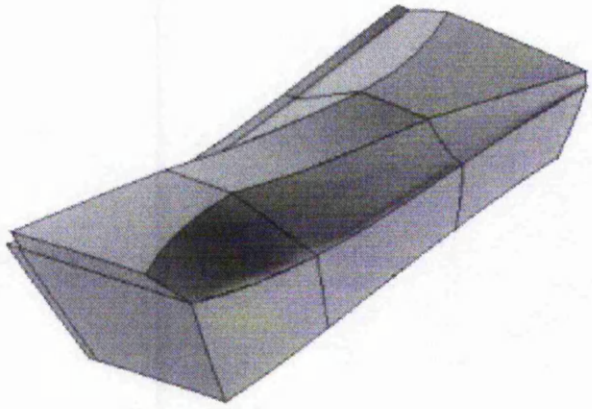


Figure 9.42 Gear tooth divided volume for mapped meshing

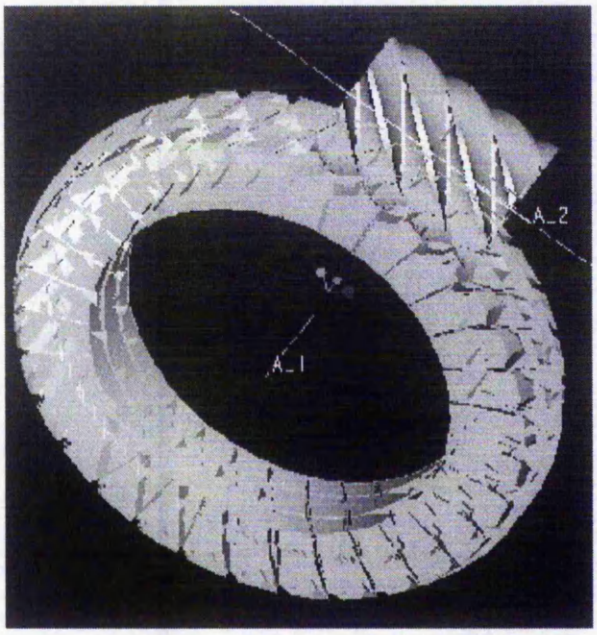


Figure 9.43 Gear assembly for FEA

The gear model for FEA consists of the 31 gear teeth's surfaces. The root parts of gear are not included. The reason for this is that if the root part is included, when it is imported into ANSYS, there will be edge gaps between the joint surfaces and the global tolerance has to be relaxed to merge them. Some of them need very large global tolerance. Merging geometry with a large tolerance will affect the accuracy of the tooth surfaces.

The worm gear assembly model is exported as one whole model. In the **Export** pop menu, select the **Surface** option and **Flat** option. Layers are used to blank out the unwanted geometry.

9.5 GENERATION OF 3D FINITE ELEMENT MODELS

9.5.1 Importing Model via the IGES Interface

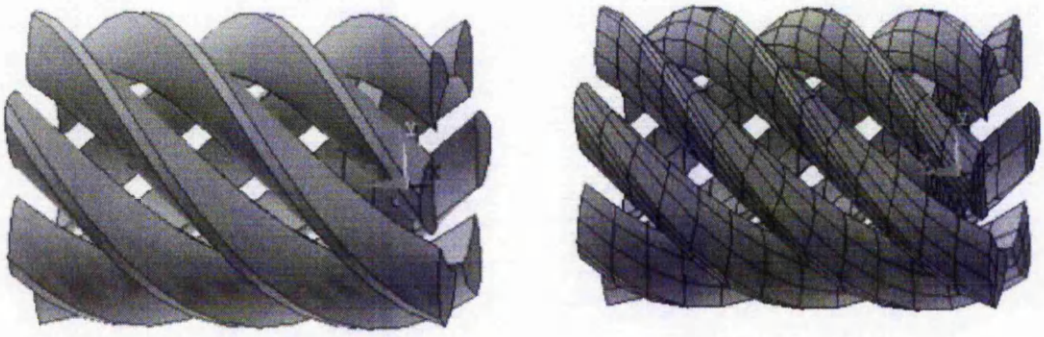
There are two IGES importing options available in ANSYS: the *default* option and the *alternate* option. The ANSYS manual recommends users always try the *default* option first. The *default* option is easy to use and also has very powerful geometry repairing tools, which is not available using the *alternate* option. However, the *default* option is not suitable for nonlinear gear contact analysis. The reason is that the *default* option represents the imported surfaces with numerous tessellated flats. This will affect the accuracy of contact force or pressure on the contact region. The other major shortcoming is that the imported geometry is not compatible with the native ANSYS geometry database. This is very inconvenient because new geometry cannot be added onto the model after it has been imported.

The IGES file of the gear geometry is imported into ANSYS using the *alternate* option in this research. Before the importing command is issued, the *merge key points* and *merge lines* options should be checked and the *creating volumes automatically* option should be switched off. During the importing process, the IGES file accuracy tolerance must be chosen. After all these have been done, the model geometry can be successfully imported into ANSYS.

9.5.2 Worm Model Mesh

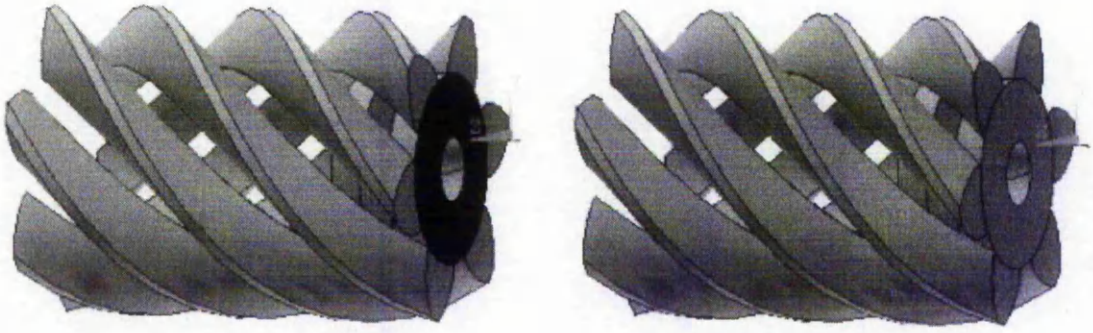
After the gear assembly model is imported, the model has only key points, lines and surfaces and its volumes have to be created in ANSYS.

For the sake of convenience, the surfaces, lines and volumes are grouped into different components. For example, the worm's six thread surfaces are grouped into a surface group named "thread". Select the "thread" group and display the surface, a figure such as Figure 9.44 (a) will be displayed. In the ANSYS preprocessor, create the volume using the *arbitrary areas* function. In the pop up menu select *pick all*, the volume is created and displayed as Figure 9.44 (a).



(a) Six-thread volumes (b) Mesh six thread volumes

Figure 9.44 Worm thread mesh



(c) Extrude volume and mesh (b) Extrude three inner volumes

Figure 9.45 Extrude the inner cylinder mesh

When the thread volumes are created, the threads can be meshed. Due to the limits on the number of nodes, the high order hexahedral element SOLID95 was used. SOLID95 can simulate the curved tooth surface more accurately than SOLID45, which is a lower order element. Set the tooth width direction 2 divisions, the height direction 4 divisions, and the lead direction 14 divisions and then mesh the thread volumes. The thread meshes are created as shown in Figure 9.44 (b).

The inner cylinder mesh uses the *extrude* function in ANSYS which allows the volumes and meshes to be extruded from the area. The area is created by sketching two circular areas and subtracting the smaller circle from the larger one. The blue area in Figure 9.45 shows the area created for extrusion.

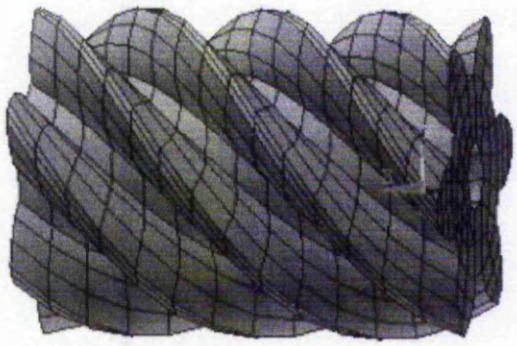


Figure 9.46 Inner cylinder meshed

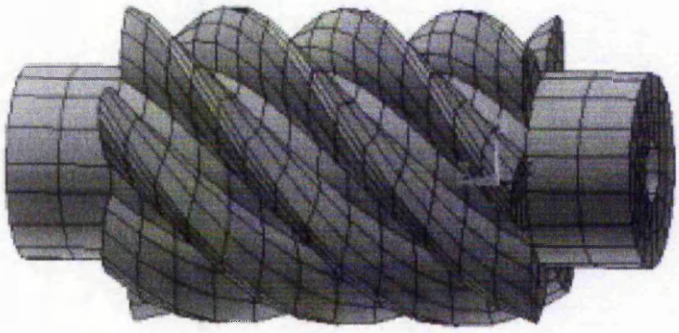


Figure 9.47 Whole worm mesh

The next step is to mesh the area with 2D shell elements which have the same nodal distribution as the surface of SOLID95. Mesh the area first and then extrude the 2D mesh to get the 3D inner cylindrical meshes. The following command can be used: Prep7/Operate/Extrude/By xyz offset. The mesh extrusion has two directions: (1) is along the z direction of the local coordinate system and (2) is along the y direction. One layer mesh is created each time. Figure 9.45 shows three volumes and meshes have been extruded and Figure 9.46 shows the entire inner cylinder meshes have been extruded. Finally the two end shafts are extruded that will be used later for applying boundary constraints and simulating the gear rotation (see Figure 9.47).

9.5.3 Gear Model Mesh

All the gear surfaces are grouped into a "gear" component. The gear tooth has to be divided into three brick shaped blocks so that it can be meshed. Selecting a few teeth surfaces in contact with the worm and the two planes and plotting the areas will produce a figure such as Figure 9.48. Choosing **Operate** from the preprocessor and selecting **Divide/ By Area** and then selecting the tooth surfaces and the two planes will divide the gear tooth surfaces into three parts.

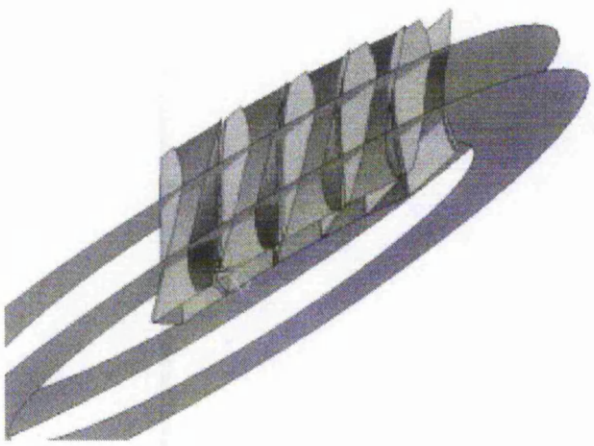


Figure 9.48 Gear tooth surface dividing

The final gear tooth for mapped meshing should be divided as shown in Figure 9.50. Since the both end surfaces of a tooth are only a single surface, it has to be divided into two surfaces. This can be divided by the *Dividing* function using the work plane.

However, aligning the work plane in the right position is a difficult task. So an alternative method was used here. Instead of dividing the surface, the end surfaces were deleted. Then a straight line was created using the key point option. The two separated areas were constructed by the *arbitrary* option.

The new created surface was not aligned with the old surface in its inner area. But this does not matter since the stress at the end surface is of little interest and it has little influence on the tooth contact forces and stresses.

The gear root area is a very thin block, which is not imported into ANSYS. They were created in ANSYS. Key points were used to draw the necessary straight lines and then the area was created using the four lines. After all the areas were created, they were used to create the volumes.

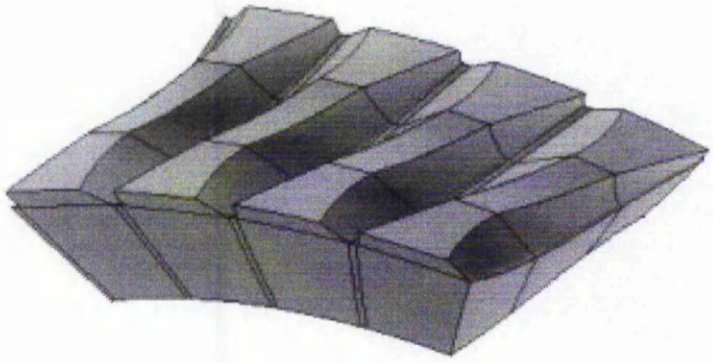


Figure 9.49 Four gear teeth volumes

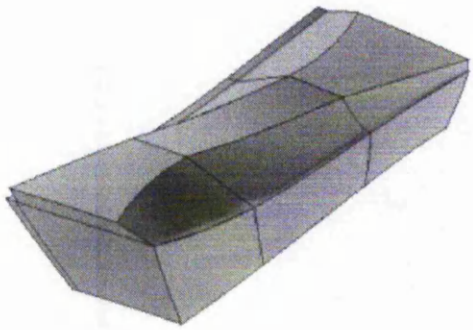


Figure 9.50 Single tooth volume dividing

For the purpose of convenience as well as for the consideration of accuracy, four teeth that are in possible contact with the worm are created for gear analysis. Figure 9.49 shows the four created gear tooth volumes.

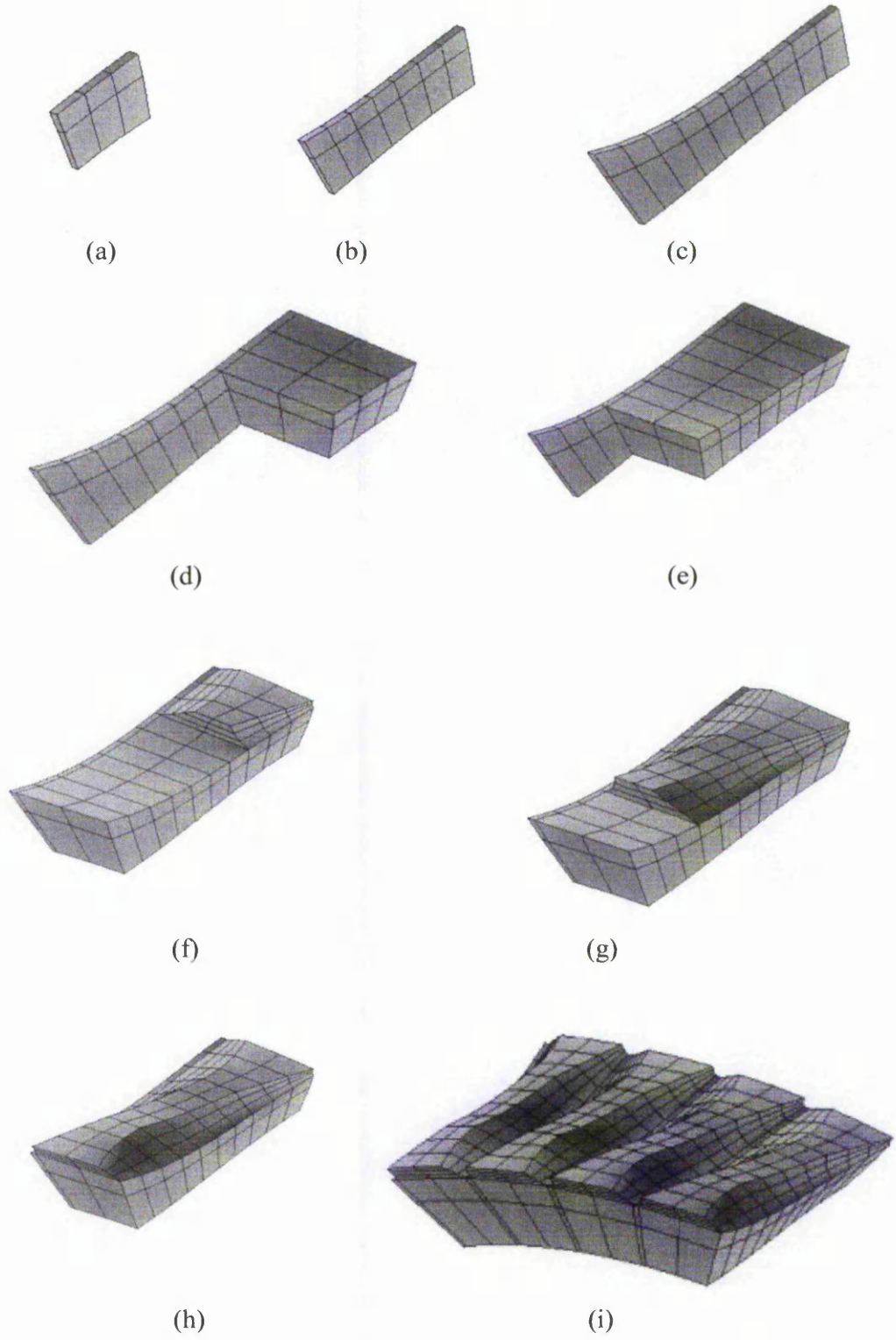


Figure 9.51 Illustration of gear tooth mapped meshing process

When the gear tooth volumes are all created, the gear is ready to mesh. Set the line divisions before issuing the mesh command. Figure 9.51 illustrates the gear tooth mesh process. Pick the volumes one by one to get the four teeth meshed. The elements will be similar to Figure 9.52.

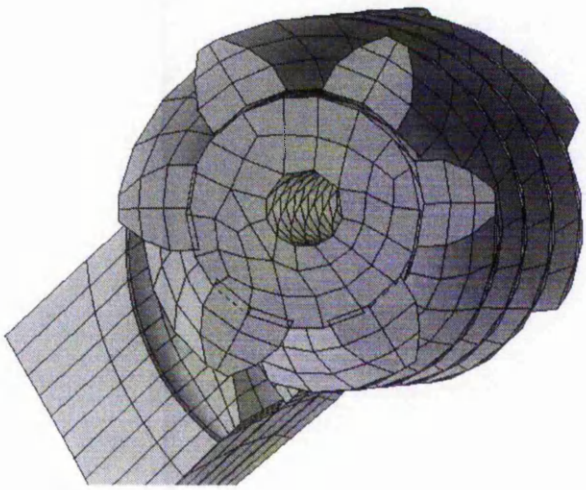


Figure 9.52 Fourth gear teeth and worm mesh



Figure 9.53 Holroyd worm gearset I assembly mesh

The meshes of the remaining gear teeth can be done in the same manner. However, it would take a substantial amount of time to create the lines, areas and set the line divisions. So an advanced technique was applied to improve the efficiency and speed up the model generation.

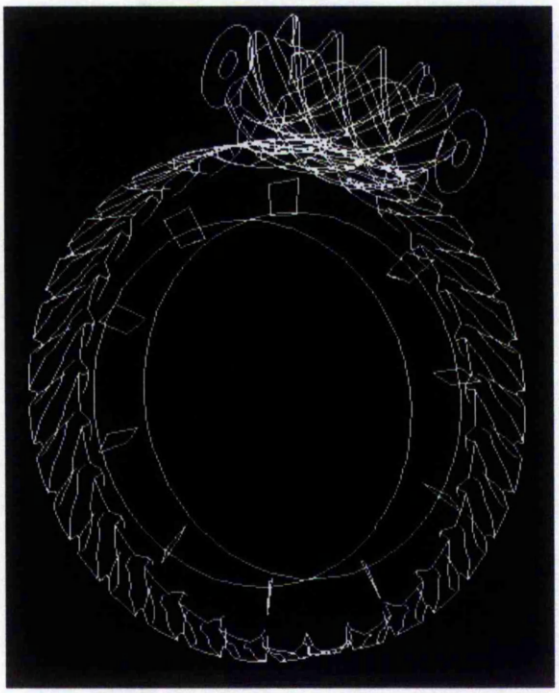


Figure 9.54 Detect separated area and mesh

The advanced *transfer coordinate system* function is used here to copy the volumes and meshes. The procedure is described as follows:

- Create a local cylindrical coordinate system. This coordinate system will be used for copying the gear teeth mesh.
- Then in ANSYS preprocessor, select **Move/Modify**.
- Choose **Transfer by coordinate**; select the local cylindrical coordinate system wanted. Special attention should be paid to the active coordinate system. The transfer performed by copying the volume and below from the active coordinate to the destination coordinate system.
- Select **Copy** option.

- Select all the four gear teeth volumes and click OK. The volume will be completely copied into the destination coordinate system.
- Now eight gear teeth's volumes and meshes have been created. Create a new local cylindrical coordinate system and repeat all the procedure mentioned above. 16 teeth's meshes will be created. Repeat the above procedure until all the gear teeth's volume and meshes have been created.

Figure 9.53 shows the whole gear assembly FEA model meshed with hexahedral elements.

During the *copy* process, the volumes are separated. The nodes at the interface between the copied volume and original volume are coincident but separated. The meshes are not an integrated whole but separate meshes. Figure 9.54 shows the gear volumes are separated inside and the surfaces exist inside the gear volume. So these gear nodes and elements in the interface have to be merged using the ANSYS *merge* function otherwise they are not integrated meshes.

Six different gear models with different contact positions have been created to simulate the whole range of gear operation. The six different positions cover the worm teeth sliding over one whole gear tooth during operation.

9.6 GENERATION OF CONTACT ELEMENTS

According to the unloaded tooth contact analysis, there are three pairs of teeth in simultaneous contact. In case all the contacts are detected in analysis, four pairs of contact elements have been created. A symmetrical contact element scheme was applied in this analysis.

The procedure for assigning contact pairs is described as follows:

- In the ANSYS preprocessor, select **Create**; in the pop up menu, select **Contact element**; then select the **Contact element wizard;** the contact wizard is shown as Figure 9.55.

- In **Target Surface**, select the **Area** option. Using areas to create the target element is easier and more flexible. Gear tooth contact is a nonlinear flexible-to-flexible contact, so check the **Flexible** target type options; finally click the **Pick Target ...** button and then pick up the worm tooth surface for contact elements.

- After the target elements have been created, click **Next>** button. In next pop up menu, check the **Areas** option to create contact surface as shown in Figure 9.56. Click the **Pick Contact...** button; then pick up the gear tooth surface. The gear tooth surface consists of three patches. Pick the three patches of gear tooth one by one to finish the creation of the target element.

- After click **Next** button, set the material ID of the contact elements. Click **Optional settings...** button to set up the 11 real constants for contact pairs (see Figure 9.56).

- The real constants are set up in the menu as shown in Figure 9.58. The model is not in initial contact, so the initial contact closure ICONT is used to establish the initial penetrations. The ICONT is set to -0.1.

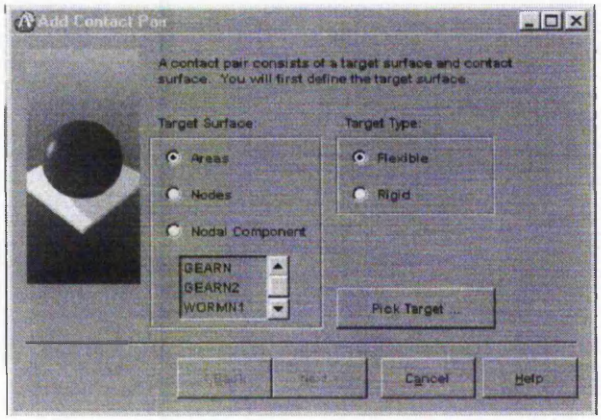


Figure 9.55 Adding target elements

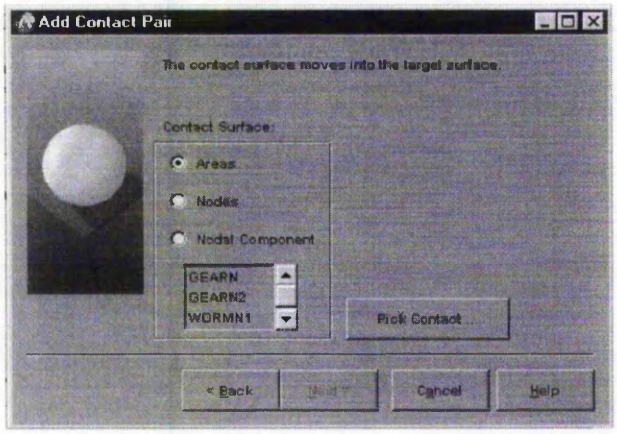


Figure 9.56 Adding contact elements

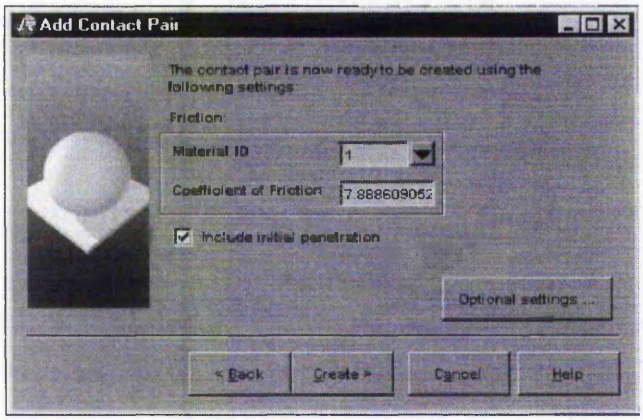


Figure 9.57 Set material ID for contact pair

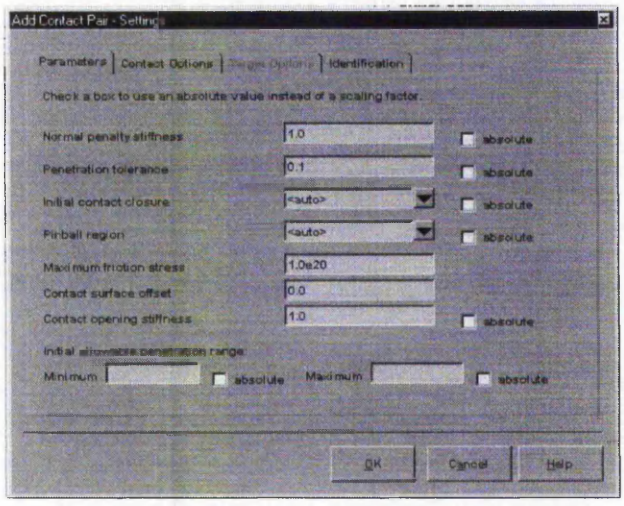


Figure 9.58 Real constants for contact element

Figure 9.59 shows the four pairs of contact elements for the worm gear. The long twisted elements are the target elements on the worm tooth surface and the others are the contact elements on the gear tooth surface.



(a) Contact pair one

(b) Contact pair two

(c) Contact pair three

(d) Contact pair four

Figure 9.59 Contact pairs in Holroyd worm gear set I

9.7 LOAD AND BOUNDARY CONSTRAINTS

In the nonlinear tooth contact analysis, the constrained scheme is that the gear is allowed to freely rotate and the worm is fixed so that the loads are applied on the gear.

The gear is constrained on its inner surface where it will have little influence on the gear tooth stresses and it is also convenient to constraint the gear rotation. The nodes on the inner surface are rotated into a nodal coordinate system situated at the centre of gear with the Z direction aligned with the gear axis. These nodes are fixed in X and Z translational freedoms in the local cylindrical coordinate system so the gear can rotate about its axis but cannot move along the X and Z directions.

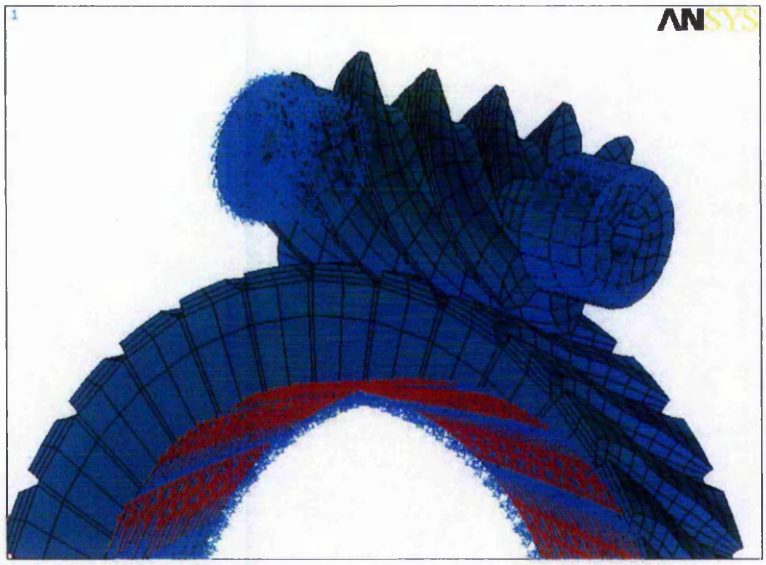


Figure 9.60 Worm gear constraints and loading scheme

The torque applied to the gear is simulated by applying the forces to the inner ring surface of the gear since the gear inner surface meshes are not even. The root part face is much smaller than the gear tooth part face so for the purpose of evenly distributing the forces, only the gear tooth part face nodes are selected for applying the forces.

A nodal coordinate system is created at the centre of one end surface of worm with its Z direction aligned with the worm's axis. The nodes on the worm surface of the shaft are fixed in the X direction but free in the Z and Y directions in the nodal cylindrical coordinate system. The nodes on one end surface of the shaft are fixed in three translational freedoms. The nodes on the other end surface of the shaft are free to rotate.

Figure 9.60 shows the constraint and loading scheme used in the worm gear contact analysis.

9.8 RESULTS AND ANALYSIS

To simulate the full gear tooth contact operation, six different contact positions have been used to simulate the whole gear range operation. The six contact position cover the range that the worm meshes over one whole gear tooth. Since every gear tooth is the same, the gear operation can be simulated by these six models.

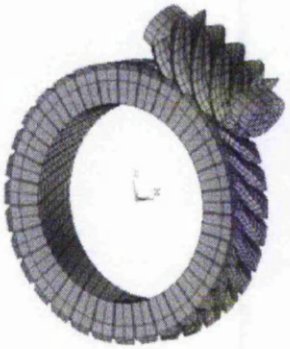
Table 9.6 The different position angles of six worm gear models (degree)

	Gear	Worm
Position 1	0	0
Position 2	1.93548	10
Position 3	3.87097	20
Position 4	5.80645	30
Position 5	7.74194	40
Position 6	9.67742	50

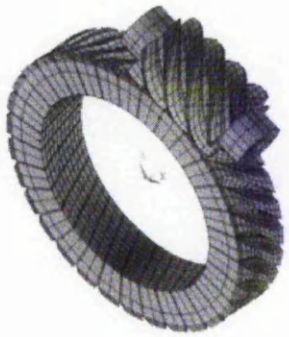
Figure 9.61 shows the six gear assembly models with different contact positions for the gear tooth contact analysis. The position angles of the six different models are listed in Table 9.6. The worm and gear rotate 10° and 1.93548° respectively from one position to the next position.

The torque applied to the gear was 2430 Nm and the loads are ramped when they are applied. There was one load step applied in the whole loading process. This one load step was divided into 10 load substeps. The automatic time step option was turned on during the solution. The first load step was finished at time 20. When the equilibrium of first load step was achieved, there were 6 or 7 load substeps depending on the contact positions.

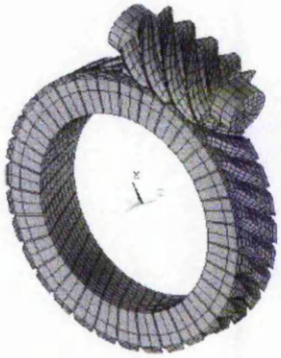
The material of the worm is phosphor bronze with Young's modulus 1.17E5 MPa and Poisson's ratio 0.35. The gear was made of hardened steel with Young's modulus 1.8E5 MPa and Poisson's ratio 0.3.



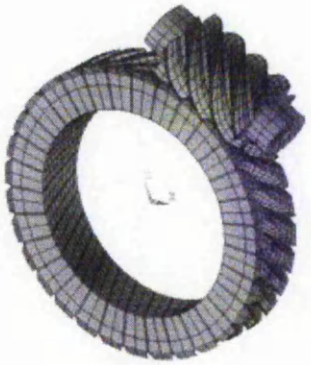
(a) Position 1



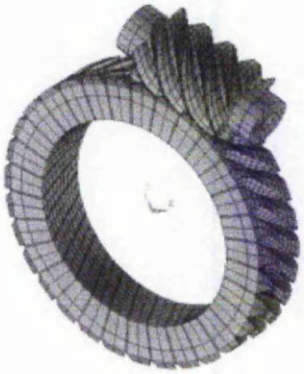
(b) Position 2



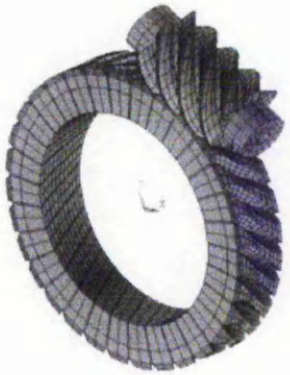
(c) Position 3



(d) Position 4



(f) position 5



(g) position 6

Figure 9.61 Six worm gear FE models with different contact positions

9.8.1 Stress Pattern

9.8.1.1 Tooth Stresses at Position 1

At position 1, there are three tooth pairs in simultaneous contact as shown teeth A, B, C in Figure 9.62. The contact region in gear tooth A is near its right end. In load substep 6, the maximum Von Mises stress reaches 376.134 MPa. Figure 9.62 shows the Von Mises stresses of the gear teeth in load step 1, substep 6. The contact region in tooth B is neither a point contact nor a line contact. It is an area contact and the contact region is over half of the tooth surface. The maximum contact forces occur near the middle of tooth B. The maximum Von Mises stress of tooth B is near the maximum tooth contact pressure (see Figure 9.63). The contact pressure in tooth B is not evenly distributed. The contact region in tooth C has two contact-point areas as shown in Figure 9.63. The larger contact-point area is near the left end and the smaller one is near the middle of the tooth. The maximum Von Mises stress happens near the smaller contact centre. The Von Mises stresses near the larger contact centre are also larger than those in other areas (see Figure 9.63).

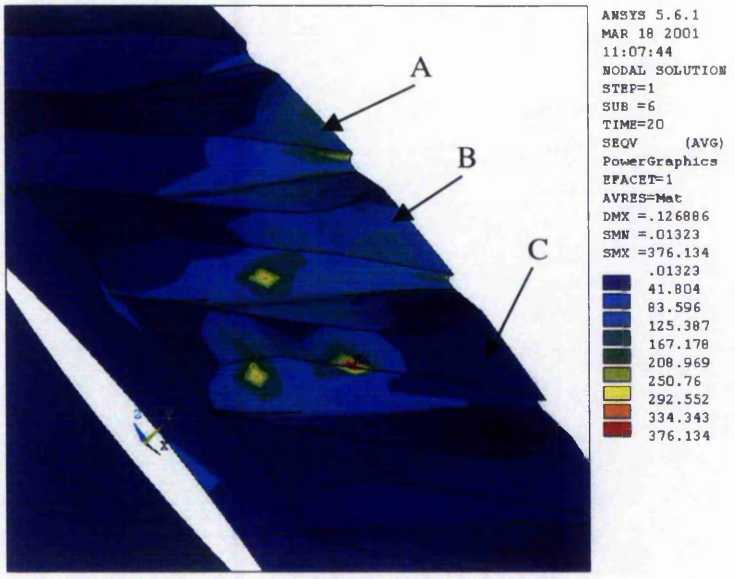


Figure 9.62 Gear I contact stresses (load step 1, substep 6), position 1

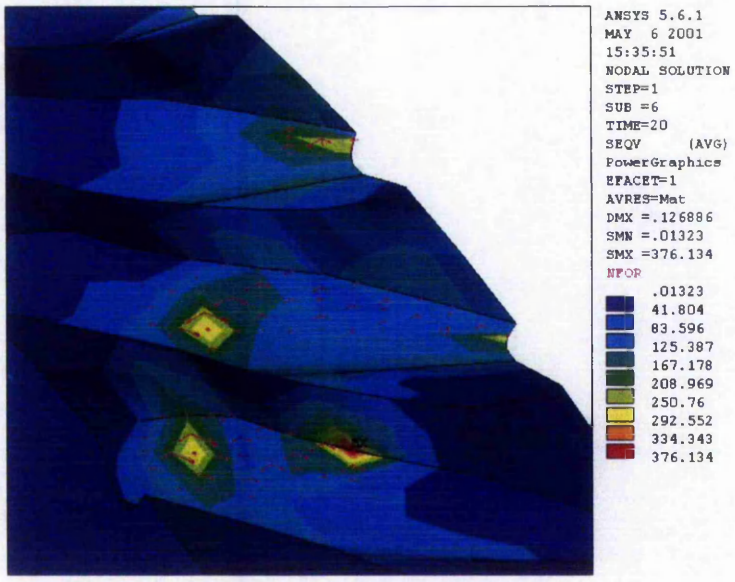


Figure 9.63 Gear I contact forces (load step 1, substep 6), position 1

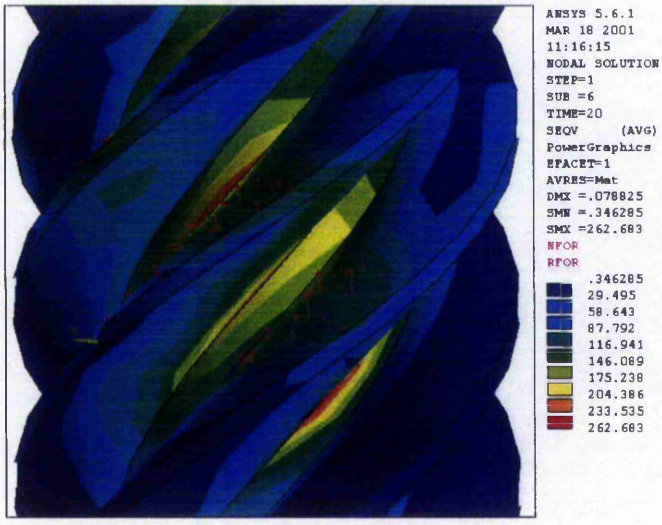


Figure 9.64 Worm I contact forces and stress pattern (load step 1, substep 6), position 1

Figure 9.64 shows the worm's Von Mises stress pattern. The maximum Von Mises stress occurs at the tooth that is in contact with gear tooth C.

The worm's maximum Von Mises stress (262.683 MPa) is smaller than their counterpart gear's (376.134 MPa). The maximum Von Mises stress in each worm tooth happens at the root of the non-contact side. The maximum tensile stress occurs at the root below the contact region centre.

9.8.1.2 Tooth Stresses at Position 2

At position 2, the gear rotates an angle of 1.93548° and the worm rotates an angle of 10°. The gear tooth A has already moved out of contact but tooth D has not come into contact yet. There are only two teeth in simultaneous contact. The maximum Von Mises stress occurs at tooth C and increases to 393.134 MPa. From Figure 9.65 it can be seen that tooth C has two contact centres. The Von Mises stresses are higher near the contact centre (see Figure 9.66).

The worm's maximum Von Mises stress increases too. The value of the maximum stress is 290.401 MPa. Though the stress values increase, the worm's stress pattern at position 2 is very similar to the worm at position 1.

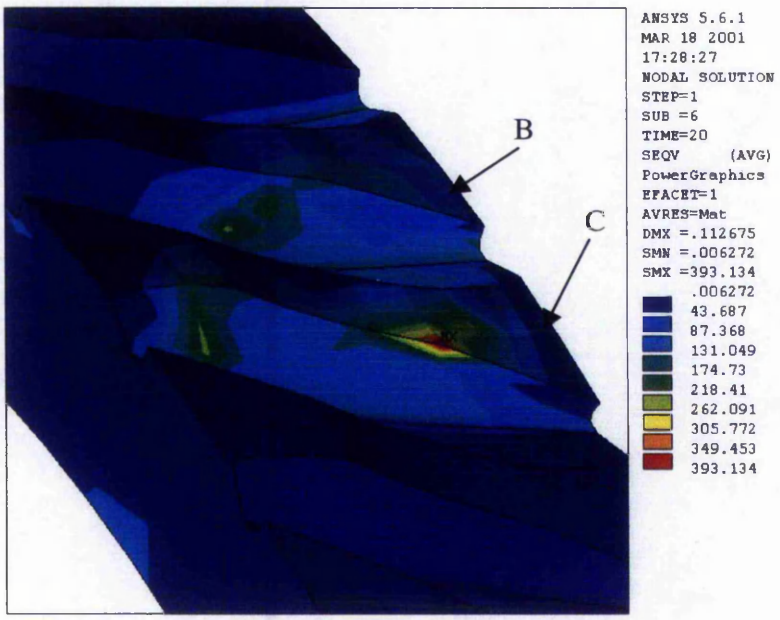


Figure 9.65 Gear I contact stresses (load step 1, substep 6), position 2

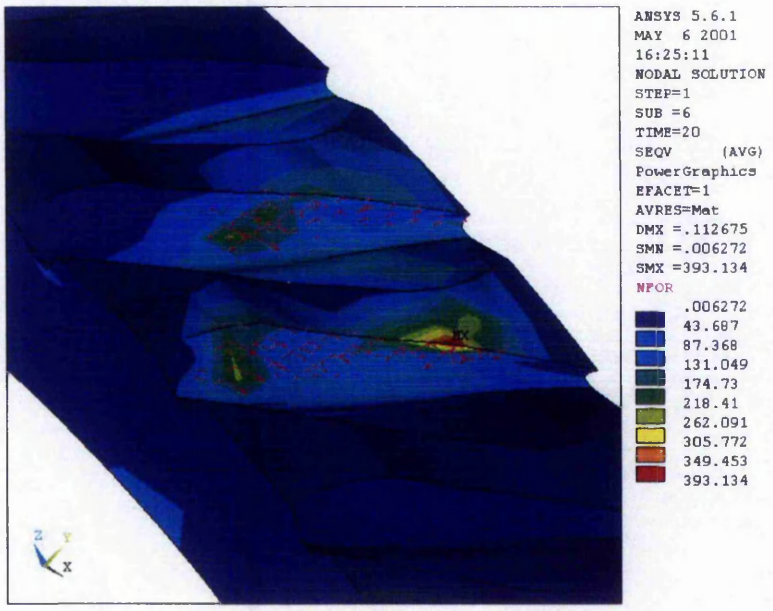


Figure 9.66 Worm I contact stresses and reaction forces (load step 1, substep 6), position 2

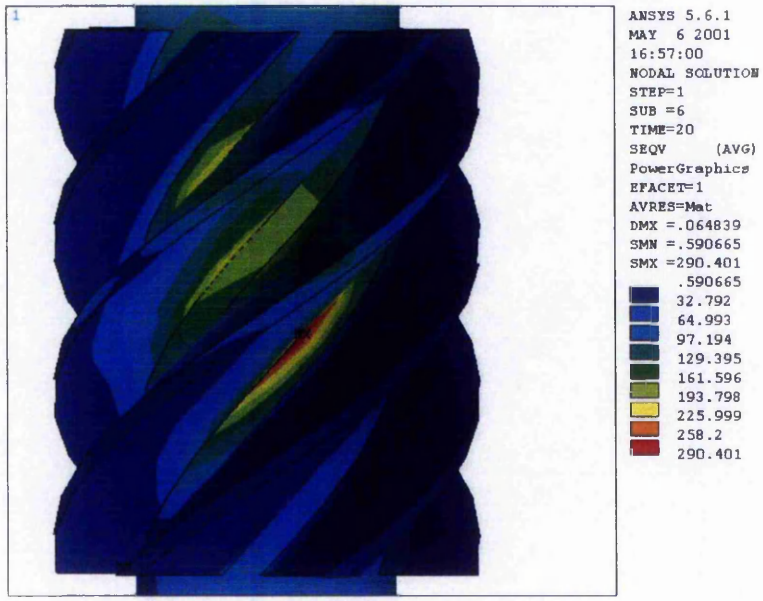


Figure 9.67 Worm I Von Mise stresses (load step 1, substep 6), position 2

9.8.1.3 Tooth Stresses at Position 3

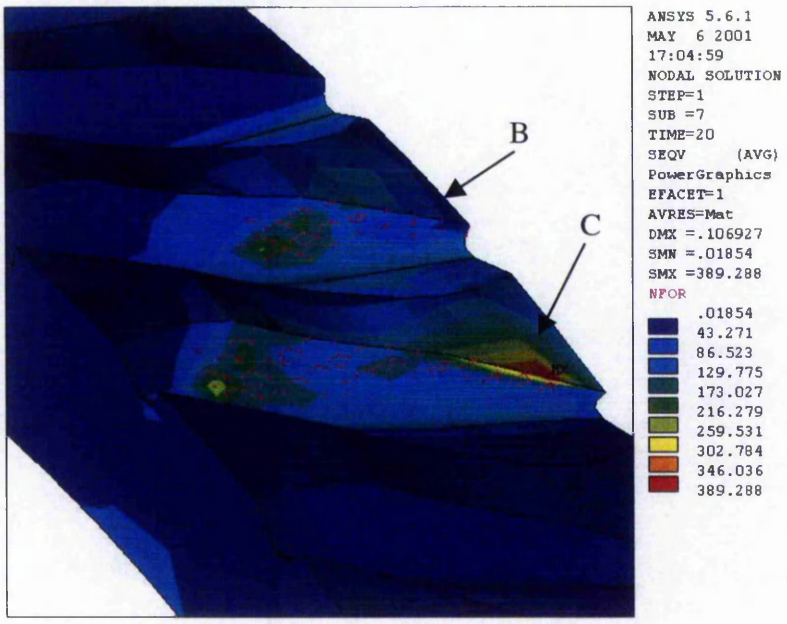


Figure 9.68 Gear I contact forces (load step 1, substep 7), position 3

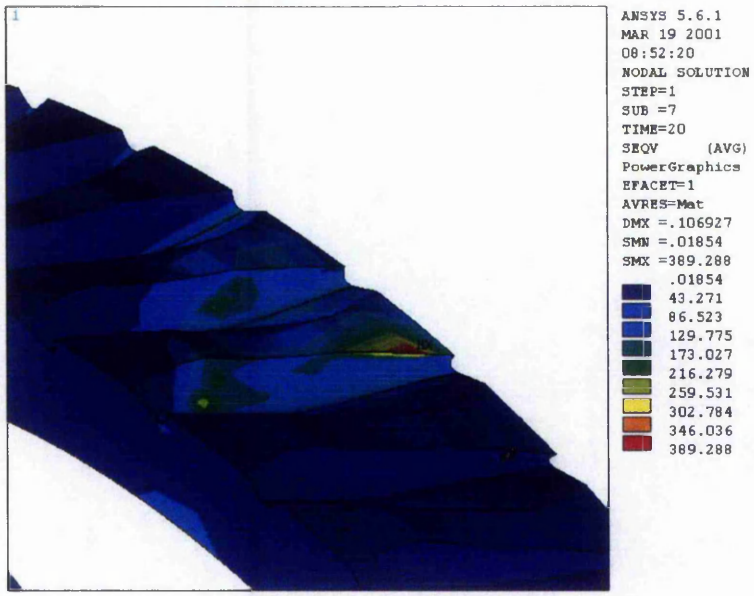


Figure 9.69 Gear I contact stresses (load step 1, substep 7), position 3

At position 3, the worm rotates another 10° and the gear 1.95348°. There are still two gear tooth pairs in simultaneous contact. The contact on tooth B moves further towards the right edge. The maximum gear Von Mises stress is nearly the same as at position 2. The contact pressure patterns of tooth B and C are also nearly the same as the preceding contact position (see Figure 9.68). The gear tooth contact stress patterns in substep 7 are shown in Figure 9.69. The worm's maximum stress increases slightly from 290 MPa to 303 MPa (see Figure 9.70).

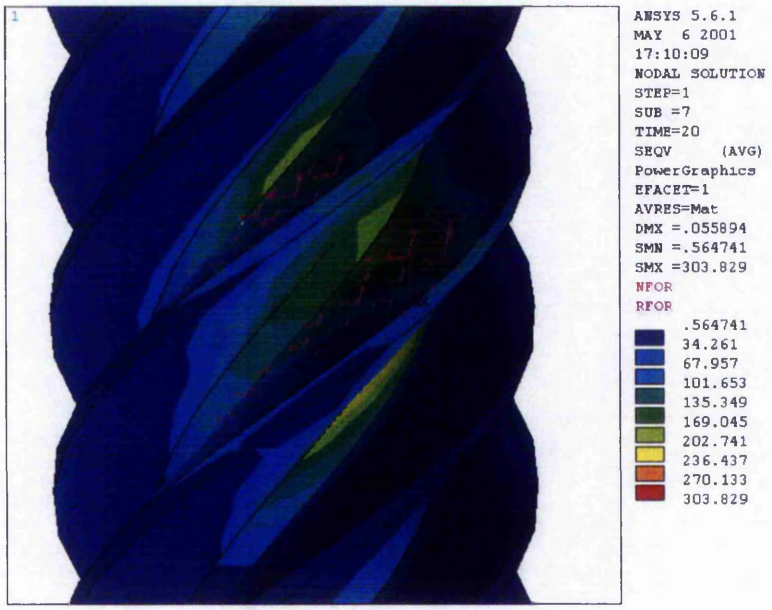


Figure 9.70 Worm I contact stresses (load step 1, substep 7), position 3

9.8.1.4 Tooth Stresses at Position 4

At position 4, there are still two tooth pairs in simultaneous contact (see Figure 9.71). Tooth D has still not come into contact. The gear maximum Von Mises stress is 308.178 MPa and is smaller than that at position 2 or 3. However, the worm's stress patterns change little (see Figure 9.73). This indicates the overall contact forces have changed little although the contact regions have shifted (see Figure 9.72 and Figure 9.68). The analysis of contact forces at position 4 (see Section 9.8.2.4) confirms the above conclusion.

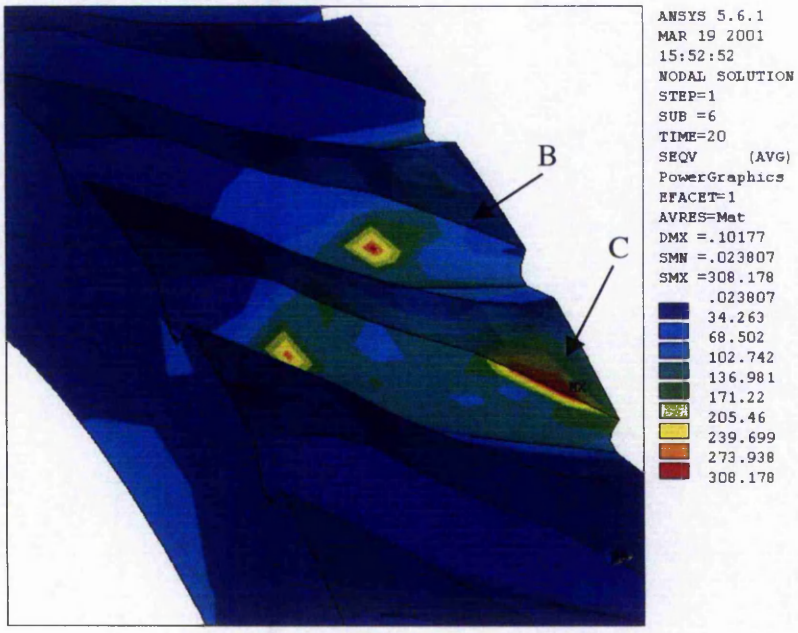


Figure 9.71 Gear I contact stresses (load step 1, substep 6), position 4

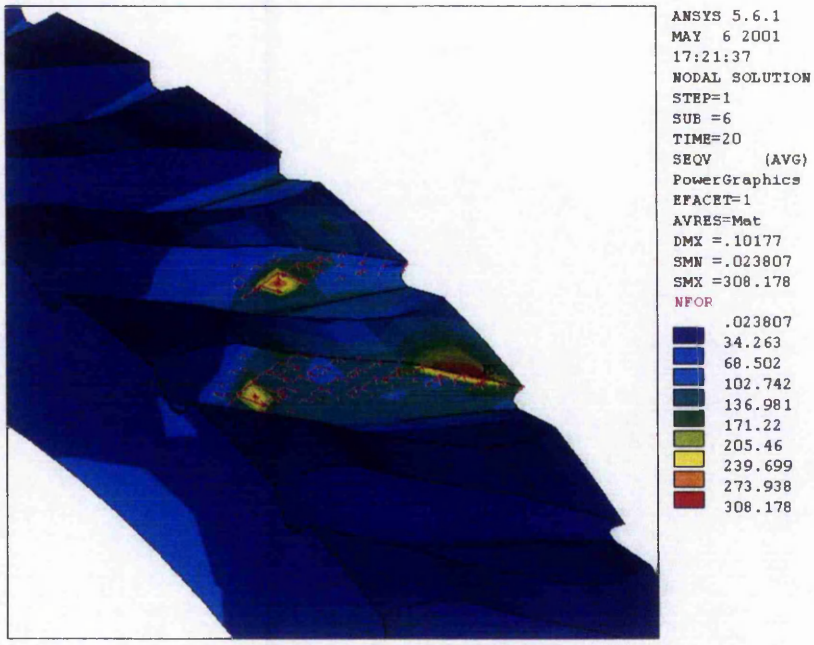


Figure 9.72 Gear I contact stresses and forces (load step 1, substep 6), position 4

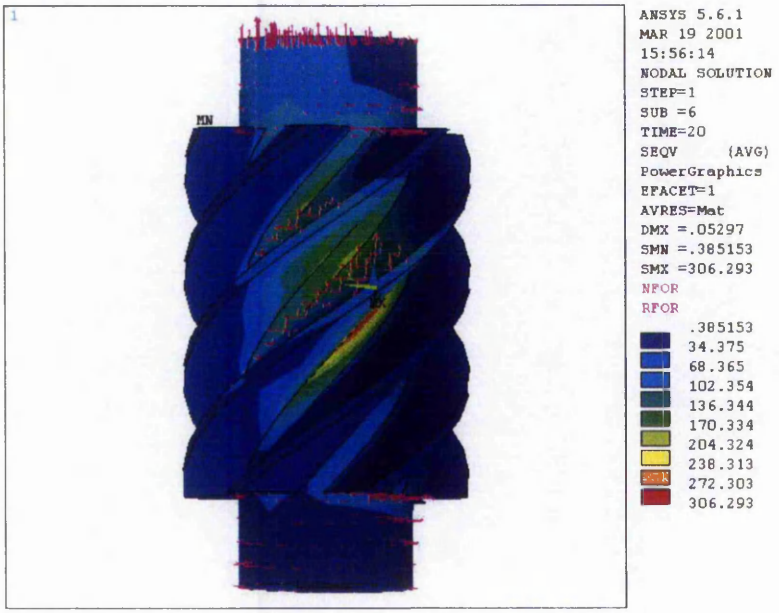


Figure 9.73 Worm I contact stresses (load step 1, substep 6), position 4

9.8.1.5 Tooth Stresses at Position 5

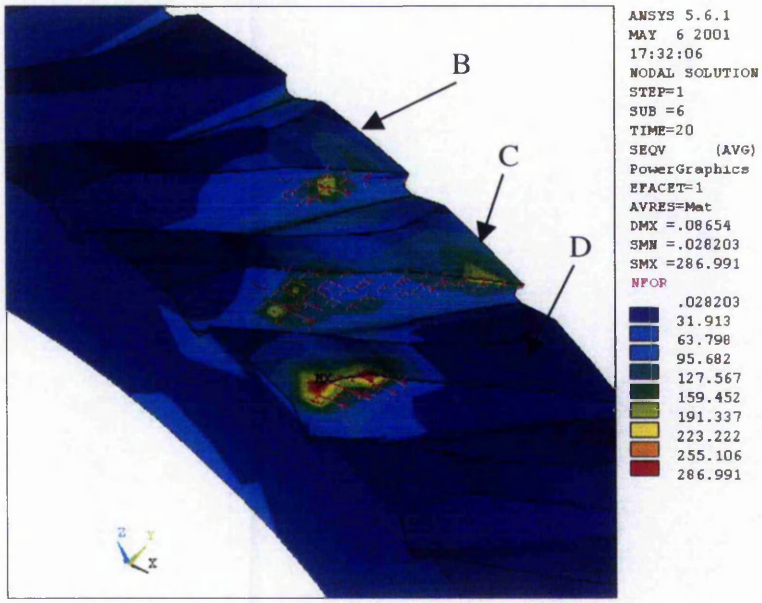


Figure 9.74 Gear I contact stresses and forces (load step 1, substep 6), position 5

At position 5, the contact status has changed from position 4. The gear tooth D comes into contact with the worm tooth (see Figure 9.74). There are three tooth pairs in simultaneous contact at this position. The gear maximum stress (286.991 MPa) occurs at tooth D near the contact centre.

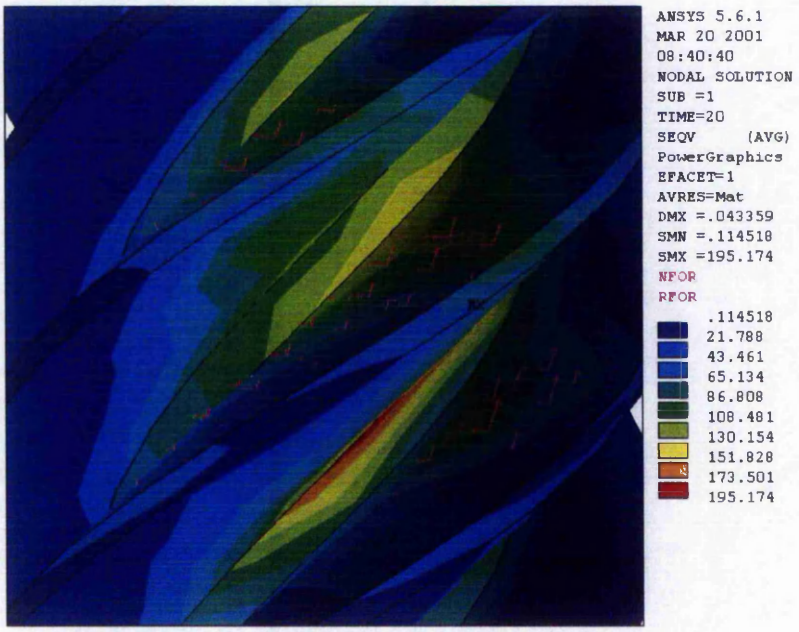


Figure 9.75 Worm I contact stresses, position 5

The worm's maximum Von Mises stress decreases from 306.293 MPa at the preceding position to 195.174 MPa. This is consistent since now there are three tooth pairs in simultaneous contact. The load share in each gear tooth is therefore smaller than that in the preceding position.

9.8.1.6 Tooth Stresses at Position 6

At position 6, there are three gear tooth pairs in simultaneous contact. Both the worm and gear's contact patterns are similar to those at contact position 1. This is consistent because after position 6, the next contact status will be the same as position 1. When the process is repeated, the gear operation can be simulated. Figure 9.76 shows the gear stress (Von Mises) pattern at contact position 6.

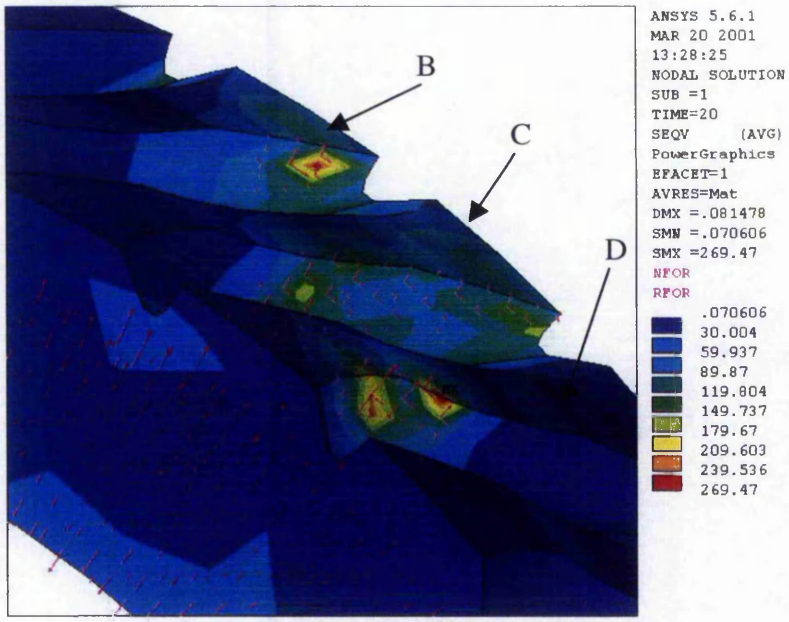


Figure 9.76 Gear I contact stresses (load step 1, substep 6), position 6

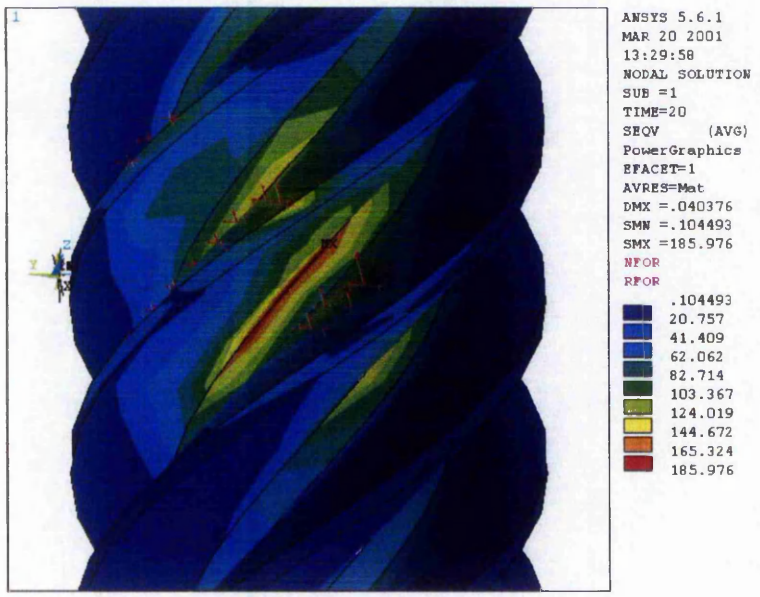


Figure 9.77 Worm I contact stresses (load step 1, substep 6), position 6

The worm tooth stresses are smaller than those in the gears. At position 6, the worm's maximum Von Mises stress is 185.976 MPa, whereas the gear's maximum Von Mises stress is 269.47 MPa.

Figure 9.78 to Figure 9.83 shows the whole gear tooth stress patterns at six different positions. The stress patterns are presented in the whole gear models so that it is easier to view the overall shift of contact regions.

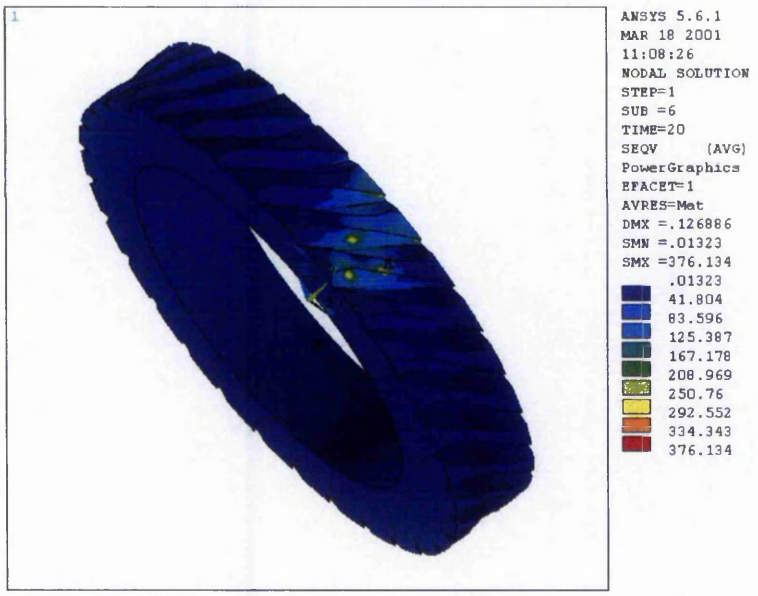


Figure 9.78 Gear I contact stresses (load step 1, substep 6), position 1

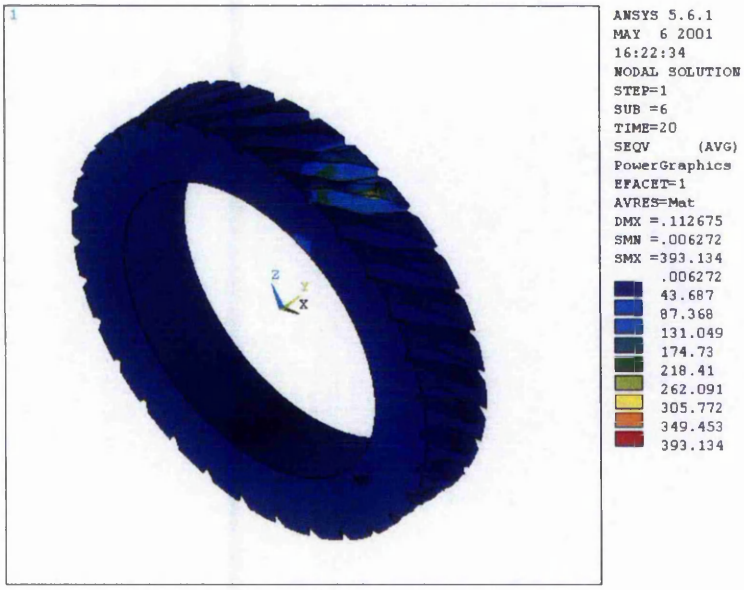


Figure 9.79 Gear I contact stresses (load step 1, substep 6), position 2

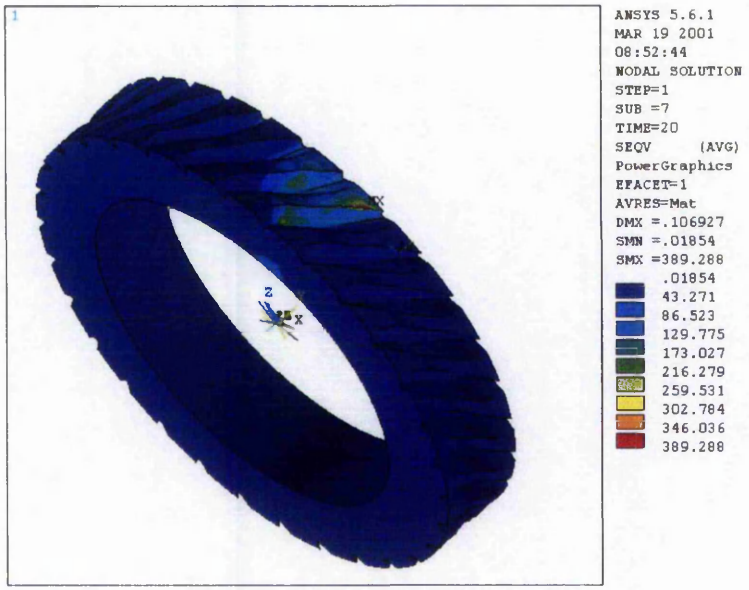


Figure 9.80 Gear I contact stresses (load step 1, substep 6), position 3

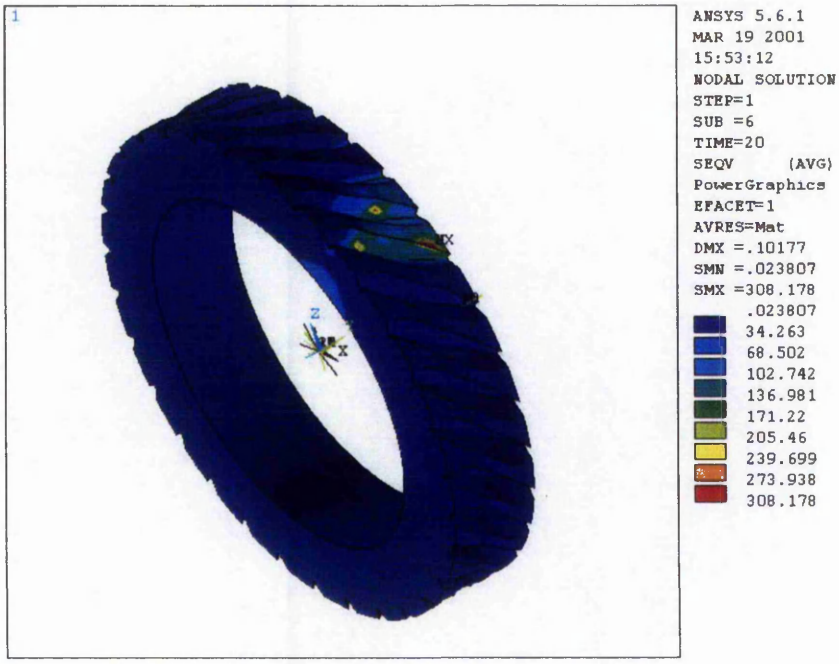


Figure 9.81 Gear I contact stresses (load step 1, substep 6), position 4

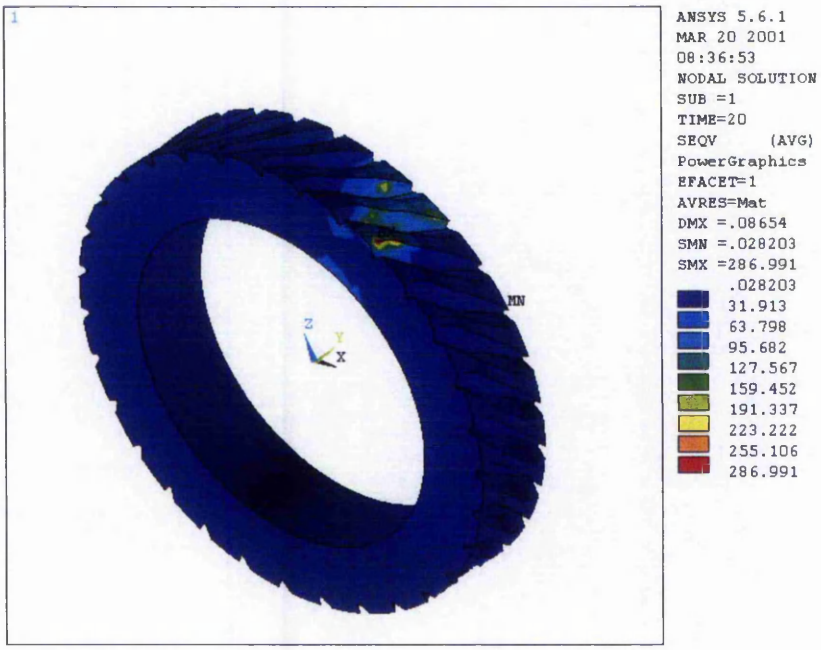


Figure 9.82 Gear I contact stresses (load step 1, substep 6), position 5

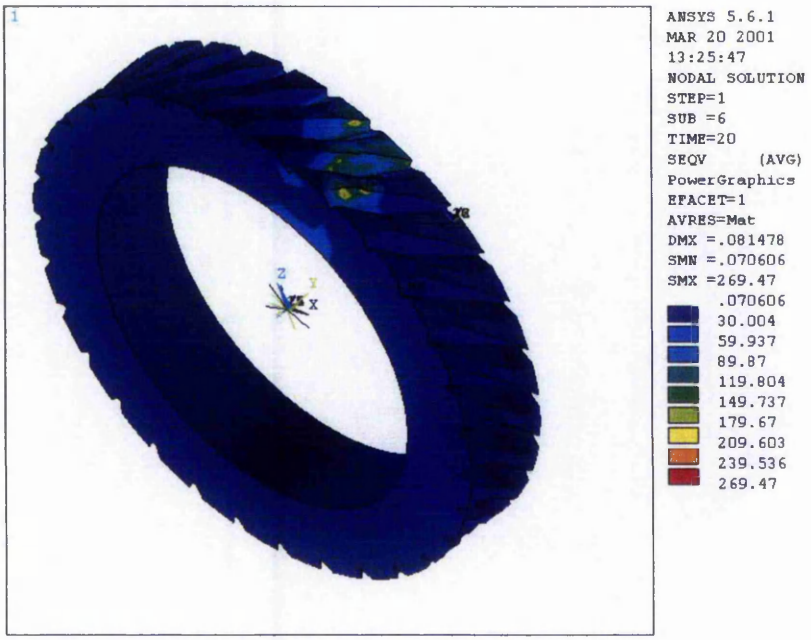


Figure 9.83 Gear I contact stresses (load step 1, substep 6), position 6

9.8.2 Load Distribution

9.8.2.1 Contact Forces and Load Share at Position 1

The contact forces are expressed in global Cartesian coordinate system. The applied gear torque is 2430000 Nmm.

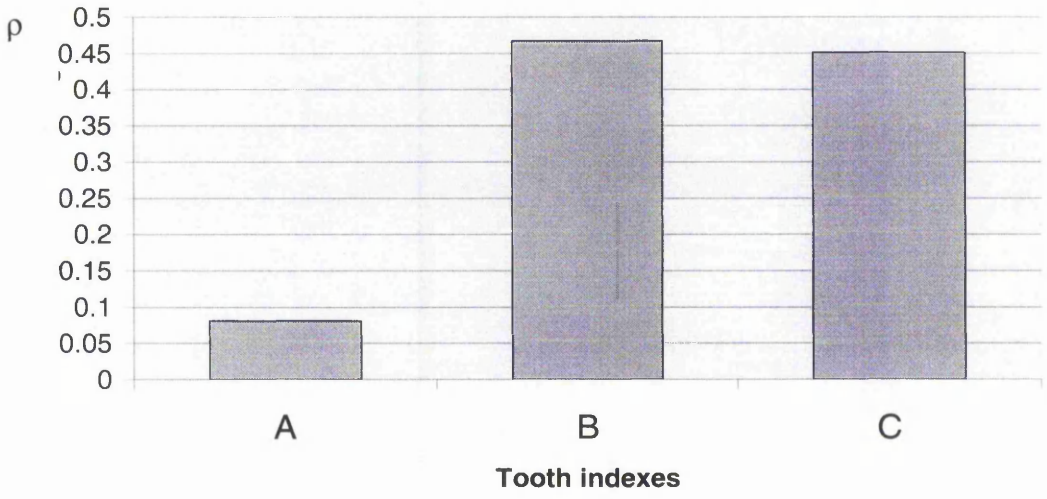


Figure 9.84 Worm gear tooth load share at position 1

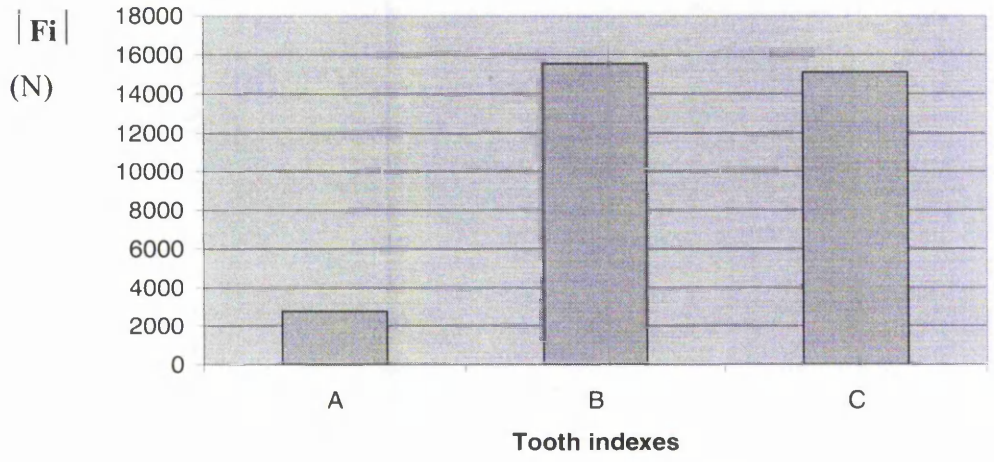


Figure 9.85 Worm gear tooth contact forces at contact position 1

The load share is calculated from the percentage of the torque each tooth contributed in the whole applied torque on the gear axis. As has been discussed in the previous section, gear tooth B has the maximum load share (46.8%). The load share of tooth C (45%) is a little bit lower than that of tooth B.

The total contact force in each tooth is the vector sum of the nodal forces on the contact region. They have different orientations. Here only the magnitudes of forces in each tooth are compared. Figure 9.85 shows the magnitude of the gear contact forces in every contact tooth. The distribution pattern of contact forces is similar to that of the load share. Tooth B has the largest force and tooth A has the smallest contact force.

9.8.2.2 Contact Forces and Load Share at Position 2

When the gear tooth contact moves from position 1 to position 2, tooth A exits from the contact. Tooth D had still not come into contact. So at position B only two teeth are in simultaneous contact. The load is shared between tooth B and C. The load share of tooth B decreases and is 40% of the whole gear torque. This agrees with the real situation since the tooth B now is at the position that will be gradually exiting from contact. The load share in tooth C has increased and contributed 60% of the applied torque.

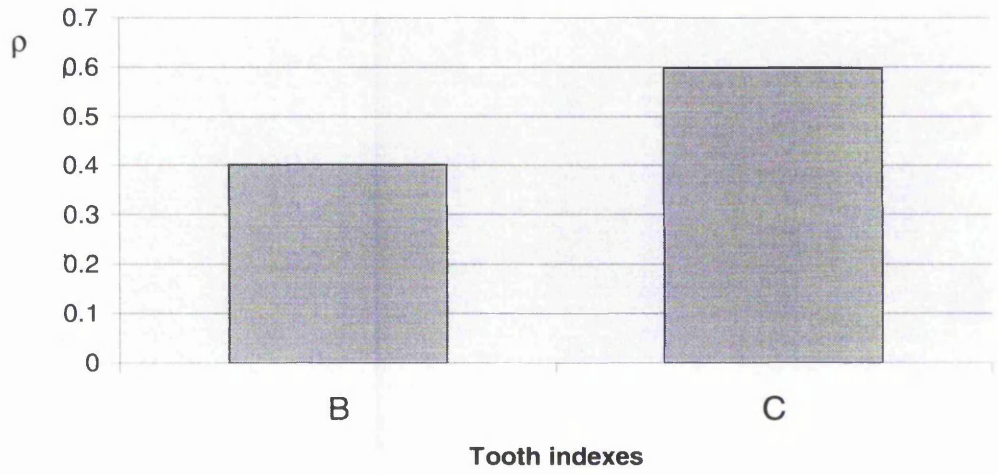


Figure 9.86 Worm gear tooth load share at position 2

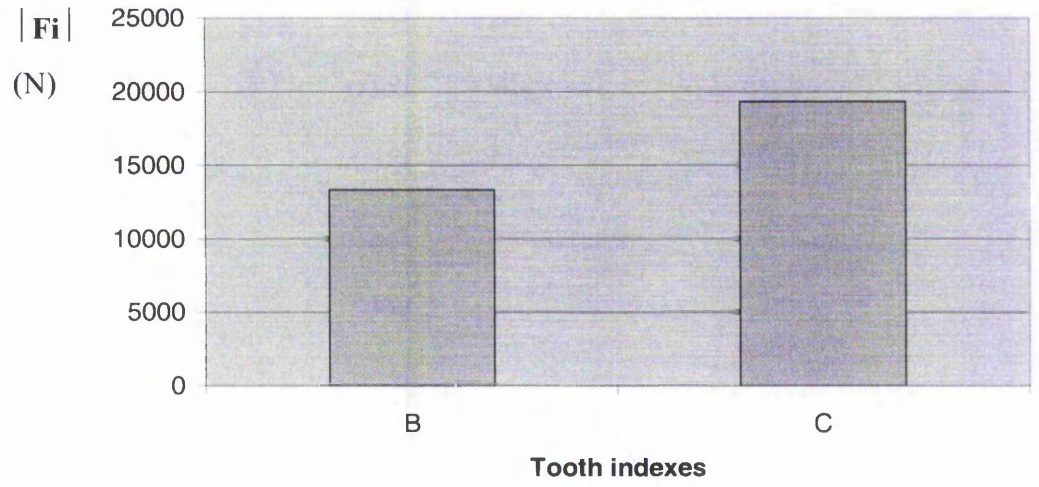


Figure 9.87 Worm gear tooth contact forces at contact position 2

9.8.2.3 Contact Forces and Load Share at Position 3

At position 3, the situation is quite similar to that at contact position 2. The load share of tooth B decreases from 40% to 32.6%. Meanwhile the load share of tooth C increases from 60% to 67.4%.

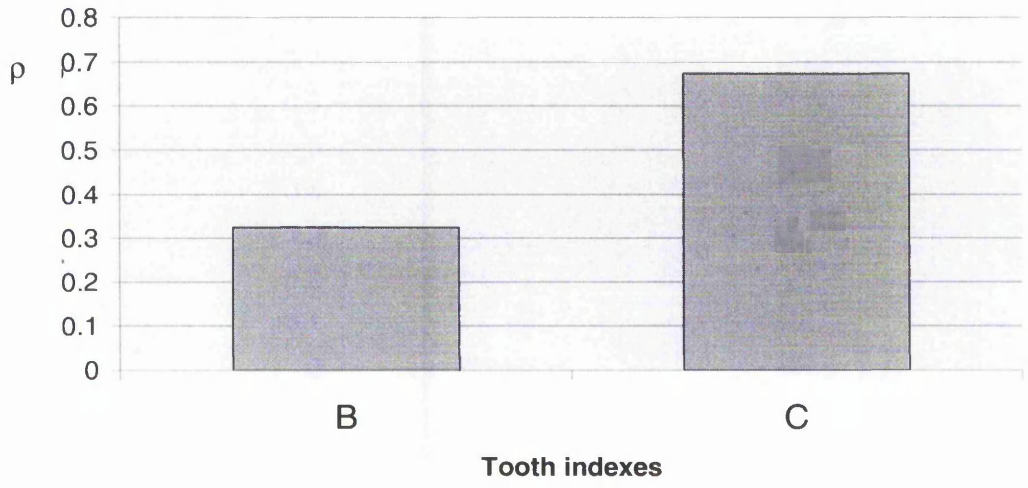


Figure 9.88 Worm gear tooth load share at position 3

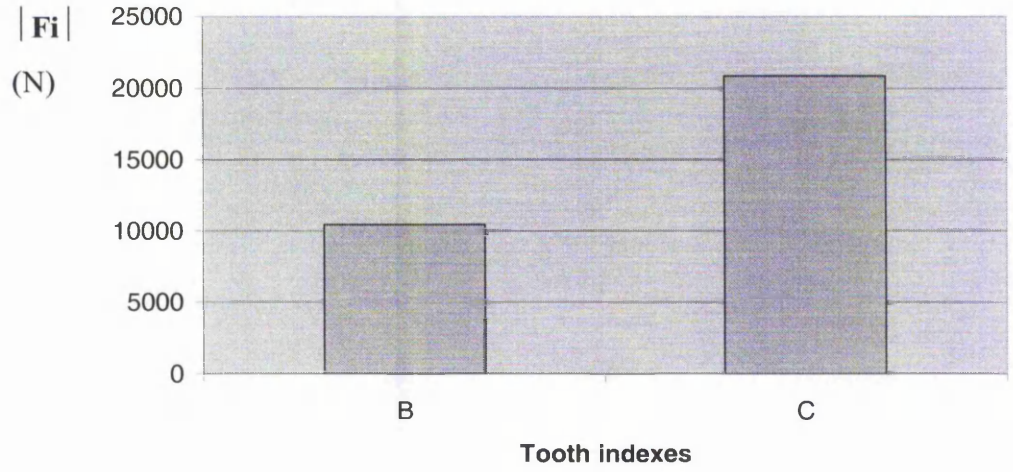


Figure 9.89 Worm gear tooth contact forces at contact position 3

9.8.2.4 Contact Forces and Load Share at Position 4

At position 4, the trends shown at position 3 continues. The load share of tooth B decreases from 32.6% to 29.6% and the load share of tooth C increases from 67.4% to 70.4%. Figure 9.90 illustrates the load share of gear teeth at position 4. Figure 9.91 shows the magnitudes of worm gear tooth contact forces.

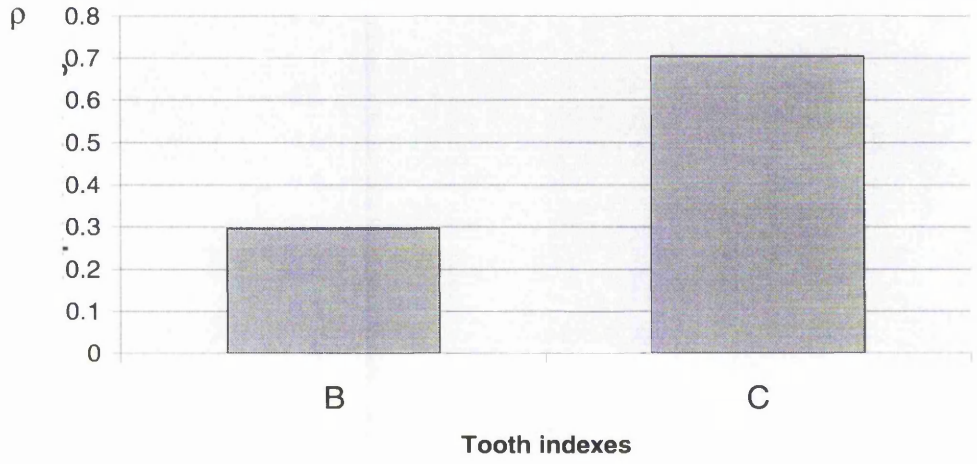


Figure 9.90 Worm gear tooth load share at position 4

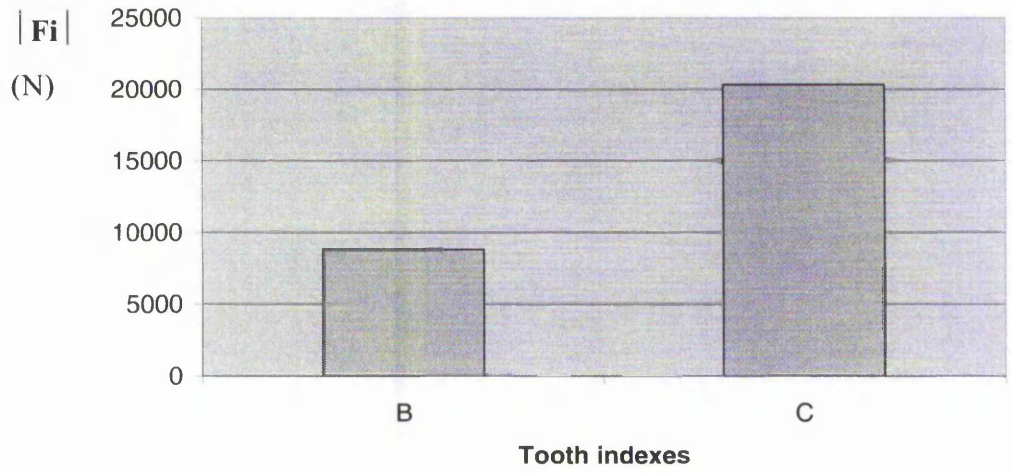


Figure 9.91 Worm gear tooth contact forces at contact position 4

9.8.2.5 Contact Forces and Load Share at Position 5

At position 5, the contact status is changed and tooth D comes into contact. Since one more tooth joins into contact, the load share of the other two teeth all decrease a little (see Figure 9.92 and Figure 9.90). Tooth C still has the maximum load share (54.8%). Tooth B has 18.3% load share and the new contacting tooth D has 26.9% load share.

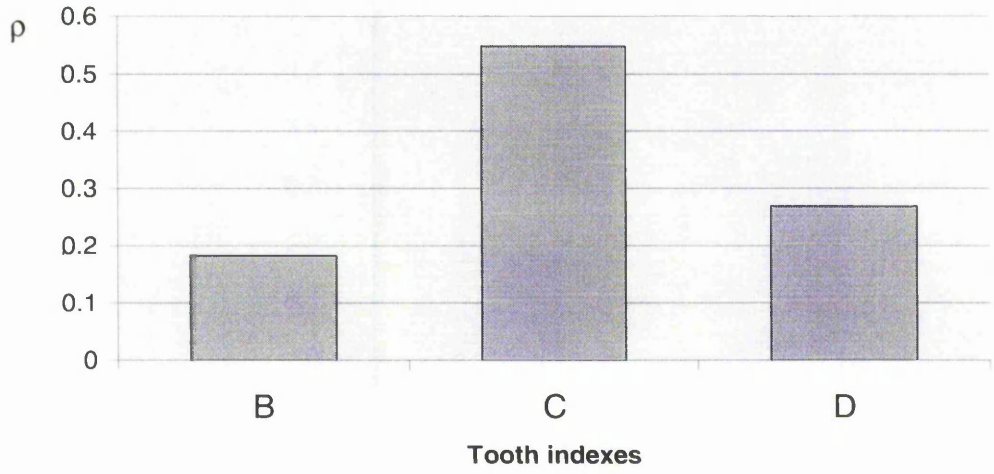


Figure 9.92 Worm gear tooth load share at position 5

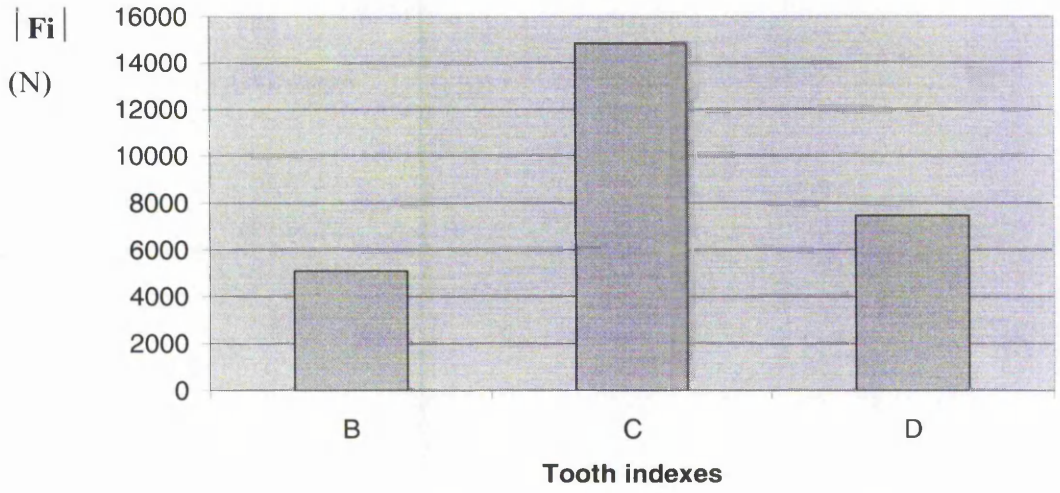


Figure 9.93 Worm gear tooth contact forces at contact position 5

9.8.2.6 Contact Forces and Load Share at Position 6

The load share of tooth B decreases from 18.3% to 11.9% and has lowest load share. Tooth C has the maximum load share though its load share decreases. The load share of tooth D increases and at the next contact position tooth D will have the maximum load share (refer to position 1).

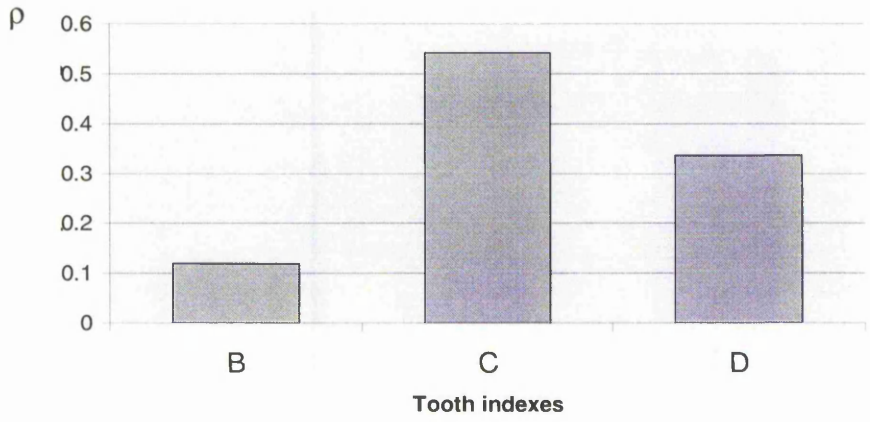


Figure 9.94 Worm gear tooth load share at position 6

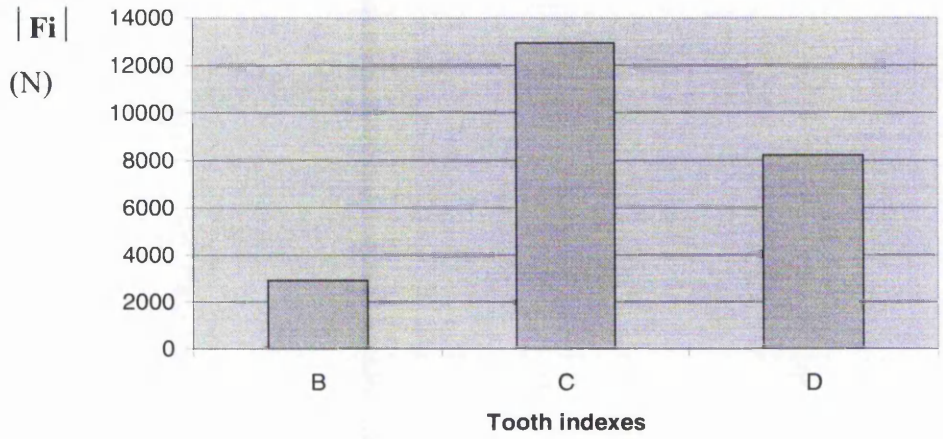


Figure 9.95 Worm gear tooth contact forces at contact position 6

9.8.3 Submodel

The meshes in the models mentioned in the previous sections are still somewhat coarse. In order to get more precise results, denser meshes are desired. However, if the computer resources are limited, it is impossible to do so using the same models. In order to solve this problem, another advanced technique, submodelling, can be used to determine more accurate stress patterns.

Figure 9.97 shows the submodel cut from the full model and is one part of tooth C which is shown in Figure 9.96 which is a coarser mesh of the full gear model. Figure 9.98 shows the tooth stress pattern (contact side) of the full gear model. Due to the coarse mesh, the stress contours are not very smooth and the stresses on the tooth fillet area are too coarse to identify the changes. However, the submodel can illustrate the details of the changes. Figure 9.99 shows the tooth stress pattern on the contact side of the submodel. The stresses in the tooth fillet area are larger than other areas except the contact region which agrees well with engineering intuition. If more detailed stress patterns in the tooth fillet area are desired, the non-uniform contour technique can be used and Figure 9.100 shows the submodel tooth stress pattern in the contact side with non-uniform contours.

Figure 9.101 shows the tooth stress pattern (non-contact side) of the full gear model. Figure 9.102 shows the submodel tooth stress pattern in the non-contact side with non-uniform contours. It clearly illustrates the smoother stress contours.

By using the submodelling techniques, the detailed tooth stress pattern can be obtained without requiring a lot of computer resources.

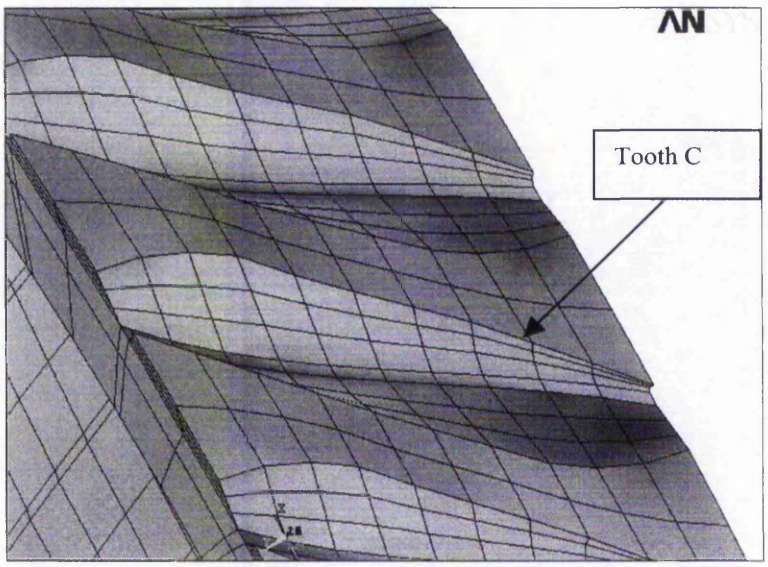


Figure 9.96 Gear tooth coarse mesh

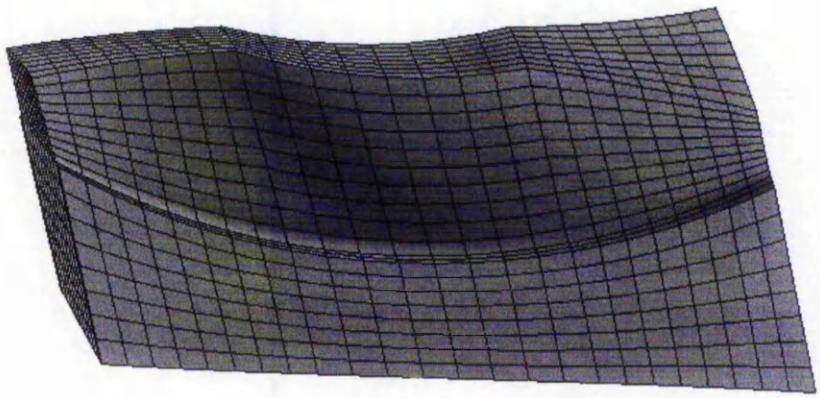


Figure 9.97 Denser mesh of one tooth submodel

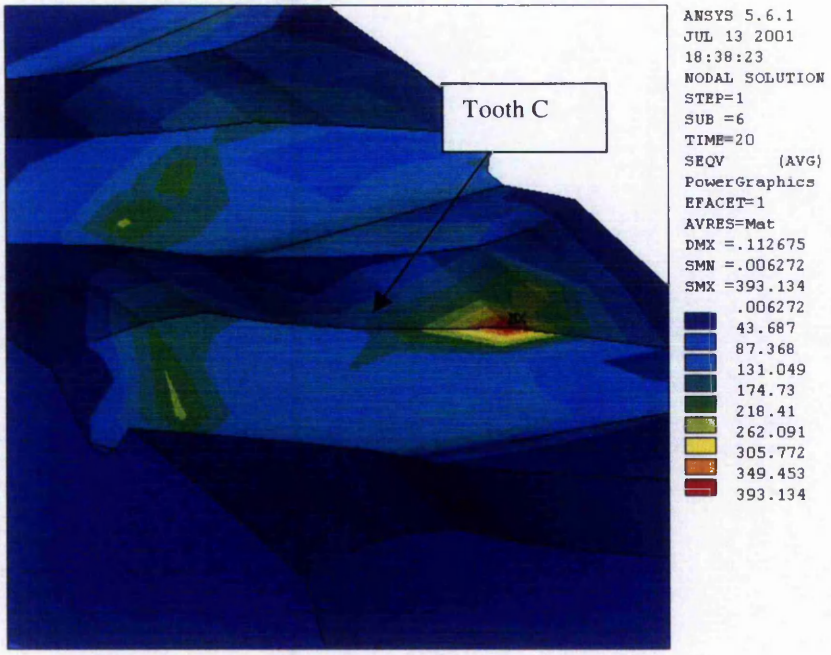


Figure 9.98 Gear tooth stresses

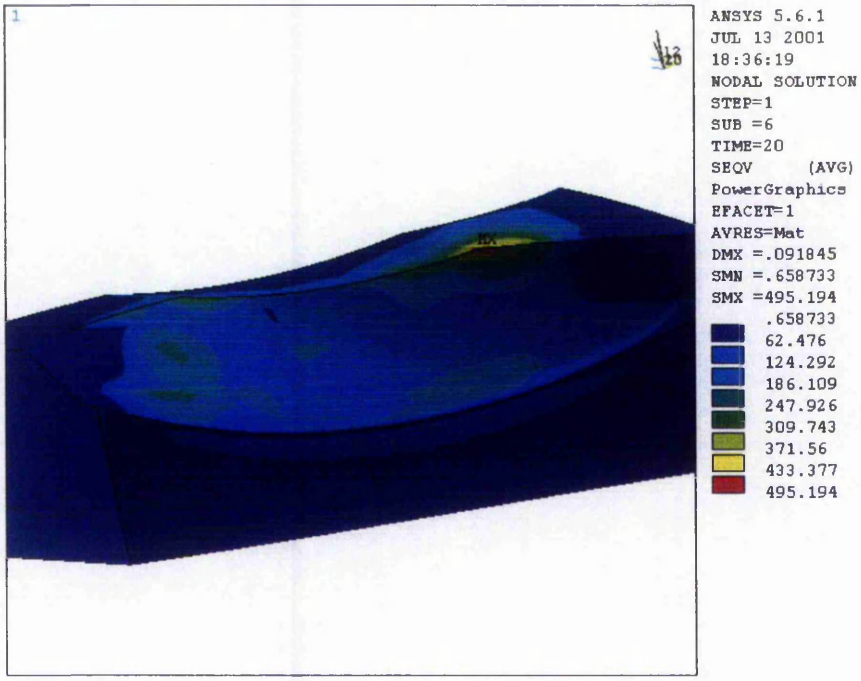


Figure 9.99 Submodel stress pattern (contact side, uniform contour)

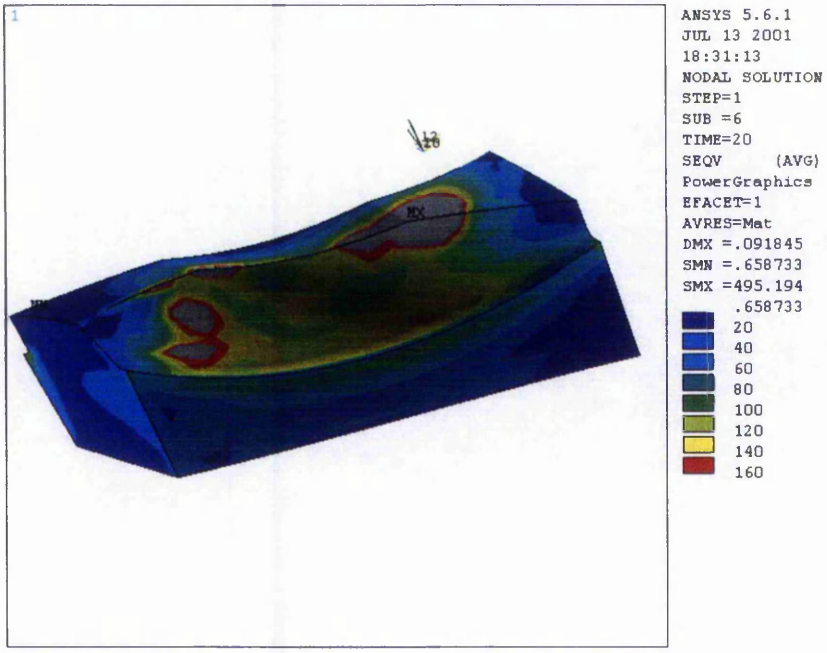


Figure 9.100 Submodel stress pattern (contact side, non-uniform contour)

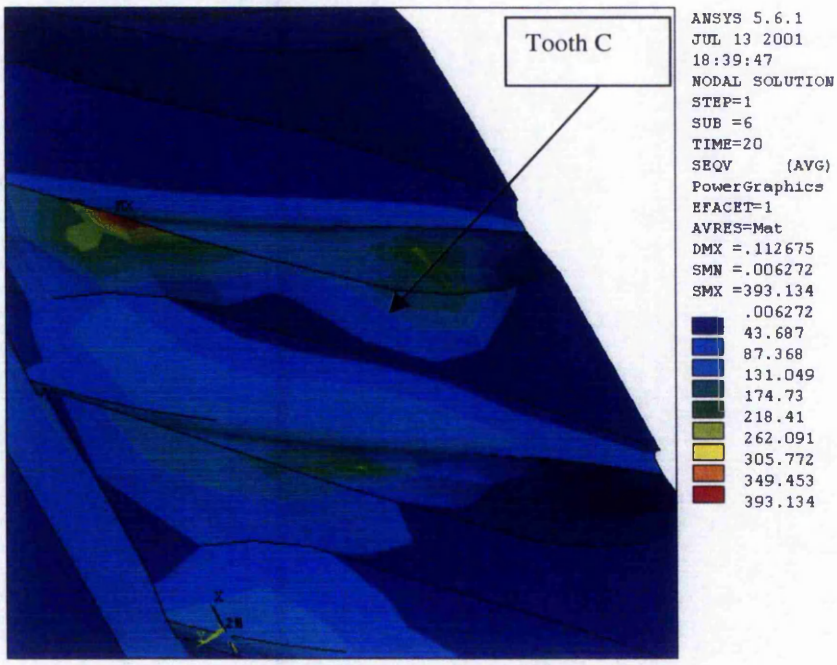


Figure 9.101 Gear stress pattern (non-contact side)

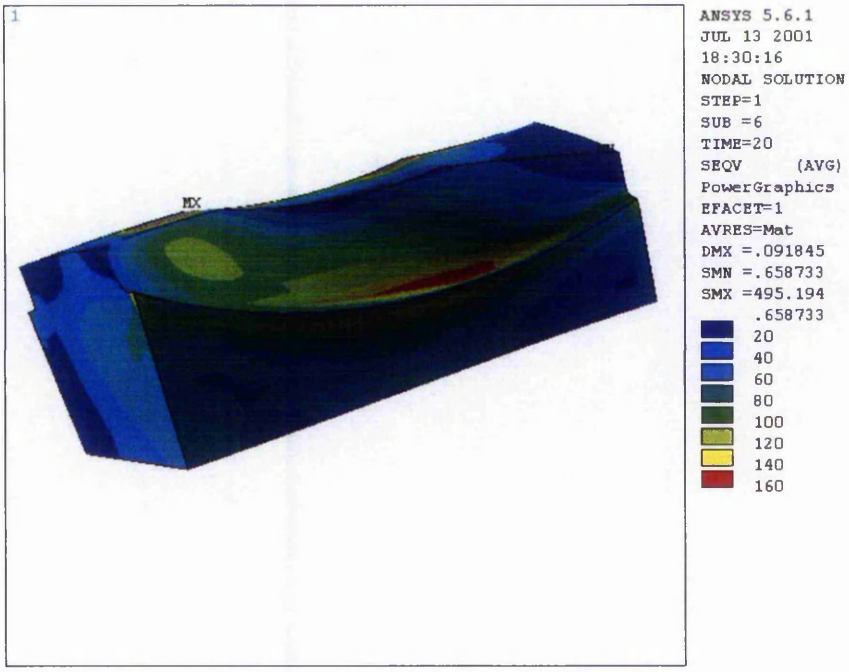


Figure 9.102 Submodel stress pattern (non-contact side, non-uniform contour)

9.9 DISCUSSION AND CONCLUSIONS

The results of the finite element contact models of worm gear can be verified by experiment. However, to obtain the worm gear contact stress by experiment is extremely difficult. Normally there are two experimental methods to obtain worm gear stresses. The first method is to place strain gauges in the gear tooth and the other is the photoelastic method. Both methods have their own advantages and disadvantages. The traditional method is simpler than the photoelastic method. However, due to the worm gear run-in characteristics, strain gauges have little room to be placed on the interested areas such as the tooth root. A research group has carried out the Holroyd worm gear experiment at Chongqing University, China in June 2001. Strain gauges were used but failed to deliver any valid results. Due to the limited space in the gear tooth, even though very small strain gauges (0.3x1.2 mm) were used, the strain gauges were all damaged after the gear tooth and worm tooth came into contact. It is planned to use the photoelastic method to estimate the gear tooth stresses in the future. This will still face a significant difficulty because the worm is made of hardened steel and the gear is phosphor bronze. The test specimens

should be made of materials that have the identical ratio of Young's modulus to the gear drive. If the test specimens are not made the same ratio of Young's modulus, the test results are useless. When the stiffness is changed, all the contact region and deformation will be changed as well. The other difficulty is that due to the running-in characteristics of a worm gear, it is impossible to observe the stresses directly on the test specimens. So special test specimen materials have to be used in order to preserve the stress status. The procedure of obtaining the stress status is that the stressed test specimen will be cooled down to preserve the stress status. The test specimen will be cut into slices and then the photoelastic method will be applied to measure the gear tooth section stresses. Such a process of course could result in a significant experimental error. According to Qin's experiment on a Hourglass gear drive (Qin and Qin, 2000), the experimental results are up to 30% different from the analytical results.

To validate the present model, the methods used to judge the spiroid gear can be applied to worm gear too. In the present analysis, commercial software is used so that if the model preparation is right, the results could be considered to be correct. When the results are assessed, firstly the simplification of the model is considered and the input condition is consistent. The stress analysis results clearly show how the tooth contact region moves and the stress pattern changes. The tooth stress changes and contact region shifts successfully simulate the gear operation. The contact force changes and load share changes in agreement with the real situation. All these provide confidence regarding the results of the model run.

The following is a brief conclusion:

Six full FE models for loaded multi-tooth contact analysis of a worm gear have been developed in this chapter. The geometrical models were built in Pro/Engineer using the advanced VGM technique. The techniques of geometry cleanup for the worm gear VGM models have been developed and illustrated in detail.

The models were imported into ANSYS via the IGES data transferring interface and meshed with high order hexahedral solid elements, which have good performance in

nonlinear tooth contact analysis. The meshing techniques for the complicated mapped mesh with hexahedral elements have been developed and illustrated.

The advanced surface-to-surface contact elements have been used to simulate the gear tooth contact. The whole range of gear operation has been simulated by six full nonlinear tooth contact models with different contact positions.

The loaded gear tooth contact stress patterns in six different models have been determined, illustrated and discussed. The gear tooth contact force and load sharing have been analysed and determined.

The feasible procedures developed in this chapter offer a solution to the unsolved problem in current worm gear design. The calculation of tooth stress and evaluation of load share are important in worm gear design but remain unknown in the existing gear design standard. The results obtained are fundamental to the design of a worm gear drive with high contact ratio and compact size.

CHAPTER 10 Conclusions

A brief conclusion of the work completed in this thesis is presented in this chapter. The major achievements of this research are summarised and suggestions for future work have been presented.

In conventional spiroid and worm gear design, the gear is generated by a hob which is identical to the worm and hence the tooth pairs are in line contact at every instant. They are sensitive to the errors arising from manufacture and assembly. In practice, due to the errors, the tooth contact may shift to the edge of the tooth surfaces which reduces the working life of a gear drive.

The solution of the above problem is to modify the gear geometry to obtain a favourable localised tooth contact pattern. However, currently there are no efficient methods available for modifying the worm and spiroid gear drives. The existing techniques for obtaining a favourable bearing contact may cause interference between the meshing teeth of the worm and its mating gear.

A fast and parametric 3D modelling of gear drives has a strong appeal for both academic researchers and industrial engineers. The conventional 3D modelling methods for worm and spiroid gears are complicated, time-consuming and non-parametric. The literature review showed that no advanced modelling method is available in the gear industry which can directly model the worm gear or spiroid gear in advanced CAD packages such as AutoCAD, SolidWork and Pro/Engineer.

The conventional tooth contact analysis (TCA) assumes gear surfaces as rigid bodies. The deformation of the two contacting teeth is simplified by an elastic approach that is uniformly imposed over the whole tooth surface and the contact between a pair of teeth is assumed to be spread over an elliptic area centred at the point of contact. This is obviously not a true reflection of reality. In reality, especially when the gears are under heavy load, the deformation and load distribution on the gear tooth surfaces affect the meshing characteristics and consequently the gear transmission errors will differ significantly from those which are expected from the TCA analysis. Most work

reported did not present an effective method to analyse the tooth behaviour under load.

The aims of this research were concerned with the optimum design and 3D CAD/CAE simulation of spiroid and worm gear drives. This research consists of three main approaches. The first approach is to develop a novel method for obtaining a favourable tooth contact pattern for spiroid and worm gearing. The second approach is to develop a novel parametric solid modelling methodology which can visualise the interference and contact paths of the new gear designs. This is achieved by simulation of the gear manufacturing process. The models allow contact path and interference to be visually investigated and controlled based on simulation of meshing. The third approach is to develop a general and feasible FEA procedure to examine the stresses, deformations, stiffness and load distributions of multi-tooth contact problems of gear drives.

10.1 OBTAINING LOCALISED TOOTH CONTACT FOR SPIROID AND HELICON GEARS

10.1.1 Existing Methods of Obtaining Localised Tooth Contact

In order to reduce the sensitivity to manufacturing and assembly errors, much attention has been focused on gear optimum design. The main idea of gear optimum design is to obtain localised tooth contact by modifying the gear tooth profile. In Chapter 2, a number of existing approaches for modifying the gear tooth profile have been reviewed. Many contributions have been made in this area. However, the existing methods of tooth profile modification of worm and spiroid gears are difficult to implement in standard gear hobbing machines.

10.1.2 A Novel Approach for Obtaining Favourable Localised Tooth Contact of Spiroid and Helicon Gears

In this project, a novel approach to obtaining the favourable localised tooth contact of gear teeth has been proposed and developed. The localised contact is achieved by

modifying the worm tooth surface. With this approach, only the worm cutter's geometrical angles and mounting position need to be adjusted.

The meshing theory of modified gear surfaces has been established. The mathematical models of gear tooth surfaces have been deduced. Programs have been written to obtain the modification parameters and to solve the nonlinear meshing equations of spiroid, helicon and ZA worm gears. Numerical simulations of meshing of localised tooth contact of spiroid, helicon and ZA worm gears have been conducted. The results confirm that the proposed gear modifying method provides better localised bearing contact and the edge contacts are avoided.

The numerical analysis of the contact path of the modified spiroid, helicon and worm gear drives proves the tooth contact of the new type of spiroid and helicon gearing is stable both in contact pattern and size.

This new approach is capable of being implemented in standard gear hobbing machines. It is more economical than the existing methods for the modification of gear teeth. The modified spiroid and worm gearing have significant advantages over the conventional ones such as less sensitivity to misalignments, more favourable lubrication condition, higher load capacity, longer working life and lower manufacturing costs. The new type spiroid, helicon and ZA worm gear drives can achieve high transmission quality and cut down the time and effort spent in production and assembly. Therefore, this project has contributed a novel method to develop a new type spiroid, helicon and ZA worm gearing with favourable localised tooth contact.

10.2 3D PARAMETRIC MODELLING AND VIRTUAL SIMULATION OF SPIROID AND WORM GEARS

Worm and spiroid gear drives have complex tooth geometry. 3D gear models are essential to view the tooth contact patterns and to detect any possible interferences between the contacting teeth in a modified gear drive. 3D gear models are also necessary in loaded tooth contact analysis using the finite element method. However, it is not an easy task to build three-dimensional models of spiroid and worm gears. In

current gear modelling approaches, complicated numerical models are involved and a set of unknowns from the surface and meshing equations has to be solved. It may be relatively easy to find the solution for part of the surfaces but it is usually difficult to obtain the full surface from these meshing equations. All the current 3D modelling methods are complicated, time-consuming, non-parametric, inflexible regarding changes and do not directly reflect the nature of gear manufacturing.

A novel 3D parametric modelling methodology, *virtual gear manufacturing*, has been first proposed and developed by the author to overcome the shortcomings of existing 3D gear modelling methods. The principle of VGM is to simulate the practical gear hobbing process to cut a gear in the advanced 3D CAD package, Pro/Engineer.

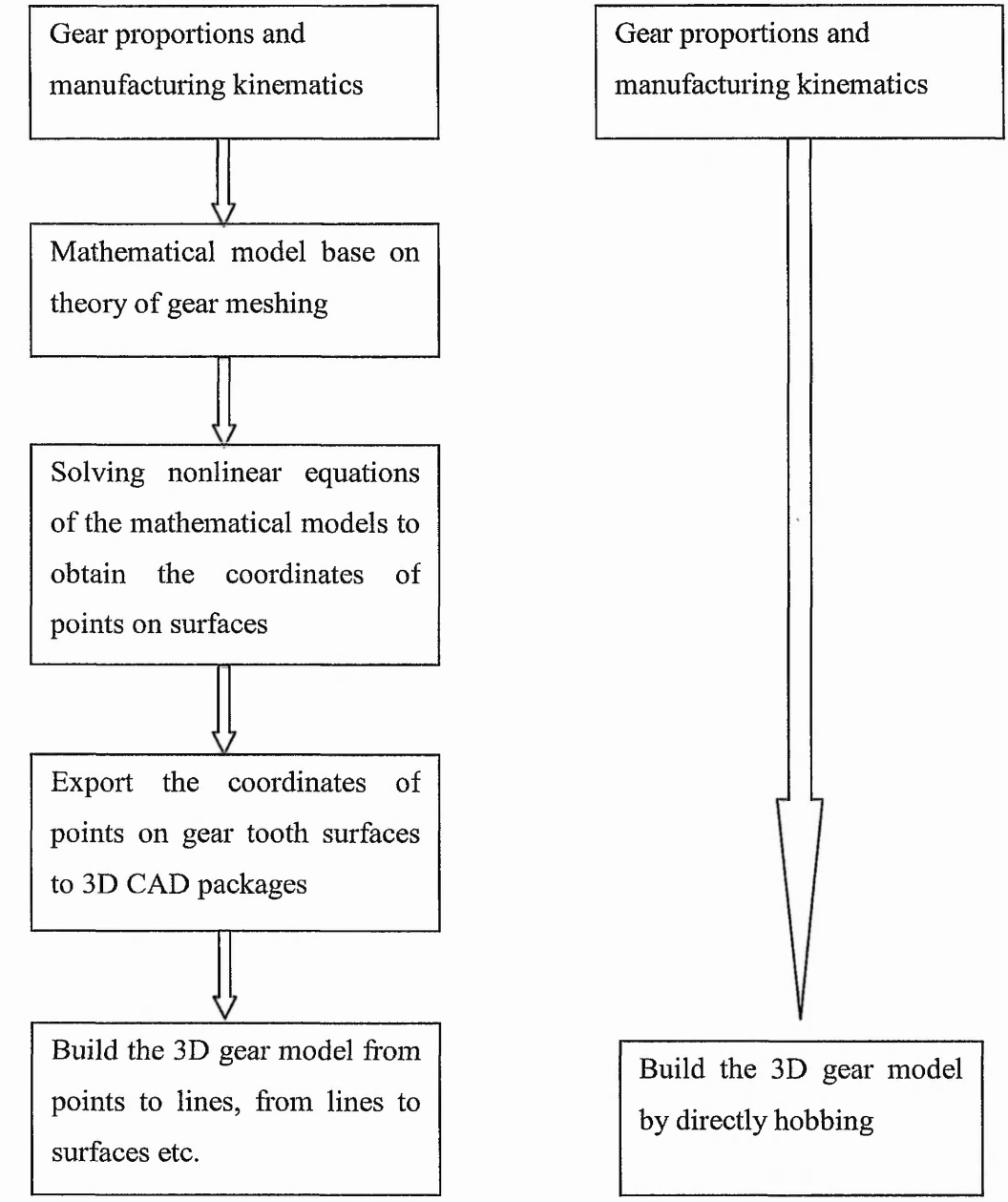
Unlike conventional 3D modelling methods, the VGM method does not involve any mathematical modelling and hence the solution of the complicated non-linear meshing equations can be avoided. One of the most difficult aspects in the VGM method - to simulate the worm and spiroid gear hobbing process in which the gear blank and hob rotate perpendicularly about their own axes – have been solved. The two-axis-rotational cut has been simulated using the advanced *helical sweep cut* and advanced patterning techniques.

The methodology and techniques have been developed for 3D spiroid and worm gear modelling. The VGM models can be used to simulate gear meshing, to analyse the contact pattern and to detect any possible tooth interference in the new gear design.

In comparison with conventional 3D gear modelling methods, the VGM method has distinct advantages as summarised below:

- The VGM method produces 3D gear models more quickly than the conventional gear modelling method. Figure 10.1 is a comparison between conventional gear modelling methods and the VGM method. It clearly shows the advantage of the VGM method. The process of solving the nonlinear meshing equation for worm and spiroid gears in the conventional gear modelling method is an extremely difficult and time-consuming process. Unlike conventional 3D gear modelling methods, the VGM method does not utilise

the coordinates of points on the gear tooth surface to build the solid gear model. Therefore, the extreme difficulty in obtaining the full solutions of gear surface points from the non-linear meshing equations can be avoided. The VGM method directly models the gears from the gear proportions.



(a) Conventional 3D modelling (b) The VGM method

Figure 10.1 Comparison between conventional gear modelling method and VGM

- The VGM process visualises and animates both the conventional and modern meshing theory of gearing. Modern computerised gear theory can only simulate the meshing of gearing in point or line contact. But, in addition to the simulation of point and line contact, The VGM process can visually simulate the more general region contact patterns.

- The VGM method provides a fast way to visualise the design of spiroid or worm gears. This will help designers to improve their work and reduce the product cycle time and costs. The 3D simulation provides a useful visual aid for investigating the tooth contact. With 3D simulation, the contact pattern of the spiroid and worm gearing and their direction of relative motion can be predicted and the interference between the modified tooth surfaces can be detected and hence avoided at the design stage. It is valuable both for academic research and industrial application.

- The VGM gear model is more accurate than the model built by the conventional gear modelling method. The solutions of the conventional model which are based on gear meshing theory are the coordinates of the points on the contact lines. So with conventional gear meshing theory it is impossible to find the solutions in the root areas where no contact lines reside and therefore it is difficult for the conventional modelling method to construct the whole accurate tooth surface. However, the VGM model simulates the gear manufacturing process in which no coordinates of surface or contact lines are required and it naturally produces the root fillet areas.

- The VGM method can produce the gear models that the conventional gear modelling method cannot. For example, the VGM method easily produces worm gear set II (see Figure D.7 Gear set II assembly) using the data from Holroyd, Inc. The gear commercial software used in Holroyd, Inc. cannot find the coordinates of the whole gear surface and only partial surface points are found (Fish, 2000). Without the surface datum points, the conventional 3D gear modelling method cannot make the gear models.



- The VGM models are parametric and very flexible for incorporating to changes. The 3D VGM models also lay a solid foundation for the loaded gear tooth contact analysis using the finite element method.

- The VGM method is a novel approach. The VGM method is completely different from the conventional 3D gear modelling method not only in concept but also in procedures.

- The VGM method can significantly reduce the manufacturing cost in the early production stage because it can visually detect and fix the problems in a new gear design before expensive prototypes are built. It is also a very powerful tool to build 3D gear models for CNC gear hobbing machines.

Based on the new modelling method, ZA worm gear, ZI worm gear, spiroid gear and helicon gear drives have been virtually manufactured in Pro/Engineer. Those gear drive models have been assembled. With the new VGM models, simulations of the meshing of spiroid and worm gears have been conducted and animated. The worm and spiroid tooth contact paths have been determined in a virtual 3D environment.

10.3 LOADED MULTI-TOOTH CONTACT ANALYSIS OF SPIROID AND WORM GEARS USING THE FINITE ELEMENT METHOD

10.3.1 Conventional Loaded Tooth Contact Analysis Methods

Since the gear teeth have very complex geometry, no simple stress analytical solution has so far been developed for any given set of gear teeth. The conventional method cannot accurately predict gear tooth stresses and load distributions.

With the rapid development of computer software and hardware, it is now possible to accurately predict the gear tooth contact stresses and deformations using the finite element method. However, loaded gear tooth contact analysis is a highly nonlinear problem and is extremely difficult.

There are few research papers published on the analysis of loaded multi-tooth contact analysis. The limited research publications available are mainly focused on a single gear tooth, not on all the teeth involved in the contact regions. This does not reflect the real situation. Partial multi-tooth contact models have boundary constraint problems. In partial models, gap elements have been used to predict the penetrations between the simultaneously contacting teeth. Therefore, the unloaded contact paths have to be used as the loaded tooth contact path in the finite element analysis. This is not accurate of course. Besides, the process of alignment of the gap elements in the anticipated contact paths is numerically tedious and difficult.

The research work in this area is still in its infancy due to the extremely complicated worm and spiroid gear tooth geometry and contact condition. No satisfactory LTCA work for the worm and spiroid gear drives has so far been carried out. Based on the model built by the VGM method, the loaded multi-teeth contact analyses of worm and spiroid gears have been successfully conducted in this research.

10.3.2 Nonlinear Tooth Contact Analysis and Techniques

10.3.3 Loaded Multi-Tooth Contact Analysis of Spiroid Gear

A feasible and general finite element method has been developed to analyse the multi-tooth contact pattern for spiroid gears. The 3D geometrical models of spiroid gear drives were exported to ANSYS from Pro/Engineer. An evaluation of solid and contact elements for nonlinear gear contact finite element analysis has been conducted. The techniques for 3D gear model geometry cleanup, importing a 3D gear model via the IGES interface, and 3D finite element meshing have been developed. The FE models enable the loaded tooth contact pattern, stress distribution, contact force and load distribution to be fully examined for the first time, which cannot be undertaken using conventional theoretical or experimental methods.

The feasible procedures for the 3D spiroid gear modelling, geometry cleanup and 3D model generation have been illustrated in detail in this research. The techniques developed for the spiroid gear geometry cleanup are general and can be used for other

types of VGM gear models. The developed FE procedures and techniques make the complicated loaded multi-tooth FE contact analysis much simpler and more efficient.

One full spiroid gear model and seven simplified full models have been developed for the loaded multi-tooth contact analysis of spiroid gears. Another ten partial spiroid models and submodels have also been developed during this research.

Advanced surface-to-surface contact techniques have been used in the multi-tooth contact analysis. The contact boundaries are simulated by the general surface-to-surface contact elements that are more convenient and more suitable to simulate the real tooth contact than gap elements. The general tooth surface-to-surface contact techniques calculate the contact and determine the contact forces automatically. This technique makes the gear finite element model more efficient and accurate.

The whole spiroid gear operation range is simulated by seven simplified full FE models with different contact positions. The spiroid gear contact stress distributions throughout the whole gear operating ranges have been illustrated and discussed in detail. The cross section stress patterns in the gear and worm are also visually presented which is almost impossible for experimental methods. The contact forces and load sharing of spiroid gears have been determined. The relation between the load distribution, the contact forces and the stresses with the different contact positions has been illustrated. The observed contact region is elliptic and the contact force distribution is similar to that of classical Hertzian contact theory.

The full contact models should be used rather than partial models for the loaded multi-tooth contact analysis. The partial models were found not to be suitable for gear tooth contact analysis in this research. In contrast to the widely used practice that applies partial models for the loaded multi-tooth contact analysis, the partial models were found to be inaccurate in the trial runs in the present partial models due to the problem of boundary simulation.

The boundary conditions have a significant influence on the final contact forces and tooth stresses. The middle tooth among the simultaneous contact teeth has the highest proportion of the load. The fraction of load on the tooth depends on the position of its

contact region. The tooth with the contact region in the middle of its width has the largest load share. The tooth with the contact region near to its edge has the smallest load share. The hexahedral high order element exhibited good performance for the loaded gear tooth contact analysis.

Non-linear multi-tooth contact analysis requires very accurate tooth geometry. Special attention should be paid to the accuracy of the FE model after the model has been imported and the subsequent geometry cleanup. Geometry importation via the IGES should use the *alternative* option rather than the *default* option for the gear contact models.

10.3.4 Multi-Tooth Contact Analysis of Worm Gears

The worm gear geometrical models are built in Pro/Engineer using the advanced VGM technique. The techniques of geometry cleanup for the worm gear VGM models have been developed and illustrated in detail.

The models are imported into ANSYS via the IGES data transferring interface. The models are meshed with the high order hexahedral solid elements, which have good performance in nonlinear tooth contact analysis. The meshing techniques for the complicated mapped meshing with hexahedral elements have been developed and illustrated.

The advanced surface-to-surface contact elements have been used to simulate the gear tooth contact. The whole range of gear operation is simulated by six full nonlinear tooth contact models with different contact positions. The loaded gear tooth contact patterns in six different models have been determined, illustrated and discussed. The gear tooth contact force and load sharing have been analysed and determined.

The feasible procedures reported offer a solution to the unsolved problem in current worm gear design. The calculation of tooth stress and evaluation of the load distribution are important in worm gear design but remain unknown in the existing gear design standard. The results obtained are the fundamentals of the design of worm gear drives.

10.4 A BRIEF SUMMARY

10.4.1 Three Major Achievements

This thesis is concerned with optimum design and 3D CAD/CAE simulation of spiroid and worm gear drives. Three original contributions have been achieved in this PhD research. They are:

- A novel approach has been proposed and developed to obtain a favourable tooth contact pattern for spiroid and worm gears. This new approach is capable of being implemented in standard gear hobbing machines. It is more economical than the existing gear tooth modification methods. The modified spiroid and worm gears have significant advantages over the conventional ones such as less sensitivity to misalignments, more favourable lubrication condition, higher load capacity, longer working life and lower manufacturing costs.

- A novel parametric solid modelling methodology, *virtual gear manufacturing*, has been developed to visualise the interference and contact paths of the new gear designs. The VGM method is a significant approach because (1) it is parametric and has much faster 3D modelling speed than the conventional gear modelling method; (2) it can model gear drives directly without involving any complicated mathematical modelling; (3) it visualises and animates both the conventional and modern meshing theory of gearing. Modern computerised gear theory can only simulate the meshing of gearing in point or line contact. The VGM method can visually simulate the more general regional contact problems; (4) it can reduce the manufacturing cost in the early production stage.

- Full nonlinear multi-tooth contact finite element models of spiroid and worm gears using the advanced surface-to-surface techniques have been developed and analysed in this thesis. The worm and spiroid gear tooth contact stress

patterns in the whole gear operation range have been determined and simulated. It is believed that this is the first time that real loaded contact tooth stresses and deformations of spiroid and worm gearings have been fully examined. The feasible standard procedures and techniques developed in this research enable engineers and researchers to conduct the loaded multi-tooth contact analysis much more easily.

10.4.2 Completed Work

During the PhD research, substantial research studies have been conducted in obtaining favourable localised tooth contact patterns, in 3D parametric modelling and in loaded multi-tooth contact analysis for spiroid and worm gears. The completed investigations in this thesis are listed as follows:

- A thorough literature review of present published research in the optimum design of gear tooth profile and 3D CAD/CAE simulation has been conducted.

- A new method has been developed to achieve the localised bearing contact for spiroid, helicon and worm gears. The new method is able to implement easily for standard gear hobbing machines and it will therefore be more cost-effective.

- The mathematical models of the modified spiroid, helicon and worm gear surfaces and meshing have been established; Programs have been developed using MathCAD and Matlab to calculate the surfaces and contact patterns; The localised contact paths have been determined and illustrated.

- A novel CAD modelling method, *virtual gear manufacturing* (VGM) method, has been developed for spiroid, helicon and worm gear drives which directly reflect the nature of gear manufacturing.

- Virtual simulations of the meshing of worm and spiroid gear tooth surfaces have been conducted.

- A general and feasible finite element modelling method for multi-tooth contact analysis of worm and spiroid gears using the advanced surface-to-surface contact algorithm has been developed.

- A reliable *finite element analysis* (FEA) procedure and technique have been developed to predict the contact stresses and load sharing of spiroid and worm gear drives using ANSYS.

- The tooth contact stress patterns and load sharing of spiroid and worm gear drives have been investigated. The trend of contact stress changes and load sharing variation during the whole gear operation agree well with the real situation.

10.4.3 Numerical Models Developed

In this project, the following numerical models have been established. The numerical models are programmed and have been simulated in MathCAD.

- Modified and unmodified spiroid gear models
- Modified and unmodified helicon gear models
- Archimedean worm gear model

10.4.4 VGM Models Developed

The following 3D geometrical models have been created using the VGM method during this PhD research.

- Two 3D models of Archimedean worm gear parts and assembly
- Three 3D models of ZI worm gear parts and assembly
- One 3D model of spiroid gear parts and assembly
- One 3D model of helicon gear parts and assembly

10.4.5 FE Models Developed for LTCA

The following multi-tooth contact FE models of gear drives have been developed during this PhD research.

- One full spiroid gear finite element contact model
- Seven simplified full spiroid gears FE models
- Ten partial spiroid gear multi-tooth contact FE models
- Six full FE worm gear contact models

10.4.6 Experimental Work

- Holroyd worm gear tooth contact patterns
- Holroyd worm gear work efficiency

10.5 SUGGESTION FOR FUTURE WORK

10.5.1 3D Parametric Modelling of Gear Drives

The VGM method developed in this research is claimed as a breakthrough in the 3D parametric modelling of gear drives. However, the current VGM method is still working within the environment of Pro/Engineer; to model a worm gear or spiroid gear, the user should be familiar with Pro/Engineer. Since Pro/Engineer is a huge program and too complicated for occasional users, there is a need to develop independent software to fully achieve automatic 3D gear modelling. Since the VGM theory has been developed, this is not difficult but just needs time to develop using the application-programming interface (API) provided by Pro/Engineer. Such automatic gear modelling software will have great application in the gear industry.

10.5.2 Loaded Multi-Tooth Contact Finite Element Analysis

The FEA software ANSYS 5.6 university option used in this research has limits on the number of nodes. Although efficient techniques have been developed for the

loaded gear tooth contact analysis, the models built in this thesis still have relatively coarse meshes. Finer mesh models are desired and the full version of ANSYS is suggested for future LTCA.

The IGES file format is used for gear geometry exchange in this research since no other choice is available. Gear geometry importing via the IGES files requires substantial knowledge of the operation techniques and the user has to fully understand how the IGES defines the geometry. If the geometrical models are built in Pro/Engineer, the Pro/E importing interface is suggested. Otherwise, the Step or Parasolid geometrical data exchanging interfaces are recommended.

The effects of friction and lubrication are not considered in this research. When the gear drive is in operation, friction and lubrication exist. Future research should consider these factors to see how much they will affect the contact stresses.

10.5.3 Dynamic Response of Gear Drives Using Finite Element Method

The FE work developed in this research is a static nonlinear tooth contact analysis. It can simulate the steady operation of worm gear and spiroid gears. However, the dynamic responses of the worm gear acceleration and impacting problems have not been included. Future work should calculate the dynamic response of impacts and accelerations so worm gears and spiroid gears under various loading conditions and operating conditions can be fully simulated and understood.

Loaded multi-tooth contact analysis of worm and spiroid gears is still in its infancy. The research completed in this thesis provides a good start.

REFERENCES

Journal and Conference

Abadjiev, V. and Petrova, D., 1997, "Testing of the Kinematic Conjugation of the Flanks Active Surfaces of Gear-Pairs of Type Spiroid", *Mechanical Machine Theory*, Vol. 32, No. 3, pp.343-348

Adams, V. and Askenazi, A., January 1999, "Building Better Products With finite Element Analysis (Common Misconceptions about FEA)", *BENCHmark*, pp.4-5

Argyris, J., Litvin, F. L., Lian, Q. M., Lagutin, S., A., 1999, "Determination of Envelope to Family of Planar Parametric Curves and Envelope Singularities", *Computer Methods In Applied Mechanics And Engineering*, Vol. 175, No. 1, pp.175-187

Bair, B. and Tsay, C., 1998a, "ZK-Type Dual-Lead Worm and Worm Gear Drives: geometry", *Journal of Mechanical Design*, Vol. 120, pp. 414-421

Bair, B. and Tsay, C., 1998b, "ZK-Type Dual-Lead Worm and Worm Gear Drives: Contact Teeth, Contact Ratios and Kinematic Errors", *Journal of Mechanical Design*, Vol. 120, pp. 422-428

Baxter, M. L., 1961, "Basic Geometry and Tooth Contact of Hypoid Gears", *Industrial Mathematics*, pp.1-28

Bibel, G. D. and Handschuh, R. F., 1996, "Meshing of a Spiral Bevel Gearset With 3D Finite Element Analysis", NASA, TM-107336, ARL-TR-1224

Bibel, G. D., Kumar, A., Reddy, S. and Handschuh, R. F., 1995, "Contact Stress Analysis of Spiral Bevel Gears Using Finite Element Analysis", *Journal of Mechanical Design*, Vol. 117, pp. 235-240

Chang, S. L., 1997, "A General Mathematical Model for Gears Cut by CNC Hobbing Machines", *Journal of Mechanical Design*, Vol. 119, pp.108-113

Chang, S. L. and Tsay, C. B., 1998, "Computerised Tooth Profile Generation and Undercut Analysis of Noncircular Gears Manufactured With Shaper Cutters", *Journal of Mechanical Design*, Vol. 120, pp. 92-99

Colborne, J., 1989, "The Use of Oversize Hobs to Cut Worm Gears", AGMA paper 89FTM8

Colborne, J., 1993, "Undercutting in Worms and Worm Gears", AGMA paper 93FTM1

Colborne, J., 1994, "The Curvature of Surfaces Formed by a Cutting Edge", *Mechanism and Machine Theory*, Vol. 29, No. 5, pp.767-775

Cornell, R., 1981, "Compliance and Stress Sensitivity of Spur Gear Teeth", *Journal of Mechanical Design*, Vol. 103, pp.447-459

Dabnichki, P. and Crocombe, A., 1999, "Finite Element Modelling of Local Contact Conditions in Gear Teeth", *Journal of Strain Analysis*, Vol. 34, No. 2, pp.129-142

Donno, M. D. and Litvin, F. L., 1999a, "Computerised Design, Generation and Simulation of Meshing of a Spiroid Worm-Gear Drive With Double-Crowned Worm", *Journal of Mechanical Design,* Vol. 121, pp.264-273

Donno, M. D. and Litvin, F. L., 1999b, "Computerized Design and Generation of Worm-Gear Drives With Stable Bearing Contact and Low Transmission Errors", *Journal of Mechanical Design*, Vol. 121, pp. 573-578

Dudas, I., Banyai, K. and Varga, G., 1996, "Simulation of Meshing of Worm Gearing", *Proceedings of 7th ASME International Power Transmission and Gearing Conference*, 6th-9th October, San Diego, California, pp 141-146

Duke, B. and Walton, D., 1999, "Some Aspects of Spiradrive Gearing Efficiency", *Proceedings of 1999 Drives & Controls Conference*, British Gear Association, 16-18 March, Telford, UK, pp. 6:1-6:7

Errichello, R., 1978a, "Bending Stress in Gear Teeth Having Circular Arc Profiles-Part 1 Analysis", *Journal of Mechanical Design*, Vol. 100, pp. 382-394

Errichello, R., 1978b, "Bending Stress in Gear Teeth Having Circular Arc Profiles-Part 2 Experiment", *Journal of Mechanical Design*, Vol. 100, pp. 394-403

Feng, P. H., Litvin, F. L., Townsend, D. P. and Handschuh, R. F., 1999, "Determination of Principal Curvatures and Contact Ellipse for Profile Crowned Helical Gears", *Journal of Mechanical Design*, Vol. 121, No. 1-2, pp.107-111

Fish, M. A., 2000, Private Communication, Holroyd Gear Company, UK

Fish, M. A. and Munro, R. G., 1999, "Modelling Contact Characteristics in Worm Gear Systems", *Proceeding of Drives and Controls Conference*, pp. 7:1-7:4

Fong, Z. and Tsay, C., 1991, "A Mathematical Model for the Tooth Geometry of Circular-Cut Spiral Bevel Gears", *Journal of Mechanical Design*, Vol. 113, pp.174-181

Gear Industry Home Page, http://www. geartechnology.com/hot/qanda.htm.

Gosselin, C., Cloutier, L. and Nguyen, Q. D., 1995, "A General Formulation for the Calculation of the Load Sharing and Transmission Error Under Load of Spiral Bevel and Hypoid Gears", *Mechanism and Machine Theory*, Vol. 30, pp. 433-450

Gosselin, C., Nonaka, T., Shiono, Y. and Tatsuno, T., 1998, "Identification of the Machine Settings of Real Hypoid Gear Tooth Surfaces", *Journal of Mechanical Design*, Vol. 120, pp. 429-439

Handschuh, R. F. and Bibel, G. D., 1999, "Experimental and Analytical Study of Aerospace Spiral Bevel Gear Tooth Fillet Stresses", *Journal of Mechanical Design*, Vol. 121, pp. 565-572

Handschuh, R. F. and Kicher, T., 1996, "A Method for Thermal Analysis of Spiral Bevel Gears", Journal of Mechanical Design, Vol. 118, pp. 580-585

Huang, C., Wen, S. and Huang, P., 1993, "Multilevel Solution of the Elastohydrodynamic Lubrication of Concentrated Contacts in Spiroid Gears", *Journal of Tribology*, Vol. 115, pp. 481-486

Janninck, W., 1988, "Contact Surface Topology of Worm Gear Teeth", *Gear Technology*, Vol. 5, part 2, pp.31-47

Kasuba, R. and Evans, J., 1981, "An Extended Model for Determining Dynamic Loads in Spur Gearing", *Journal of Mechanical Design*, Vol. 103, pp.398-407

Kawasaki, K. and Tamura, H., 1998, "Duplex Spread Blade Method For Cutting Hypoid Gears With Modified Tooth Surface", *Journal of Mechanical Design*, Vol. 120, pp.441-447

Kirov, V., 1999, "Design of Spiroid Hobs", *Journal of Materials Processing Technology*, Vol. 88, pp.208-215

Lagutin, S. and Verkhoskii, A., 1977, "Assembly Accuracy of Worm Wheel Drives With Closed Contact Lines", *Machine & Tooling*, Vol. 48. No. 8, pp.14-17

Lee, C., Lin, H., Oswald, F. and Townsend, D., 1991,"Influence of Linear Profile Modification and Loading Conditions on the Dynamic Tooth Load and Stress of

High-Contact Ratio Spur Gears", *Journal of Mechanical Design*, Vol. 113, pp.473-480

Lin, C., Tsay, C. and Fong, Z., 1996, "Tooth Contact Analysis of Hypoid Gears", *Journal of the Chinese Society of Mechanical Engineers*, Vol. 17, No. 3, pp.241-249

Lin, C., Tsay, C. and Fong, Z., 1998, "Computer-Aided Manufacturing of Spiral Bevel and Hypoid Gears with Minimum Surface-Deviation", *Mechanism and Machine Theory*, Vol. 33, No. 6, pp.785-803

Litvin, F. L., 1995, "Applied Theory of Gearing: State of the Art", ASME *Special 50th Anniversary Design Issue*, *Journal of Mechanical Design*, Vol. 117 pp.128-134

Litvin, F. L., Chaing, W. S., Kuan, C., Lundy, M. and Tsung, W. J., 1991, "Generation and Geometry of Hypoid Gear-Member With Face-Hobbed Teeth of Uniform Depth", *International Journal of Machine Tools & Manufacture*, Vol. 31, No. 2, pp.167-181

Litvin, F. L., Chaing, W. S., Lundy, M. and Tsung, W. J., 1990, "Design of Pitch Cones for Face-Hobbed Hypoid Gears", *Journal of Mechanical Design*, Vol. 112, No. 3, pp.413-418

Litvin, F. L., Chen, J. S., Lu, J. and Handschuh, R. F., 1996, "Application of Finite Element Analysis for Determination of Load Share, Real Contact Ratio, Precision of Motion, and Stress Analysis", *Journal of Mechanical Design*, Vol. 118, pp.561-567

Litvin, F. L., Chen, L. S., Sep, T. M. and Wang, J. C., 1995, "Computerized Simulation of Transmission Errors and Shift of Bearing Contact for Face-Milled Hypoid Gear Drive", *Journal of Mechanical Design*, Vol. 117, No. 2, pp.262-268

Litvin, F. L., Chen, N. X. and Chen, J. S., 1995, "Computerized Determination of Curvature Relations and Contact Ellipse for Conjugate Surfaces", *Computer Methods In Applied Mechanics and Engineering*, Vol. 125, No. 1-4, pp. 151-170

Litvin, F. L., Chen, N. X., Zhang, Y., Krenzer, T. and Handschuh, R. F., 1993, "Computerized Generation of Surfaces With Optimal Approximation to Ideal Surfaces", *Computer Methods in Applied Mechanics and Engineering*, Vol. 110, No. 1-2, pp.39-55

Litvin, F. L. and Donno, M., 1998, "Computerized Design and Generation of Modified Spiroid Worm-Gear Drive With Low Transmission Errors and Stabilized Bearing Contact", *Computer Methods In Applied Mechanics and Engineering*, Vol. 162, No. 1-4, pp.187-201

Litvin, F. L, Egelja, A. M. and Donno, M. D., 1998, "Computerized Determination of Singularities and Envelopes to Families of Contact Lines on Gear Tooth Surfaces", *Computer Methods in Applied Mechanics and Engineering*, Vol. 158, pp. 24-34

Litvin, F. L. and Gutman, Y., 1981a, "Methods of Synthesis and Analysis for Hypoid Gear-Drives of Formate and Helixform .1. Calculations for Machine Settings for Member Gear Manufacture of the Formate and Helixform Hypoid Gears", *Journal of Mechanical Design*, Vol. 103, No.1, pp.83-88

Litvin, F. L. and Gutman, Y., 1981b, "Methods of Synthesis and Analysis for Hypoid Gear-Drives of Formate and Helixform .2. Machine Setting Calculations for the Pinions of Formate and Helixform Gears", *Journal of Mechanical Design,* Vol. 103, No. 1, pp.89-101

Litvin, F. L. and Gutman, Y., 1981c, "Methods of Synthesis and Analysis for Hypoid Gear-Drives of Formate and Helixform .3. Analysis and Optimal Synthesis Methods for Mismatch Gearing and Its Application for Hypoid Gears of Formate and Helixform", *Journal of Mechanical Design*, Vol. 103, No. 1, pp.102-113

Litvin, F. L. and Gutman, Y., 1981d, "A Method of Local Synthesis of grounded on the Connections between the Principal and Geodetic Curvatures of Surfaces", *Journal of Mechanical Design*, Vol. 103, No. 1, pp.114-125

Litvin, F. L. and Hsiao, C. L., 1993, "Computerized Simulation of Meshing and Contact of Enveloping Gear Tooth Surfaces", *Computer Methods in Applied Mechanics and Engineering*, Vol. 102, No. 3, pp.337-366

Litvin, F. L. and Kim, D. H., 1997, "Computerized Design, Generation And Simulation of Meshing of Modified Involute Spur Gears With Localised Bearing Contact And Reduced Level of Transmission Errors", *Journal of Mechanical Design*, Vol. 119, No. 1, pp.96-100

Litvin, F. L. and Kin, V., 1992, "Computerized Simulation of Meshing and Bearing Contact for Single-Enveloping Worm-Gear Drives", *Journal of Mechanical Design*, Vol. 114, No. 2, pp.313-316

Litvin, F. L., Kin, V. and Zhang, Y., 1990, "Limitations of Conjugate Gear Tooth Surfaces", *Journal of Mechanical Design*, Vol. 112, No. 2, pp.230-236

Litvin, F. L., Kuan, C., Kieffer, J., Bossler, R. and Handschuh, R. F., 1991, "Straddle Design of Spiral Bevel and Hypoid Pinions and Gears", *Journal of Mechanical Design*, Vol. 113, No. 4, pp.422-426

Litvin, F. L., Peng, A. Y. and Wang, A. W., 1999, "Limitation of Gear Tooth Surfaces by Envelopes to Contact Lines and Edge of Regression", *Mechanism and Machine Theory*, Vol. 34, No. 6, pp.889-902

Litvin, F. L. and Seol, I. H., 1996, "Computerized Determination Of Gear Tooth Surface As Envelope To Two Parameter Family Of Surfaces", *Computer Methods in Applied Mechanics and Engineering*, Vol. 138, No. 1-4, pp.213-225

Litvin, F. L., Vhen, N. and Lu, J., 1995, "Computerized design and generation of low-noise Helical Gears with Modified surfaces Topology", *Journal of Mechanical Design*, Vol. 117, pp. 254-161

Litvin, F. L., Wang, A. G. and Handschuh, R. F., 1996, "Computerized Design and Analysis of Face-Milled, Uniform Tooth Height Spiral Bevel Gear Drives", *Journal of Mechanical Design*, Vol. 118, No. 4, pp.573-579

Litvin, F. L., Wang, A. G. and Handschuh, R. F., 1998, "Computerized Generation and Simulation of Meshing and Contact of Spiral Bevel Gears With Improved Geometry", *Computer Methods In Applied Mechanics And Engineering*, Vol. 158, No. 1-2, pp.35-64

Litvin, F. L., Yi, Z., Kieffer, J. and Handschuh, R. F., 1991, "Identification and Minimization of Deviations of Real Gear Tooth Surfaces", *Journal of Mechanical Design*, Vol. 113, No. 1, pp.55-62

Litvin, F. L., Zhang, J. and Handschuh, R. F., 1988, "Crowned Spur Gears - Methods for Generation and Tooth Contact Analysis .2. Generation of the Pinion Tooth Surface by A Surface of Revolution, *Journal Of Mechanisms Transmissions And Automation In Design*, Vol. 110, No. 3, pp.343-347

Litvin, F. L., Zhang, Y., Lundy, M. and Heine, C., 1988, "Determination of Settings of A Tilted Head Cutter For Generation of Hypoid and Spiral Bevel Gears", *Journal of Mechanisms Transmissions and Automation In Design*, , Vol. 110, No. 4, pp.495-500

Litvin, F. L., Zhang, Y., Wang, J. C., Bossler, R. B. and Chen, Y. J. D., 1992, "Design and Geometry of Face-Gear Drives", *Journal of Mechanical Design*, Vol. 114, No. 4, pp.642-647

Lu, J., Litvin, F. L. and Chen, J. S., 1995, "Load Share and Finite-Element Stress-Analysis for Double Circular-Arc Helical Gears", *Mathematical and Computer Modelling*, Vol. 21, No. 10, pp.13-30

Moriwaki, I., Fukuda, T., Watabe, Y. and Saito, K., 1993, "Global Local Finite Element Method In Gear Tooth Stress Analysis", *Journal of Mechanical Design*, Vol. 115, pp 1008-1012

Qin, D. T. and Qin, D. X., 2000, "Tooth Contact Analysis Of Hourglass Worm Gearing On The Condition That Errors Mixed With Deformation", *Proceeding of International Conference on Gear Transmissions and Mechanical Systems*, Professional Engineering Publishing, Nottingham, UK, pp.109-118

Seol, I. H. and Litvin, F. L., 1996a, "Computerized Design, Generation and Simulation of Meshing and Contact of Worm-Gear Drives With Improved Geometry", *Computer Methods in Applied Mechanics and Engineering*, Vol. 138, pp. 73-103

Seol, I. H. and Litvin. F. L., 1996b, "Computerised Design, Generation and Simulation of Meshing and Contact of Modified Involute, Klingelnberg and Flender Type Worm-gear Drives", *ASME Journal of Mechanical Design*, Vol. 118, pp 551-555

Shibata, Y., Kondou, N. and Ito, T., 1997, "Optimum Tooth Profile Design for Hypoid Gear", *JSAE Review*, Vol. 18, pp.283-287

Shimachi, S., Gunbara, H., Kobayashi, T. and Kawada, H., 1994, "Hourglass Worm Gears Designed to Concentrate Surface Normals", *JSME International Journal, Series C*, Vol. 37, No.2, pp. 347-354

Simon, V., 1981, " Elastohydrodynamic Lubrication of Hypoid Gears", *Journal of Mechanical Design*, Vol. 103, pp.195-203

Simon, V., 1988, " Computer Aided Manufacture of High Precision Hob", *International Journal of Machine Tools & Manufacture*, Vol. 28, No. 4, pp.443-452

Simon, V., 1993a, "Stress Analysis in Double Enveloping Worm Gears by Finite Element Method", *Journal of Mechanical Design*, Vol. 115, pp. 179-185

Simon, V., 1993b, " Load Distribution in Double Enveloping Worm Gears", *Journal of Mechanical Design*, Vol. 115, No. 3, pp.496-501

Simon, V., 1994, "A New Worm Gear Drive with Ground Double Arc Profile", *Mechanism and Machine Theory*, Vol. 29, No. 3, pp. 407-414

Simon, V., 1998, "The Influence of Misalignments on Mesh Performances of Hypoid Gears", *Mechanism and Machine Theory*, Vol. 33, pp.1277-1291

Song, Y., 1999, "Literature Review: State-of-Art of Worm and Spiroid Gearing Research", *Internal Report*, The Nottingham Trent University, 2nd October, Nottingham

Song, Y., 2000a, "Geometry of Modified ZK Worm-Gear Drive With Low Transmission Errors and Stabilised Bearing Contact", *Internal Report*, The Nottingham Trent University, 10th January, Nottingham

Song, Y., 2000b, "Geometry of Involute Spiroid Tapered Pinion", *Internal Report*, The Nottingham Trent University, 15th March, Nottingham

Song, Y., 2000c, "Computerised Design and Generation of Modified ZA Worm-Gear Drive With Localised Tooth Contact", *Internal Report*, The Nottingham Trent University, 29th November, Nottingham

Song, Y. and Su, D., 2000 "3D Virtual Manufacturing of Worm Gear Drives", *Proceedings of International Conference on Gearing, Transmissions and Mechanical Systems*, Nottingham, UK, 3-6 July, pp.119-128

Song, Y., Su, D. and Gentle, R., 2000a "A Novel Approach of 3D Spiroid Gear Modelling", *Proceedings of 3rd International Conference on Mechanics & Materials in Design*, Orlando, USA, May 29-31, pp.59-61

Song, Y., Su, D. and Gentle, R., 2000b, "Optimum Design of Spiroid Gearing With the Aid of 3D Virtual Manufacturing Method", *Proceedings of 4th International Conference on Adaptive Computing in Design and Manufacture*, Plymouth, UK, 26-28 April, pp.51-54

Song, Y., Su, D., Ianakiev, A. and Gentle, R., 2001, "Loaded Multi-tooth Contact Analysis of Spiroid Gears by General Surface-to-Surface Contact Analysis Using the Finite Element Method", *Proceedings of the International Conference on Mechanical Transmission*, 5-9 April, China, pp.131-136

Steward, J., 1990, "The Compliance of Solid, Wide-Faced Spur Gears", *Journal of Mechanical Design*, Vol. 112, pp. 590-595

Su, D., 1996, "A Computer Aided General Approach For Loading-Capacity Analysis Of Cylindrical Worm Gears", *Proceedings, The International Conference on Theory and Practice of Gearing*, 4-6 December, Izhevsk, Russia, pp 327-336

Su, D. and Song, Y., 2000a "Numerical Modelling of Spiroid Gears With Localised Tooth Contact", *Proceedings of International Conference on Gearing, Transmissions and Mechanical Systems*, Nottingham, UK, 3-6 July, pp.75-90

Su, D. and Song, Y., 2000b, "A Novel Approach of Obtaining Localised Tooth Contact for Spiroid Gear Drives", *Proceedings of 8th International Power Transmission and Gearing Conference*, ASME Design Engineering Technical Conferences, Baltimore, USA, 10-13 September, pp.131-136

Su, D., Yang, F. and Gentle, C. R., 1999, "Computer Aided Design and Simulation of Worm Gearing with Localised Tooth Contact", *Proceedings of 1999 Drives & Controls Conference*, British Gear Association, 16-18 March, Telford, UK, pp. 8:1-8:5

Su, D., Yang, F. and Gentle, R., 2000, "Tooth Stresses, Mesh Stiffness and Loaded Transmission Errors of Involute Worm Gears", *Gearing and Transmission*, Issue 3, IFToMM Gearing and Transmission TC, pp.36-44

Su, D., Yang, F., Gentle, R. and Reith, D., 1998, "A New Approach Combining Numerical Analysis and Three-Dimensional Simulation for Design of Worm Gearing With Preferable Localised Tooth Contact", *Proceedings of the 1998 ASME Design*

Engineering Technical Mechanisms Conference, Atlanta, Paper No. DETC98/MECH-5830

Su, D., Yang, F. and Song, Y., 1999, "A CAD Approach for Reducing Worm Gearing's Sensitivity to Manufacturing and Assembly Errors", *Proceedings of International Conference on Computer Aided Production Engineering*, 19-21 April, Durham, pp.101-108

Sudoh, K., Tanaka, Y., Matsumoto, S. and Tozaki, Y., 1996, "Load Distribution Analysis Method for Cylindrical Worm Gear Teeth", *JSME International Journal*, Series C, Vol. 39, No. 3, pp. 606-613

Sundaresan, S., Ishil, K. and Houser, D., 1991, "A Procedure Using Manufacturing Variance to Design Gears With Minimum Transmission Error", *Journal of Mechanical Design*, Vol. 113, pp.318-324

Tsay, C. B., Jeng, J. W. and Feng, H. S., 1995, "A Mathematical Model of the ZE-type Worm Gear Set", *Mechanism and Machine Theory*, Vol. 30, Part 6, pp. 777-789

Varatio (Special Product) Ltd., "Engineering Excellence, Spiroid Gear Systems", Berkshire, England.

Vedmar, L. and Henkriksson, B., 1998, "A General Approach for Determining Dynamic Forces in Spur Gears", *Journal of Mechanical Design*, Vol. 120, pp.593-598

Wang, K., and Cheng, H., 1981, "A Numerical Solution to the Dynamic Load, Film Thickness, and Surface Temperatures in Spur Gears, Part II, Results", *Journal of Mechanical Design*, Vol. 103, pp.177-187

Weck, M. and Mauer, G., 1990, "Optimum Tooth Flank Corrections for Helical Gears", *Journal of Mechanical Design*, Vol. 112, pp. 584-589

Wilcox, L. and Coleman, W., 1973, "Application of Finite Elements to the Analysis of Gear Tooth Stresses", *Journal of Engineering for Industry*, Vol. 95, pp. 1139-1148

Winter, H. and Wilkesmann, H., 1981, "Calculation of Cylindrical Worm Gear Drives of Different Tooth Profiles", *Journal of Mechanical Design*, Vol. 103, pp.73-81

Vedmar, L. and Henriksson, B., 1998, "A General Approach for Determining Dynamic Forces in Spur Gears", *Journal of Mechanical Design*, Vol. 120, pp. 593-598

Yang, F., 2000, "Numerical Analysis and Three Dimensional Modelling of Worm Gearing with Localised Tooth Contact", *PhD Thesis*, The Nottingham Trent University, Nottingham, UK

Yang, F., Su, D., Wang, X. and Gentle, C. R, 1998, "A Numerical Method to Obtain Preferable Localised Tooth Contact for Cylindrical Worm Gearing," *Proceedings of International Conference on Mechanics in Design*, 6th-9th July, Nottingham, UK

Yoshino, H. and Muta, Y., 1997, "Tooth Surface Modification Method Applicable to Various Types of Worm Gears", *Proceedings of International Conference on Mechanical Transmissions and Mechanisms*, July 1st-4th, Tianjin, China, pp.598-602

Zalgaller, V. A. and Litvin, F. L., 1977, "Sufficient Conditions of Existence of Envelope to Contact Lines and Edge of Regression on the Surface of the Envelope to the Family of Surfaces Represented in Parametric Form", *Proceeding of Universities,* Mathematics, Vol. 178, No. 3, pp.20-23

Zhang, Y. and Fang, Z., 1997, "Analysis of Transmission Errors Under Load of Helical Gears With Modified Tooth Surfaces." *Journal of Mechanical Design*, Vol. 119, pp.120-126

Zhang, Y. and Fang, Z., 1999, "Analysis of Tooth Contact and Load Distribution of Helical Gears With Crossed Axes", *Mechanism and Machine Theory*, Vol. 34, pp.41-57

Zhang, Y., Litvin, F. L., Maruyama, N., Takeda, R. and Sugimoto, M., 1994, "Computerized Analysis of Meshing and Contact of Gear Real Tooth Surfaces", *Journal of Mechanical Design*, Vol. 116, No. 3, pp.677-682

Zheng, C., Lei, J. and Savage, M., 1989, "General Method for Computing Worm Gear Conjugate Mesh Property, Part 1. The Generating Surface", *Journal of Mechanisms, Transmission and Automation in Design,* Vol. 111, pp.143-148

Zheng, C. and Lei, J., 1989, "General Method for Computing Worm Gear Conjugate Mesh Property, Part 1. The Mathematic Model of Worm Gear Manufacturing and Working Process", *Journal of Mechanisms, Transmission and Automation in Design,* Vol. 111, pp.149-152

Manuals and Books:

ANSYS *User's Manual for Revision 5.6*, Swanson Analysis systems, Inc., 2000.

LS-DYNA3D *User's Manual*, Livermore Software Technology Corporation, 1999.

Adams, V. and Askenazi, A., 1999, *Building Better Products With Finite Element Analysis*, Onward Press

Bohle, F. and Saari, O. E., 1955, *Spiroid Gears*, AGMA 389.01

Boresi, P. and Sidebottom, O., 1985, *Advanced Mechanics of Materials*, 4th Ed. John Wiley & Sons, Inc., New York.

Budynas, R. G., 1977, *Advanced Strength and Applied Stress Analysis*, McGraw-Hill, New York

Crockett, J. C., 1971, *Gear Cutting Practice Machines and Tools*, Machinery Publishing, Brighton

Dooner, D. B. and Seireg, A. A., 1995, *The Kinematic Geometry of Gearing: A Concurrent Engineering Approach*, John Wiley & Sons, Inc., New York

Drago, R. J., 1988, *Fundamentals of Gear Design*, Butterworths, London

Dudley, D. W., 1962, *Gear Handbook: The Design, Manufacture, and Application of Gears*, McGraw-Hill, New York

Dudley, D. W., 1984, *Handbook of Practical Gear Design*, McGraw-Hill, New York

Endoy, R., 1990, *Gear Hobbing, Shaping and Shaving: A Guide to Cycle Time Estimating and Process Planning*,. Society of Manufacturing Engineers, Publications Development Dept, Dearborn, Mich.

Ewert, R. H., 1997, *Gears and Gear Manufacture: the Fundamentals*: Chapman & Hall : International Thomson Publishing, New York

Gleason Works, 1981, *Understanding Tooth Contact Analysis*, Gleason, Rochester

Korn, G. and Korn, T., 1968, *Mathematics Handbook for Scientists and Engineers*, 2nd ed., McGraw-Hill, New York, USA

Ladouceur, N., 1997, *Inside Pro/SURFACE*, Onward Press

Litvin, F. L., 1994, *Gear Geometry and Applied Theory*, Prentice Hall, New Jersey

McMahon, C. and Browne, J., 1998, *CADCAM: Principles, Practice and Manufacturing Management* / Second Edition, Addison-Wesley, Harlow, England

Merritt, H. E., 1971, *Gear Engineering*, Pitman, London

Nelson, W. D., 1961, *Spiroid Gearing*, Illinois Tool works

Shtipelman, B. A., 1978, *Design and Manufacture of Hypoid Gears*, John Wiley & Sons, Inc., New York

Smith, J. D., 1983, Gears And Their Vibration: A Basic Approach to Understanding Gear Noise , Macmillan, New York

Steffen, D., Utz, J. and Cox, W. R., 1997, Inside Pro/ENGINEER, Onward Press

Stokes, A., 1970, *High Performance Gear Design*, Machinery Publishing, Brighton, UK

Townsend, D. P., 1991, Editor in chief, *Dudley's Gear Handbook*, Second edition, McGraw-Hill, New York, USA

Tuplin, W. A., 1962, *Involute Gear Geometry*, Chatto & Windus, UK

Tuplin, W. A., 1962, *Gear Design*, Machinery Publishing Co.

Wang, S., 1979, *Theory of Worm Gear* (in Chinese), Tianjin Science and Technology Publisher

Watson, H. J., 1970, *Modern Gear Production*, Pergamon, Oxford

Vickers, G. W., 1990, *Numerically Controlled Machine Tools*, Ellis Horwood Limited, New York

Zalgaller, V. A., 1975, *Theory of Envelopes*, Publishing House Nauka, Moscow

APPENDIX A NUMERICAL RESULTS OF LOCALISED TOOTH CONTACT OF A SPIROID GEAR

Table A.1 Results of Localised Tooth Contact (Spiroid Gear Side I)

u_1	θ_1	ϕ_1	ϕ_w	u_w	θ_w	ϕ_2
6.514	-0.1225	1.004e-5	4.423e-7	6.512	-0.1218	0
6.546	0.08831	-0.209	-0.0082	6.545	0.08901	-0.2094
6.581	0.2993	-0.418	-0.0164	6.58	0.2999	-0.4189
6.615	0.5102	-0.628	-0.0246	6.614	0.5108	-0.6283
6.65	0.7213	-0.8377	-0.0328	6.649	0.7218	-0.8378
6.684	0.9324	-1.047	-0.0410	6.684	0.9329	-1.047
6.719	1.144	-1.257	-0.0492	6.718	1.144	-1.257
6.753	1.355	-1.466	-0.0574	6.753	1.355	-1.466
6.788	1.566	-1.676	-0.0657	6.787	1.566	-1.676
6.822	1.777	-1.885	-0.0739	6.822	1.778	-1.885
6.857	1.989	-2.094	-0.0821	6.856	1.989	-2.094
6.891	2.2	-2.304	-0.0903	6.891	2.2	-2.304
6.925	2.412	-2.513	-0.0985	6.925	2.412	-2.513
6.959	2.624	-2.723	-0.1068	6.96	2.624	-2.723
6.994	2.835	-2.932	-0.115	6.994	2.835	-2.932
7.378	5.263	-3.142	-0.1232	7.38	5.262	-3.142
7.409	5.457	-3.351	-0.1314	7.41	5.457	-3.351
7.439	5.652	-3.56	-0.1396	7.441	5.651	-3.56
7.469	5.846	-3.77	-0.1478	7.471	5.845	-3.77
7.499	6.039	-3.979	-0.1561	7.501	6.038	-3.979
7.529	6.232	-4.189	-0.1643	7.531	6.231	-4.189
7.559	6.424	-4.398	-0.1725	7.561	6.423	-4.398
7.589	6.616	-4.608	-0.1807	7.59	6.615	-4.608
7.618	6.807	-4.817	-0.1889	7.62	6.806	-4.817
7.647	6.997	-5.026	-0.1971	7.649	6.996	-5.027
7.676	7.186	-5.236	-0.2053	7.678	7.185	-5.236



7.705	7.375	-5.445	-0.2135	7.707	7.374	-5.445
7.733	7.563	-5.655	-0.2218	7.736	7.562	-5.655
7.762	7.75	-5.864	-0.23	7.764	7.749	-5.864
7.79	7.936	-6.074	-0.2382	7.792	7.935	-6.074
7.818	8.121	-6.283	-0.2464	7.82	8.12	-6.283
7.845	8.306	-6.492	-0.2546	7.848	8.304	-6.493
7.872	8.489	-6.702	-0.2628	7.875	8.487	-6.702
7.899	8.671	-6.911	-0.271	7.902	8.669	-6.912
7.926	8.851	-7.121	-0.2792	7.929	8.85	-7.121
7.952	9.031	-7.33	-0.2875	7.955	9.029	-7.33
7.978	9.209	-7.54	-0.2957	7.981	9.207	-7.54
8.004	9.385	-7.749	-0.3039	8.007	9.384	-7.749
8.029	9.56	-7.958	-0.3121	8.032	9.559	-7.959
8.054	9.734	-8.168	-0.3203	8.057	9.732	-8.168
8.078	9.905	-8.377	-0.3285	8.081	9.904	-8.378
8.103	10.08	-8.587	-0.3367	8.106	10.07	-8.587
8.126	10.24	-8.796	-0.345	8.128	10.24	-8.796
8.148	10.41	-9.005	-0.3532	8.151	10.41	-9.006
8.171	10.57	-9.215	-0.3614	8.174	10.57	-9.215
8.191	10.73	-9.424	-0.3696	8.194	10.73	-9.425
8.212	10.89	-9.634	-0.3778	8.215	10.89	-9.634
8.232	11.04	-9.843	-0.386	8.235	11.04	-9.844
8.249	11.19	-10.05	-0.3942	8.252	11.19	-10.05
8.265	11.34	-10.26	-0.4024	8.268	11.33	-10.26
8.279	11.47	-10.47	-0.410	8.282	11.47	-10.47

Table A.2 Results of Localised Tooth Contact (Spiroid Gear Side II)

u_1	θ_1	ϕ_1	ϕ_w	u_w	θ_w	ϕ_2
4.23	0.2418	3.577e-6	0.00016	4.228	0.238	0
4.986	0.4329	-0.2076	-0.00805	4.984	0.432	-0.2094
5.014	0.6413	-0.4171	-0.01627	5.012	0.641	-0.418



5.042	0.8497	-0.6266	-0.02448	5.039	0.849	-0.6283
5.069	1.058	-0.8361	-0.0327	5.067	1.058	-0.8378
5.097	1.266	-1.046	-0.04091	5.094	1.266	-1.047
5.125	1.475	-1.255	-0.04913	5.121	1.474	-1.257
5.152	1.683	-1.465	-0.05734	5.149	1.683	-1.466
5.18	1.891	-1.674	-0.06555	5.176	1.891	-1.676
5.208	2.1	-1.884	-0.07377	5.203	2.099	-1.885
5.235	2.308	-2.093	-0.08198	5.23	2.308	-2.094
5.263	2.516	-2.303	-0.0902	5.258	2.516	-2.304
5.29	2.725	-2.512 -	-0.09841	5.285	2.724	-2.513
5.318	2.933	-2.721	-0.1066	5.312	2.932	-2.723
5.345	3.141	-2.931	-0.1148	5.339	3.141	-2.932
5.373	3.349	-3.14	-0.1231	5.366	3.349	-3.142
5.4	3.558	-3.35	-0.1313	5.394	3.557	-3.351
5.428	3.766	-3.559	-0.1395	5.421	3.765	-3.56
5.455	3.974	-3.769	-0.1477	5.448	3.973	-3.77
5.482	4.182	-3.978	-0.1559	5.475	4.182	-3.979
5.51	4.39	-4.188	-0.1641	5.502	4.39	-4.189
5.537	4.598	-4.397	-0.1723	5.529	4.598	-4.398
5.565	4.806	-4.607	-0.1806	5.556	4.806	-4.608
5.592	5.015	-4.816	-0.1888	5.583	5.014	-4.817
5.619	5.223	-5.026	-0.197	5.61	5.222	-5.027
5.647	5.431	-5.235	-0.2052	5.637	5.43	-5.236
5.674	5.639	-5.445	-0.2134	5.664	5.638	-5.445
5.701	5.847	-5.654	-0.2216	5.691	5.846	-5.655
5.728	6.055	-5.864	-0.2298	5.718	6.054	-5.864
5.756	6.263	-6.074	-0.2381	5.745	6.262	-6.074
5.783	6.471	-6.283	-0.2463	5.772	6.47	-6.283
5.81	6.679	-6.493 -	-0.2545	5.799	6.678	-6.493
5.837	6.887	-6.702	-0.2627	5.826	6.886	-6.702
5.865	7.094	-6.912	-0.2709	5.853	7.094	-6.912
5.892	7.302	-7.121	-0.2791	5.879	7.302	-7.121

5.919	7.51	-7.331	-0.2873	5.906	7.51	-7.33
5.946	7.718	-7.54	-0.2956	5.933	7.717	-7.54
5.974	7.926	-7.75	-0.3038	5.96	7.925	-7.749
6.001	8.134	-7.959	-0.312	5.987	8.133	-7.959
6.028	8.341	-8.169	-0.3202	6.014	8.341	-8.168
6.055	8.549	-8.378	-0.3284	6.041	8.548	-8.378
6.082	8.757	-8.588	-0.3366	6.068	8.756	-8.587
6.11	8.965	-8.797	-0.3448	6.094	8.964	-8.796
6.137	9.172	-9.007	-0.3531	6.121	9.171	-9.006
6.164	9.38	-9.216	-0.3613	6.148	9.379	-9.215
6.191	9.588	-9.426	-0.3695	6.175	9.587	-9.425
6.218	9.795	-9.635	-0.3777	6.202	9.794	-9.634
6.246	10	-9.845	-0.3859	6.229	10	-9.844
6.273	10.21	-10.05	-0.3941	6.256	10.21	-10.05
6.3	10.42	-10.26	-0.4023	6.283	10.42	-10.26
6.327	10.63	-10.47	-0.4106	6.31	10.62	-10.47
6.355	10.83	-10.68	-0.4188	6.337	10.83	-10.68
6.382	11.04	-10.89	-0.427	6.363	11.04	-10.89
6.409	11.25	-11.1 -	-0.4352	6.39	11.25	-11.1
6.437	11.46	-11.31	-0.4434	6.417	11.45	-11.31
6.464	11.66	-11.52	-0.4516	6.444	11.66	-11.52
6.491	11.87	-11.73	-0.4599	6.471	11.87	-11.73
6.519	12.08	-11.94	-0.4681	6.499	12.08	-11.94
6.546	12.28	-12.15	-0.4763	6.526	12.28	-12.15
6.574	12.49	-12.36	-0.4845	6.553	12.49	-12.36
6.601	12.7	-12.57	-0.4927	6.58	12.7	-12.57
6.629	12.91	-12.78	-0.5009	6.607	12.9	-12.78
6.656	13.11	-12.99	-0.5091	6.634	13.11	-12.99
6.684	13.32	-13.2	-0.5174	6.662	13.32	-13.19
6.712	13.53	-13.41	-0.5256	6.689	13.53	-13.4
6.739	13.73	-13.62	-0.5338	6.716	13.73	-13.61
6.767	13.94	-13.83	-0.542	6.743	13.94	-13.82



6.795	14.15	-14.04	-0.5502	6.771	14.15	-14.03
6.823	14.36	-14.24	-0.5584	6.798	14.35	-14.24
6.85	14.56	-14.45	-0.5666	6.826	14.56	-14.45
6.878	14.77	-14.66	-0.5749	6.853	14.77	-14.66
6.906	14.98	-14.87	-0.5831	6.881	14.97	-14.87
6.934	15.18	-15.08	-0.5913	6.909	15.18	-15.08
6.963	15.39	-15.29	-0.5995	6.937	15.39	-15.29
6.991	15.6	-15.5	-0.6077	6.964	15.59	-15.5
7.019	15.8	-15.71	-0.6159	6.992	15.8	-15.71
7.047	16.01	-15.92	-0.6241	7.02	16.01	-15.92
7.076	16.22	-16.13	-0.6324	7.048	16.21	-16.13
7.104	16.42	-16.34	-0.6406	7.076	16.42	-16.34
7.133	16.63	-16.55	-0.6488	7.105	16.63	-16.55
7.161	16.84	-16.76	-0.657	7.133	16.83	-16.76
7.19	17.04	-16.97	-0.6652	7.161	17.04	-16.96
7.219	17.25	-17.18	-0.6734	7.19	17.25	-17.17
7.248	17.45	-17.39	-0.6816	7.219	17.45	-17.38
7.277	17.66	-17.6	-0.6899	7.247	17.66	-17.59
7.306	17.87	-17.81	-0.6981	7.276	17.86	-17.8
7.336	18.07	-18.02	-0.7063	7.305	18.07	-18.01
7.365	18.28	-18.23	-0.7145	7.334	18.28	-18.22
7.395	18.49	-18.44	-0.7227	7.363	18.48	-18.43
7.424	18.69	-18.65	-0.7309	7.393	18.69	-18.64
7.454	18.9	-18.85	-0.7391	7.422	18.89	-18.85

APPENDIX B NUMERICAL RESULTS OF LOCALISED TOOTH CONTACT OF A HELICON GEAR

Table B.1 Results of Localised Tooth Contact (Helicon Gear Side I)

u_1	θ_1	ϕ_1	ϕ_w	u_w	θ_w	ϕ_2
1.46	0.03977	2.13e-5	0.000216	1.46	0.0404	0
1.46	0.2418	-0.203	-0.00799	1.46	0.2478	-0.209
1.46	0.4499	-0.412	-0.01621	1.46	0.4559	-0.418
1.46	0.658	-0.6224	-0.02442	1.46	0.6639	-0.628
1.46	0.8661	-0.831	-0.03264	1.46	0.872	-0.8378
1.46	1.074	-1.041	-0.04085	1.459	1.08	-1.047
1.46	1.282	-1.251	-0.04907	1.459	1.288	-1.257
1.46	1.49	-1.46	-0.05728	1.459	1.496	-1.466
1.46	1.698	-1.67	-0.0655	1.459	1.704	-1.676
1.46	1.907	-1.879	-0.07371	1.459	1.912	-1.885
1.46	2.115	-2.089	-0.08192	1.459	2.12	-2.094
1.46	2.323	-2.298	-0.09014	1.459	2.328	-2.304
1.46	2.531	-2.508	-0.09835	1.459	2.536	-2.513
1.46	2.739	-2.717	-0.1066	1.459	2.744	-2.723
1.46	2.947	-2.927	-0.1148	1.459	2.952	-2.932
1.46	3.155	-3.136	-0.123	1.459	3.16	-3.142
1.46	3.363	-3.346	-0.1312	1.459	3.368	-3.351
1.46	3.571	-3.555	-0.1394	1.458	3.576	-3.56
1.46	3.779	-3.765	-0.1476	1.458	3.784	-3.77
1.46	3.987	-3.974	-0.1559	1.458	3.992	-3.979
1.46	4.195	-4.184	-0.1641	1.458	4.2	-4.189
1.46	4.403	-4.394	-0.1723	1.458	4.407	-4.398
1.46	4.611	-4.603	-0.1805	1.458	4.615	-4.608
1.46	4.819	-4.813	-0.1887	1.458	4.823	-4.817
1.46	5.027	-5.022	-0.1969	1.458	5.031	-5.027



1.46	5.235	-5.232	-0.2051	1.458	5.239	-5.236
1.46	5.442	-5.441	-0.2133	1.458	5.447	-5.445
1.46	5.65	-5.651	-0.2216	1.458	5.655	-5.655
1.46	5.858	-5.86	-0.2298	1.458	5.863	-5.864
1.46	6.066	-6.07	-0.238	1.457	6.07	-6.074
1.46	6.274	-6.279	-0.2462	1.457	6.278	-6.283
1.46	6.482	-6.489	-0.2544	1.457	6.486	-6.493
1.46	6.69	-6.698	-0.2626	1.457	6.694	-6.702
1.46	6.898	-6.908	-0.2708	1.457	6.902	-6.912
1.46	7.106	-7.117	-0.2791	1.457	7.109	-7.121
1.46	7.313	-7.327	-0.2873	1.457	7.317	-7.33
1.46	7.521	-7.536	-0.2955	1.457	7.525	-7.54
1.46	7.729	-7.746	-0.3037	1.457	7.733	-7.749
1.46	7.937	-7.955	-0.3119	1.457	7.94	-7.959
1.46	8.145	-8.165	-0.3201	1.457	8.148	-8.168
1.46	8.353	-8.374	-0.3283	1.456	8.356	-8.378
1.46	8.56	-8.584	-0.3366	1.456	8.564	-8.587
1.46	8.768	-8.793	-0.3448	1.456	8.771	-8.796
1.46	8.976	-9.003	-0.353	1.456	8.979	-9.006
1.46	9.184	-9.212	-0.3612	1.456	9.187	-9.215
1.46	9.391	-9.422	-0.3694	1.456	9.394	-9.425
1.46	9.599	-9.632	-0.3776	1.456	9.602	-9.634
1.46	9.807	-9.841	-0.3858	1.456	9.81	-9.844
1.46	10.01	-10.05	-0.3941	1.456	10.02	-10.05
1.46	10.22	-10.26	-0.4023	1.456	10.22	-10.26
1.46	10.43	-10.47	-0.4105	1.456	10.43	-10.47
1.46	10.64	-10.68	-0.4187	1.456	10.64	-10.68
1.46	10.85	-10.89	-0.4269	1.455	10.85	-10.89
1.46	11.05	-11.1	-0.4351	1.455	11.06	-11.1
1.46	11.26	-11.31	-0.4433	1.455	11.26	-11.31
1.46	11.47	-11.52	-0.4516	1.455	11.47	-11.52
1.46	11.68	-11.73	-0.4598	1.455	11.68	-11.73



1.46	11.88	-11.94	-0.468	1.455	11.89	-11.94
1.46	12.09	-12.15	-0.4762	1.455	12.09	-12.15
1.46	12.3	-12.36	-0.4844	1.455	12.3	-12.36
1.46	12.51	-12.57	-0.4926	1.455	12.51	-12.57
1.46	12.71	-12.77	-0.5008	1.455	12.72	-12.78
1.46	12.92	-12.98	-0.5091	1.455	12.92	-12.99
1.46	13.13	-13.19	-0.5173	1.454	13.13	-13.19
1.46	13.34	-13.4	-0.5255	1.454	13.34	-13.4
1.46	13.54	-13.61	-0.5337	1.454	13.55	-13.61
1.46	13.75	-13.82	-0.5419	1.454	13.75	-13.82
1.46	13.96	-14.03	-0.5501	1.454	13.96	-14.03
1.46	14.17	-14.24	-0.5583	1.454	14.17	-14.24
1.46	14.37	-14.45	-0.5666	1.454	14.38	-14.45
1.46	14.58	-14.66	-0.5748	1.454	14.58	-14.66
1.46	14.79	-14.87	-0.583	1.454	14.79	-14.87
1.46	15	-15.08	-0.5912	1.454	15	-15.08
1.46	15.2	-15.29	-0.5994	1.454	15.2	-15.29
1.46	15.41	-15.5	-0.6076	1.454	15.41	-15.5
1.46	15.62	-15.71	-0.6158	1.453	15.62	-15.71
1.46	15.83	-15.92	-0.6241	1.453	15.83	-15.92
1.46	16.03	-16.13	-0.6323	1.453	16.03	-16.13
1.46	16.24	-16.34	-0.6405	1.453	16.24	-16.34
1.46	16.45	-16.55	-0.6487	1.453	16.45	-16.55
1.46	16.66	-16.76	-0.6569	1.453	16.66	-16.76
1.46	16.86	-16.97	-0.6651	1.453	16.86	-16.96
1.46	17.07	-17.18	-0.6733	1.453	17.07	-17.17
1.46	17.28	-17.38	-0.6816	1.453	17.28	-17.38
1.46	17.49	-17.59	-0.6898	1.453	17.48	-17.59
1.46	17.69	-17.8	-0.698	1.453	17.69	-17.8
1.46	17.9	-18.01	-0.7062	1.452	17.9	-18.01
1.46	18.11	-18.22	-0.7144	1.452	18.11	-18.22
1.46	18.31	-18.43	-0.7226	1.452	18.31	-18.43



1.46	18.52	-18.64	-0.7308	1.452	18.52	-18.64
1.46 0	18.73	-18.85	-0.7391	1.452	18.73	-18.85

Table B.2 Results of Localised Tooth Contact (Helicon Gear Side II)

u_1	θ_1	ϕ_1	ϕ_w	u_w	θ_w	ϕ_2
0.9059	-0.112	1.264e-5	0.00026	0.9021	-0.1063	0
0.9059	0.09577	-0.206	-0.00794	0.9023	0.1042	-0.209
0.9059	0.3067	-0.4156	-0.01616	0.9022	0.3151	-0.418
0.9059	0.5177	-0.625	-0.02437	0.9021	0.5262	-0.628
0.9059	0.7287	-0.8344	-0.03258	0.902	0.7373	-0.8378
0.9059	0.9398	-1.044	-0.04079	0.9019	0.9484	-1.047
0.9059	1.151	-1.253	-0.049	0.9018	1.16	-1.257
0.9059	1.362	-1.462	-0.05721	0.9017	1.371	-1.466
0.9059	1.573	-1.672	-0.06542	0.9016	1.582	-1.676
0.9059	1.785	-1.881	-0.07363	0.9015	1.794	-1.885
0.9059	1.996	-2.091	-0.08184	0.9015	2.005	-2.094
0.9059	2.208	-2.3	-0.09005	0.9014	2.217	-2.304
0.9059	2.419	-2.509-	-0.09826	0.9013	2.429	-2.513
0.9059	2.631	-2.719	-0.1065	0.9012	2.64	-2.723
0.9059	2.843	-2.928	-0.1147	0.9011	2.852	-2.932
0.9059	3.055	-3.137	-0.1229	0.901	3.064	-3.142
0.9059	3.267	-3.347	-0.1311	0.9009	3.277	-3.351
0.9059	3.479	-3.556	-0.1393	0.9008	3.489	-3.56
0.9059	3.692	-3.765	-0.1475	0.9007	3.701	-3.77
0.9059	3.904	-3.975	-0.1557	0.9007	3.914	-3.979
0.9059	4.117	-4.184	-0.1639	0.9006	4.127	-4.189

APPENDIX C NUMERICAL RESULTS OF LOCALISED TOOTH CONTACT OF A ZA WORM GEAR

Table C.1 Results of Localised Tooth Contact (ZA Gear)

u_1	θ_1	ϕ_1	ϕ_w	u_w	θ_w	ϕ_2
0.3241	-1.371	-0.003	-3.09e-5	0.324	-1.378	0
0.3288	-1.163	-0.2121	0.0034	0.3286	-1.169	-0.2094
0.3334	-0.9552	-0.4208	0.006	0.3333	-0.9599	-0.4189
0.338	-0.7471	-0.6296	0.0104	0.3379	-0.751	-0.6283
0.3427	-0.539	-0.8383	0.0139	0.3426	-0.5421	-0.8378
0.3473	-0.3308	-1.047	0.0174	0.3472	-0.3331	-1.047
0.352	-0.1226	-1.256	0.0209	0.3518	-0.1242	-1.257
0.3566	0.08558	-1.465	0.0244	0.3565	0.08479	-1.466
0.3612	0.2938	-1.673	0.0278	0.3611	0.2937	-1.676
0.3659	0.502	-1.882	0.03139	0.3658	0.5027	-1.885
0.3705	0.7102	-2.091	0.0348	0.3704	0.7117	-2.094
0.3751	0.9183	-2.3	.03837	0.3751	0.9206	-2.304
0.3798	1.127	-2.509	0.04186	0.3797	1.13	-2.513
0.3844	1.335	-2.717	0.04535	0.3843	1.339	-2.723
0.389	1.543	-2.926	0.04884	0.389	1.548	-2.932
0.3937	1.751	-3.135	0.05233	0.3936	1.756	-3.142
0.3983	1.96	-3.344	0.05582	0.3982	1.965	-3.351
0.4029	2.168	-3.553	0.05931	0.4029	2.174	-3.56
0.4075	2.376	-3.762	0.0628	0.4075	2.383	-3.77
0.4122	2.584	-3.97	.06629	0.4121	2.592	-3.979
0.4168	2.793	-4.179	0.06978	0.4168	2.801	-4.189
0.4214	3.001	-4.388	0.07327	0.4214	3.01	-4.398
0.4257	3.208	-4.597	0.07676	0.4257	3.218	-4.608
0.43	3.415	-4.806	0.08025	0.43	3.426	-4.817
0.4343	3.622	-5.015	0.08374	0.4343	3.634	-5.027
0.44	3.834	-5.224	0.08723	0.44	3.846	-5.236



0.4458	4.046	-5.432	0.09072	0.4458	4.059	-5.445
0.4493	4.251	-5.641	0.09422	0.4493	4.264	-5.655
0.4529	4.456	-5.85	0.09771	0.4529	4.47	-5.864
0.4585	4.668	-6.059	0.1012	0.4586	4.682	-6.074
0.4643	4.88	-6.268	0.1047	0.4643	4.895	-6.283
0.4678	5.084	-6.477	0.1082	0.4679	5.1	-6.493
0.4714	5.289	-6.686	0.1117	0.4715	5.306	-6.702
0.477	5.501	-6.895	0.1152	0.4771	5.519	-6.912
0.4828	5.713	-7.103	0.1186	0.4829	5.731	-7.121
0.4863	5.918	-7.313	0.1221	0.4864	5.937	-7.33
0.4899	6.123	-7.522	0.1256	0.4901	6.142	-7.54
0.4956	6.335	-7.73	0.1291	0.4957	6.355	-7.749
0.5013	6.547	-7.939	0.1326	0.5015	6.567	-7.959
0.5048	6.752	-8.148	0.1361	0.505	6.773	-8.168
0.5084	6.957	-8.357	0.1396	0.5086	6.978	-8.378
0.5141	7.169	-8.566	0.1431	0.5143	7.191	-8.587
0.5198	7.381	-8.775	0.1466	0.52	7.404	-8.796
0.5233	7.586	-8.984	0.1501	0.5236	7.609	-9.006
0.5269	7.79	-9.193	0.1536	0.5272	7.814	-9.215
0.5326	8.002	-9.402	0.157	0.5328	8.027	-9.425
0.5383	8.214	-9.611	0.1605	0.5386	8.24	-9.634
0.5418	8.419	-9.82	0.164	0.5421	8.445	-9.844
0.5455	8.624	-10.03	0.1675	0.5458	8.65	-10.05
0.5511	8.836	-10.24	0.171	0.5514	8.863	-10.26
0.5568	9.048	-10.45	0.1745	0.5571	9.076	-10.47
0.5603	9.253	-10.66	0.178	0.5607	9.281	-10.68
0.564	9.458	-10.86	0.1815	0.5643	9.487	-10.89
0.5696	9.67	-11.07	0.185	0.57	9.699	-11.1
0.5753	9.882	-11.28	0.1885	0.5757	9.912	-11.31
0.5789	10.09	-11.49	0.1919	0.5793	10.12	-11.52
0.5825	10.29	-11.7	0.1954	0.5829	10.32	-11.73
0.5881	10.5	-11.91	0.1989	0.5886	10.54	-11.94



0.5938	10.72	-12.12	0.2024	0.5943	10.75	-12.15
0.5974	10.92	-12.33	0.2059	0.5978	10.95	-12.36
0.601	11.13	-12.54	0.2094	0.6015	11.16	-12.57

APPENDIX D HOLROYD WORM GEAR SET II DATA AND 3D MODELS

Design Data of Worm Gear Set II

Holroyd worm gear set II design data are listed in Table D.1 to Table D.4.

Table D.1 Worm gear set II reference information

Threads	1
Teeth	50
Centres	125.0000 mm
Hand	Right
Lead Form	Single
Design	Inv. Hel.
Backlash	0.102 mm
Quotient	9.1365
Module	4.2950
Normal Pressure Angle	22.5
Wheel Oversize	1.27 mm
Wheel Cutter Type	Fly

Table D.1 Worm II and IIs Dimensions (length units: mm)

	WORM II	**WORM IIs**
Axial Pitch	13.4931	13.4931
Lead	13.4931	13.4931
Base Diameter	9.9693	9.9693
Pitch Diameter	39.2413	39.2413
Root Diameter	29.045	29.045
Outside Diameter	47.831	47.831

Case Depth	1.1430	
Roughing Allowance	0.0000	
Grinding Allowance	0.3048	
Normal Pitch	13.4130	13.4130
Lead Angle	6° 15′	6° 14′ 46″
Base Lead Angle	23° 18′	23° 18′ 27″
Tooth Height	9.393	
Clearance	0.8539	
Calliper Depth	3.106	
Calliper Thickness	6.047(Milled)	
Calliper Thickness	-(Ground)	
Calliper Thickness	5.742(Finished)	

Table D.2 Wheel cutter II and IIa setting (length units: mm)

	WHEEL CUTTER II	**WHEEL CUTTER IIs**
Machine Set Up	Fly	Fly
Axial Pitch	13.4882	13.4882
Lead	13.4882	13.4882
Base Diameter	9.9892	9.9892
Root Diameter	32.023	30.310
Outside Diameter	50.809	50.809
Cutting Centres	125.6350	127.590
Threads	1	1
Normal Pitch	13.4130	13.4130
Lead Angle	6° 3′	6° 3′
Base Lead Angle	23° 15′	23° 15′
Calliper Depth	3.960	3.960
Calliper Thickness	5.844	5.844
Tilt Angle	0° 12′	0° 12′

Table D.3 Wheel II dimensions (length units: mm)

	WHEEL II	WHEEL IIs
Face width	27.3487	27.3487
Outside Diameter	220.9647	227.533
Pitch Diameter	214.7500	
Root Diameter	200.4609	204.4522
Max Shrunk Bore	183.7505	
Max Bolted Bore	187.6524	
Throat Diameter	219.2467	219.2467
Throat Radius	15.3766	15.3766

In Table D.2 to D.4, worm gear IIs stand for the standard design of worm gear in same gear ratio designation. Comparison the Holroyd design with the standard design, we can set Holroyd worm gear set II is nearly a standard design. The lead angle is only 14 second difference which is very small. Holroyd wheel's outside diameter has 6.5 mm smaller and the root diameter 4mm smaller than that in standard calculation. There are two items has little change in wheel dimension: root diameter from 30.31 to 32.023, cutting centre from 127.590 to 125.635

The calculated worm centre distance is 126.99563 mm (125.00mm in Holroyd worm gear). The calculated worm minimum face width is 75.19 mm. In design it usually take 76 mm. It is the same as Holroyd design.

Axial Section Profile of Worm and Wheel Cutter

Figure D.1 and D.2 is the worm and wheel cutter's axial section profile. The method of obtaining the worm and wheel cutter's axial section profile is the same as Holyroyd worm gear set I.

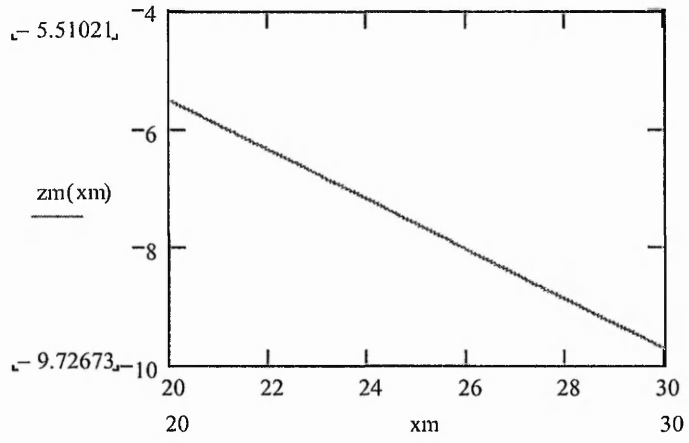


Figure D.1 Worm II axial section profile (mm)

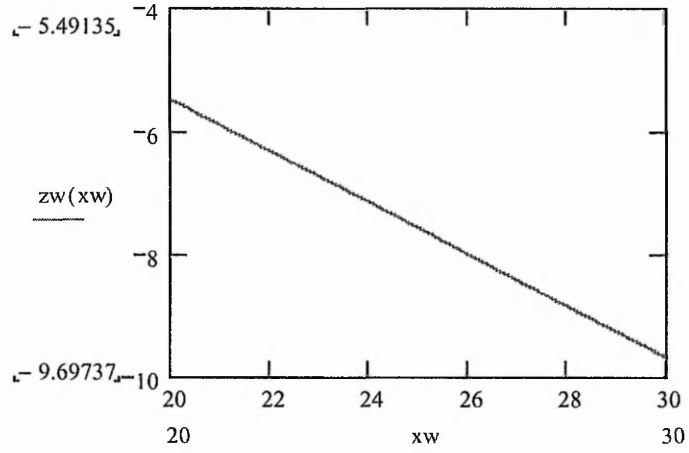


Figure D.2 Wheel cutter II tooth axial section profile (mm)

Figure D.3 and D.4 show the worm and wheel cutter's axial section profile that will be used to construct the 3D models of worm and wheel cutter. The tooth profile is obtained from Figure D.1 and D.2 and the tooth axial thickness is calculated from the calliper tooth thickness in the position of calliper depth.

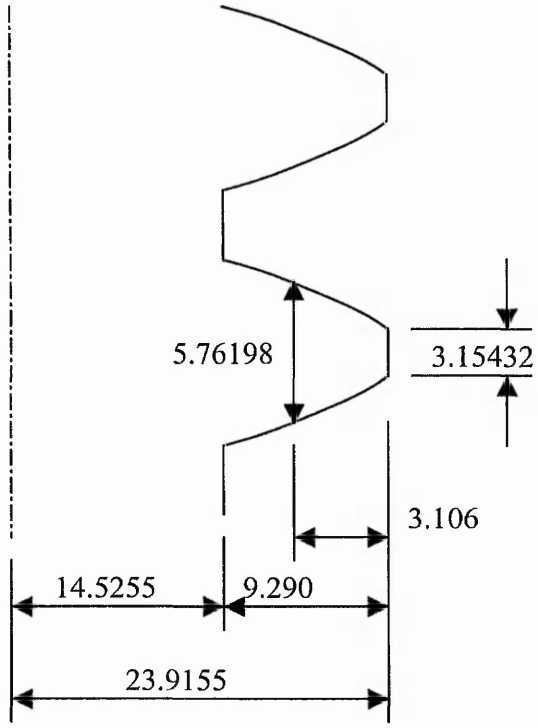


Figure D.3 Holroyd worm II tooth axial profile, pitch=13.4931 mm

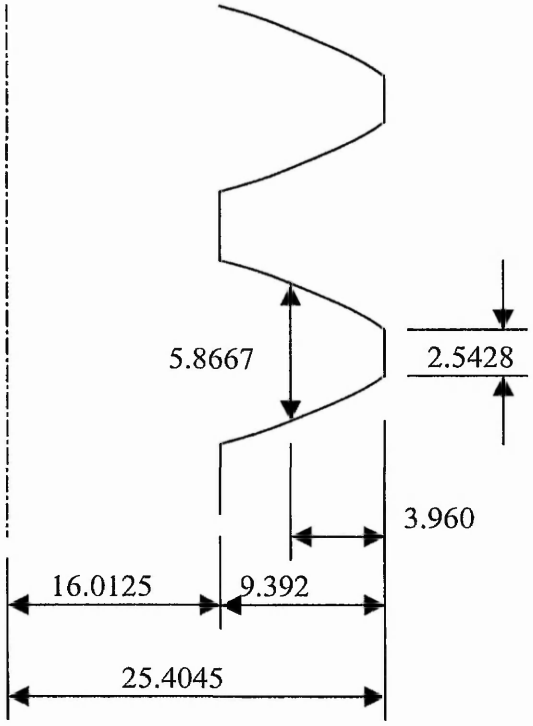


Figure D.4 Hob II axial tooth profile pitch=13.4882 mm

3D Models of Worm Gear II

The worm II is created in the same procedure as worm I. Its axial section is shown in Figure D.3. Figure D.5 showns the 3D model of worm II. The 3D model of gear II is shown in Figure D.6 and the gear assembly is shown in Figure D.7

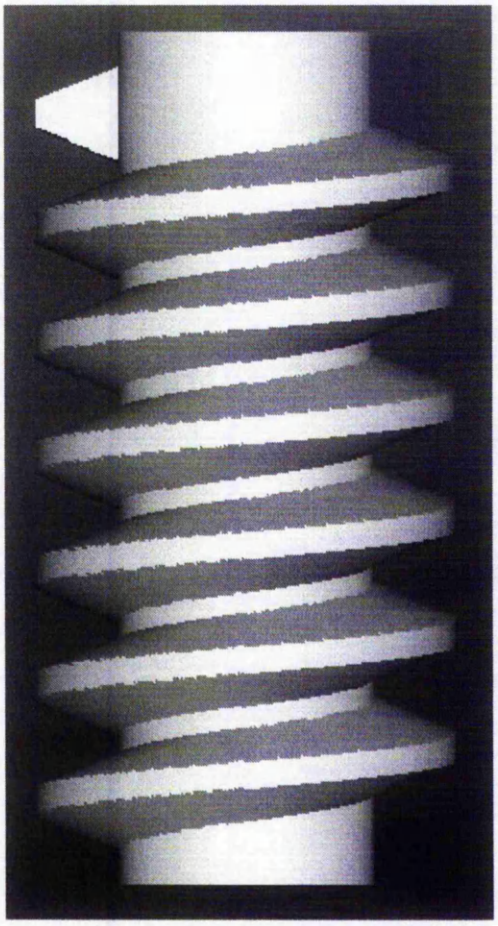


Figure D.5 3D model of worm II

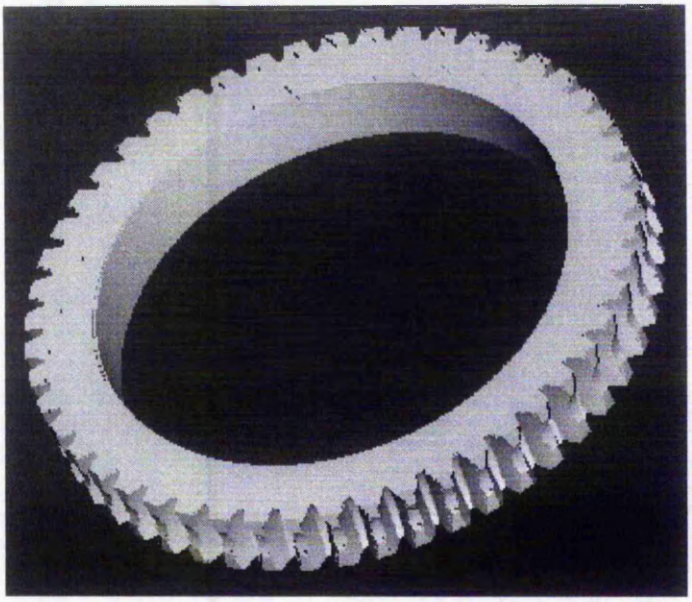


Figure D.6 3D model of gear II

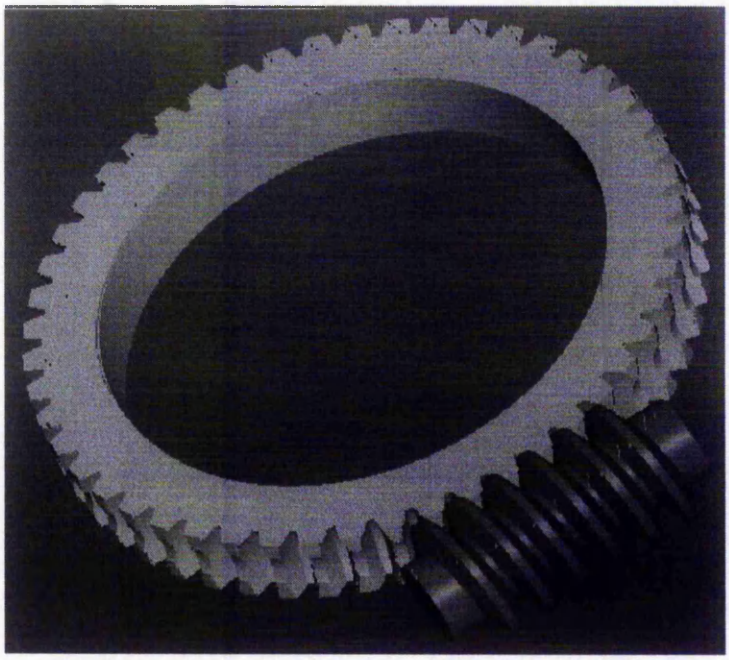


Figure D.7 Gear set II assembly

APPENDIX E WORM GEAR EXPERIMENT

E.1 Introduction

The objectives of the worm gear test were to obtain the gear tooth stress patterns under load and the comparison of efficiency between high reduction ratio gear and lower reduction ratio gears. The test specimens of worm gear were provided by Holroyd Gear Co. Ltd. The tests were carried out from 1 June 2001 in the State Key Laboratory of Mechanical and Transmission, Chonqing University, China. The experiment was conducted by Mr. Pen Cheliang, Wang Jian and Wang Lequan (Chongqing University) and were monitored by Mr. Yongle Song and Professor Daizhong Su (the Nottingham Trent University).

E.2 Test Specimens

There are two sets of worm gears for experiment. The first set has a lower reduction ratio 6/31 and the other set has higher reduction ratio 1/50. The two worm gear sets are all modified to obtain better contact and the methods of modifications are confidential of Holroyd. For the sake of convenience, the lower reduction worm gear is denoted as worm gear Ia and the higher reduction ratio worm gear IIa. The standard design of worm gear sets, which has the same designation with set Ia and IIa, are denoted as Ias and IIas respectively.

The worm is made of hardened steel and the wheel phosphor bronze. The mechanical properties of hardened steel is: E=213 GPa, Poisson ratio ν=0.285; the Young's modulus of the phosphor bronze is 88.3 Gpa and the Poisson's ratio is 0.35.

E.2.1 Worm gear Ia

The worm Ia is a right hand involute type worm and has six starts. The centre distance of gear set Ia is fixed to 125 mm. The module of the worm is 6.7564. Worm Ia cutting

depth is 8.5598mm (0.337 inch). The designation of worm gear Ia is T/t/q/m=6/31/6/6.7564. Table E.1 lists the design data of worm gear Ia. Table E.2 lists the dimension of worm Ia and the dimensions of the standard design calculated with the same designation. From the data it can be seen that the worm is a standard design. However, the wheel Ia is a modified design and its outside diameter and throat diameter is 3.7 mm and 3.8 mm smaller than that of the standard wheel respectively. The dimension data of the wheel Ia and Ias are listed in Table E.3. The parameters of wheel cutter Ia and Ias are listed in Table E.4. From the data it can be seen that the Holroyd wheel and wheel cutter have little difference from the standard design.

Table E.1 Worm gear set Ia designation T/t/q/m=6/31/6.00/6.7564

Threads	6
Teeth	31
Centres	125.0000 mm
Hand	Right
Lead Form	Single
Design	Inv. Hel.
Backlash	0.102 mm
Quotient	6
Module	6.7564 mm
NPA	22.5
Wheel Oversize	1.27 mm
Wheel Cutter Type	Fly

Table E.2 Worm Ia and Ias dimensions(units: mm)

	WORM Ia	**WORM Ias**
Axial Pitch	21.20138	21.22586
Lead	127.21141	127.35514
Base Diameter	34.94024	34.9788
Pitch Diameter		40.5384
Root Diameter		33.03022
Outside Diameter	54.000	54.0512



Case Depth		
Roughing Allowance		
Grinding Allowance		
Normal Pitch	14.99108	15.009
Lead Angle	45° 0′	45° 0′
Base Lead Angle	49° 12′ 36″	49° 12′ 36″
Tooth Height		10.51049
Clearance		0.9555
Calliper Depth	5.1054	5.1054
Calliper Thickness	8.3312 (Milled)	8.3312 (Milled)
Calliper Thickness	8.2042 (Ground)	8.2042 (Ground)
Calliper Thickness	7.8994 (Finished)	7.8994 (Finished)

Table E.3 Wheel Ia and Ias dimensions (mm)

	WHEEL Ia	**WHEEL Ias**
Face width	41.00	35.751
Outside Diameter	218.135	221.802
Pitch Diameter		209.4484
Root Diameter	194.102	194.0246
Max Shrunk Bore		
Max Bolted Bore		
Throat Diameter	211.24	215.0456
Throat Radius	19.38	19.38

Table E.4 Wheel cutter Ia and Ias (length units: mm)

	WHEEL CUTTER Ia	**WHEEL CUTTER Ias**
Machine Set Up	Fly	FLY
Axial Pitch		20.94567
Lead	125.67412	125.67412
Base Diameter	35.56	35.258

Root Diameter		33.331
Outside Diameter	54.508	54.327
Cutting Centres		123.838
Threads	6	6
Normal Pitch		
Lead Angle	44° 18′	44° 18′
Base Lead Angle	48° 22′	48° 22′
Calliper Depth	6.0706	6.0706
Calliper Thickness	8.001	8.001
Tilt Angle	0° 43′	0° 43′

Figure E.1 shows the Holroyd wheel with 6/31 gear ratio. The six-start right hand involute worm is shown in Figure E.2. Figure E.3 is the assembly of the worm and the wheel on the gearbox with the centre distance 125 mm.

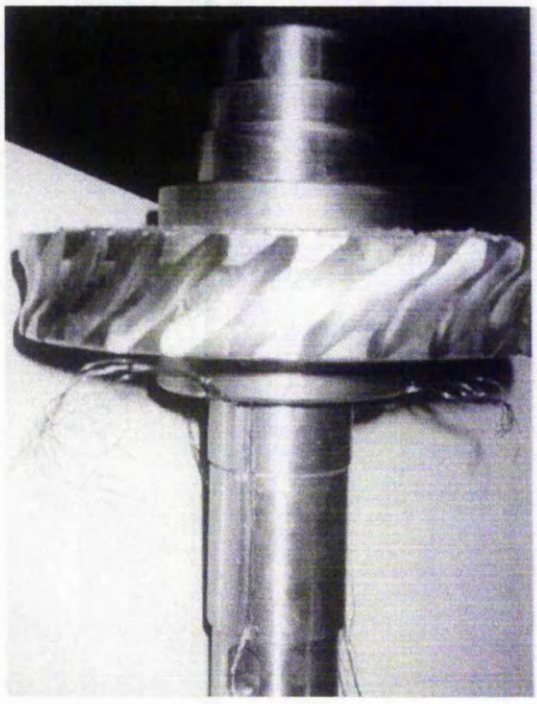


Figure E.1 Worm gear (6/31 ratio)

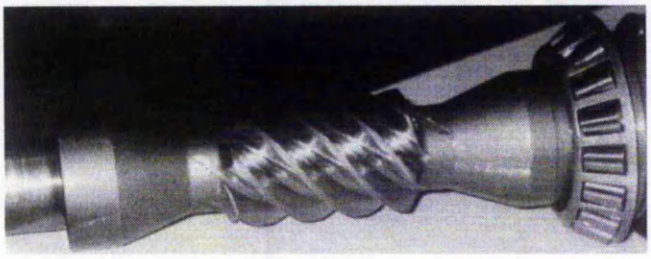


Figure E.2 Worm (6 starts)

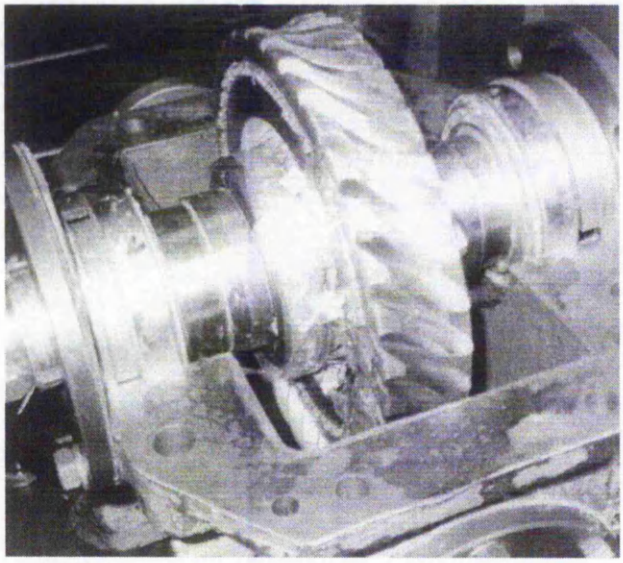


Figure E.3 Worm gear in gear box

E.2.1.1 Contact Observation

The photos of gear contact zone are not clear. It has to wait another film to be developed and posted to us by Mr. Peng.

E2.2 Worm gear IIa

The worm IIa is a right hand involute type worm and has single thread with a larger reduction ratio (see Figure E.4). The centre distance of gear set IIa is also fixed to 125 mm. The module of the worm is 4.1656. Worm IIa cutting depth is 8.5598mm (0.337

inch). The designation of worm gear IIa is T/t/q/m=1/50/10/4.1656. Table E.5 lists the design data of worm gear IIa. Table E.6 and Table E.7 lists the dimension of worm and wheel IIa and the dimensions of the worm gear standard design calculated with the same designation. From the data it can be seen that the worm gear IIa is a standard design. Figure E.5 shows the worm gear with gear ratio 1/50.

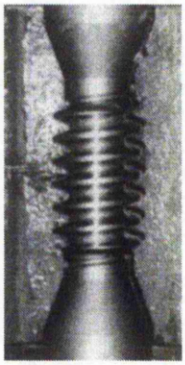


Figure E.4 Worm (1 start)

Table E.5 Worm gear set IIa designation T/t/q/m=1/50/10/4.1656

Threads	1
Teeth	50
Centres	125.0000 mm
Hand	Right
Lead Form	Single
Design	Inv. Hel.
Backlash	0.102 mm
Quotient	10
Module	4.1656 mm
NPA	22.5
Wheel Oversize	1.27 mm
Wheel Cutter Type	Fly

Table E.6 Worm IIa and IIas dimensions(units: mm)

	WORM IIa	WORM IIas
Axial Pitch	13.0861	13.0866
Lead	13.0869	13.0866
Base Diameter	9.73074	9.7299
Pitch Diameter		41.656
Root Diameter		31.74592
Outside Diameter	49.9872	49.9872
Case Depth		
Roughing Allowance		
Grinding Allowance		
Normal Pitch	13.0226	13.02167
Lead Angle	5° 42′ 38″	5° 42′ 38″
Base Lead Angle	23° 10′ 36″	23° 10′ 36″
Tooth Height	9.1186	9.11884
Clearance		0.82899
Calliper Depth	3.0226	3.0226
Calliper Thickness	5.8674(Milled)	5.8674(Milled)
Calliper Thickness	-(Ground)	-(Ground)
Calliper Thickness	5.5626 (Finished)	5.5626 (Finished)

Table E.7 Wheel IIa and IIas dimensions (mm)

	WHEEL IIa	WHEEL IIas
Face Width		27.631
Outside Diameter	218.26/218.01	220.69411
Pitch Diameter		208.28
Root Diameter	198.356	198.2908
Max Shrunk Bore		
Max Bolted Bore		
Throat Diameter	215.59	216.5285
Throat Radius	16.70	16.70

Table E.8 Wheel cutter IIa and IIas (length units: mm)

	WHEEL CUTTER IIa	WHEEL CUTTER IIas
Machine Set Up	Fly	Fly
Axial Pitch		13.08354
Lead	13.08354	13.08354
Base Diameter	9.74598	9.74682
Root Diameter		33.0794
Outside Diameter		51.3183
Cutting Centres	124.9934	127.5902
Threads	1	1
Normal Pitch	13.4130	13.4130
Lead Angle	5° 32′	5° 32′
Base Lead Angle	23° 8′	23° 8′
Calliper Depth	3.8354	3.8354
Calliper Thickness	5.6642	5.6642
Tilt Angle	0° 11′	0° 11′

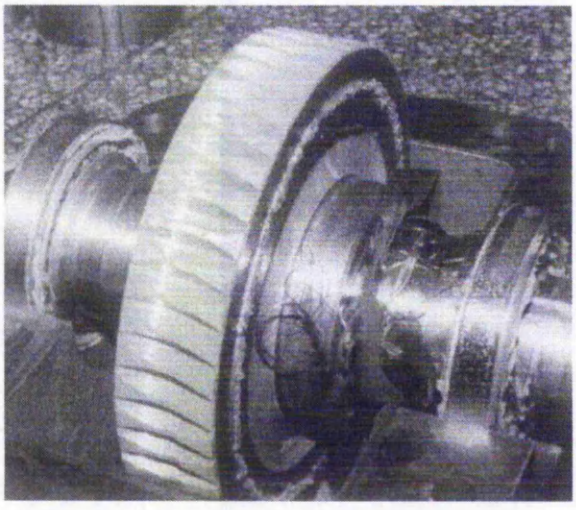


Figure E.5 Worm gear (1/50 ratio)

E2.2.1 Contact Observation

From the part of developed film, the contact region of the worm gear is recorded. Figure E.6 shows the trace of the wheel after the initial run-in without load. The wheel's contact region is almost the whole tooth surface. Obviously it is not a point contact and it is a line contact.

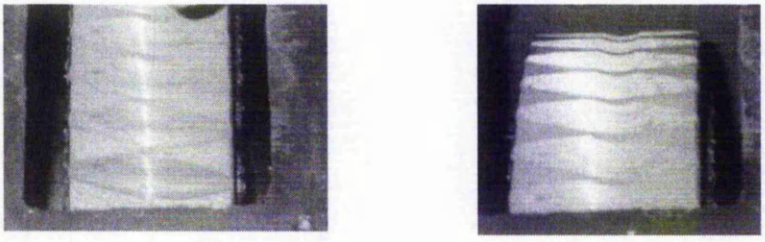


Figure E.6 Gear run in contact region

E.3 Static Strain Test

Worm gear tooth surface is a space curve surface. To determine the stress of one point on the gear tooth surface, three strain gauges are necessary. To measure the gear tooth stresses, the strain rosette scheme was planned first. Rectangular strain rosette (see Figure E.7) was going to be used in the scheme. According to our finite element analysis, there will be three teeth in simultaneously contact in most time. In order to simulate the worm gear operation, the test range should cover that the worm and the wheel rotate about each other with one tooth. The strain gauges will be placed on four continuous wheel teeth. The pace position is in the middle of gear tooth and in the root of the tooth (see Figure E.8).

However, The scheme of using strain rosette met problem that the available strain rosette is too large for the wheel tooth. There is very small room and backlash in the worm gear. So an alternative plan is used. The single strain gauges are used. Instead

of using 4 strain rosettes, 12 single strain gauges are used. There are four continuously strain gauges are in 0 degree, then four in 90 degree and four in 45 degree. The size of the smallest strain gauge available is 0.3x1.2 mm. The trail installation of worm gear revealed that such small strain gauge may be placed in the root of gear tooth. However, when the strain gauges are placed, the difficulty comes. First we faced how to insulate the gauge wires. Stick tapes were suggested and used but the working was really hard. We worked as careful as possible in placing the strain gauges. 12 gauges took us a whole day. The test results showed that such placement were not ideal that once the worm gear were engaged in the tooth with strain gauge, the signal of the strain gauges were suddenly jumped and then disappeared. This phenomenon repeated until all the gauge teeth were engaged. Dismounted the worm gear and we found that the insulate tapes were all moved and the gauges were pressed and damaged by the worm teeth.

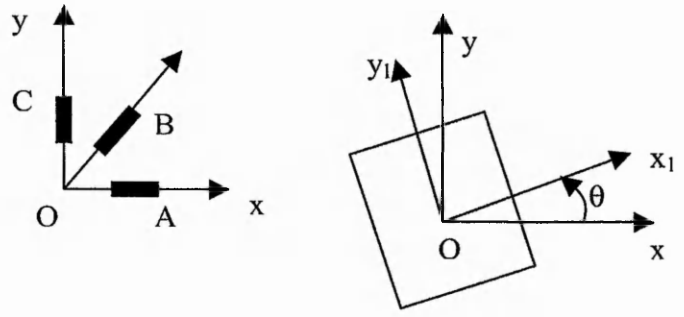


Figure E.7 Rectangular strain rosette (45 in degree)

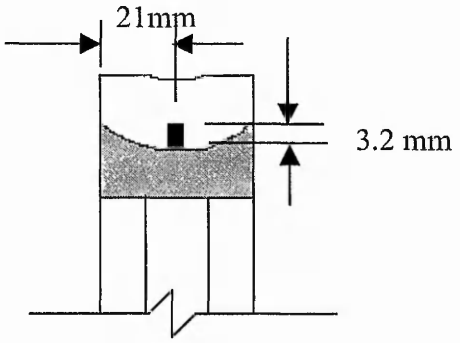


Figure E.8 Diagram of strain gauge position

Because there is so small room for placing the strain gauge in the worm gear, we had to consider other method. A wide consultation about how to do the worm gear strain test had been done. There are mainly two suggestions. The first one is to remove some part of the wheel tooth surface so that there will be room available for strain gauges. However, this method has problem in quality control and also will damage the wheel geometry. Remove a little bit does not solve the problem but if remove a lot will weaken the tooth stiffness and therefore affect the final results. The second suggestion is to place the strain gauges in the end of the gear tooth (see Figure E.9). This method is good for spur gear since it can be simplified 2D problem. However, for worm gear, this method has obviously problem because the worm gear have a twisted tooth (see Figure E.3) and the tooth ends have little strains if the contact was happen in other part of tooth. But without any other methods available, we tried the second suggestion because we thought we better do something rather than do nothing and go back with an empty hand.

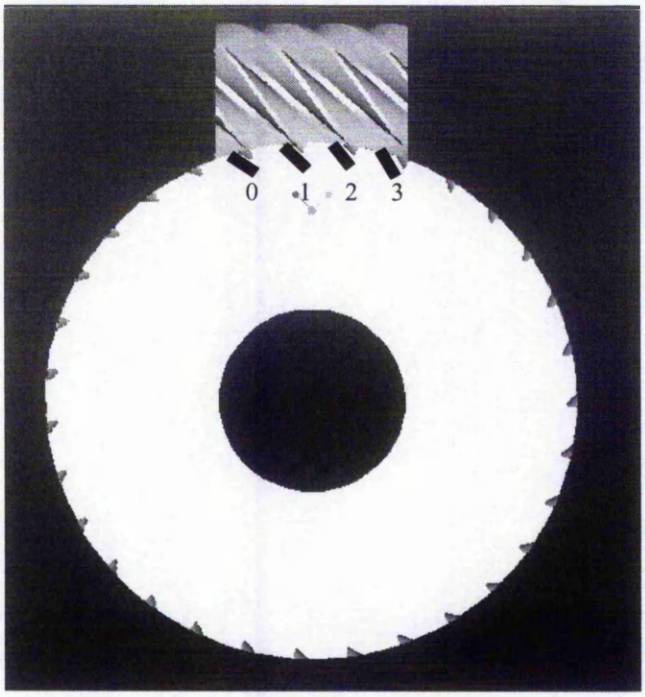


Figure E.9 Single Strain Gauge Scheme

E.3.1 Test Rig Set Up

The static strain test rig was set up as shown in Figure E.10. There are six tested positions for each gear test which covers the one gear teeth mesh over one worm tooth so that the whole gear operation range can be simulated. The load is applied on the gear and the worm is fixed.

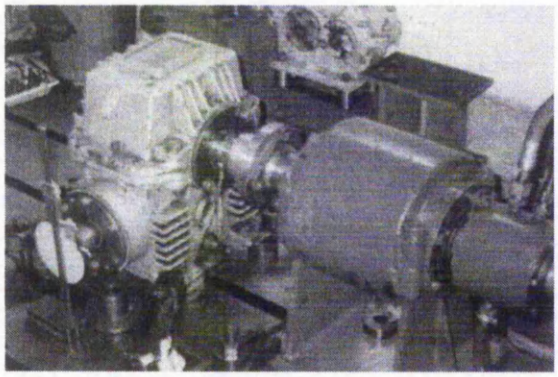


Figure E.10 Strain Test Rig

E.3.2 Test Results and Analysis

The strains of the gear tests are very small and in some load steps even no changes at all or even smaller when the load is added. This is because the strains are very small on the tooth ends and the tolerance errors of the strain instruments may be even bigger than the reading. So the strain results are useless. However, we listed the results below. Table and Table listed the test results of 6/31 ratio worm gear. Table and Table listed the test results of worm gear with 1/50 gear ratio. The number 3 strain gauge doesn't work during test. The initial value cannot be balanced and the reading is very unstable.

Table E.9 Strain Gauge Readings

Time: 12/6/01	Gear ratio 31/6	position 1



loading (unit) / Gauge no.	0	10	20	30	40	50
0	60	62	58	62	59	60
1	59	58	55	54	49	44
2	59	57	53	52	53	55
3						
4	76	64	49	36	18	4
5	61	47	28	11	-10	-30
6	26	21	21	30	45	60
7	61	61	92	90	87	55
Note: one unit loading equals to 24.30NM torque						

Table E.10 Strain Gauge Readings

Time: 12/6/01	Gear ratio 31/6				position 2	
loading (unit) / Gauge no.	0	10	20	30	40	50
0	-29	-26	-24	-24	-23	-20
1	-20	-22	-23	-25	-29	-32
2	-20	-18	-18	-14	-8	6
3						
4	-20	-35	-44	-54	-68	-82
5	-24	-41	-52	-67	-83	-102
6	-34	-38	-41	-30	-17	0
7	-6	1	14	41	52	45
Note: one unit loading equals to 24.30NM torque						

Table E.11 Strain Gauge Readings

Time: 12/6/01	Gear ratio 31/6				position 3	
loading (unit) / Gauge no.	0	10	20	30	40	50



0	5	1	1	2	1	2
1	2	2	-4	-7	-12	-17
2	22	-2	30	41	64	97
3						
4	2	-4	-18	-30	-48	-58
5	12	10	5	-12	-31	-53
6	8	13	20	38	46	55
7	-23	-7	18	41	57	58
Note: one unit loading equals to 24.30NM torque						

Table E.12 Strain Gauge Readings

Time: 12/6/01	Gear ratio 31/6				position 4	
loading (unit) / Gauge no.	0	10	20	30	40	50
0	18	17	15	14	14	13
1	13	11	6	2	-3	-7
2	70	73	83	109	152	240
3						
4	18	11	-1	-15	-32	-49
5	29	29	21	1	-19	-41
6	24	30	51	68	64	44
7	-26	-18	6	24	44	58
Note: one unit loading equals to 24.30NM torque						

Table E.13 Strain Gauge Readings

Time: 12/6/01	Gear ratio 31/6				position 5	
loading (unit) / Gauge no.	0	10	20	30	40	50
0	26	24	22	19	18	17
1	19	17	12	7	1	-5
2	158	160	169	201	254	340

3						
4	27	14	4	-11	-27	-41
5	38	40	31	10	-10	-32
6	30	39	60	39	1	-52
7	-24	-13	5	29	44	55
Note: one unit loading equals to 24.30NM torque						

Table E.14 Strain Gauge Readings

Time: 12/6/01	Gear ratio 31/6				position 6	
loading (unit) / Gauge no.	0	10	20	30	40	50
0	29	28	23	20	18	15
1	23	29	19	15	7	1
2	257	259	259	261	265	266
3						
4	48	24	11	-10	-29	-45
5	29	36	39	25	17	11
6	-29	-18	-1	-80	-132	-193
7	61	61	-2	18	30	42
Note: one unit loading equals to 24.30NM torque						

The number 6 strain gauge doesn't work during test. The initial value cannot be balanced and the reading is very unstable.

Table E.15 Strain Gauge Readings

Time: 12/6/01	Gear ratio 50/1				position 1	
loading (unit) / Gauge no.	0	10	20	30	40	50
0	-8	60	51	29	16	-12
1	-7	73	87	114	137	168
2	-8	72	85	111	133	163

3	-7	71	85	108	132	163
4	-7	65	79	101	123	150
5	-6	68	84	107	129	157
6						
7	-4	38	61	84	109	137
Note: one unit loading equals to 24.30NM torque						

Table E.16 Strain Gauge Readings

Time: 12/6/01	Gear ratio 50/1				position 2	
loading (unit) / Gauge no.	0	10	20	30	40	50
0	17	30	43	27	13	-3
1	10	30	55	67	73	81
2	30	47	76	88	106	118
3	35	53	70	99	118	132
4	34	50	67	90	108	121
5	30	46	62	81	98	110
6						
7	27	42	67	88	107	120
Note: one unit loading equals to 24.30NM torque						

Table E.17 Strain Gauge Readings

Time: 12/6/01	Gear ratio 50/1				position 3	
loading (unit) / Gauge no.	0	10	20	30	40	50
0	3	-21	-49	-72	-91	-101
1	20	18	18	19	13	5
2	36	49	61	77	91	107
3	45	54	71	91	108	129
4	44	58	73	92	107	124
5	41	52	63	77	91	104



6						
7	-42	53	70	88	104	121
Note: one unit loading equals to 24.30NM torque						

Table E.18 Strain Gauge Readings

Time: 12/6/01	Gear ratio 50/1				position 4	
loading (unit) / Gauge no.	0	10	20	30	40	50
0	-40	-45	-71	-105	-130	-149
1	23	12	1	6	4	-7
2	50	59	68	85	97	108
3	69	82	93	115	123	142
4	63	74	86	107	122	135
5	55	65	76	91	102	112
6						
7	61	64	79	97	113	127
Note: one unit loading equals to 24.30NM torque						

Table E.19 Strain Gauge Readings

Time: 12/6/01	Gear ratio 50/1				position 5	
loading (unit) / Gauge no.	0	10	20	30	40	50
0	-39	-52	-83	-111	-146	-171
1	20	12	2	8	13	17
2	57	60	98	80	97	106
3	80	85	90	114	133	146
4	71	77	80	106	126	137
5	65	70	79	90	105	113
6	30					
7	71	74	88	102	121	133
Note: one unit loading equals to 24.30NM torque						



Table E.20 Strain Gauge Readings

Time: 12/6/01	Gear ratio 50/1				position 6	
loading (unit) / Gauge no.	0	10	20	30	40	50
0	-55	-63	-88	-111	-138	-165
1	28	24	23	30	32	33
2	59	64	71	82	91	101
3	85	90	102	115	129	140
4	74	80	93	107	120	132
5	68	74	84	92	102	110
6						
7	76	80	94	107	119	130
Note: one unit loading equals to 24.30NM torque						

E.3.3 Future Strain Test

Since there is little room in worm gear for placing strain gauges, normal test methods cannot obtain the tooth strains. The more sophistic method-photoelastic method is suggested for the future stress test.

E.4 Test of Worm Gear Efficiency

E.4.1 Test Rig Set Up

The diagram of worm gear efficiency test is shown in Figure E.11. The DC Input Motor rotates the Torque and Rotational Speed Sensor. The power and rotational speed of the DC Input Motor is controlled by a DC Speed Control Instrument. The Torque and Rotational Speed Sensor is connected to the computer to take the readings. An oil temperature sensor is placed in the lubrication oil and connected to

the Temperature Display. The lubrication oil for worm gear is not available so that the oil for spur is used in the test. Figure E.12 shows the pictures of the worm gear test rig set up.

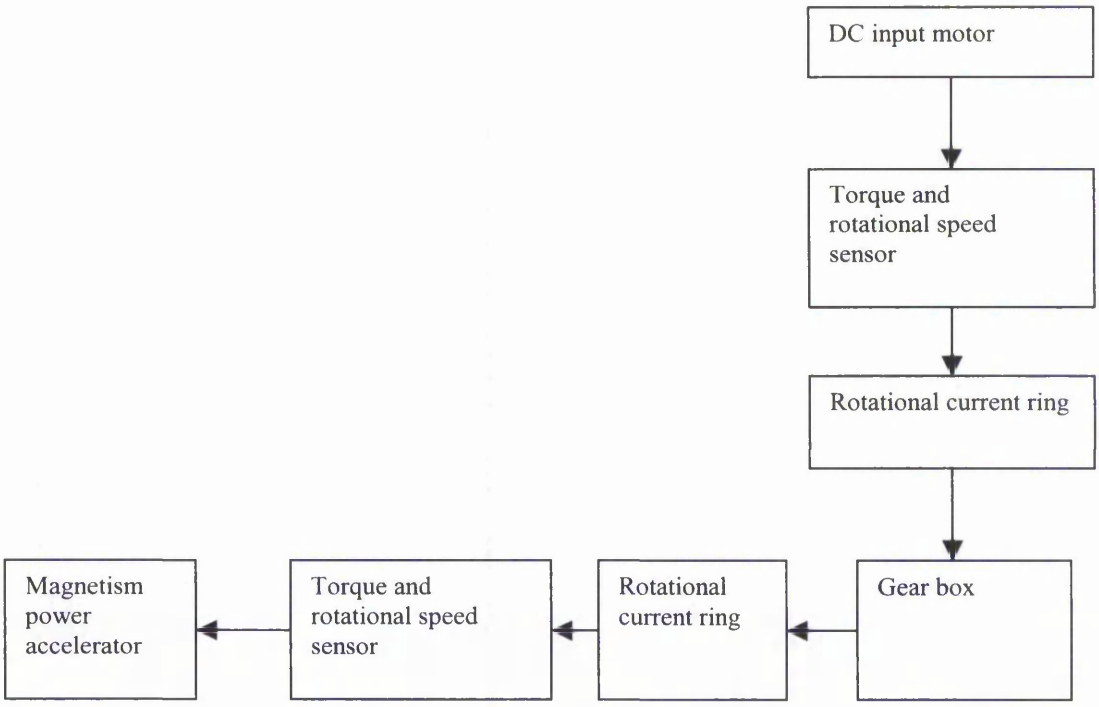
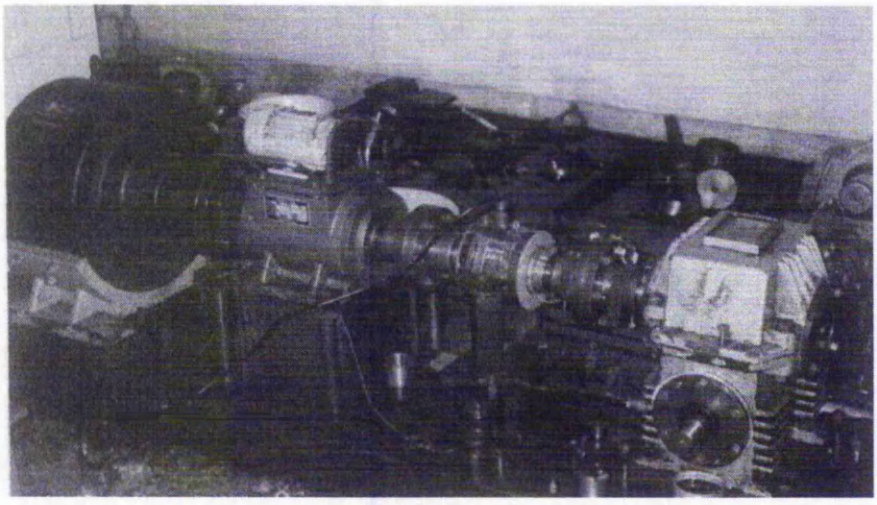
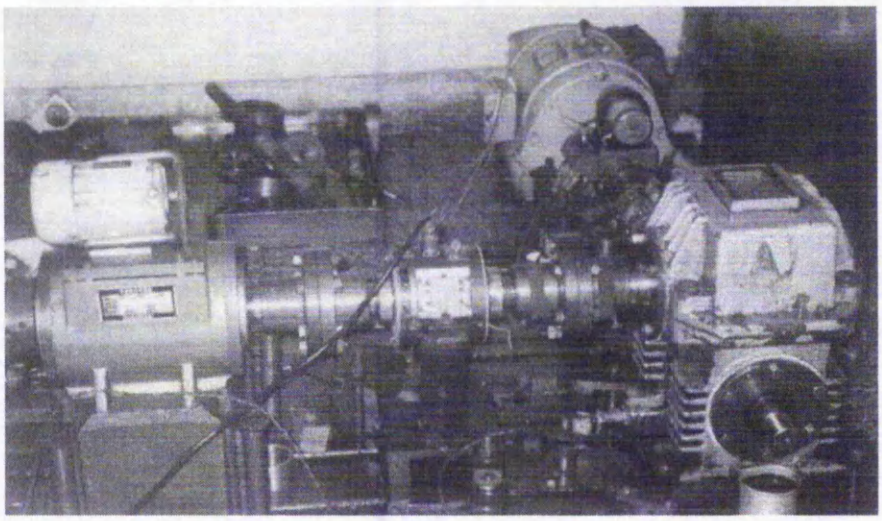


Figure E.11 Diagram of Test rig set up



(a)



(b)

Figure E.12 Test Rig of Worm Gear Efficiency

The gear tooth temperatures are measured by thermocouple which is bedded into a small hole drilled on the top of gear tooth as shown in Figure E.13. The distance of thermocouple to gear tooth surface is 2 mm. The distance of thermocouple to the gear tooth end is 80 mm.

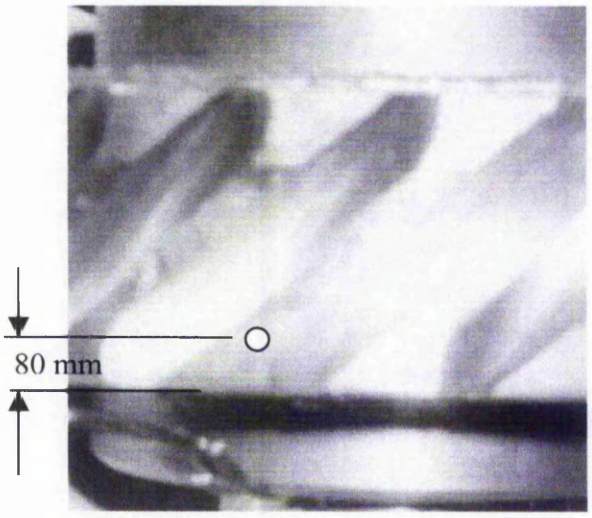


Figure E.12 Diagram of thermocouple position

E.4.2 Test Scheme

Six rotational speed steps and six powers steps are planned for the efficiency test as shown in Table E.21.

Table E.21 Loading Scheme for Efficiency Test

Maximum allowed input torque: 20 NM
Maximum allowed electric current: 20A
Rotational speed: 1000 rpm, 1400 rpm, 1600 rpm, 1800 rpm, 2000 rpm, 2200 rpm
Power: 1.0, 1.2, 1.5, 1.8, 2.5, 3.0, 3.5KW

E.4.3 Oil Temperature Curves

The oil temperature was displayed on the Temperature Display and recorded at every 10 or 15 minutes interval. Here two tests have been done. Table E.22 listed the temperature and efficiency results of worm gear with 1/50 ratio at the input rotational speed 1000 rpm and power 1KW. The room temperature was around 30 degree Celsius. The whole running lasted 5 hours and then the oil temperature became stable. The temperature increased from 30°C to 80.4 °C. The efficiency was increasing from the beginning 46% to the final 58%. The more smooth the gear set running, the higher the efficiency it is.

Table E.22 Efficiency Readings

Efficiency Test: 50/1 worm gear			
Date: 23/6/01			
Room temperature:30 degree Celsius			
1000rpm	Power: 1KW		
No.	Oil temperature (°C).	Time (minutes)	Efficiency (%)
0	38.3	10	46
1	42.4	20	52
2	46.7	30	54



3	49.8	40	51
4	55.4	50	52
5	64.7	60	52
6	69.6	70	52.8
7	71	80	50.1
8	71.2	90	54
9	72.6	100	48
10	73.7	110	51
11	74.6	120	54
12	75.3	130	56
13	76	140	55.4
14	76.5	150	55.6
15	77.1	165	57
16	77.7	180	58
17	78.2	190	56.2
18	78.5	200	57.6
19	78.8	210	54
20	78.9	220	54
21	79.1	230	47
22	79.2	240	58
23	80.4	270	58
24	80.4	300	58

Table E.23 listed the temperature and efficiency results of worm gear with 1/50 ratio at the input rotational speed 1400 rpm and power 1KW. The room temperature was around 30 degree Celsius. The whole running lasted 3 hours and 45 minutes and then the oil temperature became stable. The temperature increased from 30°C to 76.7 °C. The efficiency was increasing from the beginning 50.7% to the final 57.6%.

Table E.23 Efficiency Readings

Efficiency Test: 50/1 worm gear			
Date: 24/6/01			
Room temperature:30 °C			
1400rpm	Power: 1KW		
No.	Oil temperature (°C).	Time (minutes)	Efficiency (%)
0	53.7	0	50.7

1	61.3	10	56
2	64.6	20	52
3	63.8	30	54
4	66.4	45	55
5	69.8	60	55
6	72.8	75	55.6
7	73	90	53.6
8	73.8	105	56
9	74.4	120	58
10	75	135	56.1
11	75.4	150	57
12	79.2	165	57
13	78.4	180	61.5
14	77.2	195	59.8
15	76.6	210	59.7
16	76.6	225	57.6

Figure E.13 and Figure E.14 are the oil temperature curve changed with the running times. Figure E.13 is the first run with the input shaft speed 1000 rpm and the input power is 1 KW. Figure E.14 is the second run with the input shaft speed 1400 rpm and the input power is 1 KW. The final temperature decreases when the input speed decreases when the input power is kept the same.

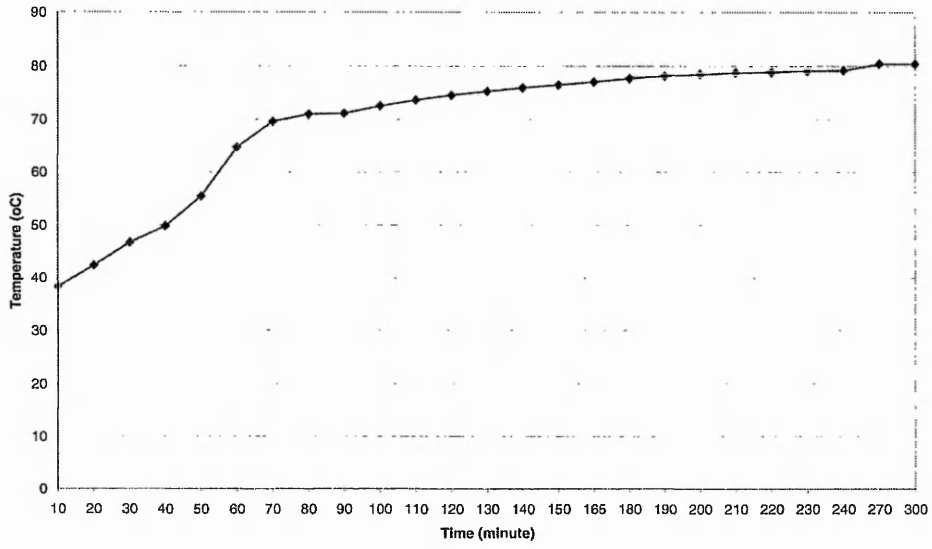


Figure E.13 Oil Temperature Rising during the Worm Gear Run-In (1000 rpm, 1 KW)

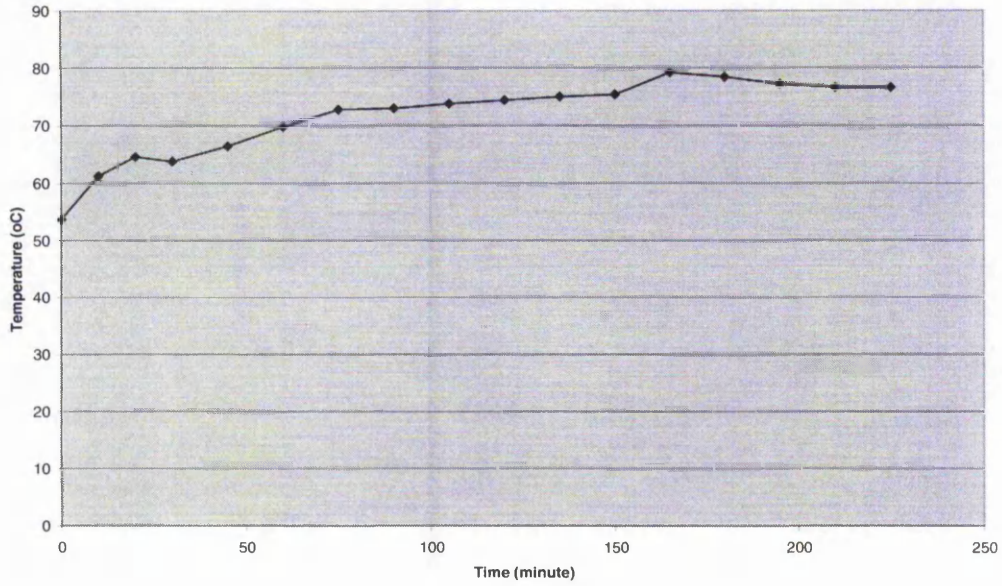


Figure E.14 Oil Temperature Rising during the Worm Gear Run-(1400 rpm, 1KW)

E.4.5 Efficiency Curves

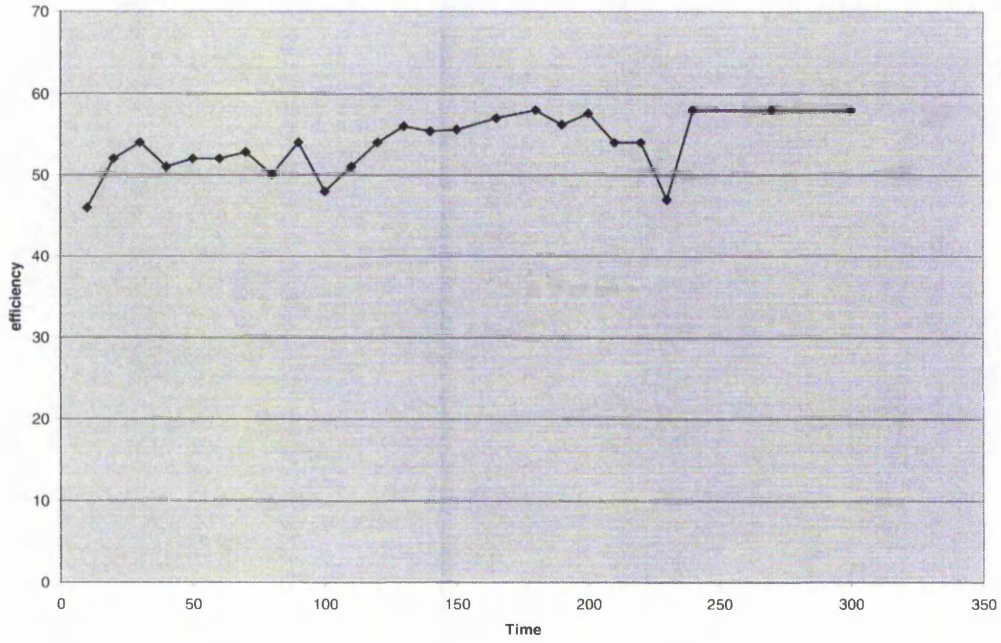


Figure E.15 Efficiency Change during the Worm Gear Run-(1000 rpm, 1KW)

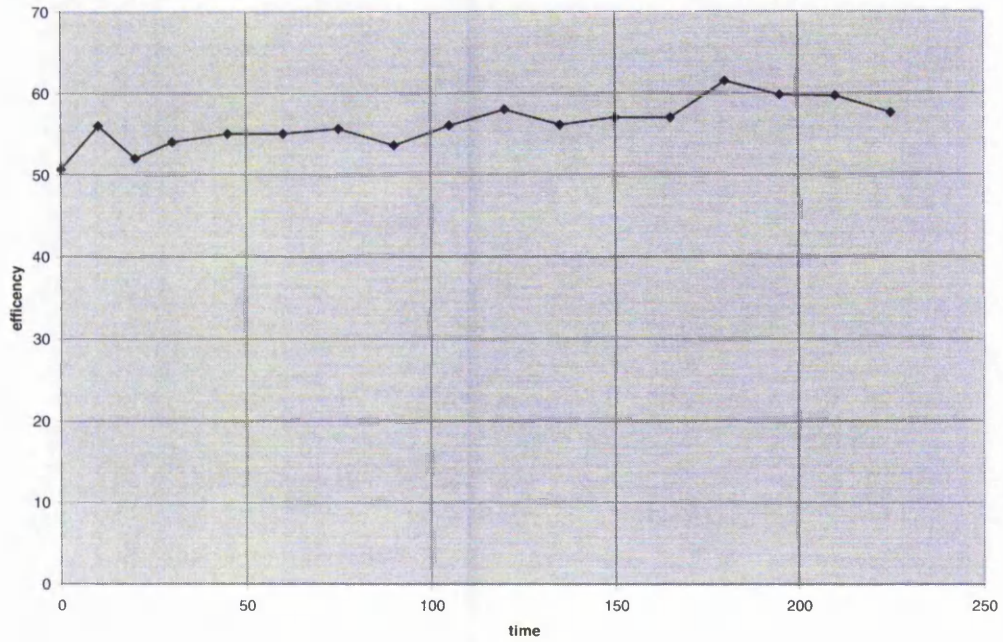


Figure E.16 Efficiency Change during the Worm gear Run-(1400 rpm, 1 KW)

The lubrication oil is the No. 200 common oil. Figure E.15 and Figure E.16 are the oil temperature curve changed with the running times. Figure E.15 is the first run with the input shaft speed 1000 rpm and the input power is 1 KW. Figure E.16 is the second run with the input shaft speed 1400 rpm and the input power is 1 KW. The final efficiency decreases when the input speed decreases when the input power is kept the same.

Table E.24 to E. 26 list the final wheel tooth temperature, lubrication oil temperatures and efficiency of the worm gear with gear ratio (1/50). Table E.27 to E. 29 list the final wheel tooth temperature, lubrication oil temperatures and efficiency of the worm gear with gear ratio (6/31).

Table E.24 Tooth Temperature (ratio 1/50)

	1.0KW	1.2KW	1.5KW	1.8KW
1000 rpm	92 °C			
1200 rpm	88 °C	92 °C		
1400 rpm	86 °C	97 °C	106 °C	

1600 rpm	91 °C	82 °C (fan cooled)	92 °C (fan cooled)	
1800 rpm	92 °C	85 °C (fan cooled)	92 °C (fan cooled)	

Table E.25 Efficiency (ratio 1/50)

	1.0KW	1.2KW	1.5KW	1.8KW
1000 rpm	63%			
1200 rpm	60%	61%		
1400 rpm	58.5%	63.5%	64%	
1600 rpm	60%	58% (fan cooled)	60% (fan cooled)	
1800 rpm	59.5%	60.5% (fan cooled)	60% (fan cooled)	64% (fan cooled)

Table E.26 Lubrication Oil Temperature (ratio 1/50)

	1.0KW	1.2KW	1.5KW	1.8KW
1000 rpm	78.8 °C			
1200 rpm	80.4 °C	84.3 °C		
1400 rpm	79.3 °C	83 °C	89.6 °C	
1600 rpm	75.4 °C	69 °C (fan cooled)	82 °C (fan cooled)	
1800 rpm	75.5 °C	60.5 °C (fan cooled)	73 °C (fan cooled)	81.1 °C (fan cooled)

Table E.27 Tooth Temperature (ratio 6/31)

	1.05 KW	1.35 KW	1.7 KW	2.0 KW
1050 rpm	66 °C	73.6 °C		
1250 rpm	68.7 °C	75.5 °C		
1450 rpm	70.2 °C	78.2 °C	80.4 °C	
1650 rpm	67.2 °C	73.1 °C	75 °C	78.9 °C

Note: the gearbox is cooled by fan.

Table E.28 Efficiency (ratio 6/31) (cooled by fan)

	1.05 KW	1.35 KW	1.7 KW	2.0 KW
1050 rpm	62.5%	69.5%		
1250 rpm	59%	68.5%		
1450 rpm	53%	62.5%	69%	
1650 rpm	51.5%	57.5%	64.5%	68%
Note: the gearbox is cooled by fan.				

Table E.29 Lubrication Oil Temperature (ratio 6/31)

	1.05 KW	1.35 KW	1.7 KW	2.0 KW
1050 rpm	52.5 °C	53.8 °C		
1250 rpm	58 °C	60.5 °C		
1450 rpm	61.2 °C	63.3 °C	64.6 °C	
1650 rpm	60.3 °C	61.2 °C	61.9 °C	63.1 °C
Note: the gearbox is cooled by fan.				

E.4.6 Conclusions

Using the conventional strain gauge method cannot obtain the worm gear tooth stresses due to its complicated geometry and running-in characteristics. There are too little room there for the strain gauge to place. When the worm gear run in, the strain gauges will be pressed and damaged. More advanced test method is needed such as photoelastic method.

The experimental results show that the higher the input power, the higher the efficiency. When the input power is constant, the efficiency of worm gear decreases when the input rotating speed increases. However, the tooth temperature and

lubrication oil temperature nearly remain constant when the rotating speed and input power changes. The lower reduction ratio worm gear (6/31) has higher output efficiency and lower tooth and lubrication oil temperatures than the higher reduction ratio worm gear (1/50) if the input shaft speed and power is the same.

APPENDIX F EXTENDED SUMMARIES OF SOME METHODS MENTIONED IN CHAPTER 2

F.1 Seol's Third Approach for Tooth Modification Using Oversized Hob

Seol et al (1996) also presented the third approach for localisation of bearing contact of worm gear tooth. In this approach, the oversized hob is designed as a conjugated one to the worm. This means that the hob and the worm thread surface have a common enveloping surface that is the surfaces of an imaginary rack simultaneously in mesh with the worm and the hob. The hob and the worm are again in internal tangency (Figure 2.5), and their axes are crossed. However, the types of the helicoid surfaces of the hob and the worm differ from each other.

The worm and the hob are considered as two helical gears that are simultaneously in mesh with two racks, c and t, that are provided with two coinciding cylindrical surfaces Σ_c and Σ_t (Figure 2.6). Surfaces Σ_c and Σ_t have the same normal section and they can slide one with respect to the other while being in mesh with the hob and the worm. It is assumed that surface Σ_c is in mesh with the hob thread surface Σ_h, and surface Σ_t is in mesh with the worm surface Σ_w.

Imagine that the hob and the worm perform rotational motions about their crossed axes. The shortest distance and the crossing angle between the axes are determined with the equations

$$\Delta r = r_{ph} - r_{pw} \tag{F.1.1}$$

$$\Delta\gamma = \lambda_{pw} - \lambda_{ph} \tag{F.1.2}$$

The two racks that are in simultaneous mesh with the hob and the worm perform related translation motions while the hob and the worm are rotated about their axes. The current displacement of both racks in the normal direction is the same. The



normal direction is considered in the plane Π that is tangent to the worm and hob pitch cylinders at point P.

A helical gear and the respective rack have an instantaneous axis of rotation P_i-P_i (i=1,2) that is the generatrix of the helical gear. There are two such instantaneous axes of rotation while the hob and the worm are in mesh with the two respective racks. These axes lie in plane Π and intersect each other at point P.

Considering the meshing of the hob and the worm gear being generated, it is recognised that the hob and the worm-gear are in line contact and there are two axes in meshing, I-I and II-II, that represents two crossed straight lines. Point P should belong to the axis of meshing II-II.

The conditions highlighted above are observed, then the surfaces of the worm and the generated worm-gear will be in point contact at every instant, that is, the contact is localised and the transmission function is a linear one with the prescribed gear ratio.

F.2 Seol et al's Another Approach for Klingelnberg and Flender Worm Gear

In 1996, Seol and Litvin presented another paper for the localisation of Involute, Klingelnberg and Flender type worm gears. Their approach aimed to reduce the sensitivity of worm gear drives to misalignment and the level of maximal transmission errors. In addition to the application of an oversized hob, a pre-designed parabolic function of transmission errors is applied in modification of worm gear drives. According to the authors, such a function is able to absorb misalignment that may cause high vibration. It was proposed to obtain the parabolic function of transmission errors by variation of the shortest distance between the hob and the worm gear during the process of generation.

The proposed approach is based on the generation of the worm gear by a hob of an increased diameter in comparison with the worm. The hob and the worm are in internal tangency as shown in Figure 2.5. Special conjugation of the hob and the



worm thread surfaces must be required. Though the hob and the worm gear are in line contact during the process of generation, the generated worm gear tooth surface and the worm are in point contact in the process of their meshing.

The above method can be illustrated as follows:

First, the tool cutter surfaces mesh with worm surface. The generated surface of the worm can be represented as the following equations:

$$\mathbf{r}_w(\theta, \nu, \psi) = \mathbf{M}_{wc}(\psi)\mathbf{r}_c(\theta, \nu) \tag{F.2.1}$$

$$\mathbf{N}_c \cdot \mathbf{v}_c^{(cw)} = f(\theta, \nu) = 0 \tag{F.2.2}$$

Where, $\mathbf{r}_c(\theta, \nu)$ is the vector function of the tool surface; ψ is the angle of rotation in the worm screw motion; $\mathbf{N}_c$ is the normal to the tool cutter surface; $\mathbf{v}_c^{(cw)}$ is the vector of relative velocity. Equation (F.1.2) is the equation of meshing and the necessary condition of envelope existence (Litvin, 1968, 1989, 1994a, Zalgaller, 1975). The subscript c in Equation (F.1.2) indicates that the vectors are represented in coordinate system S_c.

Second, design a hob surface that can generate the gear surfaces that are in point contact with the above worm. Design of such a hob is based on the following considerations: (i) The increase in pitch diameter of the hob in comparison with the worm permits localization of the bearing contact of worm-gear drives; (ii) The hob and the worm are considered as two helical gears in internal meshing; and (iii) The conjugation of the hob surfaces Σ_h and the worm surface Σ_w is provided if they are simultaneously in tangency with the surface Σ_r of an imaginary rack.

The design of the hob is based on the following procedures:



(i) The imaginary rack meshed with worm. Surface Σ_r is determined as the envelope to the family of surfaces Σ_w that is represented in S_r. The imaginary rack surface Σ_r thus can be determined as the following equations:

$$\mathbf{r}_r(\theta_w, \nu_w, \phi_w) = \mathbf{M}_{rw}(\phi_w)\mathbf{r}_w(\theta_w, \nu_w) \tag{F.2.3}$$

$$\mathbf{N}_w \cdot \mathbf{v}_w^{(rw)} = f_w(\theta_w, \nu_w, \phi_w) = 0 \tag{F.2.4}$$

(ii) Now the hob surfaces are in meshing with the imaginary rack surface. Therefore, by the theory of meshing, the hob surface Σ_h can be determined as the envelope to the family of imaginary rack surface. The hob surfaces are thus determined by the following equations

$$\mathbf{r}_h(\theta_r, \nu_r, \phi_h) = \mathbf{M}_{hr}(\phi_h)\mathbf{r}_r(\theta_r, \nu_r) \tag{F.2.5}$$

$$\mathbf{N}_r \cdot \mathbf{v}_r^{(rh)} = f_h(\theta_r, \nu_r, \phi_h) = 0 \tag{F.2.6}$$

Third, the above gear tooth surfaces are meshing with the hob surfaces. The gear surfaces are the envelope of the hob surfaces and are determined as follows

$$\mathbf{r}_g(\theta_h, \nu_h, \psi_h) = \mathbf{M}_{gh}(\psi_h)\mathbf{r}_h(\theta_h, \nu_h) \tag{F.2.7}$$

$$\mathbf{N}_h \cdot \mathbf{v}_h^{(gh)} = f_g(\theta_h, \nu_h, \psi_h) = 0 \tag{F.2.8}$$

Fourth, according to Seol and Litvin, the localised tooth contact meshing can be simulated by the following equations:

$$\mathbf{r}_f^{(1)}(u_1, \theta_1, \phi_1) - \mathbf{r}_f^{(2)}(u_2, \theta_2, \phi_2) = 0 \tag{F.2.9}$$

$$\mathbf{n}_f^{(1)}(u_1, \theta_1, \phi_1) - \mathbf{n}_f^{(2)}(u_2, \theta_2, \phi_2) = 0 \tag{F.2.10}$$

F.3 Tooth Contact Analysis

The tooth contact analysis can determine the following problems:

- Transmission errors caused by misalignment
- Paths of contact point on the gear tooth surfaces
- Bearing contact as a set of instantaneous contact ellipses.

The main idea of TCA is based on simulation of continuous tangency of gear tooth surfaces being in mesh. The continuous tangency of gear tooth surfaces indicates that at the current point of tangency the contacting surfaces have common position vectors $\mathbf{r}_f^{(i)}$ and surface unit normal $\mathbf{n}_f^{(i)}$, (i=1,2), i.e.

$$\mathbf{r}_f^{(1)}(u_1,\theta_1,\phi_1)-\mathbf{r}_f^{(2)}(u_2,\theta_2,\phi_2)=0 \tag{F.3.1}$$

$$\mathbf{n}_f^{(1)}(u_1,\theta_1,\phi_1)-\mathbf{n}_f^{(2)}(u_2,\theta_2,\phi_2)=0 \tag{F.3.2}$$

Where

$$\mathbf{r}_f^{(1)}=\mathbf{M}_{f1}\mathbf{r}_1 \tag{F.3.3}$$

$$\mathbf{n}_f^{(1)}=\mathbf{L}_{f1}\mathbf{n}_1 \tag{F.3.4}$$

$$\mathbf{r}_f^{(2)}=\mathbf{M}_{fq}\mathbf{M}_{q2}\mathbf{r}_2 \tag{F.3.5}$$

$$\mathbf{n}_f^{(2)}=\mathbf{L}_{fq}\mathbf{L}_{q2}\mathbf{n}_2 \tag{F.3.6}$$

The surface unit normal are obtained from the following equation,

$$\mathbf{n}_i = \frac{\dfrac{\partial \mathbf{r}_i}{\partial u_i} \times \dfrac{\partial \mathbf{r}_i}{\partial \theta_i}}{\left| \dfrac{\partial \mathbf{r}_i}{\partial u_i} \times \dfrac{\partial \mathbf{r}_i}{\partial \theta_i} \right|} \tag{F.3.7}$$

Vector Equations (F.3.1) and (F.3.2) yield five independent scalar equations with six unknowns, u_1, θ_1, ϕ_1, u_2, θ_2, ϕ_2 since $\left|\mathbf{n}_f^{(1)}\right| = \left|\mathbf{n}_f^{(2)}\right| = 1$. These equations are represented as

$$f_i(u_1, \theta_1, \phi_1, u_2, \theta_2, \phi_2) = 0 \qquad f_i \in C^1 \quad (\mathrm{i} = 1,2,3,4,5) \tag{F.3.8}$$

One of the unknowns, say ϕ_1, may be chosen as the input. Henceforth, Equations (F.3.2) are assumed to be satisfied at a point

$$P^0 = (u_1^0, \theta_1^0, \phi_1^0, u_2^0, \theta_2^0, \phi_2^0) \tag{F.3.9}$$

and the system Jocobian differs from zero. Thus,

$$\Delta_5 = \frac{D(f_1, f_2, f_3, f_4, f_5)}{D(u_1, \theta_1, u_2, \theta_2, \phi_2)} = \begin{vmatrix} \dfrac{\partial f_1}{\partial u_1} & \dfrac{\partial f_1}{\partial \theta_1} & \dfrac{\partial f_1}{\partial u_2} & \dfrac{\partial f_1}{\partial \theta_2} & \dfrac{\partial f_1}{\partial \phi_2} \\ \cdot & \cdot & \cdot & \cdot & \cdot \\ \cdot & \cdot & \cdot & \cdot & \cdot \\ \cdot & \cdot & \cdot & \cdot & \cdot \\ \dfrac{\partial f_5}{\partial u_1} & \dfrac{\partial f_5}{\partial \theta_1} & \dfrac{\partial f_5}{\partial u_2} & \dfrac{\partial f_5}{\partial \theta_2} & \dfrac{\partial f_5}{\partial \phi_2} \end{vmatrix} \neq 0 \tag{F.3.10}$$

According to theorem of implicit function systems existence (Korn and Korn, 1968, and Litvin, 1989b), Equation (F.3.2) can be solved in the neighbourhood of p^0 by functions,

$$\{u_1(\phi_1), \theta_1(\phi_1), u_2(\phi_1), \theta_2(\phi_1), \phi_2(\phi_1)\} \in C^1 \tag{F.3.11}$$

Functions (F.3.11) provide the complete information about the conditions of meshing of gears that are in point contact.



F.4 Gosselin's Formulae for Loaded Tooth Contact Analysis

Gosselin, et al (1995) presented a loaded tooth contact analysis method to predict the motion error of spiral bevel gear sets. In order to simplify the complexity of the problem, a few general assumptions were made:

- There is neither friction in the contact zone nor the presence of lubricant that can affect the distribution of the contact pressure, and create an oil film of varying thickness between meshing teeth
- Displacements due to tooth deflection, shearing or contact deformation are sufficiently small that the tooth surface normal at the contact point is not affected.
- The gear tooth surface coordinates, contact points along the path of contact, bearing pattern, tooth surface curvatures and principal directions and contact stresses are calculated from unloaded tooth contact analysis.
- Contact is assumed Hertzian and there are no boundary corrections made for edge contact. These can be changed to reflect different operating conditions and the path of contact and contact parameters are then recalculated accordingly.
- Tooth coupling effects are neglected, e.g. the movement of one tooth due to a load applied on an adjacent tooth, although such effects may alter load sharing.

The following two load sharing compatibility conditions were also applied:

- The pinion and the gear blank rotation caused by the displacement of any tooth under load must be the same for all simultaneously meshing tooth pairs (see Figure 2.11). This includes tooth bending deflection and shearing displacement, contact deformation and profile separation due to profile mismatch.
- The sum of the torque contribution of each meshing tooth pair must equal to the total applied torque.



According to the above compatibility conditions, the following equations were deduced:

$$\frac{[\delta\mathbf{B}_{i-1}+\Delta\mathbf{S}_{i-1}+\delta\mathbf{H}_{i-1}]_t}{|\mathbf{R}_{ci-1}|}=\frac{[\delta\mathbf{B}_i+\Delta\mathbf{S}_i+\delta\mathbf{H}_i]_t}{|\mathbf{R}_{ci}|}=\frac{[\delta\mathbf{B}_{i+1}+\Delta\mathbf{S}_{i+1}+\delta\mathbf{H}_{i+1}]_t}{|\mathbf{R}_{ci+1}|} \quad \text{(F.4.1)}$$

$$\mathbf{T}_{app}=\mathbf{T}_{i-1}+\mathbf{T}_i+\mathbf{T}_{i+1} \quad \text{(F.4.2)}$$

where subscript t indicates that the tangential direction is considered, e.g., normal to the transverse plane radius at the contact point (Figure 2.11).

$\delta\mathbf{B}_{i-1},\delta\mathbf{B}_i,\delta\mathbf{B}_{i+1}$: is the tooth displacement vector caused by bending and sharing for tooth pairs i-1, i and i+1 respectively; bending displacement is obtained by finite element analysis;

$\Delta\mathbf{S}_{i-1},\Delta\mathbf{S}_i,\Delta\mathbf{S}_{i+1}$: is the initial separation vector between tooth pairs i-1, i and i+1 respectively; Due to profile mismatch, the initial separation is obtained from the motion error curve, and is in the tangential direction (Figure 2.11);

$\delta\mathbf{H}_{i-1},\delta\mathbf{H}_i,\delta\mathbf{H}_{i+1}$: is contact deformation vector of tooth pairs i-1, i and i+1 respectively; contact is assumed to be hertizian.

$\mathbf{R}_{ci-1},\mathbf{R}_{ci},\mathbf{R}_{ci+1}$: is transverse plane contact radius vector on the pinion tooth;

$\mathbf{T}_{i-1},\mathbf{T}_i,\mathbf{T}_{i+1}$: is the individual vectorial contribution to total applied torque;

$\mathbf{T}_{app}$: is the total applied torque vector

The individual torque vectors are defined by the following cross product:

$$\mathbf{T}_j=\mathbf{R}_{cj}\times\mathbf{F}_j \quad \text{(F.4.3)}$$

where j varies from i-1, to i+1.